CONTENTS (CONTINUED)

TECHNICAL NOTES

DISCUSSION

ERRATUM

E. M. Sparrow
K. K. Tien

Department of Mechanical Engineering,
University of Minnesota,
Minneapolis, Minn.

Forced Convection Heat Transfer at an Inclined and Yawed Square Plate—Application to Solar Collectors

Experiments have been performed to determine the average heat transfer coefficients for forced convection airflow over a square plate that is inclined and yawed relative to the oncoming flow. The experiments involved mass transfer and were carried out via the naphthalene sublimation technique, with air as the working fluid. By means of the analogy between heat and mass transfer, the results are presented in a form that can be used directly for heat transfer applications. The experiments encompassed a wide range of angles of yaw and angles of attack, and extended over a Reynolds number range from about 20,000 to 100,000. It was found that owing to three dimensional flow effects, the transfer coefficients were remarkably insensitive to both the angle of attack and the angle of yaw. This enabled all the results to be correlated by the equation $j = 0.931Re^{-1/2}$ (where $j = (h/\rho c_p U_\infty)Pr^{2/3}$) with an accuracy of $\pm 2^{1}/_{2}$ percent. The correlation equation was applied to the determination of the heat transfer coefficient for wind-related heat losses from a flat plate solar collector. It was demonstrated that the currently standard computational equation (which is, in reality, not well suited to the application) substantially overestimates the heat transfer coefficient.

Introduction

The research to be reported here is a study of the heat transfer characteristics of boundary layer flows subjected both to yaw and to an angle of attack. At the same time, it serves to model the forced convection heat loss (due to wind) from the upper cover plate of a solar collector. Although the research and its results are not tied to any one application, the initial impetus for undertaking the work was provided by the aforementioned solar devices. It may, therefore, be of interest to begin with a brief recounting of the present practice for calculating forced convection heat losses from solar collectors and to identify the need for improved knowledge of the relevant heat transfer coefficients.

The cover plates of a flat plate solar collector serve both to trap radiation in the collector via the greenhouse effect and to shield the hot collector plate from direct contact with the wind. The top surface of the upper cover plate is exposed to the ambient air and, in the presence of a wind, it will lose heat via forced convection. The direction of the wind relative to the surface of the cover plate will, in general, vary with time, although there may be a preferred direction at specific sites. In particular, there appears to be no basis for assuming that the wind direction is parallel to the surface of the cover plate.

The most recent texts, (e.g., [1, 2][1]) dealing with the analysis of flat plate collectors continue to recommend evaluation of wind-related heat losses by employing average heat transfer coefficients based on the experiments of Jurges (1924), as quoted in [3]

$$\bar{h} = a + bV^n \qquad (1)$$

where V is the wind velocity. The constants a, b, and n are accorded one set of numerical values for velocities less than 16 ft/s and a second set of values for velocities between 16 and 100 ft/s. The experiments were performed for flow of room temperature air parallel to a heated vertical plate 1.64 feet square.

Among the limitations of equation (1), two are especially relevant to solar collector applications. The first limitation of the equation is that it is based on parallel flow experiments, whereas the wind direction is, in general, not parallel to the collector. The second is the

---

[1] Number in brackets designate References at end of paper.

absence of any dependence on plate length, which is a contradiction of the well established fact that boundary layer heat transfer coefficients are length dependent. For instance, for laminar boundary layer flow on a flat plate, the average heat transfer coefficients decrease with the square root of the length. In view of these inadequacies, it is difficult to envision a rational basis for employing equation (1) for wind-related heat loss calculations. This realization served as the initial motivation for the present research.

The experiments to be described here were conducted with a square plate situated in a low turbulence wind tunnel. As will be discussed later in more detail, the plate was mounted so that it could be inclined at any angle of attack relative to the oncoming flow and, in addition, it could be set at any angle of yaw. These angles are illustrated in Fig. 1, where the left-hand diagram is a schematic side view and the right-hand diagram is a view looking down on the plate along the surface normal. The angles of attack and yaw are respectively designated as α and ϕ. The 20 deg beveling of the edges (to prevent blockage) will be illustrated later in more detail.

The objective of the research was to determine average heat transfer coefficients as a function of the angles of attack and yaw, with the Reynolds number encompassing the full range provided by the wind tunnel. In view of the advantages to be discussed shortly, the experiments were performed for mass transfer rather than for heat transfer. However, with the aid of the well-established analogy between heat and mass transfer, the final results will be presented in terms of heat transfer parameters.

The mass transfer experiments were carried out using the naphthalene sublimation technique. With reasonable precautions, this technique provides a well-defined boundary condition on the transfer surface (the mass transfer boundary condition is analogous to uniform wall temperature in the corresponding heat transfer problem). Furthermore, it is virtually free of the extraneous edge losses of the type that are commonly encountered in heat transfer experiments. In addition, it facilitates highly accurate measurements of the rate of transfer.

The selection of a square plate as the object of the experiments was based on two considerations. First, the boundary layer flow on a square plate is expected to be strongly three dimensional, thereby making it an interesting subject for fundamental research. Second, the majority of flat plate solar collectors presently in use (i.e., those used to provide hot water) are square. As will be discussed later, the flow field and the corresponding heat transfer results for rectangular plates are expected to differ from those for a square plate.

A survey of the literature failed to identify any work directly related to the present research objectives. A paper by Drake [4] dealt with heat transfer on an inclined rectangular flat plate, but baffles were placed along the lateral edges to avoid three-dimensional effects. Sogin [5] measured the sublimation mass transfer from a circular disk oriented at a fixed angle (=90 deg) to an airflow.

The Experiments

Apparatus. For the experiments, the naphthalene plates were mounted in the test section of a low speed, low turbulence wind tunnel. The mounting arrangement is illustrated photographically in Fig. 2. In the photograph, the naphthalene plate is seen to be framed by a thin border. The border is the only visible part of a stainless steel cassette which houses the plate, the cassette being one of the elements

of a mold in which the plate was cast. The back face of the cassette was fitted with a connector which enabled the cassette to be attached to a sting suspended from the ceiling of the test section. The connector was designed to permit the angle of attack to be set and fixed at any desired value. The angle of yaw was set by rotating the sting in its supports. These angles were measured by protractors (not shown in the photograph).

The naphthalene plate and its frame constituted a square with a 7.62 cm (3 in.) side. The frame width, 0.238 cm ($^3/_{32}$ in.), was the narrowest border that could be machined without defacing the edge and/or the surface of the frame. The selection of the plate dimensions was made with a view to minimizing blockage of the 30.5 × 61 cm (1 × 2 ft) cross section of the wind tunnel test section. The largest blockage occurs when the plate is positioned transverse to the flow, that is, when $\alpha = 90$ deg. For this orientation, the blockage ratio was about 3 percent. As the angle of attack decreases, the blockage ratio diminishes in proportion to sin α. In light of the foregoing, blockage effects can be regarded as negligible.

The naphthalene plates were cast in a specially designed mold which consisted of two parts—the cassette and a highly polished stainless steel base plate. A photographic view of the assembled mold is presented in Fig. 3. As shown there, the cassette is positioned face down on the base plate, thereby exposing its rear face to view. To facilitate the casting process, two removable fixtures were implanted into the rear face. One of these is a funnel which enables the molten naphthalene to be poured into the mold cavity, and the second is a vent tube which permits air to escape from the cavity.

The mold cavity can be seen in Fig. 4, which is a view of the front face of the cassette as it would appear prior to the casting process. The cavity was created by hollowing out the front face, with the machining being performed so as to leave a fairly rough surface which would enhance the adhesion of the solidifying naphthalene. To further enhance adhesion, an array of crater-like drill holes was machined into the hollowed-out surface.

The surface of the base plate was subjected to a succession of painstaking hand polishing and lapping operations. As a consequence, the naphthalene surface produced by contact with the base plate possessed a very high degree of smoothness such that no further machining was required.

A new naphthalene plate was cast for each data run, and only fresh (unused) reagent grade naphthalene was used for each casting. All implements relating to the casting process were kept scrupulously clean and free from contaminants; lubricants were never used to facilitate the separation of the two parts of the mold. To hasten the progress of the research, two cassettes were employed.

From a further inspection of Fig. 3, it is seen that three of the four edges of the cassette were beveled. The beveling is also shown schematically in diagram (a) of Fig. 1, with the bevel angle indicated as 20 deg relative to the plane of the plate. The reason for the beveling was to ensure that the oncoming flow would not be diverted by blockage and/or bluntness caused by surfaces of the cassette which do not participate in the mass transfer.

Thermocouple lead wires can be seen in Figs. 2–4. These lead wires are associated with a pair of junctions buried in the naphthalene plate and positioned just beneath the exposed surface. One junction was situated about 1.3 cm ($^1/_2$ in.) downstream of the leading edge of the plate and the second was at the point of geometric symmetry of the

---

Nomenclature

c_p = specific heat at constant pressure
$\mathcal{D}$ = diffusion coefficient
h = average heat transfer coefficient
j = j-factor, equations (2a) and (2b)
K = average mass transfer coefficient, equation (4)
$\dot{m}$ = average rate of mass transfer per unit

area
Pr = Prandtl number
Re = Reynolds number, $U_\infty S/\nu$
S = side of square
Sc = Schmidt number
St = Stanton number, equation (2a)
U_∞ = free stream velocity
α = angle of attack

ν = kinematic viscosity
ρ = density
ρ_{nw} = wall concentration of naphthalene vapor
$\rho_{n\infty}$ = free-stream concentration of naphthalene vapor
ϕ = angle of yaw
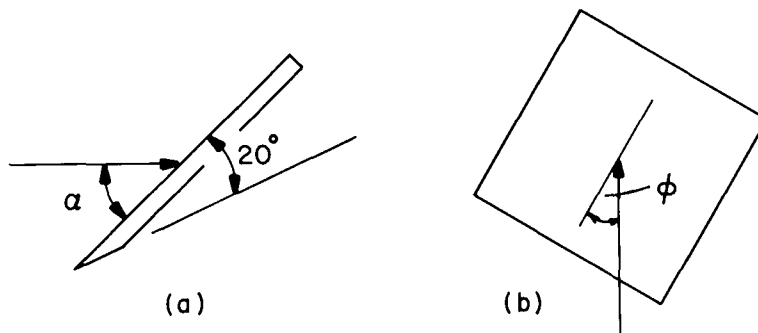
Fig. 1 Illustrations of the angle of attack and the angle of yaw, diagrams (a) and (b), respectively
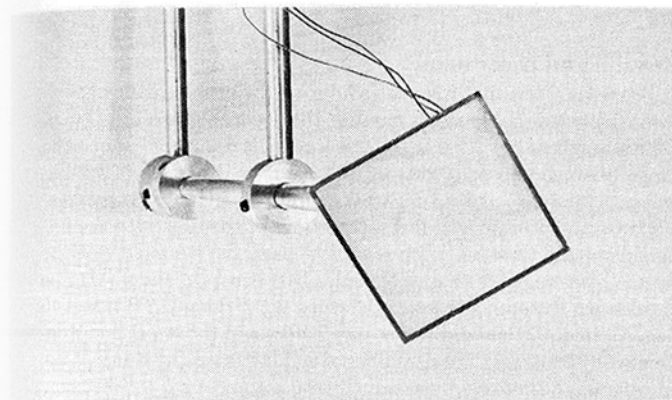
Fig. 2 Naphthalene plate mounted in the test section of the wind tunnel
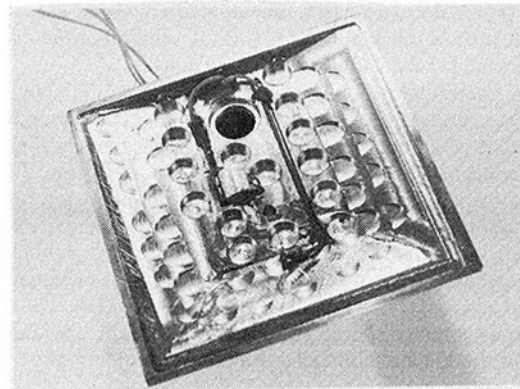
Fig. 4 Mold cavity
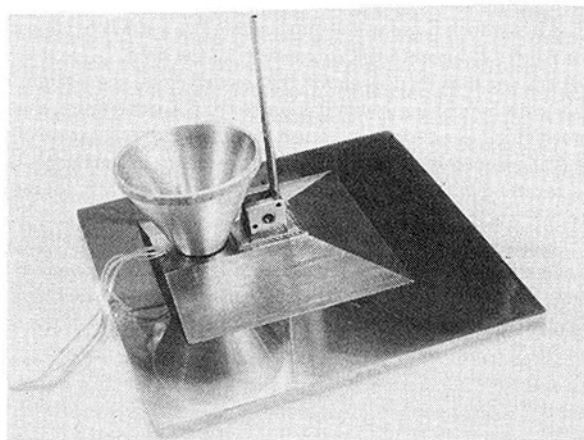
Fig. 3 Mold used for casting the naphthalene plates

surface. The thermocouples were made from 30-gage, teflon-covered copper and constantan wire. The temperatures indicated by these thermocouples never differed by more than about 0.03°C (0.05°F). A similar thermocouple, positioned just downstream and above the plate, was employed to measure the free stream temperature. All thermocouples were individually calibrated. The thermocouple emf's were measured and recorded by a digital millivoltmeter.

The velocity in the test section was measured by an L-shaped impact tube in conjunction with a wall static tap. The impact tube was situated upstream of the naphthalene plate; it was retracted during the mass transfer data acquisition period so that its wake would not impinge on the test surface. The accuracy of the velocity data provided by the impact tube-wall tap combination was validated in auxiliary experiments by comparing the results with those from a Pitot tube

having integral static taps. The two sets of results generally agreed to within 1 percent.

The amount of naphthalene sublimed during a data run was determined from measurements of the mass of the cassette (including the naphthalene plate) before and after the run. The mass measurements were made with a sensitive balance having a capacity of 200 g and a smallest scale reading of 0.1 mg. During a typical data run, about 180 mg of naphthalene was sublimed.

The wind tunnel used for the experiments was operated in the open-circuit mode, with air being drawn from the laboratory room and discharged outside the building. This mode was selected to ensure that the air delivered to the test section would be free of naphthalene vapor and would not be preheated by the fan of the wind tunnel. The turbulence level in the test section had been previously measured to be about 0.2 percent. The velocities available in the test section ranged from about 4.5 to 24 m/s (15 to 80 ft/s), and this entire range was utilized in the experiments.

Experimental Procedure. The sublimation mass transfer is driven by the difference in the concentrations of naphthalene vapor at the plate surface and in the free stream. The latter was zero in the present experiments, whereas the former is proportional to the vapor pressure of the naphthalene. The vapor pressure is very sensitive to the temperature of the surface and increases by about 10 percent per °C in the temperature range of the experiments. Therefore, the attainment of a known, steady plate temperature was a major focus in the conduct of the experiments.

Subsequent to the completion of the casting process, the mold, tightly wrapped in plastic and with the naphthalene surface pressed against the base plate, was placed in the laboratory room for a period of about 6 hr in order to attain thermal equilibrium. During the latter part of that period, the wind tunnel was activated and sufficient time allowed for steady flow to be achieved. At that point, the cassette was removed from its wrapping and its front face (i.e., the naphthalene plate) was capped with a tight-fitting teflon cap. The thus-capped

cassette was installed in the test section of the wind tunnel and allowed to remain there (~20 min) until thermal equilibrium, as sensed by the thermocouples in the naphthalene plate, was achieved.

Next, the cassette was removed from the wind tunnel and weighed, and then immediately returned to the wind tunnel. At this point, the teflon cap was removed and a stop watch was activated, thus signaling the beginning of the data run. The duration of the run was selected so that sufficient mass would be sublimed to facilitate accurate weighing, but with the constraint that the surface of the plate not be significantly altered due to the mass transfer. These criteria were fulfilled by mass transfers on the order of 180 mg, with a corresponding recession of the naphthalene surface of about 0.0025 cm (0.001 in.).

The run times ranged from 40 to 75 min corresponding to the range of plate Reynolds numbers from about 100,000 to 20,000. During each run, the temperatures were read at 2-min intervals. Timewise plate temperature variations of about 0.2°C (0.3–0.4°F) were encountered during a typical data run. The termination of a data run was marked by the capping of the naphthalene surface, removal of the cassette from the wind tunnel, and immediate weighing.

Several operations had to be performed at the beginning/end of a data run (i.e., uncapping/capping, closing/opening of the wind tunnel access hatch, activation of the stop watch). Consequently, there was a slight ambiguity (~5–10 s) in the duration time of the run. To fully remove this ambiguity, each data run was followed by a procedure whereby all of the starting and ending operations of an actual run were performed, but without the 40–75 min period of surface sublimation. The mass transfer associated with the starting/ending operations was measured and subtracted from that of the data run. The typical correction thus obtained was on the order of 1 mg, which is about 1/2 percent of the 180 mg sublimed during the data run proper.

Data Reduction

With the view to obtaining a presentation of results that would be applicable both to heat transfer and to mass transfer, the so-called j-factor was employed. The j-factors for heat and mass transfer are respectively defined as

$$j = \mathrm{St\,Pr}^{2/3}, \qquad \mathrm{St} = h/\rho c_p U_\infty \qquad (2a)$$

$$j = (K/U_\infty)\mathrm{Sc}^{2/3} \qquad (2b)$$

In equation (2a), St is the Stanton number, which is equal to Nu/RePr. The heat transfer coefficient appearing in the Stanton number is defined in the conventional manner (heat transfer rate divided by surface area and by the wall-to-airstream temperature difference). The mass transfer coefficient K and the Schmidt number Sc which appear in the mass transfer j-factor will be elucidated shortly.

According to the analogy between heat and mass transfer, the j-factors for the two modes of transfer are equal. Furthermore, it has been found by experience that j-factor results are usually correlatable in the form $j = C\mathrm{Re}^{-n}$, where $n > 0$.

The evaluation of the j-factor of equation (2b) using the experimental data will now be described. The amount of naphthalene ΔM sublimed during a data run was determined from mass measurements before and after the run (subject to the correction described at the end of the last section). Then, if τ denotes the duration time of the run and A represents the face area of the naphthalene plate, the surface-average mass flux $\dot{m}$ follows as

$$\dot{m} = \Delta M/A\tau \qquad (3)$$

As noted earlier, the mass transfer is driven by the difference in the concentrations of naphthalene vapor at the plate surface and in the free stream. Correspondingly, the mass transfer coefficient may be defined as

$$K = \dot{m}/(\rho_{nw} - \rho_{n\infty}) \qquad (4)$$

In the present experiments, $\rho_{n\infty}$ is zero. To determine ρ_{nw}, the naphthalene vapor pressure p_{nw} corresponding to the measured wall temperature was evaluated by Sogin's equation (equation (3) of [5]).

Then, ρ_{nw} was calculated from the perfect gas law using the known values of p_{nw} and T_w.

The j-factor also involves the Schmidt number $\mathrm{Sc} = \nu/\mathcal{D}$, in which $\mathcal{D}$ is the naphthalene-air mass diffusion coefficient. In view of the extremely small concentrations of naphthalene vapor, the kinematic viscosity was evaluated as that of pure air. For the diffusion coefficient, Skelland's formula ([6], p. 51) relating the value of $\mathcal{D}$ at temperature T to that at zero °C was used. The latter was taken from the International Critical Tables. For all of the data runs, the calculated Schmidt numbers were within a fraction of a percent of the value of 2.57.

The Reynolds number was based on the free stream velocity U_∞ and on the side S of the square plate. Inasmuch as the Reynolds number reflects the nature of the flow field over the entire plate (i.e., the frame as well as the naphthalene surface), S was taken as the outside dimension of the frame, that is, $S = 7.62$ cm (3 in.). Then,

$$\mathrm{Re} = U_\infty S/\nu \qquad (5)$$

Results and Discussion

The parameters that were varied during the course of the experiments included the Reynolds number, the angle of attack (Fig. 1(a)), and the angle of yaw (Fig. 1(b)). The Reynolds number spanned the range between about 20,000 and 100,000. For the angle of attack, values of 90, 65, 45, and 25 deg were chosen. Smaller angles were excluded with a view to avoiding interactions of the flow with the underside of the cassette. With regard to yaw, the symmetry of the square plate requires that only angles between zero and 45 deg be considered. Experiments were performed for angles of 0, 22.5, and 45 deg. All told, 52 final data runs were made, and these were supplemented by an almost equal number of validation and auxiliary runs. In general, the data were reproducible to within 1 or 2 percent.

The j-factor results, evaluated as described in the preceding section, have been plotted in Figs. 5–7 as a function of the Reynolds number. The successive figures correspond to yaw angles of 0, 22.5, and 45 deg. In each figure, the data for the various angles of attack are distinguished by symbols listed at the upper right. The solid lines appearing in the figures represent least squares fits of the data.

Inspection of the figures shows that as expected, the j-factor decreases with increasing Reynolds number and, furthermore, that an inverse half-power dependence is an excellent representation of the data. Aside from this, all other findings in evidence in the figures have to be regarded with a certain degree of surprise and are, therefore, especially worthy of note.

To identify these findings, attention may first be focused on one of the figures, for example, Fig. 5. From this figure, it is seen that the j-factor is quite insensitive to the angle of attack over the range investigated. Specifically, aside from the 1–2 percent scatter of the data,
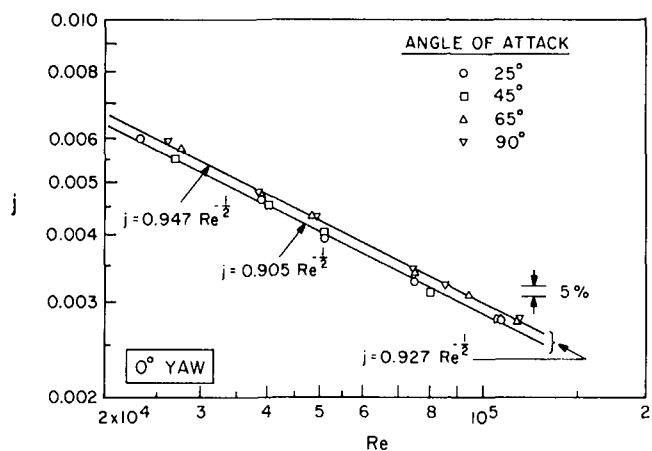

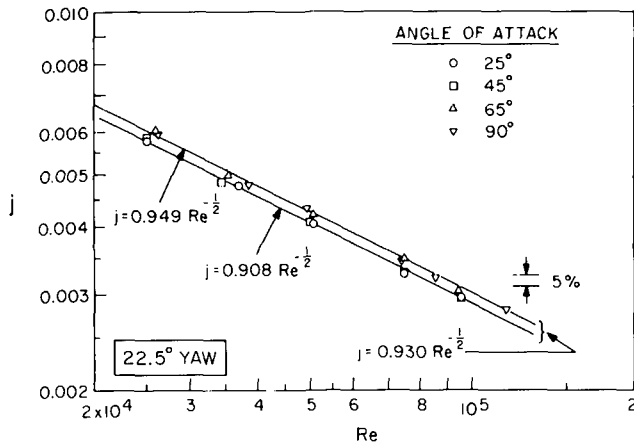Fig. 5 Variation of the j-factor with Reynolds number, yaw angle = 0 deg

Fig. 6 Variation of the *j*-factor with Reynolds number, yaw angle = 22.5 deg
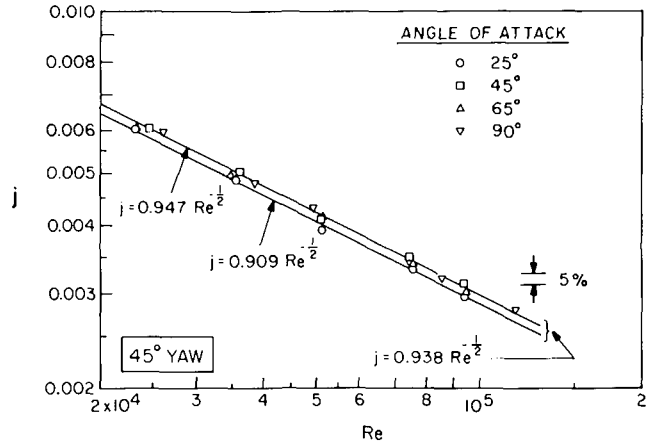
Fig. 7 Variation of the *j*-factor with Reynolds number, yaw angle = 45 deg

the *j*-factor varies (i.e., decreases) by only 5 percent as the angle of attack varies from 90 to 25 deg. This variation of the *j*-factor is very much less than would be expected on the basis of the wedge-flow solutions of conventional boundary layer theory (e.g., [7]).

This same insensitivity to angle of attack is also in evidence in Figs. 6 and 7 and, therefore, it applies to all of the yaw angles investigated.

Next, consideration may be given to how the value of the *j*-factor responds to changes in the angle of yaw. By making comparisons among Figs. 5–7 and taking note of the coefficients of the fitted curves, it is seen that *j* varies by about 1 percent over the entire range of yaw angles. Thus, for practical purposes, *j* can be taken to be independent of the angle of yaw.

To make plausible the insensitivity of the results to the angles of attack and yaw, note must be taken of the strongly three dimensional nature of the flow. Furthermore, notions based on conventional boundary layer theory have to be set aside. In particular, conventional boundary layer theory imposes a two dimensional straitjacket on the flow, thereby ruling out motions directed toward the lateral edges of the plate. Also, the textbook image of a stagnation point flow is one in which the stagnation point is the foreward-most point on the surface. Neither of these notions is applicable to the present situation.

An essential feature of the square-plate geometry studied here is that lateral motions may offer attractive escape routes as the flow seeks paths of least frictional resistance as it passes over the plate. Indeed, because the streamwise and lateral dimensions are of the same magnitude, the flow enjoys considerable freedom as it seeks to minimize its encounter with the friction forces associated with the plate surface. Thus, the streamline pattern can readily adjust to changes associated with variations of the angles of attack and yaw. One such change is the repositioning of the stagnation point, which is situated at the geometric center of the plate at 90 deg angle of attack and moves forward as the angle of attack decreases. The position of the stagnation point also responds to variations of the angle of yaw.

It is believed that the flow's successful search for minimum frictional encounters gives rise to a mean length of flow path along the plate which is nearly independent of the angles of attack and yaw. The near constancy of such a mean flow path is consistent with the observed insensitivity of the *j*-factor to variations of the attack and yaw angles.

This insensitivity is not expected to persist for plate shapes where the streamwise and lateral dimensions are of different magnitudes (e.g., rectangles). In such cases, the flow may not be able to optimize its response to imposed changes in orientation since certain directions of motion are made less attractive because they present paths of relatively high resistance. This expectation remains to be confirmed by experiment.

Attention will now be turned to the correlation of the results. As seen in Figs. 5–7, the *j*-factors for the higher angles of attack tend to

fall together, as do the *j*-factors for the lower angles of attack. These two groups of data have been fitted with separate least squares straight lines as shown in the respective figures. The two lines differ only by about 4 percent. In addition, all the data in a given figure were fitted by an equation of the form $j = C\mathrm{Re}^{-1/2}$. The resulting equation is shown at the lower right in each figure, from where it is seen that the respective values of constant C are 0.927, 0.935, and 0.938 for angles of yaw of 0, 22.5, and 45 deg. The variation of C is about 1 percent.

In view of the insensitivity of the results to the angles of attack and yaw, a single formula can be given which represents all the data to an accuracy of $\pm 2\frac{1}{2}$ percent. The formula is

$$j = 0.931\,\mathrm{Re}^{-1/2} \qquad (6)$$

The simplicity and generality of this equation makes it a useful tool for design.

From a survey of the literature, it was found that there is little available information with which the present results can be compared. The most relevant information stems from Sogin's experiments [5] on naphthalene sublimation from a circular disk oriented perpendicular to an oncoming airflow. It is appropriate to consider a comparison of Sogin's *j*-factor results with those of the present investigation for 90 deg angle of attack.

In this connection, there is some question as to how to rationalize the two Reynolds numbers inasmuch as one is based on the side of a square and the other is based on the diameter of a circle. For the comparison, it was decided to define an effective diameter of the square plate as that which preserves the cross-sectional area. This gives $D_{eff} = \sqrt{4/\pi}S$, in terms of which the correlation of the present data for 90 deg attack becomes

$$j = 1.01(\mathrm{Re}_{eff})^{-1/2} \qquad (7)$$

Sogin's correlation has the same form as equation (7), except that the multiplicative constant is 1.08 rather than 1.01. This level of agreement is entirely satisfactory, especially in view of the rather tenuous rationalization of the two geometries. If the apparent 7 percent deviation between the results were a real difference, it could easily be due to differences in free stream turbulence level.

Concluding Remarks

The present experiments have demonstrated the major role played by three dimensional effects in the flow over an inclined and yawed square plate. Inasmuch as the lateral and streamwise dimensions are of the same magnitude for a square plate, lateral motions readily occur. These lateral motions allow the flow considerable freedom to accommodate to changes in angle of attack and angle of yaw. It is believed that the freedom gives rise to a mean length of flow path along the plate surface which is nearly independent of the angles of attack and yaw.

As a consequence, the j-factor results were insensitive to these angles. This enables all the results of this investigation to be represented by the remarkably simple formula $j = 0.931 \, \mathrm{Re}^{-1/2}$, with an accuracy of $\pm2\frac{1}{2}$ percent.

It is interesting to return to the application that motivated the present research, namely, the heat transfer coefficient for wind-related heat losses from the upper cover plate of a solar collector. The absence of a logical basis for the currently standard computational equation (i.e., equation (1)) has already been discussed in the Introduction. Now, the errors associated with the use of that equation will be illustrated.

For a wind velocity of 3.05 m/s (10 ft/s), the standard equation gives a heat transfer coefficient of about 17.5 W/m² °C (3.1 Btu/hr-ft² °F), independent of the size of the collector plate. With this same wind velocity as input, the present correlation, equation (6), yields a heat transfer coefficient of 8.7 W/m² °C (1.5 Btu/hr-ft² °F) for a 1.22 m (4 ft) square collector plate. For a 2.44 m (8 ft) square plate, equation (6) predicts a heat transfer coefficient of 6.15 W/m² °C (1.1 Btu/hr-ft² °F).

The foregoing example demonstrates that the use of the currently standard computational equation leads to a substantial overestimation of the wind-related heat losses from the collector plate.

Acknowledgment

References

1 Jordan, R. C., and Liu, B. Y. H., eds., *Applications of Solar Energy for Heating and Cooling of Buildings*, American Society of Heating, Refrigerating, and Air-Conditioning Engineers, New York, Chapter VIII, 1977.

2 Duffie, J. A., and Beckman, W. A., *Solar Energy Thermal Processes*, Wiley, New York, 1974, p. 83.

3 McAdams, W. A., *Heat Transmission*, Third ed., McGraw-Hill, New York, 1954, p. 249.

4 Drake, R. M., Jr., "Investigation of the Variation of Point Unit Heat Transfer Coefficient for Laminar Flow Over an Inclined Flat Plate," *Journal of Applied Mechanics*, Vol. 71, 1949, pp. 1-8.

5 Sogin, H. H., "Sublimation From Disks to Air Streams Flowing Normal to Their Surfaces," TRANS. ASME, Vol. 80, 1958, pp. 61-69.

6 Skelland, A. H. P., *Diffusional Mass Transfer*, Wiley, New York, 1974, p. 51.

7 Eckert, E. R. G., and Drake, R. M., *Analysis of Heat and Mass Transfer*, McGraw-Hill, New York, 1972, p. 310.

Addendum

This addendum was inserted just prior to publication of this issue.

It was recently discovered, as preparations were being made to study rectangular plates, that the method for setting nonzero angles of yaw was not yielding the desired angles. A new procedure has been devised, and new experiments at nonzero yaw angles have been carried out. It was found that the average deviation of the new data from the corresponding values of the data reported in the paper is 2.7 percent. Therefore, both the qualitative and quantitative findings presented in the paper continue to apply.

R. C. C. Wang[1]
B. T. F. Chung
L. C. Thomas

Department of Mechanical Engineering, The
University of Akron, Akron, Ohio

Transient Convective Heat Transfer for Laminar Boundary Layer Flow With Effects of Wall Capacitance and Resistance

Transient forced convective heat transfer from a laminar boundary layer flow over a flat plate with appreciable thermal capacity and resistance is studied analytically. In the analysis, the flow is assumed to be steady and incompressible and the solid plate is subjected to a uniform step heat input at the lower surface. The integral method is utilized to reduce systems of nonlinear partial differential equations to a single integro-differential equation in terms of interfacial temperature which is then solved with the aid of finite difference technique. Numerical results for the fluid-solid interface temperature, heat transfer coefficient, and temperature distributions within the fluid and solid are presented. Some limiting solutions are found to agree well with the results of the previous theoretical analyses.

Introduction

Transient forced convective heat transfer has received considerable attention in modern technology. The subject is of importance in the study of time-varying systems which have been widely applied in the areas of nuclear reaction, automatic control, space flight, and the transport processes involving chemical reaction.

Most of the earlier studies in this field were based on the assumption that the temperature or heat flux at the fluid-solid interface is prescribed [1-11].[2] Consequently, the transfer coefficient could be solved by considering transport in the fluid side only. In general, the interfacial temperature or heat flux is not known a priori, but is a function of the transport within both the fluid and the solid.

In steady-state laminar convective heat transfer, the capacitance of the solid is not important. For such cases, the thermal resistance of the wall along the axial direction may affect the transport inside the fluid. Problems of this type have been solved by Sakakibara and other investigators [12-16] by coupling the steady state energy equation for the fluid with the conduction equation for the solid wall.

On the other hand, the capacitance of the solid wall is significant

under unsteady conditions. Siegel [17] solved the problem of unsteady heat transfer through a channel with a uniform velocity profile by including the effect of the solid wall capacity but excluding the wall resistance. Adams and Gebhart [18] considered thermally unsteady laminar boundary layer flow over a flat plate with appreciable thermal capacitance but without resistance. They obtained the surface temperature using the quasi-steady assumption. Chambré [19] studied the transient heat transfer of laminar slug flow over a flat plate of appreciable thermal capacity with zero thermal resistance and a time dependent heat source. Sucec [20] studied the influence of the wall capacity on transient heat convection for slug flow over a plate. The plate was assumed to have a lumped temperature (i.e., $k_s \rightarrow \infty$) in the transverse direction. The effect of the wall thermal capacity in turbulent unsteady heat transfer processes has also been studied [21, 22].

Conjugated unsteady heat transfer problems for external laminar boundary layer flow and internal laminar slug flow have been theoretically studied by several investigators [23-25]. These analyses are of interest from a purely mathematical point of view. However, no numerical results for either fluid or tube wall temperature distribution were presented. Hence, these studies provide limited physical insight into this type of problem.

In the present paper, transient forced convection heat transfer for laminar incompressible boundary layer flow over a flat plate is analyzed. A constant heat flux is imposed at the bottom of the plate. Effects of both thermal capacitance and resistance of the plate are included in the present analysis. Furthermore, the cases with uniform, linear, and third-order velocity profiles within the boundary layer are considered. The integral method is utilized to reduce the system of

---
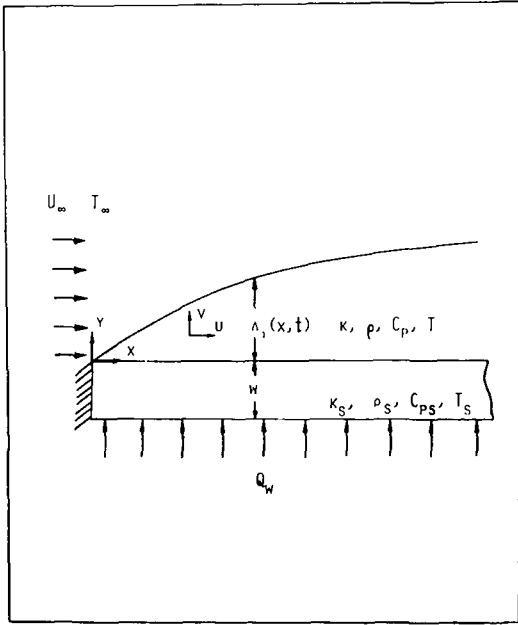
Fig. 1 Schematic model of heat transfer from a flat plate to steady laminar boundary layer flow

nonlinear differential equations to a single integro-differential equation in terms of the interfacial temperature which is then solved with the aid of a finite difference technique.

Analysis

The thermally unsteady system to be considered is two dimensional, steady, laminar, incompressible flow passing over a flat plate of finite thickness, w. The physical model is schematically shown in Fig. 1. It is assumed that: (1) the axial conduction inside both fluid and solid plate are negligible, (2) the thermal properties in both fluid and solid are constant, (3) viscous dissipation in the fluid is negligible, and (4) the plate is insulated at the end of the leading edge. Both fluid and solid plate are initially at the same temperature, T_∞. At an instant (time $t = 0$), the bottom of the plate is suddenly subjected to a uniform heat flux, q_w.

Before the heat penetrates to the fluid-solid interface (i.e., $t \leq t_0$), the fluid temperature remains unchanged and the thermal transport is analogous to unsteady heat transfer in a semi-infinite solid. The equations that describe the thermal conditions of the system may be written as

$$T = T_\infty \qquad 0 \leq y < \infty \tag{1}$$

for the fluid, and

$$\frac{\partial^2 T_s}{\partial y^2} = \frac{1}{\alpha_s} \frac{\partial T_s}{\partial t} \qquad 0 \leq (y + w) \leq w, \quad t > 0 \tag{2}$$

$$T_s = T_\infty \qquad \text{at } t = 0 \tag{3}$$

$$\frac{\partial T_s}{\partial y} = -\frac{q_w}{k_s} \qquad \text{at } y = -w \tag{4}$$

for the solid plate.

After the thermal wave reaches the fluid-solid interface (i.e., second time domain, $t > t_0$), the governing equations become

$$\frac{\partial u}{\partial x} + \frac{\partial v}{\partial y} = 0 \tag{5}$$

$$u \frac{\partial u}{\partial x} + v \frac{\partial u}{\partial y} = \nu \frac{\partial^2 u}{\partial y^2} \tag{6}$$

$$\frac{\partial T}{\partial t_2} + u \frac{\partial T}{\partial x} + v \frac{\partial T}{\partial y} = \alpha \frac{\partial^2 T}{\partial y^2} \tag{7}$$

$$u = v = 0 \qquad \text{at } y = 0 \tag{8a}$$

$$u = U_\infty \qquad \text{as } y \to \infty \tag{8b}$$

$$u = U_\infty \qquad \text{at } x = 0 \tag{8c}$$

$$T = T_\infty \qquad \text{at } t_2 = 0 \qquad \text{or } t = t_0 \tag{9a}$$

$$T = T_\infty \qquad \text{as } y \to \infty \tag{9b}$$

$$T = T_\infty \qquad \text{at } x = 0 \tag{9c}$$

for the fluid,

$$\frac{\partial^2 T_s}{\partial y^2} = \frac{1}{\alpha_s} \frac{\partial T_s}{\partial t_2} \qquad -w \leq y \leq 0, \qquad t_2 > 0 \tag{10}$$

$$T_s = T_{s0} \qquad \text{at } t_2 = 0 \qquad \text{or } t = t_0 \tag{11a}$$

$$\frac{\partial T_s}{\partial y} = -\frac{q_w}{k_s} \qquad \text{at } y = -w \tag{11b}$$

for the solid, and

Nomenclature

C_p = specific heat of fluid

C_{ps} = specific heat of solid plate

h = local heat transfer coefficient

k = conductivity of fluid

k_s = conductivity of solid plate

K = conductivity ratio (dimensionless) = k/k_s

Nu_w = Nusselt number = hw/k

Nu_{st} = Nusselt number under the steady state

P = dimensionless temperature of the fluid = $(T - T_\infty)k/q_r w$

P_s = dimensionless temperature of the solid plate = $(T_s - T_\infty)k/q_r w$

P_0 = dimensionless temperature at the fluid-solid interface = $(T_0 - T_\infty)k/q_r w$

Pr = Prandtl number = ν/α

q_w = constant heat input at the bottom of the plate

q_r = reference heat flux

Q = dimensionless heat input = q_w/q_r

R = thermal diffusivity ratio = α_s/α

$R_0 = \rho_s C_{ps}/(\rho C_p)$

Re = Reynolds number = $4wU_\infty/\nu$

T = temperature of the fluid

T_s = temperature of the solid plate

T_0 = fluid-solid interfacial temperature

T_∞ = initial temperature or temperature outside the thermal boundary layer

t = process time

t_0 = process time at which the second time domain begins

U_∞ = potential flow velocity

U = dimensionless velocity = u/U_∞

U_0 = $u_0/U_\infty (= 1$ for the present calculation)

u = flow velocity in x-direction

v = flow velocity in y-direction

w = thickness of plate

x = distance from the leading edge in flow direction

X = dimensionless distance = $4(x/w)/\text{RePr}$

y = vertical distance from the interface of fluid and plate

Y = dimensionless distance = y/w

α = thermal diffusivity of the fluid

α_s = thermal diffusivity of the solid plate

ρ = density of the fluid

ρ_s = density of the solid plate

δ_1 = momentum boundary layer thickness

$\delta = \delta_1/w$

Δ_1 = thermal boundary layer thickness

$\Delta = \Delta_1/w$

τ = dimensionless process time = $\alpha t/w^2$

τ_1 = dimensionless process time in first domain

τ_2 = dimensionless process time in second domain

τ_0 = dimensionless time at which the second time domain begins = $\alpha t_0/w^2$

$$T = T_s = T_0(x, t_2) \qquad \text{at } y = 0 \qquad (12)$$

$$k \frac{\partial T}{\partial y} = k_s \frac{\partial T_s}{\partial y} \qquad \text{at } y = 0 \qquad (13)$$

on the fluid-solid interface, where t_0 is the time required for the thermal wave to reach the interface and T_{s0} is the temperature profile within the solid at $t = t_0$.

Applying the penetration model and assuming a second-order temperature profile in the solid, we obtain the temperature distribution of the solid in the time interval $0 \leq t \leq t_0$ of the form

$$T_s - T_\infty = \frac{q_w}{2k_s} \frac{y^2}{(6\alpha_s t)^{1/2}}$$

The penetration time is given by $t_0 = w^2/6\alpha_s$, or

$$T_{s0} = T_\infty + \frac{q_w}{2k_s} \frac{y^2}{w} \qquad \text{at } t = t_0 = \frac{w^2}{6\alpha_s} \qquad (14)$$

which yields the temperature variation at the bottom of the plate of the form

$$T_s|_{y=-w} = T_\infty + \left(\frac{3}{2}\right)^{1/2} (q_w/k) \sqrt{\alpha_s t}$$

It should be pointed out that the exact solution for $T_s|_{y=-w}$ of the semi-infinite solid is $T_\infty + (4/\pi)^{1/2} (q_w/k) \sqrt{\alpha_s t}$. However, our primary objective is not to determine the temperature history at the bottom of the surface during the first time domain but to determine the fluid-solid interface temperature in the second time domain.

Integrating equation (10) with respect to y from $-w$ to 0, and equation (7) from 0 to the edge of the thermal boundary layer, Δ, and using the continuity equation, we obtain the dimensionless integral equations of the form

$$KQ + \frac{\partial P_s}{\partial Y}\bigg|_{Y=0} = \frac{1}{R} \frac{\partial}{\partial \tau_2} \int_{-1}^{0} P_s \, dY \qquad (15)$$

$$\frac{\partial}{\partial \tau_2} \int_0^\Delta P \, dY + \frac{\partial}{\partial X} \int_0^\Delta U P \, dY = -\frac{\partial P}{\partial Y}\bigg|_{Y=0} \qquad (16)$$

where $X = 4(x/w)/(\text{Re Pr})$ and $Y = y/w$. The associated dimensionless initial and boundary conditions are

$$P_s = \frac{1}{2} Q K Y^2 \qquad \text{at } \tau_2 = 0 \qquad \text{or } \tau = \tau_0 \qquad (17)$$

$$\frac{\partial P_s}{\partial Y} = -K Q \qquad \text{at } Y = -1 \qquad (18)$$

$$P = 0 \qquad \text{at } \tau_2 = 0 \qquad (19)$$

$$P = 0 \qquad \text{at } Y = \Delta \qquad (20)$$

$$\frac{\partial P}{\partial Y} = 0 \qquad \text{at } Y = \Delta \qquad (21)$$

$$P = P_s = P_0(X, \tau_2) \qquad \text{at } Y = 0 \qquad (22)$$

$$\frac{\partial P_s}{\partial Y} = K \frac{\partial P}{\partial Y} \qquad \text{at } Y = 0 \qquad (23)$$

Solutions to these equations are now obtained for both slug flow and general laminar boundary layer flow by the use of second-order approximations for P_s and P to satisfy the boundary conditions given by equations (18) and (20)–(23).

$$P_s = P_0 - 2K \frac{P_0}{\Delta} Y + \left(\frac{KQ}{2} - \frac{KP_0}{\Delta}\right) Y^2 \qquad (24)$$

$$P = P_0 \left(1 - \frac{Y}{\Delta}\right)^2 \qquad (25)$$

A higher order profile can be used which may improve the result slightly but add more complexity in algebraic manipulations.

Slug Flow Model. In this case, the fluid velocity is assumed constant throughout the entire thermal boundary layer; i.e.,

$$u = U_0 = \text{constant} \qquad (26)$$

Substituting equation (25) into (16) and using equations (19)–(23), we obtain

$$\frac{\partial}{\partial \tau_2} (P_0 \Delta) + U_0 \frac{\partial}{\partial X} (P_0 \Delta) = \frac{6P_0}{\Delta} \qquad (27)$$

Similarly, the substitution of equation (24) into (15) and the use of equations (17), (18), (22), and (23) yields

$$\frac{\partial}{\partial \tau_2} \left(\frac{P_0}{\Delta}\right) + \frac{3}{2K} \frac{\partial P_0}{\partial \tau_2} + 3R \frac{P_0}{\Delta} = \frac{3}{2} R Q \qquad (28)$$

We now have two equations, equations (27) and (28), and two unknowns, P_0 and Δ. To eliminate Δ, we first integrate equation (28) and obtain

$$\frac{P_0}{\Delta} = \frac{Q}{2} [1 - \exp(-3R\tau_2)] - \frac{3P_0}{2K} + \frac{9R}{2K} \exp(-3R\tau_2)$$
$$\times \int_0^{\tau_2} P_0(X, \xi) \exp(3R\xi) \, d\xi \qquad (29)$$

Coupling equation (29) with equation (27) leads to an expression for the interfacial temperature, $P_0(X, \tau_2)$ in terms of single dependent variable

$$\left(\frac{2G}{P_0} + \frac{3}{2K}\right) \frac{\partial P_0}{\partial \tau_2} + \left(\frac{2U_0 G}{P_0} + \frac{3U_0}{2K}\right) \frac{\partial P_0}{\partial X}$$
$$- \frac{9U_0 R}{2K} \exp(-3R\tau_2) \int_0^{\tau_2} \frac{\partial P_0(X, \xi)}{\partial X} \exp(3R\xi) \, d\xi$$
$$= -3RG + \frac{3}{2} R Q + \frac{6G^3}{P_0^2} \qquad (30)$$

where

$$G = \frac{Q}{2}[1 - \exp(-3R\tau_2)] - \frac{3P_0}{2K} + \frac{9R}{2K} \exp(-3\tau_2 R)$$
$$\times \int_0^{\tau_2} P_0(X, \xi) \exp(3R\xi) \, d\xi \qquad (31)$$

This nonlinear integro-differential equation is solved by utilizing a finite difference technique. The finite difference representation of equation (30) may be written as, after algebraic rearrangement:

$$\left[\frac{3}{2K\Delta\tau_2} + \frac{3U_0}{2K\Delta X} - \frac{9U_0 R}{4K} \left(\frac{\Delta\tau_2}{\Delta X}\right)\right] P_0^3 (i+1, j+1)$$
$$+ \left\{\frac{2}{\Delta\tau_2} G(i, j+1) - \frac{3}{2K\Delta\tau_2} P_0(i+1, j) + \frac{2U_0}{\Delta X} G(i+1, j+1)\right.$$
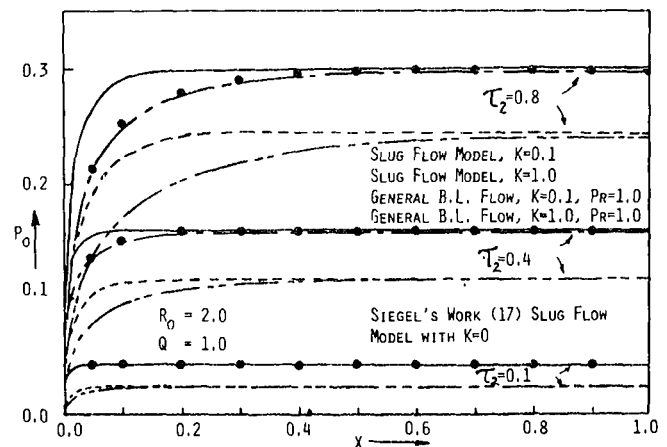

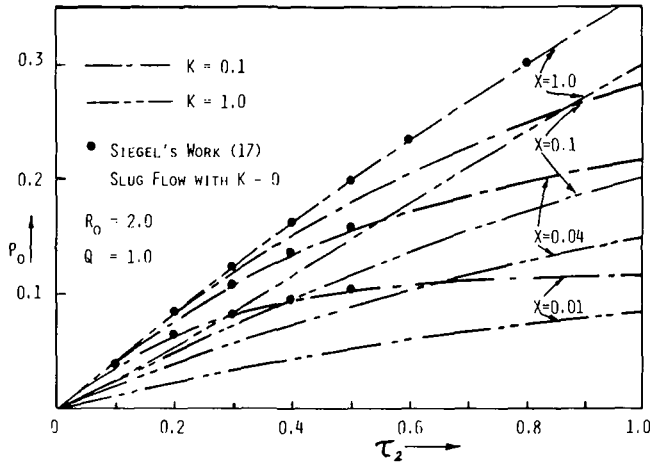Fig 2   Fluid-solid interfacial temperature under transient conditions

Fig. 3 Fluid-solid interfacial temperature history based on slug flow model

$$-\frac{3U_0}{2K\Delta X}P_0(i,j+1) - \frac{9U_0R}{2K}\left(\frac{\Delta\tau}{\Delta X}\right)\exp\left[-3R(j+1)\Delta\tau_2\right]$$

$$\times\left[\frac{1}{2}[P_0(i+1,0)-P_0(i,0)] + \sum_{m=1}^{j}[P_0(i+1,m)-P_0(i,m)]\right.$$

$$\times\exp\left(3Rm\Delta\tau_2\right) - \frac{1}{2}P_0(i,j+1)\exp\{3R(j+1)\Delta\tau_2\}\bigg]$$

$$+ 3RG(i+1,j+1) - \frac{3}{2}RQ\bigg]P_0^2(i+1,j+1)$$

$$-\left[\frac{2}{\Delta\tau_2}G(i+1,j+1)P_0(i+i,j) - \frac{2U_0}{\Delta X}G(i+1,j+1)\right.$$

$$\times P_0(i,j+1)\bigg]P_0(i+1,j+1) - 6G^3(i+1,j+1) = 0 \quad (30a)$$

where

$$G(i+1,j+1) = \frac{Q}{2}\{1-\exp\left[-3R(j+1)\Delta\tau_2\right]\}$$

$$-\frac{3}{2K}P_0(i+1,j+1) + \frac{9R}{2K}\exp\left[-3R(j+1)\Delta\tau_2\right]$$

$$\times\left[\frac{1}{2}P_0(i+1,0) + \sum_{m=1}^{j}P_0(i+1,m)\exp\left(3Rm\Delta\tau_2\right)\right.$$

$$+\frac{1}{2}P_0(i+1,j+1)\exp\{3R(j+1)\Delta\tau_2\}\bigg](\Delta\tau_2) \quad (31a)$$

The index i represents space increment and j time increment. Equation (30a) is a third-order algebraic equation in terms of the unknown $P_0(i+1,j+1)$ which is solved by Newton-Rhaphson method. Similar to the marching technique, the interfacial temperatures are computed starting from the leading edge of the plate and working toward downstream.

General Boundary Layer Flow. The slug flow assumption is not adequate for fluids with high or moderate Prandtl numbers or for very small time. Riley [7] pointed out that at very small time, the thermal boundary layer is very much thinner than the velocity boundary layer and hence the convection is affected by the velocity components regardless of Prandtl numbers. In order to obtain a solution which is applicable to liquids or gases, more realistic linear or cubic velocity profiles are assumed of the form

$$U = \frac{u}{U_\infty} = \frac{3A}{2}\left(\frac{y}{\delta_1}\right) - \frac{B}{2}\left(\frac{y}{\delta_1}\right)^3 \quad (32)$$

where $A = B = 1$ for moderate Prandtl numbers, and $A = 1.1067$, $B = 0$ for high Prandtl numbers. The constant of $A = 1.1067$ is obtained on the basis of the exact Blasius solution for the linear velocity profile

within the wall region. The steady-state hydrodynamic boundary layer thickness, δ_1, is obtained from the solution of the integral form of equations (5), (6), and (8) and is expressed by

$$\delta_1 = 5\sqrt{\frac{\nu x}{U_\infty}} \quad (33)$$

or in dimensionless form

$$\delta_1 = C\sqrt{X} \quad (34)$$

where $C = 5\sqrt{Pr}$

Following the same procedures as presented in the case of slug flow, the following expression for the interfacial temperature $P_0(x,\tau_2)$ is obtained:

$$\left(\frac{2}{3}P_0G^4 + \frac{1}{2K}P_0^2G^3\right)\frac{\partial P_0}{\partial\tau_2} + \left(\frac{3A}{8C\sqrt{X}}P_0^2G^3 + \frac{3A}{8CK\sqrt{X}}P_0^3G^2\right.$$

$$-\frac{BGP_0^4}{24C^3X^{3/2}} - \frac{BP_0^5}{20C^3KX^{3/2}}\right)\frac{\partial P_0}{\partial X} + \frac{9R}{2K}\left(\frac{-AP_0^5G^2}{4C\sqrt{X}}\right.$$

$$+\frac{BP_0^5}{30C^3X^{3/2}}\right)\exp\left(-3R\tau_2\right)\int_0^{\tau_2}\frac{\partial P_0(X,\xi)}{\partial X}\exp\left(3R\xi\right)d\xi$$

$$= 2G^6 - RG^4P_0^2 + \frac{AP_0^3G^3}{16CX^{3/2}} + \frac{Q}{2}RG^3P_0^2 - \frac{BGP_0^5}{80C^3X^{5/2}} \quad (35)$$

where G is defined by equation (31). The finite difference representation of equation (35) reduces to a sixth-order polynomial equation in terms of unknown $P_0(i+1,j+1)$ which is then solved using standard numerical technique.

Once the surface temperature is obtained, the local unsteady transfer coefficient can be calculated by

$$h = \frac{-k\frac{\partial T}{\partial y}\bigg|_{y=0}}{T_0 - T_\infty} \quad (36)$$

or

$$Nu_w = \frac{hw}{k} = \frac{-\frac{\partial P}{\partial Y}\bigg|_{Y=0}}{P_0} = \frac{2G}{P_0} \quad (37)$$

at any given instant. The transient temperature profile inside both solid and fluid also can be obtained from equations (24) and (25).

The accuracy of the numerical solutions depends on the choice of the mesh sizes, $\Delta\tau$, and ΔX. A finer mesh is required in the vicinity of the leading edge, whereas a large axial space increment is used downstream. In the present analysis, ΔX varies from 10^{-4} near $X = 0$ to 10^{-1} for $X \geq 0.1$. The time increment, $\Delta\tau$, is chosen from 10^{-4} to 0.05. With the mesh sizes given, the convergence of the solution is found to be satisfactory. Details of numerical solutions for the interface temperature and temperature distribution in both fluid and solid and the associated computer programs are available in reference [26].

Results and Discussion

Interfacial Temperature. The determination of fluid-solid interface temperature at the initial stage of the heat transfer process is a purely heat conduction problem. This conduction solution is independent of axial direction and flow condition. At infinite time the interface temperature becomes a function of X only for slug flow or a function of X and Pr only for the laminar boundary layer flow. The present analysis aims to bridge the gap between the conduction and the steady solutions.

Fig. 2–4 show the predictions for the local interfacial temperature under transient conditions for both the slug flow and the boundary layer flow. The thermal capacity ratio between the wall and the fluid is arbitrarily chosen to be 0.5 and 2.0. The dimensionless heat flux is set equal to unity (i.e., $q_r = q_w$). As can be seen from the figures, when the capacity ratio is fixed, for higher values of the conductivity ratio, K, corresponding to higher thermal resistances of the solid plate, the interfacial temperature is lower at any specific location and time.
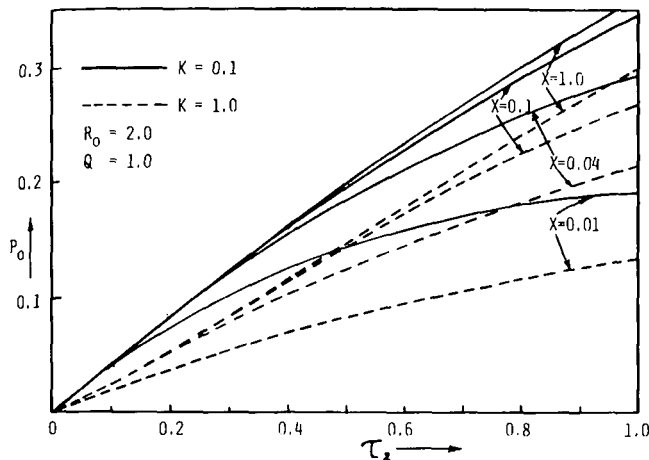
Fig. 4 Fluid-solid interfacial temperature history for laminar boundary layer flow with Pr = 1.0
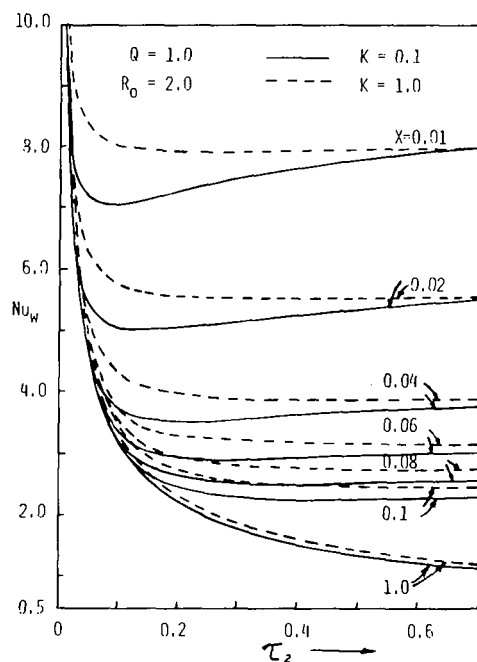

Fig. 5 Local Nusselt number for slug flow

peratures. Since the temperature gradient along the flow direction, $\partial T/\partial x$, decreases as x increases, the contribution of $u(\partial T/\partial x)$ decreases with increasing x. Therefore, as expected, the interfacial temperatures based on both slug flow model and general boundary layer flow become identical for large values of x.

Temperature Profiles. Temperature profiles in both the fluid and the solid regions can be easily obtained from equations (24) and (25), once the interface temperature or the thermal boundary layer is available. It is found that the thermal resistance of the solid plate tends to decrease the interfacial temperature and the fluid temperature, but to increase the temperature at the bottom of the plate. The temperature gradient in the plate increases significantly when the thermal resistance of the solid is increased.

As $\tau_2 \to \infty$ (i.e., steady state), the temperature profile inside the solid becomes linear. This is due to the assumption that the heat conduction along the axial direction is neglected.

Local Heat Transfer Coefficient or Nusselt Number. The predictions for local Nusselt number for the slug flow situation are illustrated in Fig. 5. At any given location x and conductivity ratio K, the transient Nusselt number decreases with the increase of the thermal capacity of the solid plate. For a fixed value of capacity ratio, an increase in the thermal resistance in the plate will increase the Nusselt number under transient conditions. This is partially due to the low interfacial temperature caused by the high resistance in the plate.

It is found that for very large values of time, the local Nusselt number is not affected by the capacity ratio. Furthermore, the effect of the conductivity ratio on Nusselt number disappears under the steady-state condition. This phenomenon also can be explained mathematically from the limiting solution for the slug flow situation, i.e.,

$$\lim_{\tau_2 \to \infty} P_0 = \sqrt{\frac{3X}{2U_0}} Q \qquad (38)$$

$$\lim_{\tau_2 \to \infty} Nu_w = 2\sqrt{\frac{U_0}{6X}} \qquad (39)$$

Note that the conductivity of the solid, k_s, does not appear in the given expressions at steady state. This result can be attributed to the fact that the axial conduction along the plate is neglected. Under steady state, the net heat flux at the interface is identical to the heat input at the bottom of the plate when the axial conduction is negligibly small [i.e., $-k (\partial T/\partial y)|_{y=0} = -k_s(\partial T_s/\partial y)|_{y=0} = q_w$]. With a constant heat flux at the surface, the local heat transfer coefficient is no longer dependent upon the conductivity of the plate. The Nusselt number at steady state is thus independent of the conductivity ratio K. However, if the axial conduction were included, as in reference [12], the steady-state temperature profile inside the solid would not be linear.

Predictions for the local Nusselt number for general boundary layer flow are shown by Fig. 6 for the case of $R_0 = 2$ and $Q = 1$. The results follow the same trends as those for the slug flow. By comparing Fig. 5 with Fig. 6, it is found that the Nusselt number for general boundary layer flow is lower than those obtained for slug flow at small values of X. This difference becomes smaller as X increases. Again, this is caused by the convective effect as explained before for the interfacial temperature.

It is of interest to note that a dip always exists in the transient local Nusselt number in Figs. 5 and 6. A similar situation has been found by other authors [19, 21, 27] for the mean transfer coefficient without wall resistance. During the early time before the influence of convection (i.e., $u(\partial T/\partial X)$) reaches a specific location, the heat transfer to the fluid at this location is totally due to conduction. At this stage, both the temperature and the heat flux at the interface increase with increasing time. However, the thermal capacity in the plate stores some of the energy and therefore causes a lower rate of increase in the net heat flux than the rate of increase of the interfacial temperature. Consequently, the Nusselt number decreases at the early times. Later, when the influence of the convective term, $u(\partial T/\partial x)$, has reached the specific location, the cooling effect of $u(\partial T/\partial x)$ brings about an in-

When K is very small, the computed wall temperatures for the case of slug flow agree very well with the theoretical predictions by Siegel [17], which were developed for the case of zero thermal resistance within the wall. It should be pointed out that the comparison of present results with those of reference [17] should be properly qualified in respect to the difference of the parallel plate problem and the boundary layer problem, as long as the slug flow model is employed. The effect of the thermal capacitance of the solid tends to decrease the interfacial temperature under transient conditions. For higher capacitance, the process takes more time to reach steady state. This agrees with the previous findings presented in references [17, 19, 20].

Numerical computations reveal that the interfacial temperature for the boundary layer flow is higher than that of slug flow for small values X. This occurs because the convective effect in the slug flow model is higher [i.e., $U_\infty(\partial T/\partial x) > u(\partial T/\partial x)$], which results in more heat transfer from the wall to the fluid and reduces the surface tem-

crease in the rate of change of the interfacial temperature. This tends to increase the local Nusselt number. Consequently, a minimum value exists in the Nusselt number at any axial location. As shown in the figures, when X increases, more time is required to reach the minimum point. This is obviously true, since more time is required for the convective wave to reach locations further downstream. When the thermal resistance of the wall becomes very large, the dip diminishes because the large thermal resistance of the wall slows down the increase rate of the interfacial temperature at early times (see Figs. 3 and 4). Consequently, the Nusselt number is greater at the early times and the minimum point due to the recovery of the convection is not so obvious. When time is very large, the capacitance becomes insignificant and the Nusselt number reaches its steady state value as shown in Figs. 5 and 6. For large value of wall capacity, the dip of Nusselt number is more pronounced, and more time is required to reach steady state.

The numerical examples presented here are restricted to the case of a step input of uniform heat flux at the bottom of the plate. To treat a more general case for arbitrary time variant heat flux, Duhamel's superposition integral method can be employed. This requires additional integrations. The computations would entail a numerical solution for the particular problem at hand.

It is of interest to examine the limiting condition of zero wall capacitance ($C_{ps} = 0$) and infinite wall conductance ($K_s \to \infty$) of the present solutions and to compare with the existing solutions in the literature. Adams and Gebhart [18] employed the integral method and the method of characteristic (with numerical integrations eventually) to solve the problem of transient heat convection from a flat plate of zero capacity subjected to a step energy input. Results for various choices of velocity profile showed an agreement of temperature within 10 percent up to 80 percent of the total temperature response. The same problem with the inclusion of dissipation effect has been solved by Chao and Cheema [6] using an analytical method involving Laplace transform and power series. Results for wall flux transients were presented graphically over a wide range of Prandtl number. Fig. 7 shows a comparison of Nusselt number ratio, Nu/Nu_{st} at $Pr = 0.72$ for various models. Both curves 1 and 2 were computed based on equation (32), while curve 3 was based on the following third-order profile suggested by Eckert and Drake [28]

$$\frac{u}{U_\infty} = 1.63 \left(\frac{y}{\delta_1}\right) - 0.645 \left(\frac{y}{\delta_1}\right)^3 \tag{40}$$

As can be seen, all solutions agree reasonably well with each other.
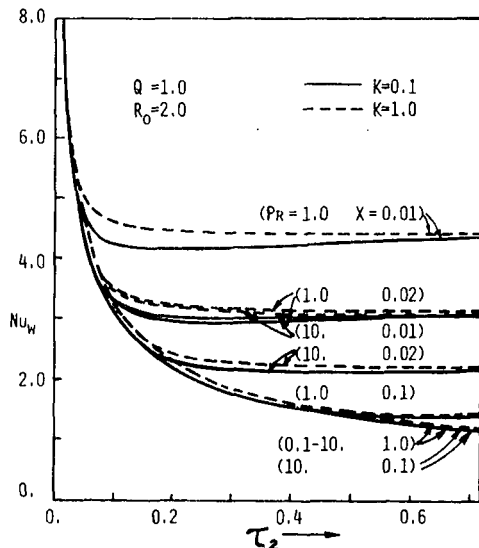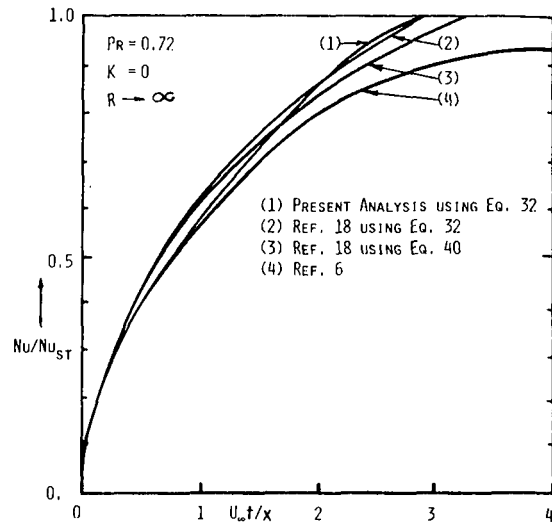
Fig. 7 Comparison of unsteady Nusselt number based on various analysis for zero wall resistance and capacity

However, the integral method yields a shorter time at which the steady state is attained. The discrepancy in numerical values between curves 1 and 2 is attributed to the different techniques involved in the solution of the boundary layer thickness.[3]

Conclusion

Transient forced convective transfer from a flat plate to a laminar boundary layer flow has been analyzed. The effects of thermal capacity and resistance of the solid plate have been included in the analysis. Typical results of fluid-solid interfacial temperature, Nusselt number, and temperature profiles have been presented for both slug flow and general boundary layer flow.

It is found that the wall capacity tends to decrease the surface temperature and Nusselt number at transient stage. The capacity effect becomes insignificant when the steady state is reached. The thermal resistance of the wall tends to decrease the interfacial temperature and increase the Nusselt number under transient conditions. The combined effects of the wall capacity and convection cause a dip in the history of the Nusselt number. The dip diminishes when the thermal resistance of the wall becomes very large. It is also found that the effect of wall resistance on the interface temperature of the slug flow is negligibly small as $K \leq 0.1$. In general, the slug flow model predicts a higher Nusselt number and lower interfacial temperature than that of the general boundary layer flow model.

In the present analysis, the integral method is utilized to reduce the complicated system of equations to a first-order intergro-differential equation. Although the final results are still evaluated with a digital computer, the complexity of the numerical computation has been greatly reduced, as compared to the direct numerical solution of equations (5)–(13).

References

1 Goodman, T. R., "Effect of Arbitrary Non-Steady Wall Temperature on Incompressible Heat Transfer," JOURNAL OF HEAT TRANSFER, TRANS. ASME, Series C, Vol. 84, 1962, p. 347.
2 Sparrow, E. M., and Gregg, J. L., "Non-Steady Surface Temperature Effects of Forced-Convection Heat Transfer," Journal of Aeronautical Sciences, Vol. 24, 1957, p. 776.
3 Cess, R. D., "Heat Transfer to Laminar Flow Across a Flat Plate With a Non-Steady Surface Temperatures," JOURNAL OF HEAT TRANSFER,

Fig. 6 Local Nusselt number for laminar boundary layer flows with various Prandtl numbers

---

[3] A typographical error exists in equation 15 of reference [18]. An "α" was missing in the denominator of the third term on the left-hand side of that equation.

TRANS. ASME, Series C, Vol. 83, 1961, p. 274.

4 Soliman, M., and Chambré, P. L., "On the Time-Dependent Convective Heat Transfer in Fluids With Vanishing Prandtl Number," *International Journal of Heat and Mass Transfer,* Vol. 12, 1969, p. 1221.

5 Biasi, L. C., "Transient Convective Heat Transfer in Fluids With Vanishing Prandtl Number: An Application of the Integral Method," *International Journal of Heat and Mass Transfer,* Vol. 14, 1971, p. 639.

6 Chao, B. T., and Cheema, L. S., "Unsteady Heat Transfer in Laminar Boundary Layer Over a Flat Plate," *International Journal of Heat and Mass Transfer,* Vol. 11, 1968, p. 1311.

7 Riley, N., "Unsteady Heat Transfer for Flow Over a Flat Plate," *Journal of Fluid Mechanics,* Vol. 17, 1963, p. 97.

8 Siegel, R., "Heat Transfer for Laminar Flow in Ducts With Arbitrary Time Variation in Wall Temperature," *Journal of Applied Mechanics,* TRANS. ASME, Series E, Vol. 82, 1960, p. 241.

9 Perlmutter, M., and Siegel, R., "Unsteady Laminar Flow in a Duct With Unsteady Heat Addition," JOURNAL OF HEAT TRANSFER, TRANS. ASME, Series C, Vol. 83, 1961, p. 432.

10 Perlmutter, M., and Siegel, R., "Two-Dimensional Unsteady Incompressible Laminar Duct Flow With a Step Change in Wall Temperature," *International Journal of Heat and Mass Transfer,* Vol. 3, 1961, p. 94.

11 Siegel, R., and Perlmutter, M., "Laminar Heat Transfer in a Channel With Unsteady Flow and Wall Heating Varying With Position and Time," JOURNAL OF HEAT TRANSFER, TRANS. ASME, Series C, Vol. 85, 1963, p. 358.

12 Sakakibara, M., Mori, S., and Tanimoto, A., "Effect of Wall Conduction on Convective Heat Transfer With Laminar Boundary Layer," *Kagaku Kogaku,* Vol. 37, 1973, p. 281.

13 Davis, E. J., and Gill, W. N., "Effects of Axial Conduction in the Wall on Heat Transfer With Laminar Flow," *International Journal of Heat and Mass Transfer,* Vol. 13, 1970, p. 459.

14 Rotem, Z., "The Effect of Thermal Conduction of the Wall Upon Convection From a Surface in a Laminar Boundary Layer," *International Journal of Heat and Mass Transfer,* Vol. 10, 1967, p. 461.

15 Sell, M. G., and Hudson, J. L., "The Effect of Wall Conduction on Heat Transfer to a Slug Flow," *International Journal of Heat and Mass Transfer,* Vol. 9, 1966, p. 11.

16 Perelman, T. L., "On Conjugated Problems of Heat Transfer," *International Journal of Heat and Mass Transfer,* Vol. 3, 1961, p. 293.

17 Siegel, R., "Forced Convection in a Channel With Wall Heat Capacity and With Wall Heating Variable With Axial Position and Time," *International Journal of Heat and Mass Transfer,* Vol. 6, 1963, p. 607.

18 Adams, D. E., and Gebhart, B., "Transient Forced Convection From a Flat Plate Subjected to a Step Energy Input," JOURNAL OF HEAT TRANSFER, TRANS. ASME, Series C, Vol. 86, 1964, p. 253.

19 Chambré, P. L., "Theoretical Analysis of the Transient Heat Transfer Into a Fluid Flowing Over a Flat Plate Containing Internal Heat Sources," L. M. K. Boelter Anniversary Volume, McGraw-Hill, New York, 1964.

20 Sucec, J., "Unsteady Heat Transfer Between a Fluid With Time Varying Temperature and a Plate: An Exact Solution," *International Journal of Heat and Mass Transfer,* Vol. 18, 1975, p. 25.

21 Soliman, M., and Johnson, H. A., "Transient Heat Transfer For Turbulent Flow Over a Flat Plate of Appreciable Thermal Capacity and Containing Time-Dependent Heat Source," JOURNAL OF HEAT TRANSFER, TRANS. ASME, Series C, Vol. 89, 1967, p. 362.

22 Chung, B. T. F., and Thomas, L. C., "A Transient Surface Renewal and Penetration Model for Turbulent Forced Convection From a Flat Plate," 5th International Heat Transfer Conference, Vol. 2, Tokyo, 1974, p. 124.

23 Perelman, T. L., Levitin, R. S., Gdalevich, L. B., and Khusid, B. M., "Unsteady-State Conjugated Heat Transfer Between a Semi-Infinite Surface and Incoming Flow of a Compressible Fluid—I. Reduction to the Integral Relation," *International Journal of Heat and Mass Transfer,* Vol. 15, 1972, p. 2551.

24 Zagary, A., and Brock, J. E., "An Integral Equation Describing Conjugated Transient Heat Transfer in Fluid Flow Through Insulated Pipes," *International Journal Heat and Mass Transfer,* Vol. 16, 1973, p. 1325.

25 Comstock, C., Zargary, A., and Brock, J. E., "On The Delayed Hot Water Problem," JOURNAL OF HEAT TRANSFER, TRANS. ASME, Series C, Vol. 96, 1974, p. 166.

26 Wang, R. C. C., "Transient Heat Transfer For Laminar and Turbulent Boundary Layer Flows With Effects of Wall Capacitance and Resistance," PhD dissertation, The University of Akron, Akron, Ohio, 1976.

27 Siegel, R., "Transient Free Convection From A Vertical Flat Plate," TRANS. ASME, Vol. 80, 1958, p. 347.

28 Eckert, E. R. G., and Drake, R. M., *Heat and Mass Transfer,* McGraw-Hill, New York, 1959.

E. M. Sparrow
S. V. Patankar
S. Ramadhyani

Department of Mechanical Engineering
University of Minnesota, Minneapolis, Minn.

Analysis of Melting in the Presence of Natural Convection in the Melt Region

An analysis of multidimensional melting is performed which takes account of natural convection induced by temperature differences in the liquid melt. Consideration is given to the melt region created by a heated vertical tube embedded in a solid which is at its fusion temperature. Solutions were obtained by an implicit finite-difference scheme tailored to take account of the movement of the liquid-solid interface as melting progresses. The results differed decisively from those corresponding to a conventional pure-conduction model of the melting problem. The calculated heat transfer rate at the tube wall decreased at early times and attained a minimum, then increased and achieved a maximum, and subsequently decreased. This is in contrast to the pure conduction solution whereby the heat transfer rate decreases monotonically with time. The thickness of the melt region was found to vary along the length of the tube, with the greatest thickness near the top. This contrasts with the uniform thickness predicted by the conduction solution. These findings indicate that natural convection effects, although unaccounted for in most phase change analyses, are of importance and have to be considered.

Introduction

Melting and freezing processes are encountered in a wide range of technologies, encompassing such diverse applications as casting of metals and glass, freeze drying of foodstuffs, and storage of thermal energy. The number and diversity of melting/freezing applications has motivated an extensive literature. As will be discussed shortly, an examination of this literature shows that, in the main, solid/liquid phase change problems are analyzed as heat conduction problems. Conduction can be accepted as the sole transport mechanism in situations where the temperature of the liquid is uniform and equal to the fusion temperature.[1] However, when the temperature of the liquid is nonuniform, consideration has to be given to the possible role of natural convection.

The presence of temperature variations in the liquid will, in most cases, activate natural convection motions. Under these conditions, the heat conduction problem in the solid has to be solved simultaneously with the natural convection flow and heat transfer problem in the liquid. Historically, the possible existence of natural convection in the liquid phase has largely gone unnoticed in the heat transfer literature. Therefore, many of the available conduction-based phase change solutions do not fully reflect physical reality.

The accounting of natural convection exposes differences between freezing and melting problems whose conduction-based solutions are interchangeable. In this connection, attention may be directed to the counterpart problems of freezing a liquid which is at its fusion temperature and of melting a solid that is also at the fusion temperature. In the freezing problem, the temperature of the unfrozen liquid remains at the fusion value, thereby precluding the possibility of natural convection. On the other hand, the liquid produced in the melting problem is necessarily nonuniform in temperature, so that natural convection motions may occur. Since the most commonly analyzed melting/freezing problems encompass media that are initially at the fusion temperature, it is worthy of note that the solutions of the melting and freezing problems are not interchangeable due to natural convection.

It is also relevant to note that there are some instances where the presence of temperature variations in the liquid does not lead to natural convection motions. One such instance is stable stratification, wherein liquid of lesser density is situated above liquid of greater density. Even when heavier fluid is situated above lighter fluid, natural convection does not occur until an instability threshold is reached. In many phase change problems, natural convection is relegated to an ineffectual role due to the high resistance offered to fluid motion by passages of small dimensions. For instance, such effects are operative in low-permeability fibrous or granular materials.

The foregoing general discussion of the role of natural convection in solid/liquid phase change problems is intended to set the stage for

the analysis and the results to be presented in this paper. The motivating application for the study is the storage of thermal energy by the melting of a salt. Qualitative laboratory experiments performed in connection with the storage work revealed a decisive influence of natural convection. In view of those findings, it appeared mandatory to take account of natural convection in the analysis and solution of the melting problem, and that dictum was followed here.

The physical situation that was analyzed is pictured schematically in Fig. 1. A vertical tube of height H and outer radius r_0 is embedded in a solid which is at its fusion temperature T_{sat}. Initially, no liquid is present, and the solid and the tube are in direct contact. At time $t = 0$, the temperature of the outer surface of the tube is raised to a value $T_w > T_{sat}$ and melting begins. Although conduction plays a dominant role at early times when the tube is surrounded by a thin melt layer, natural convection ultimately takes over. As a consequence, the interface between the solid and liquid is not vertical (in contrast with the vertical interface for pure conduction), but is sloped as indicated schematically in the figure. Under the influence of buoyancy, there is a recirculating flow within the liquid with an upflow along the heated tube and a downflow along the interface.

The analysis and solutions were aimed at two general objectives. One was to obtain information such as heat transfer coefficients and interface positions that are applicable to design. The second was to determine streamline patterns and temperature distributions in order to obtain insights into the flow and energy transport processes.

As formulated, the analysis involves the two spatial coordinates r, z as well as the time t. The complexity of the two-dimensional unsteady flow and heat transfer problem calls for the use of a numerical solution procedure. The main parameters that were varied for the solutions were the Rayleigh number and the length-to-radius ratio of the tube. The effects of two other parameters, the Stefan number and the Prandtl number, were also examined.

Attention will now be turned to previously published work dealing with problems of melting and freezing. In the heat transfer literature, it has been standard to analyze such problems by assuming that conduction is the sole transport mechanism, and the same approach has been followed in the applied mathematics literature. The effects of natural convection have been taken into account in a few papers. In [1],[2] natural convection was included in an analysis of the steady state phase change problem associated with continuous casting. Natural convection effects have been investigated in the problem of freezing or melting of water in horizontal layers, and a survey of this work is available in [2]. Experiments on the melting of a sphere of ice situated in a container of liquid water are described in [3].

In contrast to the foregoing, there appears to be a greater awareness in other literatures, particularly metallurgy, of the role of natural convection in phase change problems. This awareness was exhibited in [4] in connection with a one-dimensional analysis of freezing in a vertical slot. However, since the relevant energy equation does not
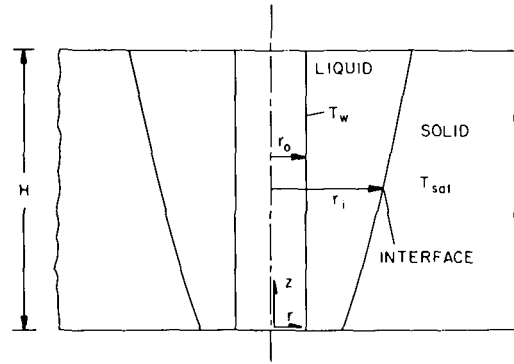
Fig. 1 Schematic diagram of the melting problem

contain velocity terms, the heat transfer processes are not affected by buoyancy, and conduction remains as the sole transport mechanism. In [5] and [6], the freezing or melting of metals and alloys was analyzed by solving the one-dimensional heat conduction equation for the solid; the heat transfer processes in the liquid were accounted for via empirical natural convection heat transfer coefficients. Experiments intended to clarify the interaction of natural convection and phase change in one-dimensional geometries are reported in [7] and [8].

It thus appears that unsteady, multidimensional coupled natural convection and melting has not yet been analyzed from first principles in the published literature. In particular, the complex recirculating natural convection flows which can occur in the liquid region have not been analytically investigated, nor have their heat transfer ramifications.

The Analysis

The starting point of the analysis is the conservation equations for axisymmetric, unsteady flow and heat transfer in the melt layer. The first task in specializing these equations is the formulation of the buoyancy term via the vertical pressure gradient and body force that appear in the z-momentum equation, that is

$$-\partial p/\partial z - \rho g \tag{1}$$

The density appearing in the foregoing expression can be related to the temperature via the Boussinesq model, according to which density variations are considered only insofar as they contribute to buoyancy, but are otherwise neglected. If T_{sat} is the fusion temperature and ρ_{sat} is the corresponding liquid density then, according to the Boussinesq model

$$\rho = \rho_{sat} - \beta\rho_{sat}(T - T_{sat}) \tag{2}$$

Furthermore, if a reduced pressure p^* is defined as

Nomenclature

c_p = specific heat at constant pressure

Fo = Fourier number, $\alpha t/r_0^2$

g = acceleration of gravity

h_{SL} = latent heat of fusion

k = thermal conductivity

P = dimensionless pressure, equation (12)

Pr = Prandtl number

p = pressure

p^* = reduced pressure, equation (3)

Q = heat transfer rate at tube surface

R = dimensionless radial coordinate, r/r_0

Ra = Rayleigh number, $(g\beta(T_w - T_{sat})r_0^3/\nu^2)$Pr

R_i = dimensionless interface coordinate, r_i/r_0

r = radial coordinate

r_i = interface coordinate

r_0 = tube radius

Ste = Stefan number, $c_p(T_w - T_{sat})/h_{SL}$

T = temperature

T_{sat} = fusion temperature

T_w = tube wall temperature

t = time elapsed from the start of heating

U = dimensionless axial velocity, $u/(\alpha/r_0)$

V = dimensionless radial velocity, $\upsilon/(\alpha/r_0)$

u = axial velocity

υ = radial velocity

z = axial coordinate

α = thermal diffusivity

β = thermal expansion coefficient

ζ = dimensionless axial coordinate, z/r_0

η = transformed radial coordinate, $(r - r_0)/(r_i - r_0)$

θ = dimensionless temperature, $(T - T_{sat})/(T_w - T_{sat})$

ν = kinematic viscosity

ρ = density

τ = dimensionless time, equation (13)

$$p^* = p + \rho_{sat} g z \qquad (3)$$

then (1) becomes

$$-\partial p^*/\partial z + g\beta\rho_{sat}(T - T_{sat}) \qquad (4)$$

the second term of which represents the buoyancy force.

Next, to further adapt the conservation equations, the constant property assumption is introduced and the subscript *sat* is deleted from ρ_{sat} in (4). With the foregoing, the equations representing conservation of mass, z-momentum, r-momentum, and energy can be written as

$$\frac{\partial u}{\partial z} + \frac{1}{r}\frac{\partial(rv)}{\partial r} = 0 \qquad (5)$$

$$\frac{\partial u}{\partial t} + \frac{\partial u^2}{\partial z} + \frac{1}{r}\frac{\partial(ruv)}{\partial r} = -\frac{1}{\rho}\frac{\partial p^*}{\partial z} + g\beta(T - T_{sat}) + \nu\nabla^2 u \qquad (6)$$

$$\frac{\partial v}{\partial t} + \frac{\partial(uv)}{\partial z} + \frac{1}{r}\frac{\partial(rv^2)}{\partial r} = -\frac{1}{\rho}\frac{\partial p^*}{\partial r} + \nu(\nabla^2 v - (v/r^2)) \qquad (7)$$

$$\frac{\partial T}{\partial t} + \frac{\partial(uT)}{\partial z} + \frac{1}{r}\frac{\partial(rvT)}{\partial r} = \alpha\nabla^2 T \qquad (8)$$

in which ∇^2 is the Laplace operator in r, z coordinates. These equations, along with an interface energy balance and other boundary conditions, are to be solved in a domain whose boundaries do not all fall along coordinate lines in a cylindrical coordinate system. In particular, the radius r_i of the liquid-solid interface varies with z as well as with time as melting proceeds. This state of affairs precludes an analytical solution and requires that, even in a numerical solution, approximations be made in order to obtain results with a realistic computational effort.

For the computational model to be employed here, it will be assumed that there is a small time lag between the heat delivery to the interface and the resulting interface motion. Specifically, during a small time interval, the fluid flow and heat transfer in the liquid region will be solved assuming that the interface is stationary. The heat transferred to the interface during that interval will then be used to compute the small finite displacement associated with the melting. With the new liquid domain which corresponds to the displaced interface, the solution for the next time interval is performed as just described.

To transform the solution domain into a more tractable shape, new coordinates ζ, η are introduced. Consistent with the aforementioned model, the interface radius r_i is independent of time during any given computational time interval. As a consequence, $r_i = r_i(z)$ during each interval. The new coordinates are defined as

$$\zeta = z/r_0, \qquad \eta = (r - r_0)/(r_i - r_0) \qquad (9)$$

so that

$$\frac{\partial}{\partial z} = \frac{1}{r_0}\frac{\partial}{\partial\zeta} - \frac{\eta}{(r_i - r_0)}\frac{dr_i}{dz}\frac{\partial}{\partial\eta} \qquad (10)$$

$$\frac{\partial}{\partial r} = \frac{1}{(r_i - r_0)}\frac{\partial}{\partial\eta} \qquad (11)$$

The key result of the transformation is that the range of η extends from zero to one at all ζ during any time interval. It may be noted that the ζ, η coordinates are nonorthogonal, as are the transformed coordinates in conventional boundary layer analyses.

In addition, to reduce the number of parameters that have to be specified for the numerical solutions, dimensionless variables and groups are introduced as

$$U = \frac{u}{\alpha/r_0}, \qquad V = \frac{v}{\alpha/r_0}, \qquad P = \frac{p^*}{\rho(\alpha/r_0)^2 Pr},$$

$$\theta = \frac{T - T_{sat}}{T_w - T_{sat}} \qquad (12)$$

$$\tau = (\alpha t/r_0^2)(c_p(T_w - T_{sat})/h_{SL}) = (Fo)(Ste) \qquad (13)$$

$$Ra = \frac{g\beta(T_w - T_{sat})r_0^3}{\nu^2}Pr, \qquad Ste = \frac{c_p(T_w - T_{sat})}{h_{SL}} \qquad (14)$$

in which h_{SL} is the latent heat for solid-liquid phase change. The motivation for using α/r_0 rather than ν/r_0 as a reference velocity and for involving the Stefan number in the dimensionless time variable will soon become apparent.

If the conservation equations were to be transformed in strict adherence with (10) and (11), the result would be a set of equations notable for length and complexity. In the main, the terms which elongate and complicate the transformed equations are spawned by the right-most member of equation (10), which involves the slope dr_i/dz of the interface. The inclusion of these terms would add significantly to the complexity and execution time of numerical solutions. Furthermore, it is highly likely that they would adversely affect the convergence of an iterative solution scheme.

Inasmuch as the present research represents the first analysis of multidimensional, unsteady natural convection phase change, it does not seem unreasonable to adopt a somewhat simplified model to enable solutions to be obtained with reasonable computational effort. It will, therefore, be assumed that the interface radius varies slowly with z, so that the terms involving dr_i/dz and d^2r_i/dz^2 can be neglected. This assumption is of the same nature as the local similarity model commonly used in the analysis of boundary layer flow and heat transfer.

With the aforementioned assumption, the transformed version of the conservation equations can be written as

$$\frac{\partial U}{\partial\zeta} + \frac{1}{R(R_i - 1)}\frac{\partial(RV)}{\partial\eta} = 0 \qquad (15)$$

$$\frac{1}{Pr}\left[Ste\frac{\partial U}{\partial\tau} + \frac{\partial U^2}{\partial\zeta} + \frac{1}{R(R_i - 1)}\frac{\partial(RUV)}{\partial\eta}\right]$$
$$= -\frac{\partial P}{\partial\zeta} + Ra\theta + \hat{\nabla}^2 U \qquad (16)$$

$$\frac{1}{Pr}\left[Ste\frac{\partial V}{\partial\tau} + \frac{\partial(UV)}{\partial\zeta} + \frac{1}{R(R_i - 1)}\frac{\partial(RV^2)}{\partial\eta}\right]$$
$$= -\frac{\partial P}{\partial\eta} + \hat{\nabla}^2 V - V/R^2 \qquad (17)$$

$$Ste\frac{\partial\theta}{\partial\tau} + \frac{\partial(U\theta)}{\partial\zeta} + \frac{1}{R(R_i - 1)}\frac{\partial(RV\theta)}{\partial\eta} = \hat{\nabla}^2\theta \qquad (18)$$

The quantities R_i and R respectively represent the dimensionless radius of the interface, which depends only on z during a given time interval, and the dimensionless radial coordinate

$$R_i = r_i/r_0, \qquad R = r/r_0 = \eta(R_i - 1) + 1 \qquad (19)$$

Furthermore, $\hat{\nabla}^2$ is the transformed Laplace operator

$$\hat{\nabla}^2 = \frac{\partial^2}{\partial\zeta^2} + \frac{1}{R(R_i - 1)^2}\frac{\partial}{\partial\eta}\left(R\frac{\partial}{\partial\eta}\right) \qquad (20)$$

It may be noted that because of the choice of the dimensionless variables, the inertia terms in equations (16) and (17) are multiplied by $(1/Pr)$ and the storage terms (i.e., $\partial/\partial\tau$ terms) contain Ste as a factor. Aside from the explicit presence of Pr and Ste, the fluid properties that make up Pr appear implicitly in Ra, while Ste is included in the dimensionless time variable τ. For typical salt storage applications, both $(1/Pr)$ and Ste $\ll 1$. The ramifications of these facts will emerge when the results are presented.

The four conservation equations (15)-(18) contain five unknowns. These include the velocity components U and V, the pressure P, the temperature θ, and the interface radius R_i. The fifth equation arises from the energy balance which applies at each point on the liquid-solid interface. This balance states that the heat delivered by the fluid to the interface during a small time interval Δt equals the latent heat absorbed by the melting material. The heat delivered ΔQ_i can be written as

$$\Delta Q_i = 2\pi r_i dz(k(\partial T/\partial z)(dr_i/dz) - k(\partial T/\partial r))\Delta t \qquad (21)$$

where the expression in brackets is a representative interfacial heat flux for the time interval. Since the interface is a surface of constant temperature ($T = T_{sat}$), it follows that

$$\partial T / \partial z = -(dr_i/dz)(\partial T/\partial r) \tag{22}$$

so that (21) becomes

$$\Delta Q_i = -k(\partial T/\partial r)2\pi r_i dz (1 + (dr_i/dz)^2)\Delta t \tag{23}$$

For gradually or even moderately sloping interfaces, $(dr_i/dz)^2 \ll 1$.

The volume swept out in response to the heat transfer ΔQ_i is $\pi \Delta(r_i{}^2)dz$ if $(dr_i/dz)^2$ is neglected compared with one, where $\Delta(r_i{}^2) = r_{i,j+1}{}^2 - r_{i,j}{}^2$ and j and $(j + 1)$ refer to the beginning and end of a time interval. With this and with the expression for ΔQ_i, the interface energy balance is

$$-k(\partial T/\partial r)2r_i\Delta t = \rho h_{SL}\Delta(r_i{}^2) \tag{24}$$

or, in dimensionless terms,

$$\frac{2R_i}{(R_i - 1)}\left(-\frac{\partial \theta}{\partial \eta}\right)\Delta \tau = \Delta(R_i{}^2) \tag{25}$$

The boundary conditions will now be discussed. For the velocity, both components are zero on all of the surfaces which bound the liquid.[3] The temperature is prescribed as being uniform on the tube surface $(T = T_w)$, while at the interface the temperature is T_{sat}; correspondingly, $\theta = 1$ at $\eta = 0$ and $\theta = 0$ at $\eta = 1$. The upper and lower bounding surfaces, $z = H$ and $z = 0$ respectively, are assumed to be adiabatic.

If the complete set of governing equations and boundary conditions is examined, it is seen that there are four prescribable parameters: Ra, H/r_0, Pr, and Ste. The relative importance of these parameters will become evident from the numerical results.

Numerical Solutions

The solutions were carried out by means of an implicit finite-difference procedure. The most challenging problem that had to be faced in devising a solution methodology was the movement of the interface. After examination of various possibilities, it appeared convenient and effective to adopt the already outlined procedure which allows for a small time lag between the convective flow and heat transfer in the liquid and the melting and movement of the interface.

To elucidate the approach, suppose that at an instant of time τ_j, all the field variables (i.e., U, V, P, and θ) are known, as is the dimensionless interface position $R_i(\zeta, \tau_j)$. Then, for a small time interval $\Delta \tau = (\tau_{j+1} - \tau_j)$, the interface is regarded as fixed. For this fixed-boundary domain, the implicit finite-difference form of equations (15)–(18) is solved, subject to their boundary conditions, to yield the distributions of the field variables at time τ_{j+1}. From the distribution of θ, the values of the derivative $\partial \theta/\partial \eta$ along the interface, which are proportional to the local heat flux, can be determined. Then, by solving the interface energy balance (25), the position of the interface at time τ_{j+1} can be evaluated; that is

$$R_i(\zeta, \tau_{j+1}) = \sqrt{\frac{2R_i}{(R_i - 1)}\left(-\frac{\partial \theta}{\partial \eta}\right)\Delta \tau + R_i{}^2} \tag{26}$$

where, on the right-hand side, $R_i = R_i(\zeta, \tau_j)$.

With the determination of R_i from equation (26), all quantities, i.e., the field variables and R_i, are known at time τ_{j+1}. An identical procedure can then be employed to proceed to time τ_{j+2}, and so forth. The effective implementation of this approach requires that $\Delta \tau$ be chosen sufficiently small to avoid errors associated with the lag between the heat delivery to the interface and the resultant interface displacement.

Another feature of the solution method is the re-evaluation of the field variables subsequent to the determination of R_i from equation (26). The need for the re-evaluation stems from the fact that the relationship between a given radial position r and the transformed coordinate η changes as r_i changes (e.g., equation (9)). Thus, a fixed

point in the ζ, η grid corresponds to different physical locations at time τ_j and time τ_{j+1}. Since the present calculations were performed with a fixed array of grid points in the ζ, η plane, the field values at these grid points correspond to one set of physical locations at time τ_j and to another set of locations at τ_{j+1}.

Re-evaluation of the field variables at the grid points has to be performed to take cognizance of this change of relationship between the physical and transformed planes. The re-evaluation was carried out by interpolation at all grid points except those which correspond to the newly created melt region between $R_i(\zeta, \tau_{j+1})$ and $R_i(\zeta, \tau_j)$. In the latter, the velocities were assumed to be zero and the temperature taken to be T_{sat} (i.e., $\theta = 0$). The interpolation for the velocities was performed by first evaluating the stream function and then differentiating it at the locations of interest. This approach was employed to ensure that both overall and local mass conservation were fulfilled. To ensure energy conservation, the temperature interpolation was carried out via an enthalpy integral, the subsequent differentiation of which yielded the local value of θ.

To avoid potential computational difficulties at $\tau = 0$ (e.g., those associated with $1/(R_i - 1) \rightarrow \infty$), the solution was started by assuming the existence of a very thin melt region concentric to the tube. The value of τ corresponding to the assumed melt layer thickness was determined from the Stefan solution. Auxiliary computations were performed to ensure that the assumed layer thickness was sufficiently small so as not to affect the subsequent results.

At each time step, it is necessary to solve a set of simultaneous algebraic equations which represent the implicit finite-difference discretization of equations (15)–(18). This two-dimensional elliptic problem was dealt with using a numerical scheme which is an adaptation of that of [9]. In actuality, the elliptic finite-difference scheme described in [9] is employed there as one of the building blocks in a procedure for dealing with three-dimensional parabolic flows. From the elliptic scheme of [9], which is set forth there for Cartesian coordinates, the discretization, grid structure, and solution method have been utilized here in constructing a computer code tailored to the ζ, η coordinates of the present problem.

The finite-difference grid encompassed 12×14 nodal points for $H/r_0 = 4$ and 12×20 nodal points for $H/r_0 = 10$, respectively in the η and ζ directions. The points were uniformly distributed in η. On the other hand, the distribution along the ζ direction was skewed so as to have a greater concentration of points near the top of the domain in order to accommodate the rapid turning of the recirculating flow in that region. The time duration of the solutions extended to $\tau \sim 0.20$ to 0.25, which corresponded to a maximum value of R_i of about 3. The time step $\Delta \tau$ required for accuracy and stability depended on the Rayleigh number, the length-radius ratio, and the value of τ itself. In general, smaller values of $\Delta \tau$ were needed at higher Ra and H/r_0. The overall range of $\Delta \tau$ used in the computations extended from 0.001 to 0.01.

Results and Discussion

In selecting values of the governing parameters to be used as input to the numerical solutions, guidance was taken from thermal storage, although the results are in no way limited to that application. The first estimates of Ra, Pr, and Ste were based on the sodium nitrate-sodium hydroxide eutectic which had been used in the laboratory experiments mentioned in the Introduction. These estimates gave Ra $\sim 7 \times 10^5$, Pr ~ 7, and Ste ~ 0.15. For a parametric study, Rayleigh numbers between 7×10^4 and 7×10^6 appeared to be relevant.

The main calculations were, therefore, carried out for Rayleigh numbers of 7×10^4, 7×10^5, and 7×10^6, with Pr = 7 and Ste = 0.15. For each of these cases, results were obtained for two length-radius ratios of the heated tube, $H/r_0 = 4$ and 10. In recognition of the higher Prandtl numbers and lower Stefan numbers that are characteristic of the liquid phase of certain phase change materials, check runs were made for Pr = 70 and for Ste = 0.05.

The heat transfer results will be presented first, followed successively by representative temperature field and flow field information and by the time evolution of the liquid-solid interface.

---

[3] At the interface, the normal component of the velocity is zero when the density change associated with the phase change is neglected, as in the present analysis.

If the rate of heat transfer at the tube surface is denoted by Q, then Q/H is the heat transfer per unit length of tube. In Fig. 2, the heat transfer per unit length, represented in dimensionless terms by $(Q/H)/k(T_w - T_{sat})$, is plotted as a function of time τ ($=$ Fo Ste), for all of the cases that were investigated. The solid and dashed lines appearing in the figure correspond respectively to length-radius ratios H/r_0 of 4 and 10. The upper, middle, and lower pairs of curves respectively portray the results for Ra $= 7 \times 10^6$, 7×10^5, and 7×10^4. For all of these cases, calculations were performed with Pr $= 7$ and Ste $= 0.15$. However, as noted in the figure, the uppermost curve corresponds to calculations made with both Pr $= 7$ and Pr $= 70$. In addition, one of the middle curves represents the solutions for both Ste $= 0.15$ and 0.05.

Inspection of the figure reveals a complex variation of the heat transfer with time which requires careful consideration. However, one fact is immediately evident, namely, that the heat transfer results are drastically different from the one for pure conduction phase change, which is characterized by a monotonic decrease with time. Clearly, another transport mode, natural convection, is playing a first order role.

Within the time scale of the figure, a greater number of events in the time history of the heat transfer are in evidence at higher Rayleigh numbers. From the curves for Ra $= 7 \times 10^6$, it is seen that the heat transfer first decreases and attains a minimum, then increases and achieves a maximum, and subsequently decreases. At lower Rayleigh numbers, the occurrence of these events is shifted to larger and larger times, so that the maximum and the subsequent decrease are not seen in the figure.

These events in the time history of the heat transfer can be tied to certain physical processes which will be mentioned briefly here and illustrated later via the temperature and fluid flow results. At early times, the natural convection, although present, is very weak, so that conduction is the dominant transport mode and, as a consequence, the heat transfer decreases with time. As the melt layer thickens, natural convection grows stronger, thereby arresting the decrease in heat transfer. The further strengthening of the natural convection causes the heat transfer to increase. During this period, heat is transported by the recirculating natural convection flow as well as directly across the melt layer.

When the melt layer becomes sufficiently thick, boundary layers are respectively established adjacent to the tube wall and adjacent to the interface. As a result, heat is no longer transported directly across the melt layer, but is carried from the tube wall to the interface only by the recirculating flow. In addition, the growing resistance encountered by the recirculating flow along the top and bottom walls (primarily the former) tends to impede the fluid motion. It is believed that these factors are responsible for the decrease in heat transfer at large times that is evident from the curves for Ra $= 7 \times 10^6$.

In general, the heat transfer per unit length appears to be greater at higher Rayleigh numbers and for shorter heating tubes. However, owing to the different paces of the various time histories, there is some crossing of the curves which locally invalidates these general trends.
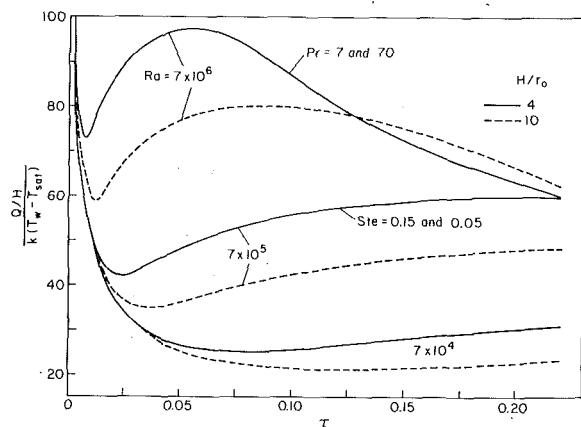
Fig. 2 also shows that when the Rayleigh number is used to characterize the natural convection effects, the results do not depend on the Prandtl number for the range investigated (Pr $= 7$–70). Furthermore, it is evident from equations (16)–(18) that if Pr has no effect for this range, it will not have an effect for any Pr ≥ 7. On the other hand, had the Grashof number (Ra/Pr) been used, then a Prandtl number dependence would have been encountered.

It is also seen from Fig. 2 and equations (16)–(18) that the involvement of the Stefan number in the dimensionless time variable τ eliminates the dependence of the results on Ste in the range from 0 to 0.15. In view of these findings, both the Prandtl number and the Stefan number can be eliminated from the list of active parameters in the aforementioned ranges. At higher values of Ste, a parametric dependence of the results on the Stefan number may be anticipated.

Attention will now be turned to illustrating representative types of temperature distributions that exist in the melt layer at various stages in its time history. Fig. 3 has been prepared for this purpose. The figure consists of three panels. In each panel, radial temperature profiles spanning the melt layer are plotted at four axial stations, $z/H = 0.15$, 0.45, 0.70, and 0.93. The Rayleigh number and the time τ that characterize the profiles in each panel are indicated therein, and $H/r_0 = 4$.

The results in the left-hand panel are representative of early times, when the influence of natural convection is small. The dashed lines plotted in the figure represent the logarithmic temperature distribution for steady state, one-dimensional radial conduction. The solid and dashed lines are nearly coincident, thereby not only confirming the dominance of the conduction mode, but also indicating a negligible effect of transient energy accumulation in the fluid.

The middle panel is intended to illustrate a temperature field which is strongly affected by natural convection, but where the boundary layer regime has not yet been established. In the panel at the right, the boundary layer regime is clearly in evidence. The temperature is uniform across most of the thickness of the melt layer, with sharp

Fig. 2 Timewise variation of the tube heat transfer rate
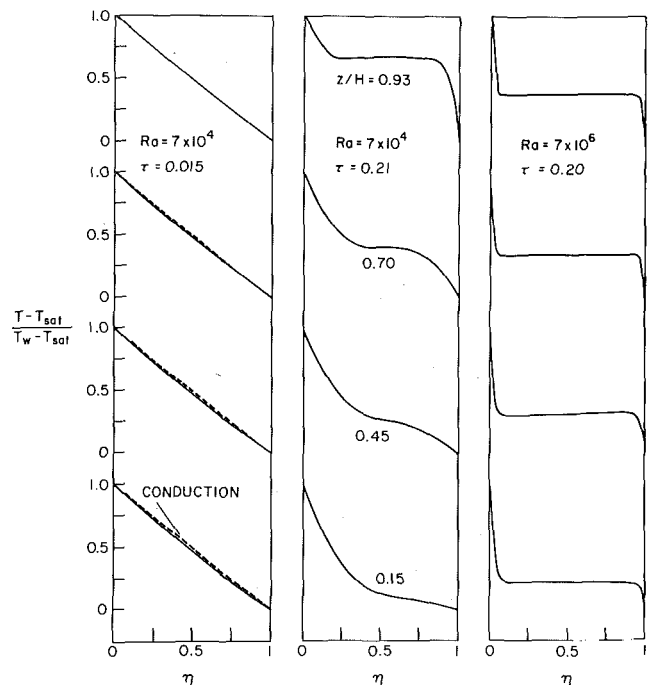
Fig. 3 Representative temperature profiles ($H/r_0 = 4$)

gradients adjacent to the tube wall and the liquid-solid interface.

The nature of the velocity field and the natural convection recirculation can be well illustrated by streamline maps, and three representative flow patterns are shown in Fig. 4. Each diagram is an r,z plane encompassing the melt region. For all cases, the general characteristic of the flow pattern is an upflow adjacent to the heated tube and a downflow adjacent to the liquid-solid interface.

The diagram at the left is representative of early times, and the trace of the melt layer in the r,z plane is nearly rectangular. Although conduction dominates, a natural convection flow definitely exists. The flow pattern that typifies most of the time history of the melt layer is illustrated by the middle diagram. There is a single recirculation zone that is centered in the upper portion of the melt region, where the melt layer thickness is greatest. The three-eddy array shown in the right-hand diagram was encountered only for the longer melt layer (i.e., $H/r_0 = 10$) and only at times corresponding to the neighborhood of the heat transfer maximum (Fig. 2).

The streamline diagrams indicate that the radial extent of the melt layer varies along the length of the heating tube, with the smallest layer thickness at the bottom and the greatest layer thickness at the top. This is in contrast to the melt layer of uniform thickness that would be predicted by an analysis in which conduction is the only mode of transport.

A more complete presentation of melt layer thicknesses and interface shapes is provided by Figs. 5 and 6, respectively for $H/r_0 = 4$ and 10. Each figure contains two panels, corresponding respectively to Ra = 7×10^4 and 7×10^6. Each panel is an r,z plane in which the heating tube encompasses the region $0 \leq r/r_0 < 1$ and the phase change material occupies the space $r/r_0 > 1$. The sequence of curves represent the successive positions of the interface at the times indicated in the figure.

The nonuniformity of the melt layer thickness that was in evidence in the streamline diagrams is confirmed by Figs. 5 and 6. In addition, these figures indicate that the interface shape and its evolution are affected markedly by the Rayleigh number and, to a lesser extent, by the length-radius ratio. At high Rayleigh numbers, the interface slopes gradually outward, with the slope being more or less uniform. On the other hand, at low Rayleigh numbers, the interface tends to lie parallel to the tube for a substantial length starting at the bottom and proceeding upward. Near the top of the region, the interfaces flare out. From these results, it is evident that at lower Rayleigh numbers, significant natural convection motions are confined to the uppermost portion of the melt region; at higher Rayleigh numbers, significant flows also occur in the lower portion of the melt. In the limit as Rayleigh number approaches zero, the interface will be vertical since natural convection vanishes and conduction is the sole transport mechanism.

Figs. 5 and 6 enable an assessment to be made of the conditions under which the interface slope $\partial r_i/\partial z$ is small, as assumed in the analysis. At high Rayleigh numbers, and especially at large H/r_0, the slopes are small to moderate. For lower Rayleigh numbers, the interface slope is small along most of the length, but may be quite large near the very top of the melt region. It is here that some deviations of the computed results from reality are to be expected, but the qualitative trends should not be affected.
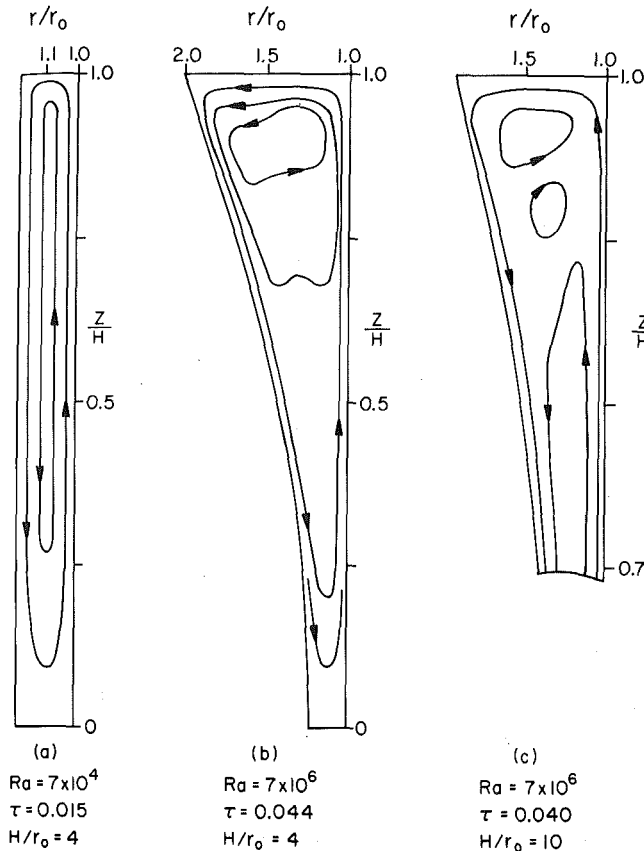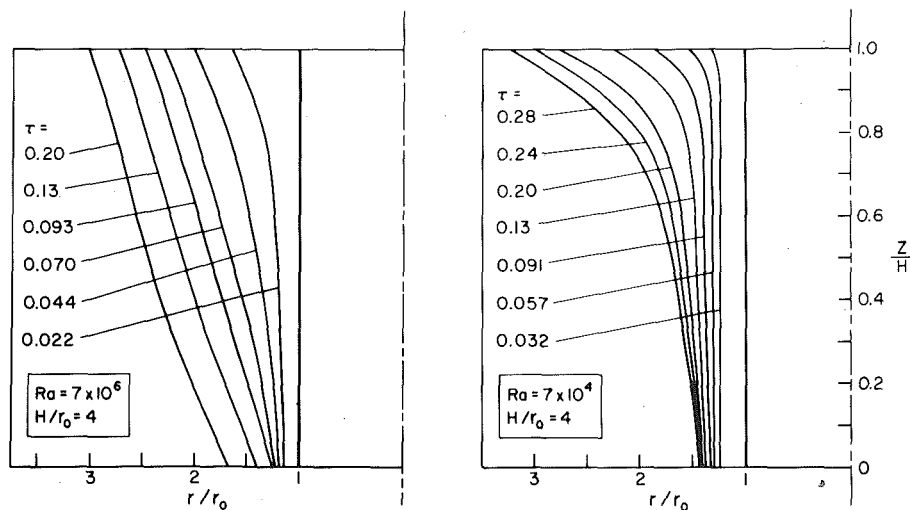

Fig. 4   Representative flow patterns

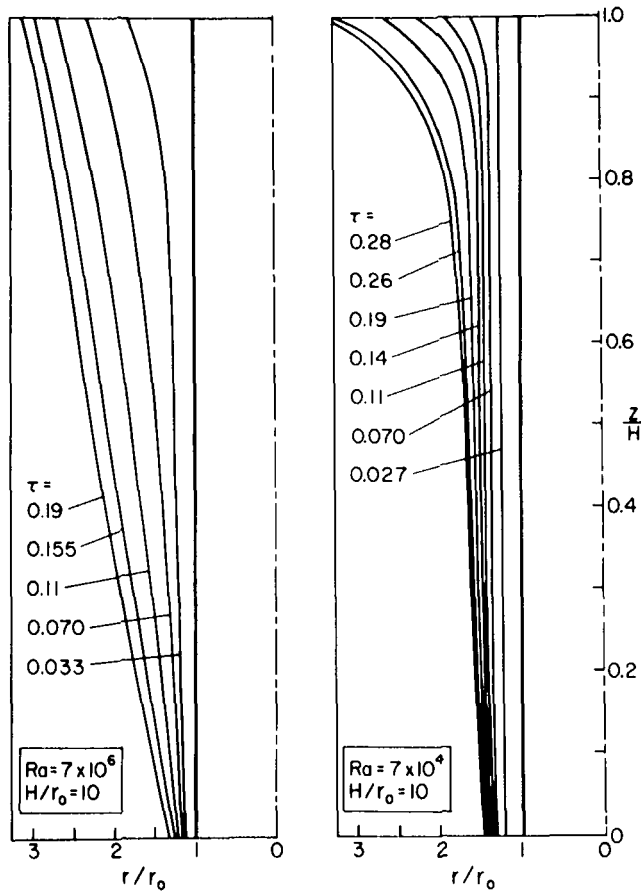Fig. 5   Melt layer thicknesses and interface shapes, $H/r_0 = 4$

Journal of Heat Transfer

Fig. 6 Melt layer thicknesses and interface shapes, $H/r_0 = 10$

Concluding Remarks

In contrast to the conventional conduction-based treatment of solid-liquid phase change, the present analysis has taken account of natural convection induced by temperature differences in the liquid melt. The analysis was performed for melting of a solid due to heat supplied by a vertical finite-length tube embedded in it. Initially, no liquid is present, and the solid, which is at its fusion temperature, is in contact with the tube. At subsequent times, the tube temperature is maintained at a uniform value that exceeds the fusion temperature, and the progressive melting of the solid gives rise to a melt region which grows larger as time passes.

Solutions were obtained by an implicit finite-difference procedure tailored to take account of the movement of the solid-liquid interface.

The calculated heat transfer rates at the tube wall were found to differ markedly from the monotonic timewise decrease that is characteristic of pure conduction phase change. Rather, the heat transfer decreased at early times and attained a minimum, then increased and achieved a maximum, and subsequently decreased. The times at which these events occurred were markedly affected by the Rayleigh number. At lower Rayleigh numbers, the pace of the timewise heat transfer variations was much slower than at higher Rayleigh numbers. The events in the time history can be tied to physical processes which were illustrated by temperature and velocity field information presented in the paper.

Another indication of the marked departures from the pure conduction model can be found in the shape of the melt region. For conduction, the thickness of the melt region is uniform along the entire length of the heating tube. On the other hand, in the presence of natural convection, the thickness of the melt layer varies along the length, with the smallest layer thickness at the bottom and the greatest layer thickness at the top.

These findings indicate that natural convection effects, although unaccounted for in most phase change analyses, are of first order importance and have to be considered.

Acknowledgment

References

1 Kroeger, P. G., and Ostrach, S., "The Solution of a Two-Dimensional Freezing Problem Including Convection Effects in the Liquid Region," *International Journal of Heat and Mass Transfer*, Vol. 17, 1974, pp. 1191–1207.

2 Seki, N., Fukusako, S., and Sugawara, M., "A Criterion of Onset of Free Convection in a Horizontal Melted Water Layer with a Free Surface," JOURNAL OF HEAT TRANSFER, TRANS. ASME, Series C, Vol. 99, 1977, pp. 92–98.

3 Vanier, C. R., and Tien, C., "Free Convection Melting of Ice Spheres," *AIChE Journal*, Vol. 16, 1970, pp. 76–82.

4 Szekeley, J., and Stanek, V., "Natural Convection Transients and Their Effects on Unidirectional Solidification," *Metallurgical Trans.*, Vol. 1, 1970, pp. 2243–2251.

5 Szekeley, J., and Chhabra, P. S., "The Effect of Natural Convection on the Shape and Movement of the Melt-Solid Interface in the Controlled Solidification of Lead," *Metallurgical Trans.*, Vol. 1, 1970, pp. 1195–1203.

6 Chiesa, F. M., and Guthrie, R. I. L., "Natural Convective Heat Transfer Rates During the Solidification and Melting of Metal and Alloy Systems," JOURNAL OF HEAT TRANSFER, TRANS. ASME, Series C, Vol. 96, 1974, pp. 377–384.

7 Cole, G. S., "Temperature Measurement and Fluid Flow Distributions Ahead of Solid-Liquid Interface," *Trans. AIME*, Vol. 239, 1967, pp. 1287–1295.

8 Heertjes, P. M., Jongenelen, J. A., and deLeeuw den Bouter, J. A., "The Effects of a Moving Boundary on Heat Transfer by Free Convection," *Chemical Engineering Science*, Vol. 25, 1970, pp. 1881–1890.

9 Patankar, S. V., and Spalding, D. B., "A Calculation Procedure for Heat, Mass, and Momentum Transfer in Three-Dimensional Parabolic Flows," *International Journal of Heat and Mass Transfer*, Vol. 15, 1972, pp. 1787–1806.

M. Epstein

Argonne National Laboratory, Reactor Analysis and Safety Division, Argonne, Ill.

Stability of a Submerged Frozen Crust

Consideration is given to the stability of a thin frozen crust of infinite extent growing between two different fluid materials. A linear, inviscid stability analysis is employed to obtain an estimate for the crust breakup time. The stability formulation parallels that of Rayleigh and Kelvin for the generation of waves at the plane interface between two different fluids and is used to develop formulas defining necessary conditions for frozen crust breakup. An approximate crust breakup criterion is proposed, viz, that the crust growth (or crystallization) time exceed the crust breakup time. The criterion shows reasonable agreement with experimental observations of the stability of a growing frozen crust in a gravity field alone (Rayleigh instability).

1 Introduction

A description of the heat-transfer characteristics between a molten ceramic fuel pool and its lower solid steel boundary is of interest in current fast breeder reactor accident analysis [1].[1] When the molten ceramic fuel (UO_2 or ThO_2) comes into contact with the solid steel boundary, as it must do, fuel crust growth begins. The underlying steel wall will melt upon contact with the molten fuel if the initial temperature of the steel is sufficiently high [2] (i.e., $\gtrsim 800°C$) and, therefore, the fuel crust becomes submerged in a fuel-steel melt. It seems likely that the fate of the crust depends on a race between the fuel crust growth process and the rate of development of buoyancy forces due to the presence of the underlying lighter steel melt. Thus, slow crust growth should lead to a thin, weak crust which becomes laterally unstable through sidewise buckling (oscillation), whereas rapid crust freezing will lead to a stable crust.

The motion of a frozen crust under buoyancy—or flow-induced excitation is similar to that at the plane interface between two different fluids, as studied by Rayleigh and Kelvin, respectively (see, e.g., [3]). In the fluid interface problem, consideration of capillarity effects alone leads to a minimum size interface wave (wavelength) below which no unstable waves are generated. Similarly, we anticipate that the presence of elasticity within a thin frozen crust stabilizes short crust wavelength perturbations. In this instance, the crust stability problem is closely related to the analysis of the stability of an infinitely long, infinitely wide plate exposed to a gas flow, as treated by Miles [4].

The analyses referenced in the foregoing are necessarily quite im-

precise. It is understandable that phenomena so complex as finite-amplitude crust wave development cannot be analyzed accurately. Moreover, the analyses do not take into account various phenomena, such as the variation of crust thickness with time, turbulence in the fluid flow, or temperature stresses within the crust, which certainly will modify the results quantitatively and some of which might produce crust disintegration in the absence of the Rayleigh or Kelvin mechanisms. There may be some ways to account for some of these phenomena; e.g., the rate of crust growth may be included formally in the differential equations that describe the instability, although at the expense of greatly increased complexity. For the purpose of obtaining a rough estimate of the conditions for frozen crust breakup, it seems best to avoid imposing further complications on existing stability theories and instead to attempt to combine the relevant theories developed in [3, 4] to obtain as simple a representation as is possible.

Accordingly, in this paper, an analysis of the instability of a submerged frozen crust of constant thickness is made on the basis of linearized flow theory. The formulation includes the effects of gravity along with both surface tension at the crust surface and elastic forces within the crust acting to stabilize the motion. Equations are derived for the breakup time of the frozen crust. A breakup criterion is proposed for a growing crust and explicit formulas providing rough estimates of critical breakup conditions are developed. Comparison of the criterion with experimental results proves favorable.

2 Physical Model

Fig. 1 represents a schematic illustration of a growing, submerged frozen crust. A fluid (material 1) occupying the space $y > 0$ flows with constant velocity U_1 in the x-direction. A layer of liquid (material 2) of depth h flows with constant velocity U_2 through the space $0 < y < -h$. A thin frozen layer (material 1 or material 2) of instantaneous thickness δ separates the flowing fluids. Several different physical processes can lead to the situation depicted in Fig. 1. For example,
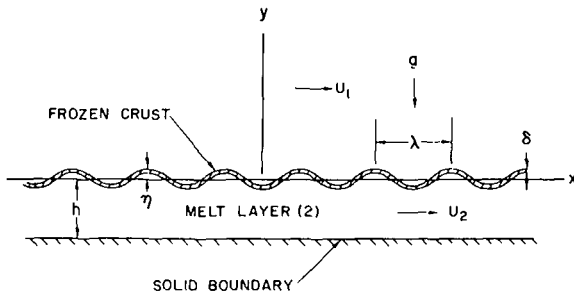

Fig. 1 Schematic of frozen layer stability model

a hot liquid may be suddenly poured over a relatively cold solid. As a result of simultaneous freezing of the liquid and melting of the solid, a crystallization front moves upward into material 1 and a melt wave moves downward into initially solid material 2. These conditions approximate the situation at the bottom of a UO_2 fuel pool [1]. If the lower material is initially cold liquid, then $h \rightarrow \infty$. On the other hand, if a cold fluid flows over a liquid surface ($h = \infty$), a crust wave moves downward into initially liquid material 2.

It is obvious that the variation of crust thickness with time plays a role in the instability analysis, and it is also obvious that a solution of the hydrodynamic equations with crust growth effects determined simultaneously is not readily obtained. Moreover, in view of the other uncertainties discussed at the end of Section 1, such an analysis is probably not justified. A rough crust breakup criterion can be obtained by first considering a linearized stability theory applicable to a crust of constant thickness. Then one could estimate a crust breakup time, τ, which depends on the crust thickness. The crust growth time, τ_f, is obtained independently from conduction theory and is set equal to τ to obtain both the frozen crust thickness at the onset of instability and the breakup criterion. This approximation is described in more detail in Section 4.

We denote by η the displacement of the frozen layer from the position of equilibrium in the plane $y = 0$ and consider the stability of a crust of constant thickness subject to the following set of simplifying assumptions:

1　The fluids are assumed to be inviscid and incompressible.

2　The displacements of the frozen layer are small so that the equations of the bending theory of beams (or plates) are applicable to the frozen layer and the fluids behave according to linearized flow theory.

3　The frozen layer is sufficiently thin so that, as far as the fluid motion is concerned, it can be treated as an interface having zero thickness and negligible inertia. The frozen layer is wide enough to preclude edge effects.

4　Thermal bending and temperature stresses are not taken into account.

5　The frozen layer is deflected and set in two-dimensional motion according to the infinitesimal disturbance

$$\eta = \eta_0 e^{ikx + nt} \qquad (1)$$

where k is the wave number and $2\pi/k$ is the wavelength λ of the disturbance.

Miles[4] analyzed a similar stability problem, but his application concerned the flow of a compressible gas over a thin panel, and so he did not include the effects of gravity nor hydrostatic pressure.

Assumptions 1–3 have been discussed extensively in the literature [3, 4] and it can be shown that their validity is assured in all cases of interest here. A temperature variation ΔT exists through the crust thickness δ. If the crust is allowed to expand freely, due to temperature change, and if the temperature distribution is approximately linear, the growing crust, in the absence of fluid motion, forms an arc of a circle with all the stress components identically zero throughout the crust. This leads us to expect negligible thermal bending effects when the ratio of the crust wave λ to the curvature of the crust R is small: $\lambda/R = \lambda \alpha_\ell \Delta T/(2\delta) \ll 1$, where α_ℓ is the coefficient of thermal expansion of the crust. From the results of the analysis, it is found that thermal bending effects, for example, are negligible for an ice crust but are not negligible for a solid UO_2 layer on molten steel. While assumption 4 cannot be justified for some material pairs, it is felt that the insights gained regarding the model amply justify our preliminary study of the initially flat frozen crust. If the crust is not allowed to expand freely, thermal bending and temperature stresses will have to be taken into account. It is then necessary to divide the solution into two parts. The first part is the solution of the problem of the stress and thermal bending of the crust and the second is the solution of oscillations of the bent crust. The principal complications foreseen are the unknown boundary-support conditions of the crust and the buckling that can occur when the frozen crust fails under the action of a load parallel to its plane. Such an analysis is not attempted herein.

3　Equations of Motion

The theoretical considerations presented in this section will refer only to a crust of constant thickness; the connection with a growing

---

Nomenclature

A = unknown coefficient; equations (14) and (15)

d = vessel diameter

D = crust stiffness; equation (8)

E = elastic modulus of frozen layer

g = acceleration due to gravity

h = depth of lower fluid (material 2); Fig. 1

i = imaginary unit in the complex number system

k = wave number of small disturbance; equation (1)

k_c = cutoff wave number

k_p = most probable wave number

L = heat of fusion of growing crust

n = growth constant of small disturbance; equation (1)

P = pressure

t = time

u = small-disturbance velocity in x-direction

U = flow velocity; Fig. 1

v = small-disturbance velocity in y-direction

x = coordinate parallel to the undisturbed crust plane; Fig. 1

y = transverse coordinate measured from crust; Fig. 1

α = thermal diffusivity of frozen crust

α_ℓ = coefficient of thermal expansion of frozen crust

α_m = thermal diffusivity of melting solid (material 2)

δ = thickness of frozen layer; Fig. 1

ϵ = Poisson's ratio for frozen layer

η = amplitude of frozen crust waves at time t; equation (1)

η_0 = original small-disturbance amplitude; equation (1)

λ = wavelength of small disturbance; $\lambda = 2\pi/k$

λ_c = cutoff wavelength

λ_p = most probable wavelength

ρ = density

σ = average interfacial tension; $\sigma = (\sigma_1 + \sigma_2)/2$

σ_1 = interfacial tension between fluid material 1 (upper fluid) and frozen crust

σ_2 = interfacial tension between fluid material 2 (lower fluid) and frozen crust

τ = growth time of unstable crust wave; equation (28)

τ_f = time for crust growth; equation (32)

ϕ = velocity potential; equation (10)

χ = growth constant for crystallization; equation (31)

χ_m = growth constant for melting; equation (38)

Subscripts

1 = upper fluid (material 1); Fig. 1

2 = lower fluid (material 2); Fig. 1

---

crust will be made in Section 4.

Subject to assumptions 1–5, the linearized hydrodynamic equations for each of the two fluid regions shown in Fig. 1 are of the form

$$\frac{\partial u}{\partial x} + \frac{\partial v}{\partial y} = 0 \tag{2}$$

$$\frac{\partial u}{\partial t} + U \frac{\partial u}{\partial x} = -\frac{1}{\rho}\frac{\partial P}{\partial x} \tag{3}$$

$$\frac{\partial v}{\partial t} + U \frac{\partial v}{\partial x} = -\frac{1}{\rho}\frac{\partial P}{\partial y} - g \tag{4}$$

and are connected through the following compatibility (matching) conditions at the frozen crust "interface" located at $y = \eta(x, t)$:

$$D \frac{\partial^4 \eta}{\partial x^4} - 2\sigma \frac{\partial^2 \eta}{\partial x^2} = P_2 - P_1 \tag{5}$$

$$v_1(x, \eta, t) = \frac{\partial \eta}{\partial t} + U_1 \frac{\partial \eta}{\partial x} \tag{6}$$

$$v_2(x, \eta, t) = \frac{\partial \eta}{\partial t} + U_2 \frac{\partial \eta}{\partial x} \tag{7}$$

Equation (5) expresses the condition of continuity of pressure across the interfacial crust. The first two terms in equation (5) represent the crust elasticity and the surface tension forces at the upper and lower crust surfaces, respectively, which act to stabilize the crust. Here D is the crust stiffness given by [4].

$$D = \frac{E\delta^3}{12(1 - \epsilon^2)} \tag{8}$$

and σ is the average surface free energy (tension) for the upper and lower crust surfaces; i.e., $\sigma = (\sigma_1 + \sigma_2)/2$. Equations (6) and (7) state that the velocity of either fluid at the crust surface is made up of the velocity of the crust itself and the velocity of the fluid relative to it. Finally, equations (2)–(4) are subject to the following conditions at $y \to \infty$ and $y = -h$:

$$v_1(x, \infty, t) = 0, \qquad v_2(x, -h, t) = 0 \tag{9}$$

Equations (2)–(4) have solutions of the form [3]

$$u = U - \frac{\partial \phi}{\partial x}, \qquad v = -\frac{\partial \phi}{\partial y} \tag{10}$$

$$P = \rho \frac{\partial \phi}{\partial t} + \rho U \frac{\partial \phi}{\partial x} - \rho g y \tag{11}$$

where the velocity potential ϕ must satisfy

$$\frac{\partial^2 \phi}{\partial x^2} + \frac{\partial^2 \phi}{\partial y^2} = 0 \tag{12}$$

and the conditions

$$\frac{\partial \phi_1}{\partial y}(x, \infty, t) = 0, \qquad \frac{\partial \phi_2}{\partial y}(x, -h, t) = 0 \tag{13}$$

For the upper fluid, we assume the solution

$$\phi_1(x, y, t) = A_1 e^{-ky} e^{ikx+nt} \tag{14}$$

and for the lower fluid,

$$\phi_2(x, y, t) = A_2 \frac{\cosh[k(y+h)]}{\sinh(kh)} e^{ikx+nt} \tag{15}$$

where A_1 and A_2 are unknown constants. Note that equations (14) and (15) are consistent with boundary conditions (13). The pressure condition across the crust, equation (5), yields (see equations (1), (10), and (11))

$$D\eta_0 k^4 + 2\sigma\eta_0 k^2 = \rho_2 (n + ikU_2)A_2 \coth(kh)$$
$$- \rho_1(n + ikU_1)A_1 + (\rho_1 - \rho_2)g\eta_0 \tag{16}$$

The kinematic conditions (6) and (7) give

$$A_1 k = \eta_0(n + ikU_1), \qquad -A_2 k = \eta_0(n + ikU_2) \tag{17}$$

Eliminating A_1 and A_2 between equations (16) and (17) results in the characteristic equation for the determination of the growth constant n:

$$[\rho_1 + \rho_2 \coth(kh)]n^2 + 2ik[\rho_1 U_1$$
$$+ \rho_2 U_2 \coth(kh)]n + Dk^5 + 2\sigma k^3$$
$$- [\rho_1 U_1^2 + \rho_2 U_2^2 \coth(kh)]k^2 - g(\rho_1 - \rho_2)k = 0 \tag{18}$$

Instability prevails if the solution of equation (18) for n, regarding all other parameters as fixed, is real and positive (see equation (1)). Thus we focus attention on the real roots of equation (18) given by the expression

$$n^2 = \frac{\rho_1\rho_2(U_1 - U_2)^2 k^2 \coth(kh)}{[\rho_1 + \rho_2 \coth(kh)]^2}$$
$$- \frac{Dk^5 + 2\sigma k^3 - g(\rho_1 - \rho_2)k}{\rho_1 + \rho_2 \coth(kh)} \tag{19}$$

4 Instability in a Gravity Field (Rayleigh Instability)

Here we are concerned with crust stability in a gravity field only $(U_1 = U_2 = 0)$, when the upper fluid is more dense than the lower fluid $(\rho_1 > \rho_2)$. In the limit $D \to 0$ we recover the classical case of Rayleigh instability at the interface between two fluids.[2]

Equation (19) for the growth constant becomes

$$n^2 = \frac{g(\rho_1 - \rho_2)k - Dk^5 - 2\sigma k^3}{\rho_1 + \rho_2 \coth(kh)} \tag{20}$$

We see from equation (20) that the amplitude of the initial disturbance grows only when $n > 0$, i.e., when

$$g(\rho_1 - \rho_2)k - (Dk^5 + 2\sigma k^3) > 0 \tag{21}$$

or crust motion is stable for wave numbers larger than a "cutoff wave number," k_c, given by

$$k_c = \left[\sqrt{\left(\frac{\sigma}{D}\right)^2 + \frac{(\rho_1 - \rho_2)g}{D}} - \frac{\sigma}{D} \right]^{1/2} \tag{22}$$

When the term $(\rho_1 - \rho_2)gD/\sigma^2 \ll 1$, crust elasticity limitations to the instability will be negligible. In such cases the crust behaves like a membrane with only the presence of surface energy to remove the instability. Equation (22) leads us to expect membrane behavior when

---

[2] The theoretical treatment of this problem is usually attributed to Taylor [5] although in fact the problem was treated earlier by Lord Rayleigh [6].
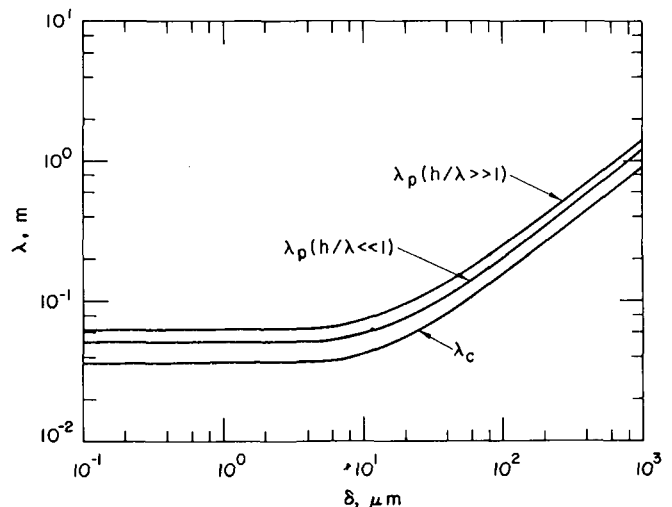
Fig. 2 Variation of the cutoff wavelength and the most probable wavelengths (for steel melt layers of infinite and finite depth) with respect to UO2 frozen layer thickness in a gravity field

the crust thickness [see equation (8)]

$$\delta \ll \left[\frac{12(1-\epsilon^2)\sigma^2}{Eg(\rho_1-\rho_2)} \right]^{1/3} \qquad (23)$$

Let us consider UO_2 crust growth on a layer of melting steel. A rough value for σ_1, the interfacial tension between molten UO_2 and solid UO_2, can be obtained from the proportion $\sigma_1 L_v = \sigma_{\ell v} L_f$ suggested by Volmer [7], where L_v is the latent heat of vaporization, L_f is the latent heat of fusion, and $\sigma_{\ell v}$ the surface tension of the liquid in contact with its vapor. For UO_2, $\sigma_{\ell v} \sim 500$ dyne cm^{-1}, $L_v \sim 460$ cal g^{-1}, and $L_f \sim 67$ cal g^{-1}, so that $\sigma_1 \sim 73$ dyne cm^{-1}. If the interfacial tension between molten steel and solid UO_2, σ_2, is taken to be comparable to the corresponding interfacial tension between molten copper and solid UO_2 [8], then, we estimate $\sigma_2 \sim 530$ dyne cm^{-1}, and $\sigma = (\sigma_1 + \sigma_2)/2 \sim 300$ dyne cm^{-1}. Accordingly, with $E \simeq 0.8(10^{12})$ dyne cm^{-2} and $\epsilon \simeq 0.3$ for solid UO_2 [9], and with $\rho_1 - \rho_2 \simeq 8.4 - 6.6 = 1.8$ g cm^{-3}, membrane-like fuel crust behavior will be evident for crust thickness $\delta \ll 8.9$ μm.

The amplitude of the disturbance grows most rapidly when the wave number k in equation (20) is such that n, or n^2, is a maximum; i.e., $dn^2/dk = 0$. At this "most probable wave number," k_p, we have

$$g(\rho_1-\rho_2) - (5Dk^4 + 6\sigma k^2)$$
$$= \frac{\rho_2 h[1 - \coth^2(kh)]}{\rho_1 + \rho_2 \coth(kh)} [g(\rho_1-\rho_2)k - (Dk^5 + 2\sigma k^3)] \quad (24)$$

In the general case, this equation is complex and cannot be solved analytically. We confine our analysis here to the two limiting cases: shallow lower liquid layers and deep lower liquid layers. When kh is small; i.e., the depth of the lower liquid is small compared with the wavelength of the disturbance, we find $\coth(kh) = 1/(kh)$, and equation (24) simplifies to

$$3Dk^4 + 4\sigma k^2 - g(\rho_1-\rho_2) = 0 \qquad (25)$$

from which the most probable wave number is obtained:

$$k_p = \left[\sqrt{\left(\frac{2}{3}\frac{\sigma}{D}\right)^2 + \frac{(\rho_1-\rho_2)g}{3D}} - \frac{2}{3}\frac{\sigma}{D} \right]^{1/2}; \qquad k_p h \ll 1 \quad (26)$$

If in equation (24) $kh \gg 1$; i.e., the depth of the melt layer is great compared with the wavelength, we find

$$k_p = \left[\sqrt{\left(\frac{3\sigma}{5D}\right)^2 + \frac{(\rho_1-\rho_2)g}{5D}} - \frac{3\sigma}{5D} \right]^{1/2}; \qquad k_p h \gg 1 \quad (27)$$

The cutoff wavelength, equation (22), and the most probable wavelengths, equations (26) and (27), are plotted as a function of crust thickness in Fig. 2 for a UO_2 crust on molten steel. For all wavelengths below the λ_c curve, there is no instability. The curves are independent of crust thickness when the interfacial tension term dominates the crust rigidity term (i.e., when $\delta \rightarrow 0$). On the other hand, when $\delta \rightarrow \infty$, crust rigidity preponderates, and equations (22), (26), or (27) reveal $\lambda \propto \delta^{3/4}$. It is noteworthy that the two λ_p curves for thin and thick steel melt layers are remarkably close to one another indicating the small effect the numerical value of h has on the most probable wavelength.

The growth time for an unstable crust wave or the breakup period of the crust is of the order of $1/n$ [10]. That is, during a time interval

$$\tau = \frac{1}{n(k_p)} \qquad (28)$$

the amplitude of the most probable wavelength increases e times (see equation (1)).[3] Again we consider the limiting case $kh \ll 1$, and from equations (20), (26), and (28) we obtain

---

[3] Levich [10] maintains that the period of fragmentation of a liquid jet is given by formula (28). This expression has also been used to estimate the bubble departure frequency in the hydrodynamic theory of boiling heat transfer [11].
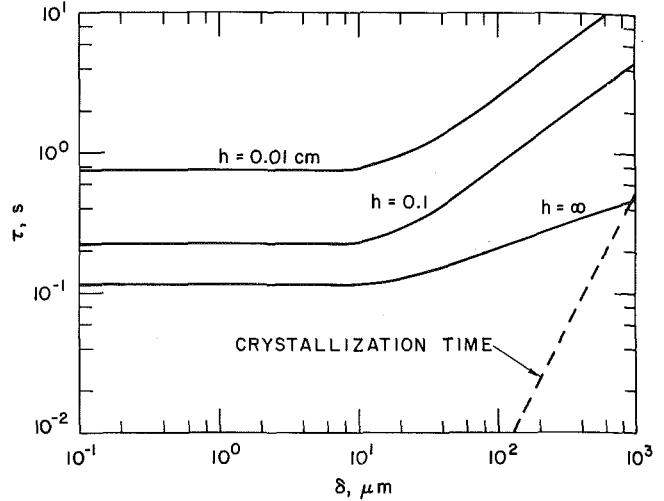
Fig. 3   Time for unstable wave growth versus UO_2 frozen layer thickness (for steel melt layers of infinite and finite depth) in a gravity field

$$\tau = \left[\frac{3\rho_2}{2hk_p^2[g(\rho_1-\rho_2) - \sigma k_p^2]} \right]^{1/2}; \qquad k_p h \ll 1 \quad (29)$$

where k_p is given by equation (26). If on the other hand we make kh large, we find

$$\tau = \left[\frac{5(\rho_1+\rho_2)}{4k_p[g(\rho_1-\rho_2) - \sigma k_p^2]} \right]^{1/2}; \qquad k_p h \gg 1 \quad (30)$$

where k_p is given by equation (27). The time, τ, it takes for the instability to develop as a function of the UO_2 fuel crust thickness is shown in Fig. 3 for selected values of the thickness of the lower steel melt layer. These values should be compared with the crust growth time. Conduction theory predicts the familiar square root crust growth law:

$$\delta = 2\chi\sqrt{\alpha t} \qquad (31)$$

where χ, the "growth constant" is a function of the physical properties and initial temperatures of the upper and lower fluid materials. Clearly, the characteristic time, τ_f, for crust growth is

$$\tau_f = \frac{\delta^2}{4\chi^2\alpha} \qquad (32)$$

This time is also plotted in Fig. 3 (dashed curve). The time for UO_2 crust growth on melting steel τ_f is completely negligible on the scale of the time for the growth of the most unstable wave for crust thicknesses below about 0.03 cm.

The two characteristic times, τ and τ_f are seen to be comparable when the effects of surface tension may be neglected (see Fig. 3). In this limit of large δ, we find the simple asymptotic behavior (see equations (8), (26), (27), (29), and (30))

$$\tau = \left[\frac{3\rho_2}{2gh(\rho_1-\rho_2)} \right]^{1/2} \left[\frac{3E\delta^3}{12(1-\epsilon^2)g(\rho_1-\rho_2)} \right]^{1/4} \qquad (33)$$

for $k_p h \ll 1$ and

$$\tau = \left[\frac{5}{4g}\left(\frac{\rho_1+\rho_2}{\rho_1-\rho_2}\right) \right]^{1/2} \left[\frac{5E\delta^3}{12(1-\epsilon^2)g(\rho_1-\rho_2)} \right]^{1/8} \qquad (34)$$

for $k_p h \gg 1$. The foregoing results are not directly applicable to a crust growing between two different fluid materials. Clearly, the variation of crust thickness with time plays a role in the instability phenomena. We should expect, nevertheless, that the assumption

$$\tau = \tau_f \qquad (35)$$

should furnish an approximation of the right order of magnitude for the crust thickness at the onset of instability. Recall that τ is the time it takes for the most unstable crust wave to develop for a particular

constant crust thickness δ. Clearly, if the time τ_f for the crust to grow through this thickness is small compared with τ the instability will not have sufficient time to develop. On the other hand, we do not expect a stable crust to grow to a thickness such that $\tau_f \gg \tau$. These two requirements imply that the crust thickness at the onset of instability is that corresponding approximately to the singular case $\tau = \tau_f$ [criterion (35)]. Considering the rough nature of the criterion, the hope that it might coincide directly with experimental data would appear vain. Qualitatively, however, we will see below that it gives an accurate picture.

Using equation (32) in equations (33) and (34) to obtain δ and substituting the results in equation (22), yields the approximations for the cutoff wavelength at the onset of crust instability:

$$\lambda_c = 7.11 \left[\frac{\chi^4 \alpha^2 \rho_2}{hg(\rho_1 - \rho_2)} \right]^{3/10} \left[\frac{E}{(1-\epsilon^2)g(\rho_1 - \rho_2)} \right]^{2/5};$$
$$k_c h \ll 1 \quad (36)$$

$$\lambda_c = 6.41 \left[\frac{\chi^4 \alpha^2}{g} \left(\frac{\rho_1 + \rho_2}{\rho_1 - \rho_2} \right) \right]^{3/13} \left[\frac{E}{(1-\epsilon^2)g(\rho_1 - \rho_2)} \right]^{4/13};$$
$$k_c h \gg 1 \quad (37)$$

For a crust growing on a melting solid we have from conduction theory

$$h = 2\chi_m \sqrt{\alpha_m t} \quad (38)$$

where χ_m is the melting constant and, like the growth constant χ, is strictly a function of the physical properties and initial temperatures of the upper and lower materials.[4] In this case the crust breakup criterion is $\tau = \tau_f = \tau_m$ where $\tau_m = h^2/(4\chi_m^2 \alpha_m)$ is the characteristic time for melting. In most cases of interest the characteristic times are

---

[4] The exact solution for the transient temperature field and the progress of the phase transformation fronts on both sides of an interface separating two semi-infinite regions can be found in reference [2]. This solution was used here to evaluate the constants χ and χ_m.

comparable when $k_p h \ll 1$. Thus, from equations (22), (31), and (33) we have the cutoff wavelength for the instability of a crust growing on a melting solid, viz

$$\lambda_c = 5.61 \left[\frac{\chi^5 \alpha^2 \rho_2}{\chi_m (\alpha_m/\alpha)^{1/2} g(\rho_1 - \rho_2)} \right]^{3/14} \left[\frac{E}{(1-\epsilon^2)g(\rho_1 - \rho_2)} \right]^{5/14}$$
$$(39)$$

The cutoff wavelength in equations (36), (37), and (39) can be interpreted as the critical wavelength for crust breakup. If the upper and lower materials are included between two parallel vertical walls, this imposes an upper limit to the admissible wavelength. Equation (39) predicts that UO_2 crust instability on melting steel must manifest itself by the formation of crust waves that exceed ~2.0 m in length. These waves are sufficiently long compared with molten UO_2 pool (reactor core) geometry to ensure the stability of the frozen UO_2 crust.

5 Experimental Results

It is of interest to compare the predictions of equations (36), (37), and (39) with experiment. A series of simple experiments were performed in which a relatively hot, heavy liquid was suddenly poured over a column of lighter cold material (liquid or solid). The lower liquid was placed in a glass test vessel. If a lower material in solid form was desired, the liquid was frozen in place at the bottom of the test vessel. The upper liquid was first placed in a pouring vessel. The test was initiated by tipping the pouring vessel, allowing liquid to impact and spread over the surface of the lower material. The liquid was poured rapidly enough to ensure that the rate of accumulation of the upper liquid (layer) exceeded the rate of phase conversion at the lower material-upper liquid interface. The initial temperature of the upper liquid was just above its melting point so that forced convection heat transfer was negligible over the duration of the experiment.

The experimental observations of the mechanical stability of the crust growing into the upper liquid along with crust stability predictions are reported in Table 1. In experiment 1, liquid Freon Fluoro-

Table 1   Results of crust-stability experiments

Expt	Material Pair (Upper) (Lower)	Melting Point, °C	Specific Gravity	Physical State and Temp, °C	Vessel Diameter d, cm	Cutoff Wavelength λ_c, cm	Crust-stability Theory	Observation[a]
1	Freon-112A H$_2$O	40 0	1.6 1.0	Liquid, 50 Liquid, 20	7	6[b]	Marginal $\lambda_c \sim d$	Stable
2	Lead Gallium	327 30	11.70 6.0	Liquid, 335 Solid, -20	7	280	Stable $\lambda_c \gg d$	Stable
3	H$_2$O C$_8$H$_{18}$	0 -57	1.0 0.7	Liquid, 2 Liquid, -30	7	3	Unstable $\lambda_c < d$	Unstable
4	" "	" "	" "	Liquid, 2 Liquid, -55	7	6	Marginal $\lambda_c \sim d$	Unstable
5	" "	" "	" "	" "	3	6	Stable $\lambda_c > d$	Stable[c]
6	" "	" "	" "	Liquid, 2 Solid, -78	7	16	Stable $\lambda_c \sim d$	Stable
7	" "	" "	" "	" "	15	16	Marginal $\lambda_c \sim d$	Stable
8	" "	" "	" "	" "	30	16	Unstable $\lambda_c < d$	Stable

[a] The crust was pronounced stable if it prevented most of the lower liquid or melt from rising to the surface of the upper liquid. Occasionally a small amount of lower liquid material was observed to escape from beneath the crust through small openings that formed between the vessel wall and the crust edge.

[b] The elastic constants of solid Freon Fluorocarbon 112A were taken to be comparable to those of other ethylene-type molecules for which such properties are available; in particular E = 400 MPa and ϵ = 0.4 for polytetrafluorethylene were chosen.

[c] A relatively thick continuous ice layer containing trapped octane droplets was observed.

carbon 112A($\sim$50°C) was poured over water at $\sim$20°C in a 7-cm diam vessel (see Fig. 4). The Freon 112A freezes upon contact with the surface of the water forming a wavy but stable crust which prevents the water ($\rho_2 = 1$g cm^{-3}) from rising through the denser liquid Freon ($\rho_1 = 1.6$g cm^{-3}). In this case a prediction of marginal (or neutral) stability was obtained since the calculated cutoff wavelength is approximately equal to the vessel diameter. In experiment 2, a very stable, smooth lead crust ($\rho_1 = 11.7$g cm^{-3}) grew above melting gallium ($\rho_2 = 6.0$g cm^{-3}) in agreement with the theory. Experiments 3–5, involving an ice crust growing on cold liquid octane, indicated a critical vessel diameter below which the crust is stable, as predicted by equation (37). For a fixed vessel diameter, ice crust breakup was observed on a column of liquid octane whereas stable crust growth was observed on melting octane (compare experiment 3 with experiment 6) in agreement with theory. For ice growth on melting octane we predict ice breakup when the vessel diameter exceeds $\sim$16 cm. This was not determined experimentally (see experiments 6–8). Instead, smooth, stable ice covers were observed to grow on melting octane in vessels as large as 30 cm in diameter. It may be that in situations where large cutoff wavelengths (say $\gtrsim$10 cm) are required, natural sources of small disturbances are insufficient to start the instability.

All the experiments in which stable crust growth was observed in small diameter vessels ($\lesssim$7 cm) were repeated under isothermal conditions. In all cases liquid-liquid interface instability was observed indicating that the experiments did indeed demonstrate the suppression of the Rayleigh instability by crystallization. In addition, only immiscible material pairs were used in these experiments to avoid any appreciable changes in material melting points and other material alloying effects.[5]

6 Concluding Remarks

The agreement between theory and experiment cited in Section 5 is not conclusive because of both theoretical and experimental inaccuracies. Nonlinear crust wave behavior must be decisive in determining the conditions for the disintegration of the frozen crust. The elastic theory employed here cannot distinguish between tough, ductile and brittle solid materials such as Freon, lead and ice, respectively. The special boundary conditions to be satisfied at the lines of contact of the crust and liquids with the vessel wall have not been accounted for. It is difficult to avoid the generation of Kelvin waves during the pouring process when the upper liquid impacts on the surface of a lower liquid material. The Kelvin-wave mechanism (flow-induced excitation) is probably partly responsible for the wavy Freon crust shown in Fig. 4. Nevertheless, despite these inaccuracies, the agreement does tend to support the validity of a Raleigh-crust wave theory.

Acknowledgments

----

[5] Gallium has only limited solubility in liquid lead (about 5 percent at 327°C) and is insoluble in solid lead [12].
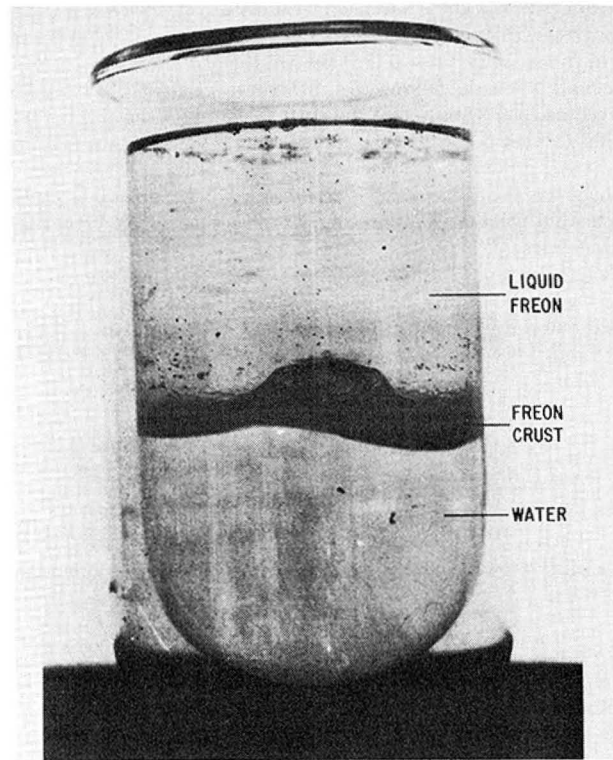
Fig. 4 Frozen layer of Freon 112A growing between water (lower fluid) and liquid Freon 112A (upper fluid)

References

1 Cheung, F. B., and Baker, L. Jr., "Core-debris Retention in the Below-core Structure Following and LMFBR Disassembly," *Trans. Am. Nucl. Soc.,* Vol. 21, 1975, pp. 309–310.

2 Epstein, M., "Heat Conduction in the UO$_2$-cladding Composite Body With Simultaneous Solidification and Melting," *Nucl. Sci. Eng.,* Vol. 51, 1973, pp. 84–87.

3 Lamb, H., *Hydrodynamics,* Dover, 1932, pp. 455–462.

4 Miles, J. W., "On the Aerodynamic Instability of Thin Panels," *Journal of the Aeronautical Sciences,* Vol. 23, 1956, pp. 771–780.

5 Taylor, G. I., "The Instability of Liquid Surfaces When Accelerated in a Direction Perpendicular to Their Planes," *Proceedings Royal Society London* Vol. A201, 1950, pp. 192–196.

6 *Scientific Papers by Lord Rayleigh,* Dover, New York, Vol. II, 1964, pp. 200–207.

7 Volmer, M., *Kinetik der Phasenbildung,* Dresden and Leipzig, T. Steinkopf, 1939, p. 181; see also McDonald, J. E., "Homogeneous Nucleation of Supercooled Water Drops," *J. Meteorology,* Vol. 10, 1953, pp. 416–433.

8 Livey, D. T., and Murray, P., "The Wetting Properties of Solid Oxides and Carbides by Liquid Metals," *Proceedings 2nd Plansee Seminar,* 1955, pp. 375–404.

9 *Uranium Dioxide: Properties and Nuclear Applications,* J. Belle, ed., U. S. Printing Office, 1961.

10 Levich, V. G., *Physicochemical Hydrodynamics,* Prentice-Hall, Chapter XI, 1962.

11 Zuber, N., "On the Stability of Boiling Heat Transfer," JOURNAL OF HEAT TRANSFER, TRANS. ASME, Series C, Vol. 80, No. 3, 1958, pp. 711–721.

12 Wilkinson, W. D., "Properties of Gallium," ANL-4109, Argonne National Laboratory, Argonne, Ill., Feb., 1948.

P. E. Frivik

Senior Research Fellow,
Division of Refrigeration Engineering,
The Norwegian Institute of Technology,
Trondheim, Norway

E. Thorbergsen

Research Fellow,
Division of Refrigeration Engineering,
The Norwegian Institute of Technology,
Trondheim, Norway

S. Del Giudice[1]

Asst. Professor,
Istituto di Fisica Tecnica,
Facoltà di Ingegneria dell' Università di Padova,
Padova, Italy

G. Comini[1]

Professor,
Istituto di Fisica Tecnica,
Facoltà di Ingegneria dell' Università di Trieste,
34127 Trieste, Italy

Thermal Design of Pavement Structures in Seasonal Frost Areas

In many practical situations, adequate thermal design of pavement structures in seasonal frost areas can be done by utilizing a model based on heat conduction alone. In this paper we present a system of computer programs which allow the solution of practically any nonlinear heat conduction problem in soils, provided that a two-dimensional description, plane or axisymmetric, is possible. The finite element method, together with the empirical correlations for thermal properties and boundary conditions, is used in the simulations. Predictions of the thermal regime in different structures are favorably compared with the results of experimental measurements, both for long-term and short-term temperature variations.

Introduction

In cold winter regions, traffic on railways and roads is often obstructed by the frost, while railway and pavement structures themselves are threatened by soil freezing. The importance of this problem is demonstrated by the extensive research on frost protection techniques that is being sponsored by national governments in several countries [1–3].[2]

Frost problems are usually related to cryosuction, which induces moisture migration to the freezing zone and ice segregation in the same area. The results are frost heaving during winter periods and loss of bearing capacity in the spring thaw, imposing speed and/or load limitations on traffic.

In the last ten years insulating materials have been used in frost protection [4–6]. Insulation, however, changes drastically the thermal regime in structures, often inducing differential icing on road surfaces. Besides, thermal design of insulated pavements should be very accurate to avoid superfluous use of expensive materials.

Adequate thermal design can only be done by utilizing numerical methods and computers, but even then simplifications must be introduced. To our knowledge, simultaneous heat and moisture transfer has never been considered in design systems. Reasons are uncertainties about the physical process, computer costs and, above all, lack

of reliable data on mass transport properties and boundary conditions for moisture movement [7 and 8].

On the other hand, experience has shown that, in many situations of practical interest, models based on heat conduction alone lead to acceptable predictions of the thermal regime. This is the case, for example, with structures where, according to the most conservative criteria for thermal design, cryosuction is eliminated by limiting the freezing zone to materials which are not frost susceptible [6 and 8].

When modeling is reduced to the solution of a nonlinear heat conduction equation, use can be made of available numerical techniques based both on finite differences or on finite elements [8–11]. The finite element method, however, offers special advantages in geometrical descriptions and in dealing with complicated nonlinear and/or time-dependent boundary conditions.

In this paper we describe a system of computer programs for thermal design of pavement structures, based on the finite element method and on a model of heat conduction alone. The general formulation of the finite element method for nonlinear heat conduction problems involving phase change has been reported elsewhere [10–12]. On the other hand, the programming system used for the present research includes several new features, such as improved techniques for the evaluation of thermal properties and boundary conditions. Besides, in this paper, the results of an extensive comparison between computed and measured temperature distributions are presented for different pavement structures, with reference both to long term and short term temperature variations. This way the accuracy of finite element simulations of realistic phase change problems is demonstrated experimentally for the first time.

Physical Aspects

It has long been established that the thermal regime in a moist soil

---

Zone	Material	Dry density (kg/m³)	Moisture content		Hydraulic conductivity
			Percent of dry mass	Degree of saturation	
I	bitumen	2300 – 2500	1 – 3	0.95 – 1.0	very low
II	crushed rock gravel sand	1900 – 2100	3 – 5	0.10 – 0.20	low to middle
III	gravel sand	1900 – 2100	3 – 5	0.10 – 0.20	low to middle
IV	insulation	30 – 40	≅ 0	≅ 0	very low
V	clay silt silty sand	1450 – 1700	15 – 25	0.8 – 1.0	middle to high

Table 1 Typical physical properties of road building materials referred to in Fig. 1
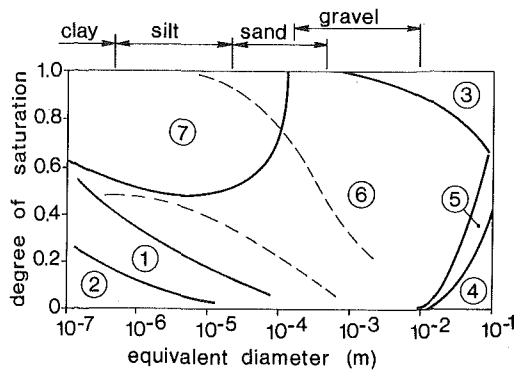

Fig. 1 Different heat transfer mechanisms and physical processes related to heat transfer in soils—The map indicates prevailing influences of: (1) moisture diffusion; (2) vapour diffusion; (3) free convection in the water phase at $t > 0$ °C or conduction; (4) free convection in air; (5) radiation; (6) conduction; (7) cryosuction at $t < 0$ °C or conduction (dotted lines show the zone of interest for road construction problems)

or structure is influenced by interconnected heat and mass transfer processes. At present, a few models, taking into account all modes of transfer, are available [8, 13, 14]. However, they are of little use for design purposes, being based on drastic simplifications such as consideration of one-dimensional geometries only, exclusion of certain mechanisms of moisture transfer etc. Besides, mass transport properties and boundary conditions for moisture movement are poorly known in most situations of technical interest.

On the other hand, three different conditions must be satisfied simultaneously in order to have phenomena such as cryosuction, moisture migration, ice segregation and frost heave. They are:
—the soil must be frost susceptible;
—the freezing zone must penetrate into areas of frost susceptible soil;
—the freezing zone must have access to underlying sources of water.

These conditions give the design engineer a choice of methods to avoid frost heave, because it is sufficient to remove or reduce one of them.

The relative influence of different mechanisms of heat transfer in soils at temperatures below 0 °C and of the physical processes related to them is described, in a qualitative manner, by Fig. 1. (This figure is reproduced from [15] and the area of cryosuction has been added after personal communication with the author.) With reference to the typical insulated pavement shown in Fig. 2 and to the physical data for standard materials reported in Table 1, the following considerations can be made.

The bituminous surface I and the insulation layer IV may be regarded as impermeable to water, compared to the soil materials. Table 1 and Fig. 1 indicate that, in the base II and in the sub-base III, heat transfer takes place mainly by conduction and cryosuction does not occur. Instead the same is true for the subgrade V only as long as freezing is avoided there.

Thus, if the insulation is effective in preventing the freezing zone from penetrating into the frost susceptible subgrade, mathematical models based on heat conduction alone can lead to acceptable predictions of temperature distributions in road structures. Accordingly, the well-known equation for nonlinear heat conduction:

$$C \frac{\partial t}{\partial \tau} = \nabla (k \nabla t) \qquad (1)$$

___Nomenclature___

C = heat capacity per unit volume (J/m³· K)

C = heat capacity matrix, equation (15)

e = emissivity of the boundary surface

F = heat load vector, equation (16)

k = thermal conductivity (W/m·K)

K = thermal conductivity matrix, equation (14)

n = outward normal to the boundary surface

N = shape function vector, equation (12)

q = heat flux density (W/m²)

r = radius, cylindrical coordinate (m)

S = cloud factor

t = temperature (°C)

t = vector of node temperatures, equation (12)

T = absolute temperature (K)

x, y = Cartesian coordinates (m)

α = convective heat transfer coefficient (W/m²·K)

Γ = boundary surface (m²)

σ = Stefan-Boltzmann constant (=5.67 W/ m²·K⁴)

τ = time (s)

Ω = domain of definition (m³)

Subscripts

a = air

c = convection

e = entering

f = final

i = initial

ℓ = leaving

p = peak

r = radiation

rr = irradiation evaluated by means of a radiometer

w = surface

x, y = in the (x, y) direction

τ = at the time instant τ

$0, 1, 2$ = reference states

Superscripts

e = element

— = average value over a one day period

⟨ ⟩ = average value over the time interval ($\tau - \Delta\tau, \tau + \Delta\tau$)
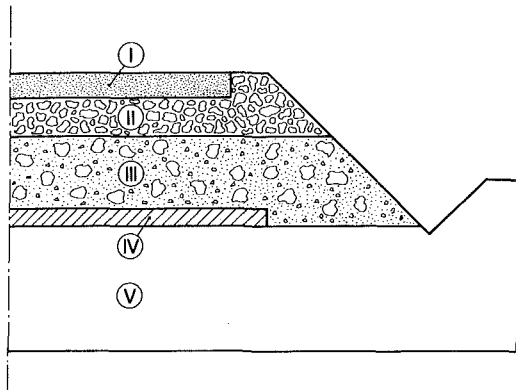
Fig. 2 Typical road structure insulated to prevent frost heaving and its different zones: (I) bituminous surface; (II) base; (III) sub-base; (IV) insulation; (V) subgrade

Fig. 3 Estimation of heat capacity and thermal conductivity in soil freezing problems

can be utilized for thermal design. The effects on thermal properties of the presence of moisture are included in the values of apparent heat capacity and thermal conductivity [8, 16, 17].

The obvious disadvantage of this approach is that the moisture content must be estimated from empirical relationships, such as the ones reported in [18]. However it is felt that, at the present stage, this is a much easier task than determining transport properties and boundary conditions for moisture movement.

The next step toward a more comprehensive modeling would be to account for cryosuction in the frost susceptible subgrade. This way, furthermore, an acceptable amount of frost heave in pavements might eventually be calculated, thus relaxing somewhat present stringent design criteria [19].

Input and Control Data

In addition to a description of the geometry considered, input data for thermal design systems include values of thermal properties of the materials used in the structure and of boundary conditions typical of the climatic region where the road is located.

Control data instead are needed to evaluate results from thermal design systems. Thus they should include, at least, measured temperature distributions.

Values of thermal properties of construction materials, climatic boundary conditions and control data for typical road structures have been collected by the Division of Refrigeration Engineering (DRE), which has been responsible for "thermal design methods and collection of design data" in the Norwegian program for research on "Frost Action in Soils" [3, 6, 15, 18, 20, 21].

Under this project, four Test Roads and nine Field Stations for recording climatic regimes (RCR) have been built [6, 21]. Each test road is supplied with a field station, and the remaining field stations are distributed according to the different climatic regions in Norway.

A typical experimental setup, complete with test road and field station, is described in [6, 21].

The test road is designed to fit an ordinary road which is regularly cleared from snow during winter. Most of the test road is insulated, but a small portion is built as a conventional road without insulation.

Several temperature transducers allow determination of two-dimensional temperature distributions in four different cross sections. Three of the measurement sections are placed in the insulated zone while the fourth one is located in the portion of the test road which is not insulated.

At the road surface, air and surface temperatures and the net heat flow into the ground are measured.

The RCR station is equipped with two smaller test fields. One is similar to an ordinary road with a bituminous surface, and it is kept free of 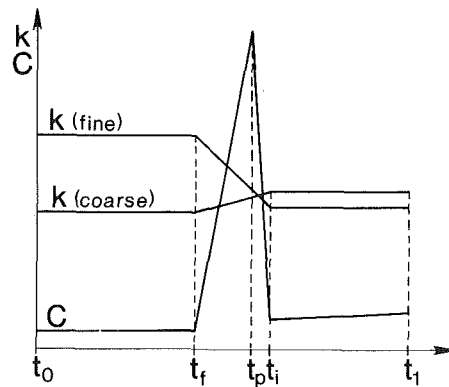snow to approximately the same extent as the test road. The other field has a natural, grass covered surface, and it is not cleared from snow in winter.

In locations where only the RCR station is placed, the test field with the bituminous surface if fitted into an ordinary road.

Temperature distributions are measured in both fields and a radiation balance is established for the bituminous surface by means of a radiation balance meter. Air temperature, evaluated according to metereological standards, relative humidity, direction and velocity of the wind were also accurately monitored.

All experimental data are recorded on magnetic tape by a data logger for subsequent computer elaboration.

This way complete heat balances for the various surfaces have been established and used for the determination of reliable climatic boundary conditions for thermal design systems.

Thermal Properties. From equation (1) it follows that the physical properties of interest are thermal conductivities k and volumetric heat capacities C, the latter accounting for the latent heat of fusion.

Material samples from all the test sites have been taken into the DRE and a great deal of experimental measurements have been performed before deciding on the most suitable procedures for the estimation of thermal properties.

In this way Johansen was able to develop a semiempirical method, which is now widely used, for prediction of thermal conductivities of soils [15]. Details of this calculation procedure are reported in [15]. Here we will only say that thermal conductivities of moist soils can be estimated from the knowledge of soil texture, density of dry soil, degree of saturation, quartz and unfrozen water contents.

Heat capacities of moist soils can be computed from very simple formulas, as suggested in [22]. Heat capacities are calculated as sums of capacities of the main components, soil particles-water-ice, plus a term depending on the variation, with respect to temperature, of the unfrozen water content [18, 22, 23].

However, if no moisture migration takes place, the total water content does not change during heat transfer processes. Therefore, thermal properties of a given soil, under the assumptions made here, can be considered as functions of temperature alone. It has been shown in [17] that, in such a case, an area-conserving triangle and a straight line can be used to interpolate heat capacity and thermal conductivity in the phase change zone. In the present study constant values have been assumed for thermal conductivity above and below freezing and for heat capacity below freezing. Heat capacity above freezing was assumed to be a linear function of temperature.

The approximations made are illustrated in Fig. 3. Thermal properties for all the materials referred to in the computations are reported in Table 2.

Boundary Conditions. The determination of reliable climatic boundary conditions for thermal design systems requires a major research effort.

The choice made here has been to rely on heat balances at the

Material and identifier		Temperatures and corresponding material properties				
		O	f	p	i	l
bitumen A	t	−30.	−0.9	−0.04	0.0	50.
	k	1.45	1.45	—	1.43	1.43
	c	1.99	1.99	87.6	2.23	2.48
gravel GR 9	t	−30.	−0.9	−0.03	0.0	50.
	k	0.80	0.80	—	1.28	1.28
	c	1.56	1.56	44.0	1.68	1.93
gravel GR 10	t	−30.	−0.9	−0.01	0.0	50.
	k	0.85	0.85	—	1.30	1.30
	c	1.60	1.60	58.2	1.76	2.01
gravel GR 11	t	−30.	−0.9	−0.04	0.0	50.
	k	2.58	2.58	—	1.70	1.70
	c	1.73	1.73	78.9	1.96	2.16
gravel GR 12	t	−30.	−0.9	−0.05	0.0	50.
	k	2.21	2.21	—	1.93	1.93
	c	1.84	1.84	118.	2.17	2.42
subgrade SG	t	−30.	−0.9	−0.05	0.0	50.
	k	2.70	2.70	—	2.20	2.20
	c	1.97	1.97	252.	2.70	2.85
clay C	t	−30.	−0.8	−0.04	0.0	50.
	k	2.18	2.18	—	1.22	1.22
	c	1.94	1.94	290.	2.64	2.79
foamed polystyrene I 1	t	−30.	—	—	—	50.
	k	0.032	—	—	—	0.033
	c	0.034	—	—	—	0.034
foamed polyurethane I 2	t	−30.	—	—	—	50.
	k	0.020	—	—	—	0.025
	c	0.141	—	—	—	0.141

Table 2 Material properties referred to in the examples of application: thermal conductivity k(W/m·K) and volumetric heat capacity C(MJ/m³·K) are given as a function of temperature t (°C)

surface of the roads. Two different types of heat balance descriptions have been utilized. The first, an instantaneous heat balance, is used for short term temperature variations, while the second, a kind of day-average heat balance, is used for long term temperature variations. These balance equations, based on data from test roads and RCR stations, are separated into a radiation component and a convective, sensible plus latent, component.

With respect to temperature boundary conditions, the heat balance technique presents several advantages. First of all it enables the design engineer to simulate temperatures in the structures as entirely dependent variables, influenced on one side by geometry and thermal properties and on the other side by the impact of the climate. Besides, when heat balances are used to establish boundary conditions, measured surface temperatures can be used as a very sensitive control of thermal regime predictions.

The heat balance technique is illustrated here with reference to both the short-term and the long-term variations in boundary conditions.

The heat balance on a road surface can be expressed as:

$$q_t = q_c + q_r \qquad (2)$$

where a distinction is made between convection and radiation fluxes.

The equations representing the short-term variations of interest for differential icing problems have a very simple structure.

The convection equation is:

$$q_c = q_{c\ell} - q_{ce} \cong \alpha(t - t_a) \qquad (3)$$

where the global coefficient α is expressed as:

$\alpha \cong 3$W/m² · K for $t - t_a < 0$;

$$\alpha \cong 4\text{W/m}^2 \cdot \text{K} \qquad \text{for } t - t_a > 0 \qquad (4)$$

and accounts both for the sensible and the latent heat transport in the test road location.

The radiation equation is:

$$q_r = q_{r\ell} - q_{re} \cong e\sigma(T^4 - T_r{}^4) \qquad (5)$$

if the ground surface is considered "gray" and an apparent sky-ra-

diation temperature is defined as:

$$T_r = (q_{rr/\sigma})^{1/4} \qquad (6)$$

q_{rr} being the measured sum of direct sky-radiation and of atmospheric radiation [21].

With long-term temperature variations, such as those of interest for seasonal frost problems, average values of heat fluxes over one-day periods are utilized in the thermal design system. High frequency temperature oscillations at the boundaries do not influence long term temperature distributions in the road structure. Therefore, with seasonal frost problems, there is no need for detailed descriptions of instantaneous heat fluxes. The additional input data would just increase the computer time without improving the accuracy.

With long-term variations, equations (3) and (5) are still used, but reference is made to one-day average values of the physical quantities involved.

The global convection coefficient is evaluated from the expressions:

$$\overline{\alpha} \cong 3\text{W/m}^2 \cdot \text{K} \qquad \text{for } \overline{t} - \overline{t}_a < 0$$
$$\overline{\alpha} = 7 + 0.2 (\overline{t} - \overline{t}_a)\text{W/m}^2 \cdot \text{K} \qquad \text{for } \overline{t} - \overline{t}_a > 0 \qquad (7)$$

which are similar, in structure, to expressions (4) and hold good for the particular area where the long-term measurements were made. (It might not be pointless to observe here that different test roads were chosen for the short-term and the long-term measurements.)

Instead, a completely different procedure, with respect to short-term radiation measurements, has been followed in the estimation of one-day average values of the total irradiation $\overline{q}_{rr}$. It has been found, in fact, that this quantity can be correlated to meteorological parameters which are easily determined. For the specific area considered in the long term simulations we have for example:

$$\overline{q}_{rr} \cong [(1 - 0.1S)(-200 \cos \phi - 25 \sin^2 \phi + 175)] + \{(\sigma \overline{T}_a{}^4 - 80) + 0.0125S[4 + \cos (\phi - 0.16)]\} \qquad (8)$$

where $\overline{q}_{rr}$ (W/m²) is the one-day average irradiation, S is the cloud factor ranging from 0, clear sky, to 8, full cloud cover, and ϕ is defined by the equation:

$$\phi = 2\pi(D + 9)/365 \qquad (9)$$

D being the day number counted from the 1st of January.

The first term in square brackets in equation (8) represents the short-wave direct sky radiation, while the second term represents the long-wave atmospheric radiation from the air and the clouds, respectively. If the part:

$$(-200 \cos \phi - 25 \sin^2 \phi + 175)$$

becomes negative, it is set equal to zero, since it means that the sun is below the horizon.

For computing purposes only, $\overline{q}_{rr}$ from equation (8) is converted into an apparent average sky temperature $\overline{T}_r$ using equation (6). Then the net radiation heat flux $\overline{q}_r$ is evaluated from equation (5).

The values $e = 0.96$ and $e = 0.93$ have been used in equation (5), respectively, for the short-term and the long-term radiation balances.

Finite Element Formulation

The problem considered in this paper is governed, in region Ω, by the nonlinear equation for heat conduction (1).

Boundary conditions are:

$$t = t_w \qquad (10)$$

on part of the boundary Γ_1 and:

$$k\nabla t \cdot \mathbf{n} + q + q_c + q_r = 0 \qquad (11)$$

on part of the boundary Γ_2.

The terms q, q_c, and q_r represent, respectively, the imposed heat flux and the rates of heat flow per unit area due to convection and radiation, while $\mathbf{n}$ is the outward normal to the boundary surface.

In the programs reference is made to two-dimensional geometries

but, by replacing k, C, q, q_c, q_r in equations (1) and (11) with rk, rC, rq, rq_c, rq_r solutions to three-dimensional axial-symmetric problems can be easily obtained [11 and 12].

The spacewise discretization of equation (1), subjected to boundary conditions (10) and (11) is accomplished using Galerkin's method as shown in [10–12].

The unknown function t is approximated, throughout the solution domain, by the relationship:

$$t = \sum_{j=1}^{n} N_j(x, y) t_j(\tau) = \mathbf{N} \cdot \mathbf{t} \tag{12}$$

where N_j are parabolic shape functions and t_j are the node temperatures.

The n equations allowing the solution for n values of t_j can be written in matrix form as [10–12]:

$$\mathbf{K} \cdot \mathbf{t} + \mathbf{C} \cdot \dot{\mathbf{t}} + \mathbf{F} = 0 \tag{13}$$

Typical matrix elements are [10–12]:

$$K_{j\ell} = \Sigma \int_{\Omega^e} \left(k_x \frac{\partial N_j}{\partial x} \frac{\partial N_\ell}{\partial x} + k_y \frac{\partial N_j}{\partial_y} \frac{\partial N_\ell}{\partial_y} \right) d\Omega$$
$$+ \Sigma \int_{\Gamma_2^e} \alpha N_j N_\ell d\Gamma \tag{14}$$

$$C_{j\ell} = \Sigma \int_{\Omega^e} C N_j N_\ell d\Omega; \tag{15}$$

$$F_j = \Sigma \int_{\Gamma_2^e} N_j (q + q_r - \alpha t_a) d\Gamma \tag{16}$$

where $(j, \ell = 1, n)$.

The set of equations (13) is nonlinear, since the matrices $\mathbf{K}$, $\mathbf{C}$ and $\mathbf{F}$ are dependent on $\mathbf{t}$.

System (13) is solved using the three-time level algorithm described in [10–12], in a slightly modified form. First a "predictor" value of $\mathbf{t}'_{\tau+\Delta\tau}$ is computed as:

$$\mathbf{t}'_{\tau+\Delta\tau} = -[\mathbf{K}_\tau + 3\mathbf{C}_\tau/(2\Delta\tau)]^{-1}[\mathbf{K}_\tau \cdot t_\tau$$
$$+ \mathbf{K}_\tau \cdot \mathbf{t}_{\tau-\Delta\tau} - 3\mathbf{C}_\tau \cdot \mathbf{t}_{\tau-\Delta\tau}/(2\Delta\tau) + 3\langle \mathbf{F} \rangle] \tag{17}$$

and $\langle \mathbf{F} \rangle$ is evaluated with reference to an average value of q_r over the time interval $(\tau - \Delta\tau, \tau + \Delta\tau)$. By assuming linear variations of T and T_r with time we obtain:

$$\langle q_r \rangle \cong e\sigma \left[T_\tau^4 - A_\tau^4 + \frac{1}{5} (T_\tau - T_{\tau-\Delta\tau})^2 \right.$$
$$\times (11 T_\tau^2 - 2 T_\tau T_{\tau-\Delta\tau} + T_{\tau-\Delta\tau}^2)$$
$$- \frac{1}{80} (A_{\tau+\Delta\tau} - A_{\tau-\Delta\tau})^2$$
$$\left. \times (11 A_{\tau+\Delta\tau}^2 + 18 A_{\tau-\Delta\tau} A_{\tau+\Delta\tau} + 11 A_{\tau-\Delta\tau}^2) \right] \tag{18}$$

where:

$$A \equiv T_r \tag{19}$$

Then a "corrector" value of $\mathbf{t}_{\tau+\Delta\tau}$ is obtained from the equation:

$$\mathbf{t}_{\tau+\Delta\tau} = -[\mathbf{K}_\tau + 3\mathbf{C}_\tau/(2\Delta\tau)]^{-1}[\mathbf{K}_\tau \cdot t_\tau + \mathbf{K} \cdot \mathbf{t}_{\tau-\Delta\tau}$$
$$- 3\mathbf{C}_\tau \cdot \mathbf{t}_{\tau-\Delta\tau}/(2\Delta\tau) + (\mathbf{F}_{\tau+\Delta\tau} + \mathbf{F}_\tau + \mathbf{F}_{\tau-\Delta\tau})] \tag{21}$$

where the predictor value $\mathbf{t}_{\tau+\Delta\tau}'$ is used to evaluate $(9r)_{\tau+\Delta\tau}$.

This way even sudden variations of the radiation heat flux can be followed very accurately. Besides, since the operations for evaluating $\mathbf{K}$, $\mathbf{C}$ and the matrix inverse are performed only once every time step, the procedure is very efficient in terms of computer time.

Thermal properties C and k are estimated as suggested in [10–12], with reference to the derivatives, with respect to temperature, of the enthalpy and of the thermal conductivity integral. This averaging process gives representative values of thermal properties even in the phase change zone. Obviously, in zones of constant temperature, recourse is made to the direct evaluation.

The programming system includes the automatic time step adjustment procedure described in [10–12]. Undulations arising from the "numerical noise" inherent in the approximations made are reduced by redefining the vector $\mathbf{t}_{\tau-\Delta\tau}$ as:

$$\mathbf{t}_{\tau-\Delta\tau} = (\mathbf{t}_{\tau+\Delta\tau} + \mathbf{t}_\tau + \mathbf{t}_{\tau-\Delta\tau})/3 \tag{22}$$

before starting the calculations for a new time step [24].

Results

The programming system used in the present investigation has been checked against the results of available analytical solutions for infinite slabs and corner regions [10, 11]. Comparisons have been made also with solutions from finite difference and triangular element programs concerning complex geometries in addition to nonlinear and/or time-dependent boundary conditions. Agreement with previous analytical and numerical solutions was of the order of 1 percent [11].

The amount of geometrical data necessary to define a problem was greatly reduced, with respect to earlier numerical simulations, by the use of isoparametric elements. The capabilities of isoparametric elements in dealing with geometrically complex problems have been illustrated in [8, 11].

In this paper the results of comparisons with experimental measurements are presented for the first time.

Comparisons have been carried out for different road structures, with reference both to long-term and short-term temperature variations.

Boundary conditions of the first kind, i.e., measured temperature values at the road surface, were used at the beginning. This way we ascertained the reliability of the mathematical model [25].

Afterwards, only convection and radiation boundary conditions were utilized. The simulations always gave acceptably uniform predictions of temperature distributions. This fact and the very large amount of comparison data produced [25], would make a detailed description of all the results obtained of little use and very space consuming. Thus only three examples of application are presented here. The first one concerns the seasonal frost problem, while the latter two pertain to the investigations on differential icing.

The Seasonal Frost Problem. The test road referred to in this example, with an insulating layer 60-mm thick placed at a depth of 71 cm, has the standard structure of the frost proof constructions illustrated in Fig. 2.

Preliminary numerical calculations indicated that detailed geometrical descriptions of the surface layers do not improve predictions of one-day-average-temperature distributions in the road structure. In fact, the bituminous layer has a small thickness and is characterized by values of thermal diffusivity which do not differ much from the corresponding values for base materials. Therefore, in later analyses of seasonal frost problems, the influence of the bituminous layers on heat conduction was disregarded. However, the emissivity values of bitumen were, all the same, attributed to the external boundary surface. Accordingly, the finite element representation illustrated in Fig. 4 looks considerably simpler than the meshes used in earlier simulations of similar problems: only 19 parabolic elements and 70 nodal points are utilized here.

Thermal properties of the materials are reported in Table 2. Simultaneous convection and radiation boundary conditions are imposed at the road surface. The air temperature $\bar{t}_a$, the cloud factor S, and the apparent sky temperature $\bar{t}_r$ resulting from meteorologic measurements are shown in Fig. 5.

Equations (3), (7) and (5), (6), (8) are used in the estimation of heat transfer by convection and radiation, respectively.

A constant temperature of 4.4 °C is imposed at the lower boundary while, as a first approximation, the lateral boundaries are assumed to be nonconductive.

The problem is started in June with the temperature distribution, calculated from a collection of measured temperatures at various levels, that is reported in Table 3.

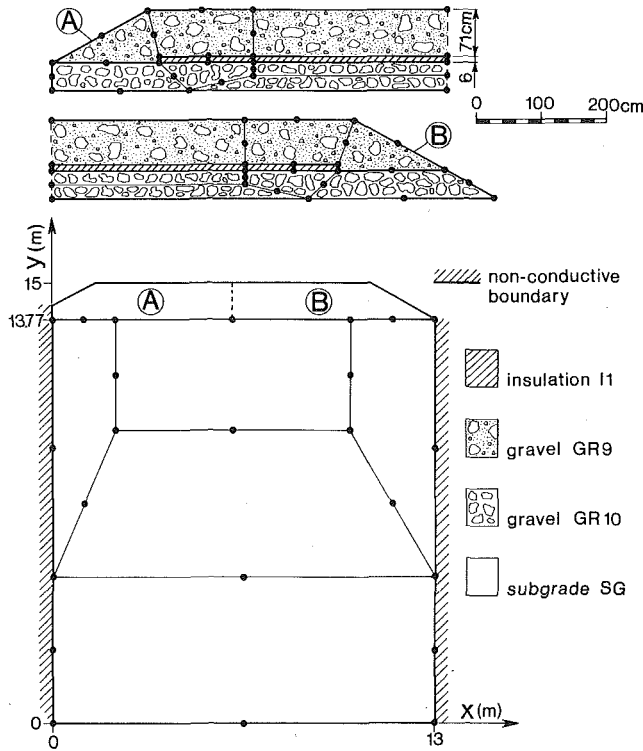Computing time is of the order of 3.4 s per time step on a UNIVAC

Fig. 4 Mesh used for studying seasonal frost problems in insulated road structures
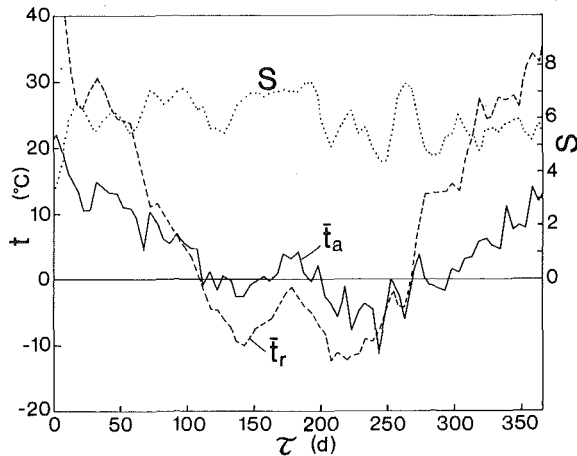

Fig. 5 Air temperature $\bar{t}_a$, cloud factor S and apparent sky temperature $\bar{t}_r$, used in the simulation of seasonal frost problems—the value $e = 0.93$ has been assumed for the emissivity of the external boundary surface

ventional road.

Therefore, in winter, low surface temperatures, resulting from outgoing night radiation to a clear sky, are a serious problem in insulated structures, expecially with top insulated roads. In order to avoid frost formation and differential icing on the road surface, the surface temperatures must be kept, approximately, at the same level

y (m)	0.00	6.08	10.08	11.00	11.75	12.25	13.00	13.50
TI (°C)	4.4	4.0	3.5	3.6	4.0	4.4	5.5	6.6
y (m)	14.00	14.23	14.30	14.33	14.70	14.82	14.90	15.00
TI (°C)	8.4	9.8	25.2	26.4	30.4	31.8	31.0	31.6

Table 3 Initial temperatures TI on June 1st, at various distances y from the lower boundary of the insulated road structure represented in Fig. 4
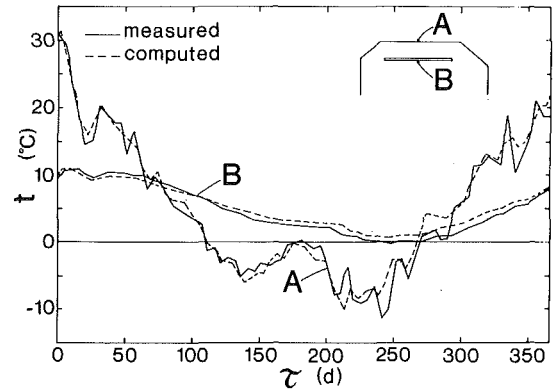
Fig. 6 Measured and computed temperatures on the surface and below the insulation layer in the road structure of Fig. 4
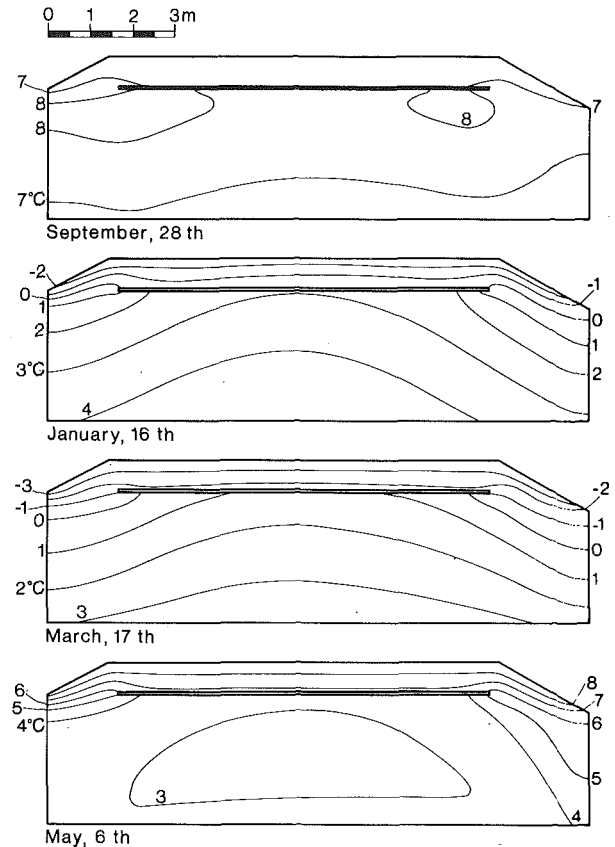
Fig. 7 Isotherm fields at different times of the year in the road structure of Fig. 4

1108 machine. A total number of 215 time steps is required to complete the one-year simulation.

Measured and computed temperatures on the surface and just below the insulation layer are compared in Fig. 6. The isotherm fields at different times of the year are shown in Fig. 7. As it can be seen, no freezing takes place in the frost susceptible subgrade below the insulation.

The Differential Icing Problem. The insulating layer reduces heat flow and, consequently, temperature gradients in the subgrade. This way, if thermal design is correct, temperature oscillations in the frost susceptible subgrade are maintained in a safe, above 0 °C, range. On the other hand, when heat flow in the subgrade is reduced by the insulation, diurnal temperature oscillations in the upper layers are increased. As a consequence, higher day temperatures in summer and lower night temperatures in winter will ensue with respect to a con-

Fig. 8 Meshes used for studying differential icing problems: (a) standard road structure; (b) top insulated road structure

Fig. 9 Air temperature t_a and apparent sky temperature t_r used in the simulation of differential icing problems—the value $I = 0.96$ has been assumed for the emissivity of external boundary surfaces

Not insulated		Top insulated	
y (m)	TI (°C)	y (m)	TI (°C)
0.00	7.2	0.00	7.2
1.10	8.1	1.10	8.1
2.10	8.8	2.10	8.8
2.60	9.0	2.60	9.0
3.30	7.5	3.30	8.6
3.80	6.0	4.40	7.3
4.30	4.3	4.84	6.6
4.80	2.2	4.90	6.3
4.94	1.2	4.93	0.7
5.00	0.0	5.00	− 0.2

Table 4 Typical initial temperatures TI in winter, at various distances y from the lower boundaries of the not insulated and the top insulated road structures represented in Fig. 8
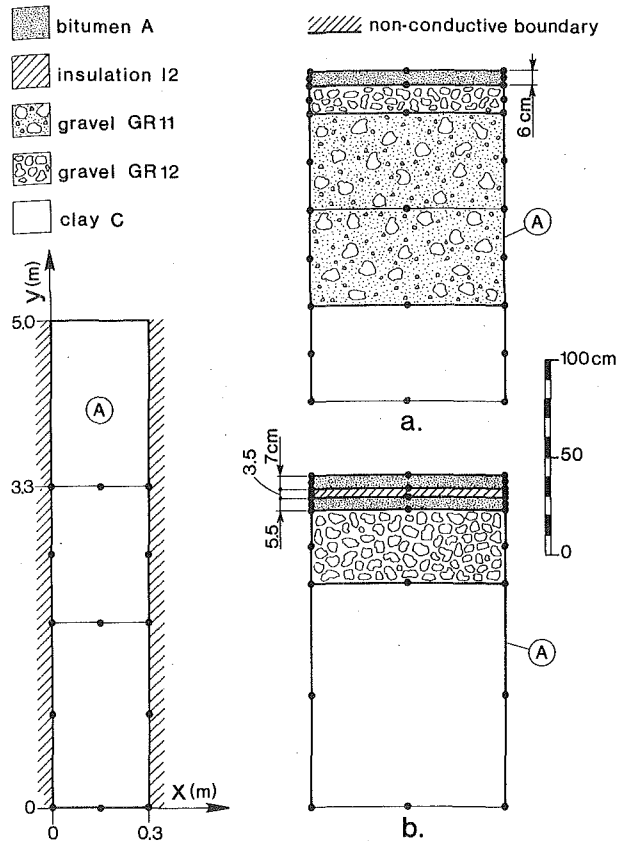
as the air temperatures. Numerical simulations of surface temperature variations are thus very useful in the comparison of different structures with respect to the fulfilment of the above mentioned design criterion.

Results concerning a conventional road with no insulation and a road with a 35-mm insulation layer close to the external surface, both subjected to the same climatic conditions, are presented here. This way the accuracy of the computer system in predicting short term temperature variations is assessed with reference to the two extreme situations of practical interest.

In differential icing problems the influence of the surface layers of bitumen on instantaneous temperature distributions must be taken into account. Instead, diurnal temperature oscillations starting at the road sides do not reach the center of the structure. Accordingly, two-dimensional heat conduction effects are not of great importance here. Thus, the one-dimensional meshes presented in Fig. 8 have been used in the analyses: seven parabolic elements and 38 nodal points have been utilized.

Thermal properties of the materials are reported in Table 2. The air temperature t_a and the apparent sky temperature t_r resulting from climatic measurements are shown in Fig. 9. Heat transfer rates by convection and radiation are computed from equations (3)–(5), respectively. The lateral boundaries and the bottom surface are assumed to be nonconductive.

The problems are started at 5 p.m. with the temperature distributions, calculated from a collection of measured temperatures at various levels, that are reported in Table 4.

Computing time is of the order of 1.4 s per time step on a UNIVAC 1108 machine. A total number of 111 time steps is required to complete a 37-hr simulation.

Measured and computed temperatures at the surface of the two road structures are shown in Fig. 10.

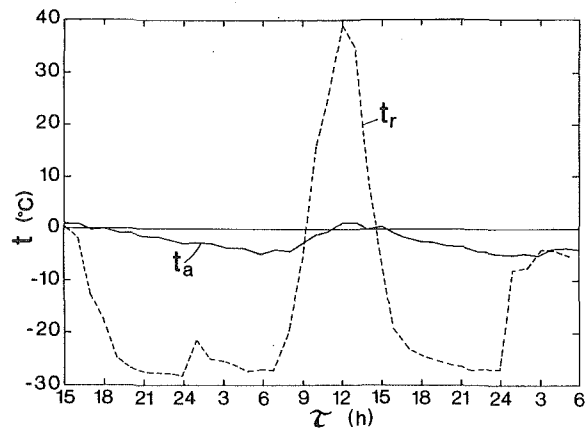As it can be seen, the greatest temperature drop occurs with the top insulated road. Since in this case the surface temperature is lower than the air temperature for most of the night, frost formation and differential icing can be expected. This result has been confirmed by temperature measurements and visual observations over a period of time [6].

Conclusions

A model based on heat conduction alone has led to acceptable predictions of the thermal regime in road structures subjected to seasonal frost and to differential icing. However, the techniques presented here can be applied also to insulated structures on permafrost, subjected to seasonal thaw.

The programming system used in this research is fast, accurate and sufficiently flexible to accommodate practically any soil freezing problem of technical interest described in terms of two-dimensional, plane, or axial-symmetric geometries, once the proper input data are available.

Future improvements of the design system might include consideration of simultaneous heat and moisture transfer to calculate acceptable amounts of frost heave. Besides, more general correlations for convection and radiation coefficients might be incorporated to enhance the transportability of the numerical results.
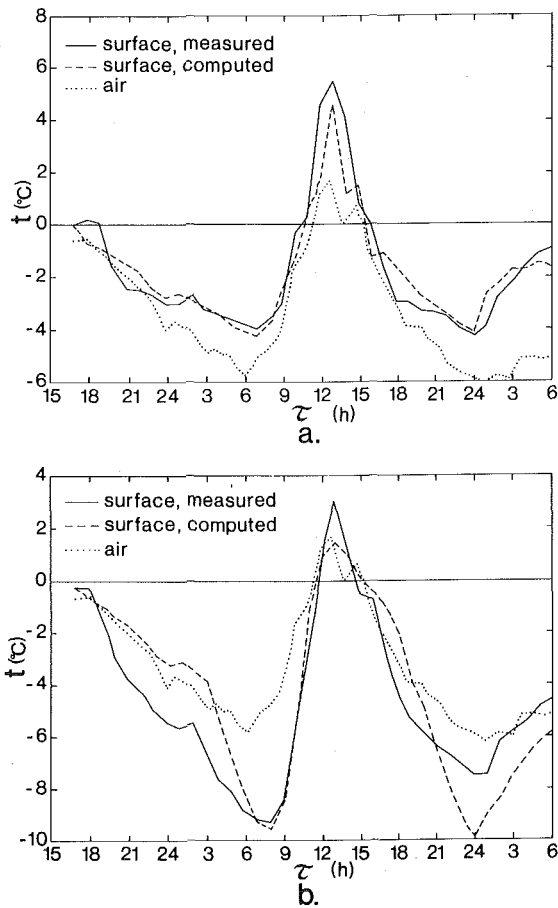
Acknowledgment

Fig. 10 Measured and computed temperatures on the surface of the road shown in Fig. 8: (*a*) Standard road structure; (*b*) Top insulated road structure

while one of the authors (SDG) was visiting, on an invited stay, the Division of Refrigeration Engineering of the Norwegian Institute of Technology at Trondheim.

References

1 OECD, "Frost Action on Roads," *Proceedings Symposium,* OECD-Road Research, Oslo, 1973.

2 Fondation Francaise d' Etudes Nordiques, "Problems Raised by Frost-Action. Fundamental and Applied Researches," *Proceedings VIth International Congress,* Le Havre, France, 1975.

3 Frivik, P. E., "Thermal Analysis of Frost Action on Roads," *Proceedings Symposium on Frost Action on Roads,* OECD-Road Research, Oslo, 1973.

4 Johnson, T. C., et al., "Roadway Design in Seasonal Frost Areas," TR 259, CRREL, Hanover, N. H., 1975.

5 Refsdal, G., "The Use of Thermal Insulating Materials in Highway Design," *Frost i Jord 9,* Oslo, 1973.

6 Frivik, P. E., and Pedersen, J. M., "Thermal Regime in Road Constructions. Measurements and Simulation," *Proceedings VIth International Congr. on Problems Raised by Frost Action,* Le Havre, 1975.

7 Andersons, D. M., and Morgenstern, N. R., "Physics, Chemistry and Mechanics of Frozen Ground: a Review," *The North American Contribution to the IInd Int. Conf. on Permafrost,* National Academy of Sciences, Washington D.C., 1973, pp. 257–288.

8 Aguirre-Puente, J., Fremond, M., and Comini, G., "Physical and Mathematical Study of Soil Freezing," (in French), *Proceedings Meeting Comm. B1, IIF/IIR,* Washington D. C., 1976.

9 Fleming, A. K., "The Numerical Calculation of Freezing Processes," thesis for the Technical Licentiate Degree, The Technical University of Norway, Trondheim, 1971.

10 Comini, G., et al., "Finite Element Solution of Nonlinear Heat Conduction Problems With Special Reference to Phase Change," *Int. J. Num. Meth. Engng.,* Vol. 8, 1974, pp. 613–624.

11 Del Giudice, S., Lewis, R. W., and Comini, G., "Finite Element Simulation of Freezing Processes in Soils," 1976, to appear.

12 Comini, G., Del Giudice, S., "Thermal Aspects of Cryosurgery," JOURNAL OF HEAT TRANSFER, TRANS. ASME, Series C, Vol. 98, 1976, pp. 543–549.

13 Harlan, R. L., "Analysis of Coupled Heat-Fluid Transport in Partially Frozen Soil," *Water Resources Research,* Vol. 9, 1973, pp. 1314–1323.

14 Guymon, G. L., and Luthin, J. N., "A Coupled Heat and Moisture Transport Model for Arctic Soils," *Water Resources Research,* Vol. 10, 1974, pp. 995–1001.

15 Johansen, Ø., "Thermal Conductivity of Soil and Rock," *Frost i Jord* 16, Oslo, 1975.

16 Bonacina, C., et al., "Numerical Solution of Phase Change Problems," *International Journal of Heat and Mass Transfer,* Vol. 16, 1973, pp. 1825–1832.

17 Bonacina, C., et al., "On the Estimation of Thermophysical Properties in Nonlinear Heat Conduction Problems," *International Journal of Heat and Mass Transfer,* Vol. 17, 1974, pp. 861–867.

18 Committee on Frost Action in Soils, "Protection Against Frost Damages," (in Norwegian), *Frost i Jord* 17, Oslo, 1977.

19 Johansen, Ø., "Frost Penetration and Ice Accumulation in Soils," *Proceedings Symposium on Frost Action in Soils,* Luleå, Sweden, 1977.

20 Saetersdal, R., "Committee on Frost Action in Soils. Annual Report 1973," *Frost i Jord* 13, Oslo, 1974.

21 Heiersted, R. S., "Thermal Climate Regime on Road and Ground Surface," *Frost i Jord* 16, Oslo, 1975.

22 Anderson, D. M., et al., "The Unfrozen Water and the Apparent Specific Heat Capacity of Frozen Soils," *The North American Contribution on the IInd International Conference on Permafrost,* National Academy of Sciences, Washington D.C., 1973.

23 Frivik, P. E., and Johansen, H., "Calorimetric Measurements of Specific Heat Capacity and Unfrozen Water Content of Soil and Organic Materials," (in Norwegian), Rep. 8, Division of Refrigeration Engineering, NTH, Trondheim, Norway, 1976.

24 Wood, W. L., and Lewis, R. W., "A Comparison of Time Marching Schemes for the Transient Heat Conduction Equation," *Int. J. Num. Meth. Engng.,* Vol. 9, 1975, pp. 679–690.

25 Frivik, P. E., Thorbergsen, E., and Del Giudice, S., 1977, unpublished results.

D. L. Siegel[1]

Senior Engineer.
Assoc. Mem. ASME

L. R. Davis

Professor.

Oregon State University,
Corvallis, Oregon.
Mem. ASME

Transient Heat and Mass Transfer in Soils in the Vicinity of Heated Porous Pipes

This paper presents an analysis which describes the time dependent heat and mass transfer in soils. Local effective thermal conductivity as a function of soil material, moisture content and temperature were used from experimental data. Diffusion of liquid and vapor are both accounted for. Local thermodynamic equilibrium between liquid and vapor is assumed. Boundary conditions were chosen to represent a subsurface soil warming and irrigation system. Surface heat exchange was included as a function of varying atmospheric and surface conditions. The spacing and depth of the pipes were varied to find their effect on moisture and temperature distribution within the soil for both summer and winter environmental conditions.

The result of expressing the governing equations in finite difference form and solving them numerically on a computer are presented in the form of temperature and moisture content distribution curves for summer and winter conditions. The results agree well with existing laboratory data. A steady-state closed form conduction solution with surface convection is also presented.

Seasonal soil temperature variations are also presented for three climates for heated and unheated soils.

Introduction

One of the techniques proposed to use the waste heat from power plants is soil heating through a series of parallel buried pipes. Soil heating increases the growing season in addition to increasing the growth rate of many plants. Initial experiments have shown drying around the pipes to be a serious problem that reduces the effective soil conductivity and moisture available for plant growth [1].[2] One method proposed to solve this problem is to allow the pipes to bleed water through a series of holes providing subsurface irrigation as well as soil heating [2]. The heat transfer problems associated with this type of system are complex due to the transient nature of environmental conditions and nonhomogeneous nature of the transport properties within the soil. The latter is further complicated by mass transfer of water, both in the liquid and vapor phases, within the soil. Most existing analyses of this problem employ steady-state assumptions, constant effective thermal conductivity, and assume

surface temperatures are known. This paper presents the differential equations which describe the transient heat and mass transfer in soils. The results of expressing the equations in finite difference form and solving numerically on a digital computer are presented for a sandy soil containing a system of parallel, heated, porous pipes. The spacing and depth of the pipes were varied to present a method for optimization of the depth and spacing for a given soil, crop, and location. The parameters for optimization were the increase in moisture content, the percent of the soil maintained above 24°C, and the average increase in temperature.

In previous methods, heat transfer in soils has been treated by assuming constant thermal conductivity and using the method of images to approximate the temperature distribution due to a buried pipe. Kendricks and Havens [3] utilized superposition to approximate the temperature due to a large number of pipes buried at uniform spacing and depth. Besides neglecting convection in the soil and assuming constant thermal conductivity, the equations of Kendricks and Havens require that the soil surface temperature be specified, which is, in most cases, not known due to heat exchange mechanisms with the environment.

Much of the work in the field of combined heat and mass transfer in soils has dealt with the thermodynamics of irreversible processes. Cary and Taylor [4, 5] developed equations from the theory of irreversible thermodynamics for the flux of heat and moisture in soils for saturated and unsaturated conditions, and experimentally found the pheomenological coefficients for these equations for various soils. Cary

---

[6] extended these experiments and equations to liquid, vapor and heat transfer in soils. These equations, however, are not applied to continuity or energy equations.

Philip and de Vries [7] adopted a more classical approach utilizing Darcy's law for liquid flux,

$$\overline{q}_\ell = -\rho_w k \overline{\nabla} \phi$$

which they transformed to

$$\overline{q}_\ell = -D_{T\ell} \overline{\nabla} T - D_{\theta\ell} \overline{\nabla} \theta - \rho_w k i$$

A diffusion equation for vapor transfer was similarly transformed from dependence on the gradient of vapor density to dependence on the gradients of temperature and liquid water content. These equations were then substituted into the continuity equations. Subsequently, de Vries [8] utilized the equations for liquid and vapor flow, and the continuity equations for vapor and liquid phases to develop an equation for evaporation rates. An energy equation was also developed utilizing the moisture flux equations. These equations were then simplified to those corresponding to a steady-state one-dimensional case in which the liquid and temperature gradients are expressed in terms of the diffusion coefficients and the heat and mass fluxes.

Fritton, et al. [9], using measured diffusion coefficients, compared results of the equations of Philip and de Vries to experimental results for soil exposed to several surface conditions. To obtain agreement between experimental and theoretical results they had to divide the measured water diffusivity by factors of 35 and 10. This discrepancy was attributed to hysteresis in the water tension curve and to the temperature dependence of the hydraulic conductivity.

Analysis

In the present analysis Darcy's equation for liquid flow in porous media was used, which can be written as,

$$\overline{q}_\ell = -\rho_w k \overline{\nabla} \phi \qquad (1)$$

Vapor flow was expressed by the diffusion equation as

$$\overline{q}_v = -D \overline{\nabla} \rho_{vo} \qquad (2)$$

The continuity equations for vapor and liquid phases are, respectively,

$$E = (S - \theta) \frac{\partial \rho_{vo}}{\partial t} - \overline{\nabla} \cdot D \overline{\nabla} \rho_{vo} \qquad (3)$$

and

$$\rho_w \frac{\partial \theta}{\partial t} - \rho_w \overline{\nabla} \cdot k \overline{\nabla} \phi = -E \qquad (4)$$

Neglecting mechanical work and assuming the magnitude of the potential, ϕ, is small and $\rho_v \ll \rho_\ell$, the energy equation is written as

$$\overline{\nabla} \cdot \lambda \overline{\nabla} T = (\theta \rho_w c_{v\ell} + \rho_{soil} c_{v soil}) \frac{\partial T}{\partial t} - \rho_w c_{p\ell} k \overline{\nabla} \phi \cdot \nabla T + h_{fg} E \quad (5)$$

In order to find ρ_v as a function of temperature and moisture content, local thermodynamic equilibrium is assumed. The free energy of the water in the soil is

$$G_\ell = g\psi$$

assuming $G = 0$ for pure water. The free energy of the vapor is

$$G_{vap} = RT \ln P_v/P_{vo}$$

where P_v is the vapor pressure and P_{vo} is the saturated vapor pressure. For equilibrium $G = G_{vap}$ and, therefore,

$$RT \ln P_v/P_{vo} = g\psi$$

or

$$\frac{P_v}{P_{vo}} = \exp [\psi g/RT]$$

Using the ideal gas law for constant temperature at the liquid-vapor interface, $P/\rho = $ constant, the relationship becomes

$$\frac{\rho_{vo}}{\rho_{v sat}} = \exp [\psi g/RT] \qquad (6)$$

Equations (3)–(6) now provide four equations which yield solutions for ρ_v, E, T, and θ, when data for ψ, k, D, and λ is provided.

One difference between these equations and those of de Vries is that these equations contain gradients of vapor density and water tension whereas de Vries' transformed equations contain temperature and water content gradients only. Equations (3)–(6) have been expressed in finite difference form and solved numerically using an implicit scheme on a CDC 3300 digital computer. A more detailed presentation of the analysis can be found in references [10, 11]. The finite difference form of the equations and a listing of the program can be found in reference [11].

The boundary conditions used for the computer simulations were chosen to approximate the conditions of the system being modeled. The vertical boundaries were modeled as insulated surfaces due to symmetry or due to the experimental configuration. The heating and irrigation pipe on a vertical boundary was modeled by specifying the temperature and moisture content at the node representing the pipe. A detailed nodalization in the vicinity of the pipe was not felt necessary due to the small expected pipe diameters. The lower horizontal boundary conditions in the soil for field simulations were specified as constant moisture content and temperature as dictated by water table data. For laboratory simulations, zero fluxes were specified.

The boundary conditions at the soil surface were calculated as [13]

$$q_\ell = \text{rain or irrigation rate}$$

$$q_v = h_v (\rho_{v surface} - \rho_{v ambient})$$

$$\text{heat flux} = h(T_{surface} - T_{ambient})$$
$$+ \epsilon \sigma T^4_{surface} - \sigma T^4_{ambient} (C_B + 0.223\sqrt{P_a})$$
$$- (1 - 0.6C^3)q_0$$

where

$C_B = $ Brunts coefficient,

Nomenclature

c_p = specific heat at constant pressure
c_v = specific heat at constant volume
D = vapor diffusivity
E = evaporation rate
g = acceleration of gravity
G = Gibbs free energy
h = surface heat conductance
h_v = surface mass conductance
h_{fg} = heat of vaporization
i = vertical unit vector
k = hydraulic conductivity

p = pressure
q = mass flux
R = universal gas constant
S = porosity
t = time
T = temperature
∇ = gradient operator
ϵ = emmisivity
θ = water content
λ = thermal conductivity

ρ = density
σ = Stefan-Boltzman constant
ϕ = total potential
ψ = thermodynamic potential of water in soil

Subscripts

ℓ = liquid
v = vapor
vo = vapor in air-filled pore
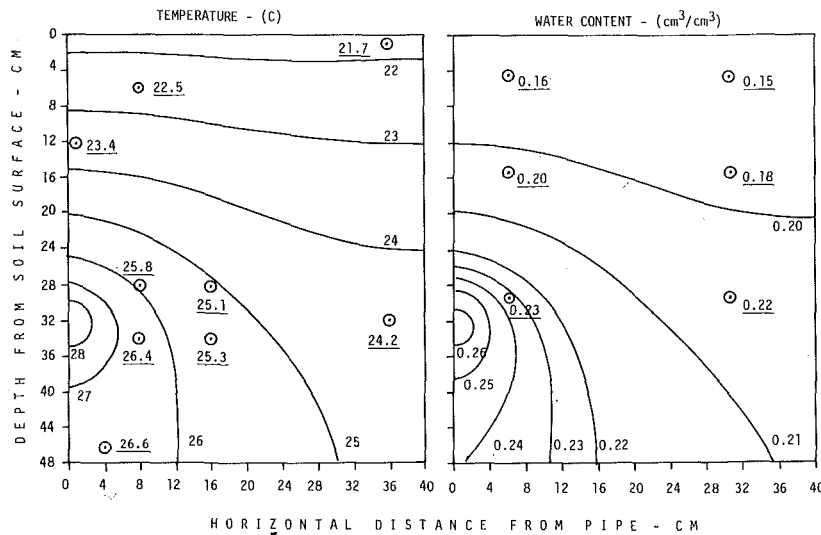w = pure liquid water

Fig. 1 Test case comparing calculated and experimental values—experimental values are underlined

P_a = the atmospheric vapor pressure,
C = the cloud cover (from 0 to 1.0), and
q_0 = the solar radiation incident upon the atmosphere.

Measured weather data was used to specify the ambient temperature, relative humidity, average wind speed, precipitation and cloud cover.

Typical node spacings were 10 cm with a 50-cm vertical spacing below a depth of 200 cm. For simulating laboratory experiments, a 4-cm node spacing was used.

Results

Several test cases were run to check the results of the computer program against the results of laboratory experiments. Plots of calculated isotherms and lines of constant moisture content for one steady-state test case are presented in Fig. 1. Also shown in Fig. 1 for comparison are selected experimental results [12] which are underlined. The experiment modeled was for a sandy soil in a container with insulated sides and bottom, atmospheric conditions 22.7°C and 70 percent relative humidity, and with a pipe on the wall at 32-cm depth. The pipe was maintained at 29°C and the moisture content of the adjacent soil was maintained at 0.27 cm³/cm³. The measured and calculated results of Fig. 1 are in good agreement.

As a further check, a closed form, steady-state solution was obtained for the configuration shown in Fig. 2. Evaporation at the soil surface was neglected and the thermal conductivity assumed constant. The temperature distribution in the experiment is approximated by the closed form solution which is

$$T = T_\infty + \frac{-T_\infty}{P} \sum_i \frac{\cos\left(\beta_i \frac{d}{D}\right) \sin\left(\beta_i \frac{t}{D}\right) \cos\left(\beta_i \frac{Y}{D}\right) \cosh\left(\beta_i \frac{X}{D}\right)}{\beta_i[2\beta_i + \sin(2\beta_i)] \sinh\left(\beta_i \frac{L}{D}\right)}$$

$$\text{where } P = \frac{\cos^2\left(\beta_i \frac{d}{D}\right) \sin\left(\beta_i \frac{t}{D}\right)}{\beta_i(2\beta_i + \sin(2\beta_i)) \tanh\left(\beta_i \frac{L}{D}\right)}$$

and the β_i are the eigenvalues of the equation

$$\tan \beta_i = \frac{hD/\lambda}{\beta_i}$$

This solution is analogous to the Kendrick and Havens equation except that surface convection is included and the surface temperature
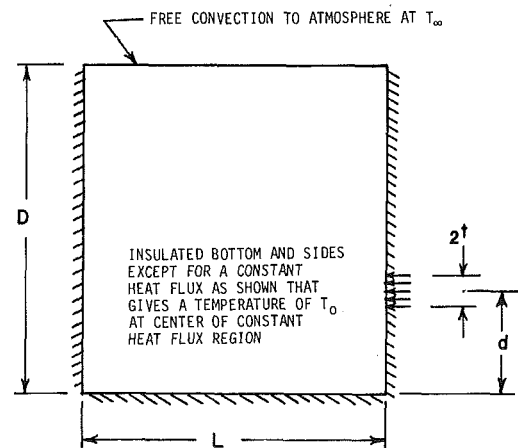

Fig. 2 Model for closed form solution simulating experimental arrangement shown in Fig. 1

does not have to be specified. Fig. 3 presents the results of this closed form approximate solution for a configuration similar to the laboratory experiment. Fig. 4 presents the results of the numerical computer program using uniform moisture content of 0.27 cm³/cm³. Figs. 3 and 4 are in good agreement. The difference is due to the lower heat transfer at the surface in Fig. 3 which resulted from neglecting evaporation.

Having thus validated the procedure, calculations were made to obtain temperature and water content profiles for various spacings and depths for summer conditions (August) and winter conditions (January). The results were obtained by imposing heat and irrigation from the subsurface system upon initial temperature and water content distributions, while assuming: (i) weather conditions for January or August, typical of the Willamette Valley in Oregon; (ii) a constant temperature of 10°C at a depth of 1200 cm; (iii) a saturated condition at a depth of 200 cm with the water content = 0.45 cm³/cm³. The computer program was run for 31 time steps of one day each. The results then represent the temperatures and moisture contents due to one month of operation of the soil warming and irrigation system. The weather conditions used were obtained by averaging the past conditions for each day over a 10-yr period. Therefore, the ambient conditions used varied from day to day. The pipe temperatures were chosen to correspond to the condenser cooling water temperature for
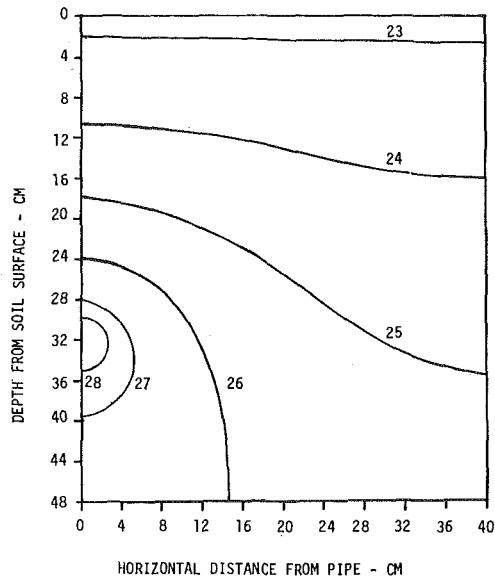
Fig. 3 Isotherms for a closed form solution for constant thermal conductivity with evaporation at the soil surface neglected
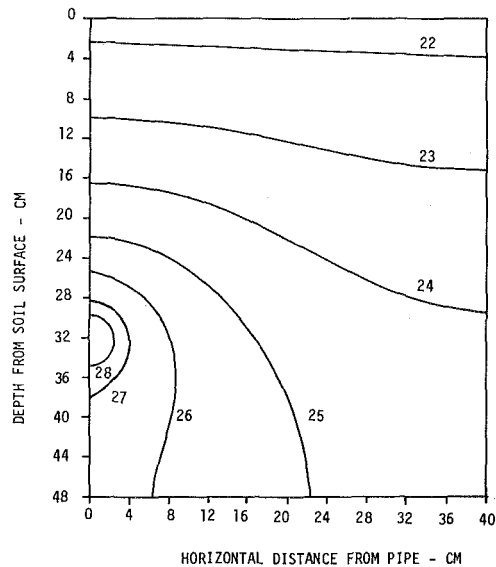

Fig. 5 Predicted moisture content (cm³/cm³) in the bottom row of figures and temperature (°C) in the top row of figures in a sandy soil for three combinations of depth and spacing with summer weather conditions

Fig. 4 Calculated isotherms (°C) for constant moisture content of 0.27 cm³/cm³

Table 1 Average temperature and moisture response of soil to a subsurface soil warming irrigation system

Depth	Spacing	Pipe Depth (cm)		Pipe Depth (cm)		Pipe Depth (cm)	
		50	100	50	100	50	100
cm	cm	Percent of Soil Above 24 C		Ave. Temp. Increase (C)		Ave. Moisture Increase (cm³/cm³)	
January 0-200	140	1.08	2.19	5.12	6.06	.0634	.0473
	280	0.57	0.86	2.44	2.83	.0386	.0264
	560	0.42	0.77	1.44	1.76	.0254	.0163
0-100	140	2.16	1.50	7.99	6.16	.104	.0673
	280	1.14	0.58	4.22	3.05	.0654	.0385
	560	0.84	0.46	2.42	1.91	.0423	.0237
August 0-200	140	65.6	77.0	7.12	8.50	.0846	.0638
	280	20.7	28.2	2.31	3.76	.0569	.0397
	560	14.5	16.4	1.99	1.65	.0337	.0211
0-100	140	83.2	72.2	9.04	7.65	.144	.0997
	280	36.8	28.2	4.15	3.69	.101	.0640
	560	10.0	16.3	2.62	1.60	.0601	.0346

a power plant near Portland, Oregon using a cooling tower as the primary heat sink. These temperatures are 41°C for August and 29°C for January. The water content of the soil at the pipe was assumed to be nearly saturated at 0.44 cm³/cm³ due to water bled from the pipe. Experimental data for ψ, k, and λ for a sandy soil were used. The data for ψ were dependent on temperature and moisture content, while the data for k and λ were dependent on moisture content.

Calculations were made for pipe depths of 50 and 100 cm and for spacings of 140, 280, and 560 cm. Fig. 5 presents typical lines of constant temperature and moisture content as functions of depth and horizontal distance from the pipe for August weather conditions. The initial temperatures and moisture contents are presented to the right of the plots.

Table 1 presents the percent of the soil maintained above 24°C, the average increase in temperature, and the average increase in moisture content in the soil from zero to 200-cm depth. These quantities are representative of the effect of the soil warming and irrigation system
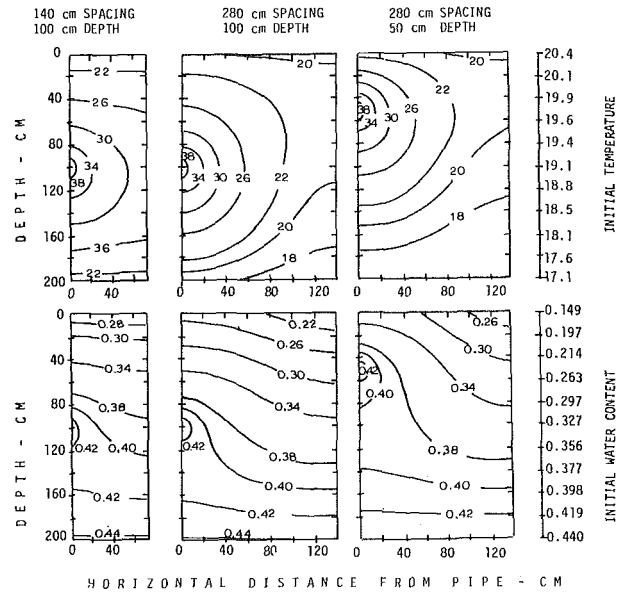
and may be used as measures of the effectiveness of a given configuration.

An estimate of the effect of different irrigation methods is gained from Figs. 6 and 7. These figures are the results of simulations of 31 days of operation in August for a pipe depth of 50 cm and a pipe spacing of 140 cm. The irrigation methods presented are for heating with: (1) no irrigation, (2) irrigation at the heating pipe, and (3) irrigation at the soil surface. The irrigation rates for cases 2 and 3 were both high at 10.8 cm/day. Fig. 6 indicates that irrigation at the soil warming pipe provides better soil heating. Fig. 7 shows that irrigation at the heating pipe also provides the highest moisture content in the soil. Much of the surface irrigation water evaporates. The moisture content did not vary appreciably at a given depth for surface or for no irrigation and the average moisture content is therefore presented. Irrigation at the heating pipe is therefore seen to be the most favorable irrigation method.

In order to assess the effect of a continuously operated soil warming system, simulations were performed using average monthly weather data for the year 1970. A time step of one week was used and the
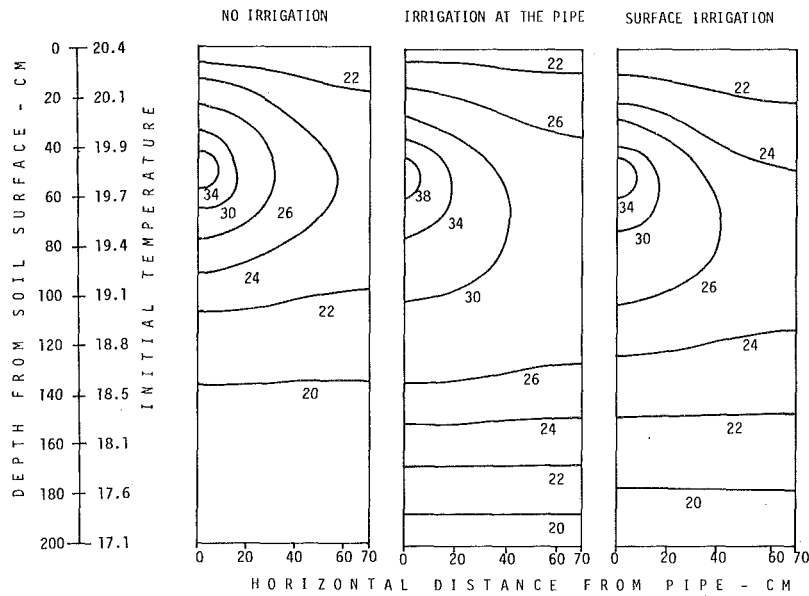
Fig. 6 Temperature distributions (°C) for various irrigation methods—the simulations are for average august weather data for Portland, Oreg. and for a pipe temperature of 41°C

simulation was performed until the temperatures repeated.

Fig. 8 presents the seasonal variation in average soil temperature at a depth of 10 cm for 1970 Portland, Oregon weather data.

Figs. 9 and 10 present simulated seasonal 10-cm depth soil temperature variations for Athens, Georgia and for St. Paul, Minnesota. Similar plots can be obtained for any depth desired.

The seasonal temperature histories could be used as an estimate of the extension of the growing season due to higher soil temperature. As an example, the growing season in Portland, Oregon, for a crop requiring a minimum soil temperature of 10°C is estimated from Fig. 8 as May to November for an unheated soil and is nearly the full year for a heated soil.

The growing season is, therefore, limited only by the air temperatures where soil heating is employed in a climate similar to that of Portland, Oregon.

Conclusions

While the results presented in Table 1 do not alone provide an optimum spacing and depth for the pipes, several generalizations can be made. The 50-cm pipe depth provides better irrigation than the 100-cm pipe depth. This is due to the effect of gravity on the flow of water and to the drying of the upper region of the soil through evaporation at the surface. From the standpoint of irrigation then, the pipe spacing should be small and the pipe depth should be as shallow as possible. Cultivation requirements demand a depth of at least 32.0 cm.

A pipe depth of 50 cm appears to produce greater heating effects for crops with a root depth of 100 cm than the 100-cm pipe depth. Furthermore, for a root depth of 200 cm, the heating effects are not greatly diminished by the shallower pipe depth. Since the cost of installation of the subsurface soil warming and irrigation system increases greatly with the depth of the pipes, it is recommended that the pipes be placed at the shallowest depth soil preparation will allow.

As expected, the heating effects increase with decreasing pipe

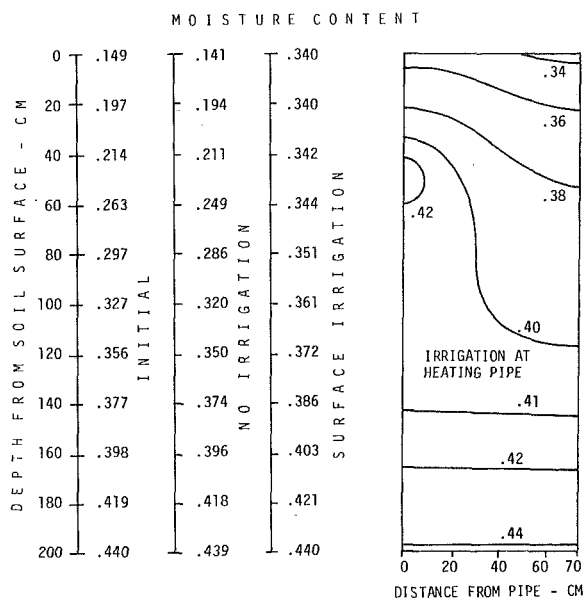**Fig. 7 Moisture content distributions (cm³/cm³) for various irrigation methods. The simulations are for average August weather data for Portland, Oreg. and for a pipe temperature of 41°C**
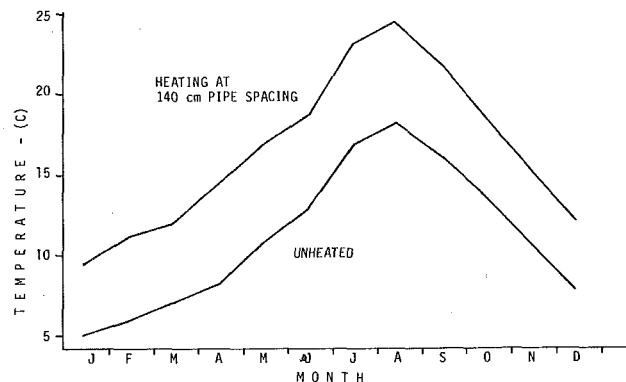

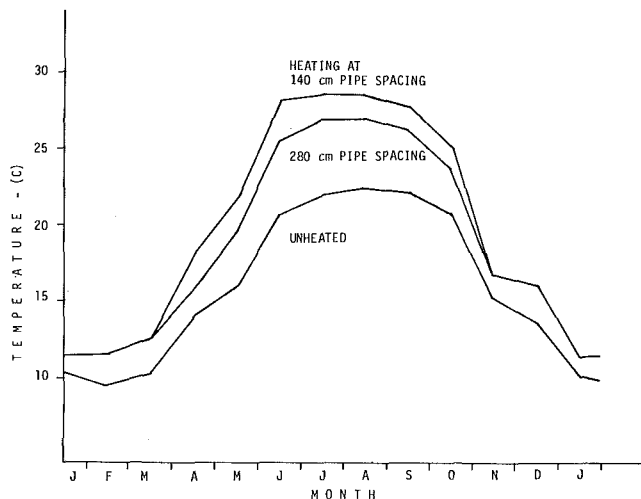**Fig. 8 Simulated Annual temperature variation at 10 cm depth in Portland, Oreg., 1970—pipe depth is 50 cm**

Fig. 9 Simulated annual temperature variation at 10-cm depth in Athens, Ga., 1970—pipe depth is 50 cm

Fig. 10 Annual temperature variation at 10-cm depth in St. Paul, Minn., 1970—pipe depth is 50 cm

spacing. Since the heating and irrigation effects increase with decreasing pipe spacing and the cost of the system is inversely proportional to the pipe spacing, an economic optimization must be performed to find the best pipe spacing. In order to perform such an optimization, one must be able to quantitatively specify the increase in crop yield due to the increased moisture content and temperature produced by the particular spacing. While such an optimization may be difficult, it is felt that an agronomist would find the results of the computer program of great use in selecting a pipe spacing and in estimating the possibility of raising two crops instead of one due to the extension of the growing season by the soil warming system.

Irrigation at the heating pipe is recommended to provide better soil warming and higher moisture content (or lower irrigation rates).

It is felt that the computer program provides a method for analyzing the effects of a soil warming and irrigation system and would be useful in selecting a pipe spacing for a given installation. It is also felt that improvements could be obtained by modeling the effects of the plant roots and foliage.

References

1 Sepaskhah, A. R., Boersma, L., Davis, L. R., and Slegel, D. L., "Experimental Analysis of a Subsurface Soil Warming and Irrigation System Utilizing Waste Heat," Paper No. 73-WA/HT-11, presented at the Winter Annual Meeting ASME, Detroit, Mich., Nov. 11–15, 1973.

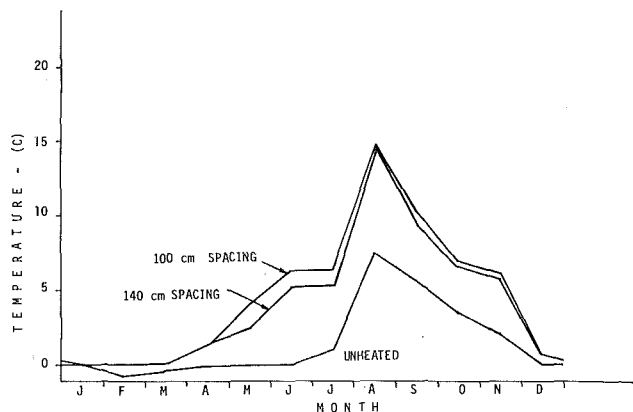2 Boersma, L., and Rykbost, K. A., "Integrated Systems for Utilizing Waste Heat From Steam Electric Plants," *Journ. Env. Qual.*, Vol. 2, 1973, pp. 179–188.

3 Kendricks, J. H., and Havens, J. A., "Heat Budget of a Subsurface Water Pipe Soil Warming System," Water Resources Research Center, University of Arkansas, 1971.

4 Cary, J. W., and Taylor, S. A., "The Interaction of the Simultaneous Diffusion of Heat and Water Vapor," *Soil Sci. Soc. Proc.*, Vol. 26, 1962, pp. 413–416.

5 Cary, J. W., and Taylor, S. A., "Thermally Driven Liquid and Vapor Phase Transfer of Water and Energy in Soil," *Soil Sci. Soc. Proc.*, Vol. 26, 1962, pp. 417–420.

6 Cary, J. W., "Water Flux in Moist Soil: Thermal Versus Suction Gradients," *Soil Sci. Soc. Amer.*, Vol. 100, 1965, pp. 168–175.

7 Philip, J. R. and de Vries, D. A., "Moisture Movement in Porous Materials Under Temperature Gradients," *Trans. Am. Geophys. Union*, Vol. 38, 1957, pp. 222–232.

8 de Vries, D. A., "Simultaneous Transfer of Heat and Moisture in Porous Media," *Trans. Am. Geophys. Union*, Vol. 39, 1958, pp. 909–916.

9 Fritton, D. D., Kirkham, D., and Shaw, R. H., "Soil Water Evaporation, Isothermal Diffusion and Heat and Water Transfer," *Soil Sci. Soc. Proc.*, Vol. 34, 1970, pp. 183–189.

10 Slegel, D. L., Davis, L. R., and Boersma, L., "Simultaneous Heat and Mass Transfer in Soils With Subsurface Heated Porous Pipes," *Proceedings of the International Conference on Heat and Mass Transfer in the Environment of Vegetation*, Dobrovnik, Yugoslavia, 1974.

11 Slegel, D. L., "Transient Heat and Mass Transfer in Soils in the Vicinity of Heated Porous Pipes," PhD thesis, Oregon State University, 1974.

12 Sepaskhah, A. R., "Experimental Analysis of Subsurface Heating and Irrigation on the Temperature and Water Content of Soils," PhD thesis, Oregon State University, 1974.

13 Hogan, T. T., Leipins, A. A., and Reed, E., "An Engineering Economic Study of Cooling Pond Performance," Environmental Protection Agency Water Pollution Research Series No. 16130DFX05/70, prepared by Littleton Research and Engineering Corp., May 1970.

A. Sakurai
Professor.

M. Shiotsu
Research Assistant.

Institute of Atomic Energy,
Kyoto University,
Kyoto, Japan

Transient Pool Boiling Heat Transfer

Part 1: Incipient Boiling Superheat

Incipient boiling superheat for exponentially increasing heat inputs to a platinum wire supported horizontally in a pool of water was measured for exponential periods ranging from 5 ms to 10 s and for subcoolings ranging from 25 to 75K under atmospheric pressure. The heat transfer coefficient before the initiation of boiling was related to those by conduction and by natural convection. The heat flux at the incipient boiling point increased with the decrease in the period. The log-log plot of the heat flux against the superheat at the incipient boiling point had a single asymptotic line of slope 2 which was independent of subcoolings in the high heat flux region. On the other hand, as the heat flux decreased to zero, the superheat tended to approach to a constant value for each subcooling. This asymptotic superheat at zero heat flux was higher for higher subcooling. Transient incipient boiling superheat was reasonably explained by the combination of two kinds of incipient boiling models.

Introduction

A step input of reactivity in a nuclear reactor will result in a power excursion in which reactor power rises exponentially with time. The exponential period is shorter for a larger size of the step reactivity. The study of the incipient boiling superheat due to an exponential increase in heater power, therefore, is important for the safety evaluation of a nuclear reactor under reactivity accident.

The heat transfer coefficient before the incipient boiling point for an exponential heat input $Q_0 e^{t/t_0}$ to the heater varies with the exponential period t_0. Therefore, the heat flux at the incipient boiling point also varies with the period. The relation between the superheat and the heat flux at the incipient boiling point for the heat inputs with various exponential period should be made clear quantitatively.

Johnson, Schrock, et al. carried out an incipient boiling study for exponentially increasing heat inputs under atmospheric and pressurized conditions [1, 2].[1] Johnson showed that the incipient boiling superheat was higher for shorter exponential period and for lower system pressure and suggested that boiling commenced at the intersection of the transient nonboiling curve and the steady nucleate boiling curve [3].

Hall and Harrison investigated extremely fast transient boiling of water at atmospheric pressure [4]. They applied the same type of

analysis as was proposed by Hsu [5] for the prediction of incipient boiling superheat due to the heat input exponentially increasing with time. They showed that the observed incipient boiling superheats were considerably higher than the predicted values.

The purpose of this study is to make clear experimentally the relation between the superheat and the heat flux at the incipient boiling points for exponentially increasing heat inputs to a heater in subcooled water under atmospheric condition and to propose a model which explains the observed relation for subcoolings.

Apparatus and Method

Boiling Vessel. A cylindrical stainless steel vessel of 20 cm in diameter and 25 cm in height was used as the boiling vessel. The water temperature in the vessel was kept constant by an outer bath. The vessel system was held on a soft cushion to prevent outer disturbances from entering into the vessel.

Test Heater. A platinum wire heater of 1.2 mm in diameter and 97.9 mm long was supported horizontally in the vessel. In order to prevent the error due to the heater terminal effect, two fine wires were spot-welded as potential taps on the heater surface 27.1 and 25.0 mm apart from each terminal. The effective length of the heater was 45.8 mm.

Heating System. The schematic diagram of the heating system is shown in Fig. 1. The platinum wire heater was heated by the electrical current from a power amplifier. The input signal of the power amplifier was controlled by a high-speed analogue computer so that the heat generation rate of the heater accorded with the desired one. Instantaneous heat generation rate in the heater was calculated by the computer and was compared with the reference signal corre-

---

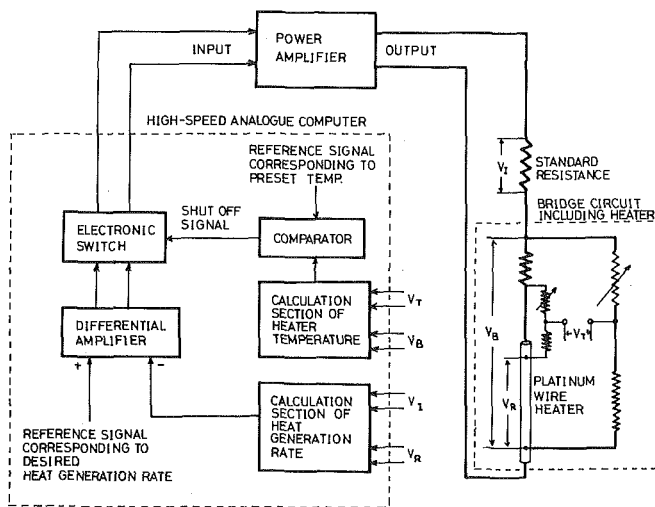[1] Numbers in brackets designate References at end of paper.

Fig. 1 Schematic diagram of the heating system

sponding to the desired heat generation rate. The difference voltage between these signals was highly amplified and fed back to the power amplifier so as to minimize the difference. The instantaneous average temperature of the heater was also calculated by the computer. As soon as it rose up to the preset value, the input signal of the power amplifier was shut off to protect the heater from melting. The power amplifier consisted of 800 transistors in parallel which supplied the current up to 2000 amperes at a power level of about 80 kW. Its power source was the storage batteries. By a modified analogue computer program, it was possible to control the input signal of the power amplifier so that the heater temperature accorded with the desired one. Stable transition boiling was realized with this system [6].

Measurement of the Heat Flux and Surface Temperature of the Heater. A bridge circuit including the heater between two potential taps as one branch shown in Fig. 1 was balanced before each experimental run for the bulk water temperature. When an exponential heat input was applied to the heater, the heater temperature increased and the bridge became unbalanced. The instantaneous output voltage of the bridge circuit V_T and the voltage drops across the bridge circuit V_B, across the heater V_R, and across the standard resistance V_I were recorded on an electromagnetic oscillograph. The instantaneous electrical resistance of the heater was determined from the values of V_T and V_B. The average temperature of the heater $T_a(t)$ was calculated from the value of the electrical resistance with the aid of the previously calibrated resistance-temperature relation. The heat generation rate of the heater $Q(t)$ was determined from the values of

V_R and V_I. The instantaneous heat flux from the heater $q(t)$ is the difference between the heat generation rate per unit surface area $DQ(t)/4$ and the rate of change of energy storage in the heater $\rho_h c_h D/4$ $(dT_a(t)/dt)$ obtained from the faired average temperature-time curve, where ρ_h, c_h are the density and the specific heat of the heater material. It was assumed that the surface temperature of the heater was uniform. The surface temperature $T_s(t)$ was calculated from the nonsteady thermal conduction equation in the heater having a time dependent heat generation rate $Q(t)$ and the heat flux $q(t)$ as a boundary condition at the surface. All these calculations were carried out by a digital computer. The uncertainties are estimated to be within ± 1 percent in the heat generation rate, ± 2 percent in the heat flux, and to be within ± 1 K in the surface temperature.

Incipient Boiling Detection. The inception of boiling was detected with the use of a piezoelectric hydrophone using a lead-zirconium-titanate crystal sensing element 40 mm away from the heater, since a pressure wave is known to be generated at an early stage of the bubble growth. Maximum allowable temperature of the hydrophone was 353 K. Its output signal was amplified and recorded on the electromagnetic oscillograph together with the signals from the bridge circuit including the heater. Frequency characteristics of the overall detection circuit were flat from 1 Hz to 1 kHz where the sensitivity was 0.1 mm/μbar on the oscillograph paper, −3 dB at 2 kHz and −22 dB at 10 kHz. It was estimated from Robinson's results of pressure disturbance caused by the bubble growth [7] that the inception of boiling would satisfactorily be detected with this sensitivity.

Experimental Procedure

Prior to each series of experiments, the test heater surface and the inner surface of the boiling vessel were cleaned with trichloroethylene followed by thorough rinsing with hot distilled water. Distilled and deionized water was then filled in the boiling vessel and the water was boiled for more than half an hour by a gas heater to remove dissolved gases. The free surface of the water was immediately covered with a sheet of Teflon to prevent the dissolution of air. This procedure was effective and the reproducibility of the incipient boiling superheat results was proved to be within ±1K. The water temperature in the outer bath had been adjusted by a thermostat with an immersion heater and a stirrer. The water temperature in the boiling vessel was measured by a mercury thermometer and when it reached the desired value, the stirrer and the immersion heater of the outer bath were turned off to prevent their noises during the experimental run. The time needed for the longest run was less than one minute and no appreciable change in the bulk water temperature in the boiling vessel was observed during the run. An exponentially increasing heat input, $Q = Q_0 e^{t/t_0}$ was then applied to the test heater by using the heating system. The heat flux and the surface superheat at the incipient boiling point were measured.

Steady boiling curve for the same heater was also measured by

---

═══════Nomenclature═══════

$a = y/r$, constant
$b = r/r_c$, constant
c_h = specific heat of heater material
c_ℓ = specific heat of liquid
D = heater diameter
Gr = Grashof number
h_c = conduction heat transfer coefficient
$h_m = (h_c{}^4 + h_n{}^4)^{1/4}$
h_n = natural convection heat transfer coefficient
k = thermal conductivity of liquid
P = pressure
Pr = Prandtl number
Q = heat input (heat generation rate per unit volume)
q = heat flux

r = radius of bubble nucleus
r_c = cavity mouth radius
r_{cu} = maximum unflooded cavity mouth radius
T = temperature
T_a = average temperature of the heater
T_i = surface temperature of the heater at the incipient boiling point
T_{ov} = maximum value of the heater surface temperature after initiation of boiling
T_s = surface temperature of the heater
T_{sat} = saturation temperature
T_∞ = liquid temperature at $y = \infty$ (uniform liquid temperature before heating commences)
t_0 = exponential period
$\Delta T_i = T_i - T_{sat}$, maximum temperature over-

ershoot
$\Delta T_{ov} = T_{ov} - T_{sat}$, incipient boiling superheat
$\Delta T_{sat} = T_s - T_{sat}$, heater surface superheat
$\Delta T_{sub} = T_{sat} - T_\infty$, liquid subcooling
y = distance from heater surface
θ_1 = advancing contact angle
θ_2 = receding contact angle
ρ_h = density of heater material
ρ_ℓ = density of liquid
σ = surface tension of liquid

Subscripts

i = incipient boiling point
ℓ = liquid
v = vapor

---

gradually decreasing the heat flux from the value near the steady critical heat flux. The reproducibility of the curve was excellent: the uncertainty of the surface superheats for the heat fluxes in the steady nucleate boiling curve was within ±1K.

Results

The incipient boiling for heat inputs exponentially increasing with time was studied by a series of experiments with the exponential periods from 5 ms to 10 s and for subcoolings of 25, 35, 50, and 75K under atmospheric condition.

Transient Boiling Process. Fig. 2 shows typical changes in the heater surface temperature and the heat flux with time for the exponential heat input. The heater surface temperature at first increases with the increase in the heat input. Boiling commences at T_i beyond saturation temperature T_{sat}. The heater temperature continues to increase up to T_{ov}, then decreases and again increases with lower rate. When the heat flux reaches a certain value, q_{max}, which is named the transient maximum heat flux, the heater temperature rapidly increases. The temperature differences of $\Delta T_i = T_i - T_{sat}$ and $\Delta T_{ov} = T'_{ov} - T_{sat}$ are called the incipient boiling superheat and the maximum temperature overshoot, respectively. This transient phenomenon is shown in Fig. 3 as a plot of $\log q$ versus $\log \Delta T_{sat}$ by the solid line. The superheat ΔT_{sat} is the difference between the surface temperature of the heater and the saturation temperature. The steady boiling curve for the same heater is also shown in the figure by a broken line for comparison. The incipient boiling point in this case lies on the left-hand side of the steady boiling curve.
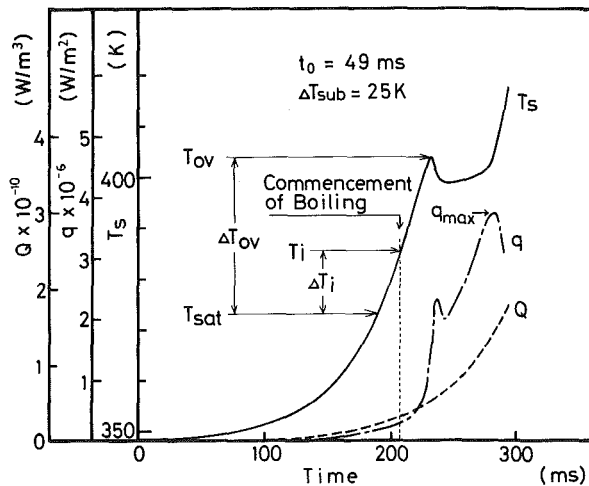

Fig. 2 Illustrative time traces of heat input Q, heater surface temperature T_s, and heat flux q
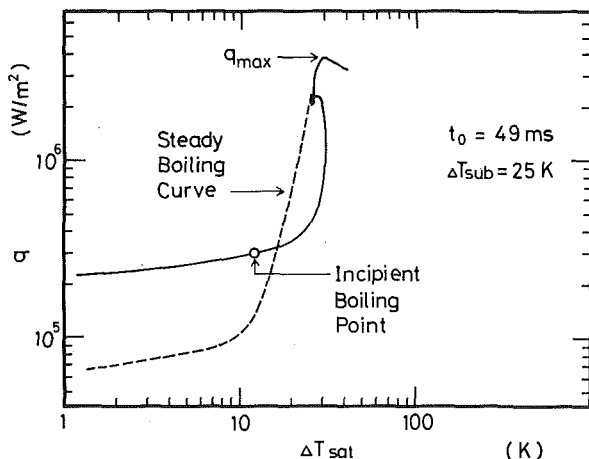

Fig. 3 The relation between heat flux and superheat for the experimental run shown in Fig. 2

Heat Transfer before the Commencement of Boiling. When an exponentially increasing heat input was applied to the heater immersed in the pool of water, the heater surface temperature and the heat flux increased as shown in Fig. 2. The heat transfer coefficients at several surface temperature points before the commencement of boiling were calculated on each of the experimental results for the periods ranging from 5 ms to 10 s. The typical results of these calculated heat transfer coefficients at $T_s = 363$ K and at $T_s = 383$K for $\Delta T_{sub} = 25$ K are shown versus period in Fig. 4(a). In the region of short periods, they are independent of the surface temperature and increase with the decrease in the period. On the other hand, in the region of long periods, they approach a constant value which is higher for higher surface temperature. Similar relations between the heat transfer coefficient and the period were obtained for the subcoolings of 35, 50, and 75K. The results for the subcooling of 50K are shown in Fig. 4(b). It is shown by the comparison between the heat transfer coefficients in Fig. 4(a) and those in Fig. 4(b) at the same periods and surface temperature that they are independent of subcooling in the region of short periods but they are higher for higher subcooling in the long period region. There seem to be two asymptotic lines; one is independent of the surface temperature and of the subcooling and the other is dependent on them.

Incipient Boiling Superheat. The values of incipient boiling superheat for periods ranging from 5 ms to 10 s and for subcooling of 25K are shown in Fig. 5. Heat transfer processes before the commencement of boiling for some of the experimental runs are shown by broken lines in the figure. The steady boiling curve for the same heater is also shown in the figure for comparison. The heat transfer coefficient and therefore the heat flux at the incipient boiling point is higher for shorter periods. The incipient boiling superheat is almost independent of the heat flux in the low heat flux region but is heat flux dependent is the high heat flux region. Incipient boiling points for the periods shorter than 1 s are on the left-hand side and those for the periods longer than 1 s are on the right-hand side of the steady boiling curve. The relation between the superheat and the heat flux at the incipient boiling point for different subcoolings are shown in Fig. 6. There seems to be an asymptotic line of slope 2 which is independent of subcoolings for high heat fluxes. On the other hand as the heat flux decreases, the superheat at the incipient boiling point tends to approach a constant value for each subcooling. This asymptotic superheat becomes higher with the increase in subcooling.

Maximum Temperature Overshoot. The maximum temperature overshoot ΔT_{0v} for various subcoolings is shown versus period in Fig. 7. The incipient boiling superheat ΔT_i is also shown in the figure for comparison. The maximum temperature overshoot is higher for shorter period and for higher subcooling and is higher than the incipient boiling superheat for the same period. The difference between ΔT_{0v} and ΔT_i becomes greater for shorter period.

Discussion

Comparison with Conventional Results. Johnson, Schrock, et al. measured the incipient boiling superheats for exponential heat inputs under subcooled conditions at atmospheric pressure [1]. Their measured values for each period were considerably scattered. Johnson took the mean of the values for each period and showed its dependence on period and on subcooling. The mean values for period 5, 15, and 50 ms were 18.9, 15.0, and 16.1 K respectively for the subcooling lower than 5.5 K. They were 25.6, 19.4, and 20.5 K respectively for the subcooling of 23.3 K and 35.6, 25.6, and 18.9 K respectively for the subcooling of 62.2 K [3]. The mean values are considerably higher than our results for the same periods shown in Fig. 7.

Johnson presented a quasi-steady state nucleate boiling model which predicted that the boiling commenced at the intersection of the transient nonboiling curve and the steady boiling curve [3]. However, it is clearly seen in Fig. 5 that the incipient boiling points do not generally lie on the steady boiling curve. Moreover, as shown in Fig. 6, the relation between the heat flux and the superheat at the incipient boiling points is different from one another depending on subcooling. These experimental results obviously reject the incipient boiling criterion by the model.
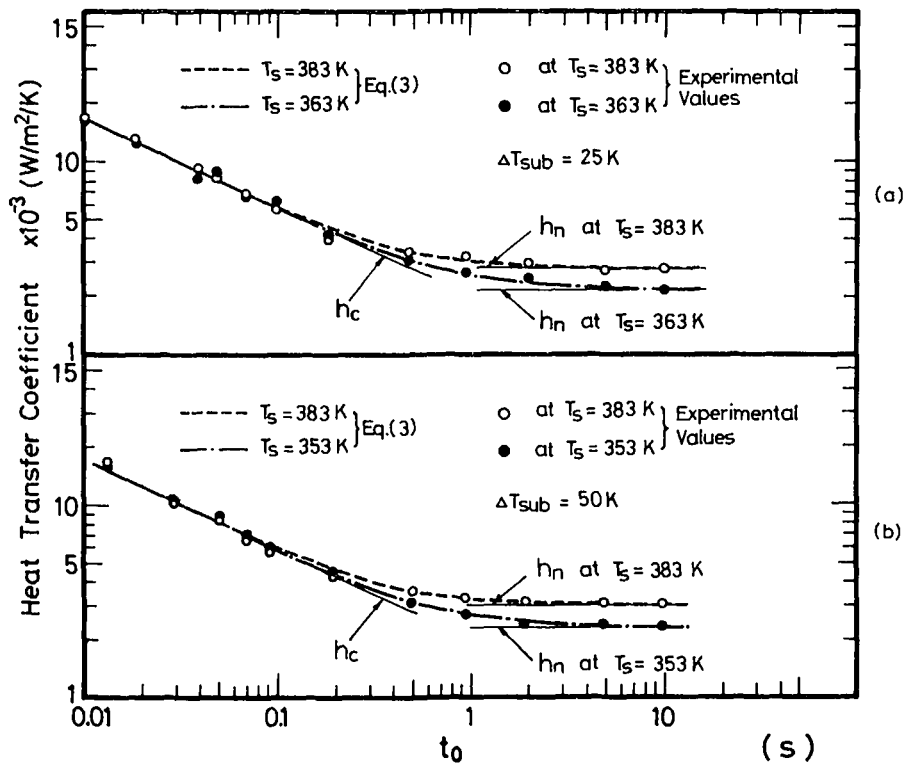
Fig. 4 Heat transfer coefficient before the initiation of boiling as a function of exponential period
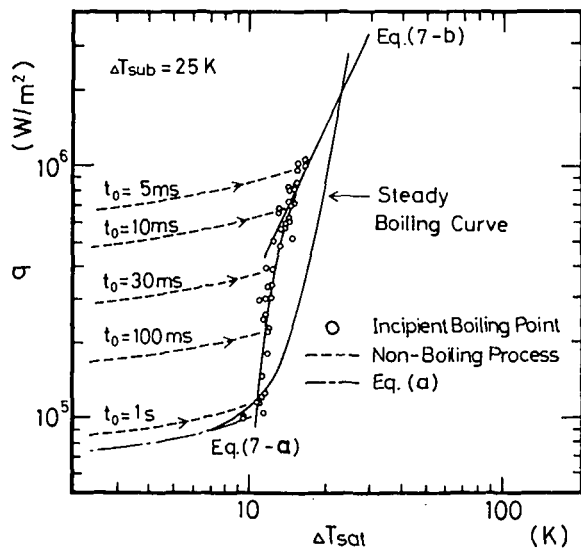

Fig. 5 The relation between heat flux and superheat at incipient boiling points for subcooling of 25 K. Some of the heat transfer processes before the incipient boiling points are shown as broken lines
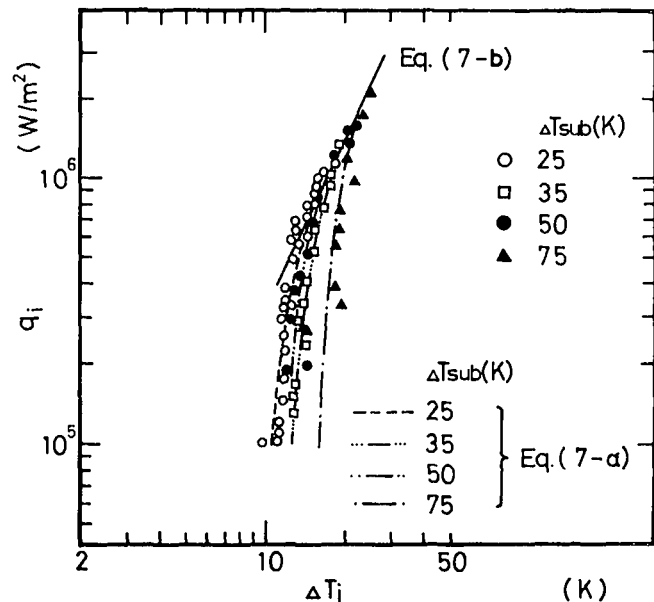

Fig. 6 The relation between heat flux and superheat at incipient boiling points for different subcoolings

Hall and Harrison measured the incipient boiling superheats under atmospheric pressure for the exponential periods ranging from 0.7 to 5 ms [4]. The longest period in their work corresponds to the shortest one in ours. The incipient boiling superheats for the period of 5 ms shown in their graph are 42 K for the subcooling of 24 and 42 K, 50 K for the subcooling of 62 K and 52 K for the subcooling of 80 K. These are 20 K or more higher than our results for the same period. They supposed that the incipient boiling superheat was equal to the maximum temperature overshoot. However, as shown in Fig. 7, the maximum temperature overshoot is higher than the incipient boiling superheat and the difference between these values is about 20 K at

the shortest period tested. They applied the same type of analysis as was proposed by Hsu [5] to the prediction of incipient boiling superheat for the exponentially increasing heat input. They reported that the incipient boiling superheat observed were about 30 K higher than the predicted values. This difference and the difference between their and our results mentioned before would be reduced if they had measured the incipient boiling superheat instead of the maximum temperature overshoot. The temperature overshoot phenomenon is investigated in more detail in Part 2 of this research which will follow in a subsequent paper.
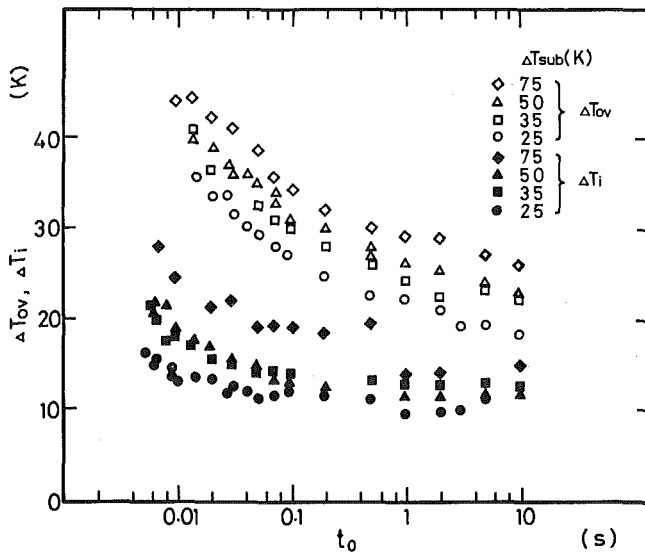
Fig. 7 Maximum temperature overshoot and incipient boiling superheat as a function of exponential period with subcooling as the parameter

Heat Transfer before the Commencement of Boiling. It was mentioned previously that the log-log plot of the nonboiling heat transfer coefficient against period shown in Figs. 4(a) and 4(b) seem to have two asymptotic lines for short and long periods respectively.

If the period is sufficiently short and therefore the increasing rate of the heat input and the corresponding increasing rate of the surface temperature are too rapid for natural convection to contribute appreciably to the heat transfer before boiling commences, water would act as an infinite solid with regard to heat transfer. The heat transfer coefficient in this case can be obtained as a function of time by solving the transient heat conduction equation. The coefficient for exponential heat input obtained with this procedure is infinite at $t = 0$ but it decreases rapidly and approaches a certain asymptotic value of h_c with the increase in t/t_0 [8]. For $t/t_0 \geqq 3$, it is well expressed by

$$h_c = (k\rho_\ell c_\ell/t_0)^{1/2}K_1(\mu D/2)/K_0(\mu D/2) \tag{1}$$

where $\mu = (\rho_\ell c_\ell/kt_0)^{1/2}$, and K_0 and K_1 are the modified Bessel functions of the second kind of zero and first orders. The initial value, Q_0, of the exponential heat input in the present investigation is so low that the increase in heater temperature before $t/t_0 = 3$ is insignificant and therefore the curve predicted by equation (1) will correspond to the asymptotic line for the short periods.

On the other hand, when the increasing rate of the heat input is sufficiently low, heat would be transferred by natural convection. Natural convection heat transfer coefficient h_n is expressed by the following equation [9].

$$h_n = 0.53 \, k \, (GrPr)^{1/4}/D \tag{2}$$

The value of h_n is dependent on the surface temperature of the heater and the subcooling. This will correspond to the asymptotic value for the long periods.

The values of h_n at $T_s = 363$ and 383 K for $\Delta T_{sub} = 25$ K and those at $T_s = 353$ and 383 K for $\Delta T_{sub} = 50$ K are shown in Figs. 4(a) and 4(b) respectively. The curve predicted by equation (1) is also shown in these figures. The curves predicted by equation (1) and equation (2) at each surface temperature are the asymptotic lines for short and long periods respectively as expected. The results of the nonboiling heat transfer coefficients for the period shorter than 0.1 s are well expressed by equation (1) and those for the period longer than 5 s are by equation (2). The intermediate period region (0.1 s < t_0 < 5 s) is the transition region from natural convection heat transfer to conduction heat transfer. The nonboiling heat transfer coefficients for the ranges of exponential period and subcooling tested including those

in the transition region are found to be well expressed by the following empirical formula

$$h_m = (h_c{}^4 + h_n{}^4)^{1/4} \tag{3}$$

The curves predicted by equation (3) for each surface temperature are shown in Figs. 4(a) and 4(b).

Incipient Boiling Superheat. It is commonly accepted that bubbles originate at small cavities on the heater surface. If the active cavities of mouth radii bigger than r_{cu} do not exist on the surface but those smaller than r_{cu} are continuously distributed, conditions required to initiate boiling for transient heat input would be presented by the following model obtained by extending the formulation by Hsu [5] and Rohsenow [10].

The bubble nucleus of radius r is sitting at the cavity mouth of radius r_c at equilibrium, where r is related to r_c by $r = br_c$. The force balance equation for the bubble nucleus is given as

$$P_v = P_\ell + 2\sigma/r \tag{4}$$

The temperature of the vapor in the bubble nucleus is higher than the saturation temperature at the liquid pressure and it can be obtained as a function of r by combining equation (4) with the temperature-pressure relation of saturated steam from steam table:

$$T_v = f(r) \tag{5}$$

The temperature profile in the liquid near the surface is expressed as a linear equation of the distance from the heater surface, y, as

$$T_\ell = T_s - qy/k \tag{6}$$

It is postulated that initial boiling will occur when the liquid temperature at the position $y = ar$ reaches the vapor temperature given by equation (5). The relation between incipient boiling heat flux and superheat is given by the following equations.

$$q_i = \frac{k}{abr_{cu}} [\Delta T_i - f(br_{cu}) + T_{sat}] \tag{7a}$$

$$\text{for } 0 \leqq q_i \leqq -\frac{k}{a}\frac{df(r)}{dr}\bigg|_{r = br_{cu}}$$

$$q_i = \frac{k}{ar_i} [\Delta T_i - f(r_i) + T_{sat}] \tag{7b}$$

$$\text{for } q_i > -\frac{k}{a}\frac{df(r)}{dr}\bigg|_{r = br_{cu}}$$

where r_i is a positive root of the equation

$$\frac{df(r)}{dr} = -\frac{a}{k}q_i$$

The relation between ΔT_i and the period can also be obtained by combining equation (3) with equations (7a) and (7b). This model is called in this paper the "superheated thermal layer model."

The values of "a" and "br_{cu}" were fitted by the least square method so that equations (7a) and (7b) may express the experimental results for each subcooling shown in Fig. 6. The reasonable value of a was 1.8 independent of subcooling and the values of br_{cu} were 2.69, 2.16, 2.29, and 1.53 μm for subcoolings of 25, 35, 50, and 75 K respectively. In fitting these values, only the data points for the period shorter than 0.1 s were used where heat transfer before the commencement of boiling is solely by conduction. The reason is that for the period longer than 0.1 s, the temperature distribution on the heater circumference may not be uniform owing to the effect of natural convection. If it is not uniform, the calculated surface temperature by supposing a uniform temperature distribution on the heater surface will be lower than that at the place of highest surface temperature where boiling commences. The curves predicted by equations (7a) and (7b) with the fitted values of a and br_{cu} are shown in Fig. 6. All of the experimental results including those for $t_0 > 0.1$ s for subcoolings of 25, 35, and 50 K are well expressed by these curves. However, for subcooling of 75 K, the experimental results for $t_0 \leqq 0.5$ s are nearly on the curves but those for $t_0 > 0.5$ s are about 3 K lower superheat side, presumably because of the aforementioned error.

If the position $y = 1.8 r$ is postulated to be at the top of the bubble nucleus, the value of "b" will be geometrically determined to be 1.67 and the values of r_{cu} are determined from the values of br_{cu} to be 1.61, 1.29, 1.37, and 0.92 μm for subcoolings of 25, 35, 50, and 75 K respectively. On the other hand, if the shape of the bubble nucleus is postulated to be hemispherical ($b = 1$), the values of r_{cu} are equal to those of br_{cu}. Two different values of r_{cu} for the same subcoolings are obtained corresponding to these two postulations. It is impossible in the present investigation to determine which postulation would be more appropriate. The values of a and b were postulated by many workers. Hsu postulated that $a = 1.6$, $b = 1.25$ [5], Bergles and Rohsenow, $a = 1$, $b = 1$ [11], and Han and Griffith, $a = 1.5$, $b = 1$ [12]. The value of a determined in this work is close to those by Hsu and by Han and Griffith. Rohsenow indicated that the trend predicted by equation (7a) with $a = b = 1$ could not clearly be observed in a large number of available experimental data [10].

The asymptotic superheat at zero heat flux for each subcooling is obtained from equation (7a) with $q_i = 0$. The superheat corresponds to the incipient boiling superheat in the isothermal liquid. Fabic suggested a model which predicts the incipient boiling superheat in the isothermal liquid [13]. In this model, the radius of the maximum unflooded cylindrical cavity under subcooled condition is give by

$$r_{cu} = \frac{2\sigma_0 \cos{(\pi - \theta_1)}}{P_{\ell_0} - P_{v_0}} \tag{8}$$

where θ_1 is the advancing contact angle and suffix "0" refers to the initial subcooled condition. Boiling commences when the force balance on the bubble meniscus in the maximum unflooded cavity breaks. The incipient boiling condition thus is

$$P_{vi} = P_\ell + \frac{2\sigma \cos{\theta_2}}{r_{cu}} \tag{9}$$

where θ_2 is the receding contact angle. The incipient boiling superheat ΔT_i is obtained from P_{vi} by the use of the steam table. This model is called in this work the "cavity model."

The values of r_{cu} predicted by this model are shown by the broken line in Fig. 8 together with those obtained from the experimentally determined values of br_{cu} with $b = 1.67$. The latter radii are more than two times as big as the former ones but the trend of dependence on subcooling is comparable. The values of r_{cu} with $b = 1$, which are not shown in the figure, are 1.67 times as big as those with $b = 1.67$ and are also comparable in the trend of dependence on subcooling.

The incipient boiling superheats predicted by the cavity model were compared in Fig. 9 with the asymptotic superheats obtained from

equation (7a) with $q_i = 0$. The superheat predicted by this model, which is shown by the broken line, is higher than the asymptotic superheat but the dependence on subcooling again is comparable. Here in both comparisons of r_{cu} and the superheat, the advancing and the receding contact angles suggested by Fabic, $\theta_1 = 108$, $\theta_2 = 66$ were used. However, these contact angles would vary for different heater materials and the disagreement in Figs. 8 and 9 may partly be due to the difference in contact angles. The shape of the cavity in the commercially prepared surface would not be cylindrical and this will also affect the incipient boiling superheat. Incidentally, if the disagreement is supposed to be solely due to the difference of contact angles, the best agreement of r_{cu} and of ΔT_i is obtained when θ_1, θ_2 are chosen to be 136 and 52 deg as shown in Figs. 8 and 9.

It is shown by the discussion herein that the incipient boiling superheat for the transient heat input would be reasonably explained by the combination of the superheated thermal layer model and the cavity model.

In forced convection systems under steady state condition, the nonboiling heat transfer coefficient varies with the flow rate. It is expected by our study that the incipient boiling superheat for the variation of flow rate would be predicted by equations (7a) and (7b).

Conclusions

The heat transfer coefficient before the commencement of boiling for the exponential heat input is given by equation (3) as the combination of the conduction and the natural convection heat transfer coefficients.

The heat flux at the incipient boiling point increases with the decrease in the exponential period. The log-log plot of the heat flux against the superheat at the incipient boiling point has a single asymptotic line of slope 2 which is independent of subcoolings for the high heat flux region. On the other hand, as the heat flux decreases to zero, the superheat tends to approach a constant value for each subcooling. This asymptotic superheat at zero heat flux is higher for higher subcooling.

The relation between the superheat and the heat flux at the incipient boiling point is well expressed by equations (7a) and (7b) with the fitted values of a and br_{cu}. The fitted value of a was 1.8 independent of subcooling. The dependency upon subcooling of the values of r_{cu} obtained from the fitted values of br_{cu} can be predicted reasonably by the cavity model. It was shown that the transient incipient boiling superheat could be reasonably explained by the combination of the superheated thermal layer model and the cavity model.
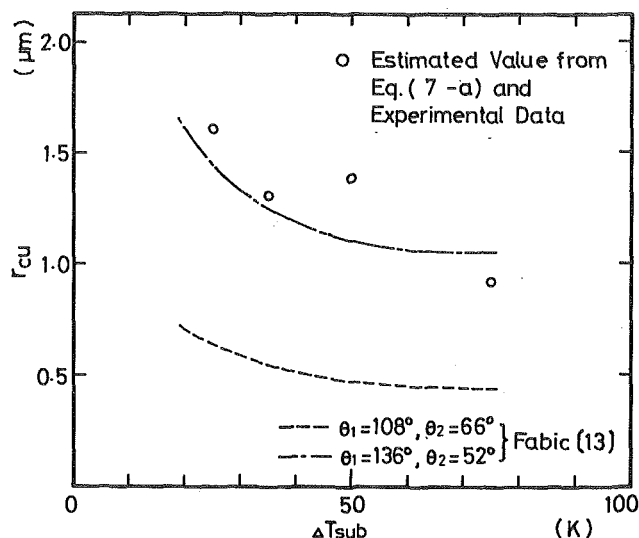

Fig. 8 Comparison of maximum unflooded cavity radius predicted by the cavity model with that estimated from equation (7a) and experimental data
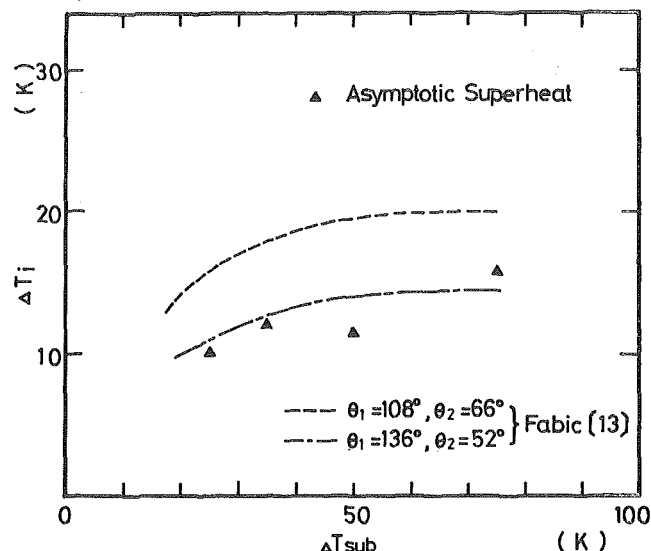

Fig. 9 Comparison of incipient boiling superheat predicted by the cavity model with the asymptotic superheat obtained from equation (7a) with $q_i = 0$

References

1 Johnson, H. A., Schrock, V. E., Selph, F. B., Lienhard, J. H., and Rosz-tóczy, Z. R., "Temperature Variation, Heat Transfer, and Void Volume Development in the Transient Atmospheric Boiling of Water," USAEC Report SAN 1001, Jan. 1961.

2 Johnson, H. A., Schrock, V. E., Fabic, S., and Selph, F. B., "Transient Boiling Heat Transfer and Void Volume Production in Channel Flow," USAEC Report SAN 1007, March 1963.

3 Johnson, H. A., "Transient Boiling Heat Transfer," *Heat Transfer 1970*, Vol. V, B3.1, Elsevier Pub. Co., Amsterdam, 1970 or *International Journal of Heat and Mass Transfer*, Vol. 14, 1971, pp. 67–82.

4 Hall, W. B., and Harrison, W. C., "Transient Boiling of Water at Atmospheric Pressure," *International Heat Transfer Conference*, Institute of Mechanical Engineering, 1966, pp. 186–192.

5 Hsu, Y. Y., "On the Size Range of Active Nucleation Cavities on a Heating Surface," JOURNAL OF HEAT TRANSFER, TRANS. ASME, Series C, Vol. 84, Aug. 1962, pp. 207–216.

6 Sakurai, A., and Shiotsu, M., "Temperature-Controlled Pool-Boiling Heat Transfer," *Heat Transfer 1974*, Vol. IV, B3.1, Scripta Book Co., Wash-ington, D.C., 1974, pp. 81–85.

7 Robinson, G. E., Schmidt, F. W., Block, H. R., and Green, G., "An Experimental Determination of Isolated Bubble Acoustics in a Nucleate Boiling System," *Heat Transfer 1974*, Vol. IV, B2.9, Scripta Book Co., Washington, D.C., pp. 75–80.

8 Hayashi, S., Sakurai, A., and Iwazumi, T., "Transient Heat Transfer in the Heterogeneous Water Reactor (1)," *Journal of Atomic Energy Society of Japan*, Vol. 5, No. 5, May 1963, pp. 403–411 or NSJ-Tr-1, 1966.

9 McAdams, W. H., *Heat Transmission*, McGraw-Hill Book Co., New York, 1954.

10 Rohsenow, W. M., "Nucleation in Boiling Heat Transfer," ASME Paper 70-HT-18, ASME Symposium, Detroit, May 1970.

11 Bergles, A. E., and Rohsenow, W. M., "The Determination of Forced-Convection Surface Boiling Heat Transfer," JOURNAL OF HEAT TRANSFER, TRANS. ASME, Series C, Vol. 86, Aug. 1964, pp. 365–372.

12 Han, C. Y., and Griffith, P., "The Mechanism of Heat Transfer in Nucleate Pool Boiling—Part I," *International Journal of Heat and Mass Transfer*, Vol. 8, 1965, pp. 887–904.

13 Fabic, S., "Vapor Nucleation on Surfaces Subjected to Transient Heating," USAEC Report SAN 1008, Aug. 1964.

A. Sakurai
Professor.

M. Shiotsu
Research Assistant.

Institute of Atomic Energy,
Kyoto University,
Kyoto, Japan

Transient Pool Boiling Heat Transfer

Part 2: Boiling Heat Transfer and Burnout

Transient boiling heat transfer for exponential heat input to a platinum wire supported horizontally in a pool of water was investigated. Transient boiling heat transfer coefficient, transient DNB heat flux, and transient maximum heat flux were obtained for exponential periods ranging from 5 ms to 10 s and for system pressures ranging from 0.1 to 2.1 MPa. Transient boiling heat transfer coefficient after the commencement of boiling becomes lower than the steady boiling heat transfer coefficient at the same heat flux. This was explained to be as a result of the time lag of the activation of originally flooded cavities for the increasing rate of the heat input. Initial heat flux was varied from zero to near the steady maximum heat flux. Effect of initial boiling condition on transient DNB and maximum heat fluxes was negligible. Mechanism of transient boiling heat transfer beyond steady DNB heat flux was suggested.

Introduction

The study of transient boiling heat transfer caused by a heat input exponentially increasing with time is important to the safety evaluation of reactivity accidents in water cooled nuclear reactors and is also interesting as a fundamental problem of time varying boiling heat transfer.

It was studied for the first time by Rosenthal under atmospheric pressure [1].[1] He showed that the temperature rise of the heater surface before the beginning of boiling could be computed by the transient conduction equation and that the maximum heat flux was not greatly influenced by the transient state of power. Johnson, et al. carried out an extensive experimental investigation of transient boiling heat transfer under the pressures of 0.10, 3.45, 6.89, and 13.78 MPa [2, 3]. They showed that the maximum heat flux for exponential heat input exceeded the steady maximum values by a factor as large as 4. Hall and Harrison investigated the exceedingly fast transient boiling of water under atmospheric pressure [4]. They showed that even at the lowest period tested (about 0.7 ms) a short burst of nucleate boiling preceded film boiling. Transient maximum heat fluxes exceeded by a factor of between 5 and 10, the maximum heat fluxes

for steady pool boiling under the same subcoolings.

In the CHIC-KIN computer program which was developed by Redfield to treat fast and intermediate reactivity transients in a water cooled heterogeneous reactor [5], the heat transfer coefficient at the fuel surface for the exponential increase in reactor power under forced convection was calculated by Jens and Lotte's correlation [6] obtained for steady boiling and the transient maximum heat flux q_{max} was calculated by the formula, $q_{max} = q_{st}e^{4.25/t_0}$. This formula was based on the data of Johnson, et al. [2] and on the steady maximum heat flux q_{st} by Bernath's correlation [7].

Sakurai, Mizukami, and Shiotsu investigated the transient boiling for exponential heat input under atmospheric pressure [8]. They reported, apparently for the first time, that heat flux increased along the steady nucleate boiling curve and its linear extension up to transient DNB (Departure from Nucleate Boiling) heat flux q_{DNB}, where it left the extension curve toward transient maximum heat flux q_{max}. Transient DNB and maximum heat fluxes were thus defined and the relations between q_{DNB}, q_{max}, and exponential period were quantitatively studied. They pointed out that the quasi-steady nucleate boiling existed with a certain lifetime on the linear extension of the steady nucleate boiling curve and they also measured the lifetime.

The major purposes of the present experimental study are to obtain the transient boiling heat transfer coefficients and the transient DNB and maximum heat fluxes for exponentially increasing heat input whose period ranges from 5 ms to 10 s under various pressures ranging from atmospheric to 2.1 MPa and to make clear the relations between these values and the corresponding steady values. It is also aimed to explain the mechanism of transient boiling heat transfer.

---

[1] Numbers in brackets designate References at end of paper.

Apparatus and Experimental Procedure

A cylindrical stainless steel pressure vessel of 20 cm in inner diameter and 60 cm in height with three sight ports was constructed. The vessel contained an electrical immersion heater which was used to control the water temperature. The test heater used was a platinum wire of 1.2 mm in diameter and 50.9 mm long supported horizontally in the vessel. In order to avoid the error due to the terminal effect of the heater, two fine wires were spot welded as potential taps on the heater surface at the position 9.7 mm and 9.0 mm respectively apart from each terminal. The effective length of the heater was 32.2 mm. The test heater was heated by electrical current controlled by a high-speed analogue computer so that the actual heat generation rate of the heater accorded with the desired one. Details of the computer controlled heating method and of instrumentation were shown in Part 1 of this paper. The experimental error is estimated to be ±1 percent in the heat input, ±1 K in the heater surface temperature, and ±2 percent in the heat flux. The reproducibility of q_{max} and q_{DNB} for slow transient seldom exceeded ±5 percent and it was better as the period became shorter.

Distilled and demineralized water was filled in the vessel and it was boiled for at least half an hour before the experimental run to remove dissolved gases. Then the pressure vessel was closed and the system pressure was raised to the desired saturated condition by heating up water with the immersion heater. Then the immersion heater was turned off and the experimental run was started by giving an exponentially increasing heat input ($Q = Q_0 e^{t/t_0}$) to the test heater. The value of Q_0 was set to be 1.5×10^7 W/m³ ($Q_0 V/S = 4.5 \times 10^3$ W/m²) throughout the present experiments which was so low that no significant change in heater temperature occurred during the early stage of the run. The period t_0 ranged from 5 ms to 10 s and the pressure ranged from 0.1 to 2.1 MPa.

Results and Discussion

Characteristics of Transient Boiling Process. Typical transient boiling curves for exponential heat inputs at the temperature saturated at 0.588 MPa are shown in Fig. 1(a) as the log-log scale plot of the transient heat flux versus the heater surface superheat. Steady boiling curve for the same heater is also shown in the figure for comparison. The curve for the exponential period of 5 s is shown as ABCDE. The heat flux increases along the nonboiling curve AB and crosses the steady boiling curve at point B. The heat flux thereafter does not increase along the steady boiling curve but increases along the curve BC. Boiling commences at a point whose superheat is slightly higher than that at point B. The heat flux increases along the curve CD and reaches the steady boiling curve at point D. The superheat along BCD is higher than that on the steady boiling curve at the same heat flux. The boiling curve beyond D agrees well with the steady boiling curve. It is almost constant in its slope up to the DNB heat flux point E and has a smaller slope up to the maximum heat flux point. The DNB and maximum heat fluxes for this period are well consistent with steady DNB heat flux, q_{stD}, and steady maximum heat flux, q_{st}, respectively. If the heat flux is forced to decrease at any point between D and E down to F with the same period and is made to increase again, the heater surface temperature decreases and increases following the steady boiling curve without the hysteresis. The process for $t_0 = 60$ ms is shown by the curve GHIJ. The surface temperature

of the heater has a maximum value at point H which is higher than that for $t_0 = 5$ s at point C. The curve from I to J coincides with the steady boiling curve and its linear extension (dashed line). It departs from the linear extension at point J. The heat flux at this departing point, which is beyond q_{stD}, is defined as the transient DNB heat flux q_{DNB}. The process has a maximum heat flux beyond q_{DNB} which is defined as the transient maximum heat flux q_{max}. This type of transient boiling process is called in this work the "regular process." For a more rapid transient of $t_0 = 5$ ms, the boiling curve KLM has its maximum heat flux (point M) without ever reaching the steady boiling curve and its linear extension. This process is different from the regular process and is called in this work the "irregular process." This irregular process was observed only for $t_0 = 5$ ms under this pressure and for t_0 shorter than 30 ms under 0.196 MPa. Under atmospheric pressure it was observed for the period shorter than 50 ms as shown in Fig. 1(b). The period at which the irregular process appears is shorter under higher pressure. Although no irregular process was observed under pressures of 1.079 and 2.059 MPa, it is thought to appear for the period shorter than the shortest period, 5 ms, used in this study.

As stated before, the heat transfer coefficient on the transient boiling process after the initiation of boiling is lower than the steady boiling heat transfer coefficient at the same heat flux. This is explained to be as follows: When the surface temperature of the heater increases due to the exponential heat input up to the incipient boiling superheat described in Part 1 of this paper, boiling commences at the unflooded cavities whose mouth radii satisfy the boiling condition also mentioned in the paper. As the heater temperature increases, cavities whose mouth radii are smaller begin to serve as bubble nuclei and the number of nucleation sites on the heater surface increases. Then, originally flooded cavities of mouth radii bigger than that of the maximum unflooded cavities will be activated by the bubbles originating from the neighboring cavities. This vapor trapping mechanism of the cavity activation was pointed out by Courty and Foust to explain the hysteresis in boiling [9]. The heater temperature would decrease with the increase in the number of the activated cavities and boiling from originally unflooded cavities would be superseded by that from the activated cavities which require smaller superheat to maintain boiling.

To make clear the activation phenomenon, the heat input was made constant at a certain level on the way of the process BCD in Fig. 1(b), fixed hereafter for 120 s, and was decreased also exponentially with the same period. The resultant processes are shown in Fig. 2. The activation process was clearly observed, where the heater temperature decreased toward the steady boiling curve EF as time elapsed along the contours shown in this figure. For a low heat flux level such as q_1, the heater temperature decreased very slowly and did not reach the steady boiling curve within 120 s. For a higher heat fluxes such as q_3 and q_4, the temperature decreased more rapidly and reached the steady boiling curve within 14 and 4 s respectively. The steady nucleate boiling is the boiling where potentially active cavities are fully activated. It is found that the rate of increase in the number of activated cavity (rate of the activation process) is very slow in the low heat flux region slightly above the incipient boiling heat flux and it becomes faster as the heat flux becomes higher. It is natural that the activation of cavities due to vapor trapping has little chance to occur soon after the initiation of boiling where the population density of nucleation
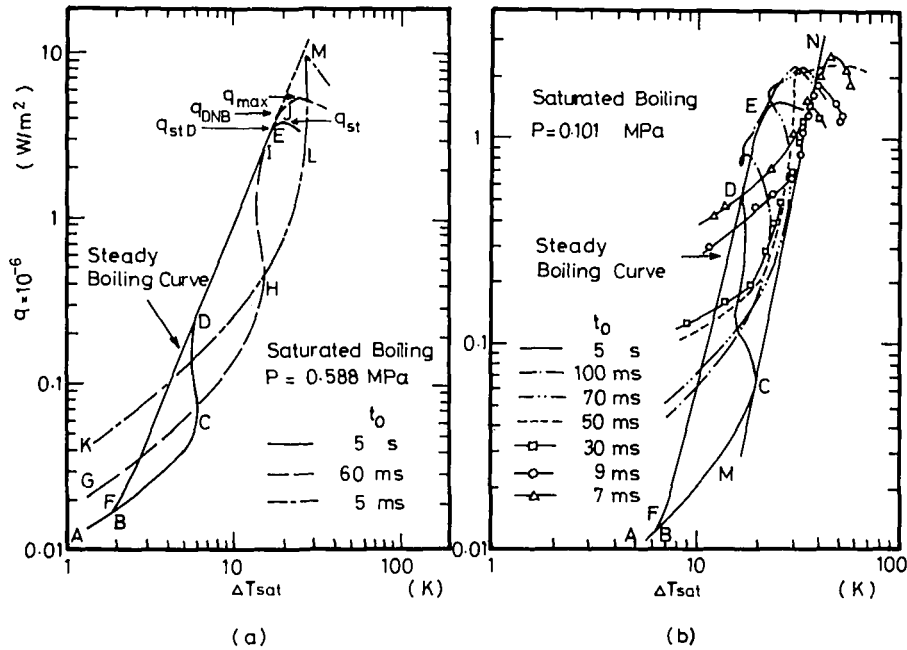
Fig. 1 Transient boiling curves for various exponential periods; (a) at 0.588 MPa, (b) at 0.101 MPa

sites on the surface is low. This cavity activation plays an important role in the transient boiling heat transfer. The boiling process becomes irregular when the boiling on the heater surface reaches a maximum heat flux condition before potentially active cavities are fully activated. If very few cavities are activated before the maximum heat flux, heat flux will increase on the nucleate boiling line due to the originally unflooded cavities. This line would correspond to the straight line MN in Fig. 1(b).

Courty and Foust examined the thermal hysteresis in steady boiling and reported that the maximum superheat was reached without any bubble formed on the heater surface, but upon further increase in heat input, the surface spontaneously broke into vigorous boiling and then the surface temperature decreased to the normal value [9]. In their experiments, the heat input was increased step by step. If the increase in heat input by one step is relatively big, the heater surface may have

spontaneously broken into vigorous boiling as they explained. As the rate of activation process is very slow in the low heat flux region, the hysteresis effect in steady boiling studied by Courty and Foust can only be characterized as a transient phenomenon for the slowest limit of heat input increase.

Transient Boiling Heat Transfer. Transient boiling heat transfer coefficient h_t normalized by the steady boiling heat transfer coefficient h_{st} for the same heat flux is shown versus heat flux for the periods of 9, 20, and 100 ms in Fig. 3(a), 3(b) and 3(c) respectively. The measured values of h_{st} were almost consistent with Rohsenow's correlation [10]. The starting point of the curve in this figure corre-

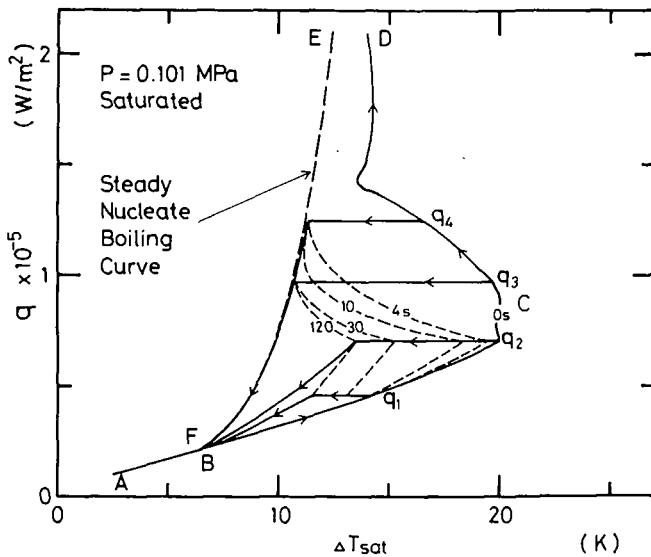**Fig. 2** Thermal hysteresis loops for the heat input first increased exponentially with the period of 5 s and then kept constant for 120 s at a certain level and decreased exponentially with the same period
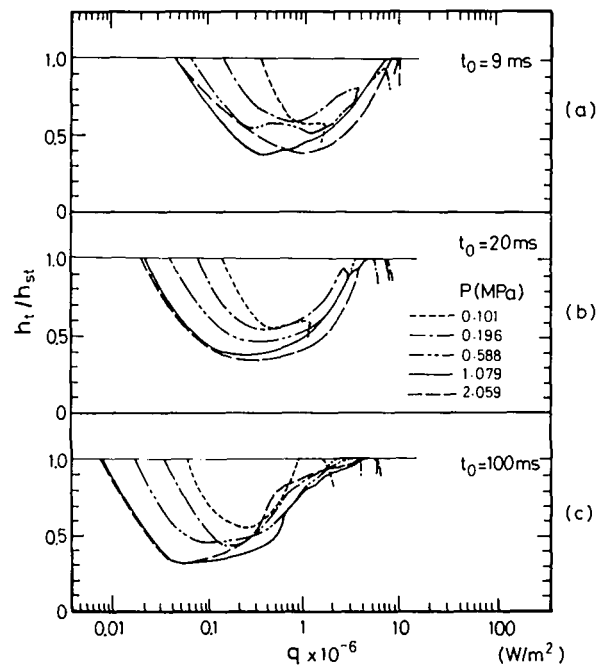

Fig. 3 Transient boiling heat transfer coefficient h_t normalized by steady one h_{st} at the same heat flux with the pressure as a parameter; for (a) t_0 = 9 ms, (b) t_0 = 20 ms, and (c) t_0 = 100 ms
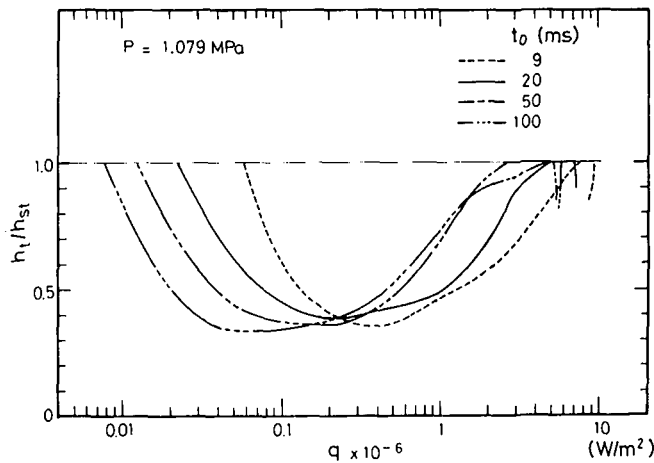
Fig. 4 The value of h_t/h_{st} versus heat flux with the period as a parameter at 1.079 MPa

Fig. 5 (a) Transient maximum heat flux and (b) transient DNB heat flux values versus exponential period for different pressures

Fig. 6 Transient boiling curve for the exponential heat input from initial heat flux on the steady boiling curve

sponds to the cross point of the transient nonboiling curve and the steady boiling curve on $\log q$ versus $\log \Delta T_{sat}$ plane. The value of h_t/h_{st} decreases with the increase in heat flux down to a minimum value. In case of the regular process, it then increases up to unity and keeps the value until q_{DNB}. In case of the irregular process, it takes a maximum value at q_{max} which is lower than unity. The minimum value of h_t/h_{st} decreases with the increase in pressure from about 0.6 at 0.101 MPa to about 0.4 at 2.059 MPa for each period. As stated in the previous section, the major cause that makes the transient boiling heat transfer coefficient lower than the steady one at the same heat flux would be the time lag of the activation of cavities. The values of h_t/h_{st} for 1.079 MPa are shown versus heat flux in Fig. 4 with the period as a parameter. This figure shows that the heat flux at the starting point and that at the minimum value of h_t/h_{st} increase with the decrease in the period but the minimum value itself is almost independent of the period. As shown in Fig. 1(b), the transient boiling processes, regular and irregular, seem to reach the line MN due to the originally unflooded cavities. Very few of cavities originally flooded are activated before this point. As this line is almost parallel to the steady boiling curve, the heat transfer coefficient normalized by the steady one at the same heat flux is almost independent of the heat flux. This value corresponds to the minimum value of h_t/h_{st} in Fig. 4.

The value of h_t before the beginning of the activation was found to be well expressed as the sum of the transient nonboiling heat transfer coefficient h_m described in Part 1 of this paper and the heat transfer coefficient due to originally unflooded cavities calculated along the line MN.

Transient Maximum and DNB Heat Flux. Transient maximum and DNB heat fluxes for various pressures are shown versus exponential period in Fig. 5. As stated before, the boiling processes at 1.079 and 2.059 MPa are regular for the whole range of period studied but those for $t_0 \leqq 5$ ms at 0.588 MPa, $t_0 \leqq 30$ ms at 0.196 MPa, and those for $t_0 \leqq 50$ ms at 0.101 MPa are irregular. The maximum heat flux by the regular process is higher for shorter period and for higher system pressure. However, when the process becomes irregular, the maximum heat flux first decreases to a minimum value with the decrease in the period and then increases. The minimum value in the case of 0.101 MPa is as low as the steady maximum heat flux. The transient DNB heat flux, which exists only for the regular process, is higher for shorter period.

The effect of initial boiling condition on q_{max} and q_{DNB} was also studied by the experiments in which heat input was increased exponentially from various initial boiling conditions. A typical boiling curve is given in Fig. 6. The line ABCD shows the process for setting the initial boiling conditions: The heat flux was increased with slow exponential function in time ($t_0 = 1$ s) up to near the steady maximum heat flux (point C) and then decreased also exponentially with the same period down to the desired initial heat flux q_{in} (point D) and was kept constant for a certain duration of time to realize steady nucleate
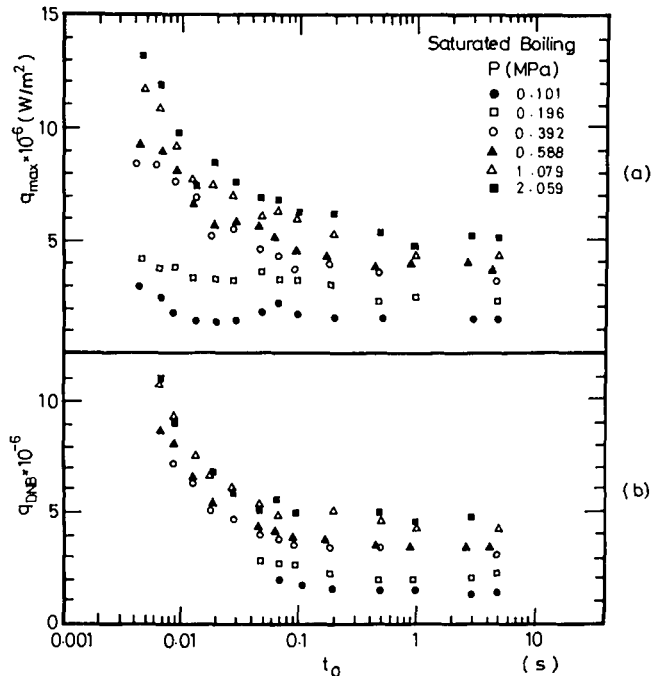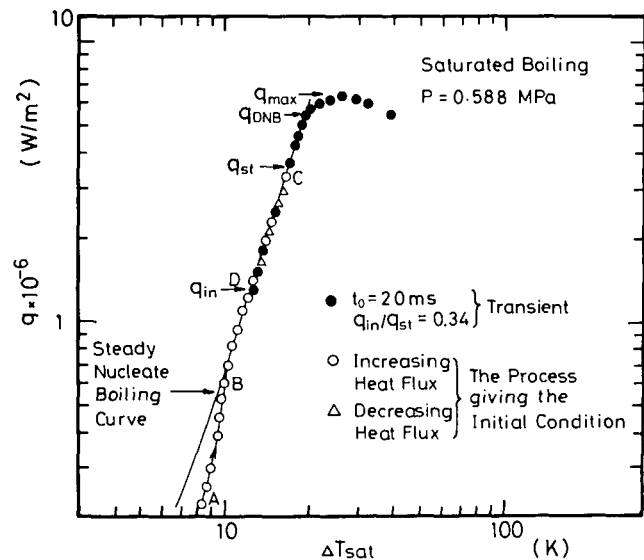
boiling. The transient boiling process started from this initial heat flux point is such that the heat flux increases along the steady nucleate boiling curve and to its extension beyond q_{stD} up to q_{DNB}. This is because the potentially active cavities are fully activated at the initial boiling condition. This process obviously is regular and called in this work the perfectly regular process.

The values of q_{max}, q_{DNB} for $q_{in}/q_{st} = 0$, 0.34, 0.8 under 0.588 MPa are shown versus period in Fig. 7(a) and 7(b) respectively. The results for $q_{in}/q_{st} = 0$ are those for 0.588 MPa in Fig. 5; i.e., those without the afore mentioned procedure for setting the initial boiling condition. Fig. 7(a) and 7(b) show that the initial heat flux has little effect on q_{max} and q_{DNB}. The curves under the lower pressures of 0.101, 0.196, 0.294, and 0.392 MPa are shown in Fig. 8(a) and 8(b). Both q_{max} and q_{DNB} are higher for shorter period and for higher pressure. It should be noted that q_{max} values by the irregular process as those for the

period shorter than 50 ms under 0.101 MPa and for the period shorter than 30 ms under 0.196 MPa shown in Fig. 5(a) are lower than the q_{max} values by the perfectly regular process at the same period shown in Fig. 8(a).

The values of q_{max} and q_{DNB} by the regular and by the perfectly regular processes can be expressed by the following empirical correlations

$$(q_{max} - q_{st})/q_{st} = 0.079\, t_0^{-0.6} \qquad (1)$$

$$(q_{DNB} - q_{stD})/q_{stD} = 0.01\, t_0^{-0.99} \qquad (2)$$

with the scattering of ±20 and ±25 percent respectively as shown in Figs. 9(a) and 9(b). Here q_{stD} is the limit of the transient DNB heat flux for the initially long period and is called in this work the steady DNB heat flux, which is about 5 percent lower than the steady maximum heat flux.

The transient DNB and the maximum heat fluxes were little affected by the variation in initial heat fluxes. This means that the process from q_{in} to q_{stD} had no effect upon the transient DNB and

maximum heat fluxes. The thermal energy transferred to water from a unit area of the heater surface during the time between t_{stD} and t_{DNB} was calculated for experimental runs of the period shorter than 500 ms except irregular ones. The values of the thermal energy divided by q_{stD} values for each pressure are plotted in Fig. 10(a) versus period. As shown in the figure, they decrease with the decrease in the period and are independent of pressure. The data are located with the scattering of ±25 percent along the line expressed by

$$\frac{1}{q_{stD}} \int_{t_{stD}}^{t_{DNB}} q(t)dt = 0.0103\,(1 + 426\, t_0^2)^{1/4} \quad (s) \qquad (3)$$

The thermal energy itself is higher for higher pressure for the same period but the dependency is canceled by dividing it with the steady DNB heat flux.

The thermal energy value transferred to water from a unit surface area between t_{stD} and t_{max} divided by q_{stD} values are plotted in Fig. 10 (b) versus period. They also decrease with the decrease in the pe-

Fig. 7 Effect of initial heat flux on (a) transient maximum heat flux and on (b) transient DNB heat flux at 0.588 MPa
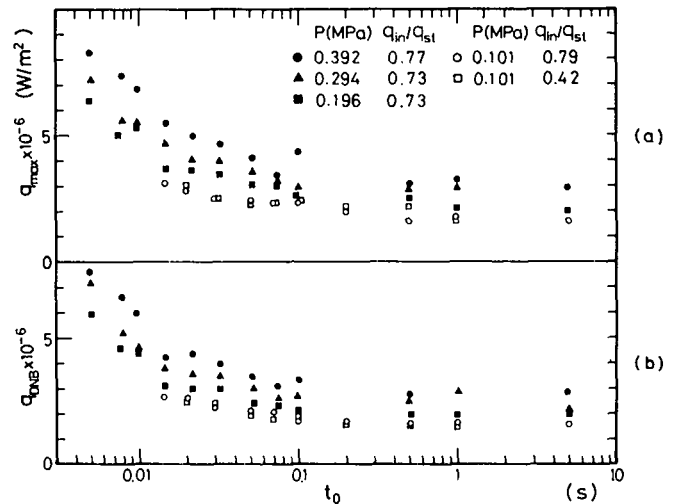
Fig. 8 (a) Transient maximum heat flux and (b) transient DNB heat flux values for the exponential heat input from initial heat flux on the steady boiling curve at pressures lower than 0.4 MPa

Fig. 9 (a) Difference between transient and steady maximum heat fluxes divided by steady maximum value, (b) difference between transient and steady DNB heat fluxes divided by steady DNB value, for regular and perfectly regular processes

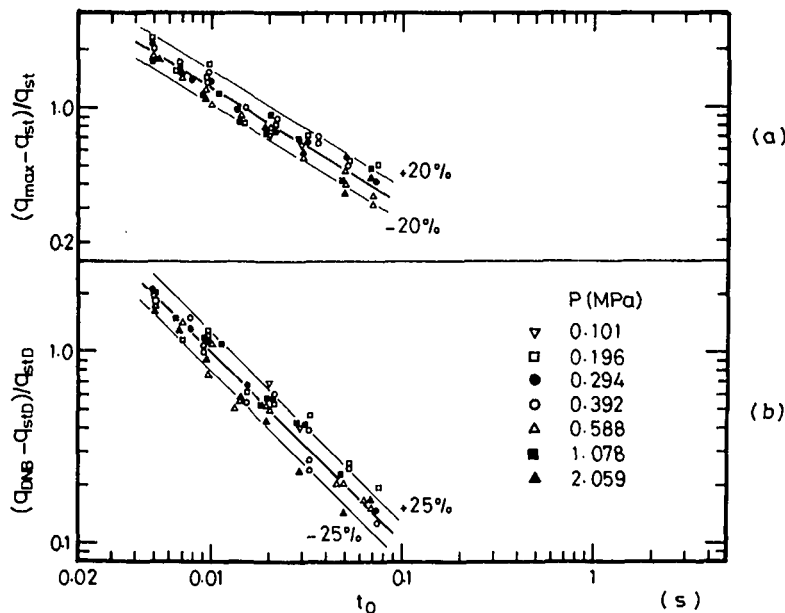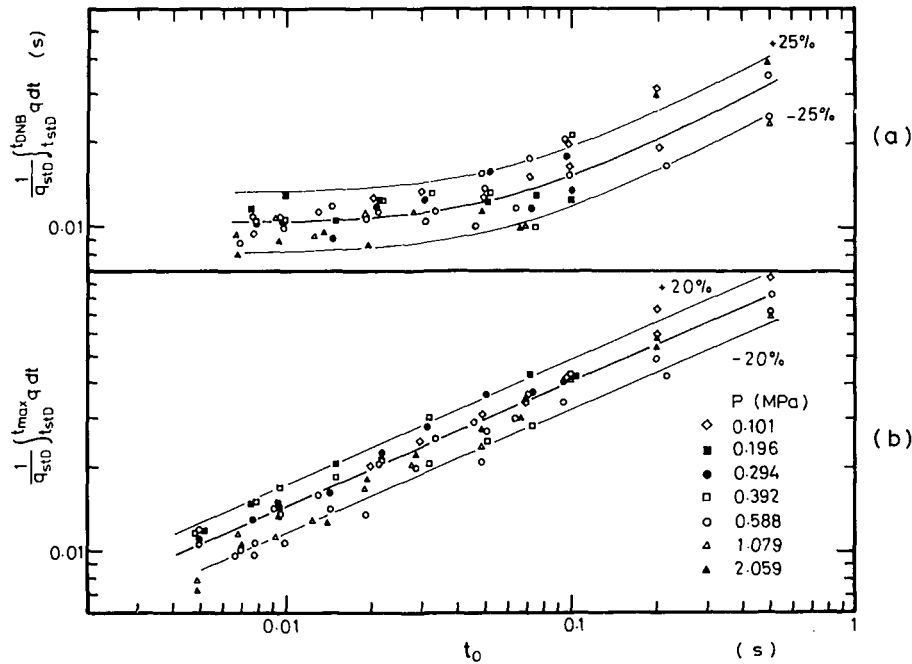**Fig. 10** Thermal energy transferred to water from unit area of heater surface in the duration of time between (a) t_{stD} and t_{DNB}, (b) t_{stD} and t_{max}, divided by steady DNB heat flux

riod and are independent of pressure. The data are located with the scattering of ±20 percent along the line expressed by

$$\frac{1}{q_{stD}} \int_{t_{stD}}^{t_{max}} q(t)dt = 0.11\, t_0^{0.44} \qquad (s) \qquad (4)$$

As stated before, when heat input was increased exponentially from the points corresponding to several initial heat fluxes on the steady nucleate boiling curve, the heat flux increased along the steady nucleate boiling curve and its linear extension up to q_{DNB} where it departed from the curve and continued to increase up to q_{max}. The mechanism of the transient boiling heat transfer for this simplified case (without a cavity activation process) can be explained to be as follows by extending the steady boiling mechanism suggested by Gaertner [11]. He classified the steady boiling heat transfer into four regions based on photographic observation; discrete bubble region, first transition region, vapor mushroom region, and second transition region with the increase in heat flux. The vapor mushroom region terminates and the second transition region starts with a smaller slope at q_{stD} point due to vapor patch formation and the latter region in turn terminates at the steady maximum heat flux.

In transient boiling, the heat flux increases beyond q_{stD} up to q_{DNB} along the linear extension of the steady boiling curve. This is considered to be because the vapor patch does not form immediately after q_{stD} until a certain thermal energy is stored in the vicinity of the heater surface, and the vapor mushroom region continues up to q_{DNB}. The slope of the boiling curve beyond q_{DNB} becomes smaller with the increase in the local surface area covered with vapor patches. The slope finally becomes zero at the transient maximum heat flux. The thermal energy stored before the vapor patch formation corresponds to that previously calculated and shown in Fig. 10(a). This energy for a fixed pressure is almost constant for the period shorter than 30 ms. The energy increase for longer period could be explained by the dispersion of a part of the energy from the thermal layer. The cause of the dispersion may be the cyclic detachment of vapor mushrooms from the heater surface whose detachment period was estimated by Gaertner [11] to be of the order of several ten milliseconds. Previously calculated thermal energy shown in Fig. 10(b) is the energy transferred to water until the vapor patch occupies the local surface area sufficient for the transient maximum heat flux to be realized.

Conclusions

Transient pool boiling heat transfer for exponential heat inputs was studied. The experimental results lead to the following conclusions.

Transient boiling process is classified into two kinds, the "regular process" and the "irregular process." The former has a maximum heat flux after reaching and following the steady boiling curve and its linear extension. On the contrary, the latter has its maximum heat flux without ever reaching and following the steady boiling curve and its linear extension. With decreasing the period, the regular process changes to be irregular. This change occurs at the longer exponential period for the lower pressure.

Transient boiling heat transfer coefficient, h_t, after the initiation of boiling becomes lower than the steady one, h_{st}, at the same heat flux level. This is explained by the time lag of the slow activation process of originally flooded cavities in the low heat flux region. h_t then recovers the steady value until q_{DNB} in the regular process. In the irregular process, the heat flux reaches the maximum value with h_t never recovering the steady value; i.e. without the full activation of potentially active cavities, which is characterized to steady boiling. The minimum value of h_t/h_{st} for a fixed pressure is almost independent of the period. This state is characterized as the boiling due to originally unflooded cavities only. The minimum value of h_t/h_{st} decreases with pressure from about 0.6 at 0.101 MPa to about 0.4 at 2.059 MPa.

Transient DNB and maximum heat fluxes by the regular process are higher for shorter period and for higher pressure. On the other hand, when the transient boiling process changes to be irregular, the value of q_{max} first decreases down to a minimum value and then increases with the decrease in the period. The results of q_{max} and q_{DNB} by the regular process are expressed by equations (1) and (2) with the error limits of ±20 and ±25 percent respectively.

When the heat input is increased from the value corresponding to the initial heat flux on the steady boiling curve, the heat flux increases along the steady boiling curve and its extension up to q_{DNB}; the process is perfectly regular even for the shortest period tested. This is supporting our explanation on the transient boiling heat transfer coefficient based on the time lag of activation process. The variation in the initial heat flux has little effect on q_{max} and q_{DNB} and the re-

sultant values are also expressed by equations (1) and (2) respectively.

The reason why the heat flux increases along the extension of steady boiling curve up to q_{DNB} when the initial boiling condition is given is as follows: It is because the vapor patch does not form immediately after q_{stD} until a certain amount of thermal energy is stored in the vicinity of the heater surface, and the vapor mushroom region continues up to q_{DNB}. Thermal energy transferred to water during the time between t_{stD} and t_{DNB} was calculated, which decreased with the decrease in the period but was almost constant for the period shorter than 30 ms. This energy would be the threshold value required for the vapor patch formation.

Acknowledgment

References

1 Rosenthal, M. W., "An Experimental Study of Transient Boiling," *Nuclear Science and Engineering*, Vol. 2, 1957, pp. 640–656.

2 Johnson, H. A., Schrock, V. E., et al., "Reactor Heat Transients Project," USAEC Report SAN 1001, Jan. 1961, to SAN 1013, May 1966.

3 Johnson, H. A., "Transient Boiling Heat Transfer," *Heat Transfer 1970*, Vol. V, B3.1, Elsevier Pub. Co., Amsterdam, 1970, and *International Journal of Heat and Mass Transfer*, Vol. 14, 1971, pp. 67–82.

4 Hall, W. B., and Harrison, W. C., "Transient Boiling of Water at Atmospheric Pressure," *International Heat Transfer Conference*, Institute of Mechanical Engineers, 1966, pp. 186–192.

5 Redfield, J. A., "CHIC-KIN, A Fortran Program for Intermediate and Fast Transients in a Water Moderated Reactor," USAEC Report WAPD-TM-479, 1965.

6 Jens, W. H., and Lottes, P. A., "Analysis of Heat Transfer, Burnout, Pressure Drop, and Density Data for High Pressure Water," USAEC Report ANL-4627, 1951.

7 Bernath, L., "A Theory of Local Boiling Burnout and its Application to Existing Data," *Chem. Eng. Progr. Symp. Series*, Vol. 56, No. 30, 1960, pp. 95–116.

8 Sakurai, A., Mizukami, K., and Shiotsu, M., "Experimental Studies on Transient Boiling Heat Transfer and Burnout," *Heat Transfer 1970*, Vol. V, B3.4, Elsevier Pub. Co., Amsterdam.

9 Courty, C., and Foust, A. S., "Surface Variables in Nucleate Boiling," *Chem. Eng. Progr. Symp. Series*, Vol. 51, No. 17, 1955, pp. 1–12.

10 Rohsenow, W. M., "A Method of Correlating Heat Transfer Data for Surface Boiling Liquids," TRANS. ASME, Vol. 74, Aug. 1952, pp. 969–976.

11 Gaertner, R. F., "Photographic Study of Nucleate Pool Boiling on a Horizontal Surface," JOURNAL OF HEAT TRANSFER, TRANS. ASME, Series C, Vol. 87, Feb. 1965, pp. 17–29.

G. L. Wedekind

Professor.
Mem. ASME

B. L. Bhatt

Graduate Student.

Oakland University,
Rochester, Mich.

An Experimental and Theoretical Investigation Into Thermally Governed Transient Flow Surges in Two-Phase Condensing Flow

The specific transient phenomenon under consideration is the outlet flowrate of subcooled liquid from a tube-type condenser where complete condensation takes place. Experimental data are presented which indicates that a small change in the inlet vapor flowrate will momentarily cause a very large transient surge in the outlet flowrate of subcooled liquid. These experimentally measured flow transients are predicted quite accurately using a system mean void fraction model. Also, some preliminary results are presented which indicate the influence of throttling at the condenser outlet as a means of attenuating the transient overshoot characteristics.

Introduction

The ability to both understand and model the principle physical mechanisms associated with the transient responses of two-phase condensing flow systems are of considerable importance as they relate to system design and control; whether the system is associated with power generation, vapor-compression refrigeration, or chemical processing.

In the literature, various types of instabilities have been reported for condensing flow; Vild, et al. [1][1] investigated condenser stability for a space power system. Soliman and Berenson [2] studied flow stability in both horizontal and vertical condenser tubes, concentrating primarily on pressure oscillations. Williams, et al. [3] studied flow stability characteristics of a radiator/condenser in one and zero "g" environments. Doroshchuk and Frid [4] reported the utilization of the outlet flowrate oscillations from a condenser as an oscillatory inlet source for a study of evaporator stability. Schoenberg [5] studied the frequency response of the inlet pressure and the point of complete condensation to sinusoidally varying inlet flowrates for a gas cooled mercury condenser.

The primary purpose of this paper is the presentation of the results of an investigation into a particular transient flow phenomenon associated with two-phase condensing flow. The specific transient phenomenon under consideration is the outlet flowrate of subcooled liquid from a tube-type condenser where complete condensation takes

place. There appears to be no reported work which has been directed at this particular transient flow phenomenon. In fact, condensing flow transients have apparently received very little attention as compared to their evaporating flow counterparts.

Experimental data are presented which indicates that a small change in the inlet vapor flowrate will momentarily cause a very large transient surge in the outlet flowrate of subcooled liquid. In fact, under certain circumstances, it is possible to make a small decrease in the inlet vapor flowrate, and momentarily have such a large decrease in the outlet liquid flowrate that for a short period of time, the flowrate will become negative, indicating that subcooled liquid will actually flow backward into the condenser. These experimentally measured flow transients are predicted quite accurately using a *system mean void fraction model* [6].

Model for Condensing Flow Transients

A schematic of the condensing flow system under consideration is shown in Fig. 1. As mentioned earlier, it is a tube-type condenser where complete condensation takes place. Therefore, it will be assumed that there is some effective position in the condenser where the last of the vapor is condensed. This position has been visually observed by Soliman and Berenson [2], as well as by the present authors. The *point of complete condensation depicted in Fig. 1 is* characteristic of these visual observations, and as can be seen, is not a sharply defined position. However, the existence of an *effective* point of complete condensation is apparent, and for thermodynamic equilibrium, it can be precisely defined from an energy perspective.

This effective transition point between the two-phase region and the subcooled-liquid region will be designated by the symbol, η. Even for what would conventionally be considered steady-state conditions,
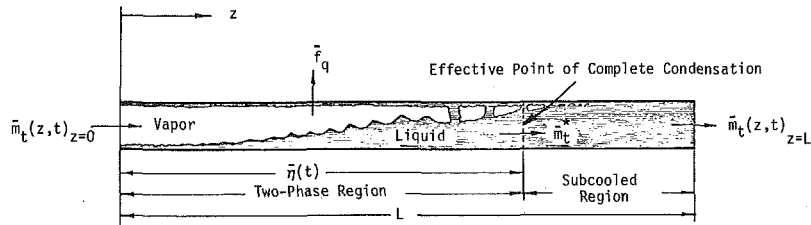

Fig. 1 Schematic of horizontal condensing flow system

the inherent stochastic nature of the two-phase condensing (or evaporating) flow process will cause random fluctuations in the length of the two-phase region. The statistical characteristics of these random fluctuations are of importance under certain circumstances, and thus have been studied for evaporating flow [7]. However, they are not being considered in this paper. Therefore, the symbol $\bar{\eta}(t)$ will be used to represent the nonfluctuating effective length of the two-phase region.

The nonfluctuating quantity here is primarily conceptual, and can be thought of as an effort to separate out the random fluctuations from the deterministic transients. The approach is similar to what is used for describing turbulent flow; that is, time averaged quantities where the averaging time is large enough to eliminate the stochastic fluctuations, but short enough not to interfere with the deterministic transients. It is important to note that the term *fluctuation* is in reference to random behavior only, and does not preclude the existence of a deterministic oscillatory behavior such as might arise in response to a sinusoidal type inlet flowrate. It is also important to recognize that this time averaging process described is conceptual, and thus related to the theoretical model only. No where in this analysis or in the presentation of the experimental data is the mechanics of the averaging process actually necessary. The foregoing discussion represents an attempt to recognize the existence of the inherent random fluctuations which are clearly present, yet to make it clear that the model currently being described does not consider them.

The two specific deterministic transient responses to be considered in this paper are those of the effective point of complete condensation, and those of the outlet flowrate of subcooled liquid.

System Mean Void Fraction. A detailed development and discussion of the physical implications of the *system mean void fraction* concept is presented in reference [6], therefore, only a brief summary will be presented here. The nonfluctuating system mean void fraction, $\bar{\alpha}_s$, will be defined as representing the instantaneous value of the nonfluctuating area mean void fraction, $\bar{\alpha}_a$, averaged over the entire length, $\bar{\eta}(t)$, of two-phase region under consideration. Therefore, the

nonfluctuating system mean void fraction, $\bar{\alpha}_s$, can be expressed as

$$\bar{\alpha}_s \equiv \frac{1}{\bar{\eta}(t)} \int_{z=0}^{\bar{\eta}(t)} \bar{\alpha}_a(z,t)dz \tag{1}$$

From this point on, only nonfluctuating quantities will be considered. Therefore, in subsequent references to these quantities, no distinction will be made.

The remaining part of this paper will be directed at the class of transient two-phase condensing flow problems where the system mean void fraction, $\bar{\alpha}_s$, is invariant with time. Mathematically, a condition sufficient for this assumption to be valid is that the area mean void fraction, $\bar{\alpha}_a(z,t)$, be expressible as a function of a single dimensionless variable, ξ; that is

$$\bar{\alpha}_a(z,t) = \bar{\alpha}_a(\xi), \qquad \text{where } \xi \equiv z/\bar{\eta}(t) \tag{2}$$

This is a type of similarity relationship such as is encountered in boundary layer theory. As was mentioned earlier, reference [6] contains a discussion of the validity of this assumption, its implications and limitations. However, one important physical implication to the condensing flow transients considered in this paper is that the time invariance of the system mean void fraction implies that the *transient* form of the momentum principle is relatively unimportant. This suggests that the transient phenomena under consideration are governed primarily by thermal mechanisms, that is, heat transfer and the conservation of mass and energy principles. This implication is verified by the experimental data presented.

Defined in this specific manner, the system mean void fraction becomes a type of *system* parameter. Its numerical value can be determined for a particular condensing flow situation by utilizing an appropriate relationship between void fraction and flow quality. Examples of how this may be done are given in the Appendix.

Conservation of Mass and Energy Principles. As mentioned earlier, when the governing equations for a condensing flow system are formulated in terms of the system mean void fraction, only the conservation of mass and energy principles are directly involved.

The condensing flow system model is formulated around the fol-

---

━━━━━━━Nomenclature━━━━━━━

A_t = total cross-sectional area of tube, m²

d = inside diameter of tube, m

f_q = local heat flux, W/m²

$\bar{f}_q$ = spatially averaged heat flux, W/m²

h = enthalpy of saturated liquid, J/g

L = total length of condenser, m

$m_t(z,t)$ = local instantaneous total mass flowrate of fluid, g/s

$\bar{m}_t^*$ = instantaneous nonfluctuating total mass flowrate of fluid leaving two-phase region relative to moving transition point boundary, g/s

$\bar{m}_{t,i}$ = initial total mass flowrate at system inlet, g/s

$\bar{m}_{t,f}$ = final total mass flowrate at system inlet, g/s

p = spatial mean system pressure, N/m²

P = inside circumference of flow channel, m

$\bar{x}$ = flow quality; ratio of vapor mass flowrate to total mass flowrate (nonfluctuating)

$\bar{x}_0$ = flow quality at inlet of condenser (nonfluctuating)

z = axial position coordinate, m

$\bar{\alpha}_a$ = nonfluctuating area mean void fraction

$\bar{\alpha}_s$ = nonfluctuating system mean void fraction

η = length of two-phase region in condenser (effective point of complete condensation), m

$\bar{\eta}_i$ = initial nonfluctuating effective point of complete condensation, m

$\bar{\eta}_f$ = final nonfluctuating effective point of

complete condensation, m

ξ = dimensionless "similarity" variable, $\xi \equiv z/\bar{\eta}(t)$

ρ = density of saturated liquid, g/m³

τ_c = time constant for condensing flow system, s

τ_m = time constant for inlet mass flowrate variation, s

Subscripts and Superscripts

Primed (′) symbols of quantities refer to saturated vapor. Unless otherwise indicated, barred (-) symbols of quantities generally refer to time-averaged quantities where the averaging time is small enough so as to just eliminate the random fluctuations.

---

lowing simplifications:

1. System mean void fraction is assumed to be invariant with time.
2. Random fluctuations due to the stochastic nature of the two-phase flow process are assumed not to influence the deterministic transients.
3. Viscous dissipation, longitudinal heat conduction, and changes in kinetic energy are neglected.
4. The specific enthalpies and densities of the liquid and vapor are considered to be saturated properties, independent of both axial position and time, and evaluated at the mean system pressure.
5. The spatially averaged heat flux, for the entire two-phase region, is assumed to be invariant with time.

Two-Phase Region. Using the system mean void fraction model, and incorporating the foregoing simplifications, the conservation of mass principle, simultaneously applied to the liquid and vapor in the two-phase region, can be expressed as

$$\frac{d}{dt}\{[\rho(1 - \bar{\alpha}_s) + \rho'\bar{\alpha}_s]A_t\bar{\eta}(t)\} = \bar{m}_t(z, t)_{z=0} - \bar{m}_t^* \quad (3)$$

The conservation of energy principle, simultaneously applied to the liquid and vapor in the two-phase region, can be expressed in terms of the system mean void fraction as

$$\frac{d}{dt}\{[\rho h(1 - \bar{\alpha}_s) + \rho'h'\bar{\alpha}_s]A_t\bar{\eta}(t)\}$$

$$= -\bar{f}_q P\bar{\eta}(t) + \{[h(1 - \bar{x}) + h'\bar{x}]\bar{m}_t(z, t)\}_{z=0} - h\bar{m}_t^* \quad (4)$$

where $\bar{f}_q$ represents the average condenser heat flux, defined as

$$\bar{f}_q \equiv \frac{1}{\bar{\eta}(t)}\int_{z=0}^{\bar{\eta}(t)} f_q\,dz \quad (5)$$

Subcooled Liquid Region. The conservation of mass principle applied to the subcooled liquid region can be expressed as

$$\frac{d}{dt}\{\rho A_t[L - \bar{\eta}(t)]\} = \bar{m}_t^* - \bar{m}_t(z, t)_{z=L} \quad (6)$$

Transient Response of the Effective Point of Complete Condensation. Consistent with the system simplifications stated earlier, equations (3) and (4) can be combined to yield the differential equation governing the transient response of the effective point of complete condensation, $\bar{\eta}(t)$, in terms of the system inlet flowrate, $\bar{m}_t(z, t)_{z=0}$; thus

$$\tau_c\frac{d\bar{\eta}(t)}{dt} + \bar{\eta}(t) = \frac{\bar{x}_0(h' - h)}{\bar{f}_q P}\bar{m}_t(z, t)_{z=0} \quad (7)$$

with the initial condition

$$\bar{\eta}(t)_{t=0} = \bar{\eta}_i \quad (8)$$

where τ_c is the time constant for the condensing flow system, defined as

$$\tau_c \equiv \frac{\rho'\bar{\alpha}_s A_t(h' - h)}{\bar{f}_q P} \quad (9)$$

and $\bar{x}_0$ represents the inlet flow quality. The condensing flow system time constant, τ_c, can be thought of as representing the time required to condense the vapor which is present within the two-phase region, providing that the rate of heat transfer from the vapor remains constant.[2] Being a first-order ordinary differential equation, equation (7), has a general closed form solution for any arbitrary inlet flowrate, $\bar{m}_t(z, t)_{z=0}$.

Transient Response of the Outlet Liquid Flowrate. The transient response of the outlet liquid flowrate, $\bar{m}_t(z, t)_{z=L}$, is directly coupled to the response of the effective point of complete condensa-

---

tion, $\bar{\eta}(t)$. This becomes apparent by combining equations (3), (6), and (7) which yield after rearrangement.

$$\bar{m}_t(z, t)_{z=L} = \left\{1 + \left[\left(\frac{\rho}{\rho'}\right) - 1\right]\bar{x}_0\right\}\bar{m}_t(z, t)_{z=0}$$

$$- \left[\left(\frac{\rho}{\rho'}\right) - 1\right]\frac{\bar{f}_q P}{(h' - h)}\bar{\eta}(t) \quad (10)$$

Therefore, for an arbitrary inlet flowrate, $\bar{m}_t(z, t)_{z=0}$, the foregoing equation will yield the response of the outlet liquid flowrate in terms of the response of the effective point of complete condensation, $\bar{\eta}(t)$.

Consider the special case where the inlet mass flowrate can be adequately represented by the following exponential function of time:

$$\bar{m}_t(z, t)_{z=0} = \bar{m}_{t,f} + (\bar{m}_{t,i} - \bar{m}_{t,f})e^{-t/\tau_m} \quad (11)$$

where τ_m, is the time constant associated with the inlet flowrate, and $\bar{m}_{t,i}$ and $\bar{m}_{t,f}$, refer to the initial and final inlet flowrates, respectively.

The transient response of the condenser outlet liquid flowrate, $\bar{m}_t(z, t)_{z=L}$, to an exponential inlet flowrate, can be obtained by solving the differential equation (7), using equation (11), and the steady-state conditions that

$$\bar{\eta}_i = \frac{\bar{x}_0(h' - h)}{\bar{f}_q P}\bar{m}_{t,i} \quad \text{and} \quad \bar{\eta}_f = \frac{\bar{x}_0(h' - h)}{\bar{f}_q P}\bar{m}_{t,f} \quad (12)$$

and then substituting into equation (10). After following through the foregoing operations, the transient response of the outlet liquid flowrate becomes

$$\frac{\bar{m}_t(z, t)_{z=L} - \bar{m}_{t,f}}{\bar{m}_{t,i} - \bar{m}_{t,f}} = e^{-(\tau_c/\tau_m)\,t/\tau_c}$$

$$+ \frac{\left(\frac{\tau_c}{\tau_m}\right)\left[\left(\frac{\rho}{\rho'}\right) - 1\right]\bar{x}_0}{\left[\left(\frac{\tau_c}{\tau_m}\right) - 1\right]}\{e^{-(\tau_c/\tau_m)\,t/\tau_c} - e^{-t/\tau_c}\} \quad (13)$$

It should be recognized that the foregoing expression reduces to the special case of a step change in the inlet flowrate as $(\tau_c/\tau_m) \to \infty$.

A display of the transient response of the outlet liquid flowrate to a particular exponential inlet flowrate is presented in Fig. 2, with

---

[3] It should be pointed out that an evaluation of equation (13) when $(\tau_c/\tau_m) = 1$ requires a limiting process.
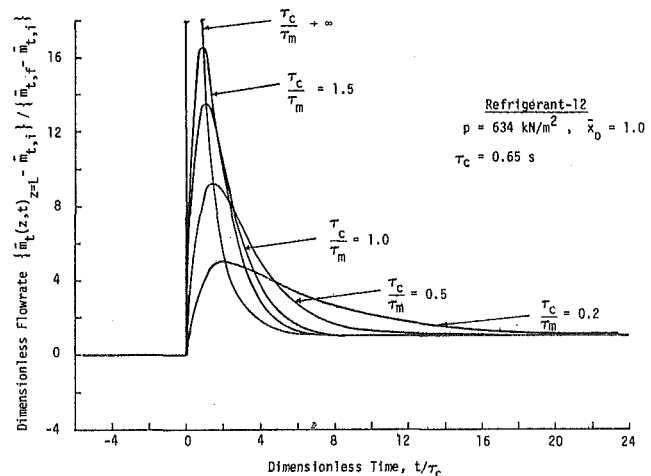
Fig. 2 **Predicted effect of the time constant ratio on outlet flowrate response**

---

[2] This becomes more apparent if both numerator and denominator of equation (9) are multiplied by the initial length, $\bar{\eta}_i$, of the two-phase region under steady-state conditions.

Journal of Heat Transfer

(τ_c/τ_m) as a parameter.[3] Since the curves are presented in dimensionless form, they represent the transient responses for both an increase and a decrease in inlet flowrate. The most interesting aspect of the model predictions is the transient *overshoot* characteristics. This type of overshoot or transient flow surge is not very common for fluid and thermal processes. Also, because the system mean void fraction is invariant with time, the transient is thermally controlled, and not a hydrodynamic phenomenon.

Further insight into the physical mechanisms behind this overshoot characteristic can be obtained from the conservation of mass principle. This is done by combining equations (3) and (6) in such a way as to eliminate the mass flowrate leaving the two-phase region relative to the moving transition point, $\overline{m}_t^*$; thus

$$\overline{m}_t(z, t)_{z=L} = \overline{m}_t(z, t)_{z=0} - (\rho' - \rho)\overline{\alpha}_s A_t \frac{d\overline{\eta}(t)}{dt} \qquad (14)$$

It can be seen from the foregoing equation, that the outlet flowrate of subcooled liquid, $\overline{m}_t(z, t)_{z=L}$, is equal to the inlet flowrate, minus the net rate at which mass is stored in the two-phase region as a result of the vapor displacing the liquid. However, with insight from equation (7), and the fact that $(\rho' < \rho)$, the net storage rate in the two-phase region is seen to be negative if the inlet flowrate is increasing, thus causing the outlet liquid flowrate to be momentarily larger than the inlet vapor flowrate. Conversely, the net storage rate in the two-phase region is seen to be positive if the inlet flowrate is decreasing, thus causing the outlet flowrate to be momentarily smaller than the inlet flowrate.

Experimental Observations

Experimental Apparatus and Measurement Techniques. A schematic of the experimental apparatus is shown in Fig. 3. Refrigerant-12 vapor was generated by circulating temperature regulated hot water through the coils inside the vapor generator (high pressure reservoir). The saturated vapor was then passed in series through a regulating valve, a superheater, a vapor turbine flowmeter, a combination sight glass-heat exchanger, and into the condenser test section. The test section was apporximately 5-m long, and was a concentric-tube configuration. It was constructed from copper tubing; a 0.95-cm OD tubing inside of a 1.91-cm OD tubing. Eleven thermocouples were mounted axially along the length of the outer tube of the test section. The condensing Refrigerant-12 flowed through the 0.80-cm ID inner tube. The inlet vapor flowrate was controlled by a quick-acting regulating valve, across which a differential pressure of about 550 kN/m^2 was maintained to insure a nonfluctuating inlet flowrate. Transient *inlet flowrates were measured by a turbine flowmeter*. They were found to be exponential in form, so a time constant, τ_m, could be determined empirically from the experimental data. Cold water was circulated in the annulus of the condenser test section.
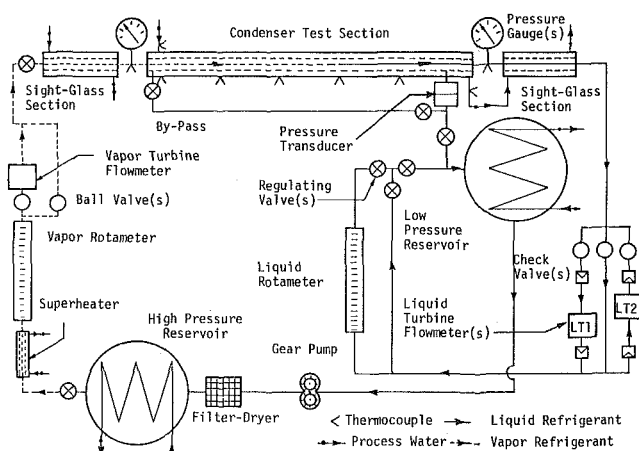

Fig. 3 Schematic of the experimental apparatus

Leaving the condenser test section, the liquid flowed through one of two liquid turbine flowmeters in the outlet flow measuring unit, and on into the low-pressure reservoir. The low pressure reservoir and hence the average condensing pressure was maintained at a constant absolute value of about 650 kN/m^2 by circulating temperature regulated cooling water through its cooling coils. At the end of a test, the liquid collected in the low pressure reservoir was pumped back into the high pressure reservoir.

For an increase in the inlet vapor flowrate, the transient in the outlet liquid flowrate was easily measured by one of the liquid turbine flowmeters in the outlet flow measuring unit. For a decrease in the inlet vapor flowrate, the outlet liquid flowrate can momentarily become negative, meaning that the liquid actually flows back into the condenser. In this situation, the outlet liquid flowrate could be measured by the other turbine flowmeter, however the lag in the flowmeter resulted in discontinuities at the point of the flow reversal.

To overcome this difficulty, a differential pressure transducer, with a much faster response than that of the turbine flowmeters was used to indirectly measure the outlet flowrate by measuring the pressure drop across the outlet flow resistance. Steady flow, single phase tests were run to calibrate the pressure drop in terms of the liquid flowrate as measured with the liquid turbine flowmeter. During an actual transient condensation test, the pressure drop measured by the differential pressure transducer was recorded on a strip chart recorder, and the flowrate at each instant of time was determined from the calibration curve obtained earlier by means of the single phase steady-state tests. A plot of flowrate measurements using the differential pressure transducer is shown in Fig. 4, along with the simultaneously recorded turbine flowmeter data.

It is interesting to note that at any instant of time, when the flowrate is increasing, the flowrate indicated by the turbine flowmeter will be lower, and that indicated by the pressure transducer will be higher than the actual flowrate. If the flowrate is decreasing, the inverse will be true. Therefore, the actual flowrate will always be between the two, and at steady state, or at a maximum or minimum, they will agree. Since it appeared from an analysis of the two flow indicating devices, that the pressure transducer indicated flowrates closer to the actual flowrate, and since it alleviated the problems discussed earlier for the bidirectional flow transients, the pressure transducer was chosen as the primary means of measuring the outlet liquid flow transients.

In order to determine the average heat flux during a particular test, it was necessary to know both the condenser heat transfer and the location of the effective point of complete condensation within the condenser tube. The heat transfer was obtained from an energy balance. The *effective point of complete condensation was obtained by* recording the temperature profile along the axis of the test section. The region where the temperature profile shows an abrupt change in slope corresponds to the location of the effective point of complete condensation.

Comparison of Theoretical Results with Experimental Data. Experimental data indicating the response of the outlet liquid flowrate to small changes in the inlet vapor flowrate has been obtained for the condition where there was negligible downstream throttling at the condenser outlet, and where the inlet flowrate could be adequately represented as an exponential function of time.

Increase in Inlet Vapor Flowrate. Fig. 4 represents the response of the outlet liquid flowrate when the inlet flowrate was increased by 11.4 percent. The inlet flowrate is also displayed on the graph. It is interesting to note the overshoot characteristics of the resulting outlet liquid flow transient. There is a sudden, relatively large increase in the outlet liquid flowrate, followed by a slower exponential decay back to the final value of the inlet flowrate.

The physics of this overshoot phenomenon can be explained as follows. During the initial part of the flow transient, a sudden increase in the inlet vapor flowrate causes the effective point of complete condensation to begin moving downstream, displacing the higher density liquid by a lower density vapor. This causes the sudden overshoot in the outlet liquid flowrate. As the transition point moves downstream, there is an increasingly larger heat transfer area for the
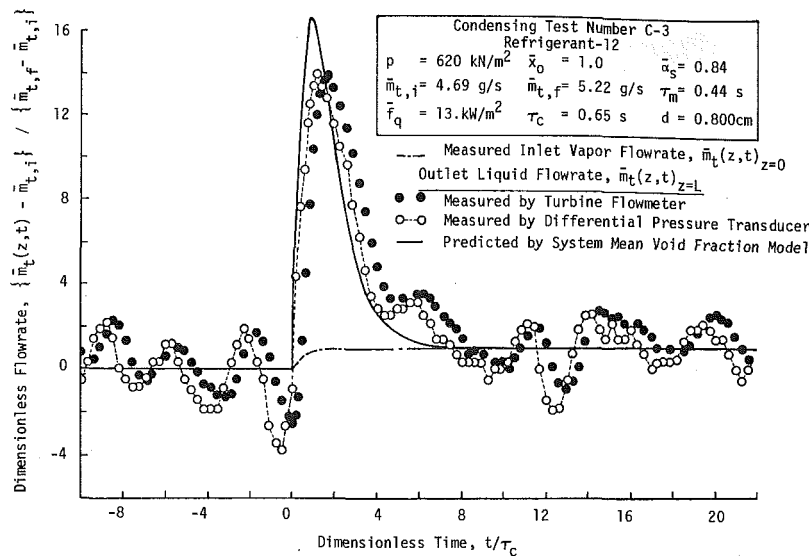
Fig. 4 Response of outlet liquid flowrate after an increase in inlet flow-rate

condensation to take place. This heat transfer area continues to increase until the rate of heat transfer is adequate to condense all of the vapor entering the condenser. At this point in time then, the outlet flowrate has decayed back to equal the inlet flowrate.

The capability of the system mean void fraction model to predict the overall transient response is clearly demonstrated by the graph. It should be noted however, that neither compressibility nor inertia effects were considered in the development of the model. It should also be noted that the model does not include the random fluctuations which are in the outlet flowrate even during what is conventionally accepted as steady-state conditions. These flowrate fluctuations appear to be caused by inherent flow instabilities within the two-phase region.

Decrease in the Inlet Vapor Flowrate. The transient response of the outlet liquid flowrate was measured when the inlet vapor flowrate was decreased by about 14.0 percent. The initial decrease in the outlet liquid flowrate is so large that it momentarily becomes negative, indicating that the flow actually reverses direction and flows back into the condenser for a short period of time before it exponentially increases back to the final value of the inlet flowrate. Experimental data for this type of situation are shown in Fig. 5. Physically, similar mechanisms to those explained for the case of the increase in the inlet flowrate are present in this situation. The only difference is that the sudden decrease in the outlet flowrate immediately after the inlet flowrate began to change is the result of a displacement of vapor by liquid rather than liquid by vapor. Here again however, the system mean void fraction model is seen to predict the overall transients quite well.

Flowrate Overshoot Attenuation. Preliminary experiments were run to investigate the effects of inlet and outlet throttling on attenuating the amplitude of the flow surges during the outlet flowrate transients. Experimental results associated with introducing various amounts of downstream throttling at the outlet of the condenser are shown in Fig. 6. The effects are significant. As the amount of throttling is increased, for approximately the same inlet vapor flowrate increase, the amplitude of the flow surge is clearly attenuated. For the case when the throttling is severe enough, it is possible to almost eliminate the flowrate overshoot. For such a situation, the outlet flowrate almost exactly tracks the changes in the inlet flowrate. Physically, what seems to be happening is as the outlet flowrate tries to increase, the flow resistance causes a corresponding increase in the condenser pressure, with a resulting increase in vapor density, which in turn reduces the rate at which vapor displaces the liquid, thus reducing the overshoot.

These experimental results suggest that an inherent downstream resistance at the condenser outlet is a positive factor in attenuating the overshoot effects. The results also indicate, however, that the attenuation is obtainable at a substantial price in terms of the pressure drop. This study is continuing in an effort to analytically include these observed effects in the system mean void fraction model.

Summary and Conclusions

The primary purpose of this paper has been the presentation of the results of an investigation into transient flow surges associated with two-phase condensing flow. The specific transient phenomenon under consideration was the outlet flowrate of subcooled liquid from a tube-type condenser where complete condensation takes place.

Experimental data have been presented which indicate that a small change in the inlet vapor flowrate momentarily causes a very large transient surge in the outlet flowrate of subcooled liquid. In fact, under certain circumstances, it is possible to make a small decrease in the inlet vapor flowrate, and momentarily have such a large decrease in the outlet liquid flowrate that for a short period of time, the flowrate actually becomes negative, indicating that subcooled liquid actually flows backwards into the condenser.

This type of overshoot characteristic represents a transient flow phenomenon which is not very common for fluid and thermal processes. It is a thermal instability, governed in part by the condenser heat transfer. It has been shown that these experimentally measured flow transients are predicted quite accurately using a system mean void fraction model, in conjunction with the conservation of mass and energy principles.

The primary purpose of the analytical portion of this paper was not directed at the formulation of the system mean void fraction model, but rather its utility in predicting the particular condensing flow transients under consideration. However, in the light of the experimental results herein presented, the model is seen to embody a certain analytical simplicity, and yet maintain the capability of accurately predicting transient flow phenomena of considerable complexity.

Preliminary experimental results were also presented which indicate the influence of throttling at the condenser outlet as a potential means of attenuating the transient flow surges. Inlet throttling appears to have relatively little influence.
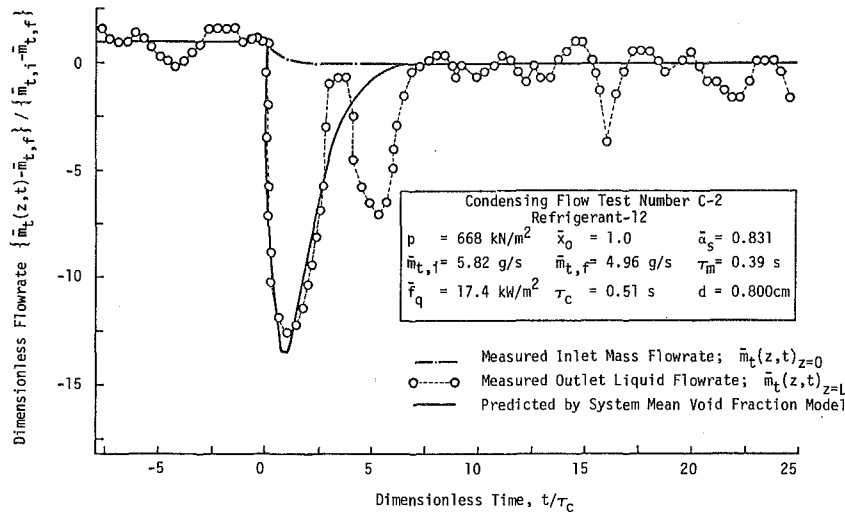
Fig. 5 Response of outlet liquid flowrate after a decrease in inlet flowrate
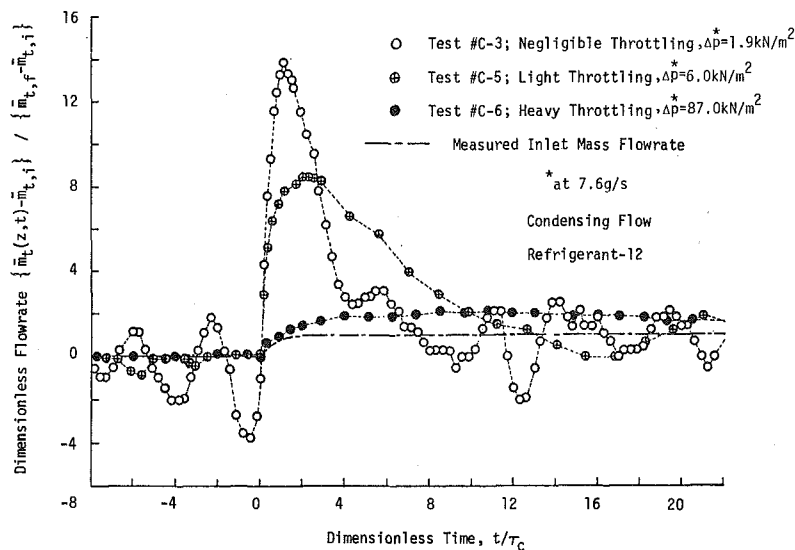
Fig. 6 Response of outlet liquid flowrate with downstream throttling

References

1 Vild, T. J., Schubert, F. H., and Snoke, D. R., "A System to Demonstrate the Zero Gravity Performance of an Organic Rankine Cycle," Intersociety Energy Conversion Engineering Conference, Boulder, Colo., 1968.

2 Soliman, M., and Berenson, P. J., "Flow Stability and Gravitational Effect in Condenser Tubes," *Proceedings From the Fourth International Heat Transfer Conference*, Paris, France, Vol. VI, 1970.

3 Williams, J. L., Keshock, E. G., and Wiggins, C. L., "Development of a Direct Condensing Radiator for Use in a Spacecraft Vapor Compression Refrigeration System," *Journal of Engineering for Industry*, Nov 1973, p. 1053.

4 Doroshchuk, V. Ye, and Frid, F. P., "The Critical Heat Flux for Water Flowing Through Round Tubes," *Problems of Heat Transfer and Hydraulics of Two-Phase Media*, S. S. Kutateladze, ed., Pergman Press, Chapter 2, 1969, p. 38.

5 Schoenberg, A. A., "Mathematical Model With Experimental Verification for the Dynamic Behavior of a Single-Tube Condenser," NASA TND-3453, 1966.

6 Wedekind, G. L., Bhatt, B. L., and Beck, B. T., "A System Mean Void Fraction Model for Predicting Various Transient Phenomena Associated With Two-Phase Evaporating and Condensing Flows," *Proceeding of the NATO Advanced Study Institute on Two-Phase Flows and Heat Transfer*, Istanbul, Turkey, Aug. 1976. Accepted for publication in the *Int. Journal of Multiphase Flow*.

7 Wedekind, G. L., and Beck, B. T., "Theoretical Model of the Mixture-Vapor Transition Point Oscillations Associated With Two-Phase Evaporating Flow Instabilities," JOURNAL OF HEAT TRANSFER, TRANS. ASME, Series C, Vol. 96, 1974, p. 138.

8 Levy, S., "Steam-Slip—Theoretical Predicting From Momentum Model," JOURNAL OF HEAT TRANSFER, TRANS. ASME, Series C, Vol. 82, 1960, p. 113.

9 Fujie, H., "A Relation Between Steam Quality and Void Fraction in Two-Phase Flow," *AICHE Journal*, Vol. 10, 1964, p. 227.

10 Zivi, S. M., "Estimation of Steady-State Steam Void Fraction by Means of the Principle of Minimum Entropy Production," JOURNAL OF HEAT TRANSFER, TRANS. ASME, Series C, Vol. 86, 1964, p. 247.

11 Martinelli, R. C., and Nelson, D. B., "Prediction of Pressure Drop During Forced Circulation Boiling of Water," TRANS. ASME, Aug. 1948, p. 695.

12 Thom, J. R. S., "Prediction of Pressure Drop During Forced Circulation of Boiling Water," *International Journal of Heat and Mass Transfer*, Vol. 7, 1964, pp. 709–724.

13 Collier, J. G., *Convective Boiling and Condensation*, McGraw-Hill, New York, 1969, pp. 24–64.

14 Sacks, P. S., "Measured Characteristics of Adiabatic and Condensing Single-Component Two-Phase Flow of Refrigerant in a 0.377-in Diameter Horizontal Tube," ASME Paper No. 75WA/HT-24, Winter Annual Meeting, Houston, Texas, 1975.

15   Chato, J. C., "Laminar Condensation," *ASHRAE Journal,* Vol. 4, 1962, p. 52.

16   Rufer, C. E., and Kezios, S. P., "Analysis of Two-Phase One-Component Stratified Flow With Condensation, JOURNAL OF HEAT TRANSFER, TRANS. ASME, Series C, Vol. 88, 1966, p. 265.

APPENDIX

For steady condensing flow conditions, with a uniform heat flux,[4] the local flow quality may be expressed as

$$\bar{x} = \bar{x}_0(1 - \xi); \qquad \xi \equiv z/\bar{\eta}(t) \qquad (15)$$

Substituting this relationship into equation (1) yields the following expression for the system mean void fraction:

$$\bar{\alpha}_s = \int_{\xi=0}^{1} \bar{\alpha}_a(\xi)d\xi = \frac{1}{\bar{x}_0} \int_{\bar{x}=0}^{\bar{x}_0} \bar{\alpha}_a(\bar{x})d\bar{x} \qquad (16)$$

A variety of relationships have been developed between void fraction and flow quality such as those given by references [8–12]. Some of these relationships as well as others are discussed by Collier [13]. In general, these relationships have been developed in part from the steady-state form of the momentum principle, although many include empirically determined constants or parameters. Although these models were formulated for adiabatic or evaporating flows, it will be assumed that they are valid for condensing flows as well. This assumption is supported by Sacks [14], who compared experimental void fraction data for adiabatic and condensing flows to the Martinelli-Nelson [11] correlation.

It is recognized that many of these correlations were developed for particular flow patterns and hence range of flow qualities. Also some were developed specifically for vertical rather than horizontal flows. Therefore, the predicted accuracy of a given model is dependent upon the range of flow qualities of interest as well as other parameters such as geometry, density ratio, slip, etc.

However, since the system mean void fraction represents an average void fraction over the entire two-phase region, then for situations where complete condensation takes place, all of the aforementioned void fraction models yield similar results. For example, using equation (16), the system mean void fraction was calculated for two of the experimental tests presented in this paper using three different void fraction models. This comparison is shown in the following.

Test number	Levy's model [8]	Fujie's model [9]	Zivi's model [10]
C-2	0.822	0.816	0.831
C-3	0.826	0.821	0.840

Also, a spot check was carried out using the Martinelli-Nelson [11] and Thom [12] correlations. The system mean void fractions so calculated varied from the foregoing table by less than 8 percent. Chato [15] and Rufer and Kezios [16] studied stratified flow condensation inside of a circular tube. Their observations of liquid level variation lend further confidence in the values of the system mean void fraction as obtained with the foregoing models.

Therefore, because of its simplicity, for the particular flow transients under consideration in this paper, Zivi's [10] model was chosen to calculate the system mean void fraction. It should be pointed out, however, that this does not preclude the use of a more appropriate or accurate flow quality model if the particular condensing flow conditions warrant it. In fact, one of the salient features of the system mean void fraction model is that it is conceptually independent of the particular void fraction-flow quality relationship which exists. It is only in the determination of a numerical value for the system mean void fraction for a specific flow situation that the particular relationship used comes in question.

The area mean void fraction due to Zivi [10] is given by

$$\bar{\alpha}_a = [1 + c(1 - \bar{x})/\bar{x}]^{-1} \qquad (17)$$

where

$$c = (\rho'/\rho)^{2/3} \qquad (18)$$

Substituting equation (17) into equation (16) and integrating yields

$$\bar{\alpha}_s = \frac{1}{(1 - c)} + \frac{c}{(1 - c)^2 \bar{x}_0} \ln \left\{ \frac{c}{(1 - c)\bar{x}_0 + c} \right\} \qquad (19)$$

Because of its simplicity, the above relationship was used to calculate the system mean void fractions which were required in this paper.

---

[4] If the heat flux is not uniform, although it would not be as accurate, an estimate could still be obtained by using this relationship.

Y. Shimada

Graduate Student.

Y. H. Mori

Research Associate.

K. Komotori

Professor.

Department of Mechanical Engineering,
Keio University,
Yokohama, Japan

Heat Transfer From a Horizontal Plate Facing Upward to Superposed Liquid-Layers With Change of Phase

This paper presents an experimental examination of a novel technique to improve the convection heat transfer to a liquid whose boiling point is higher than the temperature of heated surface. A layer of an immiscible, denser, and more volatile "secondary liquid" is placed between the heated surface and the layer of the "primary liquid" which is to be heated. The secondary-liquid boils on the heated surface, and its vapor condenses in the upper primary-liquid layer. The rate of such a heat transfer exceeds by far that of natural convection heat transfer to the single primary-liquid layer with an increase of the surface temperature, and becomes approximately equal to that of boiling heat transfer to the single secondary-liquid layer.

Introduction

Utilization of low-temperature energies such as wasted heat from industrial plants has become a very pressing problem in recent years. Heat exchangers for that use must have a high heat transfer coefficient, because the available temperature driving forces are generally small. Since the application of high power to make the working fluid flow is prohibited, however, the heat transfer to the working fluid might be primarily by natural convection. Although nucleate boiling of the working fluid is desired to obtain a high heat transfer coefficient, it cannot be expected when the temperature of heated surface does not attain the boiling point of the working fluid; such a situation is very likely because of the low-temperature heat source.

Fig. 1 illustrates the idea proposed in this paper to overcome the difficulty described in the foregoing. Superposed liquid-layers are formed on a horizontal heated plate facing upward, an immiscible, denser, and more volatile "secondary liquid" being placed between the heated plate and the "primary liquid" which is to be heated (i.e., working fluid). The secondary liquid boils, and the vapor bubbles enter the upper primary-liquid layer, entraining the secondary liquid. Such "two-phase bubbles" constituted of the secondary liquid and

its vapor become liquid drops in the course of rising in the upper layer as the result of condensation and then fall back into the lower layer. The latent heat of vaporization is transferred to the upper layer in the above circulation of the secondary-medium variable in a phase between the lower and the upper layers. The motions of bubbles and drops also promote the convection in the two layers, and serve to increase the sensible-heat transfer. On the other hand, the lower layer
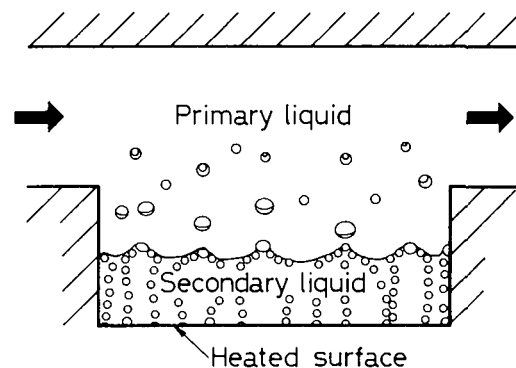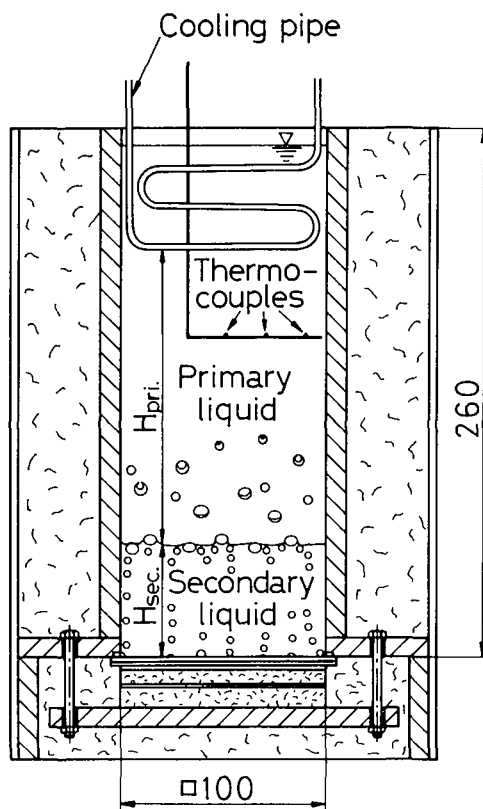

Fig. 1 Scheme of "boiling-condensation heat transfer" to superposed layers

---

Cooling pipe

Thermo-
couples

Primary
liquid

$H_{pri.}$

260

Secondary
liquid

$H_{sec.}$

□100

(Dimensions in mm)

Fig. 2 Apparatus

itself provides some resistance for the sensible-heat transfer to the upper layer. Moreover, this resistance necessarily makes the temperature of the liquid-liquid interface lower than that of the heated surface, consequently contributing to reduction of the natural convection of primary liquid. Hence an experimental examination is required to clarify whether or not the "boiling-condensation heat transfer" described previously has actually an advantage over the usual convection heat transfer to the single layer of primary liquid under certain conditions.

Although this phenomenon was described by Oktay [1][1] as a variation of boiling heat transfer to the lower-layer liquid, he presented no quantitative result about the heat transfer. Bonilla and Eisenberg [2], Bragg and Westwater [3], and Sump and Westwater [4] studied the boiling heat transfer to the superposed liquid-layers in which condensation hardly occurred. Their results are not applicable, however, to the prediction of characteristics of the boiling-condensation heat transfer with a view described previously.

In the practical application, the heat transferred to the upper layer

---

[1] Numbers in brackets designate References at end of paper.

is carried away as the enthalpy of the primary liquid, as represented in Fig. 1. Since the contribution of the forced convection in the upper layer to the heat transfer from the heated plate to the bulk of the upper layer seems to be very small in the case of low-temperature energy utilization as described before, however, the present experiment was designed so that the heat could be carried away from the upper layer by the cooling water flowing in the pipe immersed in the layer, as shown in Fig. 2. Accordingly, the combined forced and natural convection heat transfer to the single layer of the primary liquid with which the proposed boiling-condensation heat transfer is to compete, should be replaced by a simple natural convection heat transfer.

Therefore, the rate of natural convection heat transfer to the single layer of the primary liquid, as well as that of the boiling-condensation heat transfer to the superposed layers was measured using the same apparatus, in order to clarify the range in which the latter exceeds the former. The rate of boiling heat transfer to the single layer of the secondary liquid was also measured with a view to help in understanding of the characteristics of the boiling-condensation heat transfer.

Apparatus and Procedure

A schema of the apparatus is shown in Fig. 2. A pair of liquids or a kind of liquid was used to fill a square column, $100 \times 100\text{-mm}^2$ horizontal area and 260-mm depth. The upper end of the column was open to the atmosphere. The side walls were made of Bakelite and transparent acrylic plastics. The bottom plate was made of copper and was heated uniformly from below. A construction of the heating assembly is shown in Fig. 3. An auxiliary heater was installed below the main heater to reduce the downward heat loss from the main heater. Tips of constantan wires 0.1-mm dia were stuck rigidly onto the back of the top copper plate so that the three junctions of thermocouples might be located on the diagonal of the plate. Three junctions of copper-constantan thermocouples 0.1-mm dia were also located on a diagonal of each surface of an asbestos plate between the two heaters, so that the downward heat flux from the main heater could be calculated. Electric power fed to the main heater and the indications of the above thermocouples gave the net heat flux to the liquid q_w and the temperature of the heated surface (upward surface of the top copper plate) T_w. The heated surface was finished with a No. 600 emery paper and was used after it was oxidized thoroughly to insure the reproducibility of the results [5–7].

A copper pipe of 6-mm OD ran zigzag below the free surface of the liquid, through which the cooling water flowed to carry away the heat transferred from the heated surface, and to maintain the bulk temperature T_∞ in the upper layer or the single layer at a desired level. The temperature profile in the liquid layer, or layers, was measured by traversing three copper-constantan thermocouples 0.1-mm dia located on a diagonal of a horizontal area in the column. All of the thermocouples were read with a potentiometer.

Water/Freon-113 and liquid paraffin/water systems were taken up as representatives, the former in each system being the primary liquid. The former system is characterized by higher thermal conductivity and surface tension of the primary liquid than those of the secondary liquid, respectively; this is reversed in the latter. The Freon-113 used was above 99.8-percent purity. Liquid paraffin was reagent grade. Water was distilled. The properties of liquids are presented in Table 1.

The test conditions are summarized in Table 2. The values of H_{pri}

Nomenclature

h = heat transfer coefficient, $\text{kW/m}^2\text{K}$

H_{pri} = thickness of primary-liquid layer, cm

H_{sec} = thickness of secondary-liquid layer, cm

Nu = Nusselt number

q_w = heat flux, kW/m^2

Ra = Rayleigh number

T = temperature, °C

T_s = saturation temperature of secondary liquid, °C

T_w = temperature of heated surface, °C

T_∞ = bulk temperature of single liquid-layer or of upper liquid-layer, °C

y = distance from heated surface, cm
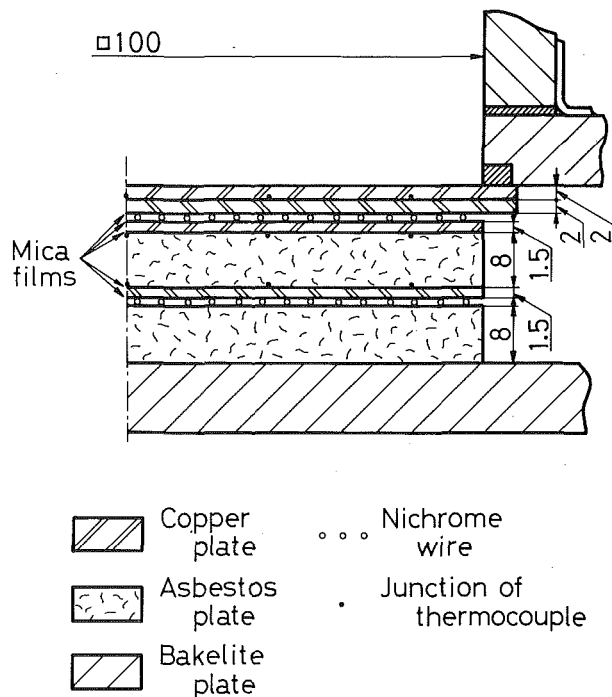
$\Delta T = T_w - T_\infty$

$\Delta T_s = T_w - T_s$

Fig. 3 Heating assembly

Copper plate
Asbestos plate
Bakelite plate
Nichrome wire
Junction of thermocouple

Table 2 Experimental conditions

	Abbreviation	T_∞ °C	$H_{pri.}$ cm	$H_{sec.}$ cm	Heat transfer mode
Water/Freon-113 system	W·N1	35	15	—	Natural convection
	W·N2	30	15	—	
	W·N3	40	15	—	
	W·N4	35	10	—	
	WF·BC1	35	15	1.0	Boiling-condensation
	WF·BC2	30	15	1.0	
	WF·BC3	40	15	1.0	
	WF·BC4	35	15	0.5	
	WF·BC5	35	15	2.0	
	WF·BC6	35	15	4.0	
	WF·BC7	35	10	1.0	
	F·B	35	—	15	Boiling
	F_w·B*	35	—	15	
Liquid paraffin/water system	P·N1	90	15	—	Natural convection
	P·N2	80	15	—	
	P·N3	70	15	—	
	PW·BC1	90	15	4.0	Boiling-condensation
	PW·BC2	80	15	4.0	
	PW·BC3	70	15	4.0	
	W·B	90	—	15	Boiling

* Freon-113 saturated with water was used.

and H_{sec} in Table 2 represent the nominal thicknesses of layers when neither boiling nor boiling-condensation occurred.

Further details of apparatus and procedure are presented elsewhere [8] with the complete data of the experiment.

Results and Discussion

The outline of dynamics of boiling-condensation phenomenon was as follows. The vapor bubbles released from the heated surface rise in the lower layer until they reach the liquid-liquid interface. There, the bubbles move along the interface and coalesce to each other, producing larger, but fewer, bubbles. When such bubbles become large enough to break away from the interface, they rise into the upper layer, each of them entraining some amount of the secondary liquid.

Table 1 Properties of liquid used

	Freon-113	Water	Liquid paraffin
Density (at 20°C), kg/m³	1577	998	880
Saturation temperature (at 101.3 kPa), °C	47.6	100	above 300
Latent heat of vaporization (at saturation temperature), kJ/kg	146.7	2255	——
Specific heat at constant pressure (at 20°C), kJ/kg-K	0.933	4.18	2.2
Thermal conductivity (at 20°C), kW/m-K	0.777×10^{-4}	6.02×10^{-4}	1.26×10^{-4}
Kinematic viscosity (at 20°C), m²/s	0.436×10^{-6}	1.00×10^{-6}	——
Prandtl number (at 20°C)	8.26	7.09	——
Surface tension (at 20°C), N/m	1.96×10^{-2}	7.24×10^{-2}	3.62×10^{-2}

Such two-phase bubbles no longer continue their ascent when the vapor phases inside them shrink to some extent, as the result of condensation, and fall back into the lower layer in the form of liquid drops. It was expected according to the study by Selecki and Gradon [9] that some difference in above behaviors might appear between water/Freon-113 and liquid paraffin/water systems since the surface-tension relation between the primary and secondary liquids in the former system is reversed in the latter system. As a matter of fact, no marked difference was found between both systems except that the liquid paraffin became opaque by the emulsification of water in the high heat-flux range, and that the liquid paraffin touched the heated surface and wetted it displacing water over a limited area, also in the high heat-flux range, as reported by Bonilla and Eisenberg [2] for styrene/water system.

Fig. 4 illustrates a typical temperature profile in each case that boiling-condensation in superposed water/Freon-113 layers, natural convection in water layer, or subcooled boiling in Freon-113 layer underwent. The heat fluxes in those examples are approximately the same. Sandwiched between thin thermal boundary layers a wide uniform-temperature region was formed in the upper layer or the single layer under each heat-transfer mode. This fact warrants the designation of the reference bulk temperature T_∞.

It is known that the natural convection of fluid between two horizontal plates in the range Ra > 10^6, a so-called "surface convection layer," appears on each plate and that the heat transfer from the heated plate to the uniform-temperature region, and that from there to the cooled plate are independent of each other [10], where the thickness of the fluid layer is employed in Rayleigh number as the characteristic geometric factor. The Rayleigh numbers in all runs of the present experiment were superior to 10^6, when H_{pri} in cases of natural convection in the single primary-liquid layer and boiling-condensation in the superposed layers or H_{sec} in case of subcooled boiling in the single secondary-liquid layer was taken as the geometric factor. It was observed that two-phase bubbles or vapor bubbles hardly entered the uniform-temperature region in case of boiling-condensation in the superposed layers or subcooled boiling in the
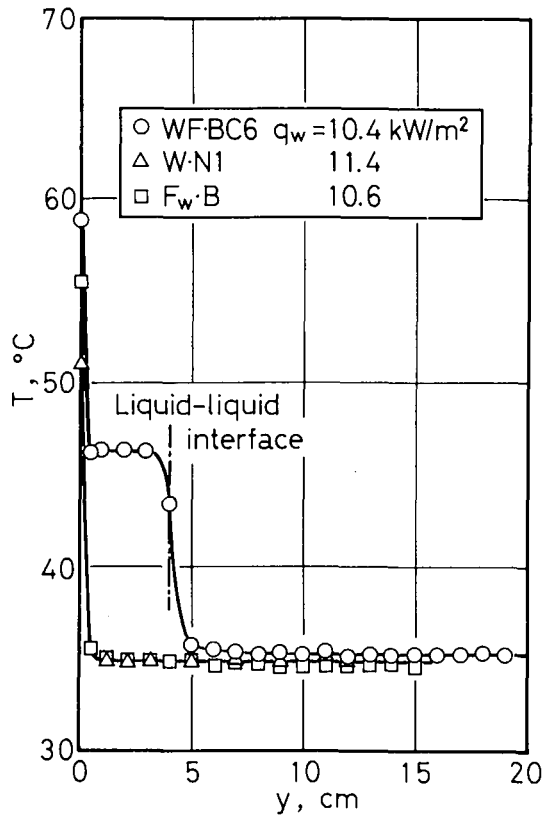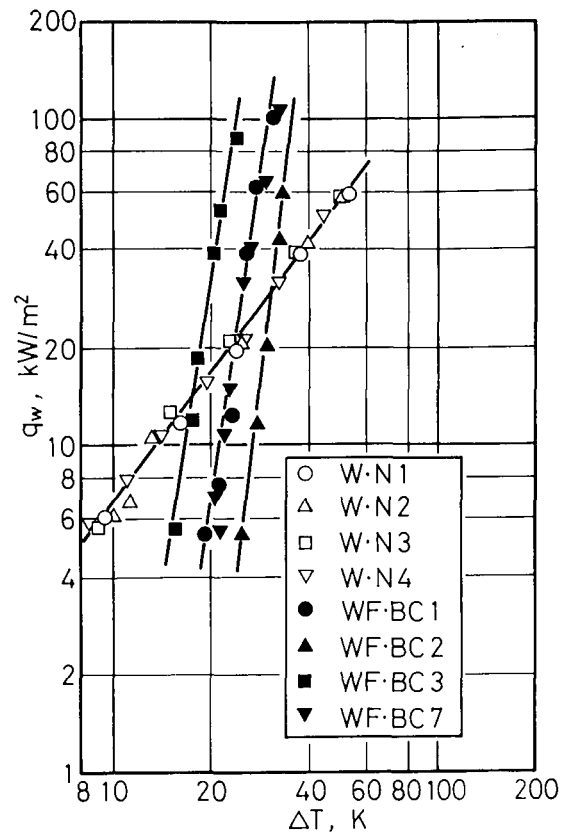
Fig. 4   Temperature profiles in liquid layers

Legend (Fig. 4):
- ○ WF·BC6 q_w = 10.4 kW/m²
- △ W·N1   11.4
- □ F_w·B   10.6

Liquid-liquid interface

Fig. 5(a)   Water/Freon-113 system

Legend (Fig. 5a):
- ○ W·N1
- △ W·N2
- □ W·N3
- ▽ W·N4
- ● WF·BC1
- ▲ WF·BC2
- ■ WF·BC3
- ▼ WF·BC7

single secondary-liquid layer. This fact suggests that the situations in and above the uniform-temperature region in those cases were similar to those under the natural convection described previously, and the heat transfer from the uniform-temperature region to the cooling pipe is expected to have affected hardly the heat transfer from the heated surface to the uniform-temperature region also in those cases. This warrants the replacement of the practical situation shown in Fig. 1 by the present experimental model.

The data of our experiment of natural convection heat transfer to the single water layer are well arranged by the following relationship

$$Nu = 0.16\,Ra^{1/3} \qquad (1)$$

where the physical properties are estimated at the bulk temperature T_∞. Note that the selection of the characteristic geometric factor does not affect the foregoing equation. The data about the natural convection heat transfer to the single liquid-paraffin layer are also related as

$$q_w = \Delta T^{4/3} \qquad \text{or} \qquad h \propto \Delta T^{1/3} \qquad (2)$$

although the relation between Nusselt and Rayleigh numbers cannot be presented since the necessary data of properties of liquid paraffin have not been available. Foregoing facts agree with the results of previous studies [10, 11], and suggest, though indirectly, that the boundary effects including the sideward heat loss from the heating assembly are small enough and that the uniform heat flux was realized with a good approximation in the present experiment.

Fig. 5 presents comparisons of relations q_w versus ΔT between the natural convection heat transfer to the single primary-liquid layer and the boiling-condensation heat transfer to the superposed layers in water/Freon-113 and liquid paraffin/water systems, respectively. It is evident that the heat flux of the boiling-condensation heat
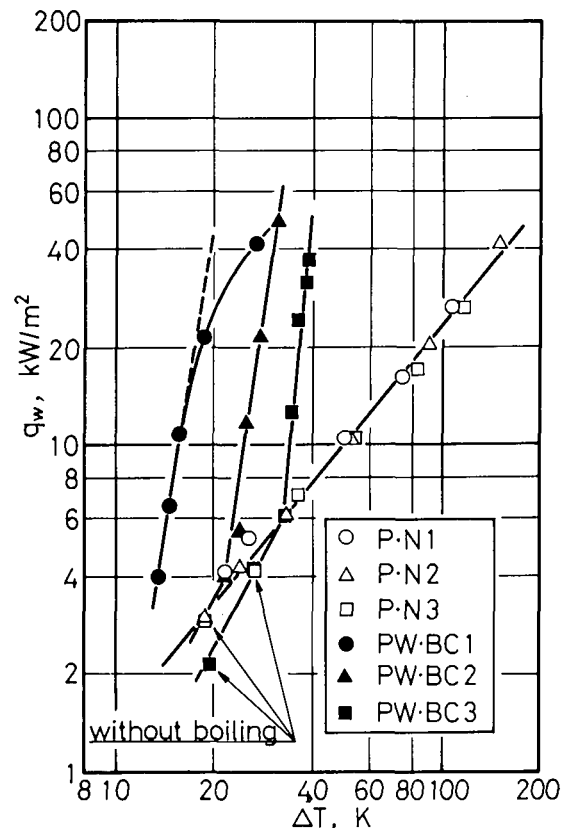

Fig. 5(b)   Liquid paraffin/water system

Legend (Fig. 5b):
- ○ P·N1
- △ P·N2
- □ P·N3
- ● PW·BC1
- ▲ PW·BC2
- ■ PW·BC3

without boiling

Fig. 5   Heat flux versus temperature difference—comparison between natural convection heat transfer and boiling-condensation heat transfer
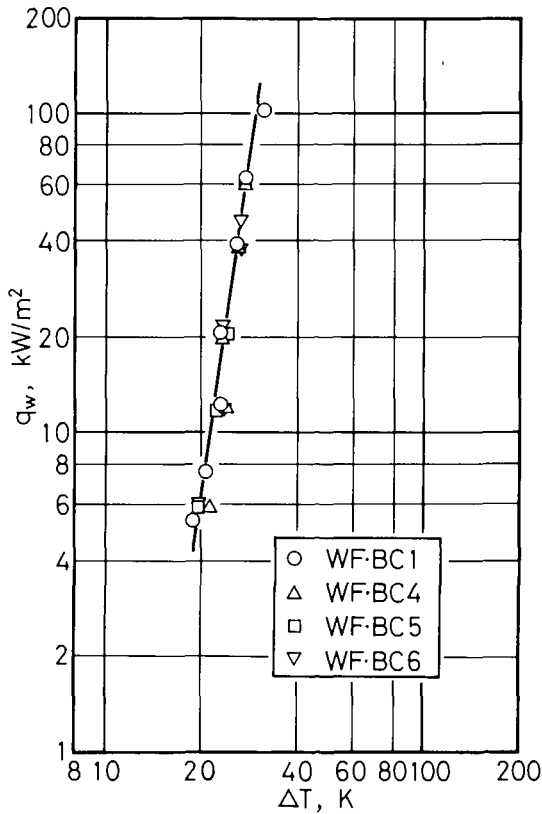
Fig. 6 Effect of the thickness of lower layer H_{sec} in water/Freon-113 system
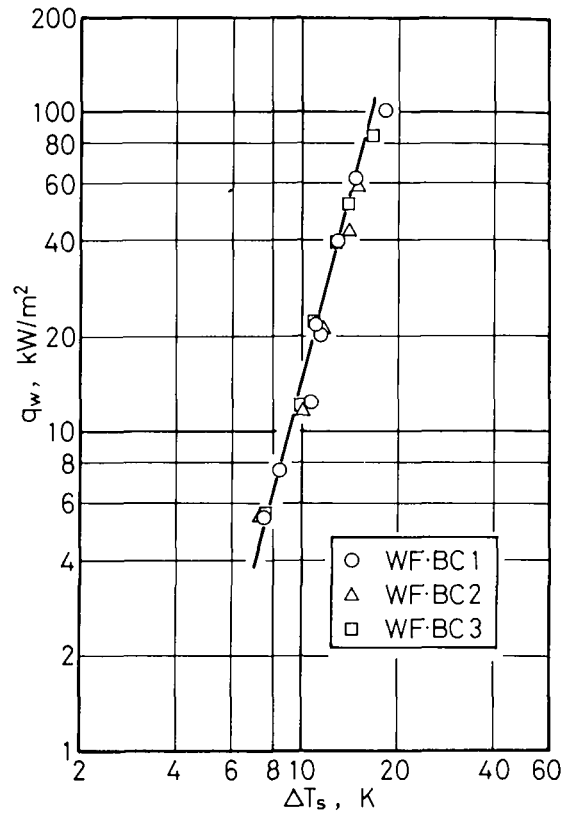

Fig. 7(a) Water/Freon-113 system

transfer exceeds that of natural convection heat transfer with an increase of ΔT, T_∞ being held constant, in each of the systems. This result insures the potential applicability of the boiling-condensation heat transfer proposed in this paper to utilization of low-temperature energies described in the Introduction. The deviation of plots for PW·BC 1 from a straight line in the high heat-flux range shown in Fig. 5(b) and also in Figs. 7(b) and 8 is ascribed to an increase of surface temperature as the result of the wetting of the surface by liquid paraffin as described before.

Fig. 5(a) suggests also that H_{pri} has little influence on the heat transfer rate (compare WF·BC1 and WF·BC7) as was expected from such temperature profiles as shown in Fig. 4. Fig. 6 shows $q_w - \Delta T$ relations in water/Freon-113 system, the parameter H_{sec} varying from 0.5 to 4.0 cm. Evidently the thermal resistance of the lower layer does not depend on its thickness at least in that range.

Seemingly, the bulk temperature T_∞ has some influence on the heat transfer in both systems. This influence can be interpreted as follows.

Fig. 7 is obtained by rearranging the data presented in Fig. 5 into the relation between q_w versus ΔT_s, the superheat of heated surface with respect to the saturation temperature of secondary liquid T_s, as in dealing with usual boiling heat transfer. The relations in water/Freon-113 system are quite the same without regard to T_∞. Although a little scatter depending on T_∞ appears in liquid paraffin/water system, those relations seem to agree in the higher heat-flux range unless a wetting of the surface by liquid paraffin occurs. That is, the heat flux is determined practically, only by ΔT_s or T_w in each system, and T_∞ has essentially little influence on the boiling-condensation heat transfer. The results presented in Figs. 5–7 indicate that the boiling-condensation heat transfer surpasses the natural convection heat transfer in the range $\Delta T_s > 11$ K in water/Freon-113 system, and insofar as T_w just exceeds T_s in liquid paraffin/water system.

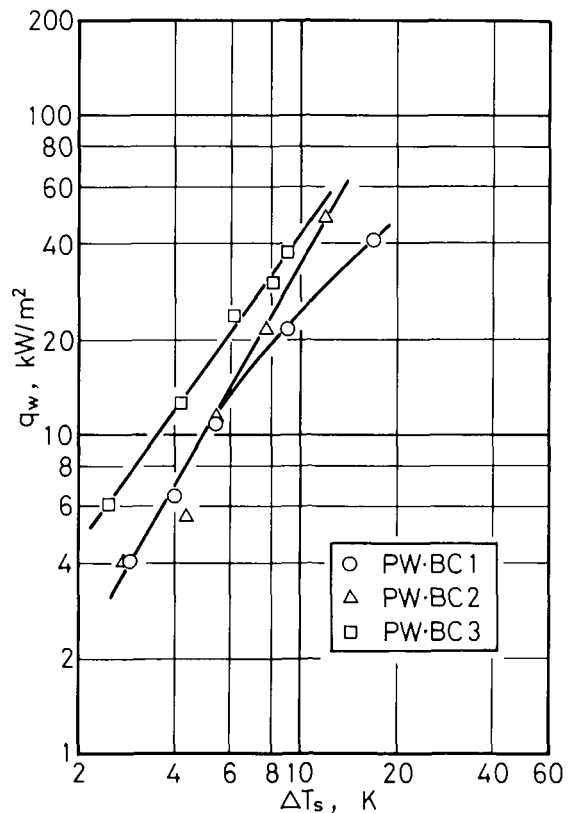The weak dependence of boiling-condensation heat transfer on T_∞

Fig. 7(b) Liquid paraffin/water system
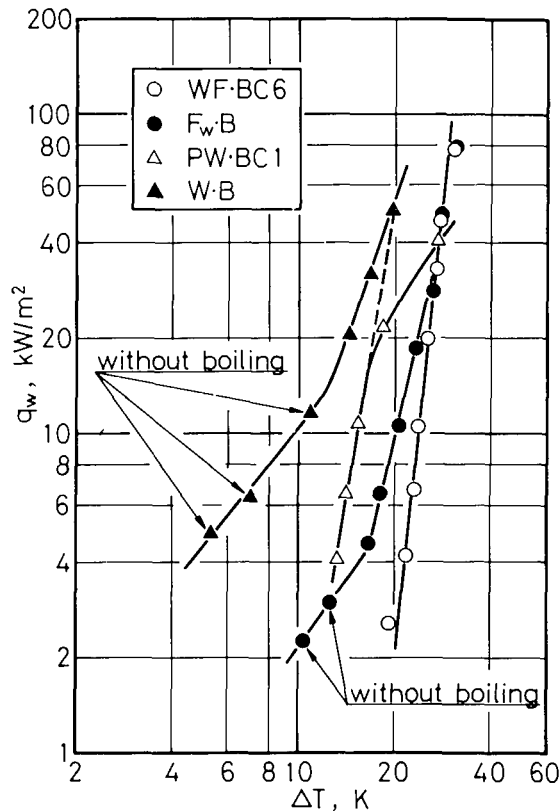
Fig. 7 Heat flux versus superheat of heated surface

Fig. 8 Comparison between boiling-condensation heat transfer (WF·BC6, PW·BC1) and boiling heat transfer to single secondary-liquid layer (F_w·B, W·B)

subcooled boiling heat transfer at the same q_w is reasonably ascribed to an increase of T_w to compensate the aforementioned dependence of sensible-heat transfer on the effective subcooling.

Concluding Remarks

An experimental study has been carried out concerning the heat transfer to the primary-liquid layer superposed on the layer of an immiscible, denser, and more volatile secondary liquid which boils on the heated surface and then condenses in the primary-liquid layer. Conclusions reached from the study are as follows.

The rate of the above heat transfer exceeds by far that of natural convection heat transfer to the single primary-liquid layer with an increase of the temperature of heated surface, unless it does not attain the saturation temperature of the primary liquid. The characteristics of this heat transfer are practically controlled by the boiling of the secondary liquid on the heated surface without regard to the other factors, and consequently the heat transfer rate approximates to that of the boiling heat transfer to the single secondary-liquid layer, provided the surface temperatures are the same. These results indicate the advantage of this heat transfer method in some practical utilizations.

It is readily presumed, however, that some practical problems will arise in the implementation of this method. The entrainment of the secondary liquid in the flowing primary liquid, for example, has to be prevented or, at least, reduced to a high degree by some means. Some refrigerants used as secondary liquids may contaminate the heated surface with deposits. These troublesome problems excluded from the scope of the present paper will have to be examined in the future.

Acknowledgment

References

1 Oktay, S., "Multi-Fluid Subdued Boiling; Theoretical Analysis of Multi-Fluid Interface Bubbles," *IBM Journal of Research and Development*, Vol. 15, No. 5, 1971, pp. 342–354.

2 Bonilla, C. F., and Eisenberg, A. A., "Heat Transfer to Boiling Styrene and Butadiene and Their Mixtures With Water," *Industrial and Engineering Chemistry*, Vol. 40, No. 6, 1948, pp. 1113–1122.

3 Bragg, J. R., and Westwater, J. W., "Film Boiling of Immiscible Liquid Mixtures on a Horizontal Plate," *Heat Transfer 1970 (Proceedings of the 4th International Heat Transfer Conference)*, Vol. 6, B 7.1, 1970.

4 Sump, G. D., and Westwater, J. W., "Boiling Heat Transfer From a Tube to Immiscible Liquid-Liquid Mixtures," *International Journal of Heat and Mass Transfer*, Vol. 14, No. 6, 1971, pp. 767–779.

5 Hirano, F., and Nishikawa, K., "Time Variation of Nucleate Boiling Heat Transfer of Water," (in Japanese), *Transactions of the Japan Society of Mechanical Engineers*, Vol. 24, No. 148, 1958, pp. 978–983.

6 Marcus, B. D., and Dropkin, D., "Measured Temperature Profiles Within the Superheated Boundary Layer Above a Horizontal Surface in Saturated Nucleate Pool Boiling of Water," JOURNAL OF HEAT TRANSFER, TRANS. ASME, Series C, Vol. 87, No. 3, 1965, pp. 333–341.

7 Iida, Y., and Kobayashi, K., "Void Fraction Distribution Above a Flat Heated Surface in Pool Boiling," (in Japanese), *Transactions of the Japan Society of Mechanical Engineers*, Vol. 34, No. 263, 1968, pp. 1247–1254.

8 Shimada, Y., "Heat Transfer From a Horizontal Plate Facing Upwards to Superposed Liquid-Layers with Change of Phase (in Japanese)," MSc thesis, Keio University, Yokohama, Mar. 1976.

9 Selecki, A., and Gradon, L., "Über den Verdampfungsmechanisms eines sich in einer nicht mischbaren Flüssigkeit bewegenden Flüssigkeitstropfens," *Chemie-Ingenieur-Technik*, Vol. 44, No. 18, 1972, pp. 1077–1081.

10 Katto, Y., *Introduction to Heat Transfer*, (in Japanese), Yokendo, Tokyo, 1967, pp. 172–175

11 Fishenden, M., and Saunders, O. A., *An Introduction to Heat Transfer*, Oxford University Press, London, 1950, pp. 180–182.

as described previously suggests that the latent-heat transfer predominates and that the heat transfer is strongly controlled by the boiling in the lower layer. Therefore, the boiling-condensation heat transfer is compared with the subcooled boiling heat transfer to the single secondary-liquid layer, T_∞ being maintained at the same level, for each system of the two in Fig. 8. Since no difference was found between the boiling of pure Freon-113 and that of Freon-113 saturated with water, only the data of the latter are presented here. The relations q_w versus ΔT for both heat transfer modes are similar in each system and seem to agree with an increase of q_w, except for the increase of ΔT caused by the wetting of heated surface by liquid paraffin in liquid paraffin/water system. A little discrepancy in the low heat-flux range is ascribed to the difference in sensible-heat transfer between both modes. The convection in the superposed layers is divided into two parts by the liquid-liquid interface, and a certain resistance is provided at the interface, as represented by the temperature profile in Fig. 4. Consequently the temperature in the lower layer must increase close to the saturation temperature of the secondary liquid T_s to bear the given heat flux when T_∞ is fixed at a certain level. Therefore, the situation in the lower layer seems to be closer to that of saturation boiling than that of subcooled boiling cited in Fig. 8. The sensible-heat transfer must decrease with a decrease of subcooling though this dependence is generally unnoticeable in higher heat-flux range. A larger ΔT in case of boiling-condensation heat transfer than that in case of

M. S. Bhatti

Senior Engineer,
Owens-Corning Fiberglas Corporation,
Technical Center,
Granville, Ohio.
Mem. ASME

Dynamics of a Vaporizing Droplet in Laminar Entry Region of a Straight Channel

A theory is developed for two-phase flow wherein droplets suspended in a gas stream penetrate the hydrodynamic boundary layer in the laminar entry region of a straight channel with isothermal walls. A fraction of the droplets is captured by the boundary layer due to isotropic turbulence superimposed at the edge of the the boundary layer. Transverse motion of the droplet is under the influence of Stokes' drag, buoyancy, gravity and inertia forces. Axial motion of the droplets is with the local gas velocity without slip. Droplet trajectories are determined by the numerical integration of the equations of motion employing the fourth order Runge-Kutta technique. Using these results, a two region model is developed for determining the convective heat transfer conductance augmented by droplet vaporization. Momentum and heat transfer results are presented for air/water-droplet system containing 10μ–50μ droplets under typical conditions encountered in dry cooling towers.

Introduction

Most of the power generation plants in the United States are equipped with evaporative cooling towers which consume large quantities of water, develop insufficient draft in certain geographic locations and produce ecologically undesirable drifts and plumes. This general consideration has engendered considerable interest in two evaporative cooling concepts: dry cooling and film cooling. The dry cooling concept consists of spraying relatively finer water droplets (10μ–50μ in diameter) into the inlet air stream thereby lowering the dry bulb temperature and in addition enhancing the air side heat transfer due to droplet vaporization. As far as possible, the wetting of the heat exchanger surface is avoided so as to minimize the problem of heat exchanger fouling. The film cooling concept consists of injecting relatively larger droplets, 100μ or more in diameter, and obtaining a liquid film which displaces the gas boundary layer from the heat exchanger surface. This results in considerable enhancement in heat transfer rates, mainly due to sensible heating and evaporation of the liquid film. The price we pay for larger enhancement is the fouling of the heat exchanger surface by the liquid film. In both these concepts, a knowledge of the droplet dynamics within the boundary layer is extremely desirable.

Up to now, a theoretical analysis of the dynamics of a vaporizing droplet in the laminar entry region of a straight channel has not been reported. Recently, Eldighidy, et al. [1][1] presented an analytical investigation of particle deposition in the entry region of a straight channel. However, their analysis is restricted to rigid particles with electrostatic charge and without gravitational force. The present paper deals with the dynamics of a vaporizing droplet in the laminar entry region of a straight channel, which is the most commonly encountered heat exchanger surface. It is an extension of a similar analysis for flat plate reported by Bhatti and Savery [2]. It also draws upon a recently reported analysis by the same authors [3] for the development of a continuous phase flow in a straight channel.

The present analysis applies to the restricted regime of two-phase flow wherein the interaction between the phases can be ignored. In other words, the analysis is uncoupled in terms of the behaviors of the dispersed droplet phase and the continuous gas phase. A practical application of this regime of two-phase flow is in dry cooling towers where starvation quantities of very fine droplets (10μ–50μ in diameter) are injected into the inlet air-stream, particularly during temporary periods of high ambient dry bulb temperatures and power demand. This analysis is also apt to be of interest in atomizers, nuclear reactors and combustion devices involving the spray of fuel droplets.

Analysis

Physical System. A gas stream containing suspended liquid droplets enters a straight channel of width $2a$, as shown in Fig. 1. The hydrodynamic boundary layers start growing on the two channel walls which are maintained at uniform temperature. The effect of viscosity

---

---

[1] Numbers in brackets designate References at end of paper.
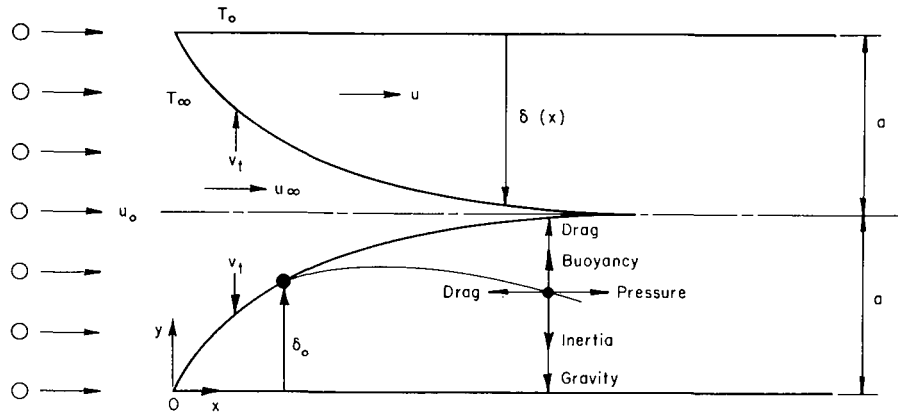
Copyright © 1977 by ASME

Fig. 1 Physical system

gradually spreads across the channel, and the droplets tend to flow preferentially in the accelerated fluid core where the effect of viscosity is not noticeable. The mechanism responsible for propelling a fraction of droplets toward the channel wall is a low-level isotropic turbulence superimposed on the invisid fluid core. Within the boundary layer, the transverse motion of the droplets is due to transverse drag, buoyancy, gravity and inertia forces, and the axial motion is due to axial drag and pressure forces. The transverse drag and gravity forces

oppose droplet penetration in the upper boundary layer, but aid it in the lower boundary layer. Thus, only the upward facing channel wall participates in the heat transfer augmentation by droplet vaporization.

Assumptions. The following simplifying assumptions enter into the analysis:

1 Droplets are spherical and obey Stokes' law. As such, the analysis is restricted to droplets with the Reynolds number (based

---

Nomenclature

a = half channel width, m

A = constant defined by equation (13), dimensionless

b = channel depth, m

B = constant defined by equation (14), dimensionless

c_p = specific heat of the gas phase, Ws/kgK

D = binary vapor diffusivity, m²/s

g = acceleration due to gravity, m/s²

h = heat transfer coefficient in the presence of droplets, W/m²K

$\bar{h}$ = average heat transfer coefficient in the absence of droplets, W/m²K

h_m = mass transfer coefficient, kg-mole/m²s

h_{fg} = enthalpy of droplet vaporization, J/kg

k = boundary layer thermal conductivity, W/mK

K = parameter defined by equation (23), s/J

m = initial droplet mass, kg

Δm = mass defect due to droplet vaporization, kg

$\dot{m}''$ = droplet mass flux in the inlet stream, kg/m²s

M = molecular weight of the droplet, kg/kg mole

$\bar{M}$ = average molecular weight of the boundary layer, kg/kg mole

$\overline{Nu}$ = $\bar{h}a/k$, average Nusselt number in the absence of droplets, dimensionless

p = local pressure within the channel, Pa

Pr = $\mu c_p/k$, Prandtl number, dimensionless

r = instantaneous droplet radius, m

r_0 = initial droplet radius, m

R = r/r_0, instantaneous droplet radius, dimensionless

R_1 = convective resistance of the inner region of the boundary layer, K/W

R_2 = convective resistance of the outer region of the boundary layer, K/W

R_3 = conductive resistance of the outer region of the boundary layer, K/W

R_{eq} = equivalent resistance of the boundary layer, K/W

Re = $u_0 a/\nu$, Reynolds number, dimensionless

Sc = ν/D, Schmidt number, dimensionless

Sh = $2rh_m/D$, Sherwood number, dimensionless

t = time, s

T_0 = channel wall temperature, K

T_∞ = fluid core temperature, K

T_i = temperature between the two regions of the boundary layer, K

u = axial boundary layer velocity, m/s

u_0 = uniform axial velocity at the channel inlet, m/s

u_∞ = axial core velocity, m/s

U = u_∞/u_0, axial core velocity, dimensionless

U_0 = axial core velocity at the point of droplet entry, dimensionless

v = transverse droplet velocity, m/s

v_t = transverse velocity due to turbulence superimposed at the boundary layer edge, m/s

V_0 = $v_t r_0/\lambda$, dimensionless

x = axial coordinate, m

X = $(x/a)/Re$, axial coordinate, dimensionless

X_∞ = $(\xi/a)/Re$, hydrodynamic entry length, dimensionless

y = transverse coordinate, m

y_d = transverse location of the droplet, m

α = parameter defined by equation (10), m²/s

α_1 = α/λ, dimensionless

β = parameter defined by equation (11), m/s²

β_1 = $\beta r_0^3/\lambda^2$, dimensionless

γ = parameter defined by equation (18), dimensionless

δ = hydrodynamic boundary layer thickness, m

δ_0 = hydrodynamic boundary layer thickness at the point of droplet entry, m

δ_t = thermal boundary layer thickness, m

ζ = δ_t/δ, boundary layer shape factor, dimensionless

λ = parameter defined by equation (9), m²/s

μ = dynamic viscosity of the gas phase, kg/ms; also unit of length, micron

ν = μ/ρ, kinematic viscosity, m²/s

ξ = hydrodynamic entry length, m

ρ = gas phase density, kg/m³

ρ_ℓ = droplet density, kg/m³

τ = $\lambda t/r_0^2$, time, dimensionless

ω_0 = vapor mole fraction at the droplet surface temperature, dimensionless

ω_∞ = vapor mole fraction at the average boundary layer temperature, dimensionless

on the turbulence velocity, v_t, droplet diameter and the average kinematic viscosity of the gas phase) less than unity.

2 Droplet concentration is low, so that there is no interference between the neighboring droplets.

3 The level of isotropic turbulence is low, so that the laminar boundary layer flow remains unaffected.

4 The velocity and the temperature gradients within the boundary layer are mild, so that the lift force arising due to droplet rotation and the reaction force arising due to nonuniform evaporation are negligible.

5 Within the fluid core, the velocity and the temperature of the droplets are the same as those of the gas phase.

6 The transverse velocity component of the gas boundary layer is negligible.

7 Droplets move axially with the local gas velocity. (There is some droplet slippage in the axial direction. However, as long as the turbulence velocity, v_t, is a small fraction of the core velocity, u_∞, this problem is relatively unimportant.)

It is extremely desirable to provide a bound on the applicability of the analysis within the confines of the foregoing assumptions. This can be accomplished by the following reasoning:

The relative axial velocity of the droplet is of the order of the turbulence velocity, v_t, whereas the axial velocity of the gas boundary layer is of the order of the core velocity, u_∞. Then, the axial momentum of the droplet, ignoring slippage, is of the order of mu_∞, while taking into account slippage it is of the order of $m(u_\infty - v_t)$. Forming the ratio of the two momenta, we notice that the droplet slippage in the axial direction can be ignored if the ratio $(u_\infty - v_t)/u_\infty$ does not differ appreciably from unity. Arbitrarily small values, such as 0.99 and 0.95, can be specified for this ratio, and thence the ratio (v_t/u_∞) can be determined. Knowing u_∞, v_t can be determined. This, coupled with the condition that the Reynolds number based on the turbulence velocity, droplet diameter and the average kinematic viscosity of the gas phase should be less than unity, provides the requisite bound on the applicability of the analysis.

Entry Region Flow Development. Before commencing the analysis of the two-phase, two-component flow within the confines of the foregoing assumptions, the problem of laminar flow development for the gas stream must be solved. There are numerous solutions, analytical as well as numerical, of this problem. A particularly simple and accurate solution is the one reported recently by Bhatti and Savery [3]. This solution consists in applying the following velocity distribution in the hydrodynamic entry region:

$$u = -\frac{1}{2\mu}\frac{dp}{dx}(2y\delta - y^2) \tag{1}$$

Equation (1) is a generalization of Hagen-Poiseuille's parabolic distribution. The physical implication of applying it in the entry region is that, as in the fully developed region, so in the developing region the pressure force and the viscous force balance each other within the boundary layer. This is tantamount to saying that the effect of the inertia force is confined to the inviscid core only where it is balanced by the pressure force.

Introducing equation (1) into the macroscopic mass balance equation, we obtain the following expressions for the local boundary layer thickness and the pressure gradient:

$$\frac{\delta}{a} = \frac{3(U-1)}{U} \tag{2}$$

$$\frac{dp}{dx} = -\frac{2}{9}\left(\frac{\mu u_0}{a^2}\right)\frac{U^3}{(U-1)^2} \tag{3}$$

When equations (2) and (3) are introduced into equation (1), it assumes the form

$$\frac{u}{u_\infty} = \left(\frac{y}{\delta}\right)\left[2 - \left(\frac{y}{\delta}\right)\right] \tag{4}$$

The remainder of the momentum transfer quantities are also expressible in terms of the dimensionless core velocity, U. Finally, the variation of U with the dimensionless axial coordinate, X, is deter-

mined from the macroscopic mechanical energy equation which yields

$$\frac{dU}{dX} = \frac{70U^2(3 - 2U)}{(U-1)^2(513 - 297U)} \tag{5}$$

whose solution subject to the boundary condition that at $X = 0$, $U = 1$, is

$$X = \frac{594U^2 + 90U - 684 - 15U\ell n(3 - 2U) - 1308U\ell nU}{280U} \tag{6}$$

At the channel inlet $U = 1$, and when the flow become hydrodynamically developed $U = 3/2$. Equations (5) and (6) correctly predict that the flow becomes developed asymptotically at $X = \infty$, which means the hydrodynamic entry length is infinite. It is customary to define the hydrodynamic entry length as that axial distance at which U is within 1 percent of its ultimate fully developed value. Thus, introducing $U = 1.4850$ into equation (6), we obtain

$$X_\infty = \frac{(\xi/a)}{\text{Re}} = 0.1674 \tag{7}$$

This value compares very well with the prediction of the well known series solution by Schlichting who predicts $X_\infty = 0.16$ [4].

Droplet Velocity Components. In reference [2], it is shown that the transverse motion of a vaporizing droplet penetrating the hydrodynamic boundary layer is governed by the equation

$$\frac{d}{dt}\left(m\frac{dy_d}{dt}\right) = mg\left(\frac{\rho}{\rho_\ell}\right) - mg + 6\pi\mu r\frac{dy_d}{dt}$$

The left hand term of this equation represents the inertia force, and the three terms on the right hand side represent buoyancy, gravity and drag force, respectively. The solution of this equation yields the transverse location, y_d, of the droplet at any instant t, after it penetrates the boundary layer [2], as

$$y_d = \delta_0 - r_0^2\left[\frac{\beta r_0^2 + 4\lambda v_t}{4\lambda(\alpha + 2\lambda)}\right] + \frac{\beta(r_0^2 - 2\lambda t)^2}{4\lambda(\alpha - 2\lambda)} \tag{8}$$

where

$$\lambda = -\frac{1}{2}\left[\frac{M}{\overline{M}}\frac{\rho}{\rho_\ell}D\,\text{Sh}\,\ell n\left(\frac{1 - \omega_\infty}{1 - \omega_0}\right)\right] \tag{9}$$

$$\alpha = 3\left(\frac{3\mu}{2\rho_\ell} - \lambda\right) \tag{10}$$

$$\beta = \left(1 - \frac{\rho}{\rho_\ell}\right)g \tag{11}$$

Introducing the dimensionless variables τ, α_1, β_1, and V_0, the foregoing can be written as

$$\left(\frac{y_d}{a}\right) = \left(\frac{\delta_0}{a}\right) + A + B(1 - 2\tau)^2 \tag{12}$$

where

$$A = -\frac{1}{4}\left(\frac{r_0}{a}\right)\left[\frac{\beta_1 + 4V_0}{(\alpha_1 + 2)}\right] \tag{13}$$

$$B = \frac{1}{4}\left(\frac{r_0}{a}\right)\left[\frac{\beta_1}{(\alpha_1 - 2)}\right] \tag{14}$$

In arriving at equation (8), the following simple equation for the droplet vaporization rate has been used

$$\frac{dr}{dt} = -\frac{\lambda}{r}$$

Treating λ as a constant [2], this equation can be integrated at once to obtain the instantaneous droplet radius, R, as a function of the dimensionless time τ. Thus

$$R^2 = 1 - 2\tau \tag{15}$$

Habib [5] compared the predictions of the simple equation (15) with those of a more cumbersome equation which, in essence, takes account of the temperature dependence of the parameter λ. The comparison

shows that along a constant area duct the predictions of the two equations agree very well. At the duct inlet, however, the latter equation exhibits somewhat anomalous behavior. Instead of predicting a decrease, it predicts an increase in the droplet radius. Habib [5] explains it as due to thermal expansion of the droplet.

Differentiating equation (12) with respect to τ, the transverse velocity component of the droplet is seen to be

$$\left(\frac{v}{v_t}\right) = -\frac{\beta_1(1 - 2\tau)}{V_0(\alpha_1 - 2)} \tag{16}$$

Since there is no droplet slippage in the axial direction, equation (4) represents the axial velocity component of the boundary layer as well as that of the droplet.

Droplet Trajectories. Noting that $u = dx/dt$, we obtain from equation (4) after the introduction of the dimensionless variables

$$\frac{dX}{d\tau} = \left(\frac{\nu}{\lambda}\right)\left(\frac{r_0}{a}\right)^2 U\left(\frac{y_d}{\delta}\right)\left[2 - \left(\frac{y_d}{\delta}\right)\right]$$

Eliminating X in terms of U via equation (5), this can be written as

$$\frac{dU}{d\tau} \approx \frac{\gamma U^3(3 - 2U)}{(U-1)^2(513 - 297U)}\left(\frac{y_d}{\delta}\right)\left[2 - \left(\frac{y_d}{\delta}\right)\right] \tag{17}$$

where

$$\gamma = 70\left(\frac{\nu}{\lambda}\right)\left(\frac{r_0}{a}\right)^2 \tag{18}$$

Here y_d is given as a function of τ by equation (12) and δ is given as a function of U by equation (2). Thus, equation (17) is an ordinary differential equation for the variation of U with τ. Unfortunately, it cannot be integrated in closed form since the variables U and τ are non-separable. Therefore, recourse has to be taken to numerical integration. With the specification of the initial condition $U = U_0$ at $\tau = 0$, equation (17) can be integrated in a straightforward fashion by the application of the fourth order Runge-Kutta technique. In the next section, we shall present the results of the numerical integration.

Knowing the variation of U with τ, the axial and the transverse coordinates of the droplets can be determined at any instant from equations (6) and (12), respectively. Thus, knowing the point of penetration and the instantaneous location of the droplet, its trajectories can be traced without difficulty.

Augmented Heat Transfer Coefficient. A simple two-region model developed in Reference [2] is used for determining the heat transfer coefficient in the presence of the droplets. The boundary between the two regions is given by the depth of penetration of the droplets. The thermal resistance of the boundary layer can be divided into three resistances, as shown in Fig. 2. The expressions for the three resistances as presented in Reference [2] are

$$R_1 = \frac{1}{\bar{h}b\xi}\left(\frac{\delta - \delta_0 + y_d}{\delta}\right) \tag{19}$$

$$R_2 = \frac{1}{\bar{h}b\xi}\left(\frac{\delta_0 - y_d}{\delta}\right) \tag{20}$$
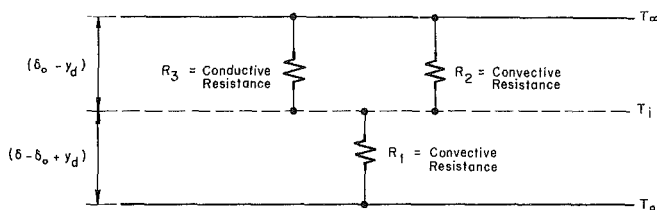
$$R_3 = K(T_i - T_\infty) \tag{21}$$

where

$$T_i = \frac{K(R_1 T_\infty + R_2 T_0) - R_1 R_2}{K(R_1 + R_2)} \tag{22}$$

$$K = \frac{3m}{\dot{m}'' \Delta m h_{fg} ba} \tag{23}$$

Implicit in the derivations of equations (19) and (20) is the assumption that the thermal boundary layer thickness, δ_t, and the hydrodynamic boundary layer thickness, δ, are coincident. In other words, the boundary layer shape factor, ζ, is unity. Strictly speaking, this assumption is true for a flat plate with zero pressure gradient involving the flow of a fluid with Prandtl number equal to unity [6]. Since the Prandtl number of practically all the industrially important gases, including air and steam, is nearly unity, the boundary layer shape factor for the gases flowing over an isothermal flat plate does not deviate significantly from unity. This can be seen more clearly from the equations [7]

$$\zeta = 1/\mathrm{Pr}^{1/3} \quad (\mathrm{Pr} \geq 1) \tag{24}$$

$$\zeta^2 - \zeta + 0.4 - \frac{3}{8\mathrm{Pr}} = 0 \quad (\mathrm{Pr} < 1) \tag{25}$$

Thus, the assumption of unity boundary layer shape factor is quite justified in the case of a flat plate. Even in the case of a straight channel where a negative pressure gradient is present, this assumption remains quite valid for fluids with $\mathrm{Pr} \leq 1$. Comparison of the ζ's computed by Sparrow [7], using equation (25) for a flat plate and the complicated differential equation applicable to a straight channel, showed that up to $\mathrm{Pr} = 0.1$, the ζ's computed from the two equations are practically indistinguishable. For $\mathrm{Pr} = 1$, ζ computed from equation (25) is about 10 percent higher than that computed from the differential equation which, unfortunately, cannot be integrated in closed form.

The resistances R_2 and R_3 are in parallel and R_1 is in series with them, so that the equivalent resistance of the boundary layer is

$$R_{eq} = \frac{R_1 R_2 + R_2 R_3 + R_3 R_1}{R_2 + R_3} \tag{26}$$

The augmented heat transfer coefficient, h, in terms of R_{eq} is given by

$$\frac{1}{h} = R_{eq}b\xi \tag{27}$$

The average heat transfer coefficient $\bar{h}$ in the combined hydrodynamic and thermal entrance region of a straight channel involving the single-phase flow can be determined from the following simple relation presented by Sparrow [7]

$$\overline{\mathrm{Nu}} = \frac{\bar{h}a}{k} = 0.664\mathrm{Pr}^{1/3}X^{-1/2}(1 + 1.825X^{1/2})^{1/2} \tag{28}$$

This relation is valid for $0.01 \leq \mathrm{Pr} \leq 2$. For a fluid with $\mathrm{Pr} \simeq 1$, the length of the combined hydrodynamic and thermal entrance region can be taken as X_∞, given by equation (7). This enables the determination of $\bar{h}$ from equation (28). Forming the ratio $h/\bar{h}$, the enhancement in the heat transfer rate due to droplet vaporization can be determined.

Results and Discussion

The use of the foregoing equations is illustrated by applying them to the following typical conditions encountered in dry cooling towers:

$\mathrm{Re} = 500$, $u_0 = 1.524$ m/s, $v_t = -0.01\, u_0$, $T_\infty = 308$K,
$$T_0 = 325\mathrm{K}, \dot{m}'' = 0.00625 - 0.025 \text{ kg/m}^2\text{s}.$$

Under these conditions, the physical properties of air/water-droplet system are:

$M = 18$ kg/kg-mole, $\overline{M} = 28$ kg/kg mole, $\rho = 1.25$ kg/m³,
$\rho_\ell = 993$ kg/m³, $\mu = 2.227 \times 10^{-3}$ kg/ms, $\nu = 1.782 \times 10^{-3}$ m²/s,
$D = 2.944 \times 10^{-3}$ m²/s, $k = 2.802 \times 10^{-2}$ J/kg, $h_{fg} = 2.4$
$\times 10^6$ J/kg, $\mathrm{Sc} = 0.61$, $\mathrm{Sh} = 2.13$, $\mathrm{Pr} = 1$.
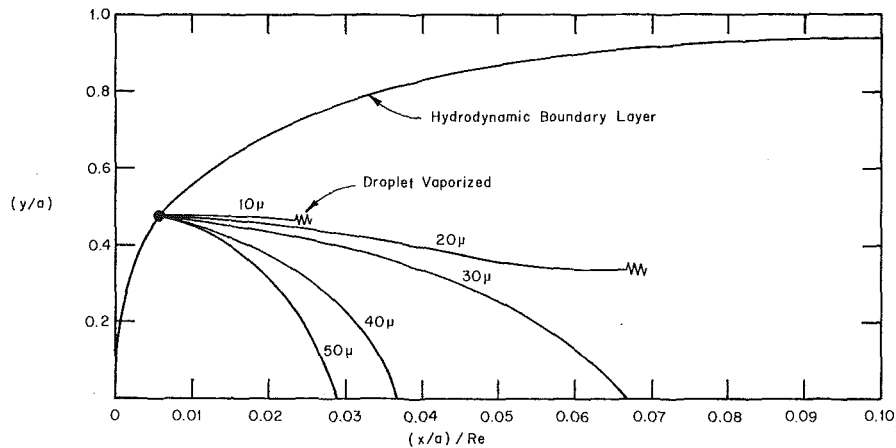
Fig. 2   Thermal resistance of the boundary layer

Fig. 3   Droplet trajectories in the entry region of a straight channel

The mole fractions, ω_∞ and ω_0, entering equation (9) are determined from the partial pressures of water vapor read from the thermodynamic tables corresponding to the average boundary layer temperature $(T_0 + T_\infty)/2$ and the average surface temperature of the droplet, which is taken as the wet bulb temperature corresponding to $(T_0 + T_\infty)/2$.

The quantities δ_0 and U_0 enter as parameters in the integration of equation (17). In order to obtain typical results, (δ_0/a) is taken as 0.5. According to equation (2), this corresponds to $U_0 = 1.2$. Introducing this value of U into equation (6), we notice that the droplet penetrates the boundary layer at the axial distance $X = 0.0071$. Knowing the value of U at any instant τ from the numerical integration of equation (17), the droplet trajectories are calculated as explained in the preceeding section. A step size of $\Delta\tau = 0.01$ is used. The calculated results are displayed in Fig. 3. Under the specified conditions, 10 and 20μ diameter droplets vaporize completely within the boundary layer. Note that from equation (15), the dimensionless vaporization time of a droplet is 0.5. Droplets having 30, 40 and 50μ diameter deposit on the channel wall before complete vaporization. The point of impact of 50μ droplet is closer to the leading edge of the channel wall than the point of impact of 30μ droplet. This is in consonance with expectation since heavier droplets gravitate more rapidly than lighter droplets.

Knowing the dwell time of the droplet within the boundary layer from equation (17), its instantaneous radius is calculated at the instant of deposition for 30, 40 and 50μ. For 10 and 20μ droplets, the final radius is zero. Thus the mass defect due to vaporization, Δm, is determined for all the droplets. This, coupled with the coordinates of the final position of the droplet, enables the determination of the boundary layer resistances from equations (19)–(23). Next, the equivalent resistance is determined from equation (26), and thence the augmented heat transfer coefficient is computed from equation (27). Finally, the percent enhancement is determined with the help of equation (28).

Fig. 4 shows the heat transfer enhancement results for 10–50μ droplets. The various curves are parametrized by the values of the droplet mass flux at the channel inlet. The smaller diameter droplets vaporize completely, but do not penetrate the boundary layer deep enough. The larger droplets, on the other hand, penetrate the boundary layer completely, but suffer very little mass defect during transit. The maximum heat transfer enhancement, therefore, is caused by a droplet penetrating the boundary layer completely and suffering maximum mass defect during transit.

Note that the heat transfer enhancement attributed to the droplets that deposit on the channel wall is due to vaporization alone. Actually, these droplets cause further heat transfer enhancement due to sensible heating and evaporization of the liquid film which they eventually form. The present heat transfer model is restricted to vaporizing droplets only and does not take account of the resistance introduced
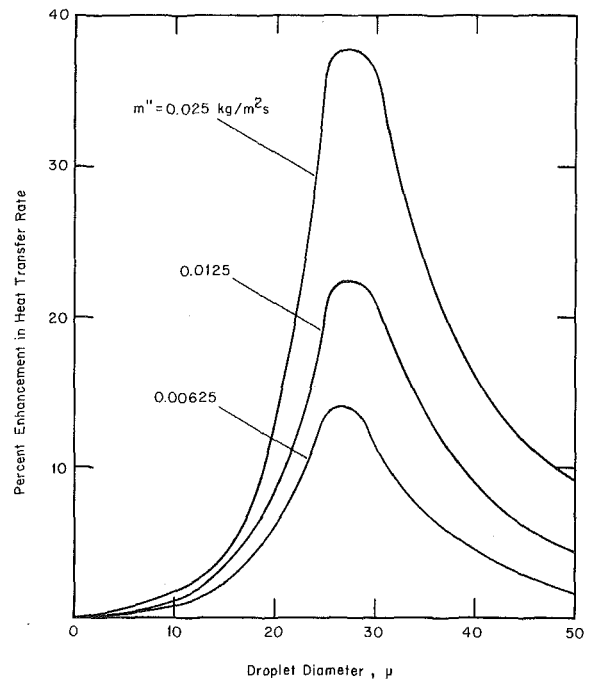

Fig. 4   Heat transfer augmentation by droplet vaporization in the entry region of a straight channel

by the liquid film. However, the momentum transfer model gives complete history of the droplets from the instant of penetration to the instant of deposition.

Finally, it may be pointed out that according to this theory, droplets do not penetrate the boundary layer formed on the downward facing wall of the channel. This fact was confirmed by the qualitative observations made on an experimental rig under similar conditions [8]. However, no quantitative measurements suitable for comparison with the theoretical predictions are available.

Concluding Remarks

An analysis of an important industrial problem hitherto unexplored has been presented. The variation of droplet radius during its transit through the boundary layer has been taken into account, which renders the analysis quite realistic. The simple two-region model for the heat transfer rate enables the determination of the augmented heat transfer coefficient, which is of major technical importance. Since the two-region model entails the solution of the energy equation in an

overall sense, the local boundary layer temperatures cannot be predicted. However, this does not limit the usefulness of the analysis. In practical applications, the augmented heat transfer coefficient rather than local boundary layer temperature is sought.

References

1 Eldighidy, S. M., Chen, R. Y., and Comparin, R. A., "Deposition of Suspensions in the Entrance of a Channel," ASME Paper No. 76-WA/Flcs-13 presented at the Winter Annual Meeting, New York, N. Y., Dec. 15, 1976.

2 Bhatti, M. S., and Savery, C. W., "Augmentation of Heat Transfer in a Laminar External Gas Boundary Layer by the Vaporization of Suspended Droplets," JOURNAL OF HEAT TRANSFER, TRANS. ASME, Series C, Vol. 97, May 1975, pp. 179–184.

3 Bhatti, M. S., and Savery, C. W., "Heat Transfer in the Entrance Region of a Straight Channel: Laminar Flow with Uniform Wall Heat Flux," JOURNAL OF HEAT TRANSFER, TRANS. ASME, Series C, Vol. 99, Feb. 1977, pp. 142–144.

4 Schlichting, H., Boundary Layer Theory, McGraw-Hill, New York, Sixth ed., 1968, pp. 176–178.

5 Habib, I. S., "The Interaction of a Hot Gas Flow and a Cold Liquid Spray in Channels," JOURNAL OF HEAT TRANSFER, TRANS. ASME, Series C, Vol. 98, Aug. 1976, pp. 421–426.

6 Kays, W. M., Convective Heat and Mass Transfer, McGraw-Hill, New York, 1966, pp. 204–205.

7 Sparrow, E. M., "Analysis of Laminar Forced Convection Heat Transfer in Entrance Region of Flat Rectangular Ducts," NACA TN 3331, 1955.

8 Wachtell, G. P., "Atomized Water Injection to Improve Dry Cooling Tower Performance," Franklin Institute Research Laboratories, Philadelphia, Pennsylvania, Report C00-2241-1, prepared for the U. S. Atomic Energy Commission under contract No. AT(11-1)-2241, Nov. 1974.

N. M. Schnurr

Professor,
Department of Mechanical Engineering,
Vanderbilt University,
Nashville, Tenn.
Mem. ASME

Numerical Predictions of Heat Transfer to Supercritical Helium in Turbulent Flow Through Circular Tubes

A numerical method is used to calculate heat transfer to supercritical helium in turbulent flow through circular tubes with constant wall heat flux. Comparisons of numerical predictions to experimental data showed good agreement. Numerical results were obtained for pressures from 2.5 to 20 atm and these results were correlated in terms of a heat flux parameter. A preliminary study of heat transfer in the thermal entry region showed the increase of the film coefficient to be larger for higher heat fluxes and for cases where the inlet bulk enthalpy was above the pseudocritical value.

Introduction

The technology of superconducting materials has advanced to the point where several types of practical systems using superconductivity are either in operation or in an advanced planning stage. Superconducting magnets have applications in fusion research. The use of superconducting materials for large-scale power transmission is now under serious consideration [1].[1] The ultra low temperatures required for these applications (~5 K) are maintained by cooling with helium. In the case of small superconducting magnets for laboratory use, the conductor is usually immersed in liquid helium at atmospheric pressure and the heat-transfer mechanism is pool boiling. For more complex systems, however, Kolm [2], Johannes [3], and Giarratano, et al. [4] indicate that there are definite advantages to using forced flow of supercritical helium for cooling.

Experimental data for forced convection heat transfer to supercritical helium are limited. Johannes [3] has provided some data at pressures of 3 6 atm (the critical pressure for helium is 2.245 atm). His results are limited to low heat fluxes and to bulk temperatures less than the pseudocritical temperature. Brechna [5] correlated some experimental data using the McAdams equation

$$Nu = 0.023 \ Re^{0.8} \ Pr^{0.4} \tag{1}$$

but the range of experimental conditions was not reported. The largest

source of data is the work of Giarratano and coworkers [4, 6]. In reference [4] they give heat-transfer coefficients for more than 100 data points in the pressure range of 3–20 atm and present a correlation in the form

$$Nu = 0.0259 \ Re^{0.8} \ Pr^{0.4} \ (T_b/T_w)^{0.716} \tag{2}$$

These data are also limited to moderate heat fluxes, however.

It has been shown by several investigators [7–9, 17] in experimental heat-transfer studies of carbon dioxide, water, oxygen, and hydrogen that for cases where $T_b < T_M$, $T_w > T_M$, and q_w is sufficiently high, the film coefficient may drop to a level well below that predicted by either equation (1) or (2). Those test conditions were not achieved in any of the experimental work reported in references [3–5]. Later studies were reported by Giarratano, et al. [6] at a pressure of 2.5 atm in which those conditions were achieved and deterioration of the film coefficients was found. The measured film coefficients were much lower than those predicted by equation (2). It does not appear that a simple correlation of the type of equation (1) or (2) will account for the severe property variations that occur at moderate to high heat fluxes.

It has been shown [10] that heat-transfer coefficients for turbulent forced convection to supercritical water ($P_r = 1.4$) in flow through circular tubes can be predicted with good accuracy over rather wide ranges of heat flux and flow rate using numerical analysis. The purpose of the work reported here is to produce numerical predictions of heat-transfer coefficients for supercritical helium and to present those results in a form useful for the designer or analyst. Verification of the analysis is provided to the extent possible by comparison of analytical results to experimental data. Some limitations of the numerical results are discussed.

Copyright © 1977 by ASME

The Numerical Method

The problem considered here is heat transfer to supercritical helium flowing through a circular tube with a constant wall heat flux. Axial conduction, viscous dissipation, and free convection effects are assumed negligible. The flow is assumed to be hydrodynamically fully developed and the enthalpy profile is uniform at the beginning of the heated section of tube.

The numerical method used here is an adaptation of the Patankar-Spalding method [11]. It is an implicit finite-difference marching procedure with modifications intended to account more accurately for the effects of the severe property variations. The most significant modification is in the "Couette flow" region very near the wall. In this region the velocities are so small that the axial convection term is negligible and the flow is adequately described by an ordinary differential equation. This equation is integrated in closed form using viscosity and Prandtl number variations characteristic of near-critical fluids. This gives values and gradients of the dependent variables, velocity and enthalpy, at the edge of the Couette flow region which are then used as boundary conditions for the finite difference solution used for the rest of the flow field. This numerical procedure is identical to that reported in [10], where a more complete discussion of the analysis can be found.

The transport and thermal property data used in this analysis are those of McCarty [12]. These data are incorporated in a subroutine in tabular form. For a fixed pressure, values of temperature, density, specific heat, viscosity, and thermal conductivity are given at various values of enthalpy. The steps in enthalpy values are small enough so that linear interpolation may be used with good accuracy.

The eddy diffusivity model used here is that of Van Driest [13], with the minor modification of using local values of density, viscosity, and shear stress rather than wall values. The resulting form is

$$\mu_{\text{eff}} = \mu + \rho \kappa^2 y^2 \left[1 - \exp \left[-y \sqrt{\tau \rho}/(\mu A_+) \right] \right]^2 |\partial u / \partial y| \qquad (3)$$

where $\kappa = 0.4$ and $A_+ = 26$. The turbulent Prandtl number is assumed to be unity.

An important aspect of the analysis was the selection of a suitable node spacing and downstream step size. It was necessary to use a nonuniform radial distribution of node points with closer spacing near the wall. The spacing was calculated from the equation

$$\Delta r_I = \Delta r_{I-1}/(2)^{1/S} \qquad 1 \leq I \leq N$$

where $I = 1$ corresponds to the node on the tube center line. As the parameter S is decreased, for a fixed value of N, the spacing of node points nearer the wall decreases and the spacing becomes wider near the tube center line. Since the Couette flow solution assumed laminar flow, the node point nearest the wall had to fall within the laminar sublayer. If that node point was too close to the wall, however, accuracy problems could result when differences were calculated between numbers of nearly identical magnitude, even though double precision was used for all calculations. For the most difficult cases (high heat flux, pressures and temperatures near the critical values) it was necessary to use 35 node points. Since computer time increased rapidly with increasing N, it was not possible to use higher values of N except to make limited comparisons with other numerical results.

Selection of a suitable downstream step size was also important. Although the numerical method is basically a forward differencing method, the values of the transport properties are evaluated at the upstream location so that the method is not universally stable. It was found that the step length had little effect on accuracy provided it was small enough to maintain computational stability. The maximum allowable step length was a complex function of fluid properties, heat flux, flow rate, and axial distance from entrance and was determined by trial and error. Computational time was minimized by lengthening the downstream step size at various stages during the computation as the entrance effects diminished and the critical region was passed. The computation time for a typical run (a bulk enthalpy increase from 10 to 90 kJ/kg) was 15 min of XDS Sigma 7 computer time.

Comparison of Numerical Results to Experimental Data

The most extensive experimental data for helium at a fixed pressure for various flow rates and heat fluxes are those of [6]. The ranges of experimental variables are:

P	$= 2.5$ atm ($P_r = 1.11$)
D	$= 0.213$ cm
T_{b_i}	$= 4$–5 K
G	$= 7, 12,$ and 22 g/s-cm^2
q_w	$= 0.008 - 0.713$ w/cm^2

Axial variations of the film coefficient are given for 18 different runs. Numerical predictions were generated for conditions matching those of the experiments. Examples of the comparisons of the numerical predictions and experimental results are shown in Fig. 1 for four runs.

The shapes of the profiles are quite well predicted. The difference between the analysis and experimental results is in the range of 10–20 percent for runs 1 and 2 except for the last 2 cm of tube length. The average deviation for these two cases (calculated by averaging the absolute values of the deviations at 1-cm intervals) are 15 percent and 13 percent, respectively, and are among the highest of the 18 cases. The overall average deviation for all cases is less than 10 percent. The numerical predictions are generally high so that any heat gain from the surroundings which might not be accounted for in the experiments would result in improved agreement.

The experimental accuracy was estimated to be in the range of 8–55 percent with the largest errors occurring at low heat flux, e.g., runs 1 and 2. In those cases the differences between the wall and bulk temperatures are only 0.1–0.2 K so that a small error in the measurement of the wall temperature causes a large error in the film coefficient.

A fairly large and consistent discrepancy occurs in the last 2 cm of

Nomenclature

C_p = specific heat
D = inside tube diameter
g = acceleration of gravity
G = mass velocity
Gr = Grashoff number = $((\rho_b - \rho_w)/\rho_w)(\rho_w/\mu_w)^2 D^3 g$
h = heat transfer coefficient
i_b = bulk enthalpy
i_{b_i} = bulk enthalpy at the beginning of the heated length of tube
i_M = pseudocritical enthalpy
k = thermal conductivity
k_b = bulk thermal conductivity

$\dot{m}_f$ = mass flow rate
Nu = Nusselt number = hD/k_b
Nu$_1$ = Nusselt number calculated from equation (1)
P = pressure
P_c = critical pressure
P_r = reduced pressure = P/P_c
Pr = Prandtl number based on bulk properties
q_w = wall heat flux
Re = bulk Reynolds number
T_b = bulk temperature
T_{b_i} = bulk temperature at the beginning of

the heated length of tube
T_M = pseudocritical temperature
T_w = wall temperature
u = local axial velocity
x = axial distance
y = distance from the tube wall
Δr = node spacing in the radial direction
μ = fluid viscosity
μ_{eff} = effective viscosity for turbulent flow
ρ = fluid density
τ = local shear stress
$\phi = q_w D^{0.2}/G^{0.8} (w \ s^{0.8} m^{-0.2} kg^{-0.8})$

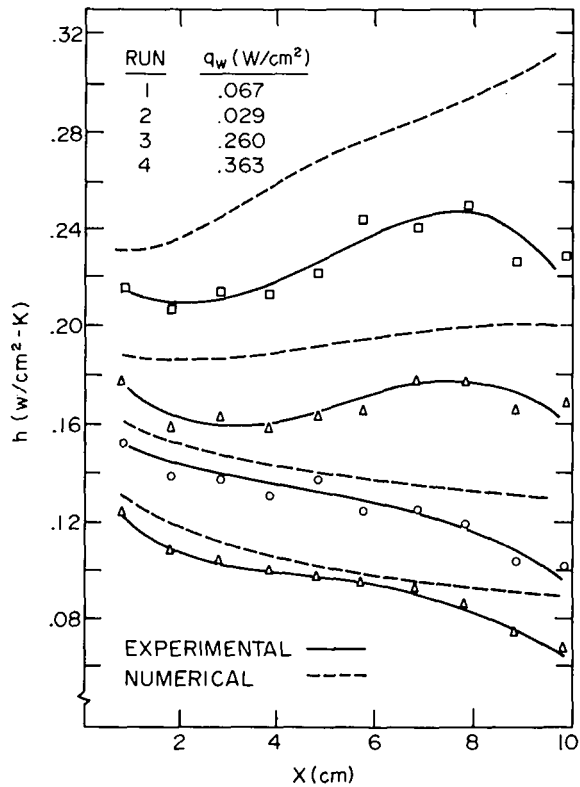**Fig. 1** Comparison of numerical predictions to experimental data of [6]. P = 2.5 atm, D = 0.213 cm, T_{b_i} = 5.04 K, G = 7.2 g/s-cm

Fig. 2 Comparison of numerical predictions to experimental correlations of [4]

the heated length of tube. The experimental data consistently show a significant drop in the film coefficient in that region regardless of the bulk temperature or other conditions. There is no apparent reason why this should occur unless it is caused by conduction at the end of the heated section. It appears that care was taken to minimize such effects in the experiments, however, and they were estimated to be small.

Considering the possible experimental error and the uncertainties in the analysis, the overall agreement is considered to be quite good.

Additional runs were made to compare the results of the analysis to the experimental data of [4]. Those data covered a range of pressures from 3 to 20 atm and are fairly well correlated by equation (2). That correlation is shown graphically in Fig. 2. The results of numerical calculations are shown for comparison. Note that the experimental correlation agrees very well with numerical results for a low heat flux case. At a higher heat flux, the peak in the curve decreases and the correlating equation and analysis no longer agree. Examination of the experimental data revealed that of the 14 data points at P = 3 atm, none are in the range $0.91 < T_b/T_M < 1.4$. Therefore, the effect of q_w on h in that range is not established by experimental results.

Direct comparisons were made to each of the data points at P = 3 atm. The average deviation from the numerical predictions was 11 percent. Comparison with a few randomly selected points at higher pressures showed better agreement.

A precise comparison of numerical results to the experimental data of [3] was not possible since the values of heat flux are not given for individual data points. Those data are all for bulk temperatures well below the transposed critical temperature and the film coefficients were found to be about 10–20 percent higher than those predicted by equation (1). This is in good agreement with low heat flux results predicted by the analysis for low heat flux cases at bulk enthalpies below the pseudocritical value.
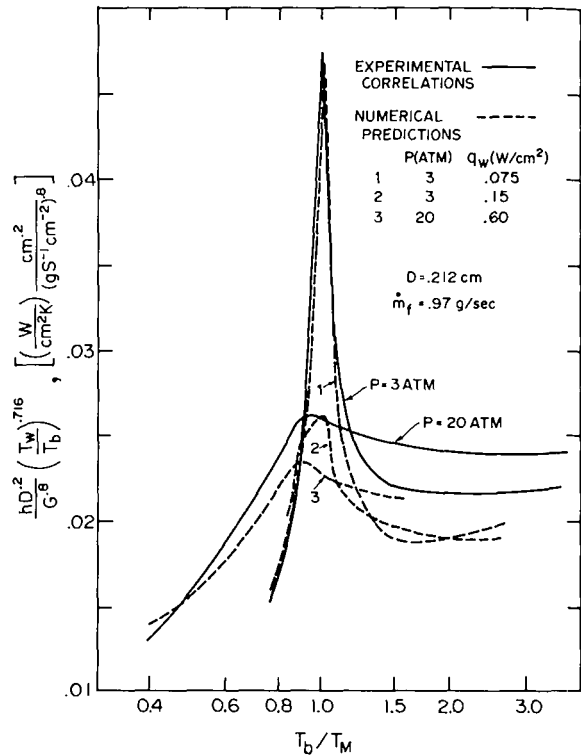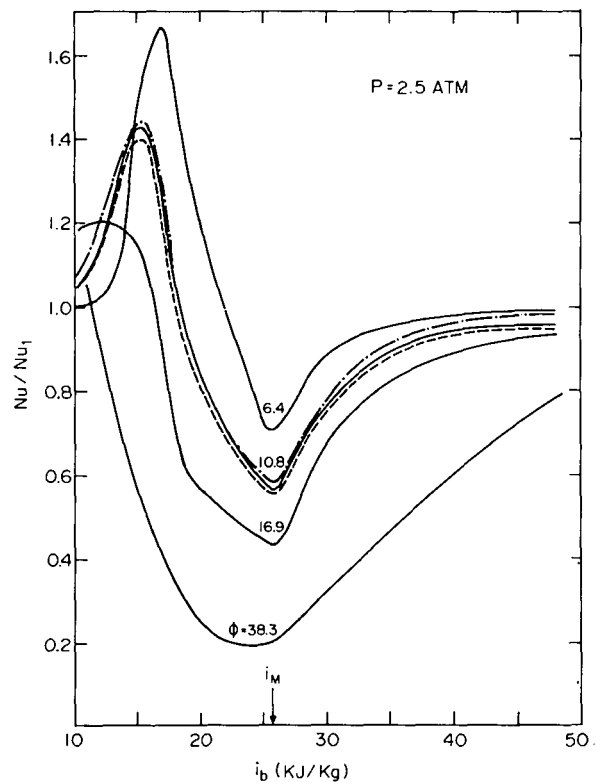

Fig. 3 Correlation of numerical results for helium at 2.5 atm

Numerical Results for Fully Developed Flow

A series of runs was made to produce numerical predictions over ranges of the independent parameters which might occur in practical applications. The independent variables are pressure, tube diameter, mass velocity, heat flux, and bulk enthalpy. It was shown in [10] that the effects of q_w, G, and D could be combined in a correlating parameter defined as
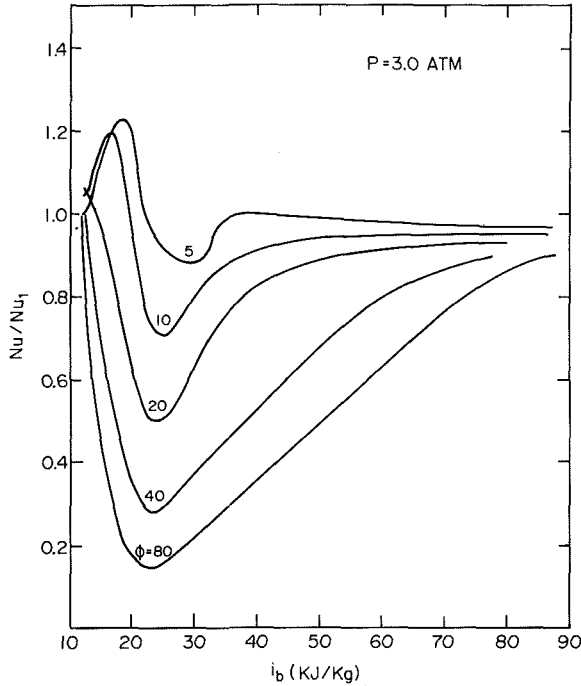
$$\phi = \frac{q_w D^{0.2}}{G^{0.8}} \qquad (4)$$
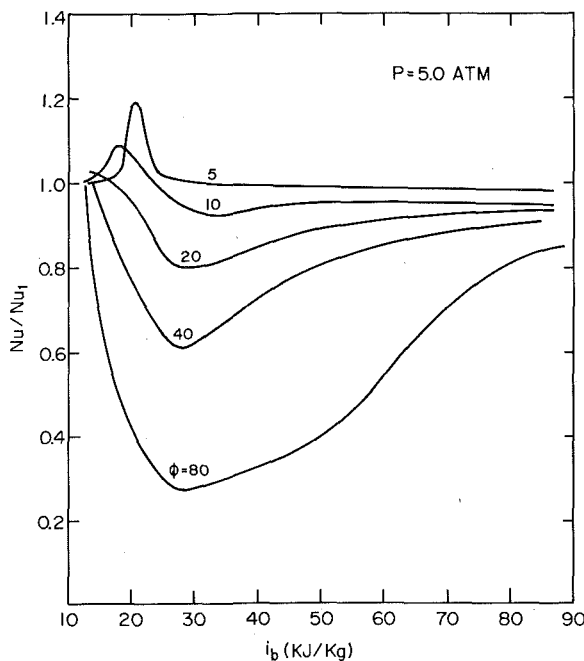
The units used here are $w\ s^{0.8}\ m^{-0.2}\ kg^{-0.8}$. This is the "heat flux parameter" suggested by Goldmann [14]. The heat-transfer coefficient is expressed in the form of a ratio of the Nusselt number divided by the Nusselt number calculated from equation (1). This parameter is plotted as a function of fluid bulk enthalpy for various values of ϕ. Results for a pressure of 2.5 atm are given in Fig. 3. Note that three curves are shown for $\phi = 10.8$. These were produced for three different combinations of q_w, G, and D and demonstrate that ϕ is indeed a correlating parameter. The correlation was also checked for other cases by varying q_w and G in such a way that ϕ remained constant and comparing the resulting curves. The agreement was within 3 percent in all cases.

The effect of increasing heat flux is clearly seen in Fig. 3. At low heat fluxes (e.g., $\phi = 6.4$) the ratio of Nu/Nu_1 increases sharply and reaches a peak at a condition where $T_w \approx T_M$. This effect was also found experimentally [6] and was of the same magnitude as predicted here. This is apparently due to a significant peak in the thermal conductivity at T_M. This causes a very low thermal resistance in the region near the wall and a significantly higher film coefficient than that predicted by equation (1), which uses fluid properties evaluated at the bulk temperature. It should be noted that the accuracy of the thermal conductivity and viscosity data is poorest in this region, however, and the accuracy of the heat transfer predictions is therefore questionable. At extremely low heat fluxes the property variations in the radial direction would become very small and the constant property solution would apply so that Nu/Nu_1 would be approximately equal to unity for all values of bulk enthalpy. At higher heat fluxes this peak decreases and eventually disappears. At pressure farther from the critical pressure, the thermal conductivity peak is smaller and the peak in Nu/Nu_1 is also much less pronounced.

The curves also have a minimum, which occurs at $T_b \approx T_M$. The deterioration is particularly severe at higher heat fluxes where T_w is much greater than T_M. These conditions result in a very low thermal conductivity and low density in the laminar sublayer. The average velocity of the fluid is still relatively low since the core of the fluid is at a temperature below T_M and the density is high. This causes very low values of h. As heating continues and T_b continues to increase, the density in the core decreases with a resulting increase in fluid velocity and improvement in the film coefficient. This minimum is
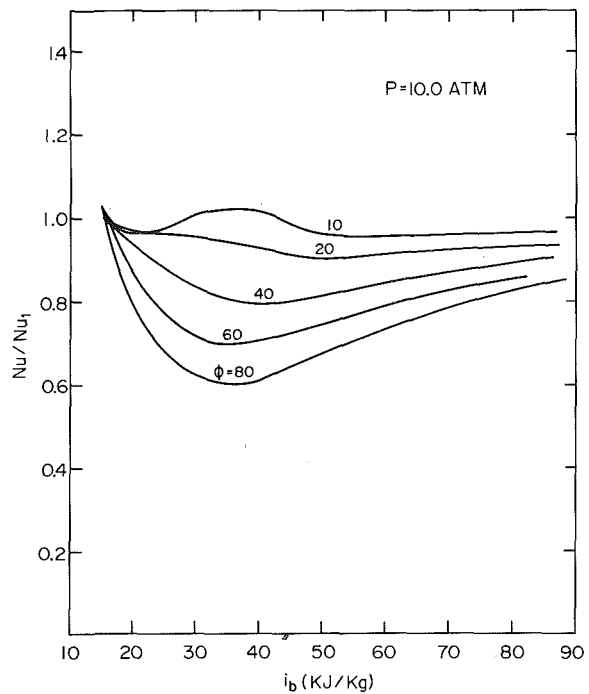

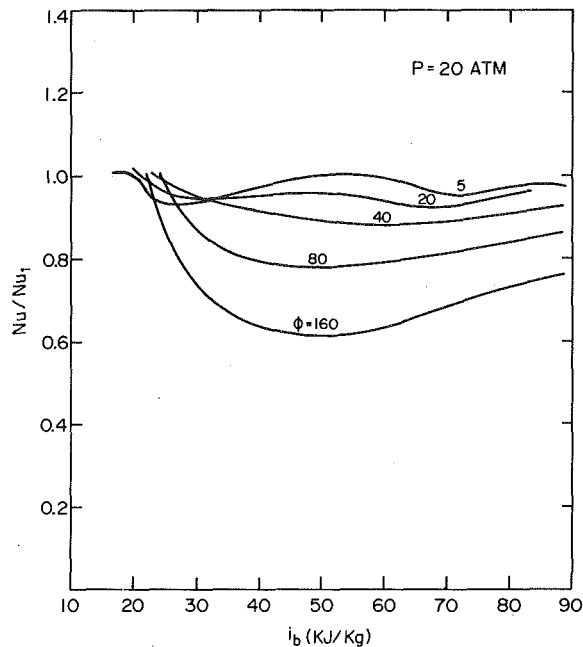Fig. 4   *Correlation of numerical results for helium at 3 atm*

Fig. 5   Correlation of numerical results for helium at 5 atm

Fig. 6   Correlation of numerical results for helium at 10 atm

Fig. 7 Correlation of numerical results for helium at 20 atm

Fig. 8 The effect of inlet enthalpy and heat flux on heat transfer in the thermal entry region

also evident in the experimental results of [15].

Additional results were produced at pressures of 3, 5, 10, and 20 atm. These results are given in Figs. 4–7. The decrease in film coefficient is less severe for pressures farther from critical.

It should be noted that the ordinate used in Figs. 3–7 can also be expressed in the form $\phi/f(T_w - T_b)$ where $f = 0.023 \, K^{0.6} \, C_p{}^{0.6}/\mu^{0.4}$ with properties evaluated at the bulk temperature. The wall temperature can therefore, be determined as a function of i_b for given values of ϕ and P using the graphical results and fluid property data. The range of fluid bulk temperatures is 4–15 K. Although peaks which may occur at temperatures below 4 K for the high heat flux cases are not shown, they are small (i.e., $Nu/Nu_1 < 1.1$) so that the McAdams correlation may be used for those conditions.

Thermal Entrance Effects

It has been shown both experimentally [7] and analytically [10] that entrance effects may continue much farther downstream for near-critical fluids than would occur with a uniform property fluid. Although a detailed study of the thermal entry region was not attempted here, a few cases were run to determine the conditions for which entrance effects would be most significant. The results are shown in Fig. 8. The axial distance for which thermal entrance effects persist is seen to be affected by the heat flux and to a lesser extent by the inlet bulk enthalpy. The entrance effects are more pronounced when the inlet bulk enthalpy is greater than the pseudocritical value and when the heat flux is high. A run was also made for comparison to experimental data points of [4] for a case very similar to curve 1 of Fig. 8. The numerical analysis predicted values of Nu/Nu_∞ of 1.65 and 1.24 at X/D of 20 and 40, respectively. The experimental film coefficients were found to be 1.50 and 1.11 times the predicted fully developed values.

Discussion

The analysis used here is based on the assumption that free convection effects are negligible. As the critical point is approached and the heat flux is increased, buoyancy effects become more important so that there will be conditions for which these results would be inaccurate. Hall [16] states that free convection effects will be negligible when $(Gr/Re^{1.8}) < 0.1$. This parameter reached a value as high as 0.5 for several of the cases run at $P = 2.5$ atm and the results still agreed
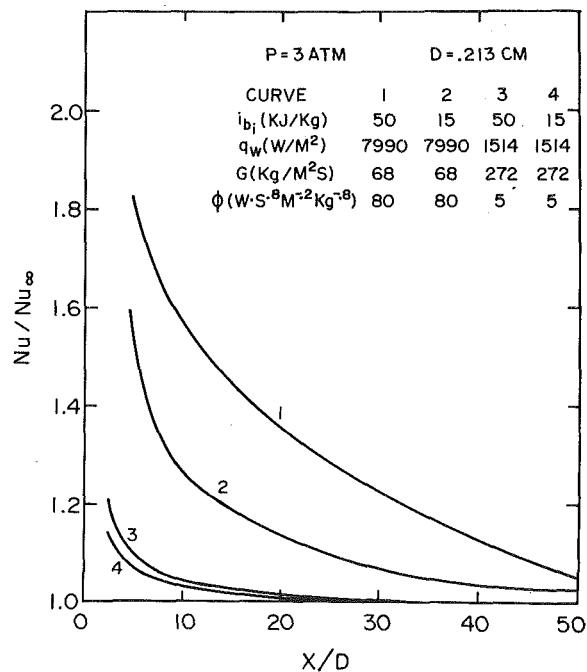
well with experimental data (for flow vertically upward). It appears, therefore, that the Hall condition is conservative.

Perhaps the most questionable aspect of the numerical method is the use of an eddy diffusivity model (equation (3)) which was originally developed for constant property flows. Several other models[2] were also used and results obtained using the various formulations were compared to experimental data for water as well as helium. The Van Driest model consistently gave the best agreement with experimental data.

A proof of the validity of the numerical analysis would require experimental verification over the entire range of conditions considered. The numerical results presented here agree with experimental data in the regions where such data exist within the quoted experimental accuracy. No experimental data are available in the regions of greatest deterioration. This analysis has, however, also been applied to supercritical water for which more extensive experimental data are available and good agreement was found in the deteriorated region.

The results given here should be applied with caution and additional experimental data will be needed to further test these results. It does appear that the use of these results may be preferable to the simpler correlating equations, particularly for conditions of moderate to high heat flux and bulk enthalpy near the pseudocritical value.

Conclusion

Numerical predictions have been obtained for heat transfer to supercritical helium in turbulent flow through a circular tube with a constant wall heat flux. Results are produced for bulk enthalpies from 10 to 90 kJ/kg and pressures of 2.5, 3, 5, 10, and 20 atm. A correlation at a fixed pressure is obtained in the form of a heat flux parameter defined by equation (4). These results are not recommended for cases where $Gr/Re^{1.8} > 0.1$.

Calculations of heat transfer in the thermal entrance region show that the film coefficient remains well above the fully developed value for a larger axial distance than would occur for uniform property fluids

---

[2] See reference [10] for a more complete discussion.

if the inlet bulk enthalpy is slightly greater than the pseudocritical value. This effect becomes more pronounced as the heat flux is increased.

Acknowledgments

References

1 Haid, D. A., "Power Transmission via the Superconducting Cable," *Mechanical Engineering*, Vol. 98, No. 11, 1976, pp. 21–25.

2 Kolm, H. H., Leupold, M. J., and Hay, R. D., "Heat Transfer by the Circulation of Supercritical Helium," *Advances in Cryogenic Engineering*, Vol. 11, 1966, p. 530.

3 Johannes, C., "Studies of Forced Convection Heat Transfer to Helium I," *Advances in Cryogenic Engineering*, Vol. 17, 1972, p. 352.

4 Giarratano, P. J., Arp, V. D., and Smith, R. V., "Forced Convection Heat Transfer to Supercritical Helium," *Cryogenics*, Vol. 11, 1971, p. 385.

5 Brechna, H., "Stanford Linear Accelerator Center," Report No. SLAC-Pub 2741, 1967.

6 Giarratano, P. J., and Jones, M. C., "Deterioration of Heat Transfer to Supercritical Helium at 2.5 Atmospheres," *International Journal of Heat and Mass Transfer*, Vol. 18, 1975, pp. 649–653.

7 Shiralkar, B. S., and Griffith, P., "Deterioration in Heat Transfer to Fluids at Supercritical Pressure and High Heat Fluxes," JOURNAL OF HEAT TRANSFER, TRANS. ASME, Vol. 91, No. 2, 1969, p. 27.

8 Shitsman, M. E., "Impairment of the Heat Transmission at Supercritical Pressures," *Teplofiz, Vsok. Temp.*, Vol. 1, 1957, p. 267.

9 Powell, W. B., "Heat Transfer to Fluids in the Region of the Critical Temperature," *Jet Propulsion*, Vol. 27, 1957, p. 776.

10 Schnurr, N. M., Sastry, V. S., and Shapiro, A. B., "A Numerical Analysis of Heat Transfer to Fluids Near the Thermodynamic Critical Point Including the Thermal Entrance Region," JOURNAL OF HEAT TRANSFER, TRANS. ASME, Vol. 98, No. 4, 1976, pp. 609–615.

11 Patankar, S. V., and Spalding, D. B., *Heat and Mass Transfer in Boundary Layers*, 2nd Ed., Intext Books, London, 1970.

12 McCarty, R. D., "Thermophysical Properties of Helium-4 From 2 to 1500 K With Pressures to 1000 atm," NBS TN 631, Nov. 1972.

13 Van Driest, E. R., "On Turbulent Flow Near a Wall," *Journal of Aeronautical Science*, Vol. 23, 1956, p. 1007- 1011.

14 Goldmann, K., "Heat Transfer to Supercritical Water and Other Fluids With Temperature Dependent Properties," Chemical Engineering Progress Symposium, Ser. II, Vol. 50, 1954, p. 105.

15 Ogata An Sato, *Proceedings of the 4th International Cryogenic Engineering Conference*, Eindhoven, Netherlands, May 24–26, 1972, p. 291.

16 *Advances in Heat Transfer*, Vol. 7, 1971, Academic Press, New York.

17 Hendricks, R. C., et al., "Experimental Heat Transfer Results for Cryogenic Hydrogen Flowing in Tubes at Subcritical and Supercritical Pressures to 800 Pounds Per Square Inch Absolute," NASA TN D-3095, Mar. 1966.

T. E. Mullin

Professor and Chairman,
Mechanical Engineering Department.
Assoc. Mem. ASME

E. R. Gerhard

Associate Dean of Academic Affairs.

Speed Scientific School,
University of Louisville,
Louisville, Ky.

Heat Transfer to Water in Downward Flow in a Uniform Wall Temperature Vertical Tube at Low Graetz Numbers

This paper presents an experimental investigation of heat transfer to water in vertical tube flow. Results from both Heating in Upflow and Heating in Downflow with the Natural Convection Parameter (Gr Pr D/L)$_w$ held constant at a value of 5.5 × 10^5 are compared with the expression developed by Martinelli and Boelter. The Nusselt numbers for Heating in Downflow were slightly higher but, within experimental error, equivalent to those values obtained for Heating in Upflow. A description of the flowfield is presented for one set of conditions for Heating in Downflow.

Introduction

When heat is transferred to a fluid, such as water in a vertical tube, the effects of natural convection on the type of flow pattern obtained is very pronounced at low Graetz numbers. As pointed out by Hanratty, Rosen, and Kabel [7][1]:

Heating in Upflow (or Cooling in Downflow). When water is heated in upflow, an overall flow pattern is observed. Three distinct flow regions were noted:

1 In the initial part of the heat transfer section the entering parabolic flow profile is distorted in such a way that the fluid in the center of the tube is slowed down and the fluid near the wall is accelerated.

2 Eventually the fluid near the tube center is decelerated to such an extent that the flow is reversed. This results in a region of inverted flow in which there is a very slow movement of fluid downward in the center part of the tube and a rapidly moving upward flow in the annulus surrounding it.

3 Far enough downstream this inverted flow becomes unstable and a region of turbulent flow is obtained.

Heating in Downflow (or Cooling in Upflow). Heating a fluid in downflow gives rise to an unstable flowfield. The fluid near the wall is retarded, and the velocity gradient at the wall may be zero.

A Reynolds number of 50 and a temperature difference of 10°F between the heat transfer medium and the incoming water produced

---

[1] Numbers in brackets designate References at end of paper.

Contributed by the Heat Transfer Division for publication in the JOURNAL OF HEAT TRANSFER. Manuscript received by the Heat Transfer Division March 1, 1976.
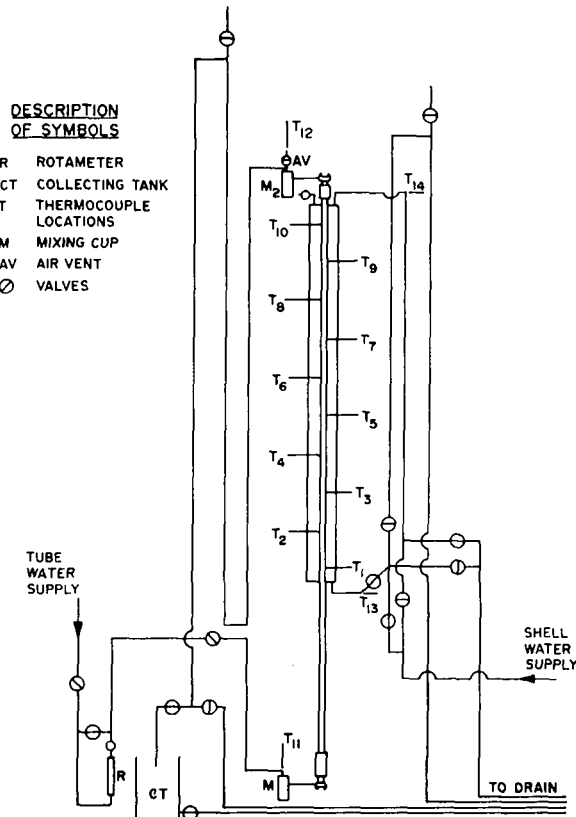
complete turbulence throughout the flowfield.

Further description of the flowfield including the effects of natural convection on the transition to turbulence in a vertical tube is presented by Scheele, Rosen, and Hanratty [8]. Martinelli and Boelter [2] and Pigford [4] have presented correlations which predict the Nusselt number for which natural convection effects are important.

The purpose of this paper is as follows:

1 To present the results of an experimental investigation on Heating in Upflow and Heating in Downflow with the Natural Convection Parameter (Gr Pr D/L)$_w$ held at a constant value;

2 To compare the experimental results with the expression developed by Martinelli and Boelter; and

3 To present a description of the flowfield for one set of conditions for Heating in Downflow.

Experimental Apparatus, Instrumentation and Experimental Error

Experiments were conducted for the heating of water both in upflow and in downflow through a vertical tube. The experimental arrangement for heating in upflow is shown schematically in Fig. 1. The experimental arrangement for heating in downflow was essentially the same except that the calming section was placed above the heat transfer section.

Cold water flowed through the inner brass tube of 27.051 mm (1.065 in.) ID. Surrounding the inner tube was a shell through which hot water passed. The heat exchange between the water in the shell and that in the tube occurred over a heat transfer section of length 3.2512 m (10 ft, 8 in.). Based on the inside diameter of the tube, the length-to-diameter ratio for the heat transfer section was 120.19.

A calming section was provided to dampen out disturbances in the

Copyright © 1977 by ASME
Transactions of the ASME

DESCRIPTION OF SYMBOLS

R   ROTAMETER
CT   COLLECTING TANK
T   THERMOCOUPLE LOCATIONS
M   MIXING CUP
AV   AIR VENT
⊘   VALVES

Fig. 1 Schematic representation of apparatus for upflow

The average value of the mass flow rates for a given run was computed and recorded. The maximum error in the mass flow rate as well as the Graetz number is estimated to be ±5 percent.

Temperatures were measured using 24-gage copper-constantan thermocouples, a selector switch, a Honeywell Twelve-point recorder and a Leeds and Northrup potentiometer. The recorder was used solely to obtain approximate temperatures. All final readings were taken using the potentiometer.

Thermocouples 1–10 had their junctions embedded in the tube wall and distributed over the heating section as shown in Figs. 1 and 2, respectively. Thermocouple 11 and 12 had junctions in the mixing cups and measured the mean fluid bulk temperature at the inlet and exit end of the tube. Thermocouples 13 and 14 had junctions at the center line of the piping and measured the temperature of water at the inlet and exit of the shell.

The cumulative error of the potentiometer, ice bath, temperature, conduction losses, contact resistances, and thermocouple calibration was estimated for the wall temperature measurements. It was found to be ±1.2°C. However, when water of the same temperature simultaneously flowed through both the shell and tube side of the experimental apparatus, it was found that the difference in readings was less than 0.2°C.

The error in the Natural Convection Parameter was determined as follows:

	$(Gr\,Pr\,D/L)_w$ Upflow	$(Gr\,Pr\,D/L)_w$ Downflow
Lowest valve	4.957×10^5	5.33×10^5
Highest valve	5.648×10^5	5.638×10^5
Average value	5.3×10^5 (for 15 runs)	5.5×10^5 (for 22 runs)
Percent variation	+2.1%; −10.3%	+2.5%; −3.1%

The value of the Nusselt number is very sensitive to experimental error. The absolute error in the value of the Nusselt number was calculated to be as high as ±23 percent; however, the probable error as calculated by the root-sum square formula was no larger than ±10 percent.

flow and to establish a parabolic velocity distribution upstream of the heat transfer section. The calming section, used only on the inlet end of the heat transfer section, was approximately 1.8034 m (5 ft, 11 in.) in length, giving an L/D ratio of 66.7. Insulation over the calming section minimized heat exchange with the surroundings, and ensured an isothermal flow ahead of the heat transfer section.

Although a calibrated rotameter was part of the experimental apparatus, all mass flow rates were determined by measuring the volume per unit of time collected in the tank "CT" and multiplying it by the density of water at that temperature. The mass flow rate was measured many times for a given run and if the variation in measurement was more than ±5 percent the results from that run were discarded.

Experimental Procedure

Fig. 1 schematically illustrates the experimental setup and valve positions for the experiments carried out with water for the constant wall temperature case in upflow. For this case, it was found that a constant wall temperature could be conveniently obtained with upflow of hot water through the shell.

The upflow experiments were conducted at a value of the product $(Gr\,Pr\,D/L)_w$ approximately equal to 5.5×10^5. From the mean fluid bulk temperature of the tube water at the inlet section (T_{11}), the value
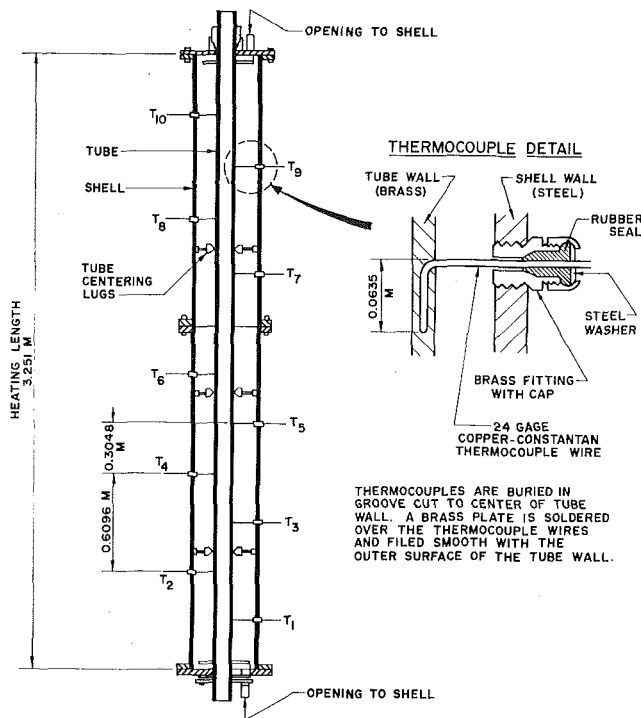

═══════Nomenclature═══════

C_p = constant pressure specific heat of the fluid

D = tube inside diameter

F_1, F_2 = functions defined by Martinelli and Boelter

g = acceleration due to gravity

Gr = Grashof number based on inside tube diameter

$$= \frac{\rho_w{}^2 g \beta D^3 (T_w - T_{in})}{\mu_w{}^2}$$

Gz = Graetz number = $WC_p/kL = (D/4L)$ RePr

h = heat transfer coefficient

k = thermal conductivity of the fluid

L = heated tube length

Nu = Nusselt number = hD/k

Pr = Prandtl number = $C_p\mu/k$

Re = Reynolds number based on the tube

inside diameter = $4W/\pi D\mu = DG/\mu$

T = temperature

T_{11} = mixed fluid temperature at the inlet section in upflow or exit mixed fluid temperature in downflow

T_{12} = mixed fluid temperature at the exit section in upflow or inlet mixed fluid temperature in downflow

T_w = average inner wall temperature

T_1–T_{10} = tube wall temperatures (see Figs. 1, 2)

T_b = arithmetic mean fluid bulk temperature

ΔT_{am} = arithmetic mean temperature difference between the wall and the fluid

$$= \frac{(T_w - T_1) + (T_w - T_2)}{2}$$

U = average axial fluid velocity

W = mass flow rate of fluid

β = volume coefficient of thermal expansion of the fluid

μ = dynamic viscosity of the fluid

ρ = density of the fluid

Subscripts

am = corresponding to quantity based on the arithmetic mean temperature difference between the wall and the fluid

b = corresponding to quantity at the arithmetic mean fluid bulk temperature

w = corresponding to quantity at the average wall temperature

---

Fig. 2 Basic structure

Fig. 3 Graetz number $Gz_b = \dfrac{WC_{pb}}{K_b L}$

that the tube wall temperature would have to be for a given value of $(Gr\ Pr\ D/L)_w$ was calculated from the equation,

$$\left[\frac{Gr\ Pr\ D}{L}\right]_w = \left[\frac{\rho_w{}^2 g \beta D^3 (T_w - T_{11})}{\mu_w{}^2}\right]\left[\frac{C_p\mu}{k}\right]_w\left[\frac{D}{L}\right] \quad (1)$$

Equations for the properties of water as functions of temperature [3, 12] were used to calculate T_w by trial and error.

The final readings of the thermocouples were taken when a steady state was assured after the temperatures remained constant for at least 20 min. The potentiometer was used to measure the final thermocouple readings. The mass flow rate was determined by finding the volume rate of water collected in the tank and multiplying it by the density of water at the temperature of the collected water. The main purpose of these experimental runs was to check the apparatus and verify the experimental procedure. This was achieved by comparing the experimental data obtained with the Martinelli-Boelter equation (2) (see Fig. 3).

For experiments conducted with the tube water in down-flow, the calming section was placed above the heat transfer section. Additional thermocouples were installed in the calming section with the aim of finding whether or not abnormal temperature changes were present. In this case, it was found that an almost uniform wall temperature could be obtained if the shell water was also run in downflow. With the exception of the fact that the flow was in the downward direction, the experimental procedure for downflow through the tube was almost the same as that used in the upflow experiments.

The desired tube wall temperature was determined from equation (1) with the exception that T_{11} is replaced with T_{12} the mean fluid bulk temperature at the inlet for downflow. All fluid properties were evaluated at the average tube wall temperature T_w.

The values of the product $(Gr\ Pr\ D/L)_w$ used in the downflow experiments were 5.5×10^5 and 3.1×10^5. Also isolated experimental points at 1.33×10^5 and 4.024×10^5 were obtained. Using these values in equation (1) and the properties of water as a function of temperature, the desired constant tube wall temperature, T_w, was calculated by a trial and error process. The time required to achieve stable conditions varied from run to run. In general, the experiments for heating in downflow required greater stabilization time. The final observations
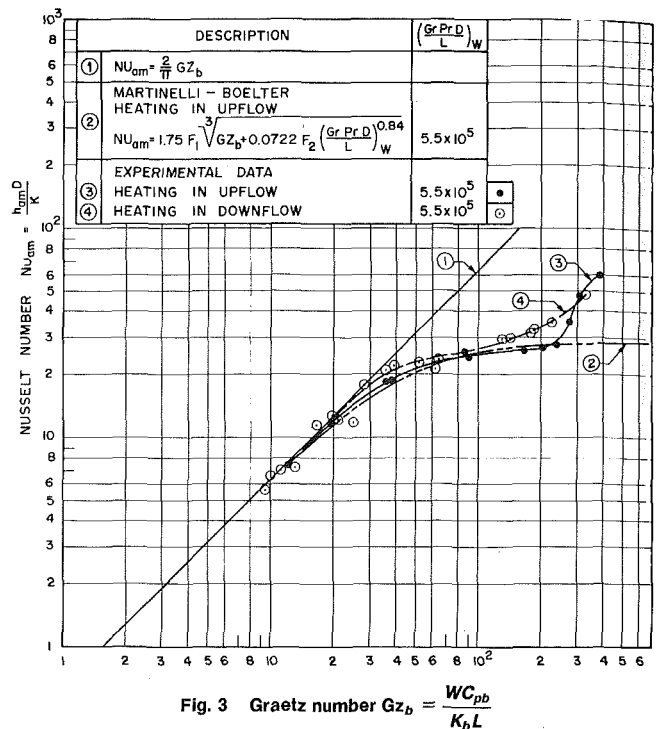
were made about 20 min after steady state was obtained. As in the heating in upflow experiments, the mass flow rates were measured by the water collection method and the potentiometer was used to measure the final thermocouple readings.

The data taken from the apparatus and its treatment may be found in references [14, 15].

Observations and Conclusions

1 The values of the Nusselt number (Nu_{am}), the Graetz number (Gz_b) and the Natural Convection Parameter ($Gr\ Pr\ D/L)_w$ computed from the experimental data for Heating in Upflow are compared with the corresponding values obtained from the Martinelli-Boelter equation and are shown in Fig. 3 (curves 2 and 3). The primary purpose of this set of experimental runs was to check the operation of the experimental apparatus. As can be seen from Fig. 3, the values of the Nu_{am} and Gz_b numbers computed from experimental data for a value of $(Gr\ Pr\ D/L)_w\ 10^{-5} = 5.5$, are in good agreement with the corresponding values predicted by the Martinelli-Boelter equation. At a value of Graetz number = 250 the Nusselt numbers computed from experimental data leave the Martinelli-Boelter curve and merge with the Sieder and Tate correlation for turbulent forced convection in tubes. It is therefore concluded that the experimental apparatus is sound.

2 The values of the Nusselt number (Nu_{am}), the Graetz number (Gz_b) and the Natural Convection Parameter ($Gr\ Pr\ D/L)_w$ which were computed from experimental data for Heating in Downflow are compared with the corresponding values obtained from the Martinelli-Boelter equation for Heating in Upflow are also shown in Fig. 3 (curves 2 and 4). The value of the Natural Convection Parameter is $(Gr\ Pr\ D/L)_w 10^{-5} = 5.5$. As can be observed from Fig. 3, the values of the Nusselt number for Heating in Downflow are, within experimental error, slightly higher than or about the same as the values for Heating in Upflow. An increase in Nusselt number for Heating in Downflow over that for Heating in Upflow have been known to occur. An example of this is the experiments of Kirschbaum [9].

An insight as to why the Nusselt numbers for Heating in Downflow are higher than might be expected may be obtained from the visual observation of Scheele and Hanratty [10] and of Mullin in conjunction with Perry [13]. The visual results reported by Perry for a Graetz
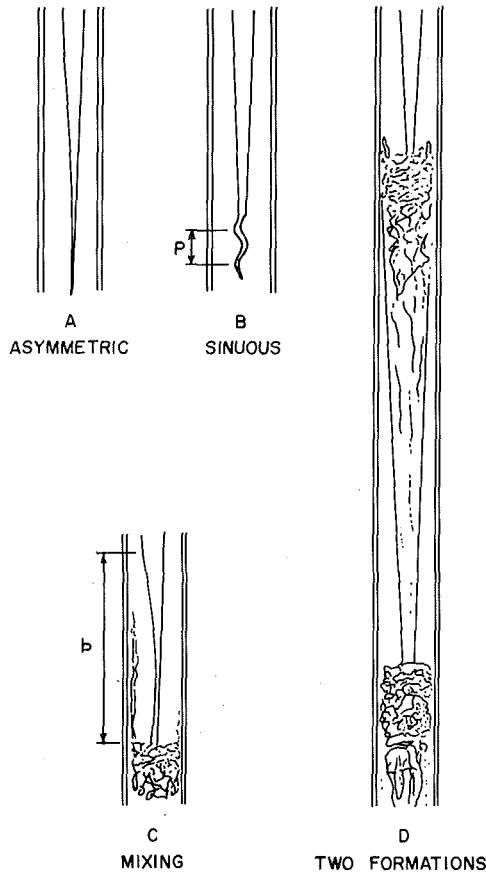
Fig. 4 Visual results

Fig. 5 Experimental results and comparison with other equations

number = 25.22 were as follows:

2(a)   The stream of dye flowing down the center line of the tube indicated a shift from center flow of the downward moving velocity profile (see Fig. 4-(A)).

2(b)   Below this shift a sinuous movement of the tip of the velocity profile occurs, which increases until complete mixing takes place below this motion (see Figs. 4-B and 4-C).

2(c)   This mixing action has the tendency to level the temperature profile which exists across the tube and as a result of this leveling the process repeats itself (see Fig. 4-D).

Time photographs of the action of the flow field as described in 2(a) and 2(b) above are shown in reference [13]. The time between each frame is $\frac{1}{3}$ s apart.

It is to be remembered that the Martinelli-Boelter equation, i.e.,

$$\mathrm{Nu}_{am} = 1.75 F_1 \sqrt[3]{\mathrm{Gz}_b + 0.0772 F_2 (\mathrm{Gr}\,\mathrm{Pr}\,D/L)_w{}^{0.84}}$$

was only intended for the determination of the Nusselt number for *Heating in Upflow* or *Cooling in Downflow*. In view of the foregoing discussion, it would appear that the practice of placing a negative sign in front of the Natural Convection Parameter, i.e.,

$$\mathrm{Nu}_{am} = 1.75 F_1 \sqrt[3]{\mathrm{Gz}_b - 0.0772 F_2 (\mathrm{Gr}\,\mathrm{Pr}\,D/L)_w{}^{0.84}}$$

in order to determine the Nusselt number for Heating in Downflow could yield values that are too low.

3   An examination of Fig. 5 shows for a given Graetz number that as the Natural Convection Parameter increases, the Nusselt number decreases. This is to be expected in view of the opposing effects of forced and natural convection. However, although the natural convection force for Heating in Downflow should reduce the heat transfer rate, it at the same time creates a flowfield which retards the decrease.
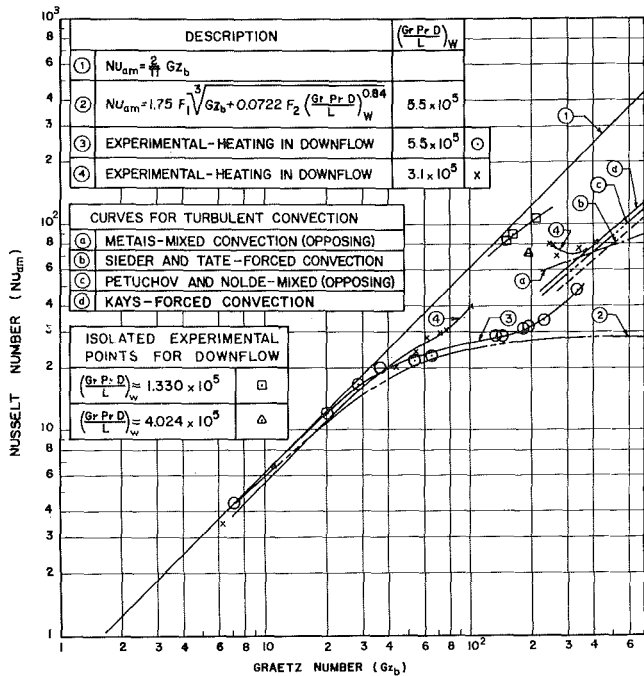
Acknowledgment

References

1   Sieder, E. N., and Tate, C. E., "Heat Transfer and Pressure Drop of Liquids in Tubes," *Ind. and Eng. Chem.,* Vol. 23, 1936, p. 1429.

2   Mantinelli, R. C., and Boelter, L. M. K., "The Analytical Prediction of Superposed Free and Forced Viscous Convection in a Vertical Pipe," *University of California Publications in Engineering,* Vol. 5, 1942, p. 23.

3   Zemansky, M. W., *Heat and Thermodynamics,* Fourth ed., McGraw-Hill, New York, 1957, p. 257.

4   Pigford, R. L., "Non-Isothermal Flow and Heat Transfer Inside a Vertical Tube," *Chem. Eng. Prog. Symp. Series,* Vol. 51, No. 17, 1952, pp. 79–92.

5   McAdams, W. H., *Heat Transmission,* Third ed., McGraw-Hill, New York, 1954.

6   Knudsen, J. G., and Katz, D. L., *Fluid Dynamics and Heat Transfer,* McGraw-Hill, New York, 1958.

7   Hanratty, T. J., Rosen, E. M., and Kabel, R. L., "Effect of Heat Transfer on Flow Field at Low Reynolds Numbers in Vertical Tubes," *Ind. and Eng. Chem.,* Vol. 50, No. 5, 1958, pp. 815–820.

8   Scheele, G. F., Rosen, E. M., and Hanratty, T. J., "Effect of Natural Convection on Transition to Turbulence in Vertical Pipes," *The Canadian Journal of Chemical Engineering,* Vol. 38, 1960, pp. 67–73.

9   Grober, H., Erk, S., and Grigull, U., *Fundamentals of Heat Transfer,* Third ed., McGraw-Hill, New York, 1961, p. 238.

10   Scheele, G. F., and Hanratty, T. J., "Effect of Natural Convection on Stability of Flow in a Vertical Pipe," *Journal of Fluid Mechanics,* Vol. 14, Part 2, 1962, pp. 244–258.

11   Kays, W. M., *Convective Heat and Mass Transfer,* McGraw-Hill, New York, 1966.

12   Holman, J. P., *Heat Transfer,* Second ed., McGraw-Hill, New York, 1968, p. 383.

13   Perry, P. F., "Visual Observation of Gravitational Force Disruption on Forced Downflow at Low Graetz Numbers," Master of Engineering Thesis in Mechanical Engineering, University of Louisville, Louisville, Ky., 1970.

14   Gonsalves, G. C., "Combined Force and Free Convection During Upward and Downward Flow of Water Through a Uniform Wall Temperature Vertical Tube," MS thesis in Mechanical Engineering, University of Louisville, Louisville, Ky., 1971.

15   McCoy, L.D., "The Determination of Heat Transfer Coefficient to Downflow in A Vertical Tube at Low Flow," Master of Engineering Thesis in Mechanical Engineering, University of Louisville, Louisville, Ky., 1972.

H. A. Simon
M. H. Chang
J. C. F. Chow

University of Illinois at Chicago Circle,
Department of Energy Engineering,
Chicago, Ill.

Heat Transfer in Curved Tubes With Pulsatile, Fully Developed, Laminar Flows

A perturbation analysis is carried out to include the second order solution for fluid flow and heat transfer for a wide range of excitation parameters and Prandtl numbers. The results show an increase in the time averaged Nusselt number in curved pipes with pulsatile flow over that achieved in straight pipes with pulsatile flow. The increases are most evident at high Prandtl numbers, high excitation relative amplitudes, and low excitation frequencies.

Introduction

Pulsatile flows in curved tubes are of common occurrence both in nature and in engineering systems. A detailed knowledge of the flow and heat or mass transfer phenomena in such cases could lead to improved performance in the design of engineering equipment. In some instances it may even be beneficial to induce pulsations in a flow system if enhanced performance will ensue.

It is only in recent years that analytical work has been initiated on unsteady pulsatile flow in curved tubes. In 1970 Lyne [1][1] considered the case of small curvature and high pressure gradient oscillation frequency. He distinguishes two regimes in the flow, an inviscid core and a boundary layer, and shows, with experimental verification, the occurrence of an additional pair of secondary circulations in the inviscid core. Zalosh and Nelson [2] in 1973, used a quasi-steady approximation for low frequency pure oscillatory flows showing it to be similar to low Dean number steady flows. Their results for high frequencies, based on a boundary layer approximation, agree with Lyne's results. Chow and Li [3] obtained a solution valid for the entire range of frequencies. They identify three distinct phases with increasing frequency: a flow dominated by viscosity with one pair of circulations, a transitional flow with either one or two pairs of circulations and a boundary layer type of flow with two pairs of circulations. The analytical work of Chandran, et al. [4] in 1974 for oscillatory flow in elastic walled tubes of small curvature shows a shift of the maximum axial velocity toward the center of curvature, opposite to that for steady flow, their results agreeing with Lyne. They also show the occurrence of two pairs of transverse circulations. Bertelson [5] in 1975 obtained experimental results which agree with the work of Lyne, and

Zalosh and Nelson. Smith [6] considers pulsatile flows in tubes of arbitrary cross section and provides a basis for deriving the attributes of several flow regimes ranging between the limiting cases of steady flow in curved tubes and pure oscillating flow in straight tubes.

An important result revealed in the references given and in the present work concerns the growth and decline of secondary circulations, often accompanied by secondary flow reversals, during a pulsation cycle. It is not unreasonable to expect that the enhanced transverse mixing that occurs in pulsatile flow would improve the heat transfer performance. The extent of this improved performance is studied in this paper. An analytical approach similar to that of Zalosh and Nelson, but including through-flow, is used to examine the flow and heat transfer characteristics of flow in tubes of relatively small curvature subjected to a wide range of applied frequencies and amplitudes. The Prandtl number is also varied over a wide range.

Problem Formulation

The equations of motion are set up in terms of the toroidal coordinates r', ϕ, and θ as shown in Fig. 1. The corresponding velocity components are U', V', and W'.

The following assumptions are made:

The fluid behavior is incompressible, Newtonian with constant properties. Both flow and temperature fields are fully developed. The curvature ratio a/R is small. Free convection, viscous dissipation, and axial conduction effects are negligible.

For the heat transfer problem it is assumed that the time averaged wall heat flux, taken over a period of oscillation, is constant. The wall temperature at one cross section and the axial temperature gradient are both constant.

The temperature distribution is expressed in the following form

$$T(R\theta, r', \phi, t') = T_w(R\theta) + N(r', \phi, t') \qquad (1)$$

The governing equations are simplified using the fact that a/R is small. Furthermore, they are written in dimensionless form using the following relations:
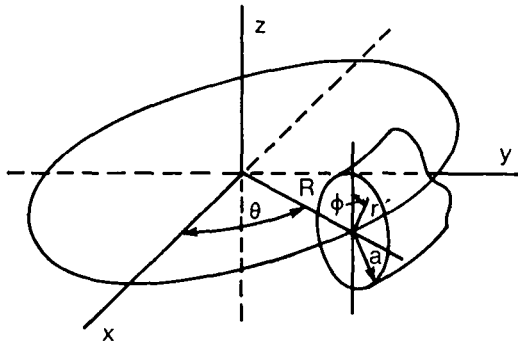

Fig. 1 The toroidal geometry, showing the orthogonal variables r', ϕ, and θ

$$t = t'\omega, \quad r = r'/a, \quad W = W'/\overline{W}, \quad \psi = \psi'/\nu$$

$$n = \frac{N}{aS}, \quad C = Ga^2/(\mu\overline{W}), \quad D = Ma^2/(\mu\overline{W}) \quad \alpha = a\sqrt{\omega/\nu},$$

$$K = \text{Re}^2(a/R), \quad \text{Re} = \frac{\overline{W}a}{\nu}, \quad S = \frac{\partial T'}{\partial(R\theta)}$$

The governing equations become:

$$\alpha^2 \frac{\partial}{\partial t} (\nabla^2 \psi) + 2KW \left(\cos\phi \frac{\partial W}{\partial r} - \frac{1}{r} \sin\phi \frac{\partial W}{\partial\phi} \right)$$
$$- \frac{1}{r} \left(\frac{\partial\psi}{\partial r} \frac{\partial}{\partial\phi} - \frac{\partial\psi}{\partial\phi} \frac{\partial}{\partial r} \right) \nabla^2\psi = \nabla^4\psi \quad (2)$$

$$\alpha^2 \frac{\partial W}{\partial t} + \frac{1}{r} \left(\frac{\partial\psi}{\partial\phi} \frac{\partial W}{\partial r} - \frac{\partial\psi}{\partial r} \frac{\partial W}{\partial\phi} \right) = C + D\cos t + \nabla^2 W \quad (3)$$

$$\text{Pr} \left(\alpha^2 \frac{\partial n}{\partial t} + \frac{1}{r} \frac{\partial\psi}{\partial\phi} \frac{\partial n}{\partial r} - \frac{1}{r} \frac{\partial\psi}{\partial r} \frac{\partial n}{\partial\phi} + W\text{Re} \right) = \nabla^2 n \quad (4)$$

The parameter α^2 may be interpreted as an oscillatory Reynolds number, or the ratio of a characteristic diffusion time a^2/ν, to a characteristic oscillation time $1/\omega$.

The boundary conditions on ψ, W, and n are

$$\frac{\partial\psi}{\partial r} = \frac{\partial\psi}{\partial\phi} = W = n = 0 \quad \text{at } r = 1$$

Also

$$\nabla^2 = \frac{\partial^2}{\partial r^2} + \frac{1}{r} \frac{\partial}{\partial r} + \frac{1}{r^2} \frac{\partial^2}{\partial\phi^2}, \quad \nabla^4 = \nabla^2(\nabla^2)$$

K, called the modified Dean number, contains a/R which is assumed to be small in this study. The secondary flow stream function ψ, the axial velocity W, and the excess temperature n can be written as power series in terms of K:

$$\psi = K\psi_1 + K^2\psi_2 + \ldots$$

$$W = W_0 + KW_1 + K^2W_2 + \ldots$$

$$n = n_0 + Kn_1 + K^2n_2 + \ldots$$

These series expansions are substituted into the governing equations. Equating equal powers of K provides sets of linear partial differential equations for zeroth, first, and second orders. Lower order solutions must be obtained first and serve as input into the higher order equations.

Zeroth Order:

$$\alpha^2 \frac{\partial W_0}{\partial t} - \nabla^2 W_0 = C + D\cos t$$

$$\text{Pr} \left(\alpha^2 \frac{\partial n_0}{\partial t} + \text{Re}W_0 \right) = \nabla^2 n_0$$

$$W_0 = n_0 = 0 \quad \text{at } r = 1$$

First Order:

$$\alpha^2 \frac{\partial}{\partial t} (\nabla^2\psi_1) - \alpha^4\psi_1 = -\frac{2W_0}{r} \left(r\cos\phi \frac{\partial W_0}{\partial r} - \sin\phi \frac{\partial W_0}{\partial\phi} \right)$$

$$\alpha^2 \frac{\partial W_1}{\partial t} - \nabla^2 W_1 = -\frac{1}{r} \frac{\partial(\psi_1, W_0)}{\partial(\phi, r)}$$

$$\text{Pr} \left(\alpha^2 \frac{\partial n_1}{\partial t} + \frac{1}{r} \frac{\partial(\psi_1, n_0)}{\partial(\phi, r)} + \text{Re}W_1 \right) = \nabla^2 n_1$$

$$\frac{\partial\psi_1}{\partial r} = \frac{1}{r} \frac{\partial\psi_1}{\partial\phi} = W_1 = n_1 = 0 \quad \text{at } r = 1$$

Second Order:

$$\alpha^2 \frac{\partial}{\partial t} (\nabla^2\psi_2) - \nabla^4\psi_2 = -\frac{2W_0}{r} \left(r\cos\phi \frac{\partial W_1}{\partial r} - \sin\phi \frac{\partial W_1}{\partial\phi} \right)$$

$$- \frac{2W_1}{r} \left(r\cos\phi \frac{\partial W_0}{\partial r} - \sin\phi \frac{\partial W_0}{\partial\phi} \right) + \frac{1}{r} \left(\frac{\partial\psi_1}{\partial r} \frac{\partial}{\partial\phi} - \frac{\partial\psi_1}{\partial\phi} \frac{\partial}{\partial r} \right) \nabla^2\psi_1$$

$$\alpha^2 \frac{\partial W_2}{\partial t} - \nabla^2 W_2 = -\frac{1}{r} \left[\frac{\partial(\psi_1, W_1)}{\partial(\phi, r)} + \frac{\partial(\psi_2, W_0)}{\partial(\phi, r)} \right]$$

$$\text{Pr} \left(\alpha^2 \frac{\partial n_2}{\partial t} + \frac{1}{r} \frac{\partial(\psi_1, n_1)}{\partial(\phi, r)} + \frac{1}{r} \frac{\partial(\psi_2, n_0)}{\partial(\phi, r)} + \text{Re}W_2 \right) = \nabla^2 n_2$$

Nomenclature

a = tube radius
C = nondimensional steady pressure gradient
D = nondimensional amplitude of oscillating pressure gradient
G = steady pressure gradient
K = modified Dean number
M = amplitude of oscillating pressure gradient
n = nondimensional excess temperature
$\overline{n}_b$ = time averaged excess bulk temperature
N = excess temperature
Nu = Nusselt number
$\overline{\text{Nu}}$ = time averaged Nusselt number
P = power

$\overline{P}$ = time averaged power
r' = radial coordinate
r = nondimensional radial coordinate
R = radius of tube curvature
Re = Reynolds number
S = axial temperature gradient
t' = time
t = nondimensional time
T = temperature
U' = radial velocity
V' = tangential velocity
W' = axial velocity
W = nondimensional axial velocity
$\overline{W}$ = average axial velocity
α = oscillatory Reynolds number
ϕ = angular coordinate in plane of tube curvature

ν = kinematic viscosity
μ = dynamic viscosity
ϕ = angular coordinate in tube cross section
ψ' = secondary flow stream function
ψ = dimensionless secondary flow stream function
ω = frequency

Subscripts

b = bulk value
w = wall value
st = steady state
0 = zeroth order
1 = first order
2 = second order

$$\frac{\partial \psi_2}{\partial r} = \frac{1}{r} \frac{\partial \psi_2}{\partial \phi} = W_2 = n_2 = 0 \quad \text{at } r = 1$$

and

$$\frac{\partial(\psi_1, W_0)}{\partial(\phi, r)} = \frac{\partial \psi_1}{\partial \phi} \frac{\partial W_0}{\partial r} - \frac{\partial \psi_1}{\partial r} \frac{\partial W_0}{\partial \phi} \quad \text{etc.}$$

The given sets of linear partial differential equations are further reduced to ordinary differential equations by use of separation of variables and superposition techniques. The resulting equations contain the harmonic and biharmonic operators indicating that the finite Hankel transformation can be usefully applied. Finally the results for the secondary stream function, the axial velocity, and the excess temperature are obtained in forms incorporating lengthy integral expressions in terms of Bessel functions in various algebraic combinations. The integral expressions are evaluated numerically. The series used are all rapidly convergent. Still, 15 or 20-term series are used in all computations to limit truncation errors [7].

In pulsatile flows the Nusselt number may be defined in several different ways. As both the heat flux and the bulk temperature vary in a complicated manner with time, it is necessary to take time averages in some way.

The local Nusselt number at some particular time is defined as:

$$\text{Nu} = \frac{2}{n_b} \left(\frac{\partial n}{\partial r} \right)_{r=1}$$

This could be time averaged in the the following way:

$$\overline{\text{Nu}} = -\frac{1}{\pi} \int_0^{2\pi} \left(\frac{\partial n}{\partial r} \right)_{r=1} \frac{1}{n_b} dt \tag{5}$$

In pulsatile flows n_b can become very small (even zero) as compared with $\partial n / \partial r$. As a result large contributions can arise to the value of $\overline{\text{Nu}}$, in equation (5), from those times when the heat transfer may be small. This can give highly misleading results.

A more suitable definition is given by:

$$\overline{\text{Nu}} = -\frac{2}{\bar{n}_b} \left(\frac{\overline{\partial n}}{\partial r} \right)_{r=1} \tag{6}$$

with

$$\bar{n}_b = \frac{\int_0^{2\pi} \int_0^{2\pi} \int_0^1 Wr\, n\, dr\, d\phi\, dt}{\int_0^{2\pi} \int_0^{2\pi} \int_0^1 Wr\, dr\, d\phi\, dt} \tag{7}$$

The role of the Nusselt number as defined in equation (6) is quite different from that encountered in steady flow cases. Here a knowledge of $\overline{\text{Nu}}$ is not sufficient to enable absolute performance in terms of temperature or heat flux to be assessed, as both these latter quantities and the velocity are variable in time. The value of $\overline{\text{Nu}}$, as defined in equation (6), lies rather in affording a guide for the comparison of pulsatile flow cases.

Results and Discussion

Solutions have been calculated up to and including the second order.

Zeroth Order Solution. The zeroth order solution corresponds to the case of pulsatile flow in a straight pipe. It is of importance here as it is used as a basis for comparison with the second order solution, revealing explicitly the effect of curvature in such flows. The discussion which follows gives physical explanations for the phase shifts which occur and also shows why the analysis gives a reduced Nusselt number in straight pipe flows.

The straight pipe velocity distributions correspond with those given by Uchida [8]. Again the maximum velocity and the forcing functions become 90 deg out of phase as α increases above a value of about 5. This shift is as expected and is predicted by the simple analysis of a rigid body undergoing forced oscillations against viscous damping. Of course, in the present case the body is not rigid and higher frequencies are required as r moves from the center line toward the

wall, before inertial forces predominate over viscous forces to the extent of causing a 90 deg phase shift between velocity and forcing function.

Fig. 2 shows the phasing of the maximum excess temperature at $r = 0$ for various Prandtl numbers. For very large Prandtl numbers the temperature distribution in the fluid is almost impervious to the different wall temperatures encountered during an oscillation. The maximum excess temperature occurs 90° after the maximum center-line velocity. This corresponds to the time of maximum pulsation displacement at which the maximum temperature excursion occurs. However, when the Prandtl number is very small the fluid very rapidly adjusts to each new wall temperature encountered. Thus maximum excess temperatures can only be maintained, at low values of α, where the velocity is a maximum.

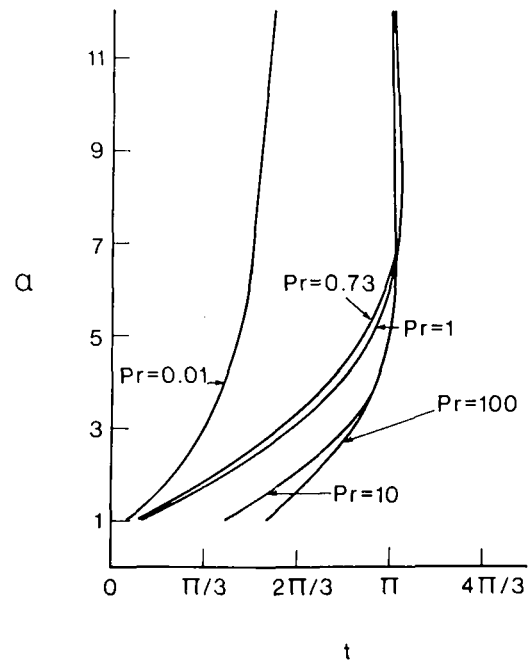Fig. 3 shows how the Nusselt number ratio varies with D/C and α

Fig. 2 The time at which maximum excess temperature occurs at the center line as a function of α for various values of Pr
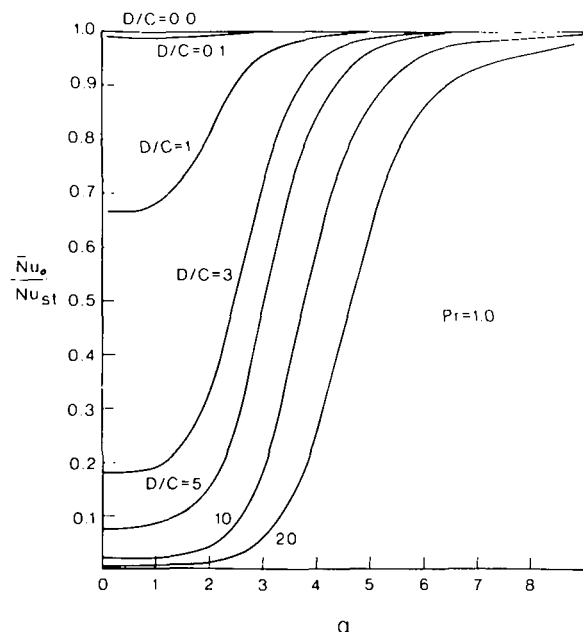

Fig. 3 Nusselt number ratio based on equation (6) as a function of α for various D/C and Pr = 1.0

for $Pr = 1.0$. This ratio approaches zero for small α and large D/C, a consequence of the method of time averaging. As described earlier, when α decreases, for any Prandtl number, a point is reached when the maximum axial velocity and the maximum excess temperature are in phase. Thus the product of W and n in equation (7) varies as the square of the forcing function amplitude. For large D/C, $\bar{n}_b$ becomes very large reducing the Nusselt number ratio to zero. The limiting values as α approaches zero are easily calculated by a quasi-steady analysis. Here the steady state velocity distribution is used but the time varying forcing function for the pressure gradient is inserted in solving the energy equation giving the result:

$$\overline{Nu}_0 = \frac{48}{11}\left(\frac{1}{1+\frac{1}{2}\left(\frac{D}{C}\right)^2}\right) \qquad (8)$$

The fact that the Nusselt number ratio does not return to the value one as α approaches zero is understandable since both α and D/C must approach zero together for the steady state to be achieved.

Fig. 4 illustrates how the local, instantaneous Nusselt number Nu_0 varies as a function of time for different values of α. Nu_0 simply oscillates about the steady value: $Nu_{ST} = 4.364$. Clearly the results portrayed in Fig. 3 arise because of the time averaging procedure and should not be used as a guide to heat transfer performance.

Barnett and Vachon [9], in an equivalent oscillating pipe case, use a similar definition of the time averaged Nusselt number, and show a slight increase in $\overline{Nu}_0$ at low α. The present authors are unable to account for this.

Both Figs. 3 and 4 show that as α becomes large the flow becomes "frozen," or in other words, the frequency becomes too high for the flow to respond significantly.

Second Order Solution The second order solution includes terms evaluated up to and including the second order. The zeroth order solution corresponds to pulsatile flows in straight pipes. The first order solution includes the zeroth order solution and shows the effects of curvature, but the secondary flows produced are symmetrical about the pipe diameter in the z direction. In the second order solution this symmetry is destroyed.

The main heat transfer results are presented in Figs. 5 and 6 in the form of a ratio of time averaged Nusselt number from the second order solution to that for a straight pipe. As α approaches 5 the flows become frozen and the results agree with the analytical results of Ozisik and Topakoglu [10] and Tyagi and Sharma [11] for steady flow in curved pipes. The first of these two references employs a constant peripheral temperature as is used here, but the second allows temperature to vary peripherally and holds the peripheral heat flux constant. The results do not appear to be too sensitive to this variation. Both the references quoted here use a perturbation analysis up to the second order. Akiyama and Cheng [12] deal with the same case numerically and show that the perturbation analysis of Ozisik and Topakoglu [10] diverges from their result, thus casting a doubt on the validity of the perturbation solutions if extended too far. Thus Figs. 5 and 6 are not extended beyond a value of $\overline{Nu}_2/\overline{Nu}_0$ of roughly 1.2. It is likely that higher order solutions may need to be included if the true nature of the complex transverse flow phenomena are to be revealed by a perturbation approach.

Figs. 7 and 8 show $\overline{Nu}_2/(48/11)$ for a range of the design parameters. Again the results show time averaged performance trends useful for comparative purposes and cannot be used as an absolute guide to heat transfer performance. The time averaging effects revealed in Fig. 3 are again evident. Fig. 7 shows that for sufficiently small D/C, the actual value depending on Pr, $\overline{Nu}_2$ becomes equal to $48/11$ as the Dean number reduces. Fig. 8 shows that for $Pr = 1.0$ and $\alpha = 1$ the Nusselt number ratio approaches the value given by equation (8) as the Dean number is reduced. The higher Prandtl number cases approach the same limit as for $Pr = 1.0$, provided that α is reduced appropriately in each case.

The frozen condition in Fig. 6 shows that at a fixed Dean number, the Nusselt number increases with Prandtl number. This type of
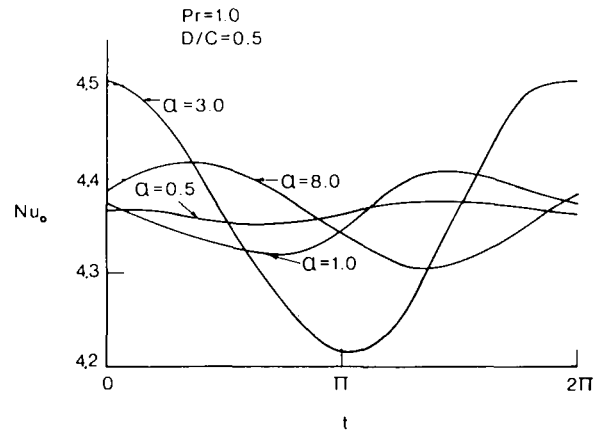

Fig. 4 Local Nusselt number as a function of time for Pr = 1.0, D/C = 0.5, and various α values
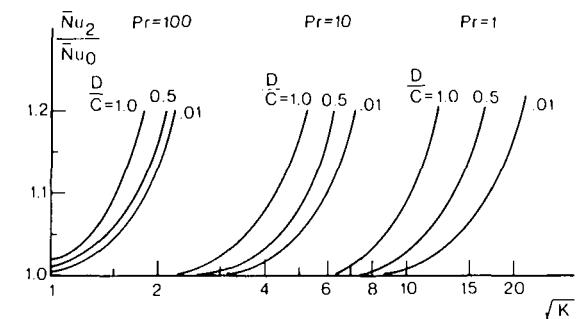

Fig. 5 Ratio of the time averaged Nusselt number for the second order solution to the zeroth order solution as a function of the Dean number for α = 1
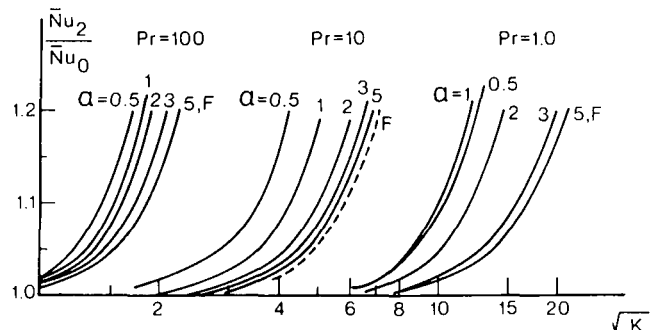

Fig. 6 Ratio of the time averaged Nusselt number for the second order solution to the zeroth order solution as a function of the Dean number for D/C = 1. Here F stands for frozen condition

dependence is expected in forced convection when boundary layer phenomena are involved. The secondary flow associated with pipe curvature causes a transverse mixing of the fluid not normally present in a straight pipe laminar flow. The character of this flow is bicellular. Fluid traverses the central region and the wall alternately, providing the boundary-layer-like behavior which leads to the expected Prandtl number dependence. The Nusselt number is insensitive to the pulsations at very small Prandtl numbers, and the Dean number needs to be increased considerably before the additional convection associated with transverse mixing becomes strong enough to influence the heat transfer.

The imposition of an oscillating pressure on the flow can have a profound and complex influence on both the axial and the secondary flows [1–6]. Secondary flow rotating cells grow and decline during the

course of a cycle in a complicated manner. One example is illustrated in Fig. 9. The occurrence of an additional cell as shown lasts for roughly 25 percent of the total period.

Figs. 5 and 6 show how the Nusselt number ratio increases in pulsatile flow for either increasing amplitude of the forcing function or decreasing α. Solutions were not obtained for α less than 0.5 due to computational difficulties and the need for excessive computer time. However, it is apparent from Fig. 6 and Fig. 10 that the Nusselt number ratio passes through a maximum value at low α. The limiting value as α approaches zero will be the same as that for steady flow in a curved tube, which is identical with the frozen case achieved at high α. The maximum value shown can only be explained in terms of the enhanced secondary flows which occur at the intermediate α values between the frozen and quasi-steady cases.

The influence of frictional dissipation on the heat transfer performance has been neglected in this analysis. If this assumption is valid in the steady state case, Fig. 11 for a straight pipe reveals that it will also be true for $D/C \leq 1$. For larger values of D/C and small α the time averaged power required increases substantially because of the large amplitude of oscillation. The assumption would need to be reexamined in such a case.

Acknowledgment

This report results from research conducted under National Science Foundation Grant No. US NSF ENG 75 14180.

References

1 Lyne, W. H., "Unsteady Viscous Flow in a Curved Pipe," *Journal of Fluid Mechanics*, Vol. 45, Part 1, 1970, pp. 13–31.
2 Zalosh, R. G., and Nelson, W. G., "Pulsating Flow in a Curved Tube," *Journal of Fluid Mechanics*, Vol. 59, Part 4, 1973, pp. 693–705.
3 Chow, J. C., and Li, C. H., to be published in the *Journal of Fluid Mechanics*.
4 Chandran, K. B., Swanson, W. M., Ghista, D. N., and Vayo, H. W., "Oscillatory Flow in Thin-Walled Curved Elastic Tubes," *Annals of Biomedical Engineering*, Vol. 2, 1974, pp. 392–412.
5 Bertelsen, A. F., "An Experimental Investigation of Low Reynolds Number Secondary Streaming Effects Associated With an Oscillating Viscous
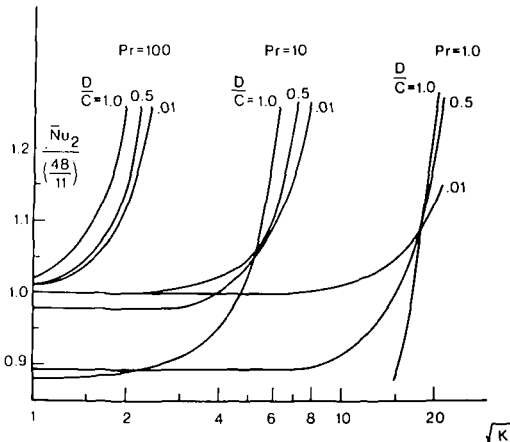
Fig. 7 Ratio of the time averaged Nusselt number for the second order solution to the straight pipe steady state value as a function of Dean number for $\alpha = 1$
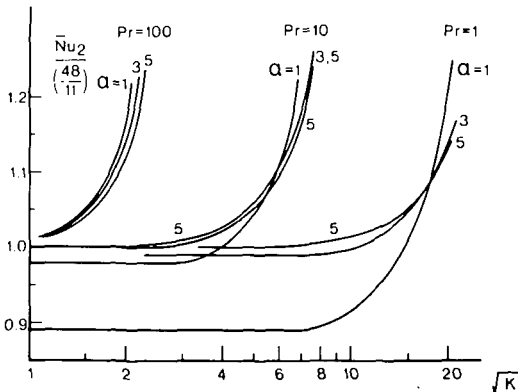

Fig. 8 Ratio of the time averaged Nusselt number for the second order solution to the straight pipe steady state value as a function of Dean number for $D/C = 1$
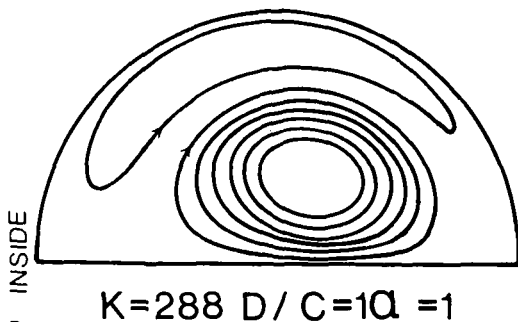

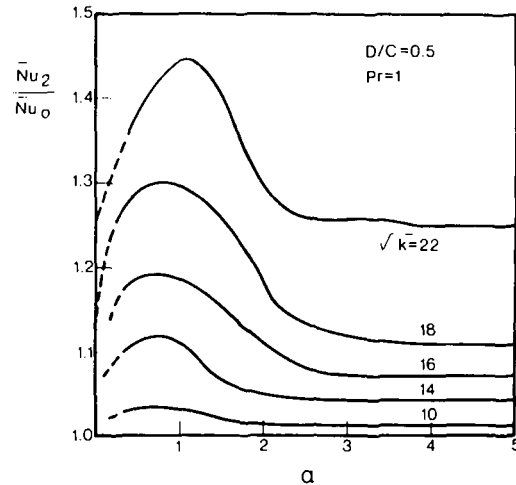**Fig. 9** Secondary flow streamlines at one instant of time

Fig. 10 Ratio of the time averaged Nusselt number for the second order solution to the zeroth order solution as a function of α for various Dean numbers
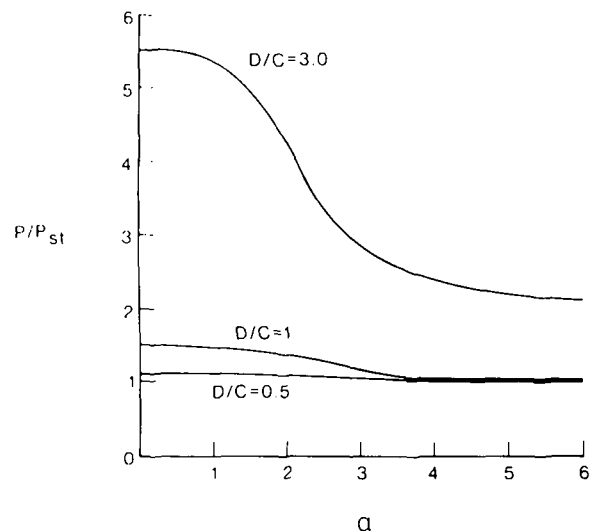

Fig. 11 Time averaged power ratio as a function of α for various D/C values

Flow in a Curved Pipe," *Journal of Fluid Mechanics,* Vol. 70, Part 3, 1975, pp. 519–527.

6   Smith, F. T., "Pulsatile Flow in Curved Pipes," *Journal of Fluid Mechanics,* Vol. 71, Part 1, 1975, pp. 15–42.

7   Chang, M. H., "Curved Tube Heat Transfer in Laminar, Pulsatile, Fully-Developed Flows," PhD thesis, University of Illinois at Chicago Circle, in preparation.

8   Uchida, S., "The Pulsating Viscous Flow Superposed on the Steady Laminar Motion of Incompressible Fluid in a Circular Pipe," *ZAMP,* Vol. 7, 1956, pp. 403–412.

9   Barnett, D. O., and Vachon, R. I., "An Analysis of Convective Heat Transfer for Pulsating Flow in a Tube," Fourth International Heat Transfer Conference, Paris -Versailles, 1970.

10   Ozisik, M. N., and Topakoglu, H. C., "Heat Transfer for Laminar Flow in a Curved Pipe," JOURNAL OF HEAT TRANSFER, TRANS. ASME Vol. 90, 1968, p. 313.

11   Tyagi, V. P., and Sharma, V. K., "An Analysis of Steady Fully Developed Heat Transfer in Laminar Flow With Viscous Dissipation in a Curved Circular Duct," *International Journal of Heat Mass Transfer,* Vol. 18, 1975, p. 69.

12   Akiyama, M., and Cheng, K. C., "Boundary Vorticity Method for Laminar Forced Convection Heat Transfer in Curved Pipes," *International Journal of Heat Mass Transfer,* Vol. 14, 1971, pp. 1659–1675.

J. R. Custer

Assoc. Mem. ASME

E. J. Shaughnessy

Asst. Professor.
Mem. ASME

Department of Mechanical Engineering and
Materials Science, Duke University, Durham, N.C.

Thermoconvective Motion of Low Prandtl Number Fluids Within a Horizontal Cylindrical Annulus

Steady natural convection in very low Prandtl number fluids is investigated using a double perturbation expansion in powers of the Grashof and Prandtl numbers. The fluid is contained in a horizontal cylindrical annulus, the walls of which either are held at constant temperature or support a constant heat flux. In both cases the evolution of the flow for increasing Grashof number is of interest. It is found that the basic flow pattern consists of one eddy. For both boundary conditions the center of this eddy falls into the lower half of the annulus as the Grashof number increases. Such behavior is directly opposite to experimental results obtained in fluids of higher Prandtl number.

Introduction

Natural convection in enclosures has been the subject of many investigations. In most of these, attention has been concentrated on fluids with large Prandtl numbers, i.e., order one and larger. Kuehn and Goldstein [1][1] present results of an experimental and numerical investigation of flows of air and water within a horizontal annulus. Included there is a very extensive bibliography of previous research. Interested readers are referred to that paper for further references to work in high Prandtl number fluids. In contrast, the behavior of fluids of small Prandtl number such as liquid metals has received much less attention. Because of their excellent heat-transfer characteristics, such fluids are being considered for use as the working fluid in several power generating cycles. It is therefore of some interest to understand the convective phenomena which occur in these fluids. In this paper we consider natural convection in low Prandtl number fluids contained within a horizontal cylindrical annulus. The flow is driven by buoyancy forces arising from density differences within the fluid. The flow is assumed to be steady, two-dimensional, and laminar. The geometry of this flow is shown in Fig. 1. Experiments have shown that such flows exist for fluids of Prandtl numbers of order one and larger. We assume that these flows are also possible in fluids of very low Prandtl number, at least for some combinations of gap width and temperature difference.

Mack and Bishop [2] investigated steady two-dimensional motion within a cylindrical annulus, the walls of which were held at different temperatures. They used a regular perturbation expansion in powers

of the Rayleigh number to obtain solutions for the stream function and temperature fields. They presented streamlines of a single flow in mercury (Pr = 0.02) at a moderate Rayleigh number (Ra = 300). The flow was composed of two weak eddies located in the top and bottom regions of the annulus. The rest of the annulus was occupied by a larger dominant eddy which rotated in the opposite sense. Huetz
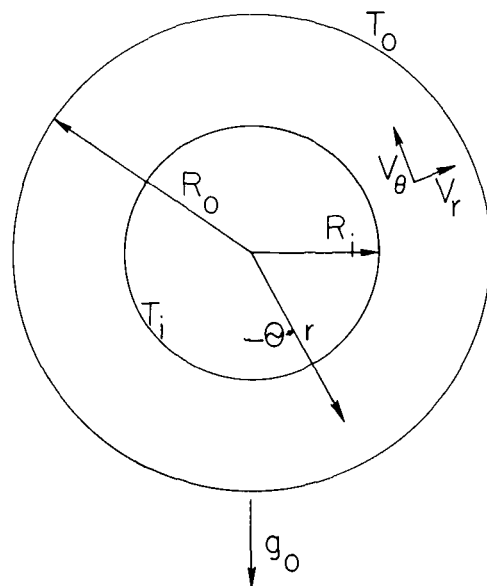

Fig. 1 Flow geometry and coordinate system

Copyright © 1977 by ASME

and Petit [3] used a similar approach to investigate the behavior of low Prandtl number fluids in an annulus. The boundary conditions they imposed were constant heat flux through one cylinder and constant temperature on the other. They too found multicellular flows.

The body of experimental work on the convective motion of air within the annulus was summarized by Powe, et al. [4] and the discrepancies noted. To resolve these discrepancies and to classify the flow regimes they also conducted extensive investigations. They determined that the various flow regimes are best correlated in terms of the inverse relative gap width $(R_i/(R_0 - R_i))$, and the Grashof number at which the steady two-dimensional flow transitions. For radius ratios greater than about 0.83, a multicelled unsteady flow with the cells located in the upper region of the annulus was the result of transition. For smaller radius ratios the steady two-dimensional flow becomes an unsteady flow which is either two- or three-dimensional. In no case were counter-rotating eddies found in the bottom of the annulus. These results were also compared with the perturbation solution of Mack and Bishop. Some limitations on that solution were noted. Powe, et al. indicated that the exact nature of the flow has some dependence on the radius of curvature.

Another paper by Powe, et al. [5] used finite differences to numerically calculate these flows for a Prandtl number corresponding to air (Pr = 0.714). They indicate that experimental evidence shows that a steady two-dimensional multiple flow with eddies occurs immediately before transition for radius ratios between 0.59 and 0.86. With this knowledge, they were able to calculate transition Grashof numbers for flows within appropriately sized cylinders. Agreement between these results and the experimental results is fairly good. Custer [6] used partial spectral expansions to investigate more thoroughly the problem of thermal convection of fluids of small Prandtl number contained within a horizontal cylindrical annulus. The stream function was assumed to be of the form $\Sigma_{n=1}^3 f_n(r) \sin n\theta$ and the temperature field was expanded as $\Sigma_{n=0}^3 g_n(r) \cos n\theta$. Substituting these expansions into the equations of motion, and using the orthogonality of the sine and cosine functions, equations governing the $f_n(r)$ and $g_n(r)$ were derived. The equations were then solved numerically. Due to the sensitivity of the problem, satisfactory convergence was obtained only for a moderate range of Grashof numbers. Several of the successful calculations were for parameter values which, according to the results of Mack and Bishop, should have produced multiple eddy flows. In no case was such a flow found.

Caltagirone [7] gave a very extensive analysis of thermal convection in a porous medium contained between horizontal concentric cylinders. Using perturbation techniques, finite-difference and finite-element solutions, Galerkin techniques, and experimental measurements, he investigated the phenomena which occur for a broad range of Grashof numbers. Using the Galerkin technique he was able to analyze the stability of these flows. He found that for sufficiently small Rayleigh numbers (Ra $\leq$ 75) the flow was two-dimensional. As the Rayleigh number increased, three-dimensional fluctuations occurred, causing a spiral flow within the annulus. Although flow within porous media is somewhat different from the present problem, these results indicate the wide range of phenomena and techniques available to analyze them.

The present research is intended to investigate more fully convection in fluids of low Prandtl number by obtaining solutions for each of two common types of boundary conditions for a broad range of radius ratios and Grashof numbers. The first of these boundary conditions is that each of the cylinders is an isothermal surface. The second is that the temperature gradient is specified at each of the cylinders. The results indicate a distinct difference between the behavior of low and high Prandtl number fluids. The single eddy which occurs for low Grashof numbers falls into the lower part of the annulus as the Grashof number increases. This behavior is in direct contrast to that of fluids of high Prandtl number such as air and water. The present results also indicate that for sufficiently large Grashof number, small counter-rotating eddies form in both the top and bottom regions of the annulus. In contrast, experimental investigations in air showed that if multiple eddies form they are found only in the top region of the annulus. Due to the lack of experimental results for liquid metals, no determination of the flow regimes has been made. The results presented here are a first attempt to do so.

In the following section the problem is formulated mathematically and the solutions are obtained as double perturbation expansions. Specific solutions for the two boundary conditions are presented and the general evolution of the flow is described. Finally, we discuss the validity of the solutions and compare these results with those in air.

Mathematical Formulation

As in many investigations of natural convection, the Boussinesq approximation is used here to incorporate the temperature dependence of the density in the equations of motion. In this approximation the density is assumed to be a linear function of temperature. Further, density fluctuations in the fluid are assumed sufficiently small that they need be included only in the body force terms of the momentum equations. Under these approximations, the system of governing equations is

$$\frac{1}{r}\frac{\partial}{\partial r}(rv_r) + \frac{1}{r}\frac{\partial v_\theta}{\partial \theta} = 0 \qquad (1)$$

$$\rho_0 \left[v_r \frac{\partial v_r}{\partial r} + \frac{v_\theta}{r}\frac{\partial v_r}{\partial \theta} - \frac{v_\theta{}^2}{r} \right] = \frac{-\partial p}{\partial r} + \mu \left[\frac{\partial}{\partial r}\left(\frac{1}{r}\frac{\partial}{\partial r}(rv_r)\right) \right.$$
$$\left. + \frac{1}{r^2}\frac{\partial^2 v_r}{\partial \theta^2} - \frac{2}{r^2}\frac{\partial v_\theta}{\partial \theta} \right] + \rho_0 g_0 [1 - \beta(T - T_0)]\cos\theta \qquad (2a)$$

$$\rho_0 \left[v_r \frac{\partial v_\theta}{\partial r} + \frac{v_\theta}{r}\frac{\partial v_\theta}{\partial \theta} + \frac{v_r v_\theta}{r} \right] = \frac{-1}{r}\frac{\partial p}{\partial \theta} + \mu \left[\frac{\partial}{\partial r}\left(\frac{1}{r}\frac{\partial}{\partial r}(rv_\theta)\right) \right.$$
$$\left. + \frac{1}{r^2}\frac{\partial^2 v_\theta}{\partial \theta^2} + \frac{2}{r^2}\frac{\partial v_r}{\partial \theta} \right] - \rho_0 g_0 [1 - \beta(T - T_0)]\sin\theta \qquad (2b)$$

$$\rho_0 C_p \left[v_r \frac{\partial T}{\partial r} + \frac{v_\theta}{r}\frac{\partial T}{\partial \theta} \right] = \kappa \left(\frac{1}{r}\frac{\partial}{\partial r}\left(\frac{r\partial T}{\partial r}\right) + \frac{1}{r^2}\frac{\partial^2 T}{\partial \theta^2} \right) \qquad (3)$$

To complete the statement of the problem, appropriate boundary conditions must be specified. These conditions are the no-slip condition at a solid surface and the thermal state of each portion of the boundary.

The motions under investigation are steady and two-dimensional. The continuity equation (1) may be satisfied exactly by the use of a stream function to represent the velocity field:

Nomenclature

C_p = specific heat at constant pressure of the fluid
g_0 = magnitude of the gravity vector
Gr = Grashof number based on radius of outer cylinder
Gr_δ = Grashof number based on gap width
p = fluid pressure
Pr = Prandtl number
r = radial coordinate
R_i, R_0 = radius of inner and outer cylinder,

respectively
T = fluid temperature
T_i, T_0 = inner cylinder temperature, outer cylinder temperature
V_r, V_θ = radial and tangential velocity component
α = thermal diffusivity of fluid
β = coefficient of thermal expansion of the fluid

δ = gap width $R_0 - R_i$
κ = thermal conductivity of fluid
η = radius ratio R_i/R_0
θ = angular coordinate
μ = dynamic viscosity
ν = kinematic viscosity μ/ρ_0
ρ, ρ_0 = fluid density and reference density
ψ, Ψ = dimensional and nondimensional stream function
∇^2 = Laplacian operator

$$v_\theta = \frac{\partial \psi}{\partial r} \qquad v_r = -\frac{1}{r}\frac{\partial \psi}{\partial \theta} \qquad (4)$$

Operating on (2a) with $(1/r)\,(\partial/\partial\theta)$ and on (2b) with $\partial/\partial r$ and then subtracting the resulting equations yields the conservation equation for the axial component of vorticity. Because the flow is two-dimensional, this is the only nonzero component of vorticity.

The equations that remain are the thermal energy equation and the axial vorticity equation. To nondimensionalize these equations the independent and dependent variables are scaled in the following way

$$r = R_0 r'$$
$$\psi = \nu \Psi' \qquad (5)$$

and either

$$T = T_i + (T_0 - T_i)T'' \text{ (case I)}$$

or

$$T = \left.\frac{\partial T}{\partial r}\right|_{r=R_0} R_0 T' \text{ (case II)}$$

The primed variables are dimensionless. The nondimensional equations of motion that result are, dropping the primes:

$$\nabla^4 \Psi = \frac{1}{r}\frac{\partial(\nabla^2\Psi, \Psi)}{\partial(r,\theta)} + \text{Gr}\left(\frac{\cos\theta}{r}\frac{\partial T}{\partial\theta} + \sin\theta\frac{\partial T}{\partial r}\right) \qquad (6)$$

$$\nabla^2 T = \frac{\text{Pr}}{r}\frac{\partial(T, \Psi)}{\partial(r, \theta)} \qquad (7)$$

Jacobian notation is used to simplify the writing of these equations. For example

$$\frac{\partial(\Psi, T)}{\partial(r, \theta)} = \frac{\partial\Psi}{\partial r}\frac{\partial T}{\partial\theta} - \frac{\partial\Psi}{\partial\theta}\frac{\partial T}{\partial r}$$

Three nondimensional parameters arise. The first is the radius ratio $\eta = R_i/R_0$, which enters the problem implicitly through the boundary conditions. The other two groups, which appear explicitly in the equations of motion, are the Grashof number Gr and the Prandtl number Pr. The exact defintion of the Grashof number depends upon the boundary conditions under consideration. For specified wall temperatures the Grashof number is $g_0\beta(T_0 - T_i)R_0^3/\nu^2$. If the inner cylinder is hotter than the outer, the Grashof number is negative. For specified wall heat flux the Grashof number is $g_0\beta\,(\partial T/\partial r)_{r=R_0}R_0^4/\nu^2$. As a result, if heat is being transferred from the fluid to the outer cylinder, the Grashof number is negative. In both cases the coefficient of expansion β has been taken to be positive. The Grashof number is a measure of the relative importance of buoyancy and viscous forces. The Prandtl number, $\text{Pr} = \nu/\alpha$, is the ratio of the diffusivity of momentum to that of heat. Alternatively it may be considered to be a measure of the importance of convection of heat versus molecular transport. Liquid metals are characterized by very small Prandtl numbers. In this limit, $\text{Pr} \to 0$, equation (7) reduces to the conduction equation, the natural limit for liquid metals.

The boundary conditions must also be nondimensionalized. For the case of isothermal boundaries, the boundary conditions are

$$\frac{\partial\Psi}{\partial r} = \frac{\partial\Psi}{\partial\theta} = 0 \qquad \text{at} \qquad r = \eta, 1 \qquad (8)$$

$$\frac{\partial^2\Psi}{\partial\theta^2} = \frac{\partial\Psi}{\partial r} = \frac{\partial T}{\partial\theta} = 0 \qquad \text{at } \theta = 0, \pi$$

and

$$T = 0 \quad \text{at} \quad r = \eta, \; T = 1 \quad \text{at} \quad r = 1 \qquad (9)$$

The conditions imposed on $\theta = 0, \pi$ are symmetry conditions. The flow in each vertical half of the annulus is assumed to be a mirror-image of that in the other half.

For the case of constant heat flux through each cylinder, conditions (8) remain unchanged. The new thermal conditions on the boundary are given by

$$\frac{\partial T}{\partial r} = \frac{1}{\eta} \quad \text{at} \quad r = \eta, \qquad \frac{\partial T}{\partial r} = 1 \quad \text{at} \quad r = 1 \qquad (10)$$

These conditions satisfy the compatibility condition for steady viscous flow. This condition states that in the absence of any volume heat sources, such as viscous dissipation, the total amount of heat passing through each cylinder is the same.

Solutions to equations (6)–(8) and either (9) or (10) are sought as double perturbation expansions in powers of the Grashof and Prandtl numbers. That is, we assume, the following forms:

$$\Psi(r, \theta) = \sum_{n=0}^{\infty}\sum_{m=0}^{\infty} \text{Pr}^n \text{Gr}^m \Psi_{nm}(r, \theta)$$

$$T'(r, \theta) = \sum_{j=0}^{\infty}\sum_{k=0}^{\infty} \text{Pr}^j \text{Gr}^k T_{jk}(r, \theta) \qquad (11)$$

Equations governing the unknown functions $\psi_{nm}(r, \theta)$ and $T_{jk}(r, \theta)$ are obtained by using the expansions (11) in the equations of motion. In each equation, terms multiplied by like powers of Prandtl number are equated. There remains an infinite set of equations in powers of Grashof number.

The thermal energy equation to zeroth order in Prandtl number is

$$\sum_{s=0}^{\infty} \text{Gr}^s \nabla^2 T_{0s} = 0 \qquad (12)$$

and the momentum equation to zeroth order in Prandtl number is

$$\sum_{m=0}^{\infty} \text{Gr}^m \nabla^4\psi_{0m} = \frac{1}{r}\left[\sum_{m=0}^{\infty}\sum_{\ell=0}^{\infty}\text{Gr}^{m+\ell}\frac{\partial\psi_{0m}}{\partial\theta}\frac{\partial(\nabla^2\psi_{0\ell})}{\partial r}\right.$$
$$\left. - \sum_{m=0}^{\infty}\sum_{\ell=0}^{\infty}\text{Gr}^{m+\ell}\frac{\partial\psi_{0m}}{\partial r}\frac{\partial(\nabla^2\psi_{0\ell})}{\partial\theta}\right]$$
$$+ \left[\frac{\cos\theta}{r}\sum_{s=0}^{\infty}\text{Gr}^{s+1}\frac{\partial T_{0s}}{\partial\theta} + \sin\theta\sum_{s=0}^{\infty}\text{Gr}^{s+1}\frac{\partial T_{0s}}{\partial r}\right] \qquad (13)$$

To first order in Prandtl number, the thermal energy equation is

$$\sum_{s=0}^{\infty}\text{Gr}^s\nabla^2 T_{1s} = \frac{1}{r}\left[\sum_{m=0}^{\infty}\sum_{s=0}^{\infty}\text{Gr}^{m+s}\left(\frac{\partial\psi_{0m}}{\partial\theta}\frac{\partial T_{0s}}{\partial r} - \frac{\partial\psi_{0m}}{\partial r}\frac{\partial T_{0s}}{\partial\theta}\right)\right]$$

$$(14)$$

and the momentum equation is

$$\sum_{m=0}^{\infty}\text{Gr}^m\nabla^4\psi_{1m} =$$
$$\frac{1}{r}\left[\sum_{m=0}^{\infty}\sum_{\ell=0}^{\infty}\text{Gr}^{m+\ell}\left\{\frac{\partial\psi_{0m}}{\partial\theta}\frac{\partial(\nabla^2\psi_{1\ell})}{\partial r} + \frac{\partial\psi_{1m}}{\partial\theta}\frac{\partial(\nabla^2\psi_{0\ell})}{\partial r}\right\}\right.$$
$$\left. - \sum_{m=0}^{\infty}\sum_{\ell=0}^{\infty}\text{Gr}^{m+\ell}\left\{\frac{\partial\psi_{0m}}{\partial r}\frac{\partial(\nabla^2\psi_{1\ell})}{\partial\theta} + \frac{\partial\psi_{1m}}{\partial r}\frac{\partial(\nabla^2 T_{0\ell})}{\partial\theta}\right\}\right]$$
$$+ \left[\frac{\cos\theta}{r}\sum_{s=0}^{\infty}\text{Gr}^{s+1}\frac{\partial T_{1s}}{\partial\theta} + \sin\theta\sum_{s=0}^{\infty}\text{Gr}^{s+1}\frac{\partial T_{1s}}{\partial r}\right] \qquad (15)$$

These equations are simplified by equating like powers of the Grashof number. The result is a set of differential equations that must be solved in a natural sequence. Equating powers of G in (12) leads to the series of problems

$$\nabla^2 T_{0s} = 0 \qquad s = 0, 1, 2, \ldots \qquad (16)$$

The solutions must satisfy the boundary conditions given by (8) and either (9) or (10) for all Grashof and Prandtl numbers for which this analysis is valid.

In order to do this, the boundary conditions (9) or (10) are imposed on $T_{00}(r)$, the conduction solution. Hence, one equation in the series (16) is

$$\nabla^2 T_{00} = 0$$

with

$$T_{00}(\eta) = 0 \qquad T_{00}(1) = 1$$

or

$$\left.\frac{\partial T_{00}}{\partial r}\right|_{r=\eta} = \frac{1}{\eta}\left.\frac{\partial T_{00}}{\partial r}\right|_{r=1} = 1$$

The rest of the equations in (16) are

$$\nabla^2 T_{0s} = 0 \qquad s = 1, 2, \ldots$$

For the case of constant wall temperature, the accompanying boundary conditions are homogenous. The solutions are all identically zero. For the case of constant wall heat flux, the imposed boundary conditions specify that the normal derivative of the temperature on the boundary is zero. Those solutions are all arbitrary constants which are taken to be zero.

Likewise, the momentum equation (13) is reduced by identifying equal powers of the Grashof number. The zeroth order equation is simply

$$\nabla^4 \psi_{00} = 0$$

The boundary conditions are all homogeneous. The solution is $\psi_{00} = 0$, which corresponds to no motion. This is to be expected because the driving force for the flow arises from density differences within the fluid. As Gr $\rightarrow$ 0 these density differences disappear and the motion should also disappear.

The zeroth-order Prandtl, first-order Grashof momentum equation is

$$\nabla^4 \psi_{01} = \frac{1}{r}\left[\frac{\partial \psi_{00}}{\partial \theta}\frac{\partial(\nabla^2 \psi_{01})}{\partial r} + \frac{\partial \psi_{01}}{\partial \theta}\frac{\partial(\nabla^2 \psi_{01})}{\partial r} - \frac{\partial \psi_{00}}{\partial r}\frac{\partial(\nabla^2 \psi_{01})}{\partial \theta}\right.$$
$$\left. - \frac{\partial \psi_{00}}{\partial r}\frac{\partial(\nabla^2 \psi_{00})}{\partial \theta}\right] + \left[\frac{\cos\theta}{r}\frac{\partial T_{00}}{\partial \theta} + \sin\theta\frac{\partial T_{00}}{\partial r}\right]$$

This sequence continues in a natural way. The equations for the unknown functions are always linear in the unknown function. The inhomogeneous term of each equation is always a nonlinear function of previously determined functions.

These equations may all be solved analytically by separation of variables. The solutions presented here were calculated from the following truncated series:

$$T(r, \theta) = T_{00}(r) + \mathrm{GrPr}T_{11}(r)\cos\theta$$

$$\psi(r, \theta) = \mathrm{Gr}\psi_{01}(r)\sin\theta + \mathrm{Gr}^2\psi_{02}(r)\sin 2\theta$$
$$+ \mathrm{Gr}^3[\psi_{031}(r)\sin\theta + \psi_{033}(r)\sin 3\theta]$$

where the functions of r are of the form $\beta_{ij}r^i(lnr)^j$ where i and j are integers and β_{ij} are constants. The index i may be any integer but the index j must be greater than or equal to zero. The streamlines to be illustrated are therefore independent of Prandtl number, but the isotherms retain first-order dependence on Prandtl number. Further details may be obtained from the first author.

Constant Temperature Results

Three parameters govern this flow, and it is natural to ask how the nature of the flow depends upon them. The solution method used here permits consideration of only very small Prandtl numbers. In fact, the streamlines which are presented are independent of Prandtl number. Conduction is the predominant mechanism of heat transfer, so the isotherms are only slightly distorted from the concentric circles which represent pure conduction. For this reason isotherms for these flows will not be plotted. For the case of a specified boundary heat flux the situation is different, but this will be discussed in the following section. For now we consider only the effect of Grashof number and radius ratio on flows for which the boundary temperatures are specified.

At low Grashof numbers the streamline patterns are similar to those found experimentally and analytically in fluids of large Prandtl number. In wide gaps the flow has the kidney shape described by Bishop and Carley (1966). This is illustrated in Fig. 2, which is a plot of selected streamlines in a flow at Gr = −200 and η = 0.2. This flow is very close to being perfectly symmetrical about the horizontal plane. In narrower gaps the flow has the crescent shape also described by Bishop and Carley.
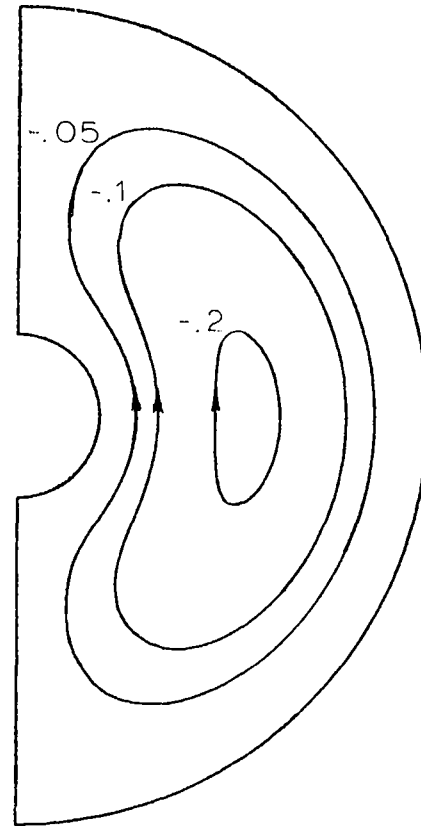

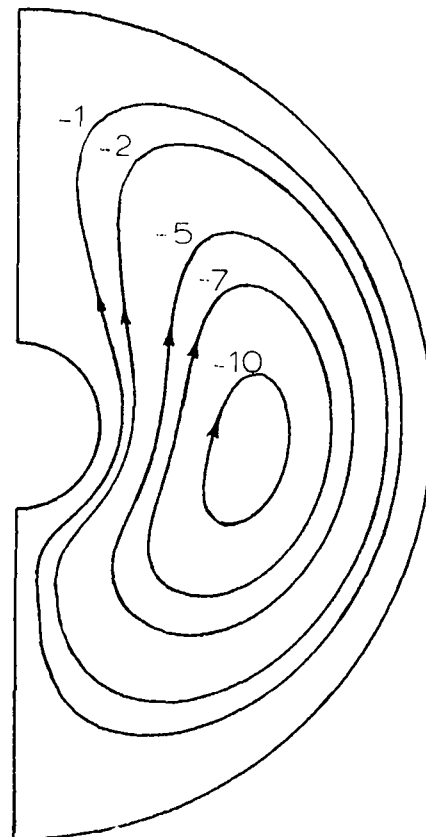**Fig. 2** Streamlines of the flow at Grashof number −200 and radius ratio 0.2

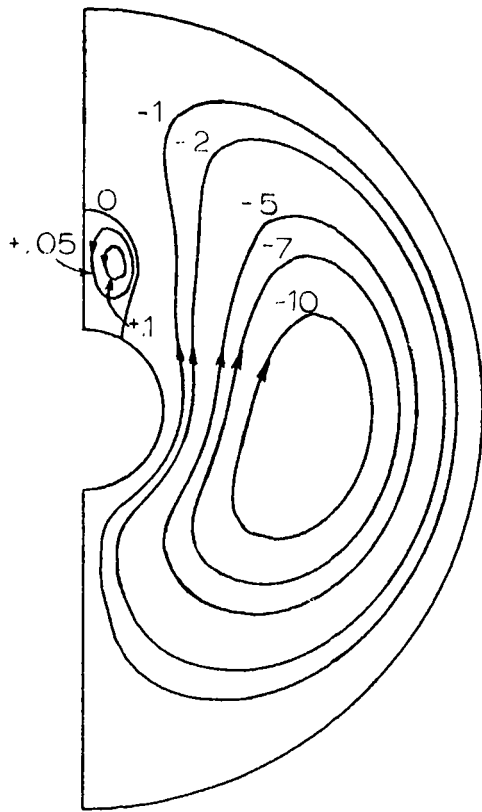**Fig. 3** Streamlines of the flow at Grashof number −10⁴ and radius ratio 0.2

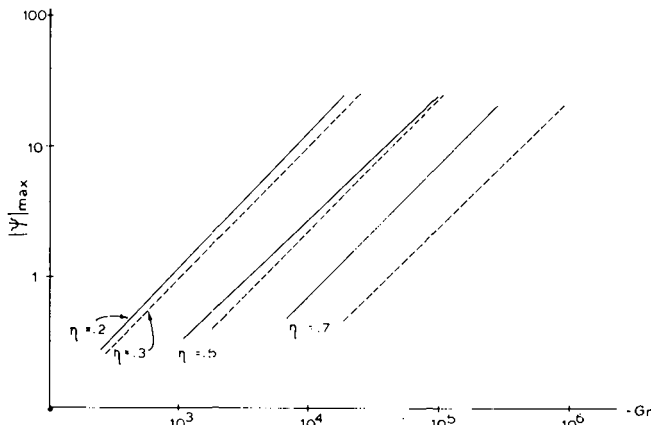**Fig. 4 Streamlines of the flow at Grashof number -12×10^4 and radius ratio 0.2**

Fig. 5 Maximum absolute value of the stream function versus Grashof number: — wall temperature specified; - - - wall heat flux specified

Fig. 6 Flow at Grashof number -10^3 and radius ratio 0.5: (a) streamlines; (b) isotherms

As the Grashof number increases, the center of the eddy, defined as the point of the extremum of the stream function, falls into the lower region of the annulus. This phenomenon is strikingly different from that which occurs in fluids of large Prandtl numbers. In those fluids the center of the eddy moves above the horizontal plane. Both Huetz and Petit [3] and Custer [6] found this difference. It was not possible to determine whether the solutions of Mack and Bishop [2] showed this behavior because they showed only one streamline pattern. Fig. 3 illustrates this behavior in a flow at Gr = -1000 and η = 0.2. Of particular interest here is the shape of the streamlines in the upper part of the annulus. The streamlines have moved outward and upward, making them seem quite pointed compared with their shape in the bottom part of the annulus. Fig. 4 shows the streamlines of a flow at Gr = $-12,000$ and η = 0.2. A small weak eddy has formed on
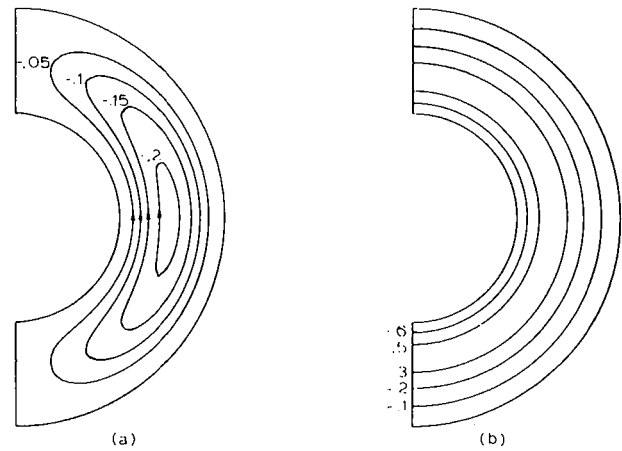
the top of the inner cylinder. The fluid within this eddy rotates counterclockwise while that in the main eddy rotates clockwise. Thus, the development of the flow in wide gaps proceeds from a single dominant eddy to a multiple eddy structure as the Grashof number increases.

In narrower gaps the process is similar but the evolution with Grashof number occurs much more slowly. The basic crescent eddy falls below the horizontal plane and the flow intensifies. Eventually one or two small counter-rotating eddies appear. For a radius ratio of 0.5, two eddies appear at a Grashof number between -7×10^4 and -8×10^4. One of these is on the top of the inner cylinder and the other is on the bottom of outer surfaces. For a radius ratio of 0.7 the flow still has the basic symmetric eddy pattern even at Gr = -2×10^5!

The maximum absolute value of the stream function is a measure of the intensity of the flow. Fig. 5 shows the maximum absolute value of the stream function plotted as a function of the Grashof number. Least-squares analysis of the data yields the following correlations:

$$\eta = 0.2: |\Psi|_{max} = 1.08 \times 10^{-3} \, (-\mathrm{Gr})^{1.002}$$

$$\eta = 0.5: |\Psi|_{max} = 2.55 \times 10^{-4} \, (-\mathrm{Gr})^{1.025}$$

$$\eta = 0.7: |\Psi|_{max} = 6.69 \times 10^{-5} \, (-\mathrm{Gr})^{1.004}$$

These results indicate that the flow is more vigorous the larger the gap. By plotting the data as a function of a Grashof number based on the gap width, these three curves may be reduced to one whose least-square correlation is given by

$$|\Psi|_{max} = 2.1 \times 10^{-3} \, \mathrm{Gr}_\delta^{1.0195}$$

This new Grashof number is $g_0\beta(T_0 - T_i)(R_0 - R_i)^3/\nu^2$

Constant Heat Flux Results

In this section we describe results which obtain when the temperature gradient is specified on the cylinders. Compared to the case of constant wall temperature, this condition has greater implications for the temperature field within the annulus than for the streamlines, so we present plots of isotherms in addition to streamlines. The Prandtl number was 0.02 for all flows illustrated.

These flows develop in the same manner as those for which the temperature of the boundaries is specified. At low Grashof numbers the streamlines are closely symmetrical about the horizontal plane. In the wide gaps the flow has the normal kidney-shaped streamline pattern previously described, while in the narrow gaps the crescent eddy is the typical shape. The isotherms are almost indistinguishable from those which would occur in the case of pure conduction, that is, they are almost concentric circles. Fig. 6 is a plot of the streamlines and isotherms for a flow at Gr = $-1,000$ and η = 0.5. The negative values of the nondimensional temperature can be explained by ex-

amining the solution for the temperature field:

$$T(r, \theta) = T^* + \ln r + GrPr\, f(r) \cos \theta.$$

T^* is a nondimensional reference temperature that corresponds to the temperature of the outer cylinder ($r = 1$) at $\theta = 90$ deg. In all the calculations, T^* was set equal to zero and the Grashof number was negative. Negative values of T represent dimensional temperatures greater than the reference temperature. For experimental purposes, it is important to note that if more terms had been included in the solution, the location of T^* would be different.

As the Grashof number increases, the streamlines follow the same development as in the case of constant wall temperature. The center of the eddy falls below the horizontal and the vigor of the flow increases. The temperature field shows increasing effects of convection, as indicated by the fact that the isotherms are no longer even close to being concentric circles. The temperature of each of the cylinders is not constant but increases in the direction of fluid flow along them. The inner cylinder temperature increases in the direction of increasing angle while that of the outer cylinder increases in the direction of decreasing angle. This is required to satisfy the constant flux boundary condition. Fig. 7 shows the streamlines and isotherms for a flow of Gr = $-50,000$ and $\eta = 0.5$. The maximum value of the stream function occurs at 86 deg and approximately halfway across the gap.

At a Grashof number of -10^5, the flow has increased in vigor by about a factor of two but it has not shifted around the gap any further.
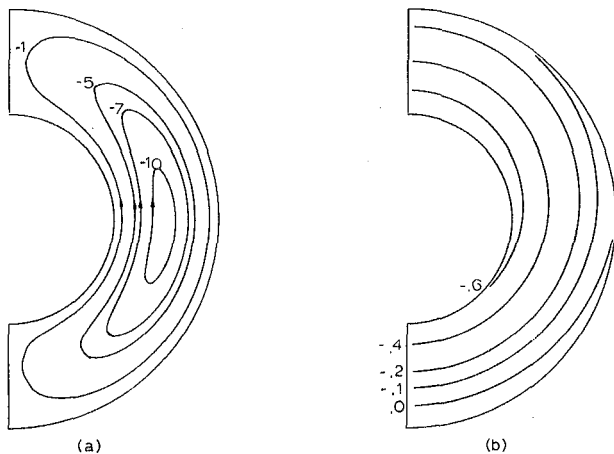

Fig. 7 Flow at Grashof number -5×10^4 and radius ratio 0.5: (a) streamlines; (b) isotherms
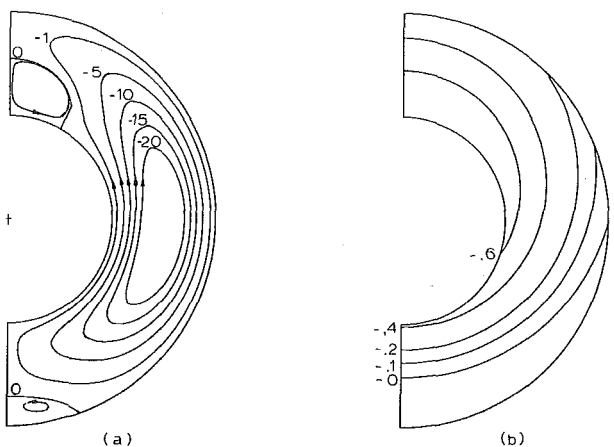

Fig. 8 Flow at Grashof number -12×10^5 and radius ratio 0.5: (a) streamlines (b) isotherms

The center of the eddy is located at the same point as it was in flow at Gr = $-50,000$. This flow exhibits the same pattern as did the flow at a Grashof number of $-10,000$ and a radius ratio of 0.2 for which the boundary temperatures were specified. The streamlines in the upper region of the annulus have been pulled outward and upward. In addition the isotherms in the upper and lower regions of the annulus are widely separated, indicating that temperature gradients in these regions are small.

In the previous analysis for constant wall temperature this behavior preceded the appearance of an eddy on the top of the inner cylinder. We expect to find that the same occurs in this case. Fig. 8 shows the streamlines and isotherms for the flow at Gr = $-120,000$ and $\eta = 0.5$. Two eddies have appeared. The flow in the eddy on the top of the inner cylinder is somewhat stronger than that in the lower eddy. The sense of rotation of both eddies is opposite that of the main flow.

As in the case of constant wall temperature, the strength of the flow is closely a linear function of the Grashof number. The correlations are

$$\underline{\eta = 0.3}\quad |\Psi|_{\max} = 8.7 \times 10^{-4}\, (-Gr)^{1.012}$$

$$\underline{\eta = 0.5}\quad |\Psi|_{\max} = 1.88 \times 10^{-4}\, (-Gr)^{1.017}$$

$$\underline{\eta = 0.7}\quad |\Psi|_{\max} = 2.47 \times 10^{-5}\, (-Gr)^{1.000}$$

These curves are also plotted in Fig. 5. It is obvious from this plot that for a given pair of parameters η and Gr, the flow is slightly more vigorous if the boundary condition is constant temperature rather than constant temperature gradient.

By defining the Grashof number in terms of the gap width, these three curves may be represented by one curve whose equation is given by

$$|\Psi|_{\max} = 1.78 \times 10^{-3}\, (-Gr_\delta)^{1.007}$$

where

$$Gr_\delta = g_0\beta \frac{\partial T}{\partial r}\bigg|_{r=R_0} R_0(R_0 - R_i)^3/\nu^2$$

Discussion

The solutions presented here are regular perturbation expansions in powers of the Grashof number and Prandtl number. It is therefore expected that they will be uniformly valid throughout the flow field for some region in parameter space. They show an interesting evolution as the Grashof number increases. At sufficiently high Grashof numbers, one or more eddies appear in the annulus and it would seem that those are no longer small perturbations superposed on the single eddy flows. The question of the range of validity of the expansions is important because the answer is crucial in understanding whether these complex flows are real or are simply results of the linearization of the equations and truncation of the series.

In order to obtain an idea of the range of applicability of these solutions, the ratio of each term of the expansion to the sum of previous terms was calculated. Such a test is not a proof of convergence, but it does show when the basic premise of a perturbation solution is violated. This premise requires that the $(n + 1)$th term of the expansion be a small correction to the solution represented by the previous n terms. Only the stream function has been so treated since the flow regimes, and not the heat transfer, are of primary interest. The curves shown in Fig. 9 mark the approximate points in the (Gr, η) plane where the last term of the series for Ψ becomes equal in magnitude to the sum of the previous terms. All flows located in the region bounded by these curves and the coordinate axes that were calculated had but a single eddy. Flows that were outside this region were composed of multiple eddies.

Inspection of the perturbation series shows how multiple eddy flows may be obtained. The terms of order Gr and Gr³ each contain angular dependence given by sin θ. Should these terms be of equal magnitude
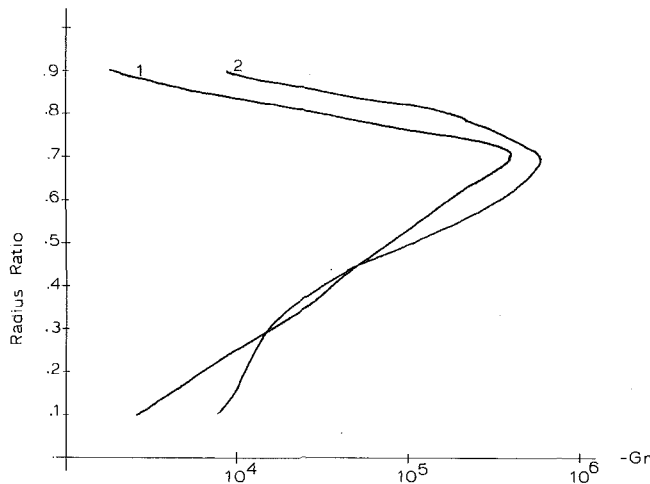
Fig. 9 Approximate region of validity of the stream function expansions: curve 1—wall temperature specified; curve 2—wall heat flux specified

but of opposite sign, the angular dependence would be determined by $\sin 2\theta$ and $\sin 3\theta$. It is these terms that yield the multiple eddies. If the terms that have been neglected are indeed small, then the multiple eddies are valid. On the other hand, the neglected terms may not really be so small that the truncated series accurately represents the true solution. Inspection of the equations indicates that the fourth-order terms have angular dependence given by $\sin 2\theta$ and $\sin 4\theta$. Another $\sin 3\theta$ does not appear until the fifth-order term. Calculating these higher-order terms involves a prohibitive amount of work. Only solutions to the full nonlinear equations or experiments can firmly establish the existence of the multiple eddy flows.

Summary

The motion of fluids with small Prandtl numbers contained within a horizontal cylindrical annulus has been investigated by a perturbation solution to the Boussinesq equations. The evolution of the flow for several radius ratios has been described and compared with published investigations of flows of high Prandtl number fluids. In both cases the flow is composed of a single eddy in each half of the annulus if the Grashof number is low. As the Grashof number grows, the eddy in low Prandtl number fluids falls, while the eddy in high Prandtl number fluids rises. This is a striking difference. At sufficiently high Grashof numbers, experiments show that flows of air and water undergo transition to some unsteady flow. While no experimental investigations of low Prandtl number fluids are known to the authors, the present results indicate that a complex multicellular flow may be possible. The rich variety of flows that occurs within this geometry provides vast possibilities for experiment and calculation. In particular the present results should be extended by both types of investigation. Extension of the spectral expansions used by Custer is underway. It is hoped that they will provide the capability to investigate the transition region of liquid metals.

Acknowledgment

References

1 Kuehn, T. H., and Goldstein, R. J., "An Experimental and Theoretical Study of Natural Convection in the Annulus Between Horizontal Concentric Cylinders," *Journal of Fluid Mechanics,* Vol. 74, 1976, p. 695.

2 Mack, L. R., and Bishop, E. H., "Natural Convection Between Horizontal Concentric Cylinders for Low Rayleigh Numbers," *Quarterly Journal of Mechanics and Applied Mathematics,* Vol. 21, 1968, p. 223.

3 Huetz, J., and Petit, J. P., "Natural and Mixed Convection in Concentric Annular Spaces—Experimental and Theoretical Results for Liquid Metals," 5th International Heat Transfer Conference, Tokyo, Vol. 3, 1974, p. 1364.

4 Powe, R. E., Carley, C. T., and Bishop, E. H., "Free Convective Flow Patterns in Cylindrical Annuli," JOURNAL OF HEAT TRANSFER, TRANS. ASME, Series C, Vol. 91, 1969, p. 310.

5 Powe, R. E., Carley, C. T., and Carruth, S. L., "A Numerical Solution For Natural Convection in Cylindrical Annuli," JOURNAL OF HEAT TRANSFER, TRANS. ASME, Series C, Vol. 93, 1971, p. 210.

6 Custer, J. R., "Natural Convection in Low Prandtl Number Fluids Within a Horizontal Cylindrical Annulus," MS thesis, Duke University, 1976 (unpublished).

7 Caltagirone, J. P., "Thermoconvective Instabilities in a Porous Medium Bounded by Two Concentric Horizontal Cylinders," *Journal of Fluid Mechanics,* Vol. 76, 1976, p. 337.

C. Chang
G. C. Vliet
A. Saberian

Department of Mechanical Engineering,
University of Texas,
Austin, Tex.

Natural Convection Mass Transfer at Salt-Brine Interfaces

*Experimental measurements of the rate of dissolution (mass transfer) at salt-brine inter-
faces have been made for variation of brine concentration from fresh water to near satu-
rated brine, and variation of surface orientation from horizontal (facing downward)
through the vertical to "near" horizontal (facing upward). Salt samples used were cut
from an underground mine and the dissolution results are for "rough" surfaces—that is,
after the surface has developed. Samples of approximately 1 m long were used, and the
results obtained and presented are for turbulent flow. The correlated results are present-
ed in the form of a coefficient C_T as a function of θ (angle from vertical) where $C_T(\theta) =
Sh/(GrSc)^{1/3}$. The coefficient is found to be a very strong function of angle, being larger
for the unstable orientations and smaller for the stable orientations than for the vertical.
The data are compared to other turbulent natural convection mass and heat transfer data
for vertical and inclined surfaces, and are found to exhibit considerably greater convec-
tion transport coefficients than for smooth surfaces.*

Introduction

There are several physical phenomena which involve turbulent
natural convection on vertical and inclined surfaces, one of these being
natural convection mass transfer during cavity development in so-
lution mining. An analogous problem is thermal stratification of liq-
uids in vessels. A numerical model for predicting the growth of solu-
tion-mined cavities has been developed by Saberian [1],[1] as part of
an ongoing study. Numerical predictive models have also been de-
veloped for thermal stratification in vessels. The purpose in obtaining
the present experimental measurements is to better quantify and
define the nature of mass transfer at a salt-brine interface.

Fluid flow in natural convection is due to density gradients within
the fluid; in heat transfer these result from thermal gradients, and
in mass transfer they result from concentration gradients. The
boundary layer will normally be laminar for some distance along the
surface and then subsequently undergo transition to turbulent flow.
In heat transfer the transition for an isothermal vertical surface is
fairly well defined by $Ra_H = Gr_H Pr$ and occurs in the approximate
range 5×10^8 to 5×10^9. In mass transfer the analogous parameters
are Gr_M and Sc, and transition has been found to occur in the range
$2 \times 10^{11} < Ra_M < 3 \times 10^{12}$. There are really no turbulent natural
convection heat transfer data available that are analogous to turbulent
natural convection mass transfer, since for liquids with Prandtl

numbers similar in magnitude to typical Schmidt numbers it is very
difficult to achieve turbulent natural convection flows.

The most recent work directly pertinent to the present study on
natural convection mass transfer is that of Lloyd, Sparrow, and Eckert
[2] and Moran and Lloyd [3], who have investigated laminar as well
as turbulent natural convection mass transfer on vertical and inclined
smooth surfaces using an electrochemical technique. These investi-
gations found natural convection mass transfer transition for vertical
surfaces to be in the range $2 \times 10^{11} < Ra_M < 3 \times 10^{12}$, that is, insta-
bilities initiate at the lower value and fully developed turbulent flow
is achieved at the higher value. In addition, there is a shift to higher
values of Ra_M for the transition range as the surface is varied from
the unstable orientation through the vertical into the stable, i.e., the
transition location moves further downstream. These investigators
found that the turbulent data could be correlated in terms of a single
angle dependent coefficient $C_T'(\theta)$ where

$$Sh_x = C_T'(\theta) (Gr_M Sc)^{1/3}$$

with the gravity in Gr_M modified to $g \cdot \cos \theta$. The coefficient $C_T'(\theta)$ was
found to increase monotonically as the surface is rotated from the
stable orientation through the vertical and into the unstable.

Mass transfer data were also obtained for vertical copper electrodes
in a copper sulfate solution by Fouad and Ibl [14] for varying electrode
length and copper sulfate concentration. Local mass transfer data
were not obtained; however, the average data were found to vary with
a Gr·Sc exponent of 0.26 to 0.28, increasing with the Gr·Sc product.
Since the data are for the entire plate (including laminar region), it
is expected that their turbulent data only, if available, should correlate
with an exponent of at least 0.28.

Wilke, et al. [4] performed some experimental mass transfer studies
for vertical surfaces. Durie [5, 6] and Saberian [1] have experimentally

---

[1] Numbers in brackets designate References at end of paper.

investigated the effect of surface inclination on the rate of dissolution of salt, and measurements of salt dissolution for vertical surfaces were also performed in [7]. Masliyah and Nguyen [8] have made mass transfer measurements for a vertical surface, and Husband [9] has made mass transfer measurements on large sugar samples in water up to $\mathrm{Ra}_M = 9 \times 10^{14}$.

The heat transfer investigations most pertinent to the present study are for turbulent natural convection heat transfer on inclined surfaces, including those of Vliet [10], Fujii and Imura [11], Hassan and Mohamed [12], and Vliet and Ross [13]. As for mass transfer, these investigations with heated surfaces show transition to move forward on the surface as the surface is rotated from the stable (facing downward) through the vertical into the unstable orientation, and the heat transfer in the turbulent regime is found to be enhanced also, although once in the unstable orientation there is little further effect.

In the present work, measurements are presented for the dissolution rate on large salt samples as a function of brine concentration and surface orientation (both upward facing, stable and downward facing, unstable). In these experiments the samples used are salt as cut from a mine and the dissolution rate was measured after the surfaces had assumed a rough character due to the dissolution process.

Experimental Apparatus

The experimental apparatus as shown in Fig. 1 accommodated salt samples approximately 1 m long, and most samples were approximately 1 m long by 0.3 m wide by 0.15 m thick, as shown in Fig. 2. Each sample[2] was coated with epoxy, except for a 1×0.3 m side, which was exposed to the brine. The sample was mounted on a stainless steel platform which could be positioned in the test vessel at any desired angle. The dissolution rate as a function of location along the sample was determined from measurements of sample thickness using a direct current displacement transducer (DCDT) located on a carriage which could be traversed along the sample while in place. The sample interface location as determined by the DCDT and the location along the sample as determined by a 10-turn potentiometer on the carriage drive assembly were plotted directly on an X-Y recorder. The measurements were made over the length of the sample along the center line, making discrete measurements at small intervals along the sample. Dissolution or surface recession rates were obtained from the change in the interface location over a specific time period.

The test vessel consisted of a $1.5 \times 1.5 \times 0.41$ m (5 ft $\times$ 5 ft $\times$ 14 in.) clear plastic tank. The test samples were suspended at the desired orientation below the liquid level in the tank as shown in Fig. 3 and center-line thickness traverses were made at time intervals. As the dissolution measurements frequently took several hours, stratification would normally build up in the vessel. To prevent this, two approximately equal-capacity reservoirs were used, a shallow one at floor level

---

[2] The salt samples used in these experiments were cut from Morton Salt's Grande Saline mine in Grande Saline, Texas. The samples exhibited some variation, however the average percent insolubles was approximately 2 percent; and the average specific gravity was 2.1 g/cm³.
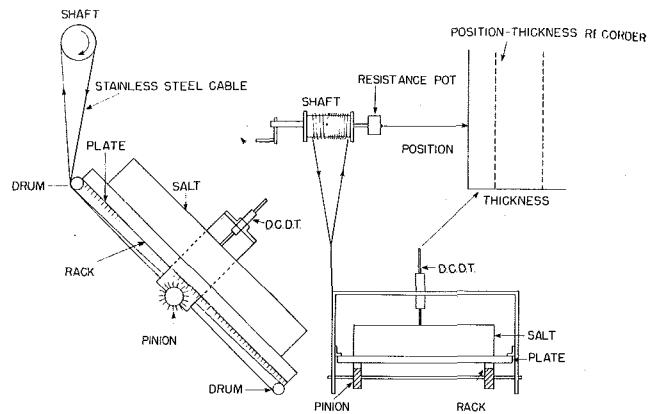

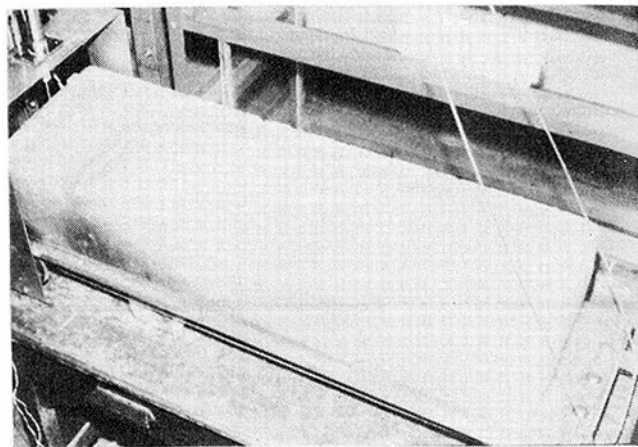**Fig. 1 Natural convection mass transfer apparatus**

Fig. 2 Mounted salt test sample

into which the more saturated brine from the bottom of the test vessel could be slowly drained, and another elevated above the test vessel, containing brine at the desired concentration which drained into the test vessel to maintain a level allowed by a float control. Brine concentration leaving the bottom of the test vessel was monitored and flow rates could be adjusted to minimize stratification.

The solubility of air in water decreases with increasing salt concentration, and unless the bulk brine is deaerated, air will come out of solution at the salt-brine interface. This becomes more severe the lower the bulk brine concentration. In the early tests the water (or brine) was not deaerated and air bubbles were observed to develop and break away from the interface, though their population was quite low. For later tests the brine used was prepared from saturated brine (hence deaerated) diluted with deaerated water. In none of the tests


Nomenclature

$C_T(\theta)$, $C_T{}'(\theta)$ = coefficients for turbulent natural convection mass transfer

$$\frac{\mathrm{Sh}_x}{\left[\dfrac{g\Delta\rho x^3}{\rho\nu^2}\mathrm{Sc}\right]^{1/3}};$$

$$\frac{\mathrm{Sh}_x}{\left[\dfrac{g\cos\theta\Delta\rho x^3}{\rho\nu^2}\mathrm{Sc}\right]^{1/3}}$$

D = diffusion coefficient of transferred

species (L^2/T)

g = gravitational acceleration (L/T^2)

Gr_x = Grashof number, $g(\Delta\rho/\rho)\,x^3/\nu^2$ (dimensionless)

m = rate of surface recession (L/T)

Ra_H, Ra_M = $\mathrm{Gr}_H\cdot\mathrm{Pr}$ or $\mathrm{Gr}_M\cdot\mathrm{Sc}$ (dimensionless)

Sc = Schmidt number ν/D (dimensionless)

Sh_x = Sherwood number $\dfrac{mx}{D}\dfrac{\rho_s}{\Delta\rho}$ (dimensionless)

x = streamwise coordinate (L)

θ = plate angle to vertical, positive being upward facing or stable orientation (deg)

ν = kinematic viscosity (L^2/T)

ρ = density (M/L^3)

Subscript

H = refers to heat transfer

M = refers to mass transfer

s = salt

x = local position

Table 1 Salt dissolution data

Angle (degrees)	Sample (No.)	$\rho\infty$ g/c.c.	$T\infty$ °C	$m^{\ddagger}$ mm/hr	Sc $= \nu/D$ (dim)	$Gr^{\dagger}$ $\times 10^{-9}$ (dim)	$Sh^{\dagger}$ $\times 10^{-3}$ (dim)	Sh $\overline{(GrSc)^{1/3}}$ (dim)
+60	2	1.0	24	2.54	831	$1600x^3$	5.69x	0.0517
+60	5	1.14	17	1.04	944	$282x^3$	3.18x	0.0495
+45	2	1.0	24	3.63	831	$1600x^3$	3.77x	0.0342
+30	2	1.0	24	5.33	831	$1600x^3$	12.0x	0.109
+30	5	1.14	17	1.61	944	$282x^3$	10.65x	0.166
0	2	1.0	24	10.2	831	$1600x^3$	22.8x	0.207
0	4	1.0	29	11.1	831	$1600x^3$	24.9x	0.226
0	5	1.14	17	1.93	944	$282x^3$	12.8x	0.199
0	6	1.14	22	1.41	944	$282x^3$	9.32x	0.145
0	7	1.10	23	2.22	899	$588x^3$	9.2x	0.116
0	7	1.14	22	1.70	944	$282x^3$	11.25x	0.0722
0	8	1.18	24	0.29	1001	$81x^3$	5.28x	0.0665
0	9	1.10	24	2.87	899	$558x^3$	11.9x	0.150
0	10	1.10	28	3.18	899	$558x^3$	13.17x	0.166
−30	4	1.0	29	16.4	831	$1600x^3$	36.8x	0.334
−30	6	1.14	22	2.49	944	$282x^3$	16.5x	0.257
−45	4	1.0	29	18.0	831	$1600x^3$	40.5x	0.368
−60	8	1.14	23	2.9	944	$282x^3$	19.2x	0.299
−90	4	1.0	28	19.4*	831	$1600x^3$	43.4x	0.394
				22.4			50.2x	0.456

* The first is measurement with DCDT and the second by weight difference.
‡ These are averaged over the lower 90% of the sample.
† The streamwise coordinate x is retained because the quantities are averages over the sample. x measured in meters.
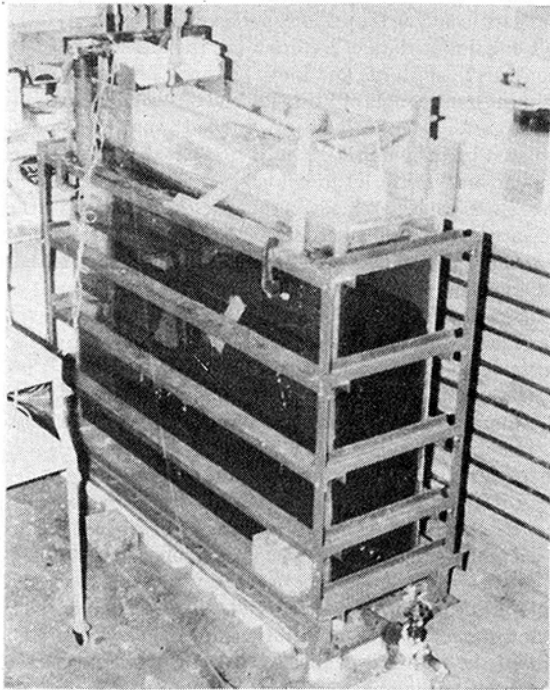
Fig. 3 Experimental test vessel

performed with water (S.G. = 1.0) was the water deaerated prior to test; however, for all subsequent tests the brine was deaerated. However, there was found to be no consistent effect of the air content of the water.

Experimental Data

Dissolution tests were conducted with water ($\rho = 1.0$) for several angles in the range from −90 to 60 deg to the vertical. In addition, tests were performed with brine ($\rho = 1.14$) at angles of +60, +30, 0, and −30 deg to the vertical, and also limited tests were made at specific gravities of 1.10 and 1.18. The approximate range of Sc for these measurements was 830–1000 based on mean boundary-layer concentration. This is approximately two to three orders of magnitude greater than the Prandtl number for typical fluids for which turbulent natural convection heat transfer data have been obtained. The values of Gr_M and Sh in this study ranged up to approximately 10^{12} and 4×10^4, respectively. Table 1 presents a summary of the present tests.

For most of the results to be reported herein, each new sample at the initiation of test was relatively smooth, that is, as cut using a large circular masonry saw; however, as dissolution progresses, the samples take on a rather rough character. This roughness development is apparently a result of several factors: the samples not being single crystal (having granular structure and inhomogeneity), erosion due to insolubles, and the nature of boundary layer flow. As a result, for each new sample the dissolution was allowed to progress until the dissolution rate appeared to approach a constant value, at which point three traverses at spaced time intervals would result in two sets of dissolution rate data over the entire length of the sample.

For these tests there were differences from sample to sample, and as a result normally three or more tests were run with each sample at different conditions (orientation or brine concentration); and for each new sample a test was conducted duplicating the conditions of a previous sample. In this way anomalous variations in dissolution rate from sample to sample could be interpreted.

The samples did not in general exhibit high dissolution rates at the forward edge as is characteristic of the laminar boundary layer, and this is attributed to impurity variations within each sample, as well as the fact that for most of the tests the critical Ra_M occurred quite early along the sample, such that few measurements occurred in what would normally be the laminar region. Therefore, these measurements do not provide useful information on the laminar regime or on transition. It should be noted that for the vertical orientation in water (S.G. = 1.0) and using the criterion of [2, 3] for incipient transition of $Ra_M = 2 \times 10^{11}$, it would normally occur approximately 0.07 m downstream of the leading edge. For the rough surfaces developed and for the unstable orientations, one would expect somewhat earlier transition, and thus the present data are applicable to turbulent flow, since sample lengths were approximately 1 m.

Some measured dissolution rates for different brine concentrations and orientations are presented in Figs. 4(a) and (b). The variation in the dissolution rate along the sample for any one test is obvious from these figures, some being greater than others, and the variation is attributed primarily to variations in the samples. The salt blocks obtained from the mine were cut (not intentionally) such that impurity (insoluble) seams ran across the samples at approximately 45
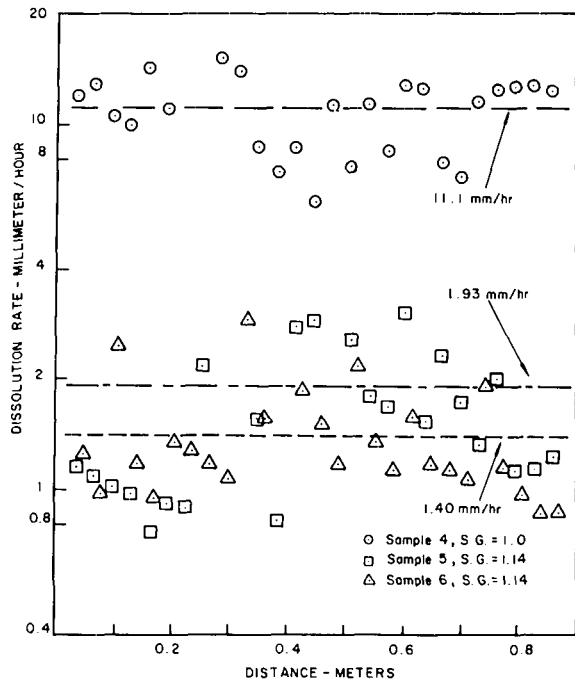
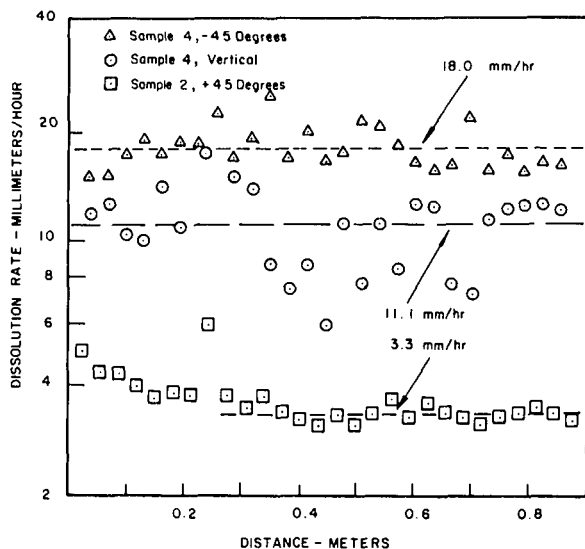**Fig. 4(a)** Dissolution rates for varying brine concentrations and vertical samples

Fig. 4(b) Dissolution rates for different orientations for fresh water (SG = 1.0)

deg, and thus on the exposed face of each sample there existed variations along the surface.

Fig. 4(a) shows vertical orientation dissolution rates for the two brine specific gravities 1.0 (water) and 1.14, using three different samples. One can see first the large effect of brine concentration on dissolution rate and also a significant difference in dissolution rate for the two sample numbers 5 and 6 at the same brine concentration. The latter is attributed to impurity variations between and throughout the samples.

Fig. 4(b) shows the variation in the dissolution rates for a particular brine concentration (S.G. = 1.0) at different angles. There is a monotonic increase in dissolution rate as the angle is varied from positive (stable, facing upward) angles through the vertical to negative (unstable, facing downward) angles.

The natural convection mass transfer data should correlate in the form $Sh_x = f(Gr_x \cdot Sc)$ with possibly an angle dependence $g \cdot \cos \theta$ introduced to form the component along the surface. This has been shown in many laminar heat and mass transfer investigations to be justified. However, for turbulent natural convection heat transfer [10, 13], it was found that no angle dependence is evident for the unstable case while even a stronger dependence than $\cos \theta$ is required for the stable case. Investigators [2, 3] used $g \cdot \cos \theta$ for all cases and introduced an angle-dependent coefficient $C_T'(\theta)$. Thus, for the turbulent case the present data are presented in the following forms:

$$Sh_x = C_T(\theta) \left[\frac{g \Delta \rho x^3}{\rho \nu^2} Sc \right]^{1/3} \qquad (1)$$

or

$$Sh_x = C_{T'}(\theta) \left[\frac{g \cos \theta \Delta \rho x^3}{\rho \nu^2} Sc \right]^{1/3} \qquad (2)$$

where the coefficients $C_T(\theta)$ and $C_{T'}(\theta)$ are functions of angle and an exponent of 1/3 is used as is customary for the turbulent region. The data correlation was not materially improved by altering the exponent from 1/3. In equation (1) the gravity is not modified, whereas in equation (2) it is modified by $\cos \theta$.

The dissolution data taken for various angles and brine concentrations are presented in Figs. 5 and 6. In Fig. 5 the data are plotted according to equation (1), while in Fig. 6 the data are plotted according to equation (2).

Also included in Figs. 5 and 6 are various other mass and heat transfer data including the salt dissolution data from the IITRI study [7], salt dissolution data of Saberian [1], the mass transfer data of Lloyd, et al. [2], of Moran and Lloyd [3], and of Fouad and Ibl [14], and the heat transfer data of Vliet [10], and of Vliet and Ross [13]. For the heat transfer data the Sherwood, Schmidt, and Grashof numbers are replaced by the Nusselt, Prandtl, and Grashof ($\beta \Delta T$ instead of $\Delta \rho / \rho$) numbers.[3] Durie [5] presents several measurements on approximately 18-cm high samples of square cross section, which exhibit coefficients $C_T(\theta)$ varying between 0.24 and 0.45. These are consistently greater than the data in Fig. 5 and this is attributed to the small cross sections (approximately 5 cm square) for these samples.

The present salt dissolution data in Figs. 5 and 6 (open symbols) show a generally monotonic decrease in the coefficient in going from the unstable to stable orientations. There is considerable scatter, which, however, is attributed mainly to sample variation. The test at −90 deg (horizontal, facing downward) was made with a smaller (0.28 m long) sample.

The present data are seen to agree quite well with the salt dissolution data of Saberian [1] for smaller samples (approximately 4 cm long by 3 cm wide), but extend over a larger range of orientations and include the positive (upward facing) angles. Some data from the IITRI study [7] are also presented. They generally fall somewhat below the present data, but show the same trend. A comparison of the IITRI data for different brine concentrations for the vertical orientation shows that the scatter is similar to that of the present data and is undoubtedly attributable to sample variations.

The mass transfer data of Lloyd, et al. [2], Moran and Lloyd [3], and Fouad and Ibl [14] are seen to fall well below the salt dissolution data. There is also seen to be a large difference between the heat transfer data of [10, 13] and the salt dissolution data. The same general trends with orientation for all the data are, however, similar.

In comparing the data presentations in Figs. 5 and 6 there appears to be no advantage in introducing $g \cos \theta$ in the turbulent natural convection correlation, since an angle-dependent coefficient is required in any case. Actually, it has the disadvantage of making the coefficient variation appear more severe, and in fact to be infinite at ±90 deg. Therefore, it is recommended that the $\cos \theta$ be omitted, and that the data presentation as in Fig. 5 be preferred for turbulent

---

[3] For the heat transfer data positive angles refer to surfaces facing downward (stable) and negative angles refer to surfaces facing upward (unstable).
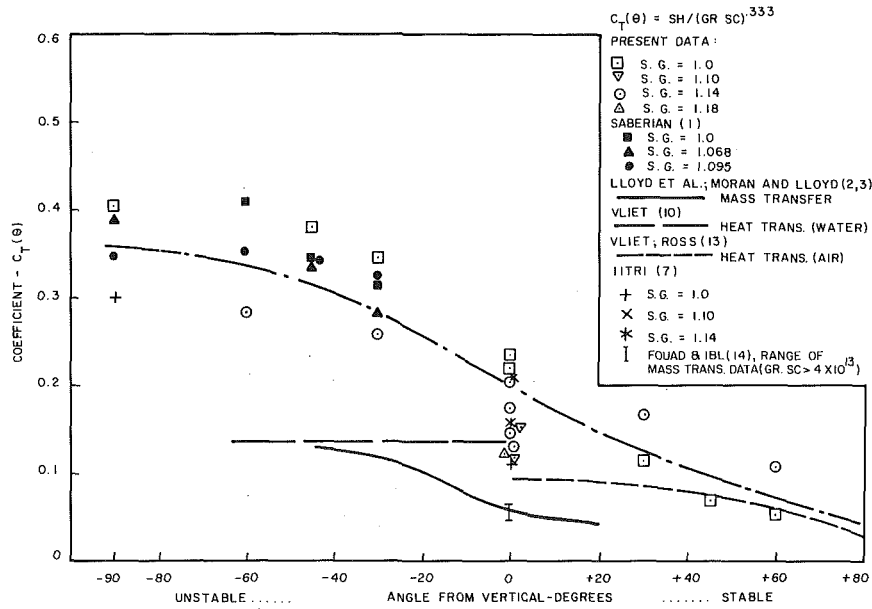
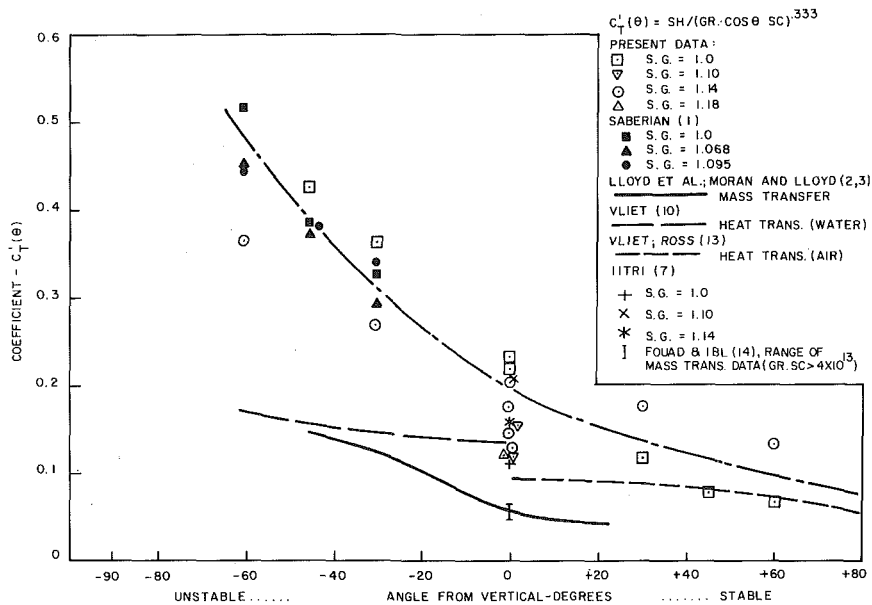**Fig. 5 Angle-dependent correlation coefficient**

Fig. 6 Angle-dependent correlation coefficient using cos θ

natural convection. Measurements were not extended beyond angles of +80 deg because in the limit of +90 deg the mass transfer would no longer be convection dominated.

The marked difference between the salt dissolution rate data versus the other heat and mass transfer data is interesting. In both the mass and heat transfer data [2, 3, 10, 13] the test surfaces are flat. In the salt dissolution data the surface after dissolution has progressed is rough and may, because of the scalloping of the surface, be significantly larger than the projected area. Thus, if the mass transfer coefficient were based on the actual surface area, the Sherwood number, and therefore $C_T(\theta)$, would be decreased, making the data more consistent. Detailed measurements were made of the surface roughness after selected tests using a depth micrometer. These indicated the actual surface area after dissolution to be approximately 10–15 percent greater than the projected area. Although this effect shifts the data in the correct direction, it does not greatly improve the agreement

between the present data and those for flat surfaces. The present data are thus not corrected for the actual surface area, but rather are based on the projected area.

Detailed measurements of the dissolution rate as a function of time were not recorded; however, the rates did generally increase with time. Durie's [5] measurements indicated that rates typically doubled between the initiation with a "smooth" sample and the final "developed" surface. The increased rates for salt dissolution are only partially explained by increased surface area, and the increase above the smooth sample rate is primarily attributed to the alteration of the boundary layer by the rough surface.

Conclusions

Salt dissolution data as a function of brine concentration and surface orientation in the turbulent regime are presented which indicate that the data correlate reasonably well in the form Sh $= C_T(\theta)$

$[\mathrm{Gr}_M \cdot \mathrm{Sc}]^{1/3}$ as has been previously suggested, though it is recommended that for the turbulent regime the gravity not be modified by angle. The present data agree reasonably well with other less extensive salt dissolution data, but exhibit significantly larger dimensionless transfer coefficients than other turbulent natural convection mass and heat transfer data for flat smooth surfaces. This is partially attributable to the actual surface being greater than the projected area but is mainly a result of an alteration of the boundary layer by the roughness which enhances the convection coefficient.

Acknowledgment

References

1 Saberian, A., "Numerical Simulation of Development of Solution-Mined Storage Cavities," PhD dissertation, University of Texas, Austin, Aug. 1974.

2 Lloyd, J. R., Sparrow, E. M., and Eckert, E. R. G., "Laminar, Transition and Turbulent Natural Convection Adjacent to Inclined and Vertical Surfaces," *International Journal of Heat and Mass Transfer*, Vol. 15, No. 3, Mar. 1972, pp. 457–474.

3 Moran, W. R., and Lloyd, J. R., "Natural Convection Mass Transfer Adjacent to Vertical and Downward-Facing Inclined Surfaces," JOURNAL OF HEAT TRANSFER, TRANS. ASME, Series C, Vol. 97, No. 3, Aug. 1975, pp. 472–474.

4 Wilke, C. R., Tobias, C. W., and Eisenberg, M., "Free Convection Mass Transfer at Vertical Surfaces," *Chem. Eng. Prog.*, Vol. 49, No. 12, Dec. 1953, pp. 663–674.

5 Durie, R. W., "Mechanism of the Dissolution of Salt in the Formation of Underground Salt Cavities," MS thesis, University of Texas, Austin, Tex., June 1962.

6 Durie, R. W., "The Boundary Region in the Salt Dissolution Process," PhD dissertation, University of Texas, Austin, Aug. 1973.

7 "Solution Mining Studies," Illinois Institute of Technology Research Institute (IITRI) Report No. IITRI-C8071-7, Apr.–June 1967.

8 Masliyah, J. H., and Nguyen, T., "Free Convection Mass Transfer: Laminar and Turbulent," *International Journal of Heat and Mass Transfer*, Vol. 18, 1975, pp. 1443–1447.

9 Husband, W. H. W., "Mass Transfer From High Vertical Surfaces to Liquids Under Free Convection Conditions," PhD dissertation, University of Saskatchewan, 1969.

10 Vliet, G. C., "Natural Convection Local Heat Transfer on Constant-Heat-Flux Inclined Surfaces," JOURNAL OF HEAT TRANSFER, TRANS. ASME, Vol. 91, No. 4, Nov. 1969, pp. 551–571.

11 Fugii, T., and Imura, H., "Natural Convection Heat Transfer from a Plate with Arbitrary Inclination," *International Journal of Heat and Mass Transfer*, Series C, Vol. 15, No. 4, May 1972, pp. 755–767.

12 Hassan, K., and Mohamed, S. A., "Natural Convection Heat Transfer from a Plate with Arbitrary Inclination," *International Journal of Heat and Mass Transfer*, Vol. 13, No. 12, Dec. 1970, pp. 1873–1886.

13 Vliet, G. C., and Ross, D. C., "Turbulent Natural Convection on Upward- and Downward-Facing Inclined Constant Heat Flux Surfaces," JOURNAL OF HEAT TRANSFER, TRANS. ASME, Series C., Vol. 97, No. 4, Nov. 1975.

14 Fouad, M. G., and Ibl, N., "Natural Convection Mass Transfer at Vertical Electrodes Under Turbulent Flow Conditions," *Electrochimica Acta*, Vol. 3, p. 233, 1960.

H. J. Nawoj
R. S. Hickman

University of California,
Santa Barbara, Calif.
Mem. ASME

An Experimental Investigation of the Plume Velocity Field Above a Horizontal Line Heat Source

The vertical velocity field of a natural convection plume arising from a horizontal line heat source was investigated experimentally in detail. The measured vertical velocities were found to be 20–25 percent less than that predicted by analysis. Various causative factors for the discrepancy between analytical and experimental results were investigated, and shown to have a minimal effect. The power law relationship between the plume vertical velocity and energy input to the line source was found to be substantially greater than that predicted by analysis. A normalized similarity function did provide an excellent representation of the lateral diffusion of energy and momentum in the plume, indicating the validity of the boundary layer approximation for the velocity field. It was postulated that further refinement of the stream functions defined by existing analyses is required to accommodate the effects of the upstream flow field that exists in the physical representation of a line source and is omitted from consideration in the development of the analyses.

1 Introduction

Laminar natural convection plumes rising from a horizontal line heat source have been extensively investigated both analytically and experimentally. Analytical treatments rely on similarity solutions and are developed using simplified momentum and energy equations obtained by order-of-magnitude analysis of the general equations. Constant fluid properties are assumed, except that the Boussinesq approximation is used to accommodate density gradients, and the continuity equation is the final equation. The equations are:

$$\rho \left(u \frac{\partial u}{\partial x} + v \frac{\partial u}{\partial y} \right) = \rho g \beta \Delta t + \mu \frac{\partial^2 u}{\partial y^2} \tag{1}$$

$$u \frac{\partial t}{\partial x} + v \frac{\partial t}{\partial y} = \frac{k}{\rho c_p} \left[\frac{\partial^2 t}{\partial y^2} \right] \tag{2}$$

$$\frac{\partial u}{\partial x} + \frac{\partial v}{\partial y} = 0 \tag{3}$$

with spatial coordinates and velocity variables as defined by Fig. 1.

Gebhart, Pera, and Schorr [1] offered numerical solutions for a range of Pr between 0.01 and 100 and provided a compendium of previous solutions. Fujii, Morioka, and Uehara [2] offered refined numerical solutions for a range of Pr between 0.01 and 100 and, in addition, provided graphs for interpolation of the profiles for the vertical velocity component and temperature at arbitrary Pr. Both authors used a similarity variable of the form:

$$\eta = C_1 x^{-2/5} y \tag{4}$$

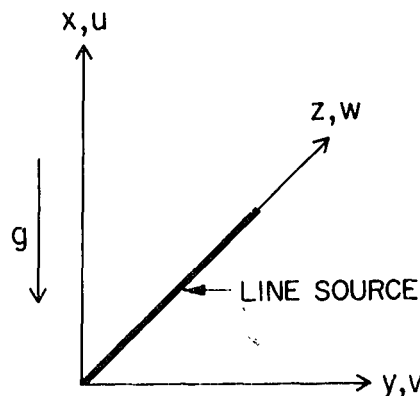a stream function of the form:

$$\psi = C_2 x^{3/5} f(\eta) \tag{5}$$

Fig. 1 Coordinate system for plume flows

---

[1] Numbers in brackets designate References at end of paper.

and a nondimensional temperature of the form

$$\frac{t - t_\infty}{\phi} = C_3 x^{-3/5} \qquad (6)$$

The vertical velocity component "u" was obtained from the stream function:

$$u = C_4 Q^{2/5} x^{1/5} f'(\eta) \qquad (7)$$

Using Fujii's values for C_1, C_2, and C_3, closed form solutions are reported for Pr of $\frac{5}{9}$ and 2, and the nondimensional profiles of the velocity and temperature are powers of hyperbolic functions. At other values of Pr, the profiles retain similar shapes. Using Gebhart's values for C_1, C_2, and C_3, no closed form solutions are reported. When the solutions given by each author are compared, they are essentially equivalent.

2 Existing Experimental Data of Plume Flow From Line Sources

The first known experimental data of natural convection plumes above line heat sources in liquids were reported by Schorr and Gebhart [3]. The data presented were temperature distributions in the plume measured interferometrically. Prior investigations had used air as the convective medium. These included experimentally determined velocity and temperature distributions by Brodowicz and Kierkus [4] and temperature distributions by Forstrom and Sparrow [5]. Experimentally determined temperature distributions in air and water and velocity distributions in water were reported by Lyakhov [6]. Similar temperature distributions for air, water, and a spindle oil of Pr $\approx$ 130-143 were reported by Fujii, Morioka, and Uehara.

Brodowicz and Kierkus used interferometry to measure temperature distributions and a streamline visualization technique to determine plume velocities. Their results showed fair agreement between experimental and analytical data for the vertical component of velocity with the experimental data consistently greater than the analytical prediction. The analytical prediction was based on Fujii's analysis. The horizontal velocity component showed poor correlation between the experimental data and the analytical prediction. The correlation of temperature profiles between the experimental data and the analytical predictions was poor. Brodowicz and Kierkus computed heat fluxes in the wake using experimental data and did achieve excellent correlation with the electrical energy input to the line source.

Forstrom and Sparrow's work, completed just after the publication of that of Brodowicz and Kierkus, presented only temperature distributions in the plume. Temperature measurements were made using a thermocouple mounted on a traversing mechanism. Their results showed that the experimental temperatures at the center line of the plume were 15 percent lower than that predicted by analysis. Normalized temperature profiles taken transversely through the plume showed excellent agreement with analytical predictions. They postulated the requirement for a virtual source to accommodate the finite thickness of the line source, and for their experimental configuration, determined the location of the virtual source as 0.083 in. below the actual wire. Also noted was a slow swaying of the plume.

Schorr and Gebhart conducted a series of plume experiments in a silicone liquid selected for its high electrical resistivity and its Prandtl number of 6.7. Only plume temperature distributions were measured, and these were determined interferometrically. Plume center-line temperatures were again 15-20 percent below those predicted from analysis, reinforcing the data shown by Forstrum and Sparrow and Brodowicz and Kierkus. The swaying motion of the plume in air, noted by Forstrom and Sparrow, was also observed in the silicone fluid by Schorr and Gebhart. The experimental normalized temperature distributions were in good agreement with the distributions predicted by analysis.

Since Brodowicz and Kierkus reported that the heat fluxes in the plume were equal to the heat input to the line source, Schorr and Gebhart noted that the end conduction effects were small and proposed that the discrepancy between the experimental and analytical data could be attributed to the existence of a flow component along the axis of the line source. The third dimension in the plume velocity would alter the temperature and velocity distributions in the flow from those predicted from similarity considerations.

Lyakhov reported good agreement between theory and measurement for the temperature and velocity distributions in both air and water. He attributed the agreement to the fact that his experimental apparatus provided closer conditions to those assumed for the analysis. He identified a virtual source at 0.12 cm below the wire center line for air, and at 0.07 cm for water. Lyakhov also pointed out that the boundary layer approximations used did not take into account the convective phenomena which must occur upstream of the line source.

Fujii, Morioka, and Uehara reported good agreement between theory and measurement of the temperature distributions for water and spindle oil at Gr $< 10^6$, fair agreement at Gr $> 10^6$, and consistently low measurements for temperature distributions in air. They attributed the difference between theory and data primarily to the swaying of the plume.

A recent paper by Goodman, Abauf, and Laufer [7] reported measurements of the velocity field in a free convection plume using laser Doppler anemometric techniques. The convective medium used was air with Pr of $\approx$0.7. The lateral diffusion of momentum, when normalized by the plume center-line velocity, was found to be in excellent agreement with the predictions of Gebhart's theoretical analysis, while the absolute value of the vertical velocity component was shown to be within 10 percent of that predicted by Gebhart's analysis. Decay of the plume velocity was noted near the end of the line source and was attributed to three-dimensional effects.

In this study, an experimental investigation of the velocity field of a free convection plume above a line source was conducted to determine the effects of using a convective medium with Pr substantially different than one and to investigate the three-dimensional effects developed by a line source of finite length.

3 Description of Experimental Apparatus

The experimental apparatus consisted of a transparent test tank constructed of Plexiglas with internal dimensions of 22.86 cm length by 19.69 cm width by 12.70 cm depth. A wall thickness of 1.91 cm was selected to minimize optical distortion due to fluid pressure and to minimize heat transfer through the walls of the tank. The surface of

---

Nomenclature

C = arbitrary constant

C_1 = similarity grouping defined by Fujii, et al., and Gebhart, et al.

C_2 = stream function grouping defined by Fujii, et al., and Gebhart, et al.

C_3 = temperature profile grouping defined by Fujii, et al., and Gebhart, et al.

C_4 = plume vertical velocity component grouping

C_p = specific heat of fluid

$f(\eta)$ = dimensionless stream function

$f'(\eta)$ = dimensionless vertical velocity component

g = gravitational acceleration

Gr, x = modified Grashof number defined by Gebhart, et al.

I = variable integral defined by Gebhart, et al.

k = thermal conductivity of the fluid

Pr = Prandtl number

Q = heat flux per unit length

t = fluid temperature

Δt = fluid temperature excess ($t - t_\infty$)

u, v = defined velocity components

x, y = defined spatial coordinates

β = volumetric temperature coefficient of fluid

η = dimensionless coordinate

μ = fluid viscosity

ρ = fluid density

ϕ = nondimensional temperature function

ψ = stream function

the liquid at the top of the tank was exposed to the atmosphere at all times.

A line source of heat located 2.22 cm above the tank base was simulated by an electrically heated Nichrome wire 11.73-cm long and 0.22 mm in diameter mounted between two cylindrical brass columns. A copper-constantan thermocouple was installed 0.95 cm below the line source and in its plane to measure the mean temperature in the undisturbed fluid. Distilled water was used as the test fluid, and the thermal power of the line source was determined from the electrical power supplied.

Velocity measurements in the flow field were made with a laser Doppler anemometer. The techniques of laser Doppler anemometry are well documented in the literature. A "dual beam" or differential anemometer was used for the experiments reported herein. The anemometer configuration precluded its movement to determine the flow field in the vicinity of the line heat source; accordingly, the entire test tank was mounted on a movable table capable of being traversed along three perpendicular axes.

The laser used was a Spectra Physics Model 120 HeNe laser with a nominal output of five mW in the TEM_{00} mode. A beam splitter divided the laser beam into two beams of approximately equal intensity. The split beams were passed through focusing biconvex lenses of 50-cm focal length and were brought to an intersection at the focal point of each lens. For the nominal case of having the point of beam intersection in the center of the test tank, the beam diameters were computed to be 0.28 and 0.43 mm for a normalized intensity of $1/e$.

The diagnostic volume of a differential anemometer for homodyning is the volume defined by the intersection of the two laser beams. The size of the diagnostic volume was approximated as a cylinder of diameter equal to the smaller beam spot diameter, and altitude determined by the large beam spot diameter and the angle of beam intersection. For the nominal spot diameters given in the previous section, the volume of the diagnostic volume was 2.6×10^{-5} cm^3.

The molecules of a fluid may be used, in principle, to act as the scattering centers for the generation of the Doppler signals in laser Doppler anemometry. Since the scattering cross section is proportional to the sixth power of the radius of the scatterer for particles with radius small compared to the wavelength of the incident beam, the intensity of molecular scattering is extremely low. Alternatives are to increase the intensity of the incident beam or to use scattering particles with radii significantly larger than the molecular radius. For the experiments reported here, spherical polystyrene latex particles were used with diameter of 0.71 microns and a refractive index of 1.59 at 6892 A. Particle concentrations used were between 20 and 50 scattering particles in the diagnostic volume.

The signal collection and processing system included a collector lens, a photomultiplier, amplifiers, a bandpass filter, and frequency analysis equipment. The photomultiplier output was amplified through two stages of amplification, passed through the bandpass filter to eliminate signals outside the frequency domain of interest, and thence analyzed with the spectrum analyzer.

The anemometer configuration used was such that a nominal flow velocity of 1 mm/s was equivalent to a Doppler signal frequency of 805 Hz. An anemometer calibration was conducted by traversing the test tank through the laser beam intersection at a known velocity. At a nominal velocity of 3 mm/s, the probable error was 1.38 percent. Representative samples of data points were checked for probable error; at a nominal flow velocity of 2 mm/s, the probable error varied between 0.81 and 2.31 percent, and at a nominal flow velocity of 1 mm/s, the probable error varied between 1.10 percent for data taken at the plume center line to 6.17 percent for data taken at the outer boundaries of the plume.

An error analysis of the anemometer was made, and the two primary sources of error identified were Doppler signal broadening due to velocity gradients within the diagnostic volume, and instrumental broadening in the spectrum analyzer due to the resolution bandwidth of the instrument. The swaying motion of the plume increased the dispersion of the individual measurements taken to develop a data point. This effect was minimized by requiring at least ten velocity

measurements for each data point, and also by making the measurement of the transverse velocity distribution of the plume relatively close to the source. The resolution bandwidth and the frequency stability of the spectrum analyzer also increased the dispersion of the individual measurements taken to develop a data point. A velocity of ≈ 0.5 mm/s was established as the minimum velocity for data recording purposes to minimize the effects of the resolution bandwidth of the analyzer, while the frequency drift of the analyzer was continuously monitored with a frequency counter and incorporated in the data reduction process.

4 Results and Discussion

Measurements were made of the transverse distribution of the vertical velocity in the plume. Measurements were taken at two elevations above the line source at the bisector of the line source. The results are shown in Fig. 2. Poor correlation exists between the predicted and measured values of the distribution of vertical velocity in the plume with the measured plume centerline velocities being approximately 20–25 percent less than the predicted velocities. When the data are normalized by their respective center-line velocities, excellent agreement exists between the predicted and measured values. This is shown in Fig. 3. When the measured velocities are expressed in terms of the nondimensional velocity of the analytical model, excellent agreement exists between the experimental measurements made at two elevations above the line source, but poor correlation exists between the analytical prediction and the experimental measurements. The results are given in Fig. 4. Of interest is the breadth of the plume for which boundary layer theory appears applicable. Although the nominal limit of applicability of boundary layer theory is $\delta/x \ll 1$, excellent correlation existed between predicted and measured normalized velocities to $\delta/x \approx 0.5$.

A series of velocity measurements was taken to determine the variation of the plume center-line velocity along the span of the line source to investigate three dimensional effects upon the plume flow
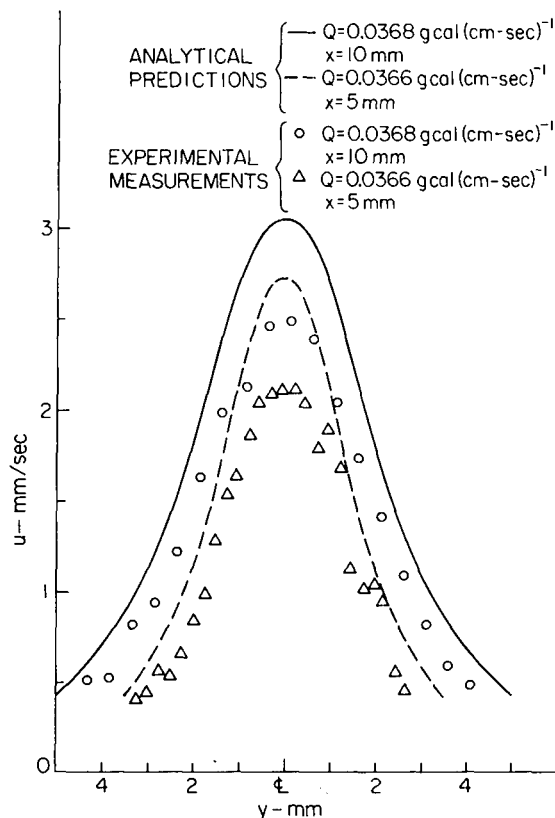

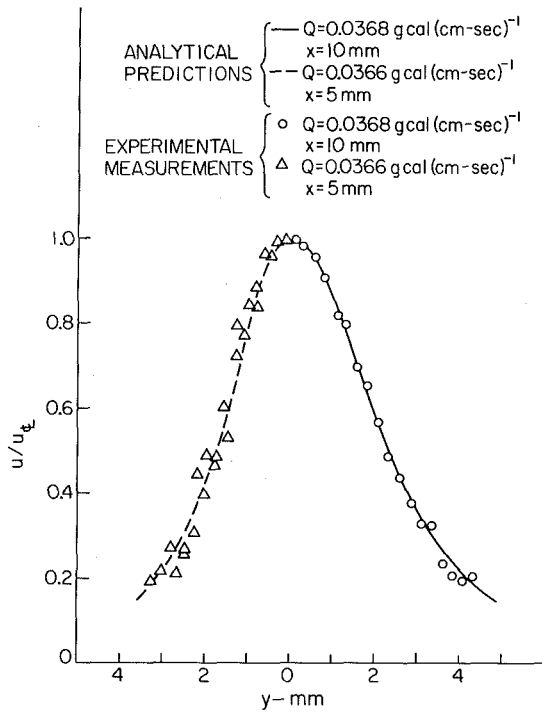Fig. 2 Transverse profiles of plume vertical velocities above a line source

Fig. 3 Transverse profiles of normalized plume vertical velocities above a line source

field. Three-dimensional effects were found to be limited to the outer 10 percent of the semispan of the line source. The results, normalized by the mean of the velocities observed over the inner 80 percent of the semispan are given in Fig. 5. Thus, the ℓ/d effects for the experimental configuration used, $\ell/d = 533$, were considered negligible, since all velocity measurements were made at the bisector of the line source. This was substantiated by the results reported by Schorr and Gebhart and Brodowicz and Kierkus.

Another series of velocity measurements was made in the vertical plane containing the line source at a fixed distance above the source. Energy input to the line source was varied over a range of Gr, x of 1.85 $\times 10^3$ to 1.62×10^4. The plume flow was laminar throughout the range of energy input since the highest Gr, x was three orders of magnitude less than the transition point to turbulent flow observed by Forstrom and Sparrow. The data are shown in Fig. 6. Using Gebhart's formulation, and writing the equation in a logarithmic form, equation (7) may be written as:

$$\log u = \log (C_4 x^{1/5} f') + \tfrac{2}{5} \log Q \qquad (8)$$

This guided the regression analysis, and the equation of the line of regression for the experimental data was:

$$\log u = 1.311 + 0.536 \log Q \qquad (9)$$

The correlation coefficient for the line of regression was 0.993. In its antilogarithmic form, the equation was:

$$u = 20.445 Q^{0.536} \text{mm/s} \qquad (10)$$

This equation was tested against the experimental data using a chi square test and found satisfactory at the 99 percent level of significance.

The discrepancy in the power law relationship between the plume vertical velocity and the energy input to the line source may be attributed to experimental errors, the existence of three-dimensional flow, the deviation of the fluid properties from the constant property assumption, conduction end effects, the requirement for a virtual source to accommodate an experimental line source of finite dimension, and the assumptions and idealizations made in the analyses.

The assumptions and idealizations made in the analyses are the typical boundary layer assumptions, i.e., that the y components of the velocity field of the plume are sufficiently small that they may be neglected, and that the upstream effects of the line source may be neglected. Brodowicz and Kierkus provided experimental confirmation that the y components of the plume flow field were an order of magnitude less than the x components of the flow field. Lyakhov did investigate the effects of the idealizations of the analyses, and found that, if the upstream flows were blocked, then excellent agreement existed between experiment and theory in the measurement of the temperature fields.

The influence of experimental errors upon the determination of the power law relationship was minimal. Velocity measurements were primarily affected by errors arising from the determination of the geometry of the dual beams, and the interpretation of the frequency analyses. Both errors tended to have a constant value, and, on a logarithmic plot, would not affect the determination of the slope. Energy measurements were made by determining the electrical parameters of the line source, and the maximum error was in the order of 0.55 percent.

Fand and Keswani [8] showed that stratification effects were minimal for the experimental geometry used, while the analyses of both Fujii and Gebhart indicated that the influence of variable fluid properties was negligible upon plume centerline velocities. Schorr and Gebhart's analysis showed that end conduction from the line source had negligible effect on the temperature field of a plume.

Forstrom and Sparrow suggested that a virtual source was required to accommodate the divergence of the plume flow from ideal due to the finite diameter of the wire used to similate the line source, and were able to predict the location of the virtual line source by extrapolation of their experimental data. Using Schlieren photography, Schorr and Gebhart confirmed that the plume origin was below the wire source, and suggested two experimental techniques for location of the virtual source, since the extrapolation of their experimental data gave ambiguous locations for the virtual source.

Attempts were made to measure vertical velocity below the line source using laser Doppler anemometry, and though vertical motion was readily discernible, the very small velocities resulted in Doppler frequencies below the lower limits of available frequency analysis equipment.

The concept of a virtual source was investigated to determine if it could be used to accommodate the effects of the idealization used in
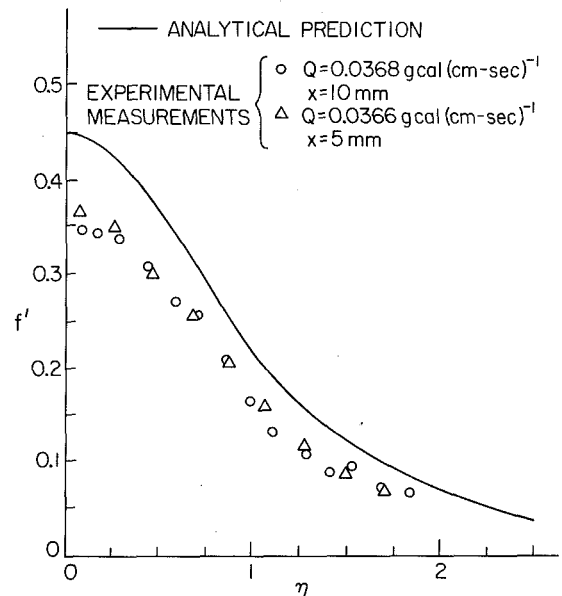

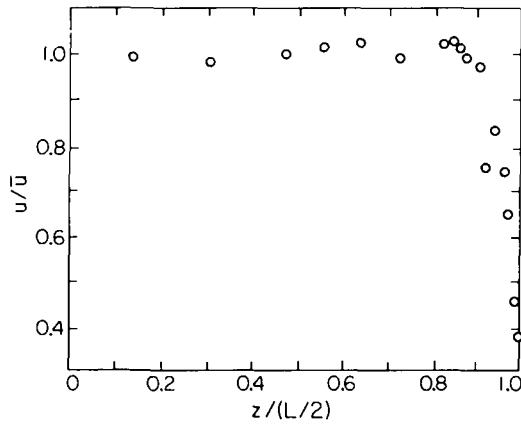**Fig. 4 Nondimensional transverse profiles of plume vertical velocities above a line source**

Fig. 5 Variation of the normalized plume center-line velocity along the semi span of a line source
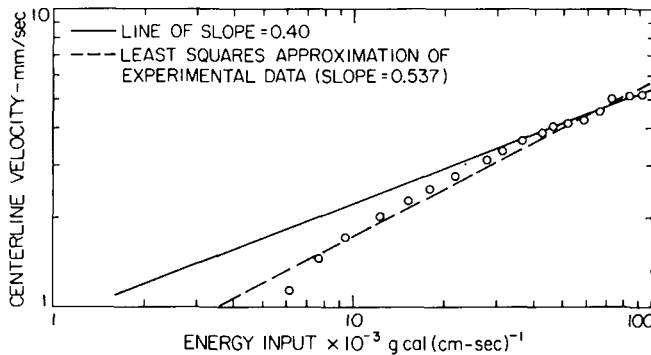

Fig. 6 Variation of plume center-line velocity above a line source

$$f(Q) = C \left(\frac{\mu}{C_p g}\right)^{1/3} \left(\frac{1}{\rho k}\right)^{2/3} \beta Q \qquad (12)$$

where C is an arbitrary multiplier. Substituting into equation (11) and expanding the bracket in a Taylor series, the variation of vertical velocity with energy input becomes, to the first approximation:

$$u = \left[\left(\frac{4}{\rho\mu}\right)^{1/2} \frac{g\beta Q}{C_p I}\right]^{2/5} x'^{1/5} f'$$
$$+ C\left[\left(\frac{4}{\rho\mu}\right)^{1/2} \frac{g\beta Q}{C_p I}\right]^{1/5} \left[\left(\frac{\mu}{C_p g}\right)^{1/3} \left(\frac{1}{\rho k}\right)^{2/3} \frac{\beta Q f'}{x'^{4/5}}\right] \quad (13)$$

Comparing equations (7) and (13), it is apparent that the inclusion of an additional term to accommodate a virtual source destroys the power law relationship that exists in the original analysis, and the corresponding logarithmic form of the equation loses its linearity. The high correlation coefficient obtained in the regression analysis of the experimental data strongly suggests that the logarithmic data were linear, and that the power law relationship between velocity and energy input to the line source was valid.

Accordingly, it is postulated that the stream functions defined by Gebhart, et al., and Fujii, et al., require further refinement to accommodate the effects of the upstream flow before the functions can be used to predict the velocities in a plume flow field. The normalized similarity function does provide an excellent representation of the lateral diffusion of energy and momentum in the plume flow field.

References

1 Gebhart, B., Pera, L., and Schorr, A. W., "Steady Laminar Natural Convection Plumes Above a Horizontal Line Heat Source," *International Journal of Heat and Mass Transfer*, Vol. 13, 1970, pp. 161–171.

2 Fujii, T., Morioka, I., and Uehara, H., "Buoyant Plume Above a Horizontal Line Source," *International Journal of Heat and Mass Transfer*, Vol. 16, 1973, pp. 755–768.

3 Schorr A. W., and Gebhart, B., "An Experimental Investigation of Natural Convection Wakes Above a Line Heat Source," *International Journal of Heat and Mass Transfer*, Vol. 13, 1970, pp. 557–571.

4 Brodowicz K., and Keirkus, W. T., "Experimental Investigation of Laminar Free Convection Flow in Air Above a Horizontal Wire With Constant Heat Flux," *International Journal of Heat and Mass Transfer*, Vol. 9, 1966, pp. 81–94.

5 Forstrom R. J., and Sparrow E. M., "Experiments on the Buoyant Plume Above a Heated Horizontal Wire," *International Journal of Heat and Mass Transfer*, Vol. 10, 1967, pp. 321–331.

6 Lyakhov, Yu. N., "Experimental Investigation of Free Convection Above a Heated Horizontal Wire," *J. Appl. Mech., Tech. Phys.* Vol. III, 1970, pp. 355–359.

7 Goodman, J., Abauf, N., and Laufer, G., "Investigation of the Velocity Field in a Free Convection Plume Using a Laser Doppler Velocity Measuring Technique," *Isr. J. Tech.*, Vol. 12, 1974, pp. 198–205.

8 Fand, R. M., and Keswani, K. K., "Mass Rate of Flow in the Natural Convection Plume above a Heated Horizontal Cylinder Immersed in a Liquid," JOURNAL OF HEAT TRANSFER, TRANS. ASME, Series C, Vol. 95, 1973, pp. 192–198.

the analysis of plume flow above a line source. Since the location of the virtual source must be a function of the energy input to the source, equation (7) may be modified to:

$$u = \left[\left(\frac{4}{\rho\mu}\right)^{1/2} \frac{g\beta Q}{C_p I}\right]^{2/5} [x' + f(Q)]^{1/5} f' \qquad (11)$$

where x' is defined as the distance from the center line of the wire, $f(Q)$ is the increment to x' needed to locate the virtual source, and Gebhart's formulation is used. Using dimensional arguments, one form of $f(Q)$ may be given as:

H. Miyazaki

E. M. Sparrow

Department of Mechanical Engineering,
University of Minnesota,
Minneapolis, Minn.

Analysis of Effects of Free-Stream Turbulence on Heat Transfer and Skin Friction

A model for the momentum eddy diffusivity induced by free-stream turbulence was constructed on the basis of measured turbulent velocity fluctuations. The thermal eddy diffusivity was obtained via the turbulent Prandtl number. The general eddy diffusivity model was applied at the stagnation point of a cylinder situated in a uniform crossflow. The expression for the eddy diffusivity contains a single unknown constant which was determined from experimental stagnation point heat transfer results. Nusselt numbers and friction factors were evaluated from solutions of the governing conservation equations, and comparisons were made with available data and other predictions. The present analytical results agree well with the data and exhibit a behavior whereby, in concert with the data, the Nusselt number (and friction factor) increases with the free-stream turbulence intensity but to a lesser extent as the turbulence intensity increases. The effect of free-stream turbulence on the friction factor is shown to be substantially less than the effect on the Nusselt number.

Introduction

It is known that free-stream turbulence augments the rate of heat transfer significantly in flows with large streamwise pressure gradients. Extensive experimental investigations have been conducted to examine the free-stream turbulence effects on heat transfer from a cylinder in a uniform crossflow as reported in [1–8].[1]

This problem has also been treated analytically by several investigators. Sutera, et al. [9] and Sutera [10] simulated the free-stream turbulence by a distributed vorticity in the free stream and showed that the stretching of the vorticity component parallel to the surface caused a substantial increase in the heat-transfer rate, while the increase in the wall friction was relatively small. This theory provides a qualitative explanation of the phenomenon but, because the free-stream vorticity was not related to the turbulence intensity, it does not enable an independent prediction of the heat transfer augmentation. Further elucidation of the mechanism by which the presence of the vortices affects the heat transfer has been provided by Kestin and Wood [11–13], but quantitative prediction of the augmentation remains to be accomplished.

Smith and Kuethe [4] employed a more direct approach and pos-

tulated an expression for the eddy diffusivity induced by the free-stream turbulence. Their model of the eddy diffusivity involves an unknown constant, which was determined from their experimental data. Galloway [14] attempted to provide a rationale for Smith and Kuethe's eddy diffusivity model. He also proposed a model of his own on the assumption that the heat transfer in the presence of free-stream turbulence is enhanced by Goertler vortices. Galloway employed his own data for evaluating unknown constants that appear in these models. He compared the thus obtained analytical predictions with his own data for the stagnation point Nusselt number, but the agreement is not satisfactory. Moreover, his curve for the Nusselt number obtained by using exactly the same eddy diffusivity model as that of Smith and Kuethe is significantly different from theirs.

The recently published paper by Traci and Wilcox [15] begins propitiously by including a two-equation model of turbulence along with the other conservation equations. In order to complete the analysis, use was made of empirical information from the experiments of Smith and Kuethe [4]. Furthermore, owing to the complexity of the analysis, certain simplifying assumptions and operations were introduced in order to facilitate the obtaining of solutions. By employing a similarity-type solution, they evaluated the Nusselt number and friction factor at the stagnation point of a cylinder in a uniform crossflow.

The objective of the present investigation is to formulate a model for the eddy diffusivity induced by free-stream turbulence using as a basis the empirical formula of Belov, et al. [16] for the local turbulent velocity fluctuations in the boundary layer. The general eddy diffusivity model will be applied at the stagnation point of a cylinder in

---

a uniform crossflow, and the Nusselt number and friction factor will be evaluated as functions of free-stream turbulence intensity by solving the relevant conservation equations. Comparison will be made with available analytical and experimental results.

Model of Eddy Diffusivity

Available experiments show that free-stream turbulence has large effects on boundary-layer flow, on both the time-averaged and fluctuating velocities. It is, however, a difficult task to formulate the effects of free-stream turbulence in a manner that can serve as an input to an analysis of the boundary layer. Since a fully predictive theory of turbulence is not yet available, it is necessary to depend on experimental findings to some extent. The present eddy diffusivity formulation makes use of experiments of Belov, et al. [13].

They obtained an empirical formula for the root-mean-square streamwise velocity fluctuations for the boundary layer over a flat plate, which is given by

$$\langle u' \rangle = \ell^* \frac{\partial u}{\partial y} + \langle u_\infty' \rangle \frac{y}{\delta} \tag{1}$$

Here, $\langle \ \rangle$ represents root-mean-square, and ℓ^* is a modified mixing length which is defined by

$$\ell^* = \ell \left\{ 1 - \exp\left(-2.5 \frac{\mathrm{Re}_x}{\mathrm{Re}_{x*}}\right) \right\} \tag{2}$$

We generalize the modified mixing length such that it is also applicable to a flow with a stagnation region. For this purpose, we alter the term $\mathrm{Re}_x/\mathrm{Re}_{x*} = x/x^*$ to $(x + x_0)/(x^* + x_0) = (\mathrm{Re}_x + \mathrm{Re}_0)/(\mathrm{Re}_{x*} + \mathrm{Re}_0)$, where x_0 is similar to an effective origin. Then,

$$\ell^* = \ell \left\{ 1 - \exp\left(-2.5 \frac{\mathrm{Re}_x + \mathrm{Re}_0}{\mathrm{Re}_{x*} + \mathrm{Re}_0}\right) \right\} \tag{3}$$

ℓ in equation (3) is the conventional mixing length without the effects of free-stream turbulence. Belov et al. used

$$\ell = \begin{cases} 0.4\, y \left\{ 1 - \exp\left(-\dfrac{y\sqrt{\tau_w/\rho}}{27\nu}\right) \right\} & \text{for } 0 \le y/\delta \le 0.225 \\ 0.09\delta & \text{for } 0.225 < y/\delta \le 1 \end{cases} \tag{4a}$$

where δ is defined by the distance from the wall where the streamwise velocity reaches 99 percent of the free-stream velocity. In Van Driest's damping factor, 26 is usually used for the empirical constant in the argument of the exponential function. However, Belov, et al. used 27 to derive the empirical representation (1).

The use of the damping factor is an accepted improvement of the mixing length representation for flow over a flat plate. The form of the damping factor which appears in (4a) is based on the assumption that the propagation velocity of the fluctuations is proportional to the friction velocity. However, at the stagnation point, the shear stress and the friction velocity vanish, and this assumption does not hold. Therefore, for an analysis at the stagnation point, the damping factor

has to be omitted, since otherwise it gives the erroneous result that $\ell = 0$.

In support of such an omission of the damping factor, attention may be called to the fact that Belov, et al. employed an alternative to (4a) to represent the mixing length, namely,

$$\ell/\delta = 0.4\,(y/\delta) - 0.59\,(y/\delta)^2 + 0.26\,(y/\delta)^3 \tag{4b}$$

They evaluated $\langle u' \rangle = \ell\,(\partial u/\partial y)$ using (4a) and (4b) along with experimentally determined values of $(\partial u/\partial y)$, and found almost identical results. Further, the present authors evaluated the stagnation point Nusselt number, employing both equation (4a) without the damping factor and equation (4b). The extreme difference in the Nusselt numbers was found to be a few percent, so that the elimination of the damping factor from the mixing length does not have a significant impact on the results at the stagnation point.

Now, we assume that the representation (1) also holds in terms of time-dependent variables, i.e.,

$$u' = \ell_x^{*\prime} \frac{\partial u}{\partial y} + u_\infty' \frac{y}{\delta} \tag{5}$$

Likewise, for the y-component of the fluctuating velocity

$$v' = \ell_y^{*\prime} \frac{\partial u}{\partial y} + v_\infty' \frac{y}{\delta} \tag{6}$$

The quantities $\ell_x^{*\prime}$ and $\ell_y^{*\prime}$ are, respectively, the time-dependent x and y components of the modified mixing length. Their relationship to the time-averaged modified mixing length ℓ^* in equation (3) will be defined shortly.

We take the product of u' and v', and its time average becomes

$$\overline{u'v'} = \overline{\ell_x^{*\prime}\ell_y^{*\prime}} \left|\frac{\partial u}{\partial y}\right| \frac{\partial u}{\partial y} + \overline{\ell_y^{*\prime}u_\infty'} \frac{y}{\delta} \frac{\partial u}{\partial y}$$
$$+ \overline{\ell_x^{*\prime}v_\infty'} \frac{y}{\delta} \frac{\partial u}{\partial y} + \overline{u_\infty'v_\infty'} \left(\frac{y}{\delta}\right)^2 \tag{7}$$

Since it is a conventional assumption that $\overline{|\ell_x^{*\prime}|} \sim \overline{|\ell_y^{*\prime}|}$ and $\overline{|u_\infty'|} \sim \overline{|v_\infty'|}$, equation (7) is reduced to

$$\overline{u'v'} = -\ell^{*2} \left|\frac{\partial u}{\partial y}\right| \frac{\partial u}{\partial y} - A\ell^* \overline{|u_\infty'|} \frac{y}{\delta} \frac{\partial u}{\partial y} + \overline{u_\infty'v_\infty'} \left(\frac{y}{\delta}\right)^2 \tag{8}$$

The negative signs on the right-hand side of equation (8) are due to the fact that $\overline{u'v'}$ is always negative when the time-averaged velocity u is an increasing function of y. ℓ^* is defined by $\ell^* = (\overline{\ell_x^{*\prime}\ell_y^{*\prime}})^{1/2}$ on the assumption that $\overline{|u'|} \sim \langle u' \rangle$. The quantity A is an empirical constant which is equal to two when the turbulence is homogeneous and isotropic.

We restrict ourselves to the case that the free-stream turbulence is homogeneous and isotropic. This is realized in the turbulence produced by grids, screens, jets, etc., at locations sufficiently downstream from the turbulence promoters. Then, the last term in equation (8) vanishes, and using the relation $\overline{-u'v'} = \epsilon_m \partial u/\partial y$, we get

---

Nomenclature

A = empirical constant in equation (9)
B = empirical constant
C = stagnation point velocity gradient
C_f = friction factor, $\tau_w/(\frac{1}{2}\rho u_\infty^2)$
d = cylinder diameter
e = constant of proportionality in ϵ_m models of [4, 14]
ℓ = mixing length
ℓ_r = representative length, $\ell_r = d$ for cylinder
ℓ^* = modified mixing length, equation (3)
L = dimensionless mixing length ℓ/ℓ_r
Nu = Nusselt number, $(h\ell_r)/k$
Pr_t = turbulent Prandtl number, ϵ_m/ϵ_h
q = heat flux

Re = Reynolds number, $(u_\infty \ell_r)/\nu$
Re_o = Reynolds number, $(u_\infty x_o)/\nu$
Re_x = local Reynolds number, $(u_\infty x)/\nu$
Re_{x*} = transition Reynolds number, $(u_\infty x^*)/\nu$
Re' = turbulence Reynolds number, $(\langle u_\infty' \rangle \ell_r)/\nu$
T = dimensionless temperature, $(t - t_w)/(t_\infty - t_w)$
t = temperature
U_s = dimensionless velocity, u_s/u_∞
u, v = velocity components
u_s = free-stream velocity
X, Y = dimensionless coordinates, x/ℓ_r, y/ℓ_r

x, y = coordinates
x_o = effective origin
x^* = transition point
α = thermal diffusivity
δ = boundary-layer thickness
ϵ_m, ϵ_h = momentum and thermal eddy diffusivities, respectively
η_m = value of η at $y = \delta$
τ = shear stress
τ_w = wall shear stress

Subscript
∞ = ambient

$$\epsilon_m = \ell*^2 \left|\frac{\partial u}{\partial y}\right| + A\ell* \langle u_\infty'\rangle \frac{y}{\delta} \qquad (9)$$

In order to obtain the thermal eddy diffusivity, we introduce the turbulent Prandtl number defined by $\mathrm{Pr}_t \equiv \epsilon_m/\epsilon_h$. Then, the shearing stress and heat flux are given by

$$\left.\begin{array}{l} \tau = \rho(\nu + \epsilon_m)\partial u/\partial y \\ q = -\rho c_p(\alpha + \epsilon_m/\mathrm{Pr}_t)\partial t/\partial y \end{array}\right\} \qquad (10)$$

Analysis

The boundary layer equations of continuity, momentum, and energy are given by

$$\left.\begin{array}{c} \dfrac{\partial u}{\partial x} + \dfrac{\partial v}{\partial y} = 0 \\[2mm] u\dfrac{\partial u}{\partial x} + v\dfrac{\partial u}{\partial y} = u_s\dfrac{du_s}{dx} + \dfrac{\partial(\tau/\rho)}{\partial y} \\[2mm] u\dfrac{\partial t}{\partial x} + v\dfrac{\partial t}{\partial y} = -\dfrac{\partial(q/\rho c_p)}{\partial y} \end{array}\right\} \qquad (11)$$

which are subject to the boundary conditions

$$\begin{array}{ll} u = v = 0 \quad \text{and} \quad t = t_w \quad \text{at} \quad y = 0 \\ u \to u_s \quad \text{and} \quad t \to t_\infty \quad \text{as} \quad y \to \infty \end{array} \qquad (12)$$

We introduce the Goertler transformation for nondimensionalization of equations (11)

$$\xi = \frac{1}{\ell_r u_\infty}\int_0^x u_s(x)dx = \int_0^X U_s(X)dX$$

$$\left.\eta = \frac{u_s(x)y}{\left\{2\nu\displaystyle\int_0^x u_s(x)dx\right\}^{1/2}} = \frac{\sqrt{\mathrm{Re}}\,U_s(X)Y}{\left\{2\displaystyle\int_0^X U_s(X)dX\right\}^{1/2}} = \frac{\sqrt{\mathrm{Re}}\,U_s(X)}{\sqrt{2\xi}}Y\right\}$$

$$(13)$$

The further introduction of the dimensionless stream function

$$F(\xi, \eta) = \frac{\psi(x, y)}{\left\{2\nu\displaystyle\int_0^x u_s(x)dx\right\}^{1/2}} = \sqrt{\mathrm{Re}}\,\frac{\Psi(X, Y)}{\sqrt{2\xi}} \qquad (14)$$

and substitution of τ from equations (10) into the second of equations (11) yields the following nondimensional equation of momentum:

$$\frac{\partial}{\partial\eta}\left\{\left(1 + \frac{\epsilon_m}{\nu}\right)\frac{\partial^2 F}{\partial\eta^2}\right\} + F\frac{\partial^2 F}{\partial\eta^2} + \beta(\xi)\left\{1 - \left(\frac{\partial F}{\partial\eta}\right)^2\right\}$$
$$= 2\xi\left(\frac{\partial F}{\partial\eta}\frac{\partial^2 F}{\partial\xi\partial\eta} - \frac{\partial F}{\partial\xi}\frac{\partial^2 F}{\partial\eta^2}\right) \qquad (15)$$

where

$$\beta(\xi) = \frac{2\left\{\displaystyle\int_0^X U_s(X)dX\right\}dU_s/dX}{U_s^2} = \frac{2\xi(dU_s/d\xi)}{U_s} \qquad (16)$$

$$\frac{\epsilon_m}{\nu} = \left\{1 - \exp\left(-2.5\frac{\mathrm{Re}_x + \mathrm{Re}_0}{\mathrm{Re}_{x*} + \mathrm{Re}_0}\right)\right\}^2 \mathrm{Re}^{3/2}\frac{U_s^2}{\sqrt{2\xi}}L^2\left|\frac{\partial^2 F}{\partial\eta^2}\right|$$
$$+ A\left\{1 - \exp\left(-2.5\frac{\mathrm{Re}_x + \mathrm{Re}_0}{\mathrm{Re}_{x*} + \mathrm{Re}_0}\right)\right\}\mathrm{Re}'L\frac{\eta}{\eta_m} \qquad (17)$$

Here, η_m is defined by the η value where the streamwise velocity in the boundary layer reaches 99 percent of the free-stream velocity u_s, and the dimensionless mixing length, L, is expressed by

$$L = \begin{cases} \dfrac{0.4\sqrt{2\xi}}{\sqrt{\mathrm{Re}}\,U_s}\eta DF & \text{for } 0 \le \eta/\eta_m \le 0.225 \\[3mm] 0.09\dfrac{\sqrt{2\xi}}{\sqrt{\mathrm{Re}}\,U_s}\eta_m & \text{for } 0.225 < \eta/\eta_m \end{cases} \qquad (18)$$

where DF is the transformation of the damping factor of equation (4a). Equation (15) is subject to the boundary conditions

$$\left.\begin{array}{ll} F = \partial F/\partial\eta = 0 & \text{at} \quad \eta = 0 \\ \partial F/\partial\eta \to 1 & \text{as} \quad \eta \to \infty \end{array}\right\} \qquad (19)$$

Using q from equations (10), the equation of energy (11) is transformed to

$$\frac{\partial}{\partial\eta}\left\{\left(\frac{1}{\mathrm{Pr}} + \frac{1}{\mathrm{Pr}_t}\frac{\epsilon_m}{\nu}\right)\frac{\partial T}{\partial\eta}\right\} + F\frac{\partial T}{\partial\eta} = 2\xi\left(\frac{\partial F}{\partial\eta}\frac{\partial T}{\partial\xi} - \frac{\partial F}{\partial\xi}\frac{\partial T}{\partial\eta}\right) \qquad (20)$$

which is subject to the boundary conditions

$$\left.\begin{array}{ll} T = 0 & \text{at} \quad \eta = 0 \\ T \to 1 & \text{as} \quad \eta \to \infty \end{array}\right\} \qquad (21)$$

Once equations (15) and (20) are solved for F and T, respectively, the friction factor and Nusselt number are found from

$$\left.\begin{array}{l} C_f = \dfrac{\tau_w}{1/2\rho u_\infty^2} = \dfrac{2}{\sqrt{\mathrm{Re}}}\dfrac{U_s^2}{\sqrt{2\xi}}\left(\dfrac{\partial^2 F}{\partial\eta^2}\right)_{\eta=0} \\[4mm] \mathrm{Nu} = \dfrac{h\ell_r}{k} = \sqrt{\mathrm{Re}}\,\dfrac{U_s}{\sqrt{2\xi}}\left(\dfrac{\partial T}{\partial\eta}\right)_{\eta=0} \end{array}\right\} \qquad (22)$$

Now, we restrict ourselves to the stagnation point of a cylinder in a uniform crossflow. In this case, the reference length ℓ_r is the diameter of cylinder d. The eddy diffusivity ϵ_m simplifies as follows. The first term of equation (9) vanishes because $\partial u/\partial y = 0$ at the stagnation point. Then, in the second term, the $A\ell*$ product is replaced by $B\ell$, where $B = (\ell*/\ell)A$. From (3), with $\mathrm{Re}_x = 0$ at the stagnation point, it follows that the quantity $(\ell*/\ell)$ depends on $\mathrm{Re}_0/\mathrm{Re}_{x*}$ alone. Although Re_{x*} is rather insensitive to both Re and Re', the quantity Re_0 is unknown and, in general, depends on Re and Re'. Therefore, it follows that B is a function of Re and Re'.

In the stagnation region, the free-stream velocity is proportional to x so that

$$U_s = CX = \sqrt{2C\xi} \qquad (23)$$

The equations of momentum and energy are simplified to the form (with $' = \partial/\partial\eta$)

$$\left.\begin{array}{l} \{(1 + \epsilon_m/\nu)F''\}' + FF'' + \{1 - (F')^2\} = 0 \\ F = F' = 0 \quad \text{at} \quad \eta = 0 \\ F \to 1 \quad \text{as} \quad \eta \to \infty \end{array}\right\} \qquad (24)$$

$$\left.\begin{array}{l} \left\{\left(\dfrac{1}{\mathrm{Pr}} + \dfrac{1}{\mathrm{Pr}_t}\dfrac{\epsilon_m}{\nu}\right)T'\right\}' + FT' = 0 \\[3mm] T = 0 \quad \text{at} \quad \eta = 0 \\ T \to 1 \quad \text{as} \quad \eta \to \infty \end{array}\right\} \qquad (25)$$

For ϵ_m/ν, we simplify equation (17) in accordance with the preceding paragraph and delete DF from equation (18) as discussed earlier, so that

$$\frac{\epsilon_m}{\nu} = \frac{B}{\sqrt{C}}\frac{\mathrm{Re}'}{\sqrt{\mathrm{Re}}}\varphi(\eta) \qquad (26)$$

$$\varphi(\eta) = \begin{cases} (0.4/\eta_m)\eta^2 & \text{for } 0 \le \eta \le 0.225\eta_m \\ 0.09\eta & \text{for } 0.225\eta_m < \eta \le \eta_m \\ 0.09\eta_m & \text{for } \eta_m < \eta \end{cases} \qquad (27)$$

Schmidt and Wenner's experiment [17] gives $C = 3.631$ for $\mathrm{Re} = 1.7 \times 10^5$. Strictly speaking, C varies slightly with Re and Re' [18]. However, the dependency of C on Re and Re' can be included in the parameter B, which is a function of these dimensionless parameters, so that the use of a specific constant value for C does not affect the model of eddy diffusivity in equation (26). The Prandtl number Pr is 0.72 for air at 20°C, and it is assumed that the conventionally used value of the turbulent Prandtl number for fully developed turbulent boundary layer flow over a flat plate is also applicable to the present flow, i.e., $\mathrm{Pr}_t = 0.9$.

Equations (24) and (25) are solved here by Keller's box method [19], which has advantages of simplicity and accuracy. The details of the

application of the box method to the present problem are described in [20]. The step sizes of the difference equations were carefully selected to ensure the accuracy of the results.

Results and Discussion

Since the present theory applied to the stagnation point of a cylinder in a uniform crossflow involves an unknown constant B, it has to be specified before the solutions of equations (24) and (25) can be undertaken. The value of B will be determined here with reference to experimental heat-transfer data. As a prelude to the determination of B, the available heat-transfer data will be examined.

To this end, the Nusselt number is plotted in Fig. 1 against the turbulence Reynolds number Re'. Since Nu is proportional to $Re^{1/2}$ for turbulence-free laminar flow, the quantity $Nu/Re^{1/2}$ is employed as the ordinate variable to diminish the dependence of the data on Re. The dashed line is the empirical correlation formula of Dyban and Epick [6]:

$$Nu/\sqrt{Re} = 0.945 + 0.00945\sqrt{Re'} \qquad (28)$$

Inspection of the figure reveals that there is a wide variation of $Nu/Re^{1/2}$ among the investigators. It is due, in some part, to possible inaccuracies in the measurements or to differences of Re.

First, we will examine the reliability of the experiments and retain those which appear to be most reliable. There are many causes of uncertainty in the data, including tunnel blockage, variation of physical properties, effect of turbulence scale, inaccurate measurement of turbulence intensity, etc. Among these, the largest source of error is believed to be inaccurate measurement of turbulence intensity. Schnautz [2] employed Schubauer's indirect method, which is inherently inaccurate, especially for the measurement of low intensities (the error is up to 100 percent). Galloway [5] did not measure the intensity. Rather, he constructed turbulence promoters similar to those of Davis and Van der Hegge Zijnen, as cited in [5]. This results in uncertainty in the estimation of the intensity. Moreover, Galloway's clear tunnel without a turbulence promoter had a very high turbulence intensity of 3 percent, while the intensity of Van der Hegge Zijnen's clear tunnel was 0.2–0.3 percent. Among the data of Kestin and co-workers, the recent data of [7] appear to be more accurate than those of [3]. In light of the foregoing discussion, no further consideration will be given to the data of [2, 3, 5].

Next, the dependence of $Nu/Re^{1/2}$ on Re should be clarified. Fig. 2 shows the data of Fig. 1 (with the aforementioned omissions) replotted in a manner which exhibits the values of Re. Dyban and Epick did not specify Re for each data point but their range of Re is 10^3 to 8×10^4.

From an examination of this figure, it is difficult to identify a consistent trend of the data with Re. However, since the variation of $Nu/Re^{1/2}$ with Re is considerable, Re' cannot be regarded as a sufficient correlation parameter. In particular, the empirical formula of
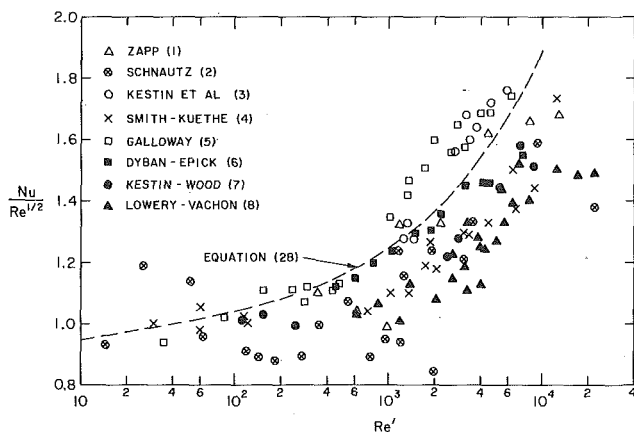
Dyban and Epick (28) fails to correlate the data because it does not account for a Re dependence. It is interesting to observe that the data of Zapp, Smith and Kuethe, and Lowery and Vachon show a trend whereby $Nu/Re^{1/2}$ decreases with Re for fixed Re'. This fact suggests the use of $Re'Re^{-n}$ as a correlation parameter. Smith and Kuethe's simple theory indicates $n = 1/2$, which will also be used here.

In accordance with the foregoing, $Nu/Re^{1/2}$ versus $Re'/Re^{1/2}$ is plotted in Fig. 3, where the spread of the data is seen to be substantially less (about half) than that of Fig. 2. Since the correlation in terms of $Re'/Re^{1/2}$ is reasonably good, it will be assumed that B is a function of $Re'/Re^{1/2}$ alone. On this basis, B was determined as follows: For each data point, solutions of equations (24) and (25) were performed for the corresponding value of $Re'/Re^{1/2}$ and for a range of B values. These solutions enabled B to be chosen so that the computed value of $Nu/Re^{1/2}$ agreed with experiment.

The results of these computations are shown in Fig. 4. The spread among the B values at small $Re'/Re^{1/2}$ is a result of the fact that in that range the mathematical structure of the model causes B to be overly sensitive to scatter in the $Nu/Re^{1/2}$ data, but with the reciprocal effect that $Nu/Re^{1/2}$ is insensitive to scatter in B. If the range of small $Re'/Re^{1/2}$ is not considered, it is seen that B is almost independent of $Re'/Re^{1/2}$ and may, therefore, be regarded as a universal constant. The average value of B is 2.2, which is indicated by a solid line.

The predictive curve of the present analysis obtained by using the aforementioned value of B is shown in Fig. 3 by a solid line IV. In addition, curves depicting the predictions of Galloway, I(a, b), of Traci
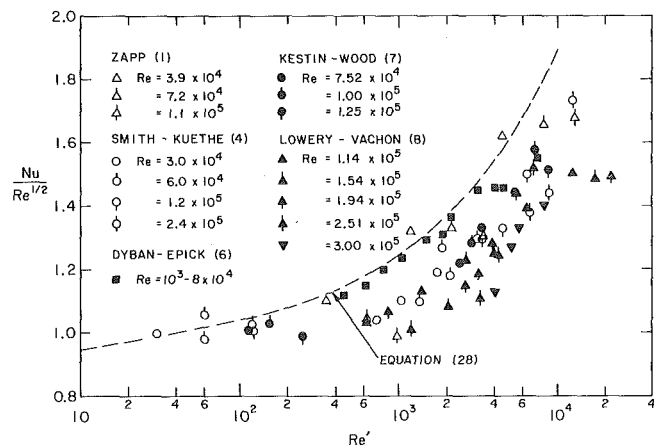

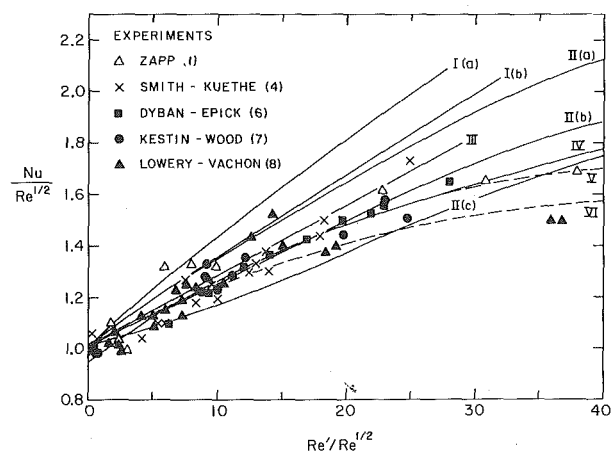**Fig. 2 Effect of Re on the Nu, Re' data correlation**

Fig. 1 Correlation of the Nusselt number data with turbulence Reynolds number Re'

Fig. 3 Presentation of Nusselt number results as a function of Re'/Re$^{1/2}$
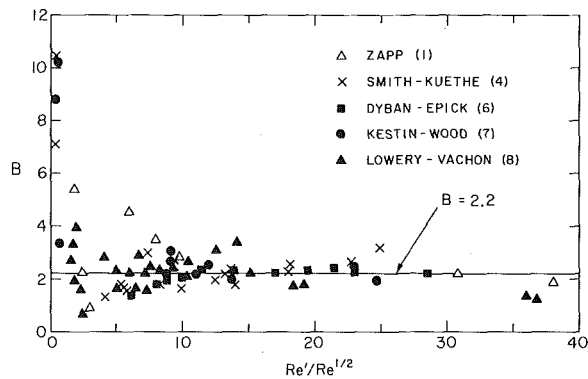
Fig. 4 Values of the constant B obtained from experimental data

Fig. 5 Friction factor results

and Wilcox, II(a, b, c), and of Smith and Kuethe, III, are presented for comparison, also as solid lines. The two Galloway curves correspond to different analytical models, whereas the three Traci-Wilcox curves are for Reynolds numbers of 10^4, 10^5, and 10^6, respectively, from lower to upper. The dashed lines represent the empirical formulas of Kestin and Wood, V, and of Lowery and Vachon, VI, both of which are second-degree polynomials in $Re'/Re^{1/2}$ which attain maximum values of $Nu/Re^{1/2}$ for $Re'/Re^{1/2} \sim 43$ and decrease thereafter.

By inspecting the figure, it is seen that the predictions of the present analysis are generally in good agreement with the data over the entire range of $Re'/Re^{1/2}$. This agreement is especially noteworthy in that only a single empirical constant was used in the analytical model. The two curves which represent Galloway's analytical models are, evidently, too high. The Smith and Kuethe curve is practically a straight line. Whereas it passes through the data at smaller $Re'/Re^{1/2}$, it does not tend to level off at higher $Re'/Re^{1/2}$ and, therefore, does not follow the trend of the data. Among the three Reynolds number curves of Traci and Wilcox, II(b) appears to be the better, but it falls on the high side of the data at larger values of $Re'/Re^{1/2}$. The empirical correlation equation of Kestin and Wood seems, on the whole, to be a somewhat better representation of the available body of data than that of Lowery and Vachon. It is interesting to note that the prediction curve of the present analysis is virtually coincident with the Kestin-Wood correlation up to $Re'/Re^{1/2} = 30$. Modest deviations occur at larger values of $Re'/Re^{1/2}$ where the correlation is less firmly established (only two data points beyond $Re'/Re^{1/2} = 30$, respectively at 32 and 38, were available for the correlation).

In the limit as $Re'/Re^{1/2}$ approaches zero, the present analysis, in common with the correlation of [7], yields a value of $Nu/Re^{1/2}$ of approximately 0.95. The other analytical models and the correlation of [8] yield values of 1.01 because they employ the potential flow field as a basis for the stagnation point velocity distribution.

The generally satisfactory performance of the present model and, in particular, the leveling off of $Nu/Re^{1/2}$ at the larger $Re'/Re^{1/2}$, can be attributed to the presence of the boundary-layer thickness in the eddy diffusivity representation. When the free-stream turbulence is increased, the boundary-layer thickness is also increased. The latter effect tends to neutralize the direct augmentation of the eddy diffusivity by the free-stream turbulence, thereby giving rise to the aforementioned leveling-off tendency.

The eddy diffusivity models of Smith and Kuethe and of Galloway did not take account of the boundary-layer thickness. It is also noteworthy that the Galloway curve, I(b), and the Smith and Kuethe curve, III, which correspond to identical models, deviate substantially from each other. As indicated in Fig. 3, the model of Traci and Wilcox predicts a significant separate dependence on Re. Careful examination of the data plotted in the figure does not substantiate such a strong dependence.

The friction factor C_f for the stagnation region is presented in Fig. 5. Since C_f varies linearly with X and inversely with $Re^{1/2}$ in the
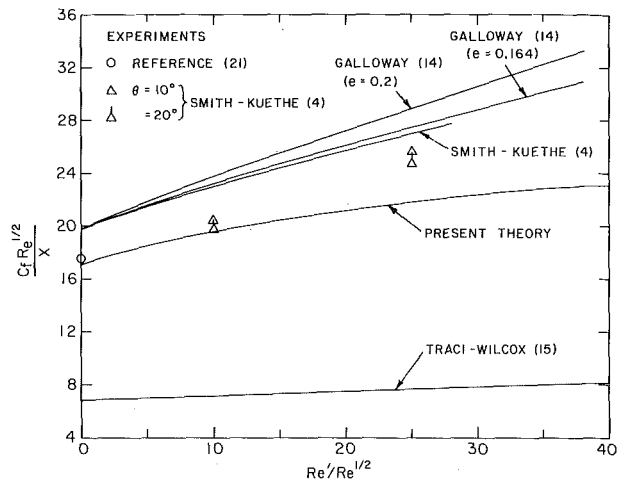
stagnation region (equations (22) and (23)), the ordinate variable $(C_f Re^{1/2})/X$ is a natural grouping. In addition to the curve representing the predictions of the present analysis, curves are also given for the predictions of Smith and Kuethe, Galloway, and Traci and Wilcox (for $Re = 10^5$).

There are not many measurements of the influence of free-stream turbulence on C_f. The experimental value of $(C_f Re^{1/2})/X$ for a nonturbulent free stream (i.e., for $Re'/Re^{1/2} = 0$) is 17.6 [21] and is shown by an open circle in Fig. 5. Smith and Kuethe are the only investigators who measured the wall shear stress in the presence of free-stream turbulence. Their measurements were in the range of angular positions from $\theta = 10$–60 deg. Since, according to [21], the wall shear stress varies linearly with θ up to about 20 deg, the Smith-Kuethe data at $\theta = 10$ and 20 deg are shown in the figure. They measured the ratio of the wall shear stresses with and without free-stream turbulence. In order to deduce $(C_f Re^{1/2})/X$ from the ratio of the stresses, it is necessary to evaluate the shear stress (or friction factor) for $Re'/Re^{1/2} = 0$. For the latter, the theoretical value of shear stress (or C_f) was used by the present authors along with the accepted experimental value of $C = 3.631$. The predictive curves of Smith and Kuethe and of Galloway are based on the potential flow value $C = 4$.

Although the accuracy of the available C_f measurements in the presence of free-stream turbulence is somewhat uncertain, they appear to be supportive of the present analysis when taken at face value. In common with the predictions for the stagnation point heat transfer, the present C_f curve tends to level off at high values of $Re'/Re^{1/2}$. When the results of Fig. 5 are compared with those of Fig. 3, it is seen that the predicted effect of free-stream turbulence on stagnation point heat transfer is much greater than the effect on the shear stress.

All of the other predictions shown in Fig. 5 increase more or less linearly in the range of larger $Re'/Re^{1/2}$. The C_f curve of Traci and Wilcox is especially noteworthy. It lies much lower than the experimental data and the other predictions. With respect to the Smith-Kuethe and Galloway curves which represent identical models, there is close agreement in contrast to the substantial deviations for the heat transfer predictions.

Concluding Remarks

In order to predict the effects of free-stream turbulence on flow and heat transfer, a model for the eddy diffusivity induced by the free-stream turbulence was derived on the basis of the representation of the turbulent velocity fluctuations of Belov, et al. The model was applied to the stagnation point of a cylinder situated in a uniform crossflow with free-stream turbulence. To facilitate the evaluation of an unknown constant appearing in the analysis, available Nusselt number data were correlated in the form $Nu/Re^{1/2}$ versus $Re'/Re^{1/2}$. With this single constant thus determined, the solutions of the con-

servation equations yielded predictions for the Nusselt number and friction factor in the presence of free-stream turbulence. These predictions were compared with the available heat transfer data, empirical formulas, and three other analytical predictions. Overall, the data are very satisfactorily represented by the present analysis. There are no fully reliable experimental data for the friction factor, but the available data are supportive of the present results. As a general finding of the analysis, it was shown that the augmentation of the friction factor due to free-stream turbulence is much less than that of the Nusselt number.

Acknowledgment

References

1   Zapp, G. M., "The Effect of Turbulence on Local Heat Transfer Coefficients Around a Cylinder Normal to an Air Stream," MS thesis, Oregon State College, 1950.

2   Schnautz, J. A., "Effect of Turbulence Intensity on Mass Transfer from Plates, Cylinders and Spheres in Air Streams," PhD thesis, Oregon State College, 1958.

3   Kestin, J., Maeder, P. F., and Sogin, H. H., "The Influence of Turbulence on the Transfer of Heat to Cylinders Near the Stagnation Point," Z. Angew. Math. Mech. Vol. 12, 1961, pp 115–131.

4   Smith, M. C., and Kuethe, A. M., "Effects of Turbulence on Laminar Skin Friction and Heat Transfer," Physics of Fluids, Vol. 9, 1966, pp. 2337–2344.

5   Galloway, T. R., "Local and Macroscopic Transport from a 1.5-in. Cylinder in a Turbulent Air Stream," AIChE Journal, Vol. 13, 1967, pp. 563–570.

6   Dyban, E. P., and Epick, E. Ya., "Some Heat Transfer Features in the Air Flow of Intensified Turbulence," Proceedings of the 4th International Heat Transfer Conference, Vol. II, Paris, 1970.

7   Kestin, J., and Wood, R. T., "The Influence of Turbulence on Mass Transfer From Cylinders," JOURNAL OF HEAT TRANSFER, TRANS. ASME, Series C, Vol. 93, 1971, pp. 321–327.

8   Lowery, G. W., and Vachon, R. I., "The Effect of Turbulence on Heat Transfer from Heated Cylinders," International Journal of Heat and Mass Transfer, Vol. 18, 1975, pp. 1229–1242.

9   Sutera, S. P., Maeder, P. F., and Kestin, J., "On the Sensitivity of Heat Transfer in the Stagnation Boundary Layer to Free-Stream Vorticity," Journal of Fluid Mechanics, TRANS. ASME, Vol. 16, 1963, pp. 497–520.

10   Sutera, S. P., "Vorticity Amplification in Stagnation-Point Flow and its Effect on Heat Transfer," Journal of Fluid Mechanics, TRANS. ASME, Vol. 21, 1965, pp. 513–534.

11   Kestin, J., and Wood, R. T., "Enhancement of Stagnation Line Heat Transfer by Turbulence," Progress in Heat and Mass Transfer, Vol. 2, 1969, pp. 249–253.

12   Kestin, J., and Wood, R. T., "The Mechanism Which Causes Free Stream Turbulence to Enhance Stagnation Line Heat and Mass Transfer," Paper No. FC 2.7, Fourth International Heat Transfer Conference, Paris-Versailles, 1970.

13   Kestin, J., and Wood, R. T., "On the Stability of Two-Dimensional Stagnation Flow," Journal of Fluid Mechanics, TRANS. ASME, Vol. 44, 1970, pp. 461–479.

14   Galloway, T. R., "Enhancement of Stagnation Flow Heat and Mass Transfer Through Interactions of Free-Stream Turbulence," AIChE Journal, Vol. 19, 1973, pp. 608–617.

15   Traci, R. M., and Wilcox, D. C., "Freestream Turbulence Effects on Stagnation Point Heat Transfer," AIAA Journal, Vol. 13, 1975, pp. 890–896.

16   Belov, I. A., Gorshkov, G. F., Komarov, V. S., and Terpigorev, V. S., "Effect of Jet Turbulence on Flow in a Boundary Layer Near a Wall" (in Russian), Zhurnal Prikladnoi Mekhaniki i Tekhnicheskoi Fiziki, Vol. 13, 1972, pp. 77–82.

17   Schmidt, E., and Wenner, K., "Waermeabgabe Ueber den Umfang eines Angeblasenen Gheitzten Zylinders," VDI-Forschungsheft No. 2, 1941.

18   Sogin, H. H., and Subramanian, V. S., "Local Mass Transfer from Circular Cylinders in Cross Flow," JOURNAL OF HEAT TRANSFER, TRANS. ASME, Series C, Vol. 83, 1961, pp. 483–493.

19   Keller, H. B., and Cebeci, T., "Accurate Numerical Methods for Boundary-Layer Flows. II: Two-dimensional Turbulent Flows," AIAA Journal, Vol. 10, 1972, pp. 1193–1199.

20   Miyazaki, H., "Flow and Heat Transfer Characteristics for a Two-Dimensional Jet Impinging on a Circular Cylinder," PhD thesis, University of Minnesota, 1975.

21   Goldstein, S., Modern Developments in Fluid Dynamics, Vol. 2. Oxford University Press, London, 1938.

D. R. Pedersen,
Argonne National Laboratory,
Argonne, Ill.

E. R. G. Eckert

R. J. Goldstein
University of Minnesota,
Department of Mechanical Engineering,
Minneapolis, Minn.

Film Cooling With Large Density Differences Between the Mainstream and the Secondary Fluid Measured by the Heat-Mass Transfer Analogy[1]

The effect of large density differences on film cooling effectiveness was investigated through the heat-mass transfer analogy. Experiments were performed in a wind tunnel where one of the plane walls was provided with a porous strip or a row of holes with three-diameter lateral spacing and inclined 35 deg into the main stream. Helium, CO_2, or refrigerant F-12, was mixed with air either in small concentrations to approach a constant property situation or in larger concentration to produce a large density difference and injected through the porous strip or the row of holes into the mainstream. The resulting local gas concentrations were measured along the wall. The density ratio of secondary to mainstream fluid was varied between 0.75 and 4.17 for both injection systems. Local film effectiveness values were obtained at a number of positions downstream of injection and at different lateral positions. From these lateral average values could also be calculated. The following results were obtained. The heat mass-transfer analogy was verified for injection through the porous strip or through holes at conditions approaching a constant property situation. Neither the Schmidt number, nor the density ratio affects the film effectiveness for injection through a porous strip. The density ratio has a strong effect on the film effectiveness for injection through holes. The film effectiveness for injection through holes has a maximum value for a velocity ratio (injection to free stream) between 0.4 and 0.6. The center-line effectiveness increases somewhat with a decreasing ratio of boundary layer thickness to injection tube diameter.

Introduction

Film cooling has found wide application as a means to protect a solid surface from the influence of a high temperature stream by injection of a cooling fluid at a discrete location. Film cooling is most effective if the coolant is ejected through a continuous slot. Structural

considerations, however, often make it necessary to use one or several rows of holes. This is, for instance, the usual arrangement when film cooling is applied to gas turbine blades. In this application there is a large temperature difference between the hot gas in the mainstream surrounding the blades and the cooling air injected through the holes in the blade. The present paper investigates the effect of large temperature differences on the cooling effectiveness for the situation when air provides the mainstream and the secondary gas stream. Also, the mainstream velocity is uniform and the boundary layer is turbulent over the film-cooled flat surface.

The heat transfer between the mainstream and the film cooled wall has to be known for an analysis of the cooling process. It is with advantage described by the following equation

$$q = h(T_{aw} - T_w) \qquad (1)$$

Copyright © 1977 by ASME

in which q denotes the heat flux from the mainstream to the film cooled surface per unit time and area, h denotes the heat transfer coefficient, T_w the wall temperature, and T_{aw} the adiabatic wall temperature; this means, the temperature which the wall assumes under the influence of film cooling when the heat flux from the surface of the wall into its interior is zero. The effect of injection on the heat transfer coefficient is discussed in a review of film cooling by Goldstein [1].[2] There experiments are described with injection through a slot or through a row of holes in which the effect of injection on the heat transfer coefficient defined by equation (1) was found to be small with the exception of a short distance downstream from the row of holes. This has also been confirmed by more recent experiments of Eriksen [2] and of Metzger and Fletcher [3]. Thus, generally available information on heat transfer coefficients for flow over a solid surface without film cooling can be used as input into equation (1) and film cooling research can concentrate on a determination of the adiabatic wall temperature T_{aw}.

This temperature is conveniently expressed in a dimensionless form called film cooling effectiveness.

$$\eta = \frac{T_{aw} - T_\infty}{T_2 - T_\infty} \qquad (2)$$

in which T_∞ denotes the temperature in the mainstream outside the boundary layer and T_2 indicates the temperature with which the secondary fluid leaves the slots or holes. For high speed flow, the temperature T_∞ has to be replaced by the recovery temperature T_r. From dimensionless analysis one can show that for a constant property situation, (i.e., for a small difference between T_∞ and T_2) the film cooling effectiveness is a function of the geometry involved, the Reynolds number in the mainstream, the parameters describing the turbulence, and the mass flux ratio

$$M = \frac{\rho_2 u_2}{\rho_\infty u_\infty} \qquad (3)$$

For variable property flows involving ideal gases with transport properties which can be expressed by a power law, the heat transfer and the film effectiveness are, in addition, a function of the ratio of the absolute temperatures T_∞/T_2 or of the density ratio ρ_∞/ρ_2.

The main parameters varied in the present experimental investigation are M and ρ_∞/ρ_2. In the presentation of the results the momentum flux ratio,

$$I = \frac{\rho_2 u_2^2}{\rho_\infty u_\infty^2} \qquad (4)$$

or the velocity ratio

$$\frac{u_2}{u_\infty} \qquad (5)$$

are also used.
Any two of the parameters 3–5 can be varied independently.

___
[2] Numbers in brackets designate References at end of paper.

Mass Transfer Analogy

Local effectiveness values are required for many applications. The limitation on the temperature level at which turbine blades can operate, for instance, is determined by the magnitude of local thermal stresses which depend on the local temperature field in the skin of the blade. The prediction of local stresses is thus based on local film cooling effectiveness and heat transfer coefficient values.

In order to obtain local effectiveness values, large scale experiments have to be performed with a locally adiabatic wall. Both conditions are difficult to fulfill. A large scale experiment requires a test setup in which the main flow is heated to a high temperature or the injected fluid is sufficiently cooled to produce the desired temperature or density ratio. To make the heat flow into the wall zero at any location requires the absence of even local heat conduction, and this again is difficult to achieve. These difficulties can be avoided by employing the heat-mass transfer analogy in which a large density difference between the main flow and the secondary flow can easily be created and where an impermeable wall gives the desired boundary condition of the adiabatic wall. A foreign gas with proper density is ejected into the main flow of the same temperature. The mass fraction of the foreign gas at the wall surface is related to the adiabatic wall temperature for the analogous heat transfer situation. Thus, the analog to the film cooling effectiveness is the following ratio of mass fractions

$$\eta = \frac{c_w - c_\infty}{c_2 - c_\infty} \qquad (6)$$

in which the indices have the same meaning as in equation (2). If the secondary fluid is a single constituent, not contained in the main stream, $c_\infty = 0$ and $c_2 = 1$. Thus,

$$\eta = c_w \qquad (7)$$

equations (6) and (7) hold when the Schmidt number, Sc, for the mass transfer experiment is equal to the Prandtl number, Pr, for the analogous heat transfer situation; otherwise, a correction has to be employed to establish the dependance of η on the Prandtl or Schmidt parameter, respectively. For convective heat transfer it has been well established that the Nusselt number describing the heat transfer coefficient is to a good approximation proportional to the third root of the Prandtl number and this correction can be applied in the mass transfer analogy. Less information on this dependence is available for the effectiveness parameter η. Therefore, its dependance on Schmidt number has been investigated in this study.

An exact analogy does not exist for the variable property situation. However, it has been shown by Eckert [4] that it holds with good approximation when the density ratio ρ_2/ρ_∞ has the same value for the mass transfer experiment and the analogous heat transfer situation. This analogy has, therefore, been used in the experiments described in the following sections. They include film cooling with injection of the secondary gas through a porous strip and through a row of holes with small and large density differences. Air with a foreign tracer gas was used to approximate a constant property situation.

___

Nomenclature

c = mass fraction
D = hole diameter
h = heat transfer coefficient
I = momentum flux ratio; equation (4)
M = mass flux ratio; equation (3)
q = heat flux to film cooled surface per unit area
Re = Reynolds number
S = center line distance between holes
s = slot width

T = temperature
u = velocity
X = dimensionless distance x/D
x = downstream distance from injection hole
Z = dimensionless distance z/D
z = distance from hole center normal to flow
η = film cooling effectiveness
μ = viscosity

ξ = distance parameter; equation (8)
ρ = density

Subscripts

aw = adiabatic wall
c = centerline
w = wall
L = lateral
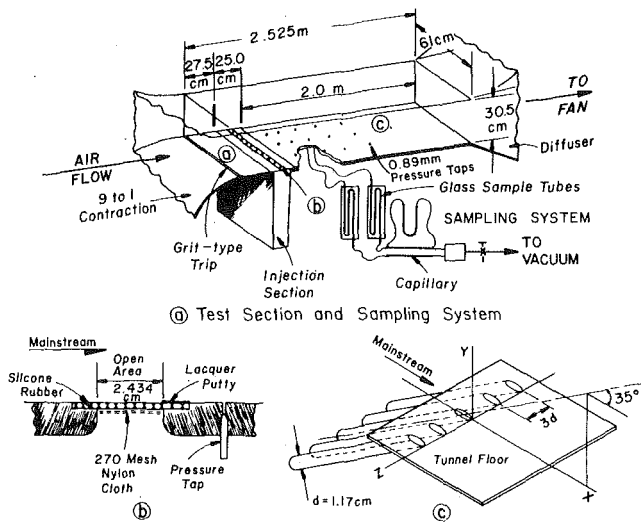∞ = mainstream
2 = secondary fluid

Fig. 1 Test section

Experiments

Wind Tunnel. The University of Minnesota Heat Transfer Laboratory low-turbulence subsonic wind tunnel [5] was used in this study. The tunnel can operate in closed or open flow. For the present experiments the open flow mode was used. The tunnel has a turbulence intensity between 0.3 and 0.4 percent achieved by a series of screens and a 9 to 1 contraction section.

The test section, shown in Fig. 1(a) is 0.305 × 0.61 m in cross section and 2.5-m long. The side walls and top are constructed of plexiglass and the tunnel floor, which constitutes the test surface, is a 12.7-mm thick anodized aluminum plate. It consists of three sections, a, b, and c. A 9.5-mm wide strip of Carborundum grit is glued near the upstream end of section a as a boundary layer trip. The grit size has been selected according to recommendations of von Doenhoff and Horton [6]. The third segment in flow direction, section c, contains taps through which samples may be drawn off to determine the wall concentration of the injected fluid. The taps are spaced exponentially in the flow direction in three parallel rows spaced 12.7-mm apart to obtain concentrations at three lateral positions. The taps are 0.89 mm in diameter and approximately 5 dia long before enlargement. Segment b contains the injection system.

Injection Geometries. The two injection geometries are shown in Figs. 1(b) and 1(c). The porous slot in Fig. 1(b) is 24.34-mm wide in the flow direction and spans the full width of the tunnel. The porous slot is made of PP129 Poroplate manufactured by Bendix Corporation and consists of four layers of 50 × 250 wires per in. stainless-steel screens sintered together. The pore size is approximately 20 microns and the ratio of open to total area is approximately 60 percent. The porous material is recessed into the surface of the test plate and the rim outside the desired width is filled with lacquer putty to provide a well-defined flow area. A plenum is arranged underneath the porous plate as shown in Fig. 1(a). It has a cross-sectional area approximately six times that of the porous slot. Nevertheless, it was found necessary to improve the uniformity of the flow through the screen by attaching various layers of 270-mesh nylon cloth to the underside of the screen at locations of high flow rates. The one sigma deviation of the flow rate from uniformity was found to be 1.1 percent after this adjustment. The apparatus for determining the flow rate is described in reference [7].

The injection geometry of the row of holes is shown in Fig. 1(c). The row of holes consisted of 15 tubes with an internal diameter of 11.7-mm spaced 3 dia apart and with their axis inclined at an angle of 35 deg toward the plate surface in main flow direction. The same ejection geometry has been studied in previous investigations at the Heat Transfer Laboratory. The tubes are ground flush with the sur-

face of the injection plate. The plate and plenum could be moved laterally allowing to measure mass concentrations at different lateral positions. Uniform flow through all of the tubes was achieved by an arrangement in which the gas enters first a large plenum and then small individual plenums for each of the tubes before it is ejected into the boundary layer. Needle valves were used to adjust the flow entering the individual plenums. The one sigma deviation of the flow rate from uniformity was found to be 1.53 percent.

In some of the experiments, only the center five holes were used for the ejection and the rest was blocked off [7, IIA]. False walls were located on both sides of the five holes to avoid a lateral spread of the jets. This was done to conserve foreign gas. The difference between measurements with 15 or five holes was negligible.

The secondary air for all of the experiments was supplied by the building air compressor. The air was filtered and passed through a pressure regulator to eliminate pressure variations with time. Uniformity of the injected mixture of foreign gas and air was obtained by a series of orifices with large pressure drop. The flow approaching the tube exits was fully developed.

Sampling System. The primary aim of the experiments was to determine the wall concentration of foreign gas at various locations. Small samples are for this purpose drawn off through the taps in the test plate shown in Fig. 1(a). The samples are sucked by a vacuum pump through glass sampling tubes with an internal diameter of 3–4 mm and a length of approximately 1 m. They then pass through capillaries to insure a known and uniform suction rate. Representative samples may be stored in the glass sampling tubes by clamping off both ends.

The ratio of the suction velocity through the pressure taps to the main stream velocity was 0.03 and 0.1, respectively, for the experiments with a row of holes and with the porous slot. These values are sufficiently small so that the sample concentration is not a function of the suction velocity. The sampling time was always greater by a factor of 10 than the time required for slug flow to move through the glass sampling tube. The foreign gas concentration of the samples was measured with a Hewlett-Packard Model 5750B Research Chromatograph with a thermal conductivity cell. A sampling valve, Hewlett-Packard Model 19020A, was used to introduce the sample into the chromatograph.

Operating Conditions. Velocity profiles were measured on and off center line with the injection holes covered by tape. The velocity profiles were found to be characteristic of a fully developed turbulent boundary layer with a lateral variation of the boundary layer thickness across the tunnel less than 5 percent. A summary of the parameters describing the operating condition of the tunnel is contained in Table 1. It can be seen that the main stream velocity was increased from 15.4 to 27.7 m/s at the smallest value of the mass flux ratio M. This was done to insure a fully developed turbulent flow at the exit of the injection tubes. More detailed information on the test conditions is contained in reference [7, III].

Results

Injection Through a Porous Slot. Two series of experiments were performed. In the first, a tracer gas was mixed with the injected air stream at a concentration sufficiently small to approximate a constant property situation in which the mass transfer analogy could be confirmed under well-defined and studied conditions. A porous slot injection was chosen because of its insensitivity to small variations in injection geometry. The concentration of the foreign gas in the ejected gas mixture was increased in the second group of tests to investigate the influence of the density ratio on the film effectiveness. The results of both test series are presented in Figs. 2 and 3. The absissa on the figures is a parameter ξ, which emerges in various semiempirical treatments of film cooling.

$$\xi = \frac{x}{Ms} \left(\frac{\mu_2}{\mu_\infty} \mathrm{Re}_2 \right)^{-0.25} \tag{8}$$

x denotes the distance from the downstream edge of the injection slot, Re_2 is the injection Reynolds number formed with the average velocity

Table 1 Operating conditions of wind tunnel

FLOW GEOMETRY	u_∞	Re_s 1)	$\frac{u_\infty}{\nu}$ 2)	Re_D 3)	δ^*_o 4)	$T\%$ 5)
	(m/sec)		(m)$^{-1}$		(mm)	
POROUS SLOT	27.7	9.1×10^5	16.9×10^5		1.53	0.4
Row of 15 holes M = 0.21	27.7	10.6×10^5	16.9×10^5	1.98×10^4	1.83	0.4
Row of 15 holes M > 0.21	15.4	5.9×10^5	9.35×10^5	1.1×10^4	1.91	0.3
Row of 5 holes M = 0.21	27.7	10.1×10^5	16.9×10^5	1.98×10^4	1.83	0.4
Row of 5 holes M > 0.21	15.4	5.6×10^5	9.35×10^5	1.1×10^4	1.91	0.3
Single hole D = 23.5 mm	15.4	5.6×10^5	9.35×10^5	2.2×10^4	1.91	0.3
Single hole D = 11.73 mm	15.4	5.6×10^5	9.35×10^5	1.1×10^4	1.91	0.3

1) Based on distance between effective starting length of boundary layer and injection location.
2) Reynolds number per unit length.
3) Based on injection tube diameter.
4) Displacement thickness at upstream edge of injection slot or holes.
5) Turbulence intensity.

of the secondary gas jet leaving the slot, the slot width is s, μ_2 is the viscosity of the injected fluid, and μ_∞ the free stream viscosity.

The data in Fig. 2 were obtained with CO_2, refrigerant-12,[3] and helium as tracer gas. The density ratio was kept close to 1, as can be seen in the Table inserted in the figure. The Schmidt numbers for these gases in air are also listed in the figure. They vary between 0.226 and 1.54. No influence of this variation of the Schmidt number, however, can be detected in studying the experimental data. This fact is remarkable because for convection heat transfer on a solid surface, the Nusselt number varies approximately proportional to the third

root of the Prandtl number as has been mentioned before. From the analogy between heat and mass transfer, one expects that the Stanton number as a dimensionless expression of the mass transfer coefficient varies also proportional to the third root of the Schmidt number. The absence of this dependence established by the present experiments can possibly be explained by a smaller effect of the viscous sublayer where the temperature (or concentration) gradient approaches a value of zero at the wall. Inserted in Fig. 2 are also a number of test points from reference [8]. The agreement for heated gas injection with a similar injection geometry with the present experiments is satisfactory, thus confirming the validity of the heat-mass transfer analogy. A small systematic deviation at the right-hand side of the figure may be caused by the difficulty to measure small effectiveness values accurately in heat transfer experiments.

Fig. 3 presents the data on the influence of density ratio on the film effectiveness. The secondary gas was a mixture of refrigerant-12 and

[3] (Dichlorodifluoromethane)
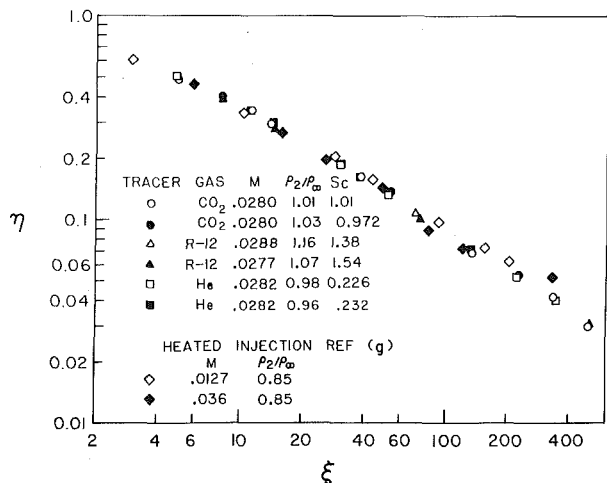
Fig. 2 Film effectiveness for ejection of air with a tracer gas through a porous strip
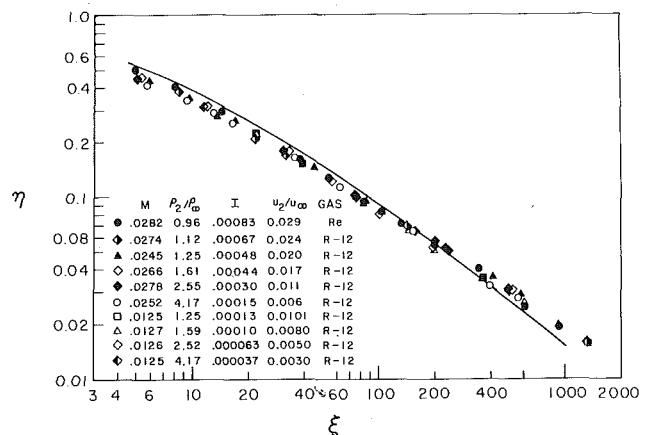
Fig. 3 Effect of large density differences between main and secondary fluid on film effectiveness for ejection through a porous strip
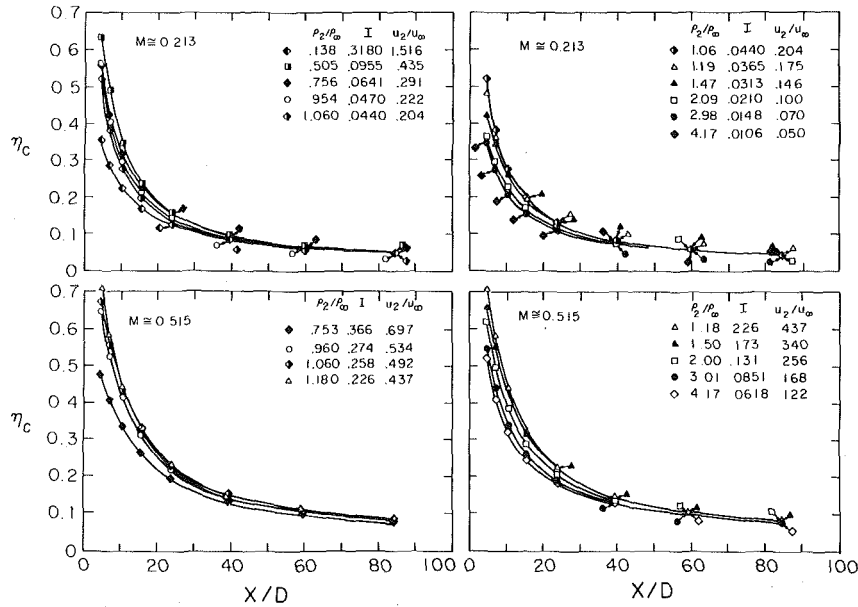
Fig. 5 Effect of density ratio on center-line effectiveness for ejection through a row of inclined holes

air with varying concentration except for one run in which helium was mixed with the secondary air. The mass velocity ratio M, the momentum ratio I, and the velocity ratio are listed together with the density ratio in the insert of the figure. The experimental points indicate over the range of variables studied that neither the density ratio nor the velocity ratio have a measurable effect on the effectiveness parameter when plotted versus the dimensionless distance ξ.

A number of equations have been analytically derived describing the film effectiveness for two-dimensional film cooling. They are summarized in reference [1]. It was found that the equation

$$\eta = \frac{1}{1 + 0.249\xi^{0.8}} \tag{9}$$

Fig. 5 (continued)

η_c
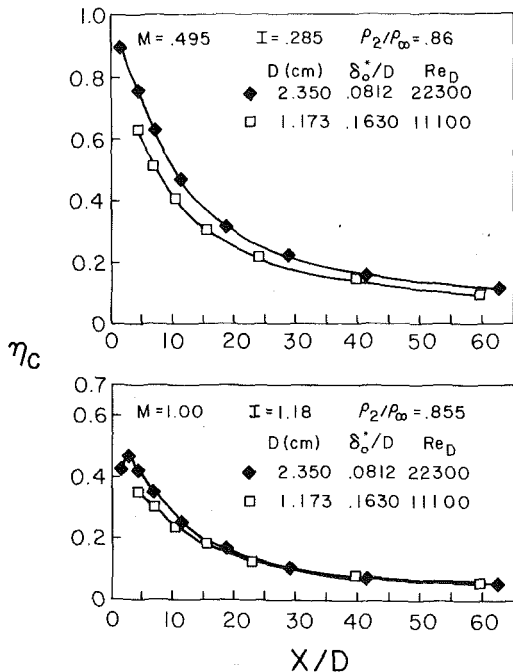
Fig. 4 Effect of boundary layer thickness on the center-line effectiveness for ejection through an inclined hole
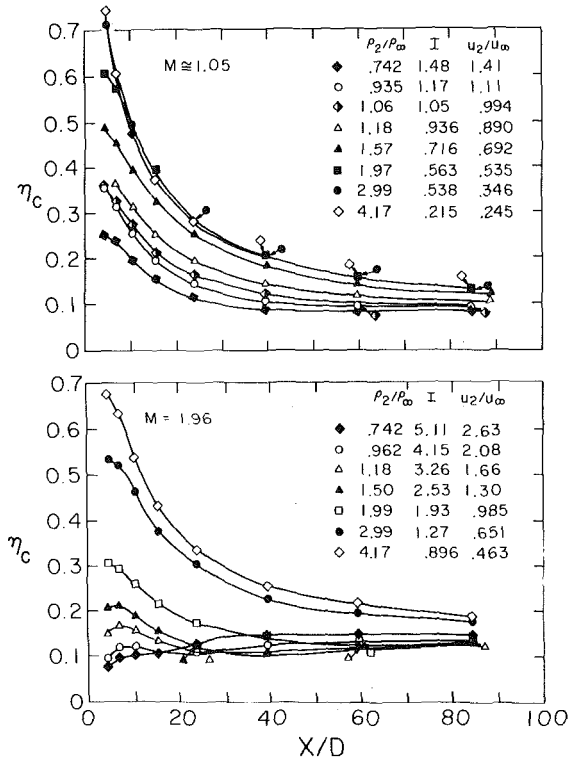
derived by Kutateladze and Leont'ev agrees best with the present measurements. It is inserted as a line in Fig. 3.

In summary, it can be stated that neither the Schmidt number, nor the density ratio influences the effectiveness parameter for film cooling with ejection through a porous strip and possibly generally for two-dimensional film cooling.

Injection Through a Row of Holes. The results obtained with injection through a row of holes are presented in Figs. 4–10. The location on the test surface is described in a coordinate system shown

Fig. 6 Lateral effectiveness as a function of the density ratio for ejection through a row of inclined holes

$$\bar{\eta} = \frac{1}{S} \int_{-S/2}^{+S/2} \eta(x, z)dz \qquad (10)$$

A first series of experiments was performed with a tracer gas to simulate a constant property situation and to compare the results with heated injection measurements. Figures presenting profiles of center-line effectiveness, lateral effectiveness, and average effectiveness values are contained in reference [7] and will not be presented here. For a detailed discussion of the results and a comparison with heat transfer experiments, the reader is also referred to the same reference. The important conclusions only are summarized in the following. The film cooling effectiveness has been studied by Eriksen [2] for air-to-air film cooling with the same geometry and a density ratio 0.85. Present mass transfer studies have been conducted at density ratios of 0.75 and 0.95; they are close to a single line. The film cooling effectiveness values reported in reference [2] lie, as expected, between the ones measured in the present mass transfer study except at some locations where large heat conduction effects in the test plate can be expected. At these locations, the centerline effectiveness measured and corrected for heat conduction effects are somewhat lower than present results but the laterally averaged effectiveness parameters are, as expected, again between the values measured here. In summary, one can, therefore, state that the heat-mass transfer analogy for a constant property situation has been verified.

The effect of boundary layer thickness has been studied in a number of previous investigations for the same geometry and a density ratio of 0.85. Results of mass transfer experiments at essentially the same density ratio are presented in Fig. 4 for two mass velocity ratios. In these studies, secondary fluid was injected through one hole only. Two different hole diameters, 11.73 and 23.5 mm, were used (see Table 1). It is observed in the figure that the centerline effectiveness increases somewhat with decreasing ratio of the boundary layer displacement thickness to the tube diameter and that the effect is somewhat larger for a mass velocity ratio close to 0.5 than for a ratio of 1. This is again in excellent agreement with the results of the previous heat transfer measurements.

The results of the experiments with a large variation of the density ratio are presented in Figs. 5–10. Fig. 5 shows the center-line effectiveness plotted over the dimensionless distance downstream from a hole with the density ratio as parameter. The mass flux M is held approximately constant for each of the individual diagrams. It may

in Fig. 1(c), x denoting the distance in downstream direction measured from the downstream edge of the injection hole, and z the distance normal to the flow direction measured from a line originating at the center of the hole. The film effectiveness is expected to be a function of the dimensionless distances x/D and z/D. Various effectiveness parameters are defined:

1 A centerline effectiveness η_c measured downstream of the centerline of a hole [$z = 0$].

2 Lateral effectiveness η_L which is a function of z/D, at a constant value of x.

3 Laterally averaged effectiveness $\bar{\eta}$ obtained at constant downstream distance x through the equation

Fig. 7 Lateral average effectiveness as a function of the density ratio for ejection through a row of inclined holes
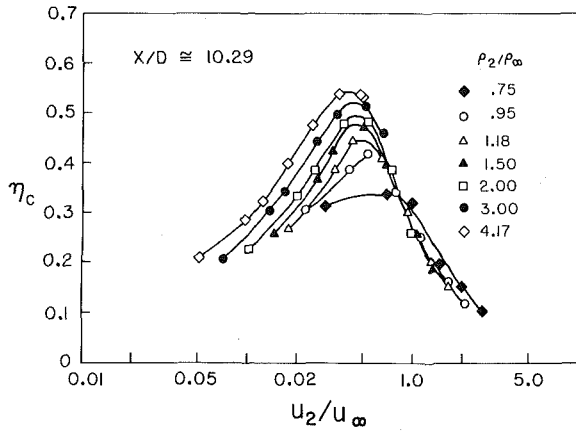
Fig. 8 Effect of injection velocity on the center-line effectiveness for injection through a row of inclined holes

be observed that the effect of the density ratio is comparatively small for the mass flux ratios 0.21 and 0.52, however, it is very pronounced for the ratio $M = 1.05$ and 1.96. The center-line effectiveness has a maximum at a certain density ratio which shifts from being between 0.50 and unity to a value between 2 and 3 as the mass flux ratio increases from 0.213 to 1.05. The maximum center-line effectiveness occurs at a density ratio larger than approximately 4 at a mass velocity ratio of 1.96.

The lateral effectiveness is plotted in Fig. 6 as a function of the lateral position at a downstream distance $x/D = 10.29$ for the four mass flux ratios with the density ratio as parameter. One expects the effectiveness to decrease as the lateral distance from the center line is increased. This is verified in the figure. However, the mode of decrease changes with varying mass velocity ratio and is obviously caused by an involved interaction between the jets. Remarkable is the large increase in the effectiveness values at a mass velocity ratio of 1.96 caused by a change of the density ratio from 1.97 to 4.17. There are indications that the penetration depth of a jet into a cross flow is determined by the value of the momentum flux ratio I. The jets may attach to the surface when the value of I is decreased from 1.90 to 0.899. Lateral effectiveness values at other downstream distances are reported in reference [7, VI, P to R].

The lateral average effectiveness is obtained by an integration of the curves in Fig. 6. The resulting values are presented in Fig. 7. The density ratio has no measurable effect on the average effectiveness for a mass flux ratio of 0.213. However, it causes a considerable variation at the mass flux ratio 0.515 and this influence increases through
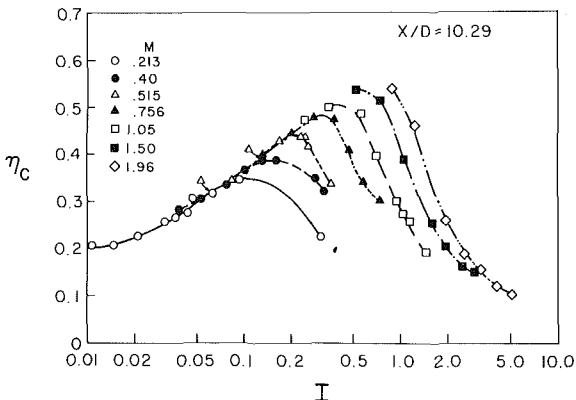
Fig. 9 Center line effectiveness as a function of the momentum flux ratio for injection through a row of inclined holes
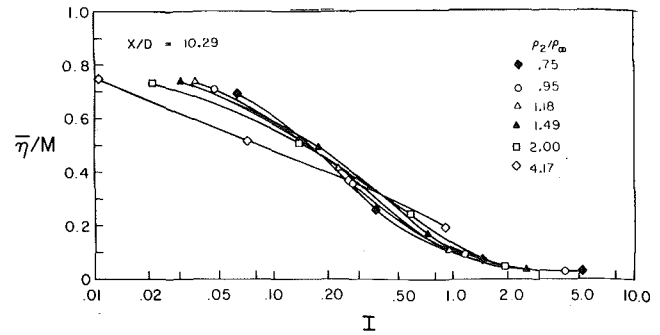
Fig. 10 Ratio of average effectiveness to mass flux ratio as a function of the momentum flux ratio for injection through a row of inclined holes

the mass flux ratios 1.05 and 1.96. One observes now a monotonic increase of the average effectiveness with increasing density ratio except at small x when the mass flux ratio is 1.96. In this case it appears that the curves presenting the effectiveness extrapolate to a value near zero for $x/D = 0$, which would mean that the jets have lifted off completely from the surface and have reattached only further downstream.

Cross plots are presented in the next figure to establish trends for the centerline effectiveness. Fig. 8 shows the center-line effectiveness for a dimensionless downstream distance of 10.29 plotted over the velocity ratio with the density ratio as parameter. One observes that the effectiveness assumes a maximum for a velocity ratio between 0.4 and 0.6. This trend has also been observed in a previous study at the Heat Transfer Laboratory of the University of Minnesota [9] and by Le Brocque, et al. [10] investigating full surface transpiration cooling by means of ejection through multiple rows of holes for a density ratio close to unity. Fig. 8 also indicates that the curves tend to converge into a single one for velocity ratios beyond the maximum. The same trends were observed for a downstream distance $x/D = 39.26$ and when the centerline effectiveness was plotted over the velocity ratio with the mass flux ratio as parameter [7, VI]. The curves arrange in a different way when the centerline effectiveness is plotted over the momentum ratio with the mass velocity ratio as parameter. Fig. 9 shows this at the dimensionless downstream distance 10.29. The curves tend now to coalesce into a single one for momentum ratios below the maximum value. This coalescence is not as pronounced at positions further downstream.

An analytic attempt to correlate effectiveness values is presented in reference [9], based on a model which locates a row of heat sinks at a given height above the surface and describes the boundary layer turbulence by a Reynolds number in which the viscosity is replaced by an average turbulent diffusivity. According to this model, the ratio η/M should only be a function of the momentum flux ratio I for a given Reynolds number and dimensionless location on the surface. A plot in which the centerline effectiveness is plotted over the momentum flux ratio correlates the experimental data only for values of the parameter η_c/M beyond the maximum η. However, an approximate correlation over the whole range of the investigated momentum flux ratio is obtained when the laterally averaged effectiveness is used. Fig. 10 shows this for a dimensionless downstream distance of 10.29. It appears that such a presentation can be used to interpolate between measured density ratios if the laterally averaged effectiveness is the desired parameter.

Conclusion. It has been demonstrated that the density ratio (or in heat transfer the temperature ratio) has no effect on the film effectiveness for injection through a porous strip, when the effectiveness is expressed as a function of the distance parameter ξ. For injection through holes, the film effectiveness is strongly dependent on the density ratio, so that this dependence certainly has to be accounted for in a performance analysis of film cooling for gas turbine blades. The film effectiveness is dependent on an involved interaction of the separation and reattachment of the jets of the injected fluid, on the

lateral spreading and on the energy transfer between jet and main flow.

References

1　Goldstein, R. J., "Film Cooling" in *Advances in Heat Transfer*, Vol. 7, Academic Press, New York and London, 1971, p. 321.

2　Eriksen, V. L., and Goldstein, R. J., "Heat Transfer and Film Cooling Following Injection Through Inclined Circular Tubes, JOURNAL OF HEAT TRANSFER, TRANS. ASME, Series C, Vol. 96, 1974, p. 239.

3　Metzger, D. E., and Fletcher, D. D., "Evaluation of Heat Transfer for Film-Cooled Turbine Components," *Journal of Aircraft*, Vol. 8, No. 1, p. 33, 1971.

4　Eckert, Ernst R. G., and Goldstein, Richard J., *Measurement Techniques in Heat Transfer*, AGARDograph 130, Technivision Services, Slough, England, Nov. 1970, with Second Ed., *Measurements in Heat Transfer*, Hemisphere Publishing Corp., Wash., 1976.

5　Raithby, G. D., "The Effect of Turbulence Parameters and Support Position on the Heat Transfer From, and Flow Around, Spheres," PhD thesis, University of Minnesota, Dec., 1967.

6　von Doenhoff, A. E., and Horton, E. A., "A Low-Speed Experimental Investigation of the Effect of a Sandpaper Type of Roughness Boundary Layer Transition," N.A.C.A. in 3858, 1956.

7　Pedersen, Dean Russell, "Effect of Density Ratio on Film Cooling Effectiveness for Injection Through a Row of Holes and for a Porous Slot," PhD thesis, University of Minnesota, Mar. 1972.

8　Goldstein, R. J., Rask, R. B., and Eckert, E. R. G., "Film Cooling With Helium Injection into a Incompressible Air Flow," *International Journal of Heat and Mass Transfer*, Vol. 9, 1966, p. 1341.

9　Goldstein, R. J., Eckert, E. R. G., Eriksen, V. L., and Ramsey, J. W., "Film Cooling Following Injection Through Inclined Circular Tubes," *Israel Journal of Technology*, Vol. 8, 1970, p. 145.

10　Le Brocque, P. V., Launder, B. E., and Priddin, C. H., "Discrete Hole Injection as a Means of Transpiration Cooling—An Experimental Study," Imperial College of Science and Technology, London, Report No. EHT/TN/ A/26, 1971.

H. Kubota

Research Scientist,
National Aerospace Laboratory,
Chofu, Tokyo, Japan

Thermal Response of a Transpiration-Cooled System in a Radiative and Convective Environment

The unsteady thermal response of a one-dimensional transpiration-cooled system in a radiative and convective environment is presented. The governing equations are solved by the Hartree-Womersley differential-difference method. The solid and fluid temperatures, the fluid pressure distributions, and the back-face heat transfer rate are obtained for a sample case of a 15 degree-entry into a Saturn nominal atmosphere.

Introduction

A transpiration-cooled system consisting of a reflecting porous matrix through which an absorbing gas is injected is a possible means of protecting a probe from the severe radiative and convective heating of outer planet atmosphere entry [1, 2].[1] For such a system, the convective heating is reduced by gas injection into the boundary layer, and the radiative heating is partially absorbed by the transpirant gas and partially reflected by the heat-shield material.

As a first step in evaluating this system, a one-dimensional analysis is used to investigate the thermal response of the heat-shield matrix exposed to incident radiative and convective heating and undergoing internal radiative transfer. In reference [3], a one-dimensional quasi-steady material response of such a transpiration-cooled system was determined analytically. In practice, however, the material response is unsteady since the entry heating pulse is short. Thus it is important to know the time-dependent heat-shield response as the ambient conditions vary.

Curry [4] has investigated the two-dimensional heat and mass transfer in a porous medium experiencing only convective heating. The present study is based on a one-dimensional version of Curry's model and extended to include an internal radiative transfer model.

The purpose of this paper is to extend the analysis of transpiration-cooled system in reference [3] to the unsteady state and to obtain the instantaneous thermal response within the heat-shield matrix.

The heat and mass transfer in the porous matrix is mathematically modeled by the momentum and energy equations for the fluid and the energy equation for the solid.

The distributions of the solid and fluid temperatures and the fluid pressure within the porous matrix and the back-face heat transfer rate are obtained by solving the aforementioned equations by the Hartree-Womersley differential-difference method [5, 6] applicable to the parabolic partial differential equation. Solutions are obtained for variations of mass flow rate of the injectant, of porosity of matrix, and of matrix thickness. Important entry probe design parameters such as peak surface temperature, time that the surface is below a certain temperature, and peak back-face heat transfer rate can be estimated.

Analysis

Physical Model and Assumptions. The physical model considered is sketched in Fig. 1. A one-dimensional porous matrix of thickness L is exposed to external convective and radiative heat fluxes. A coolant gas is injected through the matrix from back to front surface.

The major assumptions are as follows:

1 One-dimensional analysis

2 Unsteady thermal response

3 Constant mass injection rate

4 Solid and gas temperatures in the matrix not equal ("two-temperature" assumption)

5 Continuum model for the porous matrix (volume element is large with respect to individual pores)

6 No reversal flow (injected gas flows toward the heated front surface)

7 Constant thermal and optical properties (independent of temperature, pressure, and wavelength)

---

[1] Numbers in brackets designate References at end of paper.
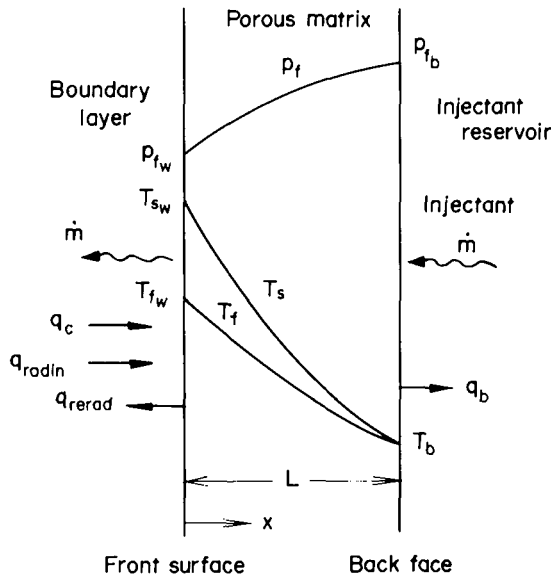
Copyright © 1977 by ASME

Fig. 1 Physical model

8   Neither chemical reactions between the porous matrix and the injected gas nor dissociation of the injected gas is allowed

9   No heat loss occurs by conduction from the back face to the oncoming coolant from the reservoir

Governing Equations. The unsteady differential equations for the conservation of mass, momentum, and energy in a porous matrix with mass transfer but without internal radiative transfer are presented in reference [4]. These equations extended to include radiation are as follows:

For fluid:

Mass conservation

$$\phi \frac{\partial \rho_f}{\partial t} + \frac{\partial(\rho_f U_f)}{\partial x} = 0 \tag{1}$$

Momentum conservation- Darcy's equation

$$-\frac{\partial p_f}{\partial x} = (\tilde{\alpha}\mu_f + \tilde{\beta}\rho_f|U_f|)U_f \tag{2}$$

Energy conservation

$$k_f \frac{\partial^2 T_f}{\partial x^2} - C_{pf}\rho_f U_f \frac{\partial T_f}{\partial x} + \frac{\partial p_f}{\partial t} + U_f \frac{\partial p_f}{\partial x} + \frac{h}{\phi}(T_s - T_f)$$

$$-\frac{\partial q_r}{\partial x} = C_{pf}\rho_f \frac{\partial T_f}{\partial t} \tag{3}$$

Perfect gas law

$$p_f = \rho_f \frac{R}{M_f} T_f \tag{4}$$

For solid:
Energy conservation

$$k_s \frac{\partial^2 T_s}{\partial x^2} - \frac{h}{1-\phi}(T_s - T_f) - \frac{\partial q_r}{\partial x} = C_{ps}\rho_s \frac{\partial T_s}{\partial t} \tag{5}$$

From assumption (3) the mass injection rate is

$$\dot{m} = -\rho_f U_f = \text{constant} \tag{6}$$

By substituting equations (1), (4), and (6) into equations (3) and (2),

$$k_f \frac{\partial^2 T_f}{\partial x^2} + C_{pf}\dot{m}\frac{\partial T_f}{\partial x} - a\frac{T_f^2}{p_f^2} + \frac{h}{\phi}(T_s - T_f) - \frac{\partial q_r}{\partial x} = b\frac{p_f}{T_f}\frac{\partial T_f}{\partial t} \tag{7}$$

$$p_f \frac{\partial p_f}{\partial x} = cT_f \tag{8}$$

where

$$a = (\tilde{\alpha}\mu_f + \tilde{\beta}\dot{m})\dot{m}^2(R/M_f)^2 \tag{9}$$

$$b = C_{pf}(M_f/R) - 1 \tag{10}$$

$$c = (\tilde{\alpha}\mu_f + \tilde{\beta}\dot{m})\dot{m}(R/M_f) \tag{11}$$

In the foregoing equations, $\tilde{\alpha}$ and $\tilde{\beta}$ are constants which depend on the porosity and h is a volumetric heat-transfer coefficient between the solid and the fluid which can be written by the experimental correlation [7] as

$$h = 0.00434 \, (C_{pf}k_f^2)^{0.333}\mu_f^{-0.227}\dot{m}^{0.56}(\tilde{\alpha}/\tilde{\beta})^{1.44} \tag{12}$$

As in reference [3] the radiative transfer term $\partial q_r/\partial x$ is given by the "two-flux" model [8] as

$$\partial q_r/\partial x = -2(A_0/A_1)e^{\alpha x}K\sum_{\nu=m}^{m'}q_{r_{e_\nu}} + 2(B_0/B_1)e^{-\alpha x}K\sum_{\nu=m}^{m'}q_{r_{e_\nu}} \tag{13}$$

where the quantities A_0, A_1, B_0, B_1, and α are given in Appendix A of reference [3].

Initial and Boundary Conditions. Initial and boundary conditions for the differential equations are
at $t = 0$:

$$T_s(x, 0) = T_f(x, 0) = T_b = \text{constant} \tag{14}$$

$$p_f(x, 0) = p_{f_w}(0) \tag{15}$$

Nomenclature

$\tilde{B}_0$ = blowing parameter defined by equation (22)

C_H = heat-transfer coefficient

C_p = specific heat

H = total enthalpy

h = volumetric convective heat-transfer coefficient

K = absorption coefficient

k = thermal conductivity

L = matrix thickness

M = molecular weight

m, m' = index on radiation bands that penetrate the matrix

$\dot{m}$ = mass injection rate

n, n' = index on radiation bands absorbed on the exposed surface

p = pressure

$\bar{p}$ = normalized pressure

q = heat-transfer rate

R = univeral gas constant

T = temperature

t = time

t^* = characteristic time

U = velocity in x direction

x = distance from front surface

$\tilde{\alpha}$ = viscous coefficient

$\tilde{\beta}$ = inertial coefficient

ϵ = emissivity

η = reflectivity

$\tilde{\eta}$ = cooling effectiveness defined by equation (45)

θ = normalized temperature

μ = viscosity

ξ = normalized distance

ρ = density

σ = Stefan-Boltzmann constant

τ = normalized time

ϕ = porosity

ψ_{con} = convective heat transfer attenuation factor due to mass injection

ψ_{rad} = radiative heat transfer attenuation factor due to mass injection

Subscripts and Superscripts

b = back face

c = convective

e = external

f = fluid

0 = without mass injection

r = radiative

radin = incident radiative

rerad = reradiative

s = solid

w = wall

∞ = free stream

ν = the νth band of radiation

$()'$ = differentiation with respect to ξ

---

at $x = 0$:

$$-k_s \frac{\partial T_s(0, t)}{\partial x} = q_c(t) + q_{\text{radin}}(t) - q_{\text{rerad}}(t) \qquad (16)$$

$$\frac{\partial^2 T_f(0, t)}{\partial x^2} = 0 \quad \text{or} \quad -k_f \frac{\partial T_f(0, t)}{\partial x} = 0 \qquad (17)$$

$$p_f(0, t) = p_{f_w}(t) \qquad (18)$$

at $x = L$:

$$T_s(L, t) = T_f(L, t) = T_b = \text{constant} \qquad (19)$$

The incident convective and radiative heating fluxes with mass injection [9, 10] are

$$q_c(t) = \rho_e U_e C_{H0} \psi_{\text{con}} (H_e - H_w) = q_{c_0}(t) \psi_{\text{con}} \qquad (20)$$

$$\psi_{\text{con}} = \tilde{B}_0/(e^{\tilde{B}_0} - 1) \qquad (21)$$

$$\tilde{B}_0 = \dot{m}/\rho_e U_e C_{H0}(t) \qquad (22)$$

$$q_{\text{radin}}(t) = \sum_{\nu=n}^{n'} (1 - \eta_e) q_{r_{e_\nu}}(t) \psi_{\text{rad}} \qquad (23)$$

and the surface reradiation heat flux is

$$q_{\text{rerad}}(t) = \epsilon \sigma T_{s_w}^4(t) \qquad (24)$$

In equations (20) and (23), ψ_{con} and ψ_{rad} are the attenuation factors for incident convective and radiative heating fluxes due to mass injection.

Method of Solution

The Hartree-Womersley Method. The governing equations (5), (7), and (8) can be written in nondimensional forms by introducing the properties

$$\theta_s(\xi, \tau) = (T_s - T_b)/(T_{s_w} - T_b) \qquad (25)$$

$$\theta_f(\xi, \tau) = (T_f - T_b)/(T_{s_w} - T_b) \qquad (26)$$

$$\bar{p}_f(\xi, \tau) = p_f/p_{f_w} \qquad (27)$$

$$\xi = x/L \qquad (28)$$

$$\tau = t/t^* \qquad (29)$$

The nondimensional equations are the partial differential equations of parabolic type having both ξ- and τ-derivatives.

The solution by the Hartree-Womersley method (the H-W method) [5, 6] is achieved by replacing the τ-derivatives with the backward-difference quotients to transform each set of partial differential equations into a system of ordinary differential equations. The basic scheme is diagramed in Fig. 2. If the solution at the previous time step is known, a solution at $\tau = \tau_n$ can be found by integration in the ξ-direction on the strip $\tau = \tau_n$.

The two τ-derivatives in the governing equations are replaced by the differences

$$\partial \theta_s/\partial \tau = (\theta_s - \theta_{s_{n-1}})/(\tau - \tau_{n-1}) \qquad (30)$$

$$\partial \theta_f/\partial \tau = (\theta_f - \theta_{f_{n-1}})/(\tau - \tau_{n-1}) \qquad (31)$$

where the subscript $(n - 1)$ represents the previous time. The subscript n representing the current time is omitted for convenience.

When equations (30) and (31) are substituted into the governing equations, the unknown variables θ_s and θ_f appear on both the right- and left-hand sides of the equations, so this difference scheme is implicit. The reduced governing equations are approximated by the system, with the constant coefficient Φ's,

$$\theta_s'' + \Phi_1(\theta_s - \theta_f) + \Phi_4 e^{\alpha L \xi} + \Phi_5 e^{-\alpha L \xi} = \frac{\Phi_{20}}{\Delta \tau} (\theta_s - \theta_{s_{n-1}}) \qquad (32)$$

$$\theta_f'' + \Phi_2 \theta_f' + \Phi_3(\theta_s - \theta_f) + \Phi_6 e^{\alpha L \xi} + \Phi_7 e^{-\alpha L \xi}$$
$$+ \frac{\Phi_{21}\theta_f^2 + \Phi_{22}\theta_f + \Phi_{23}}{\bar{p}_f^2}$$
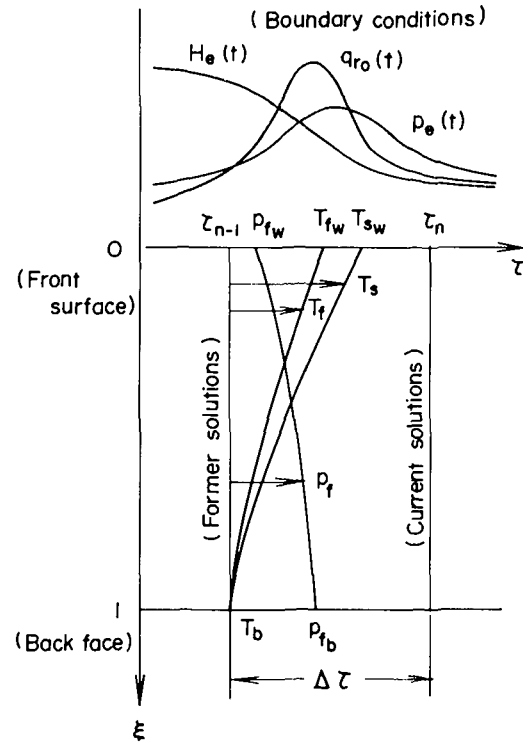
$$= \frac{\Phi_{24}\bar{p}_f}{(T_{s_w} - T_b)\theta_f + T_b} \frac{1}{\Delta \tau} (\theta_f - \theta_{f_{n-1}}) \qquad (33)$$

$$\bar{p}_f \bar{p}_f' - \Phi_8 \theta_f - \Phi_9 = 0 \qquad (34)$$

where $()'$ represents differentiation with respect to ξ, and

$$\Delta \tau = \tau - \tau_{n-1} \qquad (35)$$

The implicit difference scheme imposes no restriction on the mesh ratio $\Delta \tau/(\Delta \xi)^2$.

The initial and boundary conditions are
at $\tau = 0$:

$$\theta_s = 0 \qquad (36)$$

$$\theta_f = 0 \qquad (37)$$

$$\bar{p}_f = 1 \qquad (38)$$

And for each time step
at $\xi = 0$:

$$\theta_s' = \Phi_{10}(q_w + q_{\text{radin}} - q_{\text{rerad}}) \qquad (39)$$

$$\theta_f'' = 0 \quad \text{or} \quad \theta_f' = 0 \qquad (40)$$

$$\bar{p}_f = 1 \qquad (41)$$

at $\xi = 1$:

$$\theta_s = 0 \qquad (42)$$

$$\theta_f = 0 \qquad (43)$$

Two-Point Boundary Value Problem. The reduced simultaneous nonlinear ordinary differential equations must satisfy the boundary conditions both at $\xi = 0$ and at $\xi = 1$. In order to investigate the differential equations, the so-called shooting method is used. Initially assuming the surface temperatures T_{s_w} and T_{f_w}, the differential equations are integrated to $\xi = 1$. The values of T_{s_w} and T_{f_w} are improved by solving the fundamental equation that relates the values T_{s_w} and T_{f_w} to the errors in the boundary conditions at $\xi = 1$. Numerically, this functional equation is solved by the Secant method

[11]. The iteration is continued until the boundary conditions at $\xi = 1$ are satisfied within a certain specified tolerance. The requirement for convergence of the solution is

$$[\theta_{s1} - \theta_s(1)]^2 + [\theta_{f1} - \theta_f(1)]^2 \leqq 10^{-6} \qquad (44)$$

where θ_{s1} and θ_{f1} are the prescribed boundary conditions at $\xi = 1$. Accurate guess values for T_{sw} and T_{fw} for the ordinary differential equations at each time step are required for rapid convergence of the iteration scheme.

Sample Calculation. As in reference [3], silica (SiO_2) and carbon dioxide (CO_2) are taken as the porous matrix and the transpirant gas. Thermal and optical properties are described in Appendix C of reference [3].

The trajectory and the convective and radiative data for a 15 deg-entry into a Saturn nominal atmosphere [9, 10] are used. The pressure and enthalpy at the boundary-layer edge and radiative heating without mass injection, used as boundary conditions, are shown in Fig. 3.

Results and Discussions

Numerical results are presented for the unsteady thermal response of the CO_2-transpired porous silica matrix for 15 deg-entry into a Saturn nominal atmosphere. The ambient heating and pressure during the entry into the Saturn nominal atmosphere are derived from Fig. 3. Corresponding to the ambient conditions, the in-depth temperatures rise up to $t = 23.7$ s, when the incident radiative heating flux has a peak value, and gradually decrease after $t = 23.7$ s. An example of the instantaneous solid and fluid temperature distributions and the fluid pressure distribution within the matrix ($\xi = 0$, front surface; $\xi = 1$, back face) for $\dot{m} = 0.1$ g/cm²/s, $L = 1.0$ cm, $\phi = 0.8$, and $\psi_{\text{rad}} = 1.0$ is shown in Fig. 4. As described in reference [3], the solution is not affected whether $\theta_f'(0, \tau) = 0$ or $\theta_f''(0, \tau) = 0$ is imposed as a boundary condition; therefore, the former is used.

In this figure, the effect of radiative transfer within the porous matrix on the in-depth temperatures and fluid pressure is also presented. The solid and dashed curves represent the solutions with and without internal radiative transfer, respectively, for the same input and boundary conditions. The solid and fluid temperatures and fluid pressure for the case with internal radiative transfer, rather than those for the case without internal radiative transfer, are higher. These higher temperatures and pressure are caused by internal radiative
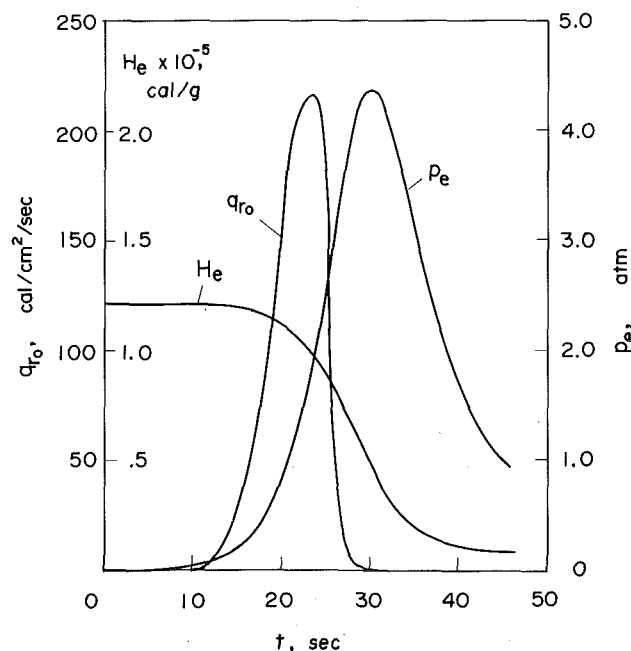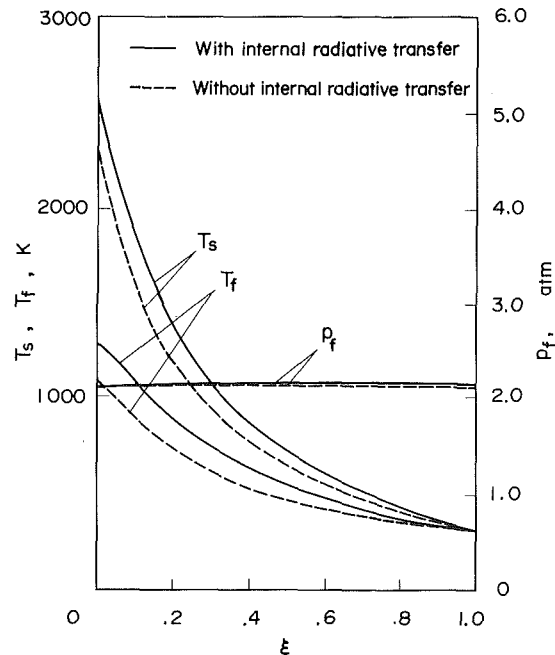
Fig. 4 Solid and fluid temperatures and fluid pressure distributions within the matrix: $t = 23.7$ s, $\dot{m} = 0.1$ g/cm²/s, $L = 1.0$ cm, $\phi = 0.8$, $\psi_{\text{rad}} = 1.0$

absorption by the absorbing coolant gas. It seems to be disadvantageous to use an absorbing gas for the transpirant; however, injection of an absorbing gas into the boundary layer can reduce the incident radiative heating more than a nonabsorbing gas when the material surface has smaller reflectivity below a break-even one [1]. The reduction of the incident heating itself dominates over the increase of the in-depth temperatures and pressure; therefore the use of the absorbing gas is advantageous for the cooling system with internal radiative transfer.

The solid and fluid temperatures decrease monotonically from the front surface of the matrix, so the surface temperature is the important factor in evaluating the performance of the cooling system. The fluid temperature is always lower than the solid temperature, so it cools the system. The fluid pressure in the wall is also influenced by the external pressure. Fig. 5(a) illustrates typical surface solid and fluid temperatures and fluid pressure histories for the same conditions as in Fig. 4. Fig. 5(b) shows the effect of increasing mass transpiration rate to $\dot{m} = 0.3$ g/cm²/s with the same other conditions as Fig. 5(a). The peaks of the surface temperature histories and the back-face fluid pressure history correspond to the peaks of the incident radiative pulse and the external pressure shown in Fig. 3, respectively.

The cooling effectiveness per mass injection rate defined in reference [3] as

$$\tilde{\eta} = (T_{sw0} - T_{sw})/(T_{sw0} - T_b)\tilde{B}_0 \qquad (45)$$

depends strongly on the mass injection rate; it decreases as the injection rate increases (see Fig. 6). Therefore, in choosing a mass injection rate for a transpiration-cooled system, a trade-off, in terms of the system design constraints, must be made between two effects: As the injection rate is increased to provide an acceptably low surface temperature, there is a proportional decrease in the cooling effectiveness of the system.

Fig. 7 shows the back-face heat-transfer rate histories with the effects of internal radiative transfer and mass injection rate. Since the back face is kept at constant temperature T_b, the back-face heat-transfer rate is variable with respect to the cooling parameters. The back-face heat-transfer rate is increased when the internal radiative transfer is included, because the presence of absorbing gas makes the solid and fluid temperatures within the matrix with internal radiative transfer higher than those without internal radiative transfer. In-
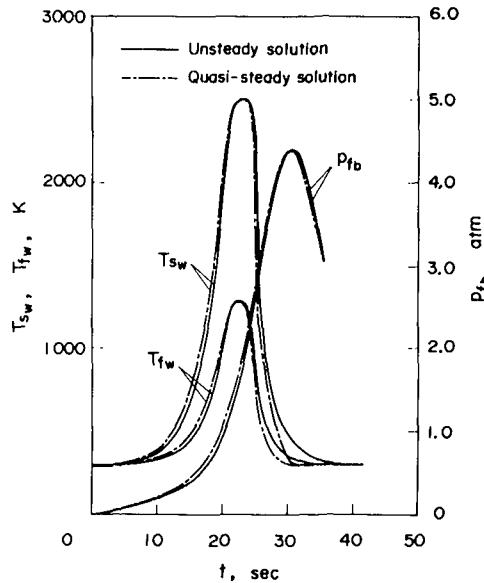

Fig. 3 Profiles of external pressure, enthalpy, and radiative heating without mass injection for 15 deg Saturn nominal entry
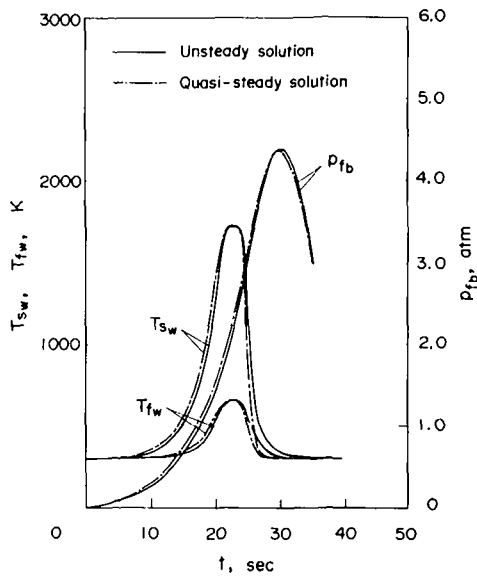
Fig. 5 (a) $\dot{m} = 0.1$ g/cm²/s

Fig. 5 (b) $\dot{m} = 0.3$ g/cm²/s

Fig. 5 Surface temperatures and back-face fluid pressure histories: $L = 1.0$ cm, $\phi = 0.8$, $\psi_{rad} = 1.0$

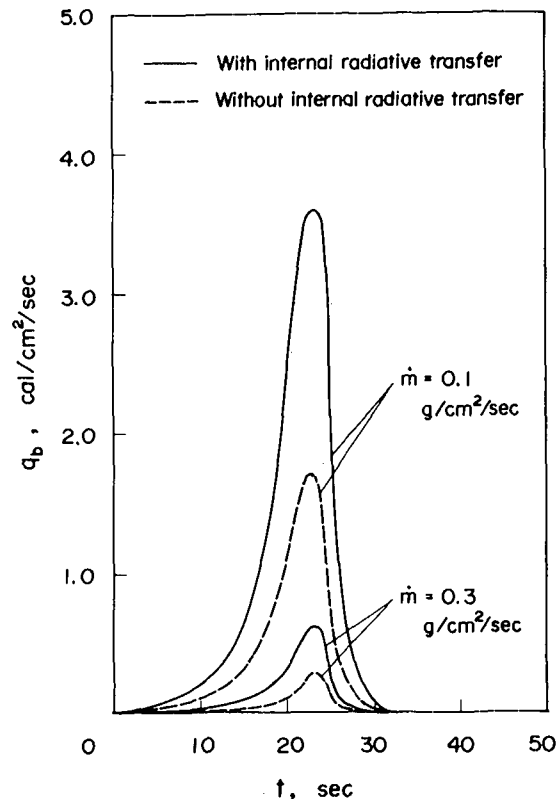Fig. 6 Cooling effectiveness: $L = 1.0$ cm, $\phi = 0.8$, $\psi_{rad} = 1.0$

Fig. 7 Back-face heat transfer rate histories: $L = 1.0$ cm, $\phi = 0.8$, $\psi_{rad} = 1.0$

creasing mass injection rate, of course, reduces the back-face heat transfer.

If the present cooling system is assumed to melt at 1981 K [10], surface ablation occurs at approximately $t = 20$ s for $\dot{m} = 0.1$ g/cm²/s (see Fig. 5(a)). Above this melting temperature, transpiration of the injected gas and the surface ablation of material simultaneously play a role of cooling. But by increasing the injection rate to $\dot{m} = 0.3$ g/cm²s, the maximum surface solid temperature is below the ablation temperature (see Fig. 5(b)), and so the probe is cooled solely by transpiration. In this analysis, for the purpose of clarifying the effect of transpiration, the surface ablation is not included. The analysis including the ablation effect will be a further extension.

The quasi-steady solutions including internal radiative transfer given in reference [3] are also shown in Figs. 5(a) and 5(b). The difference between quasi-steady solutions and the unsteady solutions by this paper indicate the effect of neglecting the transient terms in

quasi-steady analysis. When this comparison is made for a range of problem parameters, it is observed that although at peak heating the temperatures and fluid pressure of the quasi-steady solution slightly lag those of the unsteady solution (see Figs. 5(a) and 5(b)), the overall agreement of the two is quite good. As an another example of this agreement, the value of the injection rate required to keep the surface temperature below 1981 K is determined from each solution. From

Fig. 8 Desired minimum mass injection rate for transpiration-cooled system: $L = 1.0$ cm, $\phi = 0.8$, $\psi_{rad} = 1.0$

deg-entry into a Saturn nominal atmosphere was computed. The following major conclusions were obtained:

1 The surface solid and fluid temperature and the back-face heat transfer quickly respond to the incident radiative pulse.

2 Increasing the injection rate reduces the matrix temperature but also adversely reduces the cooling effectiveness per mass injection rate and increases the back-face fluid pressure.

3 The desired minimum mass injection rate to keep the surface solid temperature below the melting temperature of the matrix material is obtained. It is not much different from the result of the analysis by reference [3]; other sets of conditions also give a result close to that of reference [3], and, therefore, the simplified analysis for a transpiration-cooled system by reference [3] can be useful in engineering application.

Acknowledgment

References

1 Howe, J. T., "Shielding of Partially Reflecting Stagnation Surface Against Radiation by Transpiration of an Absorbing Gas," NASA TR R-95, 1961.

2 Chiou, J. P., and El-Wakil, M. M., "Heat Transfer and Flow Characteristics of Porous Matrices With Radiation As a Heat Source," JOURNAL OF HEAT TRANSFER, TRANS. ASME, Series C, Vol. 88, Feb. 1966, pp. 69–76.

3 Kubota, H., "A Simplified Analytical Solution for Thermal Response of One-Dimensional, Steady-State Transpiration Cooling System in Radiative and Convective Environment," NASA TN D-8129, 1976.

4 Curry, D. M., "Two-Dimensional Analysis of Heat and Mass Transfer in Porous Media Using the Strongly Implicit Procedure," NASA TN D-7608, 1974.

5 Hartree, D. R., and Womersley, J. R., "A Method for the Numerical or Mechanical Solution of Certain Types of Partial Differential Equations," *Proceedings of the Royal Society*, Vol. 161A, 1937, pp. 353–366.

6 Jaffe, N. A., and Smith, A. M. O., "Calculation of Laminar Boundary Layers by Means of a Differential-Difference Method," *Progress in Aerospace Science*, 1972, pp. 49–212.

7 Schneider, P. J., Maurer, R. E., and Strapp, M. G., "Two-Dimensional Transpiration-Cooled Nosetip," *Journal of Spacecraft and Rockets*, Vol. 8, No. 2, 1971, pp. 170–176.

8 Kortüm, G., *Reflectance Spectroscopy*, Springer-Verlag, New York, 1969.

9 Nicolet, W. E., Morse, H. L., and Vojvodich, N. S., "Outer Planet Probe Entry Thermal Protection. Part I: Aerothermodynamic Environment," AIAA Paper No. 74-700, 1974.

10 Howe, J. T., and McCulley, L. D., "Volume-Reflecting Heat Shields for Entry Into Giant Planet Atmosphere," AIAA Paper No. 74-669, 1974.

11 Nachtsheim, P. R., and Swigert, P., "Satisfaction of Asymptotic Boundary Conditions in Numerical Solution of Systems of Nonlinear Equations of Boundary-Layer Type," NASA TN D-3004, 1965.

reference [3] the quasi-steady solution gives a value $\dot{m} \simeq 0.2$ g/cm^2/s; from Fig. 8 the unsteady solution gives almost the same result. So it is verified, at least for the problems considered here, that the simple and inexpensive (computer time) analysis of reference [3] provides useful engineering results.

Conclusions

The unsteady thermal response of a one-dimensional transpiration-cooled system consisting of a reflecting porous matrix and an injected absorbing gas in a radiative and convective environment was presented. The incident radiative and convective heating are specified as boundary conditions.

The instantaneous solid and fluid temperatures and the fluid pressure distributions within the transpiration-cooled porous matrix are solved numerically by the Hartree-Womersley method.

As an application of the method, the thermal response for the 15

H. Koyama

Assoc. Professor.

A. Nakayama

Graduate Student.

K. Sato

Research Student.

T. Shimizu

Assoc. Professor.
Department of Mechanical Engineering,
Faculty of Engineering,
Shizuoka University,
Hamamatsu, Japan

Local Mass Transfer From Rotating Wedge-Shaped Blades

The purpose of this investigation is to determine the mass transfer from rotating wedge-shaped blades in an air environment. Through theoretical considerations, effect of negative pressure gradient has been emphasized wherever possible. The experimental results are correlated with local Sherwood number and Reynolds number. Furthermore, a new method has been proposed to judge the flow type by reading directly the slope of contour lines of equal sublimation drawn on the surface.

1 Introduction

To solve a number of transfer problems, the sublimation mass transfer system is being used in place of heat transfer system. Mass transfer from rotating flat blades using the naphthalene sublimation method was performed by Koyama, et al. [1].[1] They used the blades having the same span of 250 mm, but different span to side ratios ranged from 3.5 to 8.3. However, no apparent effect due to the difference in the ratios was observed. The experimental results suggested that except the region very near the center hub where shearing stress ratio is not negligible (i.e., where the ratio of the distance from the axis of rotation to the side length being less than 2.0), mass transfer coefficient for the laminar averaged over the blade chord varies approximately in proportion to the square root of the distance from the rotation axis. This suggests that, if in two-dimensional flow the peripheral velocity corresponding to the distance from the rotation axis is used in place of a free-stream velocity, local Sherwood number for the region beyond a certain distance from the axis can be correlated in the same simple relation as the conventional form of two-dimensional forced convection. A local Sherwood number correlation of the conventional form has been established through the present study as an extension of the work by Koyama, et al. [1] for the rotating system.

In this paper, theoretical and experimental studies of mass transfer from rotating wedge-shaped blades shown in Fig. 1 will be described. Experiments using the naphthalene sublimation method in an air environment were performed. The phenomena are analogous to those of the forced convection heat transfer from heated rotating blades having uniform surface temperature.

In a wedge-shaped blade, four surfaces where different phenomena can be surveyed exist. One of the objectives of the present research was to explore the effects caused by the interactions of flow among these four surfaces. Some effects are briefly noted here. For a front surface in separated flow, as well as for a back surface in wake, a contour map of equal sublimation showed that mass transfer rate increases rapidly from an upstream corner, then decreases gradually to a downstream corner, yielding a maximum sublimation ridge on a blade surface. This map pattern is quite different from the one observed for a front surface under negative pressure gradient. Particularly for a back surface, the location of the maximum sublimation depends on the flow over its adjacent front surface. When the adjacent front surface is under negative pressure gradient, the maximum sublimation occurs at the more downstream side on the back surface, compared with the case of the adjacent front surface in separate flow. For both cases of the back surface, the overall mass transfer coefficient was nearly twice as high as that for the front surface under negative pressure gradient. The highest overall mass transfer coefficient among four surfaces was observed on the front surface in separated flow, and was about two and a half times of the overall mass transfer coefficient for the front surface under negative pressure gradient.

In this paper, however, the only case treated is the front surface where the flow acceleration occurs, yielding negative pressure gradient.

2 Theoretical Considerations

2.1 **Governing Equation and Simplification.** The expressions to local skin friction coefficients are derived by solving the momentum equations which include pressure gradient and body force terms, with an integral method as well as with an extended Reynolds analogy. These results are to be used to predict local Sherwood numbers. From the standpoint of applications to practical cases, all efforts have been made to obtain a closed form solution. Cross section of a blade is shown in Fig. 1 to explain an equivalent wedge angle Φ^*, and which

---

Copyright © 1977 by ASME

is the parameter representing the angle of inclination to each surface. Then, Φ^* is evaluated from,

Case 1 (see Fig. 1), $\Phi^* = \phi + 2\alpha > 0$

Case 2 (see Fig. 1), $\Phi^* = \phi - 2\alpha > 0$

where ϕ is wedge angle, and α attack angle.

Φ^* is defined as twice the angle between the main stream direction and each surface, hence Φ^* corresponds with twice the attack angle when each surface is regarded as a flat plate. Since only the cases of flow acceleration are to be treated in this paper, it is reminded that Φ^* should be positive.

The curvilinear orthogonal coordinate system (x, r, z) is set up as shown in Fig. 1 where x is curved along the blade in the direction of the inviscid streamline, r radial and z orthogonal to both x and r. It should be noted that analysis developed here, will be quite general to the models having moderate curvature in x-direction which may be taken as $(1/2) \times (\partial\Phi^*/\partial x)$, and not restricted to the present model as far as Φ^* is treated as the function of x rather than constant.

With usual boundary layer approximations, the equations of motion can be written as follows [2].

$$u\frac{\partial u}{\partial x} + v\frac{\partial u}{\partial r} + w\frac{\partial u}{\partial z} - 2\gamma\Omega v + \gamma^2\frac{uv}{r} - u_e\frac{\partial u_e}{\partial x} = \frac{1}{\rho}\frac{\partial \tau_x}{\partial z} \quad (1)$$

$$u\frac{\partial v}{\partial x} + v\frac{\partial v}{\partial r} + w\frac{\partial v}{\partial z} + \frac{\gamma^2}{r}(u_e{}^2 - u^2) - 2\gamma\Omega(u_e - u) = \frac{1}{\rho}\frac{\partial \tau_r}{\partial z} \quad (2)$$

The equation of continuity is,

$$\frac{\partial u}{\partial x} + \frac{\partial v}{\partial r} + \frac{\partial w}{\partial z} + \frac{v}{r} = 0 \quad (3)$$

The boundary conditions are,

$$z = 0: u = v = w = 0, \tau = \tau_0$$

$$z = \delta: u = u_e, v = w = \tau = 0 \quad (4)$$

where u, v, w are velocities in x-, r-, and z-directions, Ω angular velocity, $\gamma = \cos(\Phi^*/2)$, ρ density, p static pressure, τ shear stress, δ boundary layer thickness and subscripts, x and r denote corresponding directions while 0 and e denote wall and boundary layer edge, respectively.

Equation (1) is rewritten as,

$$\frac{\partial}{\partial x}(u_e u - u^2) - \frac{\partial}{\partial x}(u_e u) + u\frac{\partial u}{\partial x} - v\frac{\partial u}{\partial r} - w\frac{\partial u}{\partial z} + 2\gamma\Omega v$$

$$- \gamma^2\frac{uv}{r} + u_e\frac{\partial u_e}{\partial x} + \frac{1}{\rho}\frac{\partial \tau_x}{\partial z} = 0 \quad (1a)$$

The continuity equation (3) gives,

$$\frac{\partial}{\partial x}(u_e u) = -u_e\frac{\partial v}{\partial r} - u_e\frac{\partial w}{\partial z} - \frac{u_e v}{r} + u\frac{\partial u_e}{\partial x}$$

$$v\frac{\partial u}{\partial r} = \frac{\partial}{\partial r}(uv) + u\frac{\partial u}{\partial x} + u\frac{\partial w}{\partial z} + \frac{uv}{r} \quad (5)$$

Substitution of equations (5) into equation (1a) reduces to,

$$\frac{\partial}{\partial x}(u_e u - u^2) + (u_e - u)\frac{\partial u_e}{\partial x} - \left(\frac{\partial}{\partial r} + \frac{1 + \gamma^2}{r}\right)(uv)$$

$$+ \left\{u_e\frac{\partial}{\partial r} + \frac{u_e + 2\gamma(r\Omega)}{r}\right\}v - \frac{\partial}{\partial z}(uw) + u_e\frac{\partial w}{\partial z} + \frac{1}{\rho}\frac{\partial \tau_x}{\partial z} = 0 \quad (6)$$

Equation (3) also gives,

$$u\frac{\partial v}{\partial x} = \frac{\partial}{\partial x}(uv) + v\frac{\partial v}{\partial r} + v\frac{\partial w}{\partial z} + \frac{v^2}{r} \quad (7)$$

Substitution of equation (7) into equation (2) reduces to,

$$\frac{\partial}{\partial x}(uv) + \frac{\gamma^2}{r}\{(u_e u - u^2) + u_e(u_e - u)\} - 2\gamma(\Omega r)\frac{u_e - u}{r}$$

$$+ \left(\frac{\partial}{\partial r} + \frac{1}{r}\right)v^2 + \frac{\partial}{\partial z}(vw) - \frac{1}{\rho}\frac{\partial \tau_r}{\partial z} = 0 \quad (8)$$

To perform the integration method, the velocity functions are suggested beforehand according to Prandtl's three-dimensional velocity profiles [3], which may be presented as,

$$v^* = \epsilon g u^* \quad (9)$$

with boundary conditions as follows

$$\eta = 0: u^* = 0, g = 1$$

$$\eta = 1: u^* = 1, \frac{\partial u^*}{\partial \eta} = g = \frac{\partial g}{\partial \eta} = 0 \quad (10)$$

where $u^* = u/u_e$, $v^* = v/u_e$, shear stress ratio $\epsilon = \tau_{0_r}/\tau_{0_x}$, and $\eta = z/\delta$. Using equation (9), the following nondimensional thicknesses are set up.

$$H_\delta = [u_e - u]_\delta/(u_e\theta) = [1 - u^*]_\delta/\theta$$
$$N = [v]_\delta/(\epsilon u_e\theta) = [gu^*]_\delta/\theta$$
$$L = [v^2]_\delta/(\epsilon^2 u_e{}^2\theta) = [g^2 u^{*2}]_\delta/\theta$$
$$K = [uv]_\delta/(\epsilon u_e{}^2\theta) = [gu^{*2}]_\delta/\theta \quad (11)$$

where $[\ ]_A$, in general, denotes the integration from zero to the focused suffix A with respect to the corresponding direction, and $\theta = [u^* - u^{*2}]_\delta$ as momentum thickness in x-direction.

Nomenclature

$c_f = 2\tau_0/(\rho u_e{}^2)$, $c_{fx} = 2\tau_{0_x}/(\rho u_e{}^2)$, local skin friction coefficients

C_n, H_c = coefficients denoted in equations (18) and (16), respectively

$C_n^* = 1/C_n$, pressure gradient parameter

$C_f{}^0$, D, E, E_ϵ, ϵ^0, θ^0 = terms denoted in equations (20)–(22)

D_v = diffusion coefficient

g = functional relation denoted in equation (9)

G^* = functional relation denoted in equation (27)

h = local mass transfer coefficient

H_δ, N, L, K ($K^* = 1/K$) = dimensionless thicknesses defined in equation (11)

I, I_ϵ = departure functions defined in equations (20) and (21)

n ($n_j = n + j$) = integer related to velocity distribution

p = static pressure

$R_{ex} = r\Omega x/\nu$, $R_{ex}^* = u_e x/\nu$, Reynolds numbers

R_n = naphthalene gas constant

S_c = Schmidt number

$Sh = hx/D_\nu$, Sherwood number

Sh^0 = coefficient denoted in equation (36)

T_w = naphthalene surface temperature

u, v, w ($u^* = u/u_e$, $v^* = v/u_e$) = velocity components on x-, r-, z-directions

u_e ($\dot{u}_e = u_e/(r\Omega)$, $\beta = \dot{u}_e(x_0)$) = main flow velocity component at boundary edge

x, r, z ($\dot{x} = x/x_0$, $\dot{r} = r/x_0$, $\eta = z/\delta$) = orthogonal curvilinear coordinate system

x_0 = distance between leading and trailing edges in x-direction

X, Y = coordinate system attached on blade surface (Fig. 4)

Δz = height difference on a naphthalene surface per unit time

α, ϕ, Φ^* ($m = \Phi^*/(2\pi - \Phi^*)$, $\gamma = \cos(\Phi^*/2)$) = attack, wedge, and equivalent wedge angles, respectively (Fig. 1)

γ_n = cast naphthalene specific weight

δ = boundary layer thickness

$\epsilon = \tau_{0_r}/\tau_{0_x}$, shear stress ratio at wall

θ ($\theta = \dot{\theta}/x_0$, $G = \theta/\delta$) = momentum thickness in x-direction

$\eta = z/\delta$, dimensionless coordinate in z-direction

ν = kinematic viscosity

ρ = density of fluid

τ, τ_0 = shear stresses inside boundary layer and at wall

Ω = angular velocity

$'$ = prime denoting the differential with respect to $\dot{x}$

$[\ ]_{\dot{x}}$, $[\ ]_\delta$ = operators for the integration from zero to the focused suffix with respect to the corresponding direction
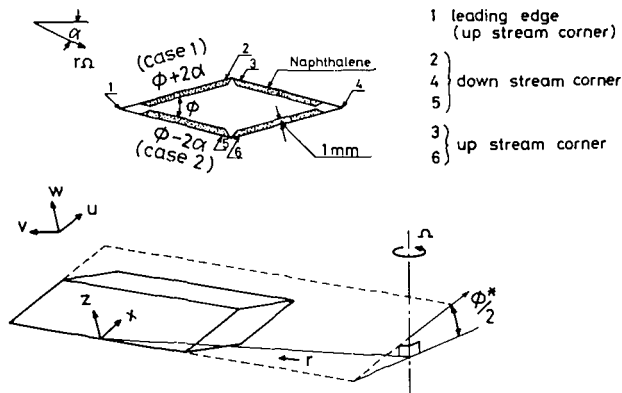
Fig. 1 Equivalent wedge angle and coordinate system

Now, equations (6) and (8) are integrated across the boundary layer with aids of equations (3), (4), and (11), which results,

$$\frac{\partial}{\partial x}(u_e{}^2\theta) + \frac{1}{2}H_\delta\theta\frac{\partial}{\partial x}(u_e{}^2) - \left(\frac{\partial}{\partial r} + \frac{1+\gamma^2}{r}\right)(Ku_e{}^2\theta\epsilon)$$
$$+ \left(u_e\frac{\partial}{\partial r} + \frac{u_e + 2\gamma r\Omega}{r}\right)(Nu_e\theta\epsilon) - \frac{\tau_{0x}}{\rho} = 0 \quad (12)$$

$$\frac{\partial}{\partial x}(Ku_e{}^2\theta\epsilon) + \frac{\gamma^2}{r}(1+H_\delta)u_e{}^2\theta - 2\frac{\gamma}{r}H_\delta r\Omega u_e\theta$$
$$+ \left(\frac{\partial}{\partial r} + \frac{1}{r}\right)(Lu_e{}^2\theta\epsilon^2) + \frac{\tau_{0x}}{\rho}\epsilon = 0 \quad (13)$$

Some simplification is still required, since the resulting partial differential equations are quite formidable. To simplify, a second order of magnitude analysis is done on these equations following Mager [4]. θ is assumed to be the order of δ, the nondimensional thicknesses and r the order of 1, u_e the same order of $r\Omega$, while $\epsilon \ll 1$. Then, terms of the order of $\epsilon\theta u_e{}^2$ in equation (12) and those of the order of $\epsilon^2\theta u_e{}^2$ in equation (13) are neglected. This makes the equations much simpler as,

$$\dot{\theta}' + \left(1 + \frac{H_\delta}{2}\right)\frac{(\dot{u}_e{}^2)'}{\dot{u}_e{}^2}\dot{\theta} - \frac{c_{fx}}{2} = 0 \quad (14)$$

$$\epsilon' + \left[\frac{(K\dot{u}_e{}^2\dot{\theta})'}{K\dot{u}_e{}^2\dot{\theta}} + K^*\frac{\dot{\theta}'}{\dot{\theta}} + K^*\left(1 + \frac{H_\delta}{2}\right)\frac{(\dot{u}_e{}^2)'}{\dot{u}_e{}^2}\right]\epsilon$$
$$- \left[2H\delta\left(\frac{\gamma}{\dot{u}_e}\right) - (H_\delta + 1)\gamma^2\right]\frac{K^*}{\dot{r}} = 0 \quad (15)$$

where the dot indicates dimensionless referred to certain scale factors such as $\dot{x} = x/x_0$, $\dot{r} = r/x_0$ and $\dot{u}_e = u_e/(r\Omega)$, while the prime denotes differential with respect to $\dot{x}$, furthermore $K^* = 1/K$ and $c_{fx} = 2\tau_{0x}/(\rho u_e{}^2)$ which is the local skin friction coefficient in x-direction.

It is noted that the simplification procedure introduced has made equation (14) of x-direction independent of r, and the same can be applied to the momentum integral equation for the two-dimensional flow.

2.2 General Solutions Common to Both Laminar and Turbulent Flow. To solve the differential equations (14) and (15), local skin friction coefficient in x-direction is assumed to be,

$$c_{fx} = H_c\left(\frac{\nu}{\theta u_e}\right)^{2/n_1} \quad (16)$$

where ν is kinematic viscosity, and the integer with suffix, $n_j = n + j$. The quantity H_c is generally a function of x when the pressure gradient exists in this direction, but here, taking account of the effective approximation, this is to be taken as constant. In fact, this assumption is often used for turbulent case, and which corresponding to Power law presented as,

$$u^* = \eta^{1/n} \quad (17)$$

Using C_n according to K. Wieghart [5.a], H_c may be correlated as,

$$H_c = 2C_n{}^{-2n/n_1}G^{2/n_1} \quad (18)$$

where C_n is constant depending on n, and $G = \theta/\delta$. The presentation for c_{fx} in equation (16) along with equation (18) can be used also in laminar case if the following relations are provided.

$$n = 1, C_n = 1 \Big/ \left(\frac{\partial u^*}{\partial\eta}\Big|_{\eta=0}\right) \quad (19)$$

Some examples of the aforementioned relations in both cases are listed in Table 1. Now, equation (16) for c_{fx} may well be regarded as the common presentation for both laminar and turbulent flow, and this enables one to solve the differential equations (14) and (15) at one time for both cases.

With H_c being assumed constant, H_δ and K have also been taken as constant so as to obtain a closed form. The correlations finally obtained are,

$$\dot{\theta} = \theta^0 R_{ex}{}^{*-2/n_3}\dot{x}I^{n_1/n_3} \quad (20)$$

where

$$\theta^0 = [(n_3/2n_1)H_c]^{n_1/n_3}, R_{ex}{}^* = u_ex/\nu, I = \{C_\theta + [\dot{u}_e{}^E]_{\dot{x}}\}/\dot{x}\dot{u}_e{}^E,$$

$E = (2n_2 + n_3H_\delta)/n_1$, and C_θ: an integration constant.

$$\epsilon = \epsilon^0(\dot{x}/\dot{r})I_\epsilon \quad (21)$$

where

$$\epsilon^0 = (H_\delta - 1)K^*/D, D = 1 + \frac{n_1}{n_3}(1 + K^*),$$

$$I_\epsilon = \frac{C_\epsilon + D\{\dot{u}_e{}^{E_\epsilon}(\dot{x}I)^{D-1}\{2H_\delta(\gamma/\dot{u}_e) - \gamma^2(H_\delta + 1)\}\dot{x}}{(H_\delta - 1)\dot{x}\dot{u}_e{}^{E_\epsilon}(\dot{x}I)^{D-1}}$$

$E_\epsilon = (2n_2/n_3)(1 + K^*) + H_\delta K^*$, and C_ϵ: an integration constant. Functions I and I_ϵ have the meaning of "departure from flat blade at zero incidence" since they tend to be unity as the angle of incidence becomes zero in the case of a flat blade.

The local skin friction coefficient is presented as follows, using equations (20) and (21) along with equation (16).

$$c_f = c_f{}^0R_{ex}{}^{*-2/n_3}I^{-2/n_3}[1 + \epsilon^2]^{1/2} \quad (22)$$

where

$$c_f{}^0 = H_c\left[\frac{n_3}{2n_1}H_c\right]^{-2/n_3}$$

On the assumption of moderate pressure gradient, Reynolds analogy may be employed, that is,

$$\text{Sh} = \frac{hx}{D_v} = \frac{1}{2}c_fS_c{}^{1/3}R_{ex}{}^* \quad (23)$$

where Sh is Sherwood number, h mass transfer coefficient, D_v diffusion coefficient, and Sc Schmidt number. Substitution of equation (22) into equation (23) yields,

$$\text{Sh} = \frac{1}{2}c_f{}^0S_c{}^{1/3}R_{ex}{}^{*n_1/n_3}I^{-2/n_3}[1 + \epsilon^2]^{1/2} \quad (24)$$

2.3 Velocity Profiles. Now, to calculate the parameters already appeared, the velocity functions u^* and g have to be selected, respectively, in laminar and turbulent flow. However, since g satisfies the boundary conditions equation (10), one may choose a second degree polynomial function common to both laminar and turbulent flow as,

$$g = (1 - \eta)^2 \quad (25)$$

For laminar, u^* may be chosen as a fourth-degree polynomial given by,

$$u^* = C_n{}^*\eta + 3(2 - C_n{}^*)\eta^2 + (3C_n{}^* - 8)\eta^3 + (3 - C_n{}^*)\eta^4 \quad (26)$$

where

$$C_n* = 1/C_n = \frac{\partial u*}{\partial \eta}\bigg|_{\eta=0}$$

Equation (26) obviously satisfies the boundary conditions of $u* = 0$ at $\eta = 0$ and $u* = 1$, $\partial u*/\partial \eta = \partial^2 u*/\partial \eta^2 = 0$ at $\eta = 1$. The pressure gradient parameter C_n* is still unknown, yet, all the assumed parameters already appeared become functions of C_n* only, because of the assumption of equation (26). As soon as C_n* is specified, all of the parameters will be calculated, by the following relationships,

$$G = G*/1260$$

$$H_\delta = 63(8 - C_n*)/G*$$

$$K* = \frac{11}{4} \frac{G*}{7C_n*^2 + 46C_n* + 184}$$

where

$$G* = 144 + 12C_n* - 5C_n*^2 \qquad (27)$$

The pressure gradient parameter C_n* may be correlated with a boundary layer edge velocity function $u_e(x)$ through the boundary condition at a surface as,

$$\nu \frac{\partial^2 u}{\partial z^2}\bigg|_{z=0} = -u_e \frac{\partial u_e}{\partial x}$$

or

$$\frac{\delta^2}{\nu} \frac{du_e}{dx} = 6(C_n* - 2) \qquad (28)$$

Noting, $G = \theta/\delta$ and $n = 1$ for laminar, substitution of equation (20) into equation (28) yields,

$$I \left(\frac{\theta^0}{G}\right)^2 \left\{\frac{\dot{x}\dot{u}_e'}{\dot{u}_e}\right\} = 6(C_n* - 2)$$

where

$$\theta^0 = \sqrt{2C_n*G} \qquad (29)$$

The preceding assumption on the constancy of the parameters such

as C_n, H_δ and $K*$ can be substantiated when $\{\dot{x}\dot{u}_e'/\dot{u}_e\}$ in equation (29) is taken as a constant m. This leads one to consider the Falkner-Skan two-dimensional potential flow as given by,

$$\dot{u}_e \propto \dot{x}^m \qquad (30)$$

A velocity distribution of this type of equation (30) may be realized for a flow passing an infinite wedge or an infinite cone, but is found also in the vicinity of a wedge-shaped leading edge of any closed body. The latter interpretation may be applied to the present model. Moreover, for properly shaped bodies, velocity profile of this type can occur at a sharp-cusped leading edge, even though the symmetry about the axis parallel to the free-stream direction is lacking. The relationship (30) specifies the departure function I as,

$$I = \frac{1}{1 + Em}$$

where

$$E = 3 + 2H_\delta \qquad (31)$$

By substituting equation (31) into equation (29) along with G and H_δ in equations (27), equation (29) finally reduces to a cubic characteristic equation with respect to C_n*,

$$5(1 + 3m)C_n*^3 - 2(11 - 30m)C_n*^2$$
$$- 120(1 + 10m)C_n* + 288(1 + 10m) = 0 \qquad (32)$$

After noting that $0 \le C_n* \le 4$ (i.e., $\max |u*| \le 1$, $\partial u*/\partial \eta|_{\eta=0} \ge 0$), furthermore for nonpositive pressure gradient, C_n* is restricted to the farther narrow range, $2 \le C_n* \le 4$ (i.e., $\dot{u}_e' \ge 0$). $C_n*(m)$ has been computed through equation (32) over the range, $0 \le m \le 1$, and finally, all the parameters as functions of $C_n*(m)$ alone have been determined.

The computed results give some prospect of calculating these parameters more simply. $C_n*(m)$ increases from 2.00 ($m = 0$) to 3.18 ($m = 1$), however, the change in nondimensional thicknesses such as G, H_δ and $K*$ are rather moderate since G varies from 0.118 to 0.112, H_δ from 2.55 to 2.41 and $K*$ from 1.34 to 1.11 when m is restricted to a moderate pressure gradient range, $0 \le m \le 0.2$. Consequently, the parameters which are the functions of the nondimensional thicknesses follow the same manner as the nondimensional thicknesses for this range of m. Hence, one may take these parameters as some representative constant values rather than depending on m. For example, since E changes from 8.11 ($m = 0$) to 7.81 ($m = 0.2$), E may be taken as either the zero pressure gradient value of 8.11 or the rounded value of 8. This indicates, the velocity profile $u*$ in the case of a flat plate, i.e., $u* = 2\eta - 2\eta^3 + \eta^4$ ($m = 0$, $C_n* = 2$), may well represent inclusively for the moderate pressure gradient range, and may be adequate for calculations of the parameters. This, in fact, was confirmed by comparing the approximate value of skin friction obtained as $E = 8$ with the exact value referred to D. R. Hartree [6] (the maximum error approximately 10 percent at $m = 0.2$). The value of eight being different from the well-known value of five [5.b] for the two-dimensional flow on a body with a blunt nose, which indicates that H_δ and G may not be treated simply constant unless the body possesses a sharp edge. However, when E is taken as the value of five instead of eight, the present results will be also valid for the body with blunt nose.

The calculated values using a selected fourth degree polynomial of zero pressure gradient for laminar and a $1/7$th power profile for turbulent are listed, respectively, in Table 1.

2.4 **Application to Present Flow Model.** General solutions can be promptly applied to the present flow model since γ is to be constant, and the edge velocity u_e may be given by the calculation over the corresponding two-dimensional potential flow with an aid of Schwarz-Christoffel's conformal mapping, which results in the same relation-ship as Falkner Skan's,

$$\dot{u}_e = \beta \dot{x}^m: 0 \le \dot{x} \le 1 \qquad (33)$$

where $\beta = u_e(x_0)/(r\Omega)$, $m = \Phi*/(2\pi - \Phi*)$, and x_0 the distance between leading and trailing (downstream corner) edges measured along

Table 1 Selected velocity profiles and their numerical values

	Laminar flow	Turbulent flow
$g(\eta)$	$(1-\eta)^2$	$(1-\eta)^2$
$\overset{*}{u}(\eta)$	$2\eta - 2\eta^3 + \eta^4$	$\eta^{\frac{1}{7}}$
n	1	7
C_n	0.500	8.74 N.B.1
H_c	0.470	0.0251
H_δ	2.55	1.29
$K*$	1.34	0.469
E N.B.2	8 or 5 (8.11) N.B.3	4 (3.86)
D N.B.2	2 (2.17)	2 (2.18)
E_c N.B.2	7 (6.93)	3 (3.25)
$\overset{0}{\theta}$	0.685	0.036
c_f^0	0.685	0.0577
$\overset{0}{\epsilon}$	0.959	0.0616

N.B.1., The value by K.Wieghart, the cases of n=7,8,9& 10 are available in [5a].

N.B.2., These values for exponents may well be taken as the integers around calculated values enclosed in parentheses for convenience over integral calculation

N.B.3., For a blade of a blunt nose, the value of 5 by A.Waltz [5b] should be recommended, while 8 for that of a sharp leading edge in laminar flow.

the free-stream direction. The substitution of equation (33) into equations (20), (21) and (24) results,

$$\dot{\theta} = \theta^0(1 + Em)^{-n_1/n_3}R_{ex}*^{-2/n_3}\dot{x} \qquad (34)$$

$$\epsilon = \epsilon^0 \left(\frac{\dot{x}}{\dot{r}}\right) \left\{ \left(\frac{2H_\delta}{H_\delta - 1}\right) \frac{\gamma/\dot{u}_e}{1 + \dfrac{E_\epsilon - 1}{D}m} - \left(\frac{H_\delta + 1}{h_\delta - 1}\right) \frac{\gamma^2}{1 + \dfrac{E_\epsilon}{D}m} \right\}$$

$$(35)$$

$$\text{Sh} = \text{Sh}^0 R_{ex}*^{n_1/n_3}[1 + \epsilon^2]^{1/2} = \text{Sh}^0 R_{ex}{}^{n_1/n_3}\dot{u}_e{}^{n_1/n_3}[1 + \epsilon^2]^{1/2} \quad (36)$$

where $\text{Sh}^0 = c_f{}^0/2\, S_c{}^{1/3}[1 + Em]^{2/n_3}$, $R_{ex} = (r\Omega)x/\nu$. Equation (34) indicates that the increase in incidence makes θ thin. And equation (35) gives,

$$\frac{\partial\epsilon}{\partial\dot{x}} \propto \dot{x}^{-m} - \left(\frac{H_\delta + 1}{2H_\delta}\right) \frac{1 + \dfrac{E_\epsilon - 1}{D}m}{1 + \dfrac{E_\epsilon}{D}m} \cdot \frac{\gamma\beta}{1 - m} \simeq \dot{x}^{-m} - 1 \geq 0 \quad (37)$$

Equation (37) shows the limiting stream angle is to grow with increasing $\dot{x}$. And equation (36) predicts that the mass transfer can be enhanced by inclining the flat blades.

The more accessible correlation for Sh can be obtained on the assumption of moderate incidence. For moderate angles of incidence, Departure function I_ϵ may be taken as a constant value of unit along x-direction, which simplifies equation (35) as,

$$\epsilon \simeq \epsilon^0(\dot{x}/\dot{r}) \qquad (38)$$

when r is large, ϵ will be

$$\epsilon \ll 1 \qquad (39)$$

Furthermore, for the moderate incidence,

$$\dot{u}_e \simeq 1 \quad \text{(Except the region near the leading edge)} \qquad (40)$$

The relations (39) and (40) allow one to simplify equation (36) as,

$$\text{Sh} = \text{Sh}^0 R_{ex}{}^{n_1/n_3}$$

When $S_c = 2.5$, using numerical values in table [1],

$$\text{Sh} = 0.465(1 + 8m)^{1/2}R_{ex}{}^{1/2} \quad \text{(laminar flow, } 0 \leq m \leq 0.2,$$
$$\text{i.e., } 0 \text{ deg} \leq \Phi^* \leq 60 \text{ deg)}$$

$$\text{Sh} = 0.0391(1 + 4m)^{1/5}R_{ex}{}^{4/5} \quad \text{(turbulent flow, } n = 7) \quad (41)$$

3 Experimental Apparatus

The schematic diagrams in Fig. 2 show the different parts of the apparatus. A duralumin blade has 1 mm depth mold on each surface. Naphthalene is heated in a glass beaker to about 100°C, and then poured to the mold of the blade which has been preheated to about 60°C.

Then, naphthalene is let cool down to the room temperature. After solidification, naphthalene surfaces are made smooth with a sharp knife.

During the operation, the room temperature is kept at 25°C with a variation of 1°C by observing the temperature-recorder, and the temperature at the periphery of blades is measured using copper-constantan thermocouple probes and the pyrometer at the beginning as well as at the end of the experiment.

81 measuring points in nine rows have been chosen on a surface at $\dot{r}$ between 2.0 and 3.6 (the span to side ratio is 4.4) following to reference [1], so that a local Sherwood number should be possibly correlated in the conventional form. Furthermore, the tip and center hub effects should be eliminated. The naphthalene height at these points on each surface is measured prior to the tests by an electronic micrometer. All data runs are done in a sealed laboratory whose volume is about 100 m³. The typical length of one data run takes as long as 4 hr, during which typically a solid naphthalene sublimation of approximately 150 μm in height is observed in the center of the surface.

① Wedge blade ④ Bearing
② Hub ⑤ Pulley
③ Rotating shaft ⑥ Motor
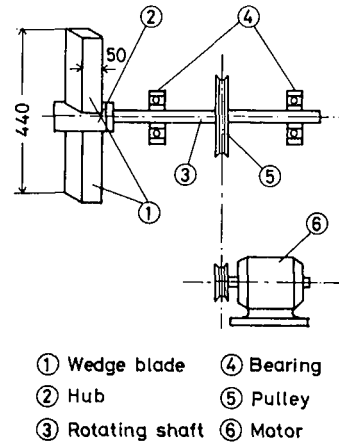
Fig. 2 Schematic diagram of experimental apparatus Naphthalene coated blades with a chord length of 100 × cos (Φ/2) mm and a span of 200 mm have 1 mm depth molds for solid naphthalene. The distance between the tips is 400 mm

After the completion of the run, the surface height at the same 81 points is measured again. The heights at four points chosen on a duralumin margin surrounding naphthalene surface are also measured to correct a positioning error. The highly precise screws connected with spiral spring are used for the adjustment in order to fix the blade surface on the same orientation as prior to the test as much as possible. This positioning error is estimated to be less than 5 μm, and has been corrected through the computation. The maximum total error over the measurements has been found to be about 5 percent.

A local mass transfer coefficient is calculated in terms of the height difference during the test. Owing to the large volume of the sealed laboratory, the mass fraction in the environment is the order of 10^{-7}, and which can be neglected, compared with the mass fraction at a surface of the order of 10^{-4}. Hence, a mass transfer coefficient can be expressed with an aid of the perfect gas law as,

$$h = R_n\gamma_n T_w \Delta z/P_n \qquad (42)$$

where R_n is naphthalene gas constant, γ_n cast naphthalene specific weight, P_n naphthalene vapor pressure, T_w surface temperature, and Δz height difference per unit time.

Naphthalene vapor pressure is determined from the vapor pressure-temperature relation by Sogin [7]. This is the same procedure followed by Koyama [1].

Three kinds of blades having wedge angle of 15, 30 and 45 deg were used by changing the attack angle as 0, 10, 12.5, 20, and 45 deg at the speed of 200, 400, 800, and 1200 rpm. No tip and center hub effect was observed from the experimental data calculated from equation (42). Some data near the downstream corner showed higher transfer coefficient than expected. Similar phenomena were reported in reference [1]. This could be due to the separation on the adjacent surface. These data were excluded from the procedure to determine a local Sherwood number correlation in the following section.

4 Experimental Results and Comparison with Predictions

4.1 Experimental Correlations for Sherwood Number.
The conventional correlation of forced convection mass transfer is,

$$\text{Sh} = CR_{ex}{}^M \qquad (43)$$

where multiplicative constant C corresponds to Sh^0 while exponent M stands for n_1/n_3 in relationships (41).

Exponent M in equation (43) was determined from the experimental data using a least square technique in the flow direction. M was found to be almost constant on the surface, however, it had two separate values to correlate variations of Ω and Φ^* in the experiments.

Allowing for an uncertainty of ±0.02, one value was found to be 0.5, and the other 0.6. The latter figure being between 0.5 and 0.8, respectively, for the laminar and the turbulent cases may indicate the flow, in this particular case, changes from laminar to turbulent somewhere along the stream line. One may call this type of flow "transient flow."

Having established a value for the exponent in equation (43), next, the least square routine was reapplied to find the multiplicative constant. Fig. 3 shows variations of the multiplicative constant C with respect to Φ^*. The data for exponent 0.5 lie along the dashed line of laminar prediction of Sh^0 in equation (41), indicating that the multiplicative constant in laminar becomes large as Φ^* increases. However, no trend like this is seen in transient flow data for exponent 0.6. In this case, data are rather dispersed around the straight line of constant shown at the lower of the figure.

In laminar flow case, the experimental results agree well with the prediction. For small inclinations, however, the points appear to be slightly over the predicted as shown in Fig. 3. The slight disagreement should be attributed mainly to the neglecting of ϵ in the approximation procedure. From Fig. 3, the data for the laminar flow suggest C to be correlated as Sh^0 of the predictions,

$$C = Sh^0 = 0.465(1 + 8m)^{1/2} \qquad (44)$$

Equation (44) gives the value of 0.465 as m tends to zero. This value has a good agreement with the value of 0.45 in reference [1].

On the other hand, for the suggested transient flow case, the data points are dispersed between 0.2 and 0.3. In this case, it is difficult to infer from the data the precise effect of increasing Φ^* on Sh^0. Dispersion of the data is not at all surprising since, for the transient flow, laminar and turbulent regions are treated collectively on the surface rather than treating two regions separately, which, then, would necessitate the information about transition point on the surface. The following correlation is proposed to be applicable for an approximation for transient flow,

$$Sh = 0.25\,R_{rx}^{0.6} \qquad (45)$$

Besides enhancing the mass transfer coefficient as shown in equations (41), the negative pressure gradient has some other effects. One such prominent effect is pertaining to a transition to turbulence. Hence, the transition should be considered not only under the effect of angular velocity increase, i.e., Reynolds number increase, but also under the effect of the negative pressure gradient.

For moderate angles of incidence in Fig. 3, Φ^* less than 60 deg ($m \leq 0.2$), the figure shows that the negative pressure gradient works to delay transition over a wide range of angular velocity. Except the data for 1200 rpm, almost all the data for C, including some of those as high angular velocity as 800 rpm appear in laminar flow for this range. This is due to the pressure gradient effect over stabilization, which has overcome the effect of angular velocity increase to help transition. Some 800 rpm data appearing in transient region show the pressure
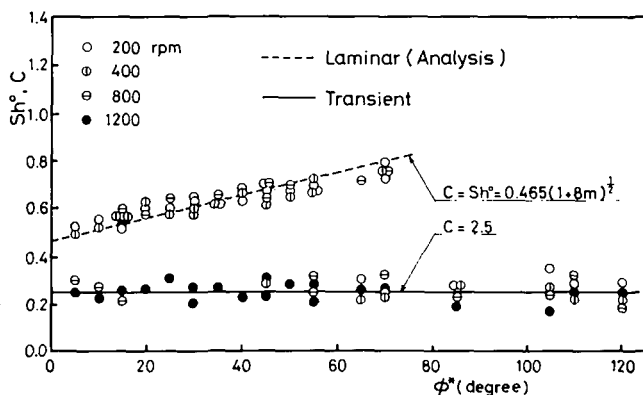
gradient effect has been at last overcome by the effect of angular velocity increase as the angular velocity reaches 800 rpm. For the range of moderate angles, 800 rpm data are the only data appearing in both laminar and transient regions if one datum point of 400 rpm at $\Phi^* = 45$ deg in transient is excluded. Therefore, the critical angular velocity for this range may be taken to be around 800 rpm. While a corresponding critical angular velocity is evaluated to be approximately 400 rpm, when the critical Reynolds number reported in [1] for a flat blade, i.e., 3×10^4, is applied into the present model. One may understand, a critical Reynolds number twice as large as that for a flat blade at zero incidence is possible simply by tilting a blade at a moderate angle, $\Phi \leq 60$ deg.

However, this negative pressure gradient effect over stabilization seems to vanish as Φ^* increases beyond 60 deg as seen in the figure. That is, not only at 1200 rpm but also some data for 200, 400, and 800-rpm appear randomly in transient flow at Φ^* between 60 and 80 deg. Moreover, when Φ^* is over 80 deg, all the data points, even the lowest 200 rpm, in the figure fall completely to the transient regime. This shows, the negative pressure gradient works for the range of large angles in a manner quite contrary to that for the range of moderate angles. That is to help transition promptly. This effect of negative pressure gradient for large angles affects even to the case of far under the critical angular velocity 400 rpm, which would be fairly laminar for the case of a flat blade at zero incidence [1].

Unfortunately, it has been found difficult to infer a precise interrelation between an equivalent wedge angle increase and a critical angular velocity increase from the figure. But, from these discussions the critical angular velocity for moderate angles, can be taken as approximately 800 rpm as a whole. Moreover, some critical equivalent wedge angle can exist between 60 and 80 deg. Beyond this value, the transition becomes strongly governed by the effect due to negative pressure gradient, and the angular velocity effect diminishes.

4.2 Contour Map of Mass Transfer Coefficient. Using equation (36), the following relation is derived,

$$h \propto \dot{x}^{-1}(\dot{u}_e\dot{x}\dot{r})^{n_1/n_3}[1 + \epsilon^2]^{1/2} \qquad (46)$$

This can be transformed into the following equation for contour lines of equal sublimation.

$$\dot{r}\dot{x}^{m-2/n_1}\left[1 + \epsilon^2\right]^{n_3/2n_1} = \text{const.} \qquad (47)$$

Again, the assumption that r is large enough to give $\epsilon \ll 1$, may lead to a simplified relations as follows.

$$r \propto x^{2/n_1 - m}$$

i.e., $r \propto x^{1-m}$ laminar

$$r \propto x^{1/4 - m} \text{ turbulent } (n = 7, m < 1/4) \qquad (48)$$

In order to clarify these results, Fig. 4 is plotted. Here, X-Y coordinates are attached to the surface with appropriately chosen dimensions. It should be noted that, for rough approximation, X and Y can be used inter-changeably with x and r, respectively.
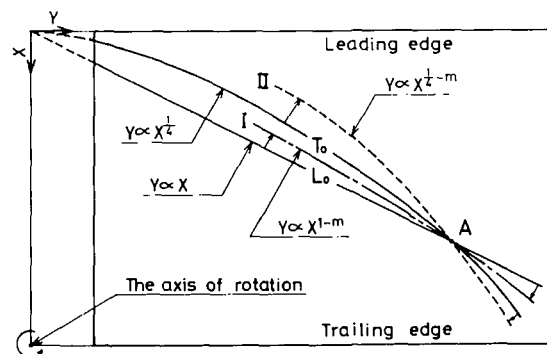

Fig. 3 Effect of incidence on multiplicative constants

Fig. 4 Schematic drawing of contour map using X-Y coordinates system

Journal of Heat Transfer

Point A is an arbitrarily chosen point on the surface. Line L^0 represents the laminar flow case at zero incidence and line T^0 represents the turbulent flow case. Now, the relations (48) indicate that these contour lines are gradually to be moved around clockwise as m increases, as shown in the figure.

The explained trend of the contour lines has been strongly confirmed by drawing contour maps for the present data. Fig. 5 is the case of equivalent wedge angle at 45 deg. Both laminar and turbulent contour lines are shown when angular velocities are 800 and 1200 rpm, respectively.

Now, the area around a given point on the surface can be divided into two regions independently of angular velocity, as shown in Fig. 4.

That is, Region I: laminar flow
             Region II: turbulent flow.

It is quite noticeable that the flow type may well be judged by the slope of the contour line passing through the focused point. Extending this discussion, these results could be reversely applied to estimate the unknown value of equivalent wedge angle by using relationship (48), provided equal height difference at more than two points on the surface is found after the sublimation.

5 Conclusions

The conclusions from this study are summarized as follows.

1 For laminar flow, reasonably good agreement is obtained between experimental results and the predictions through an extended Reynolds analogy. The resulting correlation is,

$$\text{Laminar flow } Sh = 0.465(1 + 8m)^{1/2} R_{ex}^{1/2}$$

2 For transient flow, rough approximations can be made by the equation independent of the equivalent wedge angle as follows.

$$\text{Transient flow } Sh = 0.25 R_{ex}^{0.6}$$

3 The flow type can be judged reading directly the slope of the contour lines on the surface. The expressions for contour lines are:

Laminar flow $r \propto x^{1-m}$

Turbulent flow   , $r \propto x^{1/4-m}$.
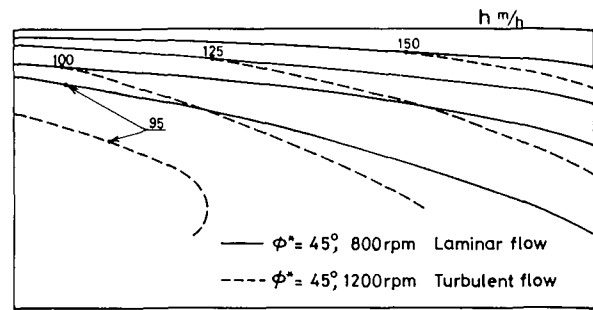
Fig. 5 Contour map of mass transfer coefficients

4 The increase of equivalent wedge angle yields high mass transfer coefficients in both cases of laminar and turbulent flow. Moreover, the negative pressure gradient works in a manner to stabilize the laminar boundary layer for $\Phi^* < 60$ deg, but this effect vanishes and finally accelerates the transition for $\Phi^* > 80$ deg.

Reference

1 Koyama, H., Osawa, S., and Izumi, R., "Mass Transfer From Inclined Rotating Plates," Preprints of the 12th Heat Transfer Symposium of Japan, A207, 1975.

2 Anand, A., and Laksminarayana, B., "Three-Dimensional Turbulent Boundary Layer in a Rotating Helical channel," *Journal of Fluids Engineering,* TRANS. ASME, 1975, p. 198.

3 Prandtl, L., "On Boundary Layers in Three-Dimensional Flow," Reports and Transactions, British MAP, No. 64, 1946.

4 Mager, A., "Generalization of Boundary Layer Momentum Integral Equations to Three-Dimensional Flows Including Those of Rotating Systems," NACA TR 1067, 1952.

5 Schlichting, H., "Boundary Layer Theory," McGraw-Hill, New York, 1960, [5a] p. 507, [5b] p. 249.

6 Hartree, D. R., "On an Equation Occurring in Flkner and Skan's Approximate Treatment of the Equations of the Boundary Layer," *Proceedings Cambridge, Philosophical Society,* Vol. 33, Part II, 1937, p. 223.

7 Sogin, H. H., "Sublimation From Discs to Air Streams Flowing Normal to Their Surfaces," TRANS ASME, Vol. 80, 1958, p. 61.

I. K. Madni

Assist. Mechanical Engineer,
Department of Applied Science,
Brookhaven National Laboratory,
Upton, N. Y.
Assoc. Mem. ASME

R. H. Pletcher

Professor,
Department of Mechanical Engineering and
Engineering Research Institute,
Iowa State University,
Ames, Iowa
Mem. ASME

Buoyant Jets Discharging Nonvertically Into a Uniform, Quiescent Ambient—A Finite-Difference Analysis and Turbulence Modeling

A differential approach for analysis of turbulent, axisymmetric, buoyant jets and plumes issuing nonvertically into a quiescent, uniform ambient is presented, in which the governing differential equations for conservation of mass, momentum, and energy, derived in a curvilinear, orthogonal coordinate system, are solved by a finite-difference method of the Dufort-Frankel type. This jet configuration is of interest with regard to the design of submerged, offshore outfalls from power plants. The analysis includes consideration of the transverse momentum equation as the jet follows a curved trajectory under the influence of buoyancy forces. The turbulent shear stress and heat flux terms in the governing equations are evaluated through a relatively simple turbulence model which accounts for the effect of buoyancy on the apparent turbulent viscosity through the gradient Richardson number. Predictions for buoyant jets discharging horizontally and at 45 deg to the horizontal are compared with recent experimental data and the results of other prediction methods.

Introduction

Jets which issue at any nonvertical angle into a denser quiescent ambient fluid follow a curved trajectory in response to the influence of buoyancy forces. Thus, a prediction scheme for such a configuration must be able to predict the jet trajectory as well as provide information on the flow properties within the jet. The buoyancy forces can be expected to influence the turbulent transport process, further complicating the prediction of the flow. The prediction of such jets is of interest with regard to environmental applications, especially in the design of submerged offshore outfalls from power plants.

The analyses and/or prediction schemes [1-7][1] proposed for this configuration to date have generally been integral in nature. Application of differential methods to buoyant jets following curved trajectories has been scant, although in [8, 9], fully three-dimensional

procedures have been described.

In the present paper, a two-dimensional differential approach for the analysis of turbulent buoyant jets and plumes discharged into a quiescent uniform ambient is presented, which would have the distinct advantage of simplicity and economy of computer time over the more involved three-dimensional approaches. Here, a reduced form of the governing partial differential equations for conservation of mass, momentum, and energy, derived in a curvilinear, orthogonal coordinate system, is solved numerically. This finite-difference procedure includes consideration of the momentum equation in the transverse direction. The turbulent shear stress and heat flux terms in the governing equations are evaluated through a relatively simple turbulence model which accounts for the effect of buoyancy on the apparent turbulent viscosity through the gradient Richardson number. Predictions for heated jets discharged horizontally and at 45 deg to the horizontal are compared with recent experimental data and the results of other prediction methods.

Analysis

Flow Configuration. Fig. 1 shows the flow configuration and the curvilinear coordinate system used for the analysis of the buoyant jet, assumed to be axisymmetric, discharging at an angle θ_0 to the hori-

---

zontal. The ambient is assumed to be uniform in temperature and at rest. The s-coordinate coincides with the jet center line. The actual flow conditions do not require that the jet be precisely axisymmetric about the center line. The assumption of symmetry, however, greatly simplifies the analysis, and the merits of a model based on this assumption were thought worth exploring considering the alternatives of employing a fully three-dimensional analysis and the associated uncertainties concerning turbulence modeling. In fact, it is questioned whether the available experimental data are sufficiently detailed to permit the verification of the turbulence modeling required for a fully three-dimensional calculation.

The analysis will proceed assuming that the ambient is infinite in extent. This excludes the prediction of the spreading region close to any free-surfaces, since in that case additional terms would have to be introduced into the governing equations, altering their parabolic nature. However, the method may still have merit for submerged shallow-water discharge calculations in the region of interest, as the most stringent thermal "mixing zone" as defined by present environmental standards applied to coastal installations usually ends before the surface field is established [10, 11]. It is true that standards, hence applications, could change with time, but a better way of calculating this class of flow is of interest. Also, some ideas from the present parabolic analysis may carry over, particularly to the partially parabolic approach and perhaps even to the fully elliptic, encompassing more complex circumstances related to the discharge problem.

Governing Equations. The fluid is assumed incompressible and density variations are neglected everywhere except in the buoyancy force terms. Viscous dissipation will be neglected in the energy equation and the usual boundary-layer assumptions will be used to eliminate the second derivatives with respect to the streamwise direction in the momentum and energy equations. Viscous terms will be neglected entirely in the momentum equation in the transverse direction; the resulting equation can be interpreted as a force balance

on a stream tube being deflected by the component of buoyancy force in the transverse direction. Accordingly, the conservation equations for the axisymmetric buoyant jet can be written

Continuity:

$$\frac{\partial}{\partial s}(uy) + \frac{\partial}{\partial y}(vy) = 0 \tag{1}$$

s-momentum:

$$u\frac{\partial u}{\partial s} + v\frac{\partial u}{\partial y} = \frac{1}{\rho y}\frac{\partial}{\partial y}(y\tau) + \frac{(\rho_\infty - \rho)}{\rho_0}g\sin\theta \tag{2}$$

y-momentum:

$$\widetilde{u^2}\frac{d\theta}{ds} = \frac{\widetilde{(\rho_\infty - \rho)}}{\rho_0}g\cos\theta \tag{3}$$

Energy:

$$u\frac{\partial t}{\partial s} + v\frac{\partial t}{\partial y} = \frac{1}{\rho c_p y}\frac{\partial}{\partial y}(-yq) \tag{4}$$

A similar equation exists for species concentration. However, for illustrative purposes, the role of temperature will be emphasized here. A detailed derivation of the equations for this flow configuration is given in [12]. The wavy lines in equation (3) denote space averages over the flow cross section. Appropriate boundary conditions are

$$\frac{\partial u}{\partial y}(s, 0) = \frac{\partial t}{\partial y}(s, 0) = 0; \quad v(s, 0) = 0$$

$$\lim_{y\to\infty} u(s, y) = u_\infty; \quad \lim_{y\to\infty} t(s, y) = t_\infty \tag{5}$$

In addition, initial distributions of u, t, and θ must be provided at a starting value of s.

The density difference terms in equations (2) and (3) are related to the temperature of the fluid through

---

Nomenclature

c_p = specific heat at constant pressure

d_0 = diameter of jet or plume at discharge

Fr_0 = discharge Froude number, $u_0^2/[gd_0(\rho_{\infty_0} - \rho_0)/\rho_0]$, dimensionless

g = acceleration of gravity

$\vec{g}$ = gravity vector, $-g\vec{k}$

H = discharge depth

$\vec{i}_s, \vec{i}_y$ = unit vectors parallel to the s, y axes, respectively

k = thermal conductivity

K_3, K_4 = constants in models for turbulent viscosity

ℓ = mixing length

ℓ_0 = mixing length uncorrected for buoyancy effects

n = total or effective kinematic viscosity

N = dimensionless total or effective kinematic viscosity n/ν

n_H = total or effective diffusivity for heat

N_H = dimensionless total or effective diffusivity for heat, n_H/ν

Pr = Prandtl number, ν/α

q = heat flux due to molecular and turbulent transport

Re_0 = Reynolds number at discharge, u_0d_0/ν, dimensionless

Ri = gradient Richardson number,

$\dfrac{-g}{\rho_a}\left(\dfrac{\partial p}{\partial y}\Big/\dfrac{\partial u}{\partial y}\right)^2$

r_0 = radius of jet or plume at discharge

s = distance along jet or plume axis

S = dimensionless axial distance, su_0/ν

ΔS = increment of S

t = temperature

T = nondimensional temperature, $(t - t_\infty)/(t_0 - t_\infty)$

$T_{0,a}$ = discharge temperature, in degrees absolute

u = s-component of time mean velocity

U = dimensionless s-component of time mean velocity, u/u_0

v = y-component of time mean velocity

V = dimensionless y-component of time mean velocity, v/u_0

x = distance along x-axis

X = dimensionless distance along x-axis, xu_0/ν

y = radial distance from jet center line

Y = dimensionless radial distance from jet center line, yu_0/ν

$y_{1/2}$ = radial distance from jet center line to point at which $(u - u_\infty)/(u_c - u_\infty) = 0.5$

$y_{t 1/2}$ = radial distance from jet center line to point at which $(t - t_\infty)/(t_c - t_\infty) = 0.5$

ΔY = increment of Y

z = vertical distance

Z = dimensionless vertical distance, zu_0/ν

α = thermal diffusivity, $k/\rho c_p$

β = isobaric volume expansivity, $-(\partial\rho/\partial t)_p/\rho_{ref}$

δ = mixing layer thickness

μ = viscosity

ν = kinematic viscosity, μ/ρ

ρ = density

τ = total or effective shear stress in s-momentum equation

θ = angle between $\vec{i}_s$ and the horizontal

Subscripts

c = evaluated at edge of core or at jet center line if no core exists

p = evaluated at constant pressure

e = evaluated at outer edge of jet

$\frac{1}{2}$ = evaluated at velocity half-radius

0 = value at jet discharge

ref = reference value

T = turbulent flow quantity

∞ = free stream or ambient value

i, j = lattice or grid indices corresponding to S, Y directions, respectively

$+, -$ = used in special notation, $\Delta Y_+ = (Y_{j+1} - Y_j)$, $\Delta Y_- = (Y_j - Y_{j-1})$, and similarly for ΔS

max = maximum

min = minimum

Superscripts

$(\ )'$ = on dependent variables, fluctuating quantities

$(\ )$ = on dependent variables, time mean quantities

$(\ \vec{})$ = vector quantities

$(\ \widetilde{})$ = space averages over flow cross section

$$\frac{(\rho_\infty - \rho)}{\rho_0} = \beta(t - t_\infty) \qquad (6)$$

An equation of the same form can be used to relate density differences to concentration differences as well. The shear stress, τ, in equation (2) includes both the viscous and apparent turbulent contributions

$$\tau = \mu \frac{\partial u}{\partial y} - \overline{\rho v' u'} \qquad (7)$$

and likewise, the heat flux, q, in equation (4) includes both molecular and turbulent transport

$$q = -k \frac{\partial t}{\partial y} + \rho c_p \overline{v' t'} \qquad (8)$$

Model for the Turbulent Transport. Using the Boussinesq concept of eddy viscosity, τ can be evaluated as

$$\tau = \rho(\nu + \nu_T) \frac{\partial u}{\partial y} = \rho n \frac{\partial u}{\partial y} \qquad (9)$$

where ν_T is the turbulent viscosity and n the total effective viscosity. It was assumed that the turbulent diffusivities for heat and momentum are related through

$$\alpha_T = \nu_T / \mathrm{Pr}_T \qquad (10)$$

where Pr_T is the turbulent Prandtl number, which was set equal to a constant value of 0.7 for the calculations described in the present paper. The heat flux, q, can be written as

$$q = -\rho c_p (\alpha + \nu_T/\mathrm{Pr}_T) \frac{\partial t}{\partial y} = -\rho c_p n_H \frac{\partial t}{\partial y} \qquad (11)$$

where n_H is the effective thermal diffusivity.

In [13] a relatively simple turbulence model was found to provide good agreement with experimental data for the vertical jet discharging to uniform and stratified ambients. One of the objectives of the present study was to determine the modifications required, if any, to this simple model in order to accurately predict jets with curved trajectories, and to determine if these modifications correlated with the gradient Richardson number in such a way as to suggest that the major additional influence on the turbulent mixing in the curved buoyant jet case, compared to the vertical jet, was due to buoyancy. The mixing length computed without accounting for the effects of buoyancy will be denoted as ℓ_0. The reference turbulence model which worked well for vertical jets [13] is given by

$$\nu_T = \ell_0^2 \left| \frac{\partial u}{\partial y} \right|, \qquad \ell_0 = 0.0762\delta \qquad (12)$$

for the initial mixing region where δ is the width of the mixing layer. After mixing penetrates to the jet center line, i.e., in the main region, the constant viscosity model was used:

$$\nu_T = 0.0246 y_{1/2}(u_{\max} - u_{\min}) \qquad (13)$$

The need to utilize two models or two sets of constants for the two regions is discussed in [14]. In the model represented by equation (13), a reference mixing length can be defined from

$$\nu_T = 0.0246 y_{1/2}(u_{\max} - u_{\min}) = \ell_0^2 \left| \frac{\partial u}{\partial y} \right|$$

whereby if $|\partial u/\partial y|$ is interpreted as $(u_{\max} - u_{\min})/y_{1/2}$, then the equivalent reference mixing length is $\ell_0 = (0.0246)^{1/2} y_{1/2}$.

It will be seen subsequently, in the Results section, that this model predicts the trajectories of horizontally discharged buoyant jets reasonably well but that the decay of center line temperature is somewhat underpredicted, suggesting that the apparent viscosity (and conductivity) is somewhat greater than indicated by equation (13).

Several investigators (see especially [15, 16]) mention the influence of buoyancy on mixing and recommend modifying the mixing length to account for this effect.

Bradshaw [16] gives a good discussion of buoyancy effects on the apparent turbulent stresses and presents some well-known empirical formulae which predict buoyancy effects as a function of Richardson
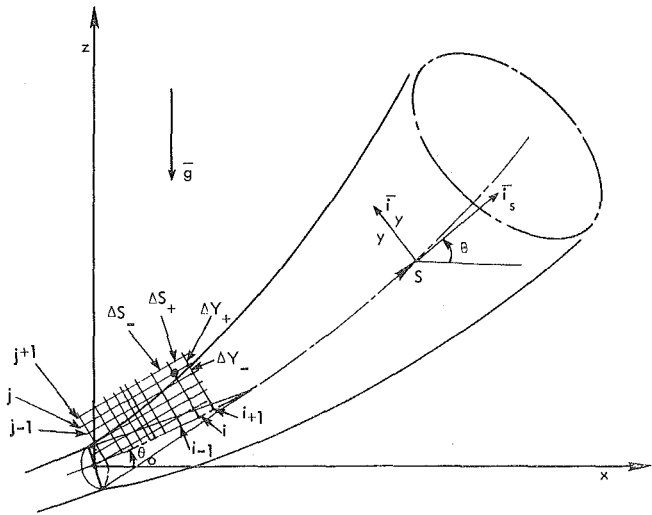
Fig. 1 Curvilinear coordinate system and finite-difference grid for buoyant jet analysis

number. In the present work, the formula of Keyps for the modification of the apparent mixing length, valid for negative Richardson numbers typically in the range $-0.5 < \mathrm{Ri} < 0$, was used. This is of the form

$$\frac{\ell}{\ell_0} = (1 - K_4 \mathrm{Ri})^{0.25} \qquad (14)$$

where ℓ_0 is the mixing length without buoyancy and ℓ is the modified mixing length. Ri denotes the gradient Richardson number, which is the ratio of buoyancy to inertia forces, and is defined as

$$\mathrm{Ri} = -\frac{g}{\rho_a} \left(\frac{\partial \rho}{\partial y} \right) \Big/ \left(\frac{\partial u}{\partial y} \right)^2 \qquad (15)$$

In equation (15) the density gradient can be expressed in terms of temperature gradient by substituting the definition of β, the thermal expansivity of fluid, i.e.,

$$\beta_a = -\frac{1}{\rho_a} \left(\frac{\partial \rho}{\partial t} \right) \qquad (16)$$

This yields

$$\mathrm{Ri} = g \beta_a \left(\frac{\partial t}{\partial y} \right) \Big/ \left(\frac{\partial u}{\partial y} \right)^2 \qquad (17)$$

For the present analysis, it was found more convenient to use a global representation of Ri as follows:

$$\mathrm{Ri} = g \beta_a \left[\frac{(t_c - t_\infty)}{\delta} \right] \Big/ \left[\frac{(u_c - u_\infty)}{\delta} \right]^2$$

$$= g \beta_a (t_c - t_\infty) \delta / u_c^2 \qquad (18)$$

A value of $K_4 = 16.34^2$ in equation (14) was found to give good results.

It is important to note that the effective turbulent viscosity appears to be mainly influenced by the components of the destabilizing derivatives involved in equation (17) which are in the direction of the earth's gravity. This was seen to be approximately true from the vertical plume results of [13], in which the deviation of predicted

center line decay values from experiment was not significant enough to suggest modifying the mixing length to include a Richardson number effect. Naturally, there may be some secondary coupling effects in the turbulent motion which could be accounted for by more complex models. However, the analytical results of [13] do suggest that it is the component of the buoyancy force in the transverse direction which is primarily responsible for altering the turbulence structure. The component of the buoyancy force in the transverse direction itself is expected to vary around the periphery of the jet having the maximum destabilizing effect at the top and maximum stabilizing influence at the bottom. The present study, which utilized an axisymmetric flow model, indicated that it was the destabilizing component which must be allowed to dominate in order to predict trends for the decay of center-line temperature which are in agreement with experimental results. This seems plausible since in the buoyant curved jet experiments where the mixing phenomena are not axisymmetric, center-line values lose their significance and it is maximum decay values (enhanced by the more intense mixing in the upper part of the jet) which most experimenters are reporting in these circumstances. Accordingly, with Ri defined as indicated in equation (17), and making use of the coordinate system indicated in Fig. 1, it is $\cos\theta \times$ Ri rather than Ri which should appear in the equation predicting the effect of buoyancy on mixing length:

$$\ell = \ell_0(1 - K_4 \text{Ri} \cos\theta)^{0.25} \qquad (19)$$

Here, θ is the local angle, so that as the jet turns upward, θ will increase, effectively reducing the effect of Ri on the mixing length.

Equation (19) was implemented in the model of equation (13) as follows:

$$\nu_T \text{ (based on } \ell_0) = \ell_0^2 \left|\frac{\partial u}{\partial y}\right| \simeq (K_3 y_{1/2}^2)\frac{(u_c - u_\infty)}{y_{1/2}}$$

$$= K_3 y_{1/2}(u_\text{max} - u_\text{min})$$

so that

$$\nu_T \text{ (based on } \ell) = \ell^2 \left|\frac{\partial u}{\partial y}\right| = \frac{\ell^2}{\ell_0^2}\left(\ell_0^2 \left|\frac{\partial u}{\partial y}\right|\right)$$

i.e.,

$$\nu_T = K_3 y_{1/2}(u_\text{max} - u_\text{min})(1 - K_4 \text{Ri} \cos\theta)^{0.5} \qquad (20)$$

where $K_3 = 0.0246$.

Equation (20), then, defines the model that was used in the present analysis to describe the turbulent viscosity in the main region of flow. It is essentially Prandtl's constant viscosity model that was employed successfully in the vertical jet configuration [13] together with a term to account for the effects of buoyancy on turbulence mixing. The constant K_3 has been carried over from the vertical configuration unchanged. In the initial region, Prandtl's mixing length model (equation (12)) was used unchanged from its earlier applications for the straight-line jet configurations [13, 14].

Solution Method. The problem formulated through equations (1)–(11) is parabolic in character, permitting the solution to be marched in the s-direction starting with initial distributions of velocity and temperature and an initial flow angle.

The method used for solving all but the y-momentum equation is similar to the explicit DuFort-Frankel procedure used in [14] for jets following straight-line trajectories. Fig. 1 shows the finite-difference grid being used. The essential details of the finite-difference formulation, truncation errors, stability of the numerical scheme, etc., can be found in [12].

Generally, step sizes in the s-direction were 8–10 percent of the width of the mixing zone.

Although various numbers of grid points in the transverse direction were used in studying the convergence properties of the procedure, most calculations were made by dividing the discharge radius into 20 Δy increments. Most jet calculations reported in this paper have required less than one minute and none more than two minutes of computation time on the IBM 360/65 computer.

Results

Nonvertical buoyant jets have been studied experimentally by Cederwall [17], Bosanquet, et al. [2], Frankel and Cumming [18], Anwar [4], Fan [3], and, most recently, Ryskiewich and Hafetz [19]. Bosanquet, et al., and Fan measured center-line trajectories; Frankel and Cumming measured the center-line concentration, but Anwar and Ryskiewich and Hafetz measured both center-line trajectories and concentration (or temperature in the case of Ryskiewich) for horizontal and inclined jets at different discharge Froude numbers. In this study, the Ryskiewich and Hafetz data were chosen for comparisons as they are the most recent and complete. With regard to the other data, Hirst [20] states that Cederwall's data were obtained with different initial conditions, making it difficult to draw conclusions from his data. Frankel and Cumming provide results only for center-line values. Also, Abraham [1] and later Pryputniewicz [21] seem to discount the validity of these data since they were not obtained under steady-state conditions. Fan's results show only trajectories. Also, Fan's data are for much larger Froude numbers, i.e., lower buoyancy effects, hence less deflection, so that the jet travels much farther to turn the same distance upward as a more buoyant jet. Apart from being of less interest to us, this would also involve more computer time; hence it was not compared.

The importance of the effect of buoyancy on the turbulent viscosity is demonstrated in Fig. 2 for a jet discharged horizontally at $\text{Fr}_0 = 64$. In the initial mixing region, equation (12) was used in all calculations. For the results shown in Fig. 2(a), the buoyancy effect on turbulence was neglected, i.e., $K_4 = 0.0$ was used in equation (20). For the results of Fig. 2(b), $K_4 = 16.34$ was used in equation (20). The predicted trajectory remains close to measurements in both cases, but using equation (20) with $K_4 = 16.34$, which permits turbulent viscosity to be influenced by buoyancy, considerably improves predictions of center-line temperature. From this comparison the Richardson number is seen to have a strong effect on the decay of center-line temperature but only marginal effect on the jet trajectory. No previous discussion of this finding has been noted in the literature to date.

In Fig. 3 the trajectory predicted by the present method is compared with the recent experimental data of Ryskiewich and Hafetz [19] for the horizontally discharged jet with $\text{Fr}_0 = 16$. The predictions of Hirst [5], Fan and Brooks [6], and Abraham [1] are also shown. The prediction of the present method is seen to agree well with the experimental data.

Fig. 4 gives a similar comparison for a horizontal discharge with $\text{Fr}_0 = 64$. The predictions of the present method are again seen to provide the best agreement with the experimental data. Good agreement with the data of Ryskiewich and Hafetz has also been noted for $\text{Fr}_0 = 256$, but the comparison will not be shown here due to space limitations.

Comparisons of the predicted and measured decay of center-line temperature for the same two flows considered in Figs. 3 and 4 are shown in Figs. 5 and 6. The present method is seen to provide excellent agreement with the experimental measurements.
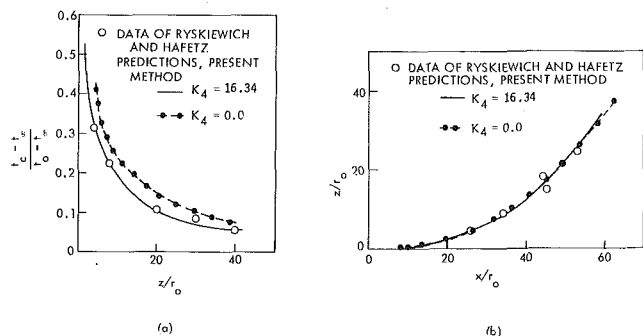

Fig. 2 Comparisons to show the influence of Ri on predictions for $\text{Fr}_0 = 64$; buoyant jet discharged horizontally to a uniform ambient (a) decay of center-line temperature, (b) jet trajectory
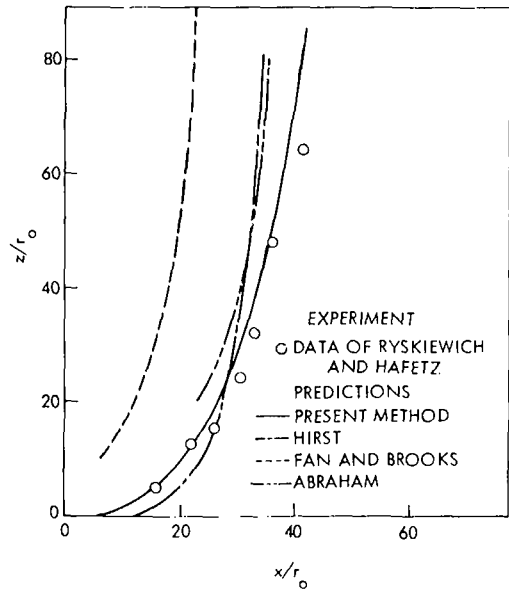
Fig. 3   Predicted and experimental trajectory for Fr_0 = 16; buoyant jet discharged horizontally to a uniform ambient
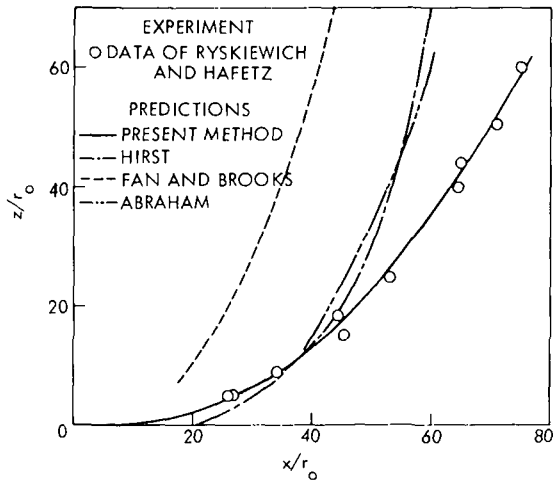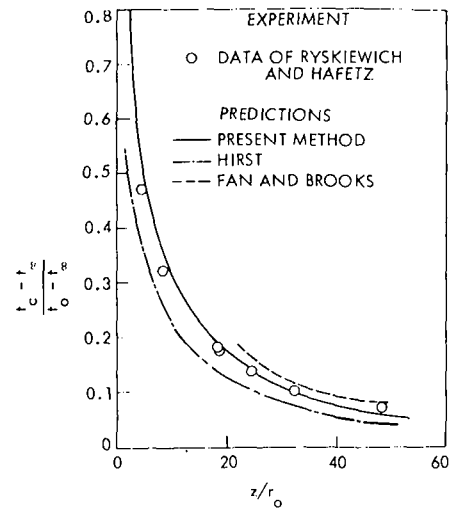

Fig. 5   Predicted and experimental decay of center-line temperature for Fr_0 = 16; buoyant jet discharged horizontally to a uniform ambient
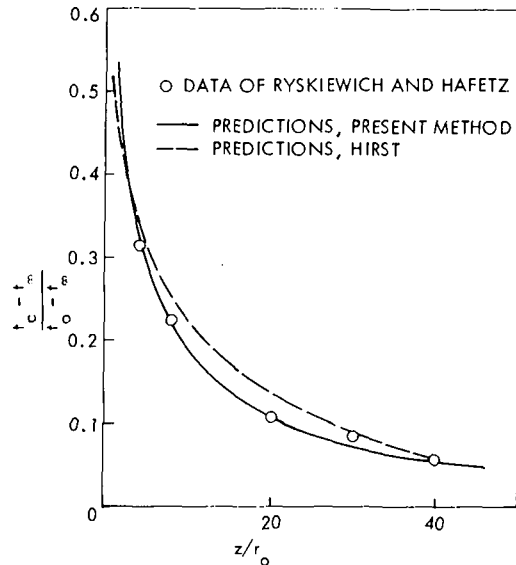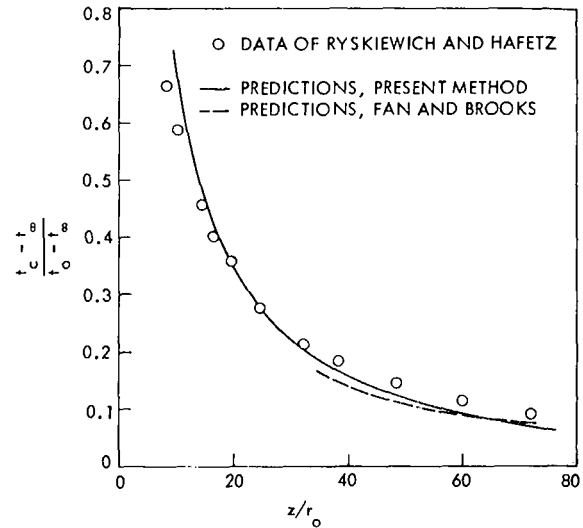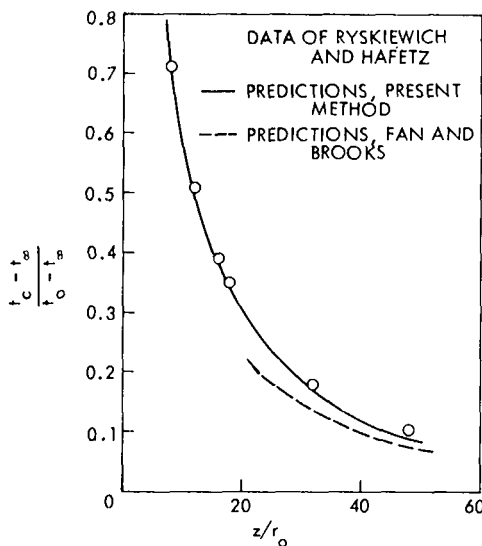

Fig. 4   Predicted and experimental trajectory for Fr_0 = 64; buoyant jet discharged horizontally to a uniform ambient

Fig. 6   Predicted and experimental decay of center-line temperature for Fr_0 = 64; jet discharged horizontally to a uniform ambient

Comparisons are not shown with the experimental results of Anwar [4] for this flow configuration. For Fr_0 = 16, Anwar's results agree very closely with those of Ryskiewich and Hafetz [19]. For Fr_0 = 64, however, there is a significant difference. The reason for this discrepancy between the experimental results is not clear. If free surface effects were a factor, they would cause greater deviation in the data of Anwar, since in his experimental setup, H/d_0 varied from 27 to 70, whereas the results of Ryskiewich and Hafetz that have been used for comparison were obtained at H/d_0 = 80.

Results for the buoyant jet discharged at 45 deg to a uniform quiescent ambient are presented in Figs. 7–9. In Fig. 7 good agreement is noted between predicted and the experimental trajectories measured by Ryskiewich and Hafetz [19] for Fr_0 = 16, 64, and 256. Figs. 8 and 9 compare predicted and measured decay of center-line temperature for Fr = 16 and 256, respectively. Predictions by the method of Fan and Brooks [6] are also shown in Figs. 8 and 9.

Although it would be desirable to test the present prediction method over even a wider range of discharge angles, it is encouraging to note that the level of agreement appears to be about as good for θ_0

= 45 deg as for θ_0 = 0 deg, suggesting that the mathematical and turbulence modeling employed has a useful degree of generality.

Concluding Remarks

A finite difference prediction method which includes a lumped parameter treatment of the transverse momentum equation is seen to work well for the analysis of buoyant turbulent jets following curved trajectories in quiescent ambients. A simple turbulence model which utilized a global evaluation of the gradient Richardson number to account for the effects of buoyancy on the apparent turbulent viscosity was shown to be adequate to predict the available experimental data in terms of both trajectory and flow properties within the jet. It is interesting to note, however, that the jet trajectories themselves could be predicted fairly well while ignoring the effects of buoyancy on the turbulent viscosity.

For the range and type of data available with which to test the analysis, the results tend to justify the use of the axisymmetric assumption as a convenient means for simplifying the analysis without significant loss of accuracy. In fact, for the comparisons shown, there
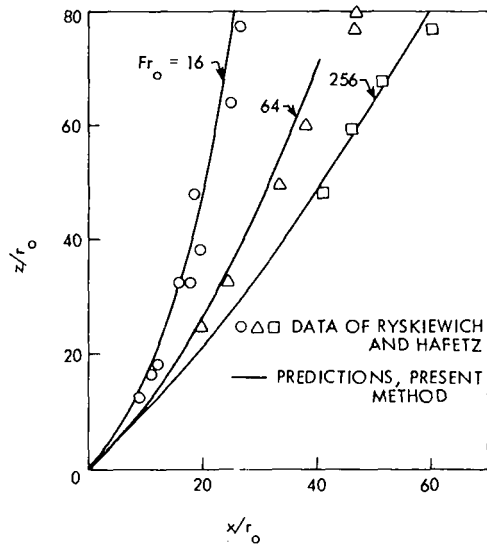
Fig. 7 Predicted and experimental trajectories for different discharge Froude numbers; buoyant jets discharged at 45 deg to a uniform ambient

Fig. 9 Predicted and experimental decay of center-line temperature for Fr_0 = 256; buoyant jet discharged at 45 deg to a uniform ambient

Fig. 8 Predicted and experimental decay of center-line temperature for Fr_0 = 16; buoyant jet discharged at 45 deg to a uniform ambient

is no indication that the use of a fully three-dimensional analysis or the use of a more complex turbulence model could provide better predictions for the flow configuration considered.

The present analysis could be used essentially intact to predict jets such as from sewage outfalls where the initial density difference is due entirely to differences in species concentration (as for example, differences in salinity) rather than temperature differences. The reason for this generality is that for fully turbulent flows, the partial differential equations and boundary conditions in nondimensional form are identical for both the equation for conservation of species and the energy equation. The density difference formulation should be used for the buoyancy terms in the momentum equation in this application, however, rather than the temperature difference relationship, equation (6).

Acknowledgment

References

1 Abraham, G., "Horizontal Jets in Stagnant Fluid of Other Density," *Journal of Hydraulics Division*, ASCE, Vol. 91, No. HY4, 1965, pp. 139–153.

2 Bosanquet, C. H., Horn, G., and Thring, M. W., "The Effect of Density Differences on the Path of Jets," *Journal Royal Society of London*, No. A263, 1961, pp. 340–352.

3 Fan, L. N., "Turbulent Buoyant Jets Into Stratified or Flowing Ambient Fluids," Keck Laboratory of Hydraulics and Water Resources, California Institute of Technology, Report No. KH-R-15, 1967.

4 Anwar, H. O., "Behavior of Buoyant Jet in Calm Fluid," *Journal of the Hydraulics Division*, ASCE, Vol. 91, No. HY4, 1969, pp. 139–153.

5 Hirst, E. A., "Buoyant Jets Discharged to Quiescent Stratified Ambients," *Journal of Geophysical Research*, Vol. 76, No. 30, 1971, pp. 7375–7384.

6 Fan, L. N., and Brooks, N. H., "Numerical Solutions of Turbulent Buoyant Jet Problems," Keck Laboratory of Hydraulics and Water Resources, California Institute of Technology, Report No. KH-R-18, 1969.

7 Chan, D. T. L., and Kennedy, J. F., "Submerged Buoyant Jets in Quiescent Fluids," *Journal of the Hydraulic Division*, ASCE, Vol. 101, No. HY6, 1975, pp. 733.

8 Schetz, J. A., Chien, C. J., and Sill, B. L., "Heat Transfer and Fluid Mechanics of the Thermal Pollution Problem," *Heat Transfer 1974*, Proceedings Fifth International Heat Transfer Conference, Vol. V, 1974, pp. 129–133.

9 McGuirk, J. J., and Spalding, D. B., "Mathematical Modeling of Thermal Pollution in Rivers," *Proceedings International Conference on Mathematics Models for Environmental Problems*, University of Southampton, England, Sept. 1975.

10 Water Pollution Control Research Series, "Potential Environmental Effects of an Offshore Submerged Nuclear Power Plant," Vol. 1, General Dynamics Report No. 16130 GFI 06/71, June 1971.

11 Marble, R. W., and Robideau, R. F., "Thermal Field Resulting From an Offshore-Submerged Nuclear Electric Power Generating Station," Paper No. 71-WA/NE-3. Presented at the ASME Winter Annual Meeting, Washington, D. C., 1971.

12 Madni, I. K., "A Finite-Difference Analysis of Turbulent, Axisymmetric, Buoyant Jets and Plumes," PhD thesis, Mechanical Engineering, Iowa State University, 1975.

13 Madni, I. K., and Pletcher, R. H., "Prediction of Turbulent Force Plumes Issuing Vertically Into Stratified or Uniform Ambients," JOURNAL OF HEAT TRANSFER, TRANS. ASME, Series C, Vol. 99, Feb. 1977.

14 Madni, I. K., and Pletcher, R. H., "Prediction of Jets in Coflowing and Quiescent Ambients," *Journal of Fluids Engineering*, TRANS. ASME, Vol. 97, 1975, pp. 558–567.

15 Launder, B. E., and Spalding, D. B., *Mathematical Models of Turbulence*, Academic Press, New York, 1972.

16 Bradshaw, P., "The Analogy Between Streamline Curvature and Buoyancy in Turbulent Shear Flow," *Journal of Fluid Mechanics*, Vol. 36, Part 1, 1969, pp. 177–191.

17 Cederwall, K., "The Initial Mixing on Jet Disposal Into a Recipient," Chalmers Institute of Technology, Goteburg, Sweden, 1963 (in Swedish).

18 Frankel, R. J., and Cumming, J. D., "Turbulent Mixing Phenomena of Ocean Outfalls," *Journal of Sanitary Engineering Division*, ASCE, SA2, 1965,

pp. 33–59.

19 Ryskiewich, B. S., and Hafetz, L., "An Experimental Study of the Free Surface Effect on a Buoyant Jet," General Dynamics Report No. U440-74-103, 1975.

20 Hirst, E. A., "Analysis of Round Turbulent, Buoyant Jets Discharged to Flowing Stratified Ambients," Report No. ORNL-4585, Oak Ridge National Laboratory, 1971.

21 Pryputniewicz, R. J., and Bowley, W. W., "An Experimental Study of Vertical Buoyant Jets Discharged Into Water of Finite Depth," JOURNAL OF HEAT TRANSFER, TRANS. ASME, Series C, Vol. 97, 1975, pp. 274 281.

ERRATUM

Figs. 10 and 11 contained incorrect curves for the isentropic homogeneous model (IHE). The curves were taken from R. A. Brown's thesis (reference [2] of the paper) where the IHE procedure was correctly described. The source of the error is not clear. Corrected figures are given here. The results shown are based upon neglect of liquid compressibility which was found to influence IHE predictions on the order of one percent only. To simplify the appearance of the figures, the curves labeled Two-Step II have been deleted, since that model produced poor comparison with the experimental data.

The first conclusion of the paper must be modified in light of this error. As the corrected figures show, the experimentally observed flowrates are higher than predicted by the IHE model, but by a much smaller margin. The difference is generally less than 60 percent of the experimental value or 150 percent of the IHE prediction. It remains true that the data show a delay in the onset of nucleation and therefore a degree of metastability in the expansion process.

The erroneous results for the IHE model also appeared in an earlier version of the paper under the same title, i.e., ASME Paper 76-HT-12. The authors are grateful to Professor R. L. Collins of the University of Louisville, who called attention to the error.

In Table 1 the temperature entry for run 3 (166.1) is incorrect. The correct value is 221.
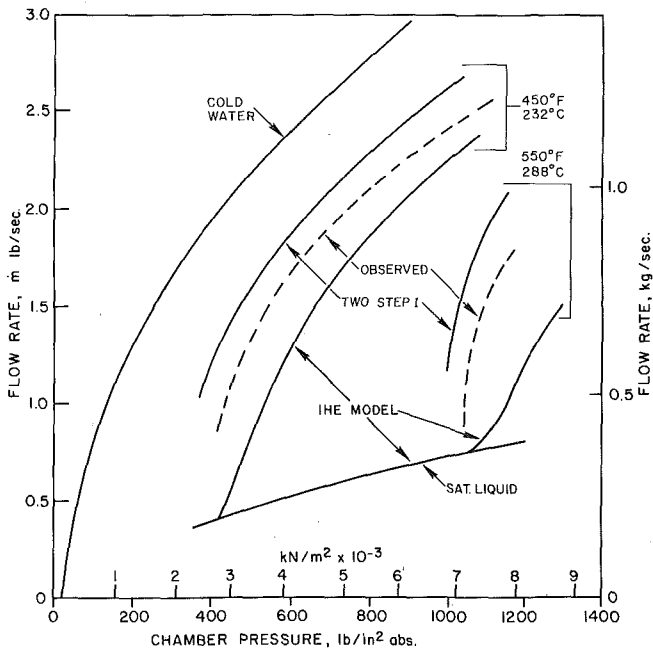
Corrected Fig. 10 Comparison of observed and theoretical flowrate for nozzle 3 at 232 and 288 C
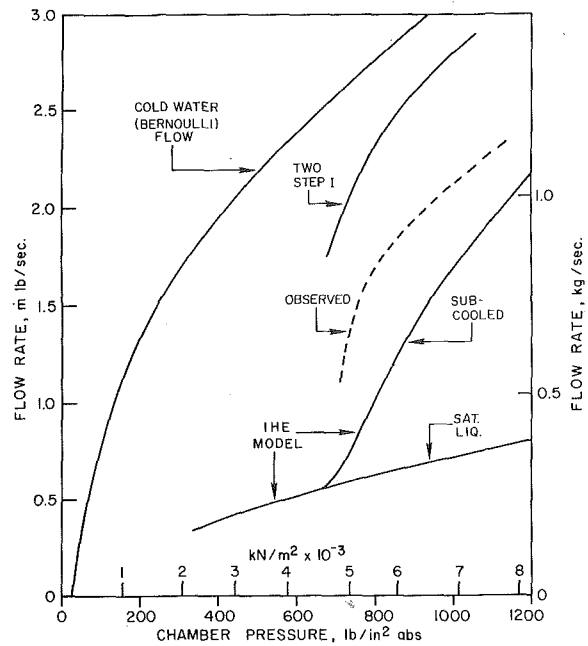
Corrected Fig. 11 Comparison of observed and theoretical flowrate for nozzle no. 3 at 260 C

L. D. Kannberg

Battelle—Northwest,
Richland, Wash.
Assoc. Mem. ASME

L. R. Davis

Oregon State University,
Corvallis, Ore.
Mem. ASME

An Analysis of Deep Submerged Multiple-Port Buoyant Discharges

The results of an experimental study of deep submerged multiple-port thermal discharges are compared to the predictions of a theory treating the dilution of merging multiple-port buoyant jets discharge from a row of equally spaced ports. The paper summarizes the considerable alteration of the Hirst [11] model necessary to adequately treat merging multiple jets. The essential features of the analysis are: (1) the gradual transition of the profiles from simple axisymmetric profiles to merging profiles and finally to fully merged, pseudo-slot, two-dimensional profiles, and (2) an entrainment based on the available entrainment surface. Results indicate that the overprediction of plume characteristics associated with certain other models as compared to experimental data may be overcome using such an analysis and that suitable prediction may be obtained.

Introduction

It is predicted that the future energy needs of this country will be met primarily by nuclear- and fossil-fueled electric generating stations. Since these plants are for the most part 35–40 percent thermodynamically efficient, a considerable amount of the energy will be released as waste heat. With this magnitude of waste heat, the effects of large thermal discharges to the environment become a legitimate concern. Regulating agencies have developed specifications concerning ambient temperature and dilution requirements for the regions near the waste-heat discharges. It is, therefore, necessary for the utility (or other appropriate industries) to design and construct discharge systems which meet dilution requirements and are cost effective. One design which has been advanced to meet these goals is the multiport diffuser. This paper presents a multiport discharge model recently advanced and compares the predictions of this method to those of other models and to experimental data.

The plumes from submerged multiport discharges can be divided into distinct flow regions characterized by their velocity and temperature profiles. Near the source is the zone of flow establishment where the "top hat" profiles of each discharge change to gaussian-shaped profiles. In the zone of established flow, these profiles remain similar, changing only in magnitude. In the merging zone, these single plumes slowly merge into one another forming a long pseudo-slot plume. This merging region can occur anywhere along the trajectory of the plume, depending upon ambient conditions and the initial port spacing. If the plumes reach the free surface, there is an additional surface transition zone where they change to drifting surface plumes.

Since it was desired to investigate the effects of merging, in this paper the plume is considered unconfined and attention is focused on the zone of established flow and the merging zone.

Historical Background

Most of the analysis performed to date has dealt with either the single round jet or the single slot jet, both of which were successfully treated by two-dimensional integral analyses with the assistance of similarity assumptions. Only recently have attempts been made to treat discharges in which similarity is not possible using numerical methods (Trent and Welty [1],[1] Shetz [2]).

Efforts to extend beyond the single port outfall or the slot jet have not been directed toward modeling the merging process of several jets but rather to adapting the solutions of the single round jet and the slot jet to give predictions for the multiple jet case. The two notable works in this regard are those of Koh and Fan [3] and Jirka and Harleman [4]. Koh and Fan simulated the multiple buoyant discharges as single jets until certain merging criteria were met and then shifted simulation to the slot analysis. Transition occurred when the entrainments for both cases were equal or when the width of the round jets equaled the spacing between the jets. Jirka and Harleman suggested that the multiple round jet discharges could be treated as a slot jet provided certain adjustments were made in the parameters describing the plume. For their "equivalent slot" method, the same discharge per unit diffuser length and the same momentum flux per unit length as the multiport discharge is required. This results in a theoretical slot of width, $B = D^3\pi/4L$ where D and L are the actual port diameter and spacing between ports.

Experimental studies have been performed by Jirka and Harleman

[1] Numbers in brackets designate References at end of paper.

Copyright © 1977 by ASME

[4], Koh, et al. [6], Argue [7], Liseth [8], Iwasa and Yatsuzuka [9], and Kannberg and Davis [5]. With the exception of Kannberg and Davis [5] and Kannberg [10], all of these studies involved discharges that were either into confined ambients or from diffusers that did not constitute a single row of discharge ports. Thus, little work has been done on the effects of merging on dilution and trajectory.

The Merging Jet Model

Hirst [11, 12] presented an excellent analysis of the single port discharge. He developed the axisymmetric equations of motion and energy from the Navier-Stokes and energy transport equations. He employed the Bousinesq assumption, boundary-layer approximations, low Eckert number, fully turbulent, steady, and incompressible flow considerations to make the equations tractable. By assuming axisymmetry and integrating in the radial direction the equations may be reduced to the following form:

Continuity

$$\frac{d}{ds}\int_0^\infty \overline{u}r\,dr = -\lim_{r \to \infty}(r\overline{v}) = E \tag{1}$$

Energy

$$\frac{d}{ds}\int_0^\infty \overline{u}(\overline{T}-\overline{T}_\infty)r\,dr = -\frac{d\overline{T}_\infty}{ds}\int_0^\infty \overline{u}r\,dr - \lim_{r \to \infty}\overline{(rv'T')} \tag{2}$$

s-momentum

$$\frac{d}{ds}\int_0^\infty \overline{u}^2 r\,dr = \overline{U}_\infty E \sin\theta_1 \cos\theta_2$$

$$+ \int_0^\infty g\beta\,(\overline{T}-\overline{T}_\infty)r\,dr \sin\theta_2 - \lim_{r \to \infty}\overline{(ru'v')} \tag{3}$$

Curvature equations

$$\frac{d\theta_2}{ds} = g\int_0^\infty [\beta(\overline{T}-\overline{T}_\infty)r\,dr \cos\theta_2 - EU_\infty \sin\theta_1 \sin\theta_2]/\overline{q}$$

and

$$\frac{d\theta_1}{ds} = \kappa_1 = \frac{EU_\infty \cos\theta_1}{\overline{q}\cos\theta_2} \tag{5}$$

where

$$\overline{q} = \int_0^\infty \overline{u}^2 r\,dr - \frac{E^2}{4} - \lim_{r \to \infty}\overline{(r^2v'^2)} \tag{6}$$

The various terms in these equations are defined in the Nomenclature.

The equations have been divided by 2π and the specific heat where appropriate. The curvature equations are formed from appropriate combinations of the component momentum equations. Fig. 1 illustrates the coordinate system used and defines θ_1 and θ_2. The integrals in these equations can be easily evaluated once suitable velocity and temperature profiles are assumed. Most researchers employ gaussian profiles; however, for this work the 3/2 power profiles successfully employed by Stolzenbach [13] were found to be more convenient since they have a defined edge.

In the zone of established flow, axisymmetric profiles of temperature and velocity are assumed to be

$$u = \Delta u + U_\infty \cos\theta_2 \sin\theta_1$$

where

$$\Delta u = \Delta u_c \left(1 - \left(\frac{r}{b}\right)^{3/2}\right)^2$$

and

$$\Delta T = \Delta T_c \left(1 - \left(\frac{r}{b}\right)^{3/2}\right)^2$$

where b is the full half-width of the plume. These profiles are very
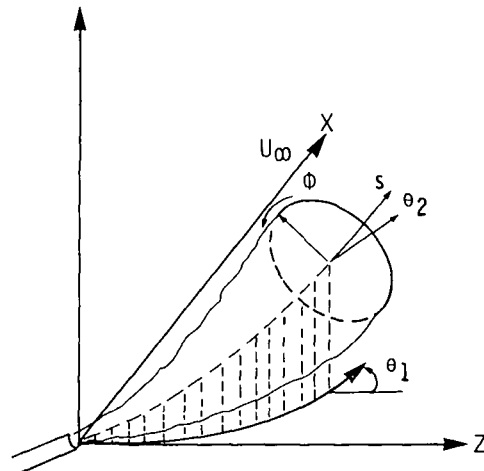
Fig. 1 The coordinate system employed by Hirst [11]

Nomenclature

A = area
a = entrainment coefficient
$a_{0,1,2,\ldots}$ = entrainment coefficients
B = slot plume discharge point width
b = 3/2 power profile plume half width
C_D = drag coefficient
D = port diameter
E = entrainment
F = Froude number = $U_0/(\Delta\rho/\rho_0 gD)^{1/2}$
F_D = drag force
F_L = local Froude number
$\overline{f}$ = time averaged quantity
f' = fluctuating quantity
$G_{1,2,3,4}$ = flux quantities in the zone of single plume flow
$\overline{g}$ = gravitational force (without bar--the gravitational constant)
$H_{1,2,3,4}$ = flux quantities in the merging zone
$h_{1,2,3}$ = incomplete integrals defined in the merging zone

L = distance between ports
$N_{1,2,3}$ = normal terms, employed in the drag force relation
$\overline{q}$ = defined in the text
R = towing ratio = U_∞/U_0
r = plume radius and radial coordinate
S,s = distance along center line and center-line coordinate
T = temperature
T_∞ = ambient temperature
T_c = center-line temperature
$\Delta T_c = (T_c - T_\infty)$
U_0 = port discharge velocity
U_∞ = ambient velocity
u = velocity in the S-direction
u_c = center-line velocity in the S-direction
$\Delta u_c = (u_c - U_\infty \cos\theta_2 \sin\theta_1)$
v = velocity in radial, r-direction
w = plume width
X = horizontal downstream distance and coordinate

Y = vertical coordinate and height above ports
Z = transverse coordinate along line of ports
α = measure of merging = L/b
β = coefficient of thermal expansion
ζ = merging coordinate along line of jet center lines
η = merging coordinate perpendicular to the S-ζ plane
θ_2 and θ = angle of plume center line to the X-Z plane
θ_1 = angle of projection of the plume center line on the plume center line on the X-Z plane from the Z-axis
ρ = density
$\Delta\rho = (\rho - \rho_\infty)$
ρ_0 = discharge density
ρ_∞ = ambient density
ϕ = circumferential plume coordinate

similar in shape to Gaussian profiles, but their defined edge and the assumption that velocity and temperature are the same give a definite point for merging calculations to start. With these relations the integrals may be evaluated and the following differential equations obtained:

Continuity of mass

$$\frac{d}{ds} G_1 = E \qquad (7)$$

Energy

$$\frac{d}{ds} G_2 = -\frac{dT_\infty}{ds} G_1 \qquad (8)$$

s-momentum

$$\frac{d}{ds} G_3 = EU_\infty \sin \theta_1 \cos \theta_2 + G_4 g \sin \theta_2 \qquad (9)$$

Curvature equations

$$\frac{d\theta_1}{ds} = EU_\infty \cos \theta_1 \Big/ \left[\left(G_3 - \frac{E^2}{4}\right) \cos \theta_2 \right] \qquad (10)$$

and

$$\frac{d\theta_2}{ds} = \left(-EU_\infty \sin \theta_2 \sin \theta_1 + g \cos \theta_2 G_4\right) \Big/ \left(G_3 - \frac{E^2}{4}\right) \qquad (11)$$

where G_i become the independent variables, defined as

$$G_1 = 0.12857 \Delta u_c b^2 + \frac{b^2}{2} U_\infty \cos \theta_2 \sin \theta_1 \qquad (12)$$

$$G_2 = 0.066758 \Delta u_c \Delta T_c b^2 - 0.12857 b^2 \Delta T_c U_\infty \cos \theta_2 \sin \theta_1 \qquad (13)$$

$$G_3 = 0.066758 \Delta u_c{}^2 b^2 + 0.25714 b^2 \Delta u_c U_\infty \cos \theta_2 \sin \theta_1$$

$$+ \frac{b^2}{2} U_\infty{}^2 \cos^2\theta_2 \sin^2\theta_1 \qquad (14)$$

$$G_4 = 0.12857 b^2 \beta \Delta T_c \qquad (15)$$

The ambient turbulence terms have been omitted from this presentation for brevity, but they are included in the computer program for use when information is available. The quantities G_i ($i = 1,2,3,4$) are the local mass flux, energy flux, momentum flux, and density deficiency, respectively, divided by 2π and specific heat where appropriate. The values of G_i can be obtained by stepwise integration of equations (7)–(11) using a Runge-Kutta or Hamming Predictor-Corrector scheme once a proper entrainment function, E, is obtained. The subsequent calculation of the center-line temperature and velocity and the plume width is an exercise in solving three equations in three unknowns. The initial conditions for these calculations can be obtained from zone of flow establishment calculations similar to those presented by Hirst [12] using the appropriate 3/2 power profiles.

The calculation continues in the streamwise (s) direction until the width of the plume is equal to the spacing between the jets. At this point the jets begin to merge and the profiles are no longer axisymmetric. For the purposes of smooth transition and a continuous solution of the differential equations between the zone of established flow and the zone of merging, the profiles employed for the merging region should have the following qualities:

1 The profiles should be smooth in all directions.

2 The slopes should be zero at $\zeta = 0, \eta = 0$, and $\zeta = L/2, \eta = 0$ (see Fig. 2).

3 When the plumes just begin to merge they should retain their single-plume profiles.

4 The profiles should be the superposition of the single-plume profiles (where applicable) with no point allowed to exceed center-line properties.

5 The profiles should maintain the characteristics of similar profiles in s.

With the foregoing considerations, the following profiles are assumed in the zone of merging:
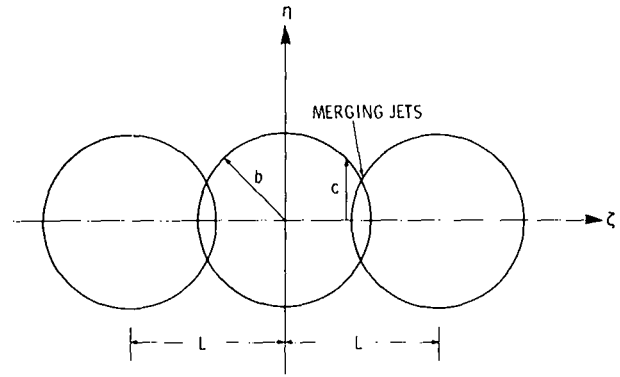
Fig. 2 The coordinate system for the merging plume analysis

$$u = \Delta u + U_\infty \cos \theta_2 \sin \theta_1$$

$$\Delta u = \Delta u_\zeta \left[1 - \left(\frac{\eta}{c}\right)^{3/2} \right]^2$$

$$\Delta u_\zeta = \Delta u_c \left[1 - \left(\frac{\zeta}{b}\right)^{3/2} \right]^2 \qquad \text{for} \quad 0 \le \zeta \le L - b$$

$$\Delta u_\zeta = \Delta u_c \left[\left(1 - \left(\frac{\zeta}{b}\right)^{3/2}\right)^2 + \left(1 - \left(\frac{L - \zeta}{b}\right)^{3/2}\right)^2 \right]$$

$$\text{for} \quad L - b \le \zeta \le L/2$$

$$\Delta T = \Delta T_\zeta \left[1 - \left(\frac{\eta}{c}\right)^{3/2} \right]^2$$

$$\Delta T_\zeta = \Delta T_c \left[1 - \left(\frac{\zeta}{b}\right)^{3/2} \right]^2 \qquad \text{for} \quad 0 \le \zeta \le L - b$$

$$\Delta T_\zeta = \Delta T_c \left[\left(1 - \left(\frac{\zeta}{b}\right)^{3/2}\right)^2 + \left(1 - \left(\frac{L - \zeta}{b}\right)^{3/2}\right)^2 \right]$$

$$\text{for} \quad L - b \le \zeta \le L/2$$

where

$$c^2 = b^2 - \zeta^2$$

After $\Delta u_\zeta = \Delta u_c$ at $\zeta = L/2$, then it is assumed that $\Delta u_\zeta = \Delta u_c$ for all ζ. The same is assumed for temperature. Theoretically, before $\Delta u_\zeta = \Delta u_c$ at $\zeta = L/2$, $b > L$ implying that there are three plumes merging instead of two. The contribution of nonadjacent plumes is considered minor and is neglected in the analysis. This is consistent with other fluid dynamic assumptions.

With the profiles described, the governing relations may be written as follows.

The continuity equation becomes

$$\frac{d}{ds} \left[\frac{1}{2\pi} \int \int_A u \, dA \right]$$

$$= \frac{d}{ds} \left[\frac{2}{\pi} \int_0^{L/2} \int_0^c (\Delta u + U_\infty \cos \theta_2 \sin \theta_1) d\eta d\zeta \right]$$

$$= \frac{d}{ds} H_1 = E \qquad (16)$$

where

$$H_1 = \frac{0.90}{\pi} b^2 \Delta u_c h_1(\alpha) + \frac{b^2}{\pi} U_\infty \cos \theta_2 \sin \theta_1 h_2(\alpha) \qquad (17)$$

$$\alpha = L/b$$

$$h_1(\alpha) = \int_0^{\alpha/2} \sqrt{1 - \chi^2} \, (1 - \chi^{3/2}) d\chi$$

$$+ \int_{\alpha-1}^{\alpha/2} \sqrt{1 - \chi^2} \, (1 - (\alpha - \chi)^{3/2})^2 \, d\chi \qquad (18)$$

and

$$h_2(\alpha) = 2 \int_0^{\alpha/2} \sqrt{1 - \chi^2} d\chi^2$$

$$= \frac{\alpha}{2} \sqrt{1 - \left(\frac{\alpha}{2}\right)^2} + \sin^{-1}\left(\frac{\alpha}{2}\right) \quad (19)$$

After $\Delta u_\zeta = \Delta u_c$ at $\zeta = L/2$, one obtains,

$$H_1 = \frac{b^2}{\pi} 0.45 \Delta u_c + U_\infty \cos\theta_2 \sin\theta_1 \, h_2(\alpha) \quad (20)$$

For the energy equation,

$$\frac{d}{ds}\left[\frac{1}{2\pi} \int \int_A u\Delta T dA\right] = \frac{d}{ds}\left[\frac{2}{\pi} \int_0^{L/2} \int_0^c (\Delta u\right.$$

$$\left. + U_\infty \cos\theta_2 \sin\theta_1)\Delta T_\eta d\eta d\zeta\right] = \frac{d}{ds} H_2 = -\frac{dT_\infty}{ds} H_1 \quad (21)$$

where,

$$H_2 = \frac{0.63116}{\pi} b^2 \Delta T_c \Delta u_c h_3(\alpha)$$

$$+ \frac{0.90}{\pi} b^2 \Delta T_c U_\infty \cos\theta_2 \sin\theta_1 h_1(\alpha) \quad (22)$$

$$h_3(\alpha) = \int_0^{\alpha/2} \sqrt{1 - \chi^2} (1 - \chi^{3/2})^4 \, d\chi + \int_{\alpha-1}^{\alpha/2} \sqrt{1 - \chi^2}$$

$$\cdot [(1 - \chi^{3/2})^2 (1 - (\alpha - \chi)^{3/2})^2 + (1 - (\alpha - \chi)^{3/2})^4] d\chi \quad (23)$$

With the given profile description, Δu_ζ approaches Δu_c at $\zeta = L/2$ to the same degree that ΔT_ζ approaches ΔT_c. Hence, when $\Delta T_\zeta = \Delta T_c$, $\Delta u_\zeta = \Delta u_c$, and one obtains

$$H_2 = \frac{b^2}{\pi} \Delta T_c (0.31558\Delta u_c + 0.45U_\infty \cos\theta_2 \sin\theta_1)h_2(\alpha) \quad (24)$$

The s-momentum equation takes the following form for the zone of merging:

$$\frac{d}{ds}\left[\frac{1}{2\pi} \int \int_A u^2 dA\right]$$

$$= \frac{d}{ds}\left[\frac{2}{\pi} \int_0^{L/2} \int_0^c (\Delta u + U_\infty \cos\theta_2 \sin\theta_1)^2 d\eta d\zeta\right]$$

$$= \frac{d}{ds} H_3 = EU_\infty \cos\theta_2 \sin\theta_1 + H_4 g \sin\theta_2$$

where

$$H_3 = \frac{0.63116}{\pi} b^2 \Delta u_c h_3(\alpha) + \frac{1.8}{\pi} b^2 \Delta u_c U_\infty \cos\theta_2 \sin\theta_1 h_1(\alpha)$$

$$+ \frac{1}{\pi} b^2 U_\infty^2 \cos^2\theta_2 \sin^2\theta_1 h_2(\alpha) \quad (26)$$

and

$$H_4 = \frac{0.9}{\pi} b^2 \beta \Delta T_c h_1(\alpha) \quad (27)$$

After $\Delta u_\zeta = \Delta u_c$,

$$H_3 = \frac{b^2 h_2(\alpha)}{\pi} (0.31558\Delta u_c^2 + 0.9\Delta u_c U_\infty \cos\theta_2 \sin\theta_1$$

$$+ U_\infty^2 \cos^2\theta_2 \sin^2\theta_1) \quad (28)$$

and

$$H_4 = \frac{0.45b^2}{\pi} \beta \Delta T_c h_2(\alpha) \quad (29)$$

For the zone of merging the curvature equations are

$$\frac{d\theta_1}{ds} = \frac{EU_\infty \cos\theta_1}{\left(H_3 - \frac{E^2}{4}\right)\cos\theta_2} \quad (30)$$

and

$$\frac{d\theta_2}{ds} = \frac{-EU_\infty \sin\theta_2 \sin\theta_1 + H_4 g \cos\theta_2}{H_3 - \frac{E^2}{4}} \quad (31)$$

In these equations the term $\alpha = L/b$ represents the degree of merging since for $\alpha = 2$, the plumes are just beginning to merge and for $\alpha = 1$, the plumes are nearly merged. The functions $h_1(\alpha)$, $h_2(\alpha)$, and $h_3(\alpha)$ are incomplete integrals in α. These integrals are not solved in closed form at present but are readily solved numerically.

The quantities H_i ($i = 1, 2, 3, 4$) are the same as G_i in the previous section. They represent the local mass flux, energy flux, momentum flux, and density deficiency. As in the previous section, the quantities Δu_c, ΔT_c, and b may be obtained from these relations by solving three equations simultaneously. The initial conditions for the zone of merging are the final plume conditions of the zone of established flow.

The proper governing differential equations have now been developed and the initial and boundary conditions specified. The only element remaining for closure is the entrainment.

The Entrainment Function

Taylor [14] was the first to suggest the formulation of an entrainment function, and the use of characteristic values of the plume to describe this function. Morton, et al. [15] have employed this concept to develop the expression

$$E = ab\Delta u_c$$

which forms the basis for all the entrainment functions developed since. Numerous other researchers have modified this relation to obtain better agreement with the widely varying discharge and ambient conditions that affect the plume. Some have used the first moment of the momentum equation to determine the form of the entrainment function. Any alterations to the entrainment function should be based on the probable changes in the mechanics of jet mixing at different discharge orientations and ambient conditions.

The entrainment function employed for this study is based on the one proposed by Hirst with modifications for merging effects.

For the Zone of Established Flow (before merging), the entrainment (for $\theta_1 = 90°$) is expressed as

$$E = \left(a_1 + \frac{a_2}{F_L}\right)$$

$$\times \left[b|u_c - U_\infty \cos\theta_2| \left(1 - \frac{a_4 b}{L}\right) + a_3 U_\infty b \sin\theta_2\right] \quad (32)$$

and for Zone of Merging, it is expressed as

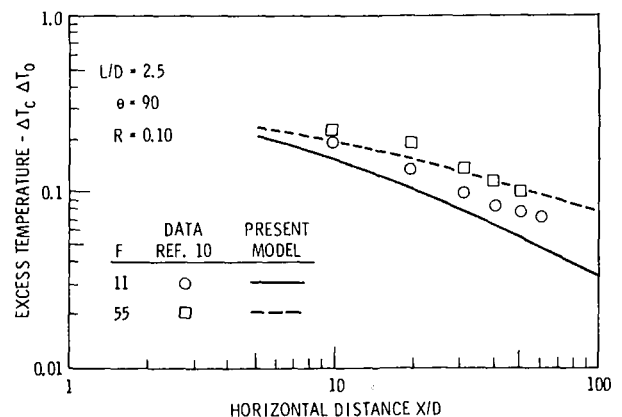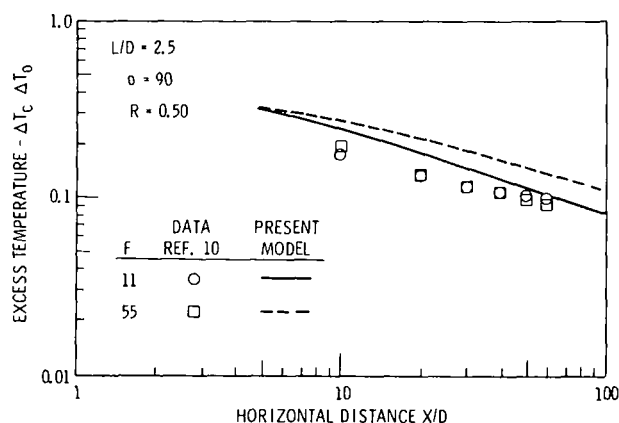Fig. 3 Comparison of experimental and model predicted excess temperature for $L/D = 2.5$, $R = 0.10$, and $\theta = 90$

$$E = \left(a_1 + \frac{a_2}{F_L}\right)\left[b|u_c - U_\infty \cos\theta_2|\left(1 - \frac{a_4}{2}\right)\right.$$

$$\left. \times\left(1 - \frac{2}{\pi}\cos^{-1}\frac{L}{2b}\right) + a_3 U_\infty \frac{L}{2}\sin\theta_2\right] \quad (33)$$

The coefficients, a_1, a_2, and a_3 are similar to those used by Hirst. a_4 accounts for reduced entrainment due to plume competition. The term $(1 - 2/\pi \cos^{-1} L/2b)$ is the entraining surface during merging.

Results

The computer code employed was originally that of the Hirst model. Extensive revision of the code was performed in order to accommodate the different profiles and the merging process. The code was then used in the present study by tuning the entrainment coefficients so that predictions best matched experimental data. The calculations were carried out on an IBM 370/158 computer operated by Optimum Systems, Inc., Bethesda, Maryland. The coefficients were determined by successively simulating more complex discharge conditions starting with single momentum jet data without current, progressing to multiple buoyant merging plumes with current.

Data for this tuning process were taken from [10, 15–17]. In tuning the model for single buoyant plumes, it was found that the best overall fit could be obtained with $a_1 = 0.05$, $a_2 = 0.0$, and $a_3 = 11.5$. Better fit to a particular case could be obtained by adjusting these coefficients for each type of flow, but this procedure reduces the generality of the model. In trying to model the multiple-port data for ambient flow of Kannberg [10], it was found that good agreement could not be obtained for both trajectory and dilution by adjusting a_3 alone, particularly for closer port spacings. It was found that a drag force term had to be included in the momentum equation before satisfactory agreement could be obtained. The drag force was assumed to be a function of plume size, spacing, and ambient current dynamic head. For the unmerged plume this gave

$$F_D = C_D \frac{b}{\pi}\left(\frac{b}{L}\right)\frac{U_\infty^2}{2}N$$

for the merging plume

$$F_D = C_D \frac{L}{\pi}\frac{U_\infty^2}{2}N$$

where

$$N = \sqrt{N_1^2 + N_2^2 + N_3^2}$$

and

$$N_1 = \cos^2\theta_2 \sin\theta_1 \cos\theta_1$$

$$N_2 = \sin^2\theta_2 + \cos^2\theta_2 \cos^2\theta_1$$

$$N_3 = \sin\theta_2 \cos\theta_2 \sin\theta_1$$

This gave a zero drag force for single plumes and a maximum drag force for closely spaced multiple plumes.

With this drag force included the best overall agreement was obtained with $a_4 = 0.2$ and $C_D = 2$. Although the effect was minor, better agreement was obtained for $R = U_\infty/U_0$ values near 0.1 if C_D was increased to 3.0, and reduced to 1.0 or below for $R = 0.5$.

The following figures show the final model predictions as compared to multiport data using the values of coefficients giving the best overall agreement. Fig. 3 is a plot of excess temperature ratio versus horizontal distance for vertical discharge into a cross current with $R = 0.1$.
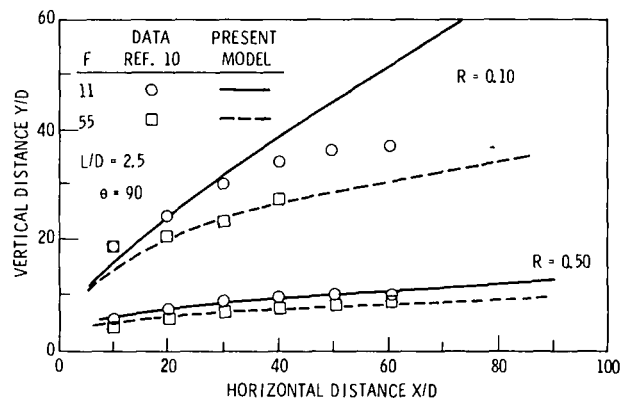
Fig. 5 Comparison of model predicted trajectories with data for $L/D = 2.5$, $F = 11$ and 55, $R = 0.10$ and 0.50
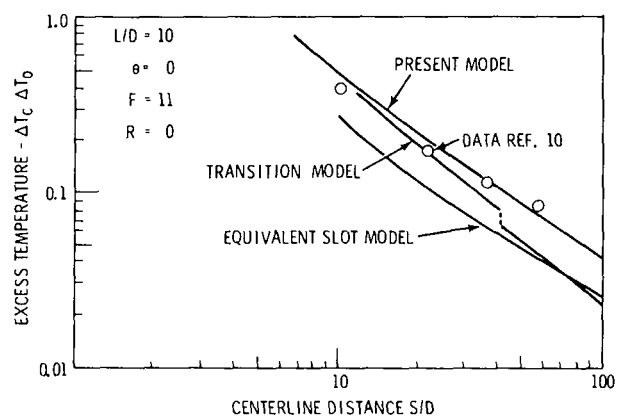
Fig. 6 Comparison of excess temperature predicted by several models and experimental data for $L/D = 10$, $R = 0.0$, and $F = 11$

Fig. 4 Comparison of experimental and model predicted excess temperature for $L/D = 2.5$, $R = 0.5$, and $\theta = 90$
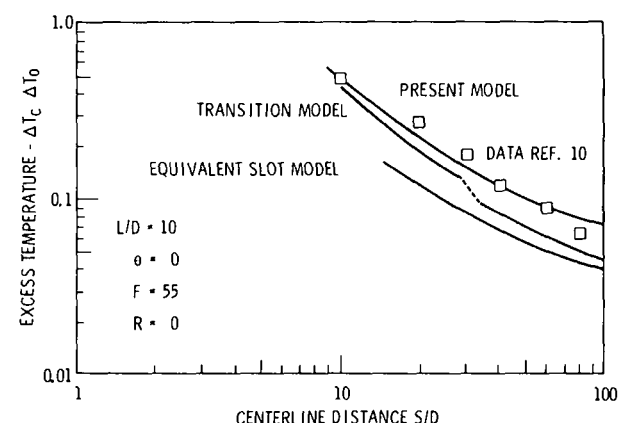
Fig. 7 Comparison of excess temperature predicted by several models and experimental data for $L/D = 10$, $R = 0.0$, and $F = 55$

The port spacing is 2.5 dia; values for discharge Froude numbers of the order of 10 and 60 are shown. The data points represent the mean of the experimental multiport data presented in reference [10]. The lines are predicted values from the model described in this paper. Fig. 4 presents similar information for $R = 0.5$. The agreement is seen to be quite good. Fig. 5 is a plot of plume trajectory for the foregoing cases. Again both experimental values and model predictions are shown. The agreement is very good for the high-current cases but not as good for the low-current cases.

Excess temperature decay along the plume center line, s/D, are shown on Fig. 6 and 7 for horizontal discharge into a stagnant ambient, for discharge Froude numbers of about 10 and 60. The port spacing in this case is 10 dia. For comparison, the experimental values of reference [10] are plotted along with predictions from the Koh and Fan transition model, the Jirka and Harleman equivalent slot model, and the merging model described here. The Koh and Fan and Jirka and Harleman models rely on entrainment coefficients determined for single round and slot jets, respectively. While it is possible to change the entrainment coefficients of these models, it would not be consistent with the nature of those models, nor would reliable predictions be obtained for extreme port spacings. Therefore the entrainment coefficients suggested by the respective authors were used in the other models. It is seen that the transition model and the equivalent slot model, although giving reasonable values, both overpredict the measured dilution, whereas the merging model does much better. The final two figures, Fig. 8 and 9 show trajectory and width comparisons for horizontal discharge into stagnant ambients, where the spacing is again 10 dia. The agreement between experimental data and merging model predictions is seen to be very good for both tra-

jectory and width within the experimental Froude number ranges of reference [10].

Conclusions

The model presented here successfully treats the merging of adjacent round jets from a row of equally spaced ports into a pseudo-slot jet in a manner that is more continuous than other methods advanced in recent years. Use of the model gives better agreement with experimental data than other models considered. The model requires additional terms in the entrainment function to account for competition of entraining fluid and for the reduction in the entrainment area of the jet as merging progresses. Unfortunately, agreement with crossflow data could not be obtained for multiple jets without the addition of a drag term and a corresponding additional coefficient. The values of these coefficients were easily determined by comparing data from progressively more complex flow cases with model predictions.

Fig. 8 **Comparison of model predicted trajectories with experimental data for L/D = 10, R = 0.0, and θ = 0.0 for several Froude numbers**

Fig. 9 **Comparison of width predictions of the Koh and Fan transition model and present model with experimental data**

References

1 Trent, D. S., and Welty, J. R., "Numerical Thermal Plume Model for Vertical Outfalls in Shallow Water," Environmental Protection Agency Technology Series, EPA-R2-73-162, Mar. 1973.

2 Shetz, J. A., Chien, C. J., and Sill, B. L., "Heat Transfer and Fluid Mechanics of the Thermal Pollution Problem," Thermal Pollution Analysis, Vol. 36 c.f. Progress in Astronautics and Aeronautics, J. A. Shetz, ed., American Institute of Astronautics and Aeronautics, 1975.

3 Koh, R. C., and Fan, L. N., "Mathematical Models for the Prediction of Temperature Distributions Resulting From the Discharge of Heated Water in Large Bodies of Water," Environmental Protection Agency Water Pollution Control Research Series Report No. 1613DW/1/70, Oct. 1970.

4 Jirka, G., and Harleman, D. R. F., "The Mechanics of Submerged Multiport Diffusers for Buoyant Discharges in Shallow Water," Massachusetts Institute of Technology, Ralph M. Parsons Laboratory for Water Resources and Hydro-dynamics, Report No. 169, Mar. 1973.

5 Kannberg, L. D., and Davis, L. R., "Experimental Investigation of Deep Submerged Multiple Buoyant Jets Into Stagnant and Co-Moving Ambients," Paper presented at Thermal Pollution Analysis Conference held at Virginia Polytechnic Institute and State University, Blacksburg, Va., May 1974.

6 Koh, R. C., Brooks, N. H., Wolanski, E. H., and List, E. J., "Basin Model Studies of Diffusers," SCE Report No. 4, W. M. Keck Hydraulics Laboratory, California Institute of Technology, May 1973.

7 Argue, J., "The Mixing Characteristics of Submerged Multiple Port Diffusers for Heated Effluents in Open Channel Flow," MA thesis, University of Iowa, May, 1973.

8 Liseth, P., "Mixing of Merging Buoyant Jets From a Manifold in Stagnant Receiving Water of Uniform Density," Hydraulic Engineering Laboratory Report HEL 231, University of California, Berkeley, Nov. 1970.

9 Iwasa, Y., and Yatsuzuka, M., "Spread of Heated Waters From Multiport Diffuser," Proceedings of the U. S.-Japan Joint Seminar on Engineering and Environmental Aspects of Waste Heat Disposal, Paper No. 9, Tokyo, Japan, Apr. 15, 1974.

10 Kannberg, L. D., "An Experimental and Analytical Investigation of Deep Submerged Multiple Buoyant Jets," PhD thesis, Oregon State University, 1976.

11 Hirst, E. A., "Analysis of Round Turbulent, Buoyant Jets Discharged to Flowing Stratified Ambients," Oak Ridge, Oak Ridge National Laboratory, Report No. ORNL-4685, 1971, p. 36.

12 Hirst, E. A., "Analysis of Buoyant Jets Within the Zone of Flow Establishment," Oak Ridge National Laboratory, Report No. ORNL-TM-3470, Aug. 1971.

13 Stolzenbach, K. D., and Harleman, D. R. F. "An Analytical and Experimental Investigation of Heated Water," Ralph M. Parsons Laboratory for Water Resources and Hydrodynamics, Report No. 135, Cambridge, Massachusetts Institute of Technology, 1971, p. 212.

14 Taylor, Sir Geoffrey, "Dynamics of a Mass of Hot Gas Rising in Air," United States Atomic Energy Commission, MDDC 919, LADC 276, 1945.

15 Morton, B. R., Taylor, Sir Geoffrey, Turner, J. S., "Turbulent Gravitational Convection From Maintained and Instantaneous Sources," Proceedings of the Royal Society of London, Series A, Vol. 234; pp. 1-23.

16 Fan, L-N., "Turbulent Buoyant Jets Into Stratified or Flowing Ambient Fluids," Keck Laboratory of Hydraulic and Water Resources, California Institute of Technology, Report No. KH-R-15, June 1967.

17 Anwar, H. O., "Behavior of Buoyant Jets in Calm Fluid," Journal of the Hydraulics Division, ASCE, Vol. 95, No. HY4, 1969, pp. 1289-1303.

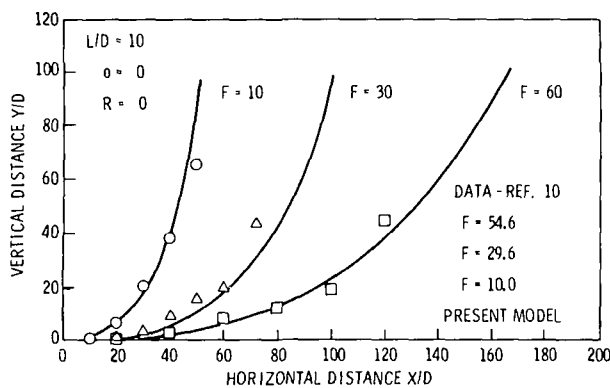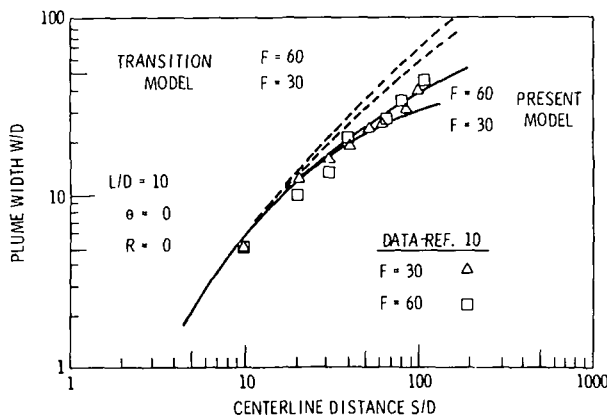18 Fox, D. G., "Forced Plume in a Stratified Fluid," Journal of Geophysical

Research, Vol. 75, No. 33, 1970, pp. 6818–35.

19   Abraham, G., "Horizontal Jets in Stagnant Fluid of Other Density," *Journal of the Hydraulics Division*, ASCE, Vol. 91, No. HY4, 1969, pp. 139–153.

20   Platten, J. L., and Keffer, J. F., "Entrainment in Deflected Axisymetric Jets at Various Angles to the Free Stream," Mechanical Engineering Department, University of Toronto, UTME-TP-6808, 1968.

21   Hoult, D. P., Fay, J. A., and Forney, L. J., "A Theory of Plume Rise Compared with Field Observations," *Journal of the Air Pollution Control Association*, Vol. 19, No. 9, 1969, pp. 585–90.

Research, Vol. 75, No. 33, 1970, pp. 6818–35.

19 Abraham, G., "Horizontal Jets in Stagnant Fluid of Other Density," *Journal of the Hydraulics Division*, ASCE, Vol. 91, No. HY4, 1969, pp. 139–153.

20 Platten, J. L., and Keffer, J. F., "Entrainment in Deflected Axisymetric Jets at Various Angles to the Free Stream," Mechanical Engineering Department, University of Toronto, UTME-TP-6808, 1968.

21 Hoult, D. P., Fay, J. A., and Forney, L. J., "A Theory of Plume Rise Compared with Field Observations," *Journal of the Air Pollution Control Association*, Vol. 19, No. 9, 1969, pp. 585–90.

DISCUSSION

G. H. Jirka[1]

Kannberg and Davis address two important points in the design and analysis of multiple-port diffusers: (1) What is the mechanism of jet merging and how to model it? (2) What is the effect of jet merging on the mixing capacity of such diffusers?

(1) The lateral merging of the individual jets emanating from the diffuser nozzles appears to be a complicated process. As the jet boundaries approach each other, the space for the entrainment flow is limited between the jets leading to low pressure zones and dynamic attachment effects. The turbulent diffusion characteristics change from an axisymmetric shearing zone to a two-dimensional one. Clearly, jet integral techniques, with their assumptions of jet similarity and hydrostatic pressure distribution, can describe this transition in an approximate fashion only. Kannberg and Davis' profile specification in the transition region represents a reasonable approach in this direction and has advantages over Koh and Fan's earlier model, inasmuch as it avoids abrupt changes in the center line temperature prediction. Questions, however, remain as to the choice of the entrainment coefficient (two- or three-dimensional value) and the assumptions of a turbulent Prandtl number of unity, which is in contradiction with experimental observations on jets and plumes. The pressure effect on the merging process caused by ambient currents is even more difficult. The form drag assumption, equation (34), proposed by the authors seems a tenuous one in view of the complicated geometry. Such model deficiencies, however, could be corrected through the best-fit choice of the drag coefficients, at least within the parameter range of the author's experiments.

(2) The basic argument of the two-dimensional slot diffuser concept, as used in the model by Jirka and Harleman [4], is that beyond the line of merging the flow field of the actual multiple-port diffuser is equal to that of a slot discharge. Or in other words, the initial three-dimensional details have no distinguishable effects at longer distances. This concept is physically reasonable, as the equivalent slot diffuser has the same kinetic energy input per unit length, which is ultimately expanded in turbulent jet mixing. This behavior of laterally limited jets is in analogy with the nozzle shape effects on free turbulent jets in which, after a certain characteristic distance, the initial shape effects are no longer felt and all jets approach an wxisymmetric shape (Sforza, et al. [22][2], experiments by Yevdjevich reported in [21]). The equivalent slot concept is useful for diffuser classification as the number of governing parameters is reduced. It has been found of sufficient accuracy for multiple-port diffusers by Liseth [8] and more recently by Buhler [23]. The lack of agreement which is indicated by Kannberg and Davis' experiments may be due to equipment effects, since the horizontal momentum input of the jets is likely to cause some circulation and possibly re-entrainment in a finite size laboratory facility. This may account for the lower centerline temperatures which were observed.

Finally, some caution has to be expressed regarding Kannberg and Davis' introductory claim that their analysis is applicable for the predictions of condenser heat discharges from electric power generation. In fact, the low buoyancy of such heated discharges in combi-
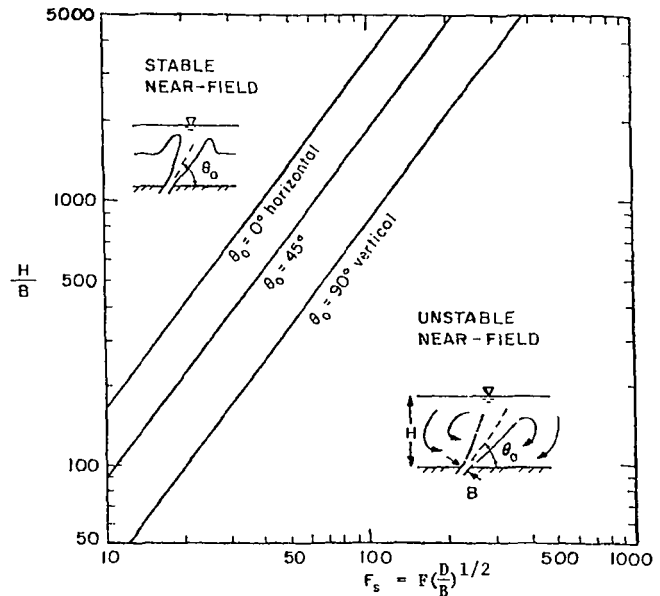
Fig. 10 Stability of the flow field for multiport diffusers discharging into shallow water as a function of slot densimetric Froude number F_s, relative water depth H/B, and discharge angle, θ_0. ($B = D^2\pi/4L$ is the equivalent slot width); after Jirka and Harleman [24]

nation with the limiting water depth at usual disposal sites gives rise to dynamic instabilities in form of a recirculating eddy extending over the entire water depth. This discharge condition cannot be analysed by means of simple buoyant jet models as proposed by the authors. Stability criteria, which depend on relative water depth, discharge Froude number and angle, have been developed by Jirka and Harleman [4, 24] and are plotted in Fig. 10. Multiple-port diffuser designs for condenser heat discharge generally fall into the unstable discharge range. The practical application of the stable range, in which the authors' model is applicable, relates to sewage and blowdown diffusers, usually with higher buoyancy and lower flowrates.

Additional References

22 Sforza, P. M. Steiger, M. H., and Tentracosts, N., "Studies on Three-Dimensional Viscous Jets," *AIAA Journal*, Vol. 4, 1966.

23 Buhler, J., "Model Studies on Multiport Outfalls in Unstratified, Stagnant or Flowing Ambient Water," PhD thesis, Department of Civil Engineering, University of California, Berkeley, 1974.

24 Jirka, G. H., and Harleman, D. R. F., "Buoyant Jets in Confined Surroundings," in *Thermal pollution Analysis*, J. A. Schetz, ed., Vol. 36 of Progress in Astronautics and Aeronautics, AIAA, New York, 1975.

Authors' Closure

We appreciate Dr. Jirka's taking time to comment on the analysis and results of this paper. We agree with much of what he has said, but feel a few points need to be further clarified.

A unity turbulent spreading parameter was introduced into the analysis to make the smooth merging of both temperature and velocity easier. The authors realize that this may not be exactly the case but

---

[1] Massachusetts Institute of Technology, Cambridge, Mass.

[2] Numbers in brackets designate Additional References at end of discussion.

it is felt that the errors introduced are minor in light of the complexity of the problem.

The equivalent slot concept is a useful approach in analyzing the characteristics of certain multiport discharges, but as with most simplified analyses, the limits of use should be understood. The fundamental premise behind the equivalent slot is that beyond the point of merging the plumes from a row of equally spaced jets become the same as the plume from a slot jet having the same mass and momentum flux per unit length as the multiple jets. This presumes that up to the point of merging, the mixing mechanisms of the two are the same, and of course they are not. The effect of this difference on the ultimate dilution would be minor if the major portion of the dilution occured after merging. This would either be for large distances away from the point of discharge or for closely spaced discharge ports. Most researchers realize this. For example, Liseth [8] suggested the use of an equivalent slot for closely spaced ports and only attempted to compare results at $y/L = 80$. For an $L/D = 10$, this at a $y/D = 800$. At this point the dilution is so great that the excess temperature, regardless of how it is calculated, is usually no longer of interest.

In the near and intermediate field where most of the data reported in this paper were taken, the story is different. One of the causes of this difference is the development length. To illustrate, consider a diffuser with 1-ft dia ports spaced 10-ft apart discharging into stagnant water. The jets for this system merge about 30 ft from discharge and have a development length where the temperatures begin to decay of about 6 ft. The equivalent slot for this system has a width, B, of 0.08 ft. Therefore, at the end of the actual single jet development zone where the excess temperature is of the order of 1.0–0.8, the equivalent slot is at an s/B of 75 where it predicts an excess temperature of the order of 0.2.

In addition to the development zone problem, entrainment is also different for the two systems. Entrainment has been suggested as $2\pi(0.082)bu_c$ and $2(0.16)Lu_c$ for the round and slot jets, respectively [3]. For the example case considered in the foregoing, the slot jet entrainment is $3.2u_c$ while the round jet entrainment varies due to plum growth from $0.26u_c$ at discharge to $2.6u_c$ at merging. Thus, even though a multiport discharge merges into essentially a two-dimensional plume where the individual character of the original jets no longer exists, its properties are different from those of a plume that originated from a slot. As a result, the authors feel that the indiscriminate use of the equivalent slot to model multiple port diffusers could lead to gross errors.

We agree with Dr. Jirka that the present model should not be used in shallow stagnant receiving water where surface effects and instabilities are present. In flowing ambients, however, even at low velocities these effects are reduced and in some cases eliminated. In many cases the receiving water is sufficiently deep to use the model to predict the major portion of the plume's characteristics.

S. Sengupta

Assistant Professor, Department of Mechanical Engineering, University of Miami, Coral Gables, Florida, Mem. ASME

A Three-Dimensional Rigid-Lid Model for Closed Basins

A numerical rigid-lid model for wind driven circulation and temperature fields in closed basins has been developed. The horizontal momentum equations each include the non-steady, non-linear inertia, Coriolis, pressure gradient and all three viscous terms. The energy equation includes the non-steady, convective and all three diffusion terms. The hydrostatic and Boussinesq approximations have been used. A Poisson equation derived from the vertically integrated horizontal momentum equations has been used as the predictive equation for surface pressure. An iterative scheme with normalization has been developed to solve the Poisson equation for pressure with Neumann boundary conditions. A vertically normalized system of equations which maps variable depth domains to a constant depth has been used. The model has been applied to a pond located near Cleveland, Ohio. The effect of topography and buoyancy on wind driven circulation has been investigated. The relative importance of the terms in the transport equations has been analyzed.

Introduction

One of the earliest investigations of wind-driven circulation was conducted by Ekman [1].[1] He developed a theory for sea-level fluctuations produced in a deep sea by steady wind stress. The steady state and time dependent, finite-depth cases were modelled by Welander [2]. These models were analytical. Pioneering work in modelling the Great Lakes was done by Csanady [3].

A numerical application of the Welander forumlation to the steady-state, wind-driven circulation in Lake Erie was made by Gedney and Lick [4]. Gedney et al. [5, 6], investigated the effects of bottom topography and eddy diffusivity on wind driven currents in two layer stratified lakes. Goldstein et. al. [7], obtained analytical solutions to investigate the effect of an island on wind-driven circulation. Numerical models of a more elaborate nature have been developed by Bryan [8], and Crowley [9-11]. Bryan [8], developed a rigid-lid model for circulation of world oceans. Crowley developed numerical models for oceanic transport with rigid-lid and free-surface formulation. He concluded that the rigid-lid model was computationally superior, though erroneous in Rossby wave predictions. Freeman [12], modelled Lake Huron using a free-surface formulation and vertical normalization suggested by Phillips [13].

Analytical models have been critically discussed in a review by Csanady [14]. Cheng et al. [15], in a recent review, has presented some numerical models for lake circulation.

In the present investigation a rigid-lid, divergence of Navier-Stokes formulation has been developed. The model has been applied to simple and complex domains. Insight has been obtained regarding numerical behavior, influence of transport parameters, driving forces and the fundamental transport mechanisms.

Formulation of the Mathematical Model

The system of equations which describes the circulation in a variable density basin is the three Navier-Stokes equations, the energy equation, the conservation of mass equation and an equation of state. The fluid is considered incompressible. In order to avoid surface gravity waves, and consequent small time scales and small integration time steps, the rigid-lid approximation is invoked. The vertical momentum equation has been reduced to the hydrostatic approximation. The effects of turbulence are incorporated by using mean equations with eddy transport coefficients; the zeroth order turbulent closure. The eddy coefficients are assumed constant, though of different magnitudes for horizontal and vertical directions. The Boussinesq approximation is applicable. A similar model without vertical normalization for constant depth basins was used by Paul and Lick [16] to simulate discharge of Cuyahoga River into Lake Erie.

Governing Equations. The vertical coordinate has been normalized by the local depth in the form of

$$\gamma = \bar{z}/\bar{h} \ (x, y)$$

This maps the basin to a constant depth one. The details of the derivation are presented by Sengupta and Lick [17]. The non-dimensional governing equations in the conservative form in the normalized coordinates (α, β, γ) are:

Continuity $\qquad \dfrac{\partial(hu)}{\partial\alpha} + \dfrac{\partial(hv)}{\partial\beta} + h\dfrac{\partial\Omega}{\partial\gamma} = 0 \qquad$ (1)

Momentum $\qquad \dfrac{\partial(hu)}{\partial t} + \dfrac{\partial(huu)}{\partial\alpha} + \dfrac{\partial(huv)}{\partial\beta} + h\dfrac{\partial(\Omega u)}{\partial\gamma} - \dfrac{h}{RB}\,v$

$$= -h\frac{\partial P_s}{\partial\alpha} - h\,B_x + \frac{1}{Re}\frac{\partial}{\partial\alpha}\left(h\frac{\partial u}{\partial\alpha}\right) + \frac{1}{Re}\frac{\partial}{\partial\beta}\left(h\frac{\partial u}{\partial\beta}\right)$$
$$+ \frac{1}{\epsilon^2 Re}\frac{1}{h}\frac{\partial}{\partial\gamma}\left(A_V^*\frac{\partial u}{\partial\gamma}\right) \quad (2)$$

$$\frac{\partial(hv)}{\partial t} + \frac{\partial(huv)}{\partial\alpha} + \frac{\partial(hvv)}{\partial\beta} + h\frac{\partial(\Omega v)}{\partial\gamma} + \frac{h}{RB}\,u$$
$$= -\frac{\partial P_s}{\partial\beta} - hB_y + \frac{1}{Re}\frac{\partial}{\partial\alpha}\left(h\frac{\partial v}{\partial\alpha}\right) + \frac{1}{Re}\frac{\partial}{\partial\beta}\left(h\frac{\partial v}{\partial\beta}\right)$$
$$+ \frac{1}{\epsilon^2 Re}\frac{1}{h}\frac{\partial}{\partial\gamma}\left(A_V^*\frac{\partial v}{\partial\gamma}\right) \quad (3)$$

Hydrostatic Equation

$$\frac{\partial\rho}{\partial\gamma} = Eu(1 + \rho)h \qquad (4)$$

where α, β are along constant γ planes.

The pressure terms are now divided into two parts, namely, the part due to surface or lid pressure, P_s, and the part due to density variations. The expressions for B_x and B_y are presented in the Appendix I.

Energy

$$\frac{\partial(hT)}{\partial t} + \frac{\partial(huT)}{\partial\alpha} + \frac{\partial(hvT)}{\partial\beta} + h\frac{\partial(\Omega T)}{\partial\gamma}$$
$$= \frac{1}{Pe}\frac{\partial}{\partial\alpha}\left(h\frac{\partial T}{\partial\alpha}\right) + \frac{1}{Pe}\frac{\partial}{\partial\beta}\left(h\frac{\partial T}{\partial\beta}\right) + \frac{1}{Pe\epsilon^2}\frac{1}{h}\frac{\partial}{\partial\gamma}\left(B_v^*\frac{\partial T}{\partial\gamma}\right) \quad (5)$$

Equation of State

$$\tilde{\rho} = 1.000428 - .000019\tilde{T} - .0000046\tilde{T}^2 \qquad (6)$$

where $\quad \tilde{\Omega} = \dfrac{\partial\gamma}{\partial\tilde{t}}$

and $\quad \tilde{\omega} = \gamma\left(\tilde{u}\dfrac{\partial\tilde{h}}{\partial\tilde{x}} + \tilde{v}\dfrac{\partial\tilde{h}}{\partial\tilde{y}}\right) + \tilde{h}\tilde{\Omega} \qquad (7)$

The rigid-lid condition $w\,(z = 0) = 0$ implies $\Omega\,(\gamma = 0) = 0$ where

$$u = \tilde{u}/U_{ref}; \quad v = \tilde{v}/U_{ref}; \quad w = \tilde{w}/\epsilon U_{ref}; \quad t = \tilde{t}/t_{ref}$$
$$x = \tilde{x}/L; \quad y = \tilde{y}/L; \quad z = \tilde{z}/H; \quad \epsilon = H/L$$

$$P = \tilde{P}/\rho_{ref}U_{ref}^2; \quad T = \frac{\tilde{T} - T_{ref}}{T_{ref}}; \quad \rho = \frac{\tilde{\rho} - \rho_{ref}}{\rho_{ref}}; \quad \Omega = \tilde{\Omega}\,t_{ref}$$

$$A_H^* = A_H/A_{ref}; \quad A_V^* = A_V/A_{ref}; \quad B_H^* = B_H/B_{ref};$$
$$B_V^* = B_V/B_{ref}$$

$$t_{ref} = L/U_{ref}$$

Quantities with subscript "ref" are reference quantities. H and L are vertical and horizontal length scales. The variables with wavy lines on top are dimensional quantities.

If $A_H = A_{ref}$ and $B_H = B_{ref}$
then $A_H^* = 1$ and $B_H^* = 1$.

$$Re = \frac{U_{ref}L}{A_{ref}}; \quad RB = \frac{U_{ref}}{fL}; \quad Pr = \frac{A_{ref}}{B_{ref}}$$

$$Pe = Re\,Pr = \frac{U_{ref}L}{B_{ref}}; \quad Eu = \frac{gH}{U_{ref}^2}$$

If Prandtl number is equal to 1, then $A_{ref} = B_{ref}$. A_H and A_V are eddy viscosities in horizontal and vertical directions. B_H and B_V are eddy diffusivities in horizontal and vertical directions.

It should be noted that the diffusion terms in equations (2, 3 and 5) are not the complete terms. Terms with higher derivatives of h with respect to α, β have been neglected. Detailed derivations are given by Sengupta and Lick [17].

To obtain a predictive equation for pressure, the horizontal momentum equations (2) and (3) are integrated from $\gamma = 0$ to $\gamma = 1$. The integrated equations are then differentiated with respect to α and β, respectively, and summed. The resulting equation for surface pressure is:

$$\frac{\partial^2 P_s}{\partial\alpha^2} + \frac{\partial^2 P_s}{\partial\beta^2} = \frac{1}{h}\frac{\partial}{\partial\alpha}\left(-A_{x1} + A_{x2} + C_x - X_p\right)$$
$$+ \frac{1}{h}\frac{\partial}{\partial\beta}\left(-A_{y1} - A_{y2} + C_y - Y_p\right)$$
$$- \frac{1}{h}\left\{\frac{\partial h}{\partial\alpha}\cdot\frac{\partial P_s}{\partial\alpha} + \frac{\partial h}{\partial\beta}\frac{\partial P_s}{\partial\beta}\right\} - \frac{\partial(\Omega)}{\partial t}\,(\gamma = 0) \quad (8)$$

The last term is the Hirt and Harlow [18] correction term which accounts for non-zero vertical velocities at the rigid lid. The variables A_x, A_{x2}, etc. are given in Appendix I. The first derivative terms for pressure are included in the forcing terms for numerical advantages discussed in a later section.

The set of equations (1–8), together with the appropriate boundary conditions, constitute the mathematical model.

Initial and Boundary Conditions. The equations are parabolic in time, requiring complete specification of all dependent variables at the start of integration. In the present study zero circulation and

---

Nomenclature

A_H = horizontal kinematic eddy viscosity
A_V = vertical kinematic eddy viscosity
A_z = vertical eddy viscosity
A_{ref} = reference kinematic eddy viscosity
$A_V^* = A_V/A_{ref}$
B_H = horizontal diffusivity
B_V = vertical diffusivity
B_{ref} = reference diffusivity
$B_V^* = B_V/B_{ref}$
B_z = vertical conductivity $\rho C_p B_V$
C_p = specific heat at constant pressure
Eu = Euler number
f = Coriolis parameter
g = acceleration due to gravity
h = depth at any location in the basin
H = reference depth
I = grid index in x-direction or α direction

J = grid index in y-direction or β direction
K = grid index in z-direction or γ direction
k = thermal conductivity
K_s = surface heat transfer coefficient
L = horizontal length scale
P = pressure
P_s = surface pressure
Pr = turbulent Prandtl number (A_{ref}/B_{ref})
Pe = Peclet number
Re = Reynolds number (turbulent)
RB = Rossby number
T = temperature
T_{ref} = reference temperature
T_E = equilibrium temperature
t = time
t_{ref} = reference time
u = velocity in x-direction

v = velocity in y-direction
w = velocity in z-direction
x = horizontal coordinate
y = horizontal coordinate
z = vertical coordinate
α = horizontal coordinate in stretched system
β = horizontal coordinate in stretched system
γ = vertical coordinate in stretched system
ρ = density
$\epsilon = H/L$

Superscripts

$(\sim)$ = dimensional quantity
$(\ )$ = dimensionless quantity
$(\ )_{ref}$ = reference quantity

Journal of Heat Transfer

isothermal initial conditions have been used.

At the air-water interface, the boundary condition on the momentum equations is wind stress obtained from Wilson [19] for wind velocities six meters above the water surface.

Edinger and Geyer [20] have determined the heat flux relations at the air-water interface. They define an equilibrium temperature as that at which no heat flux takes place at a surface, and equate heat flux to the product of the difference between surface temperature and equilibrium temperature and surface heat transfer coefficient.

The conditions on the sidewalls are no slip and no normal velocity for the momentum equation except that w is undetermined due to the hydrostatic approximation. The walls are taken as adiabatic.

At the bottom, the conditions of no slip and no normal velocity are applicable. The bottom is also considered adiabatic. The adiabatic conditions at the sidewalls and the bottom could be relaxed without an increase in conceptual difficulty or change in solution technique.

The boundary conditions on the pressure equation are obtained by evaluating the values $\partial P_s/\partial \alpha$ and $\partial P_s/\partial \beta$ from the momentum equation. Therefore the pressure solution requires a solution to a Neumann problem. The solution is unique to within a constant. However, since only the derivatives of pressure enter the momentum equations, the actual values of the pressure solution surface are unimportant as long as the shape is correct.

Numerical Procedure. A brief review of numerical techniques in geophysical flow has been presented by Simons (21). Cheng (15), has discussed some techniques relevant to lake circulation models. Roache (22) has presented several methods for incompressible flows in general.

In the present model a finite-difference method is used. A staggered mesh is used where u, v are located at integral nodes (I, J, K) on the horizontal α, β plane. P, w, T, ρ are located at half-grid points $(I + \frac{1}{2}, J + \frac{1}{2}, K)$ in the horizontal plane. The arrangement is repeated in the z or γ direction, represented by K. Constant grid sizes are used in α, β directions except at lateral boundaries where the horizontal grid spacings are halved for the non-integral node points.

The finite difference equation for the u-momentum equation is:

$$\frac{u^{n+1} - u^n}{\Delta t} = (\text{Inertia})^n + (\text{Pressure})^n + (\text{Viscous})^{n,n+1,n-1}$$

This is the forward time central space scheme, except for the diffusion terms which are approximated by the Dufort-Frankel scheme. This is a modified version of the Dufort-Frankel scheme where the time derivative has been forward differenced rather than central differenced. This was done to avoid time-splitting of the solution which often results with central differencing of first derivatives in time, eg. Bryan [8]. The schemes are similar for the v momentum equation and energy equation.

No rigorous stability analysis can be made of the system of difference equations. However, the one-dimensional Burgers equation has been analyzed. The stability criteria can be heuristically extended to three-dimensional cases. The convective stability criterion applies. The diffusive criterion has been somewhat relaxed by the modified Dufort-Frankel differencing. The Courantlewy-Fredrichs conditions for surface gravity waves has been eliminated by the rigid-lid assumption.

The Elliptic equation for pressure is solved by successive overrelaxation using a five point scheme. The first derivatives of pressure in the right hand side of equation (8) are evaluated after each time step, and are not a part of the iterative procedure; they merely contribute to the forcing term. This gave faster convergence of the iterative procedure. In this sense the equation may be termed a Poisson equation. Iterative solution of this Neumann problem poses the possibility of the solution surface "floating" to large numbers, since the solution is only unique to a constant. A point in the domain is chosen. The change in pressure at this point is computed after each iteration. The pressure solution surface is adjusted by this change such that the particular point is brought back to the original value. The procedure is repeated at each iteration.

The Hirt and Harlow [17] correction term is evaluated using a backward difference in time, with present time value equated to zero. This correction adjusts surface pressure solution so that nonzero vertical velocities (and therefore mass leaks) at the surface are corrected, allowing conservative, long time integration.
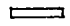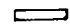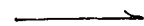
The solution is explicit. The values of u, v, w, P, ρ, T are specified initially. Using values at time 'n', the forcing term for the pressure equation is evaluated. The pressure equation is solved iteratively. The values of u and v are computed from the horizontal momentum equation. The vertical velocity is obtained by integrating the continuity equation using u and v at "$n + 1$." Temperatures are then calculated from the energy equation. The density is computed from the equation of state. A static stability check is made for the density field. If unstable stratification exists, an infinite mixing approximation is invoked, as suggested by Bryan [8] and Bennett [22].

Results and Discussions

Constant Depth Results. The model has been applied to simple geometries to obtain insight into the numerical behavior and to obtain velocity and temperature results that are relatively easy to analyze. A 100 M × 100 M square basin of constant depth 4 M is considered. A 100 KM × 100 KM basin of constant depth 20 M was used to simulate flows in the central basin of Lake Erie. A 10 × 10 mesh was used at each horizontal level; there were five nodal points in the vertical direction. Then $I = 1,10$ in the x-direction and $J = 1,10$ in the y-direction; $K = 1,5$ from surface to the bottom of the basin. A number of combinations of eddy viscosities, wind stresses and heat transfer parameters were used. A complete list of the cases investigated are presented by Sengupta and Lick [17]. Some of the important features are presented here. Numerical experiments with the constant depth, rectangular approximation of Squire Vallevue Pond (located near Cleveland Ohio) indicated some interesting features. The elimination of convective terms in the momentum equations allowed larger integration time steps and gave steady-state results which were only slightly altered near the side walls. The time to reach steady state was reduced. Increase in vertical eddy transport coefficients decreased horizontal components of surface velocities in inverse proportion, and the solutions were relatively insensitive to horizontal eddy viscosities, even with changes by a factor of 10, as would be expected from a non-dimensional ordering of the terms. The surface flows were in the direction of the wind stress, indicating the minor role of Coriolis forces in the smaller basin. The horizontal boundary layer thickness was smaller than the grid size employed. Eddy transport coefficients of 5 cm²/s and 125 cm²/s were chosen for the vertical and horizontal directions respectively. These were obtained by length scaling values used by Gedney and Lick [4]. Wind stress of .1 dyne/cm² was used. A time step of 50 s was used, and steady-state results were obtained by 9050 secs of real time. This is considerably less than the viscous time scales (L^2/A_H and H^2/A_V) indicating the importance of convection in the transient processes. A combination of viscous diffusion of vorticity and convective momentum transport is the mechanism by which the pond reaches steady state. The circulation is best described as a two-dimensional cell-like structure as shown in Fig. 1. The upwelling and downwelling regions are confined to the near and far shore regions. The velocity profiles are compared in Fig. 2 to analytical solutions obtained by Sengupta and Lick [16]. The analytical solutions were obtained by simplifying the momentum equations to a balance between vertical viscous term and the pressure gradient term. The agreement is excellent at steady state, indicating that for a constant depth basin, away form the side walls, pressure gradient and vertical viscous stress are the dominant terms.

To study the thermal characteristics of the basin, surface heating was introduced to the steady-state velocity field. A surface heat transfer coefficient of 150 BTU/day − °F-ft² and an equilibrium temperature of 20°C was used. The basin was considered initially isothermal at 15°C.

Fig. 3 and 4 show temperatures and velocities at near shore, middle, and far shore of the domain after 4 hours of heating. Cooler fluid from deeper regions is brought to the surface by near-shore upwelling. As the fluid travels towards the far-shore it is heated by surface heat
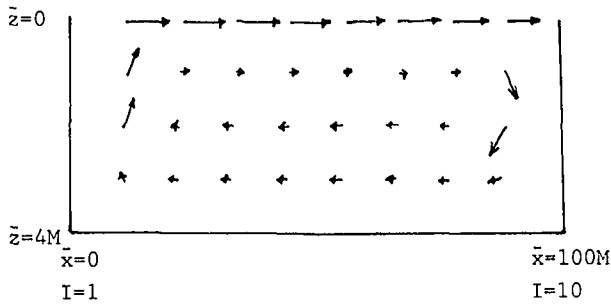
Fig. 1 Velocities at Section J = 5

transfer, and warmer fluid is convected to lower layers by far-shore downwelling. A horizontal gradient of temperature results with near shore being cooler than the far shore. The heating also results in a bouyancy field which enhances upwelling of warm fluid that is convected down at the far shore. This results in upwelling over a larger area than for the unheated case. A somewhat skewed cell results. Fig. 4 when compared with Fig. 1 shows clearly the extended upwelling region caused by bouyancy effects in the return flow.

The 100 KM × 100 KM basin was modelled using 20 cm²/s and 10^5cm²/s for vertical and horizontal eddy viscosities (as used by Gedney and Lick [4] in their studies of Lake Erie). A wind stress of 1 dyne/cm² was used. The results showed the Ekman-Spiral structure and velocities agreed well with Gedney and Lick's results, showing that low Rossby number flow situations can also be executed.

Solutions for the Pond. Before simulating the variable topography Squire Vallevue Pond, two simple cases were executed. Results for 100 M × 100 M rectangular domain with constant bottom slope (2M to 4M) showed that even with constant wind stress parallel to bottom slope, horizontal velocities increased with depth, and the upwelling region was no longer confined to the near shore. A simulation with shoreline, as shown in Fig. 5, and constant depth revealed cell-like motions similar to rectangular basins; the coastal boundary layers were smaller than grid-resolution. This suggests that the general circulation pattern will be more influenced by bottom topography
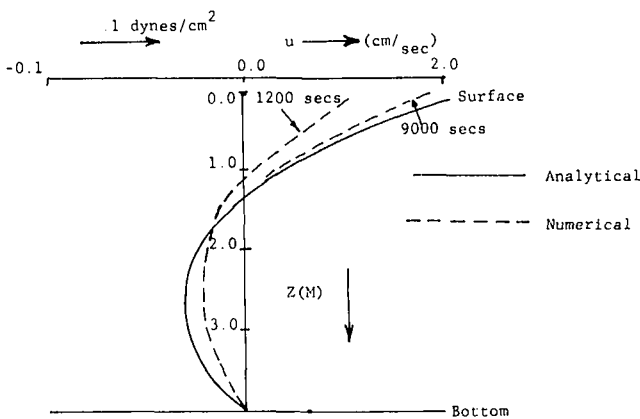
Fig. 2 Comparison of Numerical Results with Analytical Solution
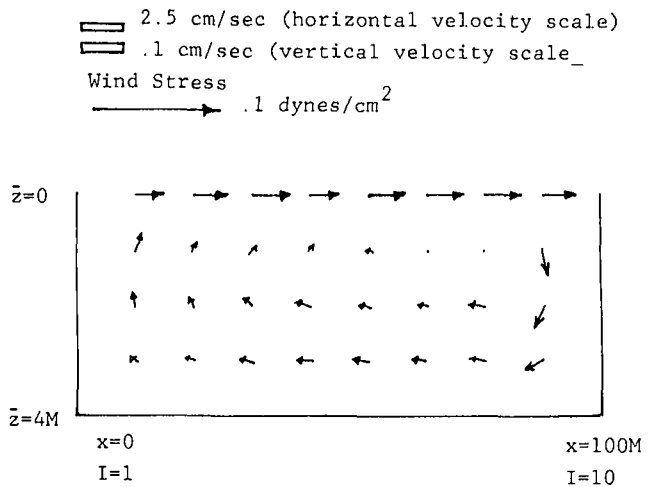
Fig. 4 Velocities at Section J = 5 after 4 hours of heating
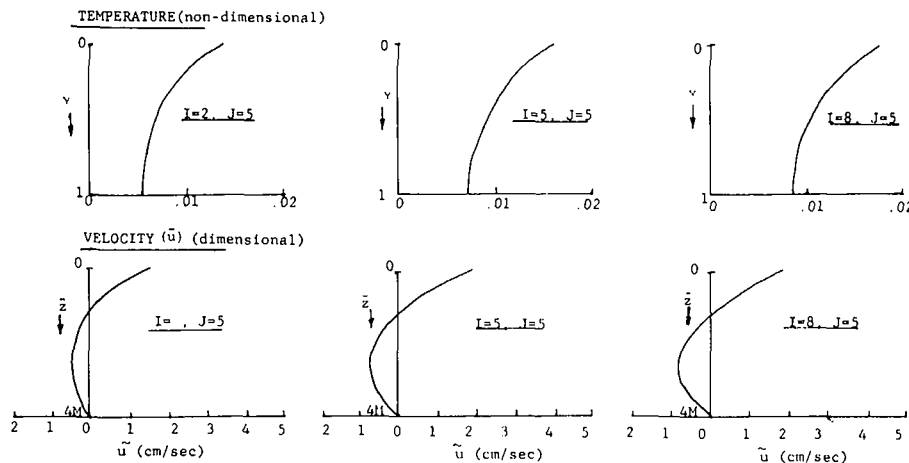
Fig. 3 Velocity and temperature profiles at Section J = 5 after 4 hours of heating; nearshore (I = 2, J = 5), middle (I = 5, J = 5), and farshore (I = 8, J = 5)

Journal of Heat Transfer
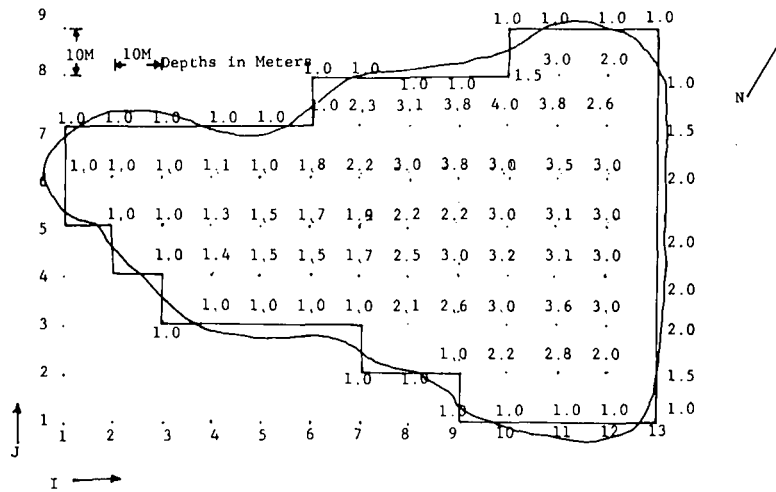
Fig. 5　Arrangement of Grid-System and Depths
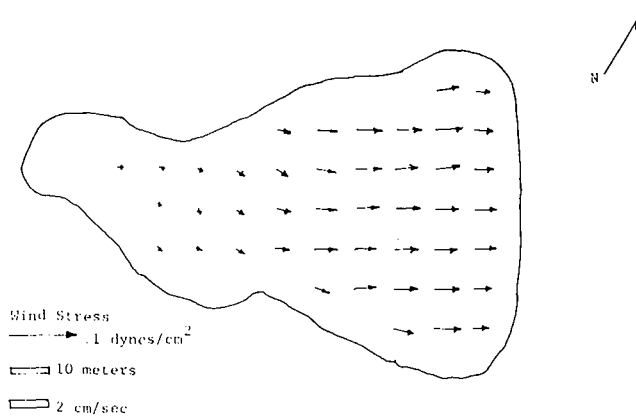
Fig. 6　Surface velocities
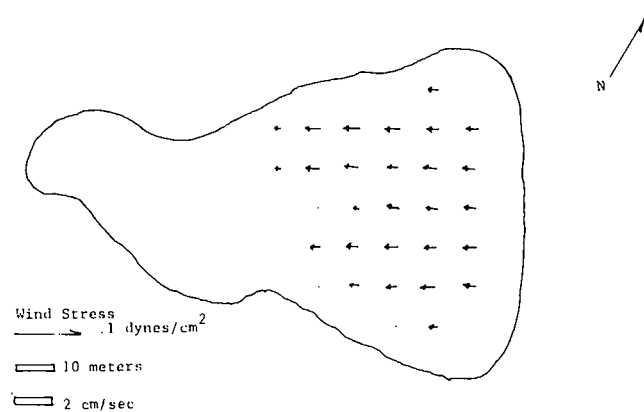
Fig. 7　Velocities at depth of 2 meters

Fig. 8　Velocities in Section $J = 4$

effects compared to shoreline effects.

The basin with realistic topography, as shown in Fig. 5, was finally executed for various meteorological and parametric situations. Results for a representative case are presented. Vertical and horizontal eddy transport coefficients were 25 cm²/s, and 125 cm²/s, respectively. These were chosen to give currents magnitudes approximately the same as those encountered in Squire Vallevue Pond.

The average wind velocities over the pond are usually around five mph from the SW or NW, the SW direction being more common. A wind stress of .1 dyne/cm² dynes was chosen. The southwest wind results are presented here.

Steady-state solutions were obtained after two hours of real time. The velocities increased rapidly at first, and then gradually approached steady state as viscous effects propagated; typical rigid-lid behavior. Fig. 6 shows the steady-state surface velocities. Velocities are smaller in shallower regions. The velocities are no longer parallel to wind direction. Transverse velocities result owing to bottom slope effects. The decrease in velocities near shore is owing to reduced depth and not horizontal boundary layer. Fig. 7 shows the return velocities at two meters depth.

The dominant cell-like structure of the flow is seen in Fig. 8. It is apparent that there are strong horizontal gradients in velocities u, v. This results in vertical velocities in order to satisfy continuity. Fig. 9 shows the vertical velocities at a depth of 1m. Vectors in the first quadrant indicate upwelling and those in the third quadrant indicate downwelling. The severest downwelling occurs at the northeast shore, owing to the almost vertical incline of the shore at this location. The upwelling regions are near the sloping portion of the pond connecting
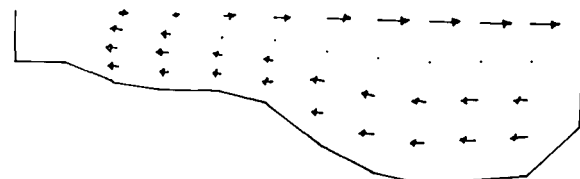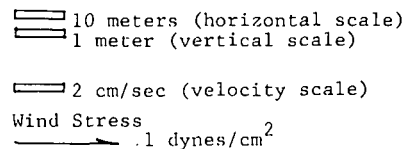
the shallow part of the pond to the deep part. This is in marked contrast to the constant depth basin, where upwelling and downwelling are confined to the regions near the near and far shores.

For a constant depth basin the solutions agreed well with the simplified analytical solution, indicating that in the interior at steady state a balance between vertical viscous terms and pressure gradient terms is a good approximation. The terms in the u-momentum equation are shown in Fig. 10. The solutions are for near steady state.

Fig. 9 Vertical velocities at a depth of 1 m

P   -   Pressure Term
I   -   Inertia Terms
H.V -   Horizontal Viscous Terms
V.V -   Vertical Viscous Terms
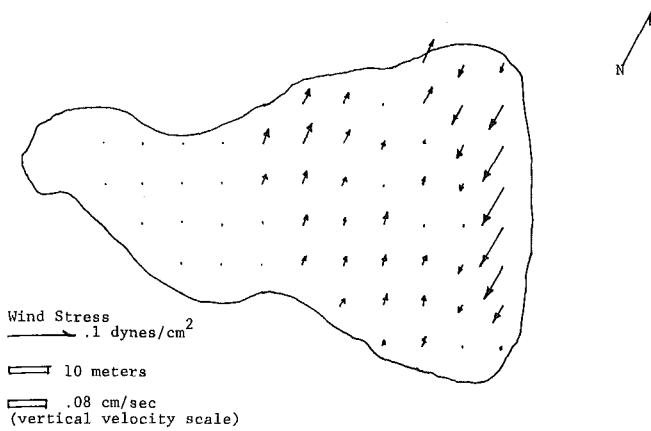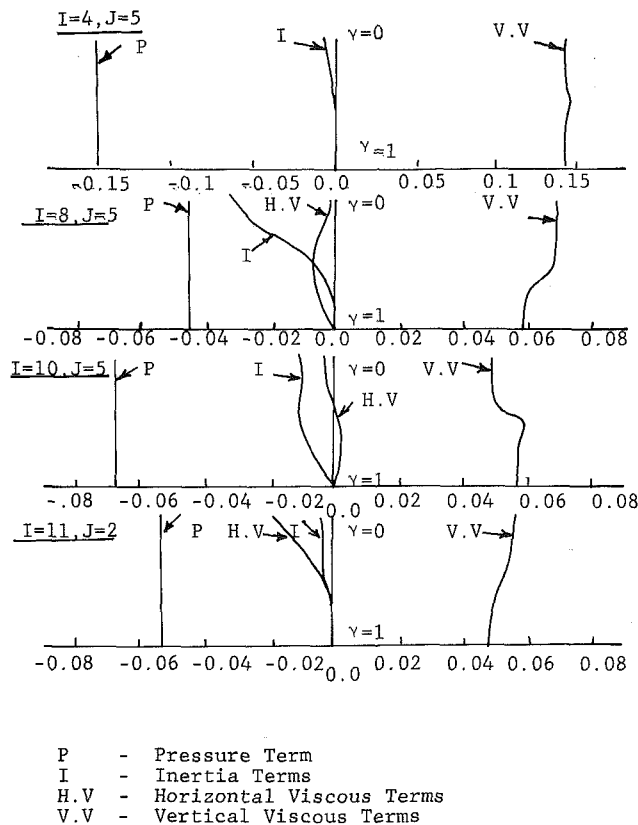
Fig. 10 Comparison of Terms in u-momentum equation (Time elapsed = 7830 secs) U_{ref} = 10 cm/s; L = 100 m; H = 4 m
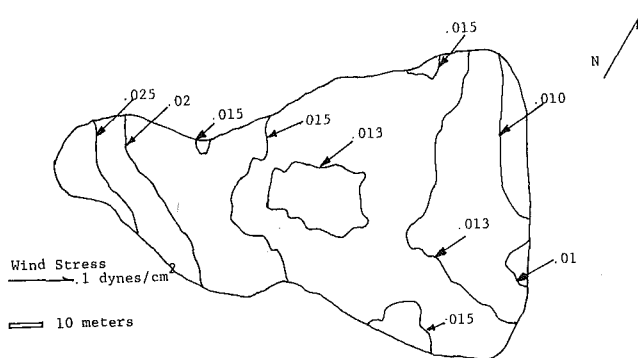
Fig. 11 Constant temperature lines at the surface after 2 hours of heating

Minor adjustments were still occurring. The variation with γ of the pressure gradient, inertia, and vertical viscous terms are plotted for these locations in the pond. Point (I = 4, J = 5) shows that a balance between the pressure gradient and vertical viscous term is quite accurate. The reason for this is that the shallow end of the pond is almost a constant depth basin with a depth of one meter. Comparisons of other locations indicate that the inertia terms are not negligible. This is because horizontal gradients of u and v are not zero at these locations, leading to appreciable values for the non-linear inertia terms. Therefore for variable depth basins, the inertia terms can be non zero even at steady state.

Temperature Fields in the Pond. To investigate the temperature distribution in the pond, solutions with 20°C equilibrium temperature and 15°C initial water temperature were obtained. Steady-state velocities for the southwest wind were taken as the initial velocity field.

Figure 11 shows the isotherms at the surface after two hours of heating. It is seen that the shallower southwest basin has a higher temperature than the deeper basin. Since the heat transfer through the surface initially is approximately the same throughout the domain, the shallower region having less fluid, and therefore thermal capacity, is heated to a higher temperature. Therefore horizontal gradients of density are far more severe than for constant depth cases. However, the convective transfer of fluid also plays a part and therefore the constant temperature lines are not identical to the constant depth lines. As the pond is heated, hotter fluid from the shallower end is convected to the deeper end.

The dominant mechanisms of heat transfer are apparent from a comparison of the various terms in the energy equation. Fig. 12 shows the vertical variation of the terms at three locations. The significant terms are the vertical diffusion term and the convective terms. The horizontal diffusion terms are negligible. It is important to note that the convective terms are quite comparable to the diffusion terms. Therefore, a simplified analysis of the heat transfer problem which ignores the convective terms will be erroneous. The heat transfer in
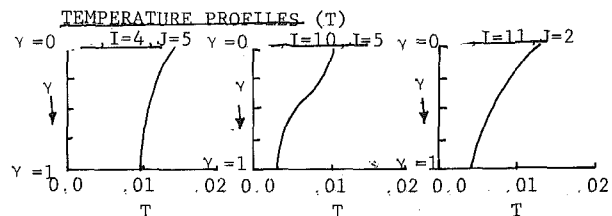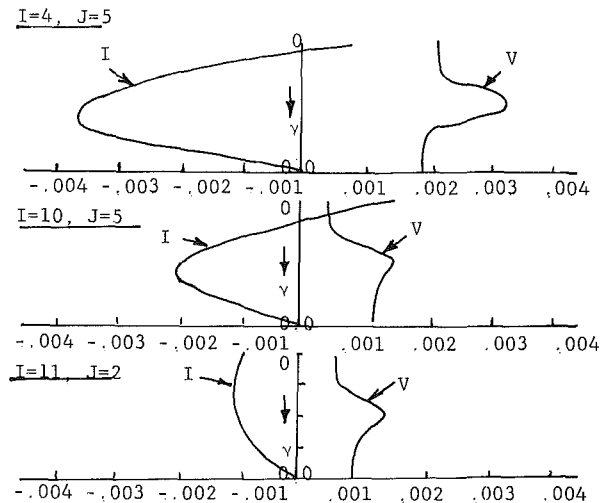
Fig. 12 Terms in the Energy Equation after 2 hours of heating U_{ref} = 10 cm/s; L = 100 m; H = 4 m; T_{ref} = 15°C

the pond is not a simple diffusion of heat through the surface into the interior. The temperature solution is strongly coupled to the general circulation in the pond.

Concluding Remarks. Numerically, the model is well behaved with few oscillations in the solution. The time steps are relatively small, owing to the rather stringent requirements of the vertical diffusive criterion, which was the most restrictive in the case of the pond. The time step sizes allowable were considerably smaller than those indicated by one-dimensional stability analyses of the Burgers equation. However, the elimination of the Courant-Lewy-Fredrichs condition by using the rigid-lid approximation leads to considerable economy compared to free-surface formulations. A major part of the computation time is expended in the iterative solution to the Poisson equation. With the introduction of direct Poisson solvers, the computation time may be reduced considerably. However, no adequate direct solution method for irregular domains is presently available.

The numerical model developed in the present investigation is comprehensive. It incorporates the effects of heat transfer, variable density and variable bottom topography on the wind-driven circulation. The program may be used with suitable modifications to flows in lakes, bays, and oceans. Since the model includes the horizontal viscous terms, horizontal boundary layers may be investigated. Small regions near the boundary may be modelled using the far field solutions as boundary conditions.

At present the model is being used as a predictive tool in power plant thermal pollution studies in South Florida [23, 24].The application is integrated with a rigorous verification effort using remote sensing and in-situ measurements.

References

1 Ekman, V. X., "Uber Horizontal Cirkulation Winderzengten Meeress-tromungen," *Arkue, Mat. Astr. Fysik,* Vol. 17, No. 26, 1923.

2 Welander, P., "Wind Action on a Shallow Sea: Some Generalizations of Ekman's Theory." *Tellus,* Vol. 9, No. 1, Feb., 1957.

3 Csanady, G. T., "Turbulent Diffusion in Lake Huron," *Journal of Fluid Mechanics* TRANS ASME, Vol. 17, 1963.

4 Gedney, R. And Lick, W.: "Wind-Driven Currents in Lake Erie." *J. Geo. Res.,* Vol. 77, 1972.

5 Gedney, R. T., et. al., "Effect of Bottom Topography, Eddy Diffusivity, and Wind Variation on Circulation in a Two-Layer Stratified Lake", NASA Technical Note TN D-7235, Mar. 1973.

6 Gedney, R. T., et. al., "Effect of Eddy Diffusivity on Wind-Driven Currents in a Two-Layer Stratified Lake", NASA Technical Note TN D-6841, June, 1972.

7 Goldstein, M. E., and Gedney, R. T., "Analytical Solution for the Wind-Driven Curculation in a Lake Containing an Island", NASA Technical Note TN D-6541, Nov. 1971.

8 Bryan, K., "A Numerical Method for the Study of the World Ocean," *J. Comp. Phys.,* Vol. 4, 1969.

9 Crowley, W. P., "A Global Numerical Ocean Model: Part I." *J. Comp. Phys.* Vol. 3, 1968.

10 Crowley, W. P., "A Numerical Model for Viscous Free Surface Barotopic Wind-Driven Ocean Circulation," *J. Comp. Phys.* Vol. 5, 1969.

11 Crowley, W. P., "A Numerical Model for Viscous Non-Divergent, Barotopic, Wind-Driven Ocean Circulations," *J. Comp. Phys.* Vol. 6, 1970.

12 Freeman, N. G., Hale, N. G., and Danard, M. B., "A Modified Sigma Equations Approach to the Numerical Modelling of Great Lakes Hydrodynamics," *J. Geo. Res.,* Vol. 77, No. 6, 1972.

13 Phillips, N. A., "Co-ordinate System Having Some Special Advantages for Numerical Forecasting," *J. Meterorol.,* Vol. 14, 1957.

14 Csanady, G. T., *A Rev. Fluid Mech.* Vol. 7, 1975, p. 357.

15 Cheng, R. T., Powell, T. M., and Dillon, T. M., "Numerical Models of Wind-Driven Circulation in Lakes," *Appl. Math. Modelling,* Vol. 1, Dec. 1976.

16 Paul, J., and Lick, W., "A Numerical Model for Three Dimensional Variable Density Jet," *Proc. 16th Conf. Great Lakes Research,* 1973.

17 Sengupta, S., and Lick W., "A Numerical Model for Wind Driven Circulation and Temperature Fields in Lakes and Ponds," FTAS-TR-74-90 Case Western Reserve University, 1974.

18 Hirt, C. W., and Harlow, F. H., "A General Corrective Proceedure for the Numerical Solution of Initial-Value Problems," *J. Comp. Phys.* Vol. 2, 1967.

19 Wilson, B. W., "Note on Surface Wind Stresses over Water at Low and High Wind Speeds," *J. of Geo. Res.,* Vol. 65, No. 10, 1960.

20 Edinger, J. E., and Geyer, J. C., "Heat Exchange in the Environment," E.E.I. Publication, No. 65-902, Edison Electric Institute, 1971.

21 Simons, T. J., "Development of Three-Dimensional Numerical Models of the Great Lakes," *Scientific Series* No. 12, Canada Centre for Inland Waters, Burlington, Ont., 1973.

22 Roache, P. J. *Computational Fluid Dynamics,* Hermosa Publishers, 1972.

23 Bennett, J. R., "Thermally Driven Lake Currents During the Spring and Fall Transition Periods," *Proc. 14th Conf. Great Lakes Res.,* IAGLR, 1971.

24 Sengupta, S., Lee, S. S., and Veziroglu, T. N., "Application of Remote Sensing to Numerical Modelling," *Proceedings of the Symposium on Remote Sensing Applied to Energy Related Problems,* Miami, 1974.

25 Sengupta, S., Lee, S. S., and Bland, R., "Three Dimensional Model Development for Thermal Pollution Studies," *Proceedings of the EPA Conference on Modelling,* Cincinatti, 1976.

APPENDIX I

The variables in the integrated equations are defined below:

$$A_{x1} = \int_0^1 \left\{ \frac{\partial}{\partial \alpha} (huu) + \frac{\partial}{\partial \beta} (hvu) + h \frac{\partial}{\partial \gamma} (\Omega u) \right\} d\gamma$$

$$A_{x2} = \frac{h}{RB} \int_0^1 v d\gamma$$

$$C_x = \frac{1}{Re} \int_0^1 \left\{ \frac{\partial}{\partial \alpha} \left(h \frac{\partial u}{\partial \alpha} \right) + \frac{\partial}{\partial \beta} \left(h \frac{\partial u}{\partial \beta} \right) + \frac{1}{\epsilon^2} \frac{1}{h} \frac{\partial}{\partial \gamma} \left(A_V^* \frac{\partial u}{\partial \gamma} \right) \right\} d\gamma$$

$$x_p = Eu \int_0^1 h \left\{ \frac{\partial h}{\partial \alpha} \int_0^\gamma \rho d\gamma + h \frac{\partial}{\partial \alpha} \int_0^\gamma \rho d\gamma - \gamma \frac{\partial h}{\partial \alpha} \rho \right\} d\gamma$$

$$A_{y1} = \int_0^1 \left\{ \frac{\partial}{\partial \alpha} (huv) + \frac{\partial}{\partial \beta} (hvv) + h \frac{\partial (\Omega v)}{\partial \gamma} \right\} d\gamma$$

$$A_{y2} = \frac{h}{RB} \int_0^1 u d\gamma$$

$$C_y = \frac{1}{Re} \int_0^1 \left\{ \frac{\partial}{\partial \alpha} \left(h \frac{\partial v}{\partial \alpha} \right) + \frac{\partial}{\partial \beta} \left(h \frac{\partial v}{\partial \beta} \right) + \frac{1}{\epsilon^2} \frac{1}{h} \frac{\partial}{\partial \gamma} \left(A_V^* \frac{\partial v}{\partial \gamma} \right) \right\} d\gamma$$

$$Y_p = Eu \int_0^1 h \left\{ \frac{\partial h}{\partial \beta} \int_0^\gamma \rho d\gamma + h \frac{\partial}{\partial \beta} \int_0^\gamma \rho d\gamma - \gamma \frac{\partial h}{\partial \beta} \rho \right\} d\gamma$$

$$B_x = Eu \frac{\partial h}{\partial \alpha} \int_0^\gamma \rho d\gamma + Eu h \frac{\partial}{\partial \alpha} \int_0^\gamma \rho d\gamma - Eu \gamma \frac{\partial h}{\partial \alpha} \rho$$

$$B_y = Eu \frac{\partial h}{\partial \beta} \int_0^\gamma \rho d\gamma + Eu h \frac{\partial}{\partial \beta} \int_0^\gamma \rho d\gamma - Eu \gamma \frac{\partial h}{\partial \beta} \rho$$

D. E. Metzger

Professor and Chairman.
Mem. ASME

L. D. Grochowsky

Graduate Student.
Assoc. Mem. ASME

Mechanical Engineering Department,
Arizona State University, Tempe, Ariz.

Heat Transfer Between an Impinging Jet and a Rotating Disk

An experimental study of the flow interaction and heat transfer between a single impinging jet and a rotating disk is presented. Tests were conducted over a range of jet flowrates, impingement radii, and disk rotational speeds with various combinations of three jet and three disk sizes. Flow visualization using smoke addition to the jet flow reveals the presence of a flow regime transition which is correlated in terms of the rotationally induced disk pumping flow acting as a cross-flow influence on the jet. Higher rotational speeds, larger impingement radii, and smaller jet flowrates favor a rotationally dominated flow interaction whereas the opposite trends favor an impingement dominated interaction. Heat transfer rates are essentially independent of jet flowrate in the rotationally dominated regime, but increase strongly with increasing flowrate in the impingement dominated regime.

Introduction

The use of impinging gas jets for component cooling in modern engineering devices is a well-established practice, and heat transfer data have been accumulated for a wide variety of application geometries [1–3].[1] The principal virtues of this method of cooling are the large heat transfer rates attainable relative to nonimpinging flows and the relative ease with which both the heat transfer rate and distribution can be controlled. The foregoing comments apply to jet impingement onto stationary surfaces; impingement onto a rotating surface raises questions which are not answered by the existing literature. Applications involving impingement cooling of rotating surfaces are currently found in bearing and gear cooling and in the cooling of gas turbine disks.

In the case of gas turbine disk cooling, the coolant is usually air supplied from the compressor section of the engine, and its use generally penalizes the engine cycle performance. Thus the objective of disk cooling scheme design is to provide the minimum necessary coolant consistent with desired engine life and reliability. The air supplied to turbine disk cooling jets is usually viewed as having two functions. First, it is expected that the high heat transfer rates normally associated with impingement onto stationary surfaces will be present even when the surface is rotating, and that they will probably be enhanced by the rotation and correspondingly increased relative velocity between jet and surface. Second, it is anticipated that if multiple jets are used and properly placed, they can prevent the undesired radial inflow of hot combustion gases into the cavity between the disk and adjacent stationary shroud.

Although estimates of the heat transfer performance can be made for these applications by using stationary impingement correlations in terms of relative jet-to-surface velocities and impingement angles, they do not account for possible effects of the pumped boundary layer on the rotating surface. The pumped flow induced by rotation at inward radial positions from the impingement location constitutes a cross-flow which can affect the trajectory and heat transfer performance of the jet. Cross-flow effects on jet trajectories [4 and 5] and their influence on impingement heat transfer [6 and 7] have received considerable past attention, but it should be noted that the nature of the cross-flow induced by rotation is quite different from the cases studied. With rotation, the crossflow is confined to a thin layer with the maximum cross-flow velocity located at the surface. The more common cross-flow situation over a stationary surface has a cross-flow velocity with a maximum value away from the surface and a zero value at the surface.

The present study was initiated to explore these effects of surface rotation and rotationally induced cross-flow on the heat transfer characteristics of a single normal jet impinging on the face of a plane disk in the absence of hubs or seals to modify the pumped flow. The geometrical arrangement is indicated in Fig. 1. The study is intended to provide a foundation for later examination of more complex geometries with both single and multiple jets. The experiments were conducted with three jet sizes and three disk diameters operated with a variety of different jet flowrates, radial impingement locations, and rotational speeds. Both smoke flow visualization and heat transfer experiments were conducted.

Apparatus and Procedures

Fig. 2 shows schematically the arrangement of experimental

---

[1] Numbers in brackets designate References at end of paper.

Contributed by the Heat Transfer Division and presented at the Winter Annual Meeting, New York, N. Y., December 5–10, 1976. Revised manuscript received by the Heat Transfer Division March 4, 1977. Paper No. 76-WA/HT-2.

equipment used in the present tests. The dashed line denotes the test cell which is a cubical steel enclosure approximately 90 cm on a side. The floor and one side of the test cell are stationary; the remaining three sides and top of the cell are welded together and roll in tracks to permit access to the inside. When fully closed the cell completely encloses the rotating portion of the apparatus with 2.5-cm thick steel and was designed to contain a bursting failure of a 15-cm dia, 2.5-cm thick aluminum disk rotating at 50,000 rpm. The heat transfer tests of the present study were conducted with the cell closed. The flow visualization was conducted with the steel test cell open and a Plexiglas enclosure was fabricated to cover the open area. A small exhaust fan and associated ducting was used to remove the smoke-laden air from the test cell. Early flow visualization was performed with the test cell both open and closed, and both with and without the exhaust fan; no differences in the observed flow patterns were noted.

The test disks are rotated with a motor-bearing combination designed for use as a tool-post grinder in machining operations. This unit is commercially available, and has an induction motor driving a two-bearing quill through a flat belt drive. Continuous control of the disk speed is provided by an auto-transformer in the motor power supply. The disk speed is monitored continuously with a photoelectric pick up sighting on the disk shaft and indicating remotely on a digital frequency counter.

Air is provided to the experiment from the laboratory compressed air supply through filters and dryers to a combination orifice and rotameter metering station. Before entering the test cell the flow passes through a smoke generating section constructed as described in reference [8]. It consists of a 60-cm long section of 5-cm dia pipe with a coiled wire nichrome heater installed inside the cap at the upstream end. Wood shavings packed into the pipe are ignited by applying a voltage to the heater for several minutes. The burning front moves downstream in the pipe producing smoke for approximately 1 hr. Downstream, the smoke-laden flow is filtered through steel wool and cooled in a water bath. A plenum chamber installed downstream of the water bath removes most of the undesirable moisture and tars. The dry, filtered smoke is then routed inside the test cell to the jet nozzles.

Three jet sizes are used in the present tests with inside exit diameters of 0.159, 0.238, and 0.635 cm. The nozzles are interchangeably mounted on a rotary micrometer table which allows accurate positioning in both the radial and axial directions. In all of the present tests the jet nozzles are aligned parallel to the axis of rotation of the disks. Jet nozzle-to-disk spacing is 0.64 cm for the two smaller jets and 1.27 cm for the largest jet. Preliminary testing showed no significant spacing effect in the range $1.0 \leq z/d \leq 5.0$.

Three different bearing-disk assemblies were fabricated and used in the present tests. Flow visualization studies were conducted on a 22.9 cm-dia steel disk which is painted black to provide a contrasting background for the smoke. Average disk face heat transfer rates were determined using two oxygen-free, high-conductivity solid copper disks, 7.6-cm dia and 12.7-cm dia. Each of the copper disks is tapered from an axial thickness of 1.27 cm at the center of 0.25 cm at the rim to reduce the influence of the rim heat transfer. A transient heat transfer test procedure was used which is identical to that previously described in reference [9]; a brief summary of the procedure will be repeated here.

The heat transfer tests are initiated by heating the copper disk while stationary with a small clamp-on electric resistance heater. The
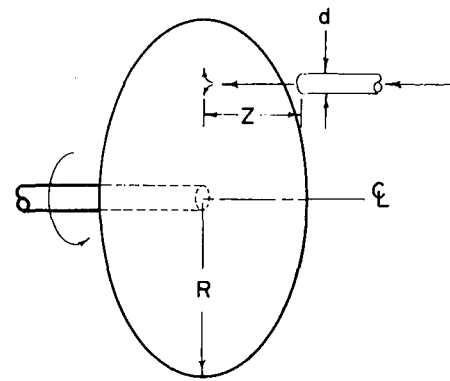
Fig. 1 Test geometry and nomenclature
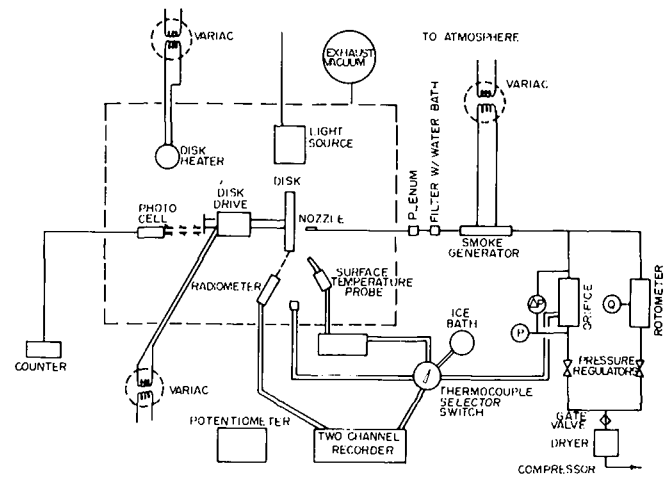
Fig. 2 Schematic of experimental apparatus

disk temperature rise is monitored simultaneously with an infrared detector sighting on the blackened disk rim and a surface temperature probe (Leeds and Northrup Surtemp) applied to the disk face. Both instrument outputs are recorded on a two-channel recorder, and the heating cycle provides an in-place calibration of the infrared unit for each test run. When the disk temperature reaches approximately 90°C, the heater and surface temperature probe are removed, the test cell is closed; and the disk is brought up to the test speed and allowed to cool in the presence of the induced and impinged flows. Typically, disk speed can be stabilized within the first 5° of cooling. The overall disk cooling rate is determined by representing the high conductivity disk as a single lumped capacitance system and evaluating the rate of change of disk internal thermal energy from the cooling transient recorded from the infrared detector. It should be noted that the disk cooling rate is very slow compared to the residence time of the fluid on the disk; and thus it should be valid to interpret the results in terms of steady-state performance.

Nomenclature

A = disk face area
d = jet diameter
D = disk diameter
h = disk face average heat transfer coefficient, $= \dot{q}/(A)(t_d - t_j)$
k = fluid thermal conductivity
N = disk rotational speed

$\dot{q}$ = disk face heat transfer rate
Q_j = jet volumetric flowrate
$Q_{p,\ell}$ = laminar disk pumping flow
$Q_{p,t}$ = turbulent disk pumping flow
r = impingement radial position
R = disk radius
t_d = disk temperature
t_j = jet and ambient temperature

z = jet nozzle-to-disk spacing
ν = fluid kinematic viscosity
Nu = disk face average Nusselt number, = hR/k
Re_j = jet Reynolds number, $= 4Q_j/(\pi d\nu)$
Re_r = rotational Reynolds number, $= 2\pi Nr^2/\nu$

The adequacy of the single lump data reduction method was verified through use of a numerical finite-difference model of the experiment. In this model a 30 node numerical representation of the test disk was subjected to various convective heat transfer distributions on the disk face and the imposed heat transfer rates were compared with those that would be inferred from measurement of the rim temperature transient. The largest differences between imposed and inferred average heat transfer rates was 4 percent for distributions simulating those encountered in the present experiments.

The overall disk heat transfer rates measured are corrected for the effects of back-side convection and conduction losses through the disk shaft, and a Nusselt number based on the average jet-side heat transfer coefficient is determined. The uncertainty in the experimentally determined Nusselt numbers is estimated to be ±12 percent, using the methods of reference [10]. Further details of the experimental apparatus and test procedures are available in reference [11].

Results

Flow Visualization. The flow patterns revealed with the presence of smoke in the impinging jets are of two general types depending on the geometrical, rotational, and flow parameters. One of the flow pattern types appears rotationally dominated while the other type appears impingement dominated. Higher rotational speeds, larger impingement radii, and smaller jet flowrates favor the former type.

Fig. 3 shows a sketch of the typical impingement dominated flow pattern observed in the flow visualization tests. In this regime the jet appears to flow radially outward (relative to the jet nozzle) for a short distance before being lifted from the surface, probably by a combination of the disk rotation and the cross-flowing induced boundary layer. As the impingement flow is lifted a portion of it is able to continue traveling radially inward toward the disk center.

Fig. 4 depicts a typical rotationally dominated flow pattern observed in the flow visualization tests. In this regime, there is typically very little penetration of the jet flow in either the clockwise (against rotation) or radially inward directions. For a given jet size, transition between the two flow types can be observed by changing any one of the three variables (flowrate, impingement position, disk speed) independently while holding the remaining two at constant values. In most cases the transition between these two flow types was observed to be quite abrupt, and could be heard as well as seen. In a small minority of cases, however, transition was not nearly as abrupt, and an intermediate flow pattern appeared which exhibited lifting of the impinged jet but no radially inward penetration.
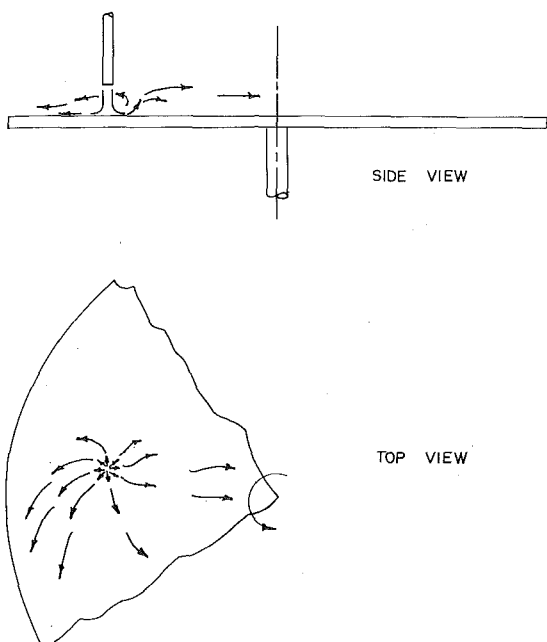
After the initial discovery of the transition phenomena described, the flow visualization experiments concentrated on documentation of the conditions existing at transition. An extensive series of tests were conducted with all three jet sizes and a variety of combinations of jet flowrate, disk speed, and radial impingement position. The ranges of variables encompassed by these tests are given in Table 1. The tests were conducted by maintaining jet flowrate and rotational speed constant while slowly increasing the radial impingement location until transition was observed. In some cases a small, repeatable hysteresis effect was observed; that is, when the impingement position was moved radially inward transition occurred at a different radius than it did when the impingement position was moved radially outward. This effect was not significant in terms of the overall correlation of the results.

A reasonably concise correlation of all the observed transition conditions was attained by utilizing the calculated values of rotationally induced pumping flow passing the impingement radius as given in reference [12]. For the rotationally induced laminar boundary layers expected for most of the test range:

$$Q_{p,\ell} = 0.886\pi r \nu \text{Re}_r^{0.5} \tag{1}$$

Fig. 5 shows the correlation attained in terms of the ratio of Q_j to $Q_{p,\ell}$ versus Re_r. Each of the data points represents conditions at an observed transition point; the resulting band of points separates the

Fig. 4 Typical rotationally dominated flow pattern
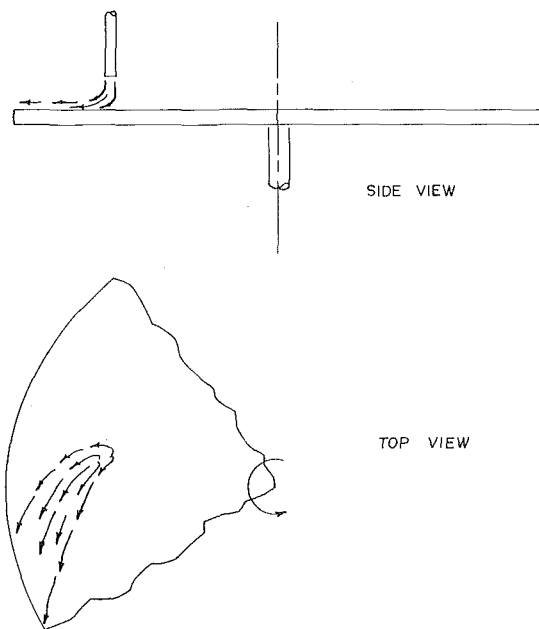
Fig. 3 Typical impingement dominated flow pattern

Table 1 Variable ranges for flow visualization tests

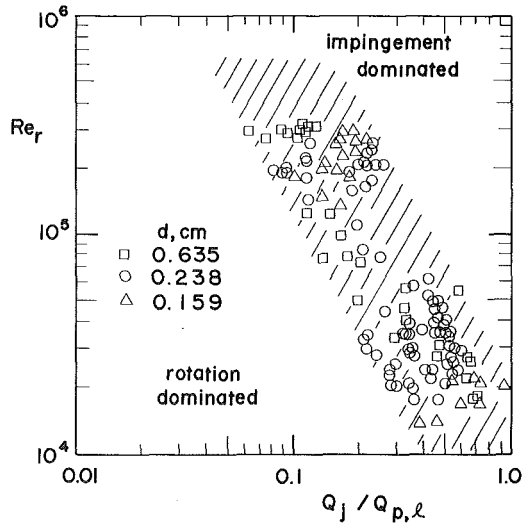| cm	d = 0.159	d = 0.238	d = 0.635
cm³/s	$141 \leq Q_j \leq 506$	$122 \leq Q_j \leq 461$	$107 \leq Q_j \leq 351$
rpm	$360 \leq N \leq 5040$	$480 \leq N \leq 4980$	$1860 \leq N \leq 4920$
cm	$3.18 \leq r \leq 10.48$	$3.81 \leq r \leq 10.61$	$2.22 \leq r \leq 10.48$
—	$10^4 \leq \text{Re}_r \leq 3 \times 10^5$	$1.8 \times 10^4 \leq \text{Re}_r \leq 2.7 \times 10^5$	$8 \times 10^3 \leq \text{Re}_r \leq 3 \times 10^5$
—	$7 \times 10^3 \leq \text{Re}_j \leq 25 \times 10^3$	$5 \times 10^3 \leq \text{Re}_j \leq 16 \times 10^3$	$10^3 \leq \text{Re}_j \leq 4 \times 10^3$

Fig. 5 Correlation of observed transition with $Q_{p,\ell}$

Fig. 6 Correlation of observed transition with $Q_{p,t}$

Fig. 7 Heat transfer, $Re_r = 5 \times 10^3$, $r/R = 0.67$

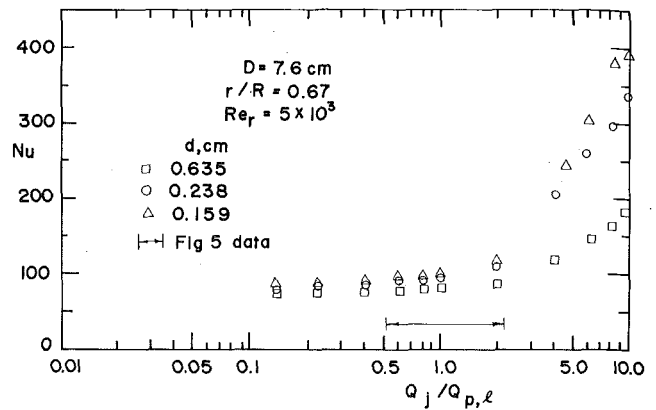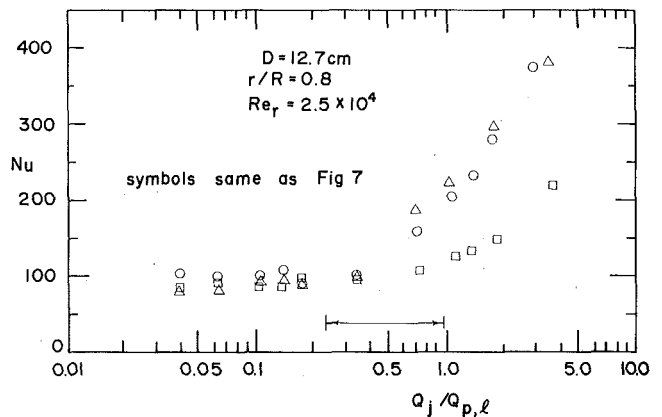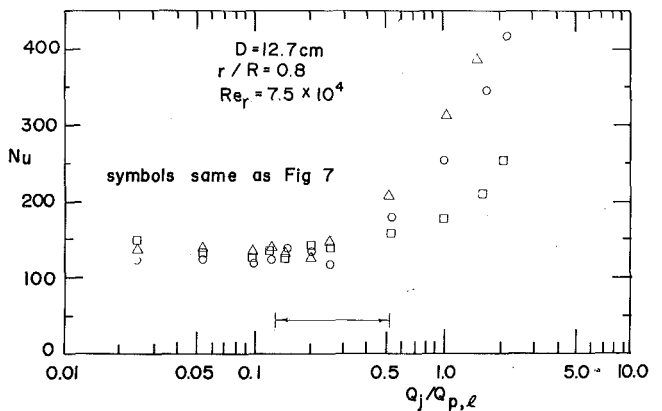Fig. 8 Heat transfer, $Re_r = 2 \times 10^4$, $r/R = 0.80$

Fig. 9 Heat transfer, $Re_r = 7.5 \times 10^4$, $r/R = 0.80$

rotational and impingement dominated zones.

No direct determination of the laminar or turbulent character of the pumped boundary layer was made in the present study; nevertheless, laminar-to-turbulent transition of this flow almost certainly takes place somewhere within the present test range which extends from $Re_r = 8 \times 10^3$ to $Re_r = 3 \times 10^5$. Transition may not occur at the same value of Re_r for all tests since rotating disk flows are known to be sensitive to outside influences which, in this case, include the impinging jet. The fact that the flow regime transition results do not display any behavior attributable to a pumped flow boundary layer transition suggests that the turbulent or laminar character of this layer is of minor importance in determining the type of interaction with the impingement flow. This conclusion is supported by the fact that the Fig. 5 data correlates equally well with the calculated pumping flows for a turbulent boundary layer [12]:

$$Q_{p,t} = 0.0697\pi r \nu Re_r^{0.8} \qquad (2)$$

This correlation is shown in Fig. 6.

Heat Transfer. Following correlation of the flow visualization results, an extensive series of heat transfer tests were conducted with all parameters held constant except jet flowrate which was increased in small increments in order to traverse from the rotationally domi-

nated zone to the impingement dominated zone. 21 such series were conducted, encompassing various combinations of jet and disk sizes, rotational speeds, and radial impingement locations. Typical results are shown in Figs. 7–9.

In all cases there is a clear correspondence between the transition location predicted from the flow visualization results and the measured heat transfer rates. At low jet flowrates relative to the amount necessary to cause transition there is, on the average, no experimentally significant effect of the jet size on the average disk surface heat transfer. This result is surprising since there is a 16 to 1 variation in

Fig. 10 Nonimpingement and rotationally dominated heat transfer

Graph legend:
- ○ no Impingement, D = 7.6 cm
- ▽ "   "   , " 12.7 "
-    "   "   , " Ref. 13
- ▨ rot. dominated, Figs 7-13

Axes: Nu (vertical), Re_r (horizontal)

applications are associated with operation in the impingement dominated regime. Also, it is apparent that heat transfer is dependent on jet velocity in the impingement dominated regime, with higher velocity jets yielding larger heat transfer rates. Thus, for a given available jet flow, it appears that better cooling can be obtained through use of a fewer number of high velocity jets if the available pressure differential across the jet orifices is great enough.

References

1   Gardon, R., and Cobonpue, J., "Heat Transfer Between a Flat Plate and Jets of Air Impinging on It," *International Developments in Heat Transfer, Proceedings, 2nd International Heat Transfer Conference,* ASME, New York, 1962, pp. 454–460.

2   Chupp, R. E., et al., "Evaluation of Internal Heat-Transfer Coefficients for Impingement Cooled Airfoils," *Journal of Aircraft,* Vol. 6, 1969, pp. 203–208.

3   Metzger, D. E., et al., "Impingement Cooling Performance in Gas Turbine Airfoils Including Effects of Leading Edge Sharpness," *Journal of Engineering for Power,* TRANS. ASME, Series A, Vol. 94, No. 3, July 1972, pp. 219–225.

4   Keffer, J. F., and Baines, W. D., "The Round Turbulent Jet in a Cross Wind," *Journal of Fluid Mechanics,* Vol. 15, 1963, pp. 481–496.

5   Bowley, W. N., and Sucec, J., "Trajectory and Spreading of a Turbulent Jet in the Presence of a Crossflow of Arbitrary Velocity Distribution," ASME Paper No. 69-GT-33.

6   Kercher, D. M., and Tabakoff, W., "Heat Transfer by a Square Array of Round Jets Impinging Perpendicular to a Flat Surface Including the Effect of Spent Air," *Journal of Engineering for Power,* TRANS. ASME, Series A, Vol. 92, No. 1, Jan. 1970, pp. 73–82.

7   Metzger, D. E., and Korstad, R. J., "Effects of Cross Flow on Impingement Heat Transfer," *Journal of Engineering for Power,* TRANS. ASME, Series A, Vol. 94, No. 1, Jan. 1972, pp. 35–42.

8   Yu, J. P., et al., "A Smoke Generator for Use in Fluid Flow Visualization," *International Journal of Heat and Mass Transfer,* Vol. 15, 1972, pp. 557–558.

9   Metzger, D. E., "Heat Transfer and Pumping on a Rotating Disk With Freely Induced and Forced Cooling," *Journal of Engineering for Power,* TRANS. ASME, Series A, Vol. 92, No. 3, 1970, pp. 342–348.

10   Kline, S. J., and McClintock, F. A., "Describing Uncertainties in Single Sample Experiments," *Mechanical Engineering,* Vol. 75, Jan. 1973, pp. 3–8.

11   Grochowsky, L. D., "An Investigation of Flow Interactions and Heat Transfer Characteristics For Single Jet Impingement on Rotating Disks," MS thesis, Arizona State University, Tempe, Ariz., 1975.

12   Schlichting, H., *Boundary Layer Theory,* Sixth ed., McGraw Hill, New York, 1968.

13   Cobb, E. C., and Saunders, O. A., "Heat Transfer From a Rotating Disk," *Proceedings of the Royal Society,* A, 1956, p. 343.

average jet velocity from the largest to smallest jet at a given value of Q_j. Moreover, the disk heat transfer is remarkably independent of the amount of impinging flow in the rotationally dominated flow regime.

The latter behavior indicates that the average disk heat transfer at small values of Re_r can be significantly increased over the no-impingement levels by impingement with small jet flowrates. This is illustrated in Fig. 10 which shows a comparison of the no-impingement results of the present study with those of reference [13] and also with the present rotationally dominated zone heat transfer. The cross-hatched band encompasses all of the rotationally dominated results for the 21 test series.

In all cases the measured heat transfer rates begin to increase somewhere within the transition location predicted from the flow visualization results. The increase is most pronounced for the smaller jets, and indicates that large increases in cooling rates in jet cooling

L. W. Hunter
S. Favin

The Johns Hopkins University,
Applied Physics Laboratory,
Laurel, Md.

Steady State Temperature Distribution in a Solid Cylinder Moving in the Direction of its Axis Through a Cross-Flow of Hot Gas[1]

*A range of boundary value problems is solved that describe the steady state tempera-
ture distribution in a solid circular cylinder of infinite length, moving in the direction of
its axis. The cylinder is heated by a hot gas flowing perpendicularly to the cylinder. The
problems differ in complexity depending on whether or not the cylinder is radially iso-
thermal and the gas temperature uniform. Dimensionless charts are presented. This work
pertains to the "moving wire techniques" for studying polymer flammability and measur-
ing heat transfer from gases.*

Introduction

The temperature distribution in a cylinder moving in the direction
of its axis is an old problem in heat transfer. In 1910 and soon there-
after, Nettleton [1][2] and Owen [2] solved problems of this type which
applied to a column of mercury flowing in a tube between two reser-
voirs at fixed temperatures; their theory enabled measurements of
the thermal diffusivity of mercury. In more recent experiments on
this system, Rosner [3] heated the tube in a flame and was able to
measure certain heat transfer characteristics of the flame. A few other
moving cylinder systems are treated in reference [4].

This paper takes a second look at the moving cylinder problem with
a view to filling in some of the gaps in the theory. Our motivation is
provided by recent experiments [5–8] using "moving wire techniques"
to measure polymer flammability and, also, heat transfer charac-
teristics of flames. In the moving wire techniques (Fig. 1) a wire is
drawn at a controlled speed in the direction of its length through a
cross-flow of hot gas. The wire is a thermocouple, stretched taut, when
the heat transfer characteristics of the gas are of interest; the tem-
perature of the junction rises at a rate proportional to the heat transfer
coefficient. To study polymer flammability, the wire consists of a
metal or fiberglass strand supporting a coating of the polymer, and
the hot gas contains oxygen for the polymer combustion. A steady

state is rapidly reached, in which residence time in the hot gas (cal-
culated as distance divided by speed) corresponds to real time. By
controlling the residence time, the experimenter can resolve the in-
stantaneous stages of polymer combustion and carry out detailed
chemical analyses of both the solid and gas phases. The surface
temperature at which combustion begins provides a useful measure
of the ignitability of the polymer.

The boundary value problems solved here range from simple
problems toward successively more flexible ones. The problems differ
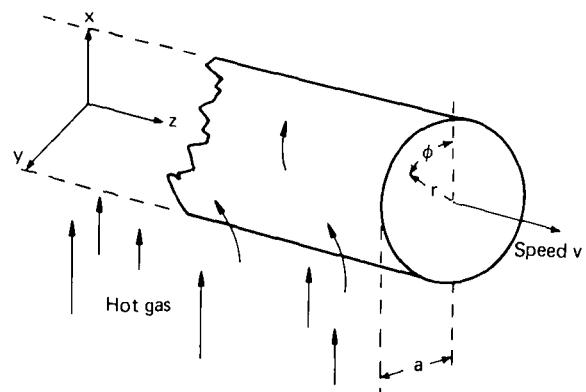
Fig. 1   Coordinate axes of the moving cylinder. The origin is on the cylinder
axis; the x-axis is vertical. The heat source is a hot gas approaching in the
x-direction from below. The conventional cylindrical coordinates r and ϕ of
a point are shown

---

[2] Numbers in brackets designate References at end of paper.

in complexity depending on whether the cylinder is radially isothermal, and whether the gas temperature is uniform. Interconnections between the various solutions are established and physical interpretations brought out. Particular attention is given to defining the exact nature of the time resolution mentioned, in which residence time corresponds to real time. In all the boundary value problems, the heat transfer coefficient is assumed to be independent of azimuthal angle ϕ at each longitudinal position. This simplification is necessary to make exact solutions possible. In applications, the Reynolds number is often small enough for this approximation to be useful [9].

Although the cylinder here has only one material phase, both radially and throughout its length, the present results can be applied to the moving wire experiments. Essentially, applications are possible to the moving thermocouple experiments when the two lead wires have equal or nearly equal heat capacities; applications to polymer coated wires are possible when the shell is thin, for then the only difference with a one-phase cylinder problem is the interpretation of the heat transfer coefficient.

Residence Time

The moving cylinder is a flowing solid. The simplest boundary value problem describing its temperature is one in which the cylinder is isothermal in every cross section:

$$\kappa \frac{\partial^2 T}{\partial z^2} - v \frac{\partial T}{\partial z} + \frac{2\kappa h}{a} (T_{gas} - T) = 0 \qquad (1)$$
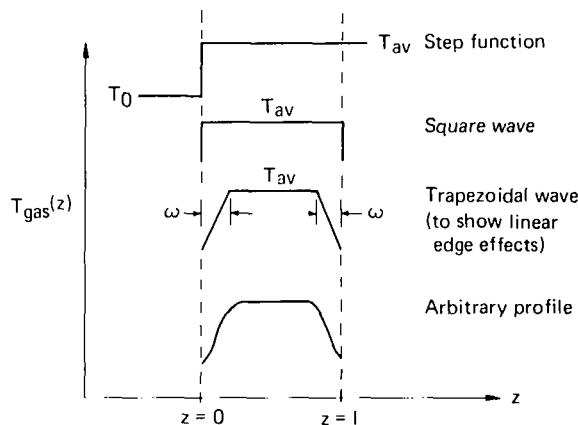
Fig. 2 Longitudinal gas temperature profiles between the cut-off points at $z = 0$ and $z = l$. Heat transfer is defined at $z < 0$ and $z > l$ either by the requirement that $T_{gas} = T_0$ in these regions (in which case h is constant everywhere) or by the requirement that $h = 0$ here

and the gas temperature is an angle-independent step function in z (Fig. 2). The terms in the differential equation [4] describe heat conduction, convection due to the effective flow of the solid at speed v, and forced convection transfer due to the gas; κ is the thermal diffusivity and a is the radius of the solid, while $h = H/k$ is the ratio, in units of reciprocal length, of the heat transfer coefficient H (heat flux for unit temperature difference) to the thermal conductivity k of the solid. The solution is chosen so that

$$T \to T_0 \quad \text{as} \quad z \to -\infty \qquad (2)$$

and

$$T \to T_{av} \quad \text{as} \quad z \to \infty \qquad (3)$$

In addition, both T and $\partial T/\partial z$ must be continuous at $z = 0$.

The solution may be written in terms of a dimensionless speed (v^*) and position (z^*) as follows:

$$\frac{T - T_0}{T_{av} - T_0} = \frac{1}{2} (1 - R^{-1}) \exp \left[(R + 1)v^*z^*\right] \text{ if } z < 0 \qquad (4)$$

$$\frac{T_{av} - T}{T_{av} - T_0} = \frac{1}{2} (1 + R^{-1}) \exp \left[-(R - 1)v^*z^*\right] \text{ if } z > 0 \qquad (5)$$

where

$$R = \left[1 + \frac{2}{(v^*)^2} \right]^{1/2}, \quad v^* = \frac{a^{1/2}v}{2\kappa h^{1/2}}, \quad z^* = \frac{h^{1/2}z}{a^{1/2}} \qquad (6)$$

When $v^* > 5$ (approximately), the solution is simply determined by a dimensionless residence time in the heat source region:

$$T = T_0 \text{ if } z < 0 \qquad (7)$$

and

$$\frac{T_{av} - T}{T_{av} - T_0} = e^{-t^*} \text{ if } z > 0, \qquad (8)$$

where

$$t^* = z^*/v^* \equiv 2\kappa ht/a \qquad (9)$$

and

$$t = z/v \qquad (10)$$

The last form satisfies a "quasitransient" boundary value problem:

$$\frac{\partial T}{\partial t} = \frac{2\kappa h}{a} (T_{av} - T) \text{ if } t > 0 \qquad (11)$$

subject to

$$T = T_0 \text{ at } t = 0 \qquad (12)$$

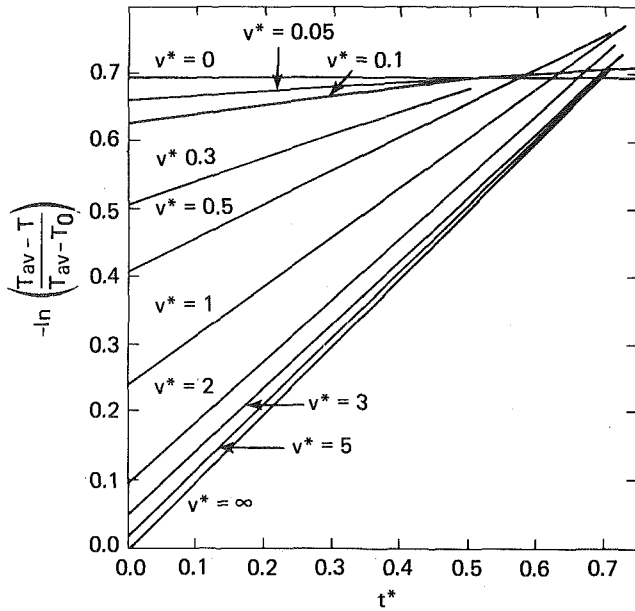and hence has a simple physical interpretation; namely, equation (8)

Fig. 3 Radially isothermal cylinder temperature, as a function of Residence time at fixed speed. The gas temperature is an angle-independent step function in z. Note that T can exceed T_0 at zero residence time
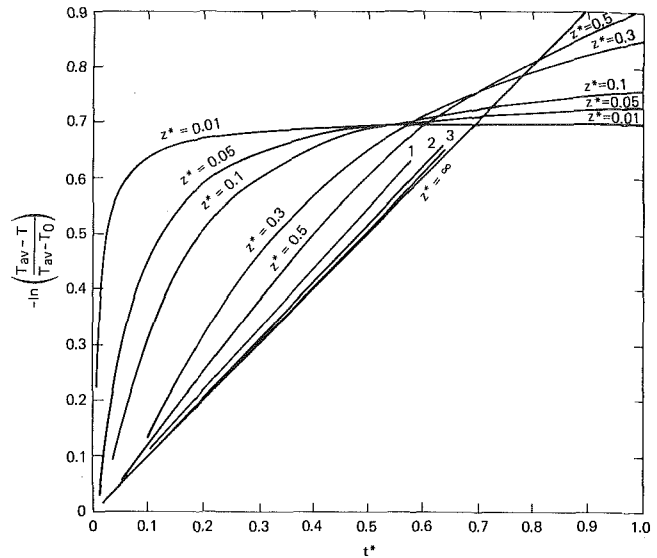

Fig. 4 Radially isothermal cylinder temperature at fixed position. The gas temperature is an angle-independent step function in z. Note that T can be less than T_{av} at infinite residence time

is the temperature which the cylinder would attain over its entire length if held stationary in a heat source for a real time equal to the residence time. This is the intuitive approximation in which a flow system (in this case, the moving cylinder) provides a time resolution of a corresponding transient system. It is valid when v^* is large and hence (from equation (6)) much more heat is carried by the flow of the solid than by conduction in the solid or forced convection from the gas. Indeed, the quasitransient differential equation, equation (11), is obtainable from the full equation, equation (1), by dropping the z-conduction term.

Residence time, $t = z/v$, can vary in two ways, either at fixed speed (z varying) or at fixed position (v varying). Correspondingly, by a change of variables from v^* and z^*, we can express the reduced temperatures in equations (4) and (5) in terms of t^* and v^*, or in terms of t^* and z^*. The residence time dependence of equation (5) is shown at fixed v^* in Fig. 3 and at fixed z^* in Fig. 4. The two procedures are equivalent in the quasitransient limit but not when z-conduction is important. In addition, the fact that heat is conducted partly in the upstream direction (against the cylinder motion) is responsible for two striking deviations from quasitransient behavior; specifically, Fig. 3 shows that T can exceed T_0 at zero residence time, while Fig. 4 demonstrates the fact that T can be less than T_{av} at infinite residence time.

Edge Effects

This section compares the radially isothermal temperature distributions resulting from a number of possible distributions of heat transfer to the moving wire. The temperature profiles of the hot gas flowing across the wire are shown in Fig. 2 in the region between $z = 0$ and $z = l$ where heat is supplied to the wire. Two possibilities are considered in the regions $-\infty < z \leqslant 0$ and $l \leqslant z < \infty$. Either $T_{gas} = T_0$ in these regions, in which case heat is removed from the wire, or else $h = 0$ here, in which case no heat transfer occurs. With the $T_{gas} = T_0$ cut-off, h is constant everywhere. The step function problem in Fig. 2 was treated in the previous section. This result is now extended to the other cases.

The differential equation, equation (1), may be solved for arbitrary $T_{gas}(z)$ by Lagrange's method of variation of parameters. To cover the cases with constant h we choose the solution which reduces to the step function case:

$$T = \frac{1}{v^*R} \int_0^\infty d\left(\frac{vZ}{2\kappa}\right)$$

$$\times \left\{ \begin{array}{l} \exp\left[-(R-1)\left(\frac{vZ}{2\kappa}\right)\right] T_{gas}(z-Z) \\ + \exp\left[-(R+1)\left(\frac{vZ}{2\kappa}\right)\right] T_{gas}(z+Z) \end{array} \right\} \quad (13)$$

To help distinguish which effects are due to z-conduction and which are not, we note that the large v^* limit of equation (13) is

$$T = T_0 + e^{-t^*} \int_0^{t^*} d(t^*)' e^{(t^*)'} T_{gas}(z') \quad (14)$$

with

$$(t^*)' \equiv \frac{2\kappa h z'}{av} \quad (15)$$

The last expression satisfies the differential equation, equation (1), without the z-conduction term. However, equation (14) is not in general quasitransient because position and speed can enter separately, not just through their ratio, residence time.

The other cases with constant h are obtained by substitution into equation (13). When T_{gas} is a square wave, the solid temperature is, for $0 < z < l$,

$$\frac{T_{av} - T}{T_{av} - T_0} = \frac{1}{2}(1 + R^{-1}) \exp\left[-(R-1)v^*z^*\right]$$

$$+ \frac{1}{2}(1 - R^{-1}) \exp\left[-(R+1)v^*z_{co}^*\right] \quad (16)$$

where

$$z_{co}^* \equiv \frac{h^{1/2}(l-z)}{a^{1/2}} \quad (17)$$

is the dimensionless distance back from $z = l$ where T_{gas} is cut off. The first term is the step function solution while the remainder is a cut-off correction. As shown in Fig. 5, the correction vanishes at large distances from the cut-off point. It also vanishes in the large v^* limit, except at $z = l$. The cylinder temperature at $z = l$ is given in Figs. 6 and 7, in which l^* is the dimensionless source length,

$$l^* = \frac{h^{1/2}l}{a^{1/2}} \quad (18)$$

A comparison with Figs. 3 and 4 shows the cut-off effects at $z = l$; one

effect, for example, is that the logarithmic temperature is no longer linear in residence time at fixed v^*.

We next consider a T_{gas} profile having tails at $z = 0$ and $z = l$ which fall off linearly with a width of w (see Fig. 2). In the region where the heat source is flat, $w < z < (l - w)$, the solid temperature is

$$\frac{T_{av} - T}{T_{av} - T_0} = \frac{1}{2}(1 + R^{-1}) \exp\left[-(R - 1)v^*z^*\right]W((R - 1)v^*w^*)$$

$$+ \frac{1}{2}(1 - R^{-1}) \exp\left[-(R + 1)v^*z_{co}^*\right]W((R + 1)v^*w^*) \quad (19)$$
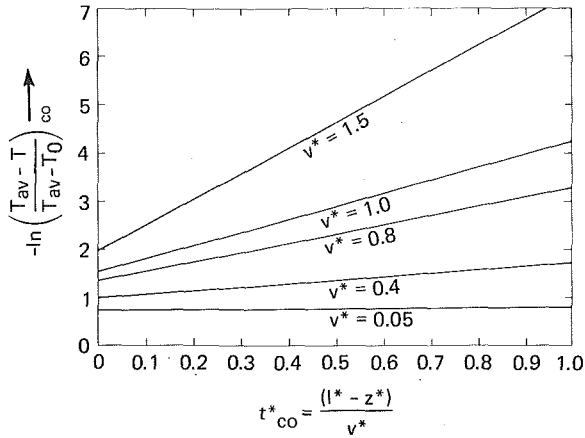
Fig. 5   The correction to the radially isothermal cylinder temperature due to the cut-off in a square wave gas Temperature Profile. The correction is small in the quasitransient regime (large v^*) and at large distances from the cut-off point
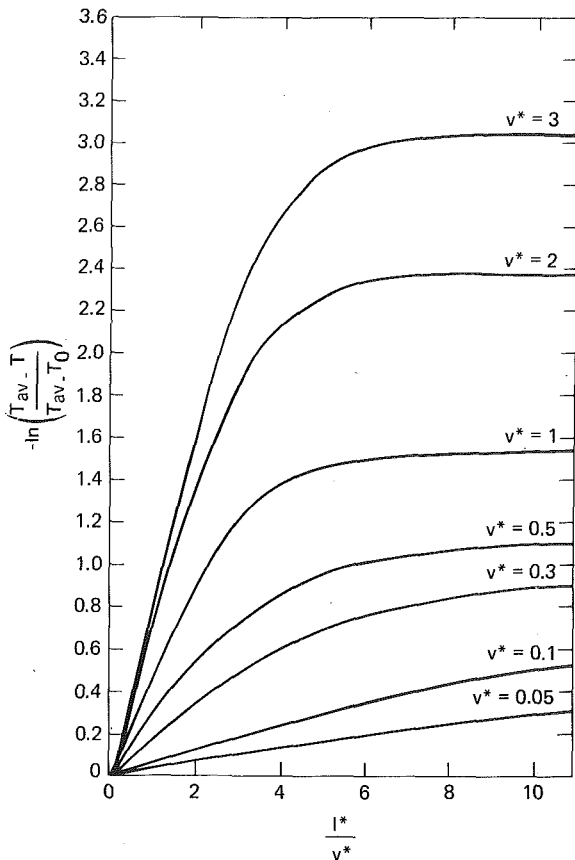
Fig. 6   Radially isothermal cylinder temperature at the cut-off point in a square wave angle-independent gas temperature profile. The source length (l^*) is varied at fixed speed (v^*)

where

$$w^* \equiv \frac{h^{1/2}w}{a^{1/2}} \quad (20)$$

is the dimensionless half-width, and

$$W(x) \equiv \frac{e^x - 1}{x} \quad (21)$$

It is seen that the two terms in the previous square wave result are now multiplied by factors, $W((R \pm 1)v^*w^*)$ which correct for the effect of the sloping edges. As shown in Fig. 8, these factors approach unity when $w^*/v^* \to 0$. However, their influence survives in the large v^* limit; if $w < z < (l - w)$,

$$\frac{T_{av} - T}{T_{av} - T_0} \to e^{-t^*}\left[\frac{e^{w^*/v^*} - 1}{w^*/v^*}\right], \quad (21)(a)$$

and when $z = l$, it may be shown from equation (14) that

$$\frac{T_{av} - T}{T_{av} - T_0} \to \left\{1 - \left[\frac{1 - e^{-w^*/v^*}}{w^*/v^*}\right]\right\}$$

$$+ e^{-l^*/v^*}\left[\frac{e^{w^*/v^*} - 1}{w^*/v^*}\right]. \quad (21)(b)$$
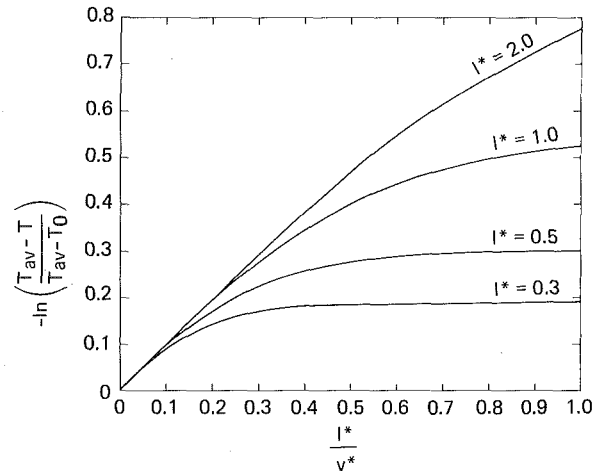
Fig. 7   Radially isothermal cylinder temperature at the cut-off point in a square wave angle-independent gas temperature profile. The speed (v^*) is varied at a fixed source length (l^*)

$W+ \equiv W((R + 1)v^*w^*)$

$W_- \equiv W((R - 1)v^*w^*)$
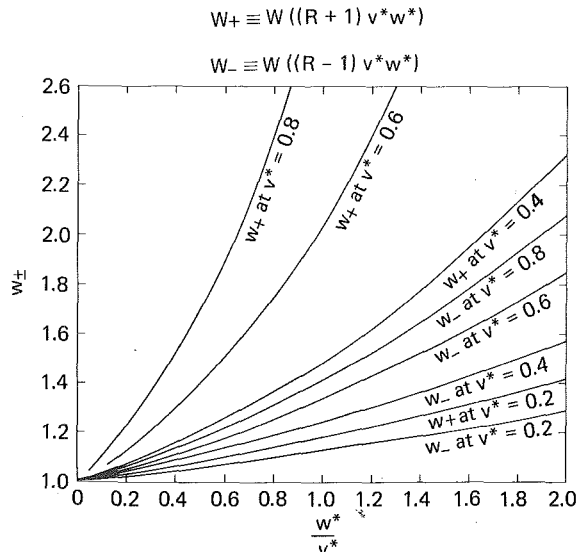
Fig. 8   Correction factors in equation (19) for the cylinder temperature when the gas profile has tails of width w at its edges

A useful boundary value problem is one in which there is no heat transfer to the cylinder in the regions $z < 0$ and $z > l$. Between the two cut-off points heat transfer is by forced convection and the gas temperature is uniform. Equation (1) applies in the heat source region, but elsewhere, T satisfies

$$\kappa \frac{\partial^2 T}{\partial z^2} - v \frac{\partial T}{\partial z} = 0 \quad \text{if } z < 0 \text{ or } z > l \tag{22}$$

With the auxiliary conditions that T and $\partial T/\partial z$ are continuous at $z = 0$ and $z = l$, and that

$$T \to T_0 \text{ as } z \to -\infty \tag{23}$$

$$T \to \text{constant as } z \to \infty \tag{24}$$

it turns out that T rises exponentially at $z < 0$, due to back-conduction, but is constant at $z \geq l$, where

$$\frac{T_{av} - T}{T_{av} - T_0}$$
$$= 4R \left[(R + 1)^2 e^{(R-1)v^*l^*} - (R - 1)^2 e^{-(R+1)v^*l^*} \right]^{-1} \tag{25a}$$

This expression has the proper limits:

$$T \to T_0 \text{ as } l^* \to 0, \text{ and } T \to T_{av} \text{ as } l^* \to \infty$$

In addition, it approaches the quasitransient limit $\exp(-l^*/v^*)$ as $v^* \to \infty$. Figs. 9 and 10 are charts of equation (25a) in the same format as Figs. 3 and 4, for ease of comparison. Between the cut-off points, the cylinder temperature is

$$\frac{T_{av} - T}{T_{av} - T_0}$$
$$= \frac{(R + 1) e^{Rv^*l^*} e^{-(R-1)z^*} + (R - 1)e^{-Rv^*l^*}e^{(R+1)z^*}}{(R + 1)^2 e^{Rv^*l^*} - (R - 1) e^{-Rv^*l^*}} \tag{25b}$$

This expression also becomes quasitransient, as $\exp(-z^*/v^*)$, in the large v^* limit.

When $T_{gas}(z)$ has an arbitrary shape between the $h = 0$ cut-off points, the cylinder temperature at $z \geq l$ is

$$T = \frac{2R (R + 1) \mathscr{A}(l) + 2R (R - 1) \mathscr{J}(0) + RT_0}{(R + 1)^2 e^{(R-1)l^*v^*} - (R - 1)^2 e^{-(R+1)l^*v^*}} \tag{26a}$$

while at $0 < z < l$ it is

$$T = \frac{e^{-v^*(l^*-z^*)}}{(R + 1)^2 e^{(R-1)l^*v^*} - (R - 1)^2 e^{-(R+1)l^*v^*}}$$

$$\times \left\{ e^{-Rv^*(l^*-z^*)} (R - 1) \left[2T_0 + (R + 1)\mathscr{A}(l) + (R - 1)\mathscr{J}(0) \right] \right.$$

$$+ e^{Rv^*z^*} \mathscr{J}(z) \left[(R + 1)^2 e^{Rv^*l^*} - (R - 1)^2 e^{-Rv^*l^*} \right]$$

$$+ e^{-Rv^*z^*} \left[(R - 1)^2 \mathscr{A}(l) e^{-Rv^*l^*} \right.$$

$$+ \frac{2}{(v^*)^2} \mathscr{J}(0) e^{Rv^*l^*} + 2(R + 1) e^{Rv^*l^*} T_0 \right]$$

$$\left. + e^{-Rv^*z^*} \mathscr{A}(z) \left[(R + 1)^2 e^{Rv^*l^*} - (R - 1)^2 e^{-Rv^*l^*} \right] \right\} \tag{26b}$$

where (cf. equation (15)),

$$\mathscr{J}(z) = \frac{1}{R} \int_{t^*}^{l^*/v^*} d(t^*)' T_{gas}(z') e^{-(R+1)(v^*)^2(t^*)'} \tag{27}$$

and

$$\mathscr{A}(z) = \frac{1}{R} \int_0^{t^*} d(t^*)' T_{gas}(z') e^{(R-1)(v^*)^2(t^*)'} \tag{28}$$

Equations (26) reduce properly to equations (25) when T_{gas} is constant between the cut-off points. In addition, equation (14) is obtained in the source region when v^* is large; the large limit here is evidently independent of the type of cut-off, depending only on the intermediate shape of the source. At $z > l$, the temperature equation (26b) reduces to equation (14) evaluated at $z = l$.

Radial Effects

To generalize further the description of the moving cylinder, the radial (r) dependence of its temperature is now added. It is shown how the isothermal cross section results appear in a well-defined mathematical limit.

The boundary value problem considered is

$$\left[\frac{1}{r} \frac{\partial}{\partial r} \left(r \frac{\partial}{\partial r} \right) + \frac{\partial^2}{\partial z^2} - \frac{v}{\kappa} \frac{\partial}{\partial z} \right] T = 0 \tag{29}$$

subject to

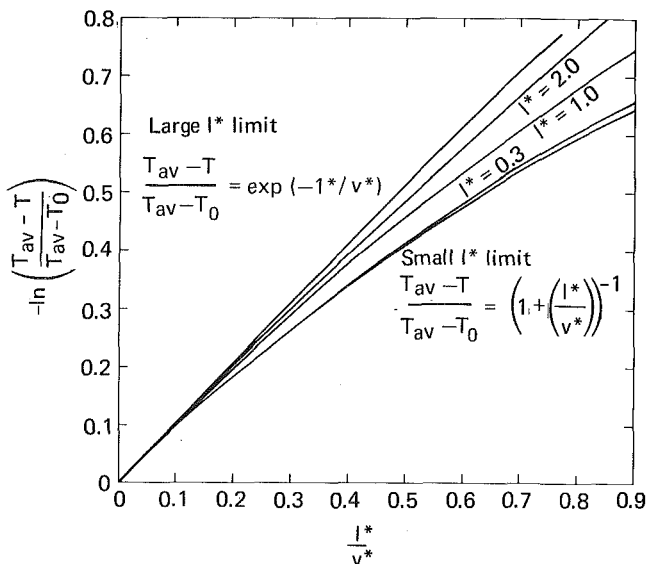$$\frac{\partial T}{\partial r} = h(T_{gas} - T) \text{ at } r = a \tag{30}$$

Fig. 9 Radially isothermal cylinder temperature to the right of a heat source which is bounded by regions of no heat transfer at $z < 0$ and $z > l$. The source length (l^*) is varied at fixed speed (v^*)
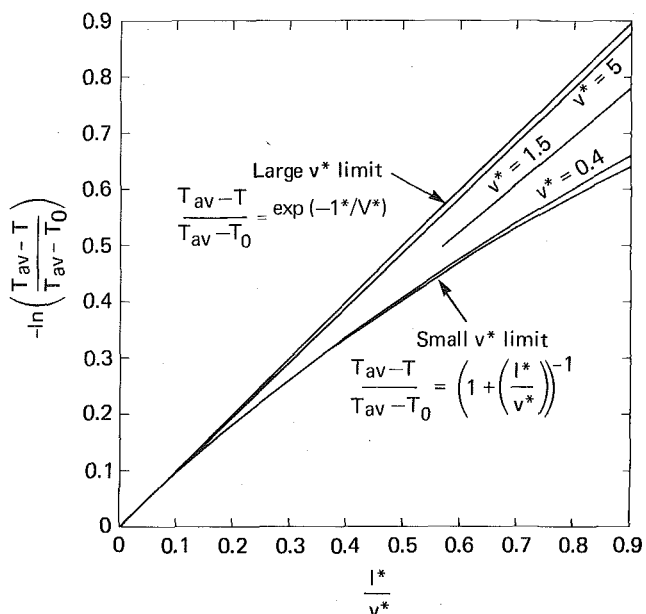

Fig. 10 Radially isothermal cylinder temperature to the right of a heat source which is bounded by regions of no heat transfer at $z < 0$ and $z > l$. Speed (v^*) is varied at a fixed source length (l^*)

and the requirement that T is everywhere finite. Again, T_{gas} is to be an arbitrary function of z. A finite Hankel transform (reference [10]) of T is now introduced:

$$H_s = \int_0^1 dr^* r^* J_0(x_s r^*) T \tag{31}$$

where

$$x_s J_0'(x_s) + N J_0(x_s) = 0 \tag{32}$$

$N \equiv ah$ is a dimensionless heat transfer coefficient, and $r^* = r/a$. The inverse transform is given by

$$T = 2 \sum_{s=1}^\infty \frac{x_s^2}{N^2 + x_s^2} \frac{J_0(x_s r/a)}{[J_0(x_s)]^2} H_s \tag{33}$$

The advantage of this transform is that it removes the r derivatives in the differential equation:

$$\left[\frac{\partial^2}{\partial z^2} - \frac{v}{\kappa} \frac{\partial}{\partial z} - \left(\frac{x_s}{a}\right)^2 \right] H_s = -J_0(x_s) N T_{gas} \tag{34}$$

and the problem is reduced mathematically to one considered in the previous section. The full solution is

$$T = \frac{1}{(v^*)^2} \sum_{s=1}^\infty \frac{x_s^2}{N^2 + x_s^2} \frac{J_0(x_s r^*)}{J_0(x_s)} \frac{1}{R_s}$$

$$\times \int_0^\infty d\left(\frac{vZ}{2\kappa}\right) \left\{ \begin{array}{l} \exp\left[-(R_s - 1)\left(\frac{vZ}{2\kappa}\right)\right] T_{gas}(z - Z) \\ + \exp\left[-(R_s + 1)\left(\frac{vZ}{2\kappa}\right)\right] T_{gas}(z + Z) \end{array} \right\} \tag{35}$$

where

$$R_s \equiv \left[1 + \frac{x_s^2}{N(v^*)^2}\right]^{1/2} \tag{36}$$

The last result readily simplifies when $T_{gas}(z)$ is a step function or square wave. For this purpose, we note that

$$2N \sum_s \frac{J_0(x_s r^*)}{(x_s^2 + N^2) J_0(x_s)} = 1 \tag{37}$$

The step function solution for $z > 0$ is then

$$\frac{T_{av} - T}{T_{av} - T_0} = N \sum_s \frac{(1 + R_s^{-1})}{(x_s^2 + N^2)} \frac{J_0(x_s r^*)}{J_0(x_s)} \exp\left[-(R_s - 1) v^* z^*\right] \tag{38}$$

while the square wave case is

$$\frac{T_{av} - T}{T_{av} - T_0} = \frac{1}{(v^*)^2} \sum_s \frac{x_s^2}{(x_s^2 + N^2) R_s} \frac{J_0(x_s r^*)}{J_0(x_s)}$$

$$\times \{(R_s - 1)^{-1} \exp\left[-(R_s - 1) v^* z^*\right] + (R_s + 1)^{-1} \exp\left[-(R_s + 1) v^* (l^* - z^*)\right]\} \tag{39}$$

These two formulas merge when $l^* - z^* \to \infty$.

With r-dependence, a quasitransient limit is obtained as $v^* \to \infty$, but *with N fixed*. Both the last two formulas then approach the limit

$$\frac{T_{av} - T}{T_{av} - T_0} = 2N \sum_s \frac{1}{x_s^2 + N^2} \frac{J_0(x_s r^*)}{J_0(x_s)} \exp\left(-x_s^2 t^*/2N\right) \tag{40}$$

This is the solution of the corresponding quasitransient boundary value problem.

$$\frac{1}{r} \frac{\partial}{\partial r}\left(r \frac{\partial T}{\partial r}\right) = \frac{1}{\kappa} \frac{\partial T}{\partial t} \tag{41}$$

subject to

$$T = T_0 \text{ at } t = 0 \tag{42}$$

and

$$\frac{\partial T}{\partial r} = h(T_{av} - T) \text{ at } r = a \tag{43}$$

The large v^* limit of the solution for arbitrary $T_{gas}(z)$ is not quasi-

transient in general:

$$T = \sum_{s=1}^\infty \frac{x_s^2}{N^2 + x_s^2} \frac{J_0(x_s r^*)}{J_0(x_s)} e^{-t^* x_s^2/2N}$$

$$\times \int_\infty^{t^*} d(t^*)' e^{(t^*)' x_s^2/2N} T_{gas}(z') \tag{44}$$

This is the extension of equation (14) appropriate when radial gradients are nonzero.

The parameter N is the additional degree of freedom that arises when radial effects are present. When T_{gas} is a step function, for example, the r-dependent distribution, equation (38), has the form

$$\frac{T_{av} - T}{T_{av} - T_0} = O(z^*, v^*, r^*, N) \tag{45}$$

whereas the corresponding isothermal core distribution, equation (5), has the form

$$\frac{T_{av} - T}{T_{av} - T_0} = \Theta(z^*, v^*) \tag{46}$$

Note that, from the boundary condition at $r^* = 1$

$$N = -\frac{d}{dr^*} \ln \Theta \text{ at } r^* = 1 \tag{47}$$

We now show that as $N \to 0$ *with v^* fixed*, the radial effects drop out. The proof relies simply on the fact that, as $N \to 0$
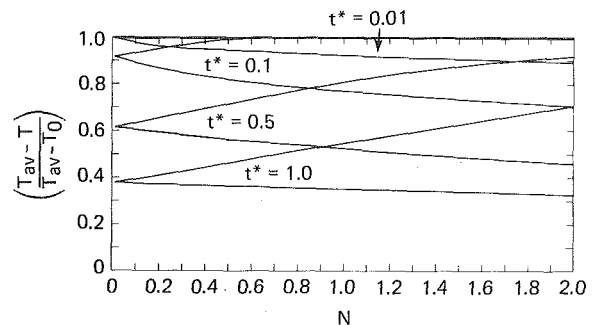

Fig. 11 Typical temperatures on the axis and on the surface, in the quasitransient limit when T_{gas} is a step function or square wave. At each t^*, the upper branch is at $r^* = 0$ and the lower branch at $r^* = 1$
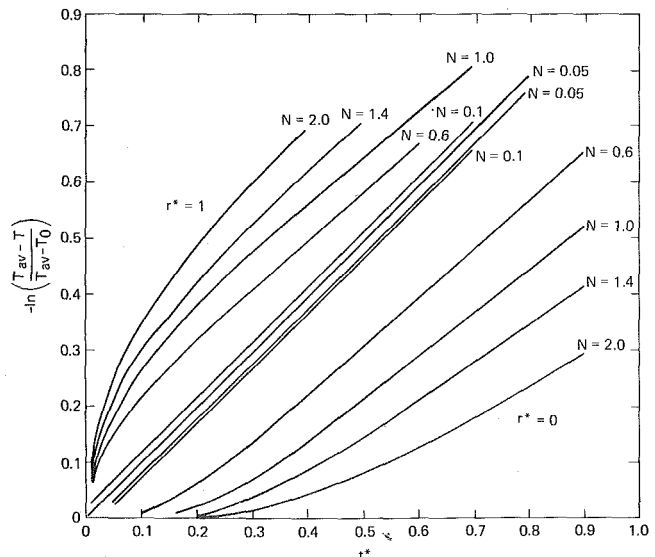

Fig. 12 Surface temperature ($r^* = 1$) and axis temperature ($r^* = 0$) in the quesitransient limit when $T_{gas}(z)$ is a step function or square wave. At each N, the upper branch is at $r^* = 1$ and the lower branch at $r^* = 0$

$$x_s \rightarrow \begin{cases} (2N)^{1/2} \text{ if } s = 1 \\ \text{bounded away from 0 if } s > 1 \end{cases} \qquad (48)$$

It follows that, keeping v^* fixed,

$$R_s \rightarrow \begin{cases} R \text{ if } s = 1 \\ \infty \text{ if } s > 1 \end{cases} \qquad (49)$$

It now readily follows that the radial distributions for the arbitrary T_{gas} profile equation (35), for the step function equation (38), and for the square wave profile equation (39), reduce to the corresponding isothermal cross section results, equations (13), (5) and (16), respectively. The large v^* radial distributions, equations (40) and (44), reduce to their isothermal cross section limits when $N \rightarrow 0$, with no accompanying restriction on t^*.

The simplest demonstration of radial effects is possible in the quasitransient limit when $T_{gas}(z)$ is a step function or square wave. Figs. 11 and 12 show how the temperatures at the axis and on the surface depart from the isothermal cross section prediction ($N = 0$). The deviations are small, especially at the surface, except when N is large; then the axis lags more behind the surface and the thermal wave takes longer to penetrate. Newman [11] has charted the cylinder temperature as a function of another set of variables, N and $t^*/2N$, not correlated with the isothermal cross section limit. The N-dependence of $(T_{av} - T)/(T_{av} - T_0)$ at fixed $t^*/2N$ is much steeper than at fixed t^*.

References

1 Nettleton, H. R., *Proc. Physical Society of London*, Vol 22, 1910, p. 278, ibid Vol. 26, 1913, p. 28.

2 Owen, S. P., *Proc. London Math. Society*, Vol. 23, 1925, p. 238.

3 Rosner, D. E., "Convective Heat Transfer with Chemical Reaction," report ARL 99 of Aeronautical Research Laboratory, Office of Aerospace Research, USAF, Wright-Patterson Air Force Base, Aug. 1961.

4 Carslaw, H. S., and Jaeger, J. C., *Conduction of Heat in Solids*, Oxford at the Clarendon Press, 1959.

5 Fristrom, R. M., and Grunfelder, C., "Moving Wire Technique Studies of Ablation, Ignition, and Extinction of Polymer Flames," *Fire and Materials* Vol. I, 1976 p. 48.

6 Fristrom, R. M., Grunfelder, C., and Hunter, L. W., "Exploratory Studies in Polymer Ablation, Ignition, and Extinction by the Moving Wire Technique," *Combustion and Flame*, Vol. 27, 1976, p. 33.

7 Hunter, L. W., Schacke, H., Grunfelder, C., and Fristrom, R. M., "Surface Temperature Measurements in the Moving Wire Technique," *Combustion Science and Technology*, Vol. 15, 1976, p. 41.

8 Schacke, H., Hunter, L. W., Fristrom, R. M., and Grunfelder, C., "Combustion of Poly (Vinyl Chloride) Studied by the Moving Wire Technique," *Sixteenth International Symposium on Combustion*, The Combustion Institute, 1977.

9 Eckert, E. R. G., and Soehngen, E., TRANS. ASME Vol. 74, 1952, p. 343.

10 Sneddon, I. N., "Finite Hankel Transforms," *Phil. Mag.*, Series 7, Vol. 37, 1946, p. 17.

11 Newman, A. B., "Heating and Cooling Rectangular and Cylindrical Solids," *Ind. Eng. Chem.*, Vol. 28, 1936, p. 545.

Natural Convection in Liquid Metals in an Enclosure

J. R. Custer and E. J. Shaughnessy[1]

We report here the results of a numerical investigation of natural convection in liquid metals contained within a horizontal cylindrical annulus [1].[2] The bounding cylinders are each at constant, but different, temperature. The flow is assumed two-dimensional and steady. The Boussinesq approximation is used to account for the temperature dependence of the density. The problem is formulated in terms of a stream function and a temperature function. The derivation of the equations is given in a companion paper [2].

To nondimensionalize the equations the radius of the inner cylinder, R_i, is chosen for the length scale, the temperature scale is $T_i - T_0$, the temperature difference between the inner and outer cylinders, and the stream function is scaled by ν, the diffusivity of momentum. Three nondimensional parameters occur. These are the Grashof number $g_0 \beta (T_i - T_0) R_i^3 / \nu^2$, the Prandtl number ν/α, and the radius ratio R_0/R_i. It is important to note that the length scale in [2] is the radius of the outer cylinder R_0, while the temperature scale is $(T_0 - T_i)$, the negative of the temperature scale used in this note. As a result, the radius ratio of one paper is the inverse of the radius ratio in the other. Likewise, the Grashof number of this note is $(R_i/R_0)^3$ times that of the other paper and of opposite sign.

The results presented here were obtained with the technique of partial spectral expansions. The principle of this approach is to expand the dependent variables in a set of known basis functions. These functions ae generally chosen to satisfy known symmetries or invariants of the flow. In this case the following expansions are chosen:

$$\psi(r, \theta) = \sum_{n=1}^{\infty} f_n(r) \sin n\theta$$

$$T(r, \theta) = \sum_{n=0}^{\infty} g_n(r) \cos n\theta$$

By truncating these expansions and using the orthogonality of the sines and cosines, differential equations governing the $f_n(r)$ and $g_n(r)$ are obtained. These equations are then solved numerically. The results reported here were obtained with series truncated after $n = 3$.

---

[1] Graduate Student and Asst. Professor, respectively, Department of Mechanical Engineering and Materials Science, Duke University, Durham, N. C.

[2] Numbers in brackets designate References at end of technical note.

Results

Calculations were carried out for Prandtl numbers 0.005, 0.01, and 0.10 and radius ratios of 1.1, 2.0, and 4.0. Due to the extremely high conductivity of these fluids the conduction heat transfer rates are used to normalize the heat transfer results. The local temperature gradient due to conduction alone is denoted by q_c. The overall heat transfer rate by conduction is denoted by Q_c. Fig. 1 is a plot of the local non-dimensional temperature gradient at each cylinder for a radius ratio of 4.0, Prandtl number of 0.01, and a Grashof number of 100. The angular coordinate is measured counter-clockwise from the direction of the gravity vector. Similar plots were obtained for all runs. Heat transfer rates above the conduction value occur where $(q - q_c)/|q_c|$ is negative. This corresponds to regions where the fluid is moving toward one of the cylinders. For the inner cylinder this occurs along the bottom surface ($\theta < 90°$) while enhanced heat transfer to the outer cylinder occurs along its upper surface ($\theta > 90°$). The overall heat transfer is obtained by integrating the local flux over the surface of one of the cylinders. Because the flow is steady, this quantity must be the same for each cylinder. The results are
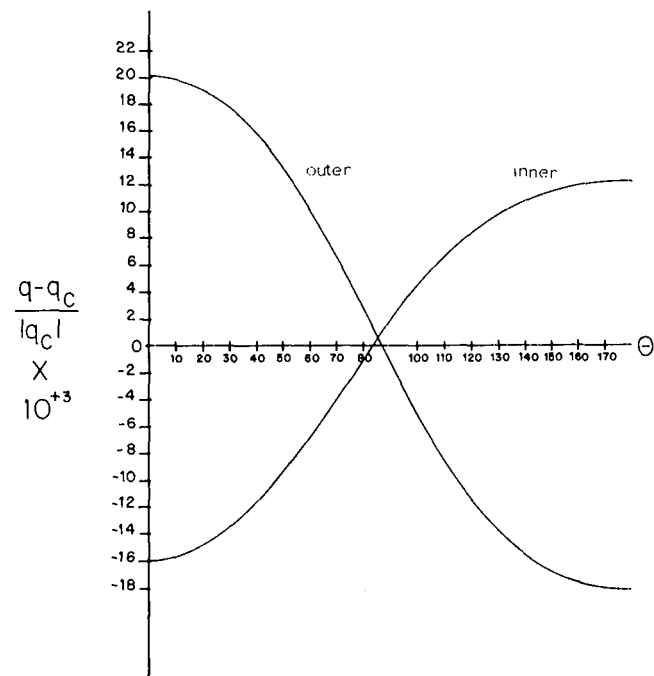

Fig. 1 Local heat flux on inner and outer cylinders for radius ratio of 4.0, Prandtl number 0.01 and Grashof of 100

radius ratio = 2.00

$$\frac{Q}{Q_c} = 1 + 5 \times 10^{-8} \, \mathrm{Ra}^{2.014}$$

radius ratio = 4.00

$$\frac{Q}{Q_c} = 1 + 1 \times 10^{-4} \, \mathrm{Ra}^{1.935}$$

These results are valid for Rayleigh numbers less than 50. The corresponding Grashof numbers are less than 5×10^3. For a radius ratio of 1.1, Q/Q_c was equal to 1 out to a Grashof number of 10^6.

It is not possible to compare these results with heat transfer results from [2] since the number of terms retained in the expression in [2] for the temperature field is insufficient to permit meaningful comparison.

In all cases investigated, the flow pattern consisted of a single eddy in each vertical half of the annulus. As the Grashof number increased, the center of each of these eddies fell below the horizontal plane. Although the perturbation results of Mack and Bishop [4] and the previously referenced investigation of the present authors both indicate the possibility of transition to a multicellular flow, none was observed here.

Acknowledgment

References

1   Custer, J. R., "Natural Convection in Low Prandtl Number Fluids Within a Horizontal Cylindrical Annulus," MS's thesis, Duke University, 1976.

2   Custer, J. R., and Shaughnessy, E. J., "Thermoconvective Motion of Low Prandtl Number Fluids Contained Within a Horizontal Cylindrical Annulus," [to be published in the JOURNAL OF HEAT TRANSFER], TRANS. ASME, Series C.

3   Bishop, E. G., and Carley, C. T., "Photographic Studies of Natural Convection Between Concentric Cylinders," *Proceedings 1966 Heat Transfer and Fluid Mechanics Institute,* 1966, p. 63.

4   Mack, L. R., and Bishop, E. G., "Natural Convection Between Horizontal Concentric Cylinders for Low Rayleigh Numbers," *Quart. J. Mech. Appl. Math.,* Vol. XXI, 1968.

An Exact Solution of the Boussinesq Equations for an Infinite Wall in a Stratified Fluid[1]

M. C. Jischke[2]

Introduction

An exact solution of the two-dimensional Boussinesq equations has been obtained for an infinite vertical wall bounding an infinite fluid half-space. Both the wall and the fluid far from the wall have arbitrary (stable) linear stratification. The fluid motions are the result of buoyancy forces due to gravity.

Chen and Eichhorn [1],[3] Cheesewright [2], and Yang, Novotny and Cheng [3] have studied the problem of a finite wall in a stably-stratified fluid using the natural convection boundary-layer equations. Similarity solutions are not possible in the isothermal wall case, and various approximate analytical-numerical methods have been employed to solve the boundary-layer equations. Similarity solutions have been obtained [3] for the case where the wall and ambient fluid have the same stratification. These results show that stratification increases the heat transfer above the isothermal value (e.g., corresponding to an isothermal fluid with the mean temperature of the stratified case), in agreement with experiment.

Doty and Jischke [4] have examined the unsteady linearized problem in which the wall and fluid temperatures differ only slightly. The resulting steady state solutions are of the boundary layer type and show that the temperature difference is communicated to the fluid through viscous and thermal boundary layers whose thickness if of the order $\mathrm{Gr}^{-1/4}$. We shall later compare these linearized results with the new exact solution.

Gill [5] in his study of laminar free convection in enclosures showed that there is another exact solution of the Bossinesq equations if the wall and fluid far from the wall have the same linear stratification, giving temperatures that differ by a constant. The resulting solution is similar to the linearized solution of Doty and Jischke [4] and shows the oscillatory nature of the resulting velocity and temperature fields. Our results here differ from those of Gill in that we assume the wall and fluid stratifications differ.

Finally, it is useful to recognize that the present solution is analogous to the exact solution of the Navier-Stokes equations developed by Karman [6] for the case of a rotating infinite disk bounding a viscous, incompressible fluid. Karman's result has been generalized by Rogers and Lance [7] to allow for rotation of both the disk and the fluid far away. Although the analogy is not mathematically precise, the structure of these rotating flows is quite similar to that of the solutions developed in this paper, again showing the qualitative similarity of rotating and stratified flows.

Analysis

The two-dimensional Navier-Stokes equations can be written

$$\frac{\partial u}{\partial x} + \frac{\partial v}{\partial y} = 0 \tag{1}$$

$$u\frac{\partial u}{\partial x} + v\frac{\partial u}{\partial y} = \frac{-1}{\rho_0}\frac{\partial p}{\partial x} + g\beta(T - T_0) + \nu\left(\frac{\partial^2 u}{\partial x^2} + \frac{\partial^2 u}{\partial y^2}\right) \tag{2}$$

$$u\frac{\partial v}{\partial x} + v\frac{\partial v}{\partial y} = -\frac{1}{\rho_0}\frac{\partial p}{\partial y} + \nu\left(\frac{\partial^2 v}{\partial x^2} + \frac{\partial^2 v}{\partial y^2}\right) \tag{3}$$

$$u\frac{\partial T}{\partial x} + v\frac{\partial T}{\partial y} = \alpha\left(\frac{\partial^2 T}{\partial x^2} + \frac{\partial^2 T}{\partial y^2}\right) \tag{4}$$

where x and y, respectively, represent the coordinates parallel and normal to the plate.

Here, we have employed the Boussinesq approximation in which the density changes are due to temperature changes only and are important only in the buoyancy force due to gravity. The kinematic viscosity ν, thermal expansion coefficient β, and thermal diffusivity α are all assumed to be constant.

We wish to develop the solution of these equations for the case of an infinite vertical wall boundary an infinite half-space of fluid. The wall and distant fluid are assumed to be linearly stratified in the vertical direction with different stratifications.

$$T_w = T_0 + a_w x, \qquad a_w = dT_w/dx \tag{5}$$

$$T_\infty = T_0 + a_\infty x, \qquad a_\infty = dT_\infty/dx \tag{6}$$

where both a_w and a_∞ must be positive if the flow is to satisfy the inviscid stability criterion. Here x is defined such that at $x = 0$ the wall and distant fluid have the same temperature.

We assume a solution of the following form

---

radius ratio = 2.00

$$\frac{Q}{Q_c} = 1 + 5 \times 10^{-8} \, \text{Ra}^{2.014}$$

radius ratio = 4.00

$$\frac{Q}{Q_c} = 1 + 1 \times 10^{-4} \, \text{Ra}^{1.935}$$

These results are valid for Rayleigh numbers less than 50. The corresponding Grashof numbers are less than 5×10^3. For a radius ratio of 1.1, Q/Q_c was equal to 1 out to a Grashof number of 10^6.

It is not possible to compare these results with heat transfer results from [2] since the number of terms retained in the expression in [2] for the temperature field is insufficient to permit meaningful comparison.

In all cases investigated, the flow pattern consisted of a single eddy in each vertical half of the annulus. As the Grashof number increased, the center of each of these eddies fell below the horizontal plane. Although the perturbation results of Mack and Bishop [4] and the previously referenced investigation of the present authors both indicate the possibility of transition to a multicellular flow, none was observed here.

Acknowledgment

The authors wish to thank the National Science Foundation for the support provided by grant ENG-7518398.

References

1 Custer, J. R., "Natural Convection in Low Prandtl Number Fluids Within a Horizontal Cylindrical Annulus," MS's thesis, Duke University, 1976.

2 Custer, J. R., and Shaughnessy, E. J., "Thermoconvective Motion of Low Prandtl Number Fluids Contained Within a Horizontal Cylindrical Annulus," [to be published in the JOURNAL OF HEAT TRANSFER], TRANS. ASME, Series C.

3 Bishop, E. G., and Carley, C. T., "Photographic Studies of Natural Convection Between Concentric Cylinders," *Proceedings 1966 Heat Transfer and Fluid Mechanics Institute,* 1966, p. 63.

4 Mack, L. R., and Bishop, E. G., "Natural Convection Between Horizontal Concentric Cylinders for Low Rayleigh Numbers," *Quart. J. Mech. Appl. Math.,* Vol. XXI, 1968.

An Exact Solution of the Boussinesq Equations for an Infinite Wall in a Stratified Fluid[1]

M. C. Jischke[2]

Introduction

An exact solution of the two-dimensional Boussinesq equations has been obtained for an infinite vertical wall bounding an infinite fluid half-space. Both the wall and the fluid far from the wall have arbitrary (stable) linear stratification. The fluid motions are the result of buoyancy forces due to gravity.

Chen and Eichhorn [1],[3] Cheesewright [2], and Yang, Novotny and Cheng [3] have studied the problem of a finite wall in a stably-stratified fluid using the natural convection boundary-layer equations. Similarity solutions are not possible in the isothermal wall case, and various approximate analytical-numerical methods have been employed to solve the boundary-layer equations. Similarity solutions have been obtained [3] for the case where the wall and ambient fluid have the same stratification. These results show that stratification increases the heat transfer above the isothermal value (e.g., corresponding to an isothermal fluid with the mean temperature of the stratified case), in agreement with experiment.

Doty and Jischke [4] have examined the unsteady linearized problem in which the wall and fluid temperatures differ only slightly. The resulting steady state solutions are of the boundary layer type and show that the temperature difference is communicated to the fluid through viscous and thermal boundary layers whose thickness if of the order $\text{Gr}^{-1/4}$. We shall later compare these linearized results with the new exact solution.

Gill [5] in his study of laminar free convection in enclosures showed that there is another exact solution of the Bossinesq equations if the wall and fluid far from the wall have the same linear stratification, giving temperatures that differ by a constant. The resulting solution is similar to the linearized solution of Doty and Jischke [4] and shows the oscillatory nature of the resulting velocity and temperature fields. Our results here differ from those of Gill in that we assume the wall and fluid stratifications differ.

Finally, it is useful to recognize that the present solution is analogous to the exact solution of the Navier-Stokes equations developed by Karman [6] for the case of a rotating infinite disk bounding a viscous, incompressible fluid. Karman's result has been generalized by Rogers and Lance [7] to allow for rotation of both the disk and the fluid far away. Although the analogy is not mathematically precise, the structure of these rotating flows is quite similar to that of the solutions developed in this paper, again showing the qualitative similarity of rotating and stratified flows.

Analysis

The two-dimensional Navier-Stokes equations can be written

$$\frac{\partial u}{\partial x} + \frac{\partial v}{\partial y} = 0 \tag{1}$$

$$u \frac{\partial u}{\partial x} + v \frac{\partial u}{\partial y} = \frac{-1}{\rho_0} \frac{\partial p}{\partial x} + g\beta(T - T_0) + \nu \left(\frac{\partial^2 u}{\partial x^2} + \frac{\partial^2 u}{\partial y^2} \right) \tag{2}$$

$$u \frac{\partial v}{\partial x} + v \frac{\partial v}{\partial y} = -\frac{1}{\rho_0} \frac{\partial p}{\partial y} + \nu \left(\frac{\partial^2 v}{\partial x^2} + \frac{\partial^2 v}{\partial y^2} \right) \tag{3}$$

$$u \frac{\partial T}{\partial x} + v \frac{\partial T}{\partial y} = \alpha \left(\frac{\partial^2 T}{\partial x^2} + \frac{\partial^2 T}{\partial y^2} \right) \tag{4}$$

where x and y, respectively, represent the coordinates parallel and normal to the plate.

Here, we have employed the Boussinesq approximation in which the density changes are due to temperature changes only and are important only in the buoyancy force due to gravity. The kinematic viscosity ν, thermal expansion coefficient β, and thermal diffusivity α are all assumed to be constant.

We wish to develop the solution of these equations for the case of an infinite vertical wall boundary an infinite half-space of fluid. The wall and distant fluid are assumed to be linearly stratified in the vertical direction with different stratifications.

$$T_w = T_0 + a_w x, \qquad a_w = dT_w/dx \tag{5}$$

$$T_\infty = T_0 + a_\infty x, \qquad a_\infty = dT_\infty/dx \tag{6}$$

where both a_w and a_∞ must be positive if the flow is to satisfy the inviscid stability criterion. Here x is defined such that at $x = 0$ the wall and distant fluid have the same temperature.

We assume a solution of the following form

$$u = 4\nu(g\beta|a_w - a_\infty|/4\nu^2)^{1/2}xf'(\eta) \tag{7}$$

$$v = -4\nu(g\beta|a_w - a_\infty|/4\nu^2)^{1/4}f(\eta) \tag{8}$$

$$T = T_\infty + (T_w - T_\infty)\theta(\eta) \tag{9}$$

$$p = p_0 - \rho_0\frac{v^2}{2} + \rho_0 g\beta a_\infty\frac{x^2}{2} + \mu\frac{\partial v}{\partial y} \tag{10}$$

where $\eta = y(g\beta|a_w - a_\infty|/4\nu^2)^{1/4}$. Aside from constants inserted for convenience, this solution assumes the streamfunction and temperature change are proportional to x, the vertical coordinate. The resulting ordinary differential equations for f and θ, then, are

$$4(f'^2 - ff'') = f''' + \text{sgn}(m)\theta \tag{11}$$

$$\frac{1}{\text{Pr}}\theta'' - 4mf' - 4\theta f' + 4f\theta' = 0 \tag{12}$$

with boundary conditions

$$\eta = 0: f = f' = 0, \theta = 1 \tag{13}$$

$$\eta \to \infty: f', \theta \to 0 \tag{14}$$

The stratification parameter m,

$$m = a_\infty/(a_w - a_\infty) \tag{15}$$

is a measure of the buoyancy force driving the motion. The stratification parameter m and the Prandtl number are the only parameters in the problem for f and θ. Provided $m > 0$, the equations for f and θ are identical to those derived by Yang, et al. [3] for the similarity solutions of the laminar boundary layer equations for free convection flow from a nonisothermal plate immersed in a temperature stratified medium (see equations (7), (8) of reference [3] for $n = 1$). The terms normally neglected in the boundary layer approximation are identically zero in the flow being considered in this paper. Thus we see that for the special case of a linearly stratified fluid and wall, the streamfunction and temperature obtained in the boundary layer approximation are identical to those obtained from the exact solution. The results for the pressure field differ, however, the exact solution accounting for variations in the pressure normal to the wall,

$$p = p_0 + \rho_0 g\beta a_\infty\frac{x^2}{2} - 2\mu(g\beta|a_w - a_\infty|)^{1/2}(2f^2 + f') \tag{16}$$

The heat transfer and shear stress at the wall (q_w and τ_w, respectively) are given by

$$q_w = -k(a_w - a_\infty)\text{Gr}^{1/4}\theta'(0) \tag{17}$$

$$\tau_w = 2\rho\nu^2 x^{1/4}\text{Gr}^{3/4}f''(0) \tag{18}$$

where the Grashof number Gr is defined as

$$\text{Gr} = \frac{g\beta|a_w - a_\infty|x^4}{4\nu^2} \tag{19}$$

The result for the heat transfer can be rewritten in terms of a Nusselt number, Nu, as

$$\text{Nu} = \frac{q_w x}{k(T_w - T_\infty)} = -\text{Gr}^{1/4}\theta'(0) \tag{20}$$

Equations (11) and (12) were solved numerically in much the same manner as in reference [3].

Results

Typical numerical results are shown in Fig. 1, where the non-dimensional temperature and streamfunction are shown for Prandtl number equal to unity and various values of the stratification parameter m.

If a_w, a_∞ must both be positive for stability, then the range of m for which stable solutions are possible is restricted. Since $a_w/a_\infty = (m + 1)/m$ must then be positive, unstable solutions must correspond to the range of m values

$$-1 < m < 0, \text{ unstable} \tag{21}$$
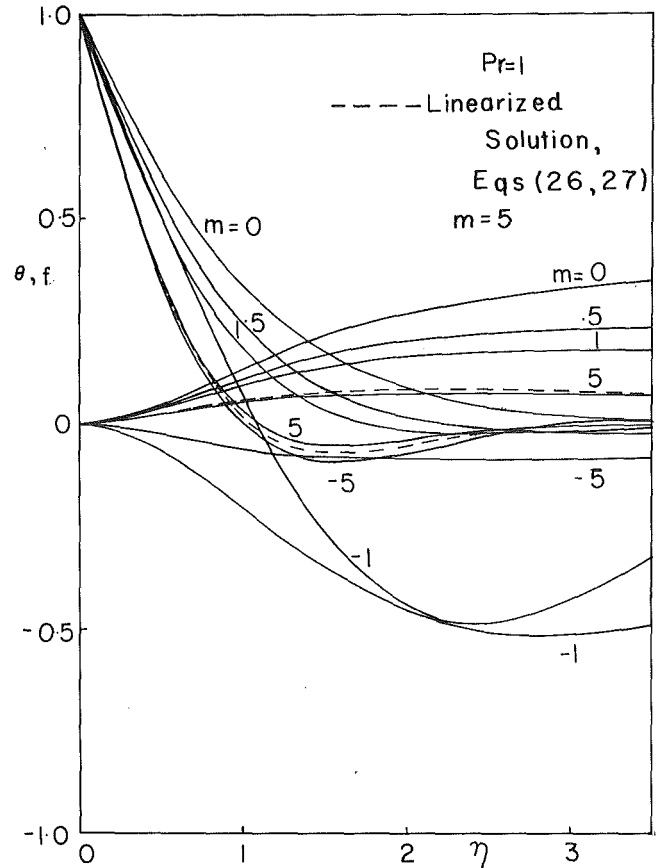

Fig. 1 Temperature and streamfunction profiles for various stratification ratios (Pr = 1).

Numerical solutions could not be obtained in this range of values of m.[4]

The present numerical results illustrate the boundary layer nature of the flow. That is, if we define the thermal boundary layer thickness δ_T as

$$\delta_T = \int_0^\infty \frac{T - T_\infty}{T_w - T_\infty}dy \tag{22}$$

then we have

$$\frac{\delta_T}{x} = \text{Gr}^{-1/4}\int_0^\infty \theta(\eta)d\eta \tag{23}$$

and the thermal boundary layer thickness decreases with increasing Grashof number, becoming very thin for large Gr.

Thus for large Grashof number, the difference in the wall and fluid temperatures is communicated to the fluid through viscous and thermal boundary layers whose thicknesses are of the order $\text{Gr}^{-1/4}$.

---

[4] Numerical solutions were obtained in [3] for the range of m corresponding to equation (21), apparently contradicting this discussion. However, the analysis in [3] implicitly assumes $T_w > T_\infty$ (see equation (16) of [3] for $n = 1$ and the assumption $L > 0$). For $n = 1$, equations (5) and (6) of [3] can be combined to show

$$L^4 = \left(g\beta\frac{(T_w - T_\infty)}{4\nu^2 x}\right)^{-1/4}$$

Thus L is real only if $T_w > T_\infty$—corresponding to $a_w > a_\infty$ and $m > 0$ if $a_\infty > 0$. However, if $a_\infty < 0$ (corresponding to $m < 0$), the flow is hydrodynamically unstable and stable solutions do not exist. Equation (11) of this paper and equation (7) of [3] differ by the coefficient, sgn(m), of θ, and this appears to be an error in [3]. As a result, the solutions in [3] for $m < 0$ appear to be physically unrealistic.
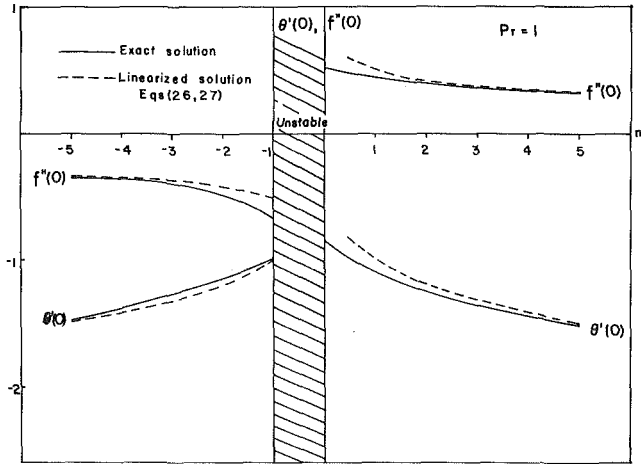
Fig. 2 Wall heat transfer, wall shear stress for various stratification ratios (Pr = 1).

Fig. 3 Effect of Prandtl number on the temperature profiles (m = 1).

Within the boundary layer, buoyant forces are resisted by viscous shear stresses and the pressure remains relatively constant. Fluid particles above $x = 0$ near the plate are heated ($a_w > a_\infty$) because of conduction and the increased buoyancy force causes the fluid to rise. Fluid particles below $z = 0$ near the plate are cooled ($a_w > a_\infty$) and fall. The vertical mass flow near the wall induces a horizontal velocity, which is of the order of $Gr^{-1/4}$ relative to the vertical velocity.

These results also show that because of stratification, the approach to conditions far from the wall is a damped oscillation, with frequency ω (e.g., $f, \theta \propto e^{\omega x}$) that satisfies the quartic equation

$$\omega^4 + 4f(\infty)(1 + Pr)\omega^3 + (4f(\infty))^2 Pr\omega^2 + 4|m|Pr = 0 \qquad (24)$$

Note that if $f(\infty) \ll 1$,

$$\omega \sim (-1 \pm i)(|m|Pr)^{1/4} \qquad (25)$$

the linearized result.

The numerical results in Fig. 1 show that as m increases from zero, the boundary layer thickness decreases and the heat transfer increases. These results can also be compared with those of the linearized theory in which $|m| \gg 1$ (e.g., $|a_w/a_\infty - 1| \ll 1$). The linearized temperature and streamfunction are

$$\theta_{1in} = \exp(-\bar{\eta})\cos(\bar{\eta}) \qquad (26)$$

$$f_{1in} = sgn(m)(1 - \exp(-\bar{\eta}(\cos \bar{\eta} + \sin \bar{\eta})/4(1m/Pr)^{3/4} \qquad (27)$$

($\eta = \eta(|m|Pr)^{1/4}$ and are compared with the exact nonlinear results for $m = 5$ in Fig. 1. Surprisingly close agreement (within 10 percent for $|m| \geq 3$) is obtained, suggesting that the linearized theory may provide a useful approximation in many problems of interest.

The effect of the stratification ratio on the heat transfer and shear stress at the wall is shown in Fig. 2 for Pr = 1. The linearized result is also given. As Fig. 2 again shows, the linearized theory gives results which are accurate to within 10 percent for $|m|$ exceeding about 3.

The effect of variations in the Prandtl number on the temperature is illustrated by the results in Fig. 3 for $m = 1$ and Prandtl numbers ranging from 0.5 to 100. As the Prandtl number increases at fixed m, the damping effect of viscosity becomes more pronounced and the thickness of the boundary layer decreases.
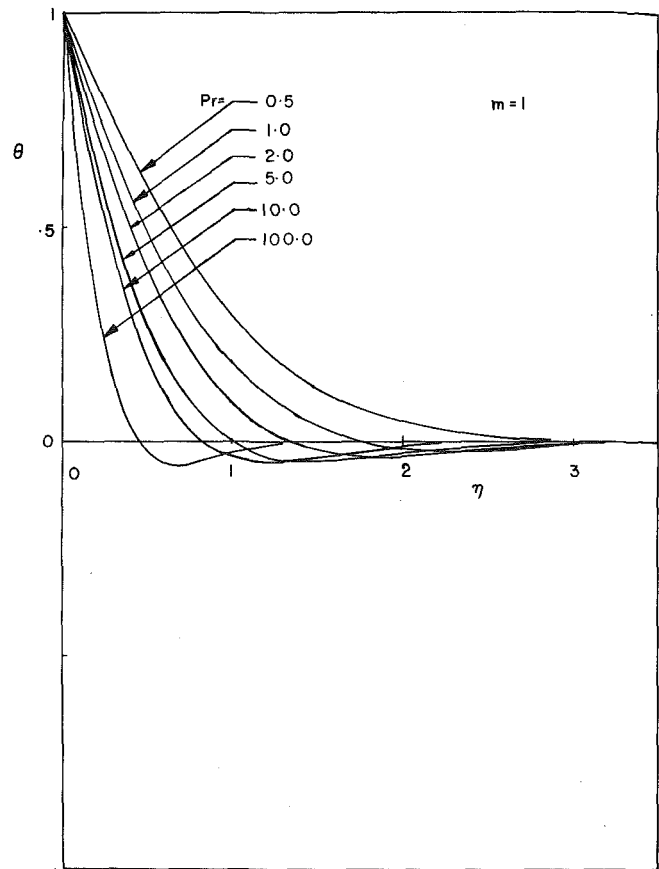
Acknowledgments

References

1 Chen, C. C., and Eichhorn, R., "Natural Convection from a Vertical Surface to a Thermally Stratified Fluid," JOURNAL OF HEAT TRANSFER, TRANS. ASME, Series C, Vol. 98, 1976, pp. 446–451.

2 Cheesewright, R., "Natural Convection from a Plane Vertical Surface in Non-Isothermal Surroundings," International Journal of Heat and Mass Transfer, Vol. 10, 1967, pp. 1847–1959.

3 Yang, K. T., Novotny, J. L. and Cheng, Y. S., "Laminar Free Convection from a Nonisothermal Plate Immersed in a Temperature Stratified Medium," International Journal of Heat and Mass Transfer, Vol. 15, 1972, pp. 1097–1109.

4 Doty, R. T. and Jischke, M. C., "Linearized Buoyant Motion Due to Impulsively Heated Vertical Plates(s)," International Journal of Heat and Mass Transfer, Vol. 17, 1974, pp. 1617–1620.

5 Gill, A. E., "The Boundary Layer Regime for Convection in a Rectangular Cavity," Journal of Fluid Mechanics, Vol. 26, part 3, 1966, pp. 515–536.

6 Karman, Th.v., "Uber Laminare und Turbulente Reibung," Zeitschrift fur Angewandte Matematik und Mekanik, Vol. 1, 1921, pp. 233–251.

7 Rogers, M. H. and Lance, G. N., "The Rotationally Symmetric Flow of a Viscous Fluid in the Presence of an Infinite Rotating Disk," Journal of Fluid Mechanics, Vol. 7, 1960, pp. 617–631.

Mixed Convection Across a Horizontal Cylinder With Uniform Surface Heat Flux

A. Mucoglu[1] and T. S. Chen[1]

Introduction

Recently, a new analysis of mixed convection across a horizontal cylinder was presented by the present authors [1][2] who employed a new finite-difference method [2, 3] to solve the transformed nonlinear conservation equations. This solution method is simple and efficient to use, and can provide accurate numerical results even for a region very close to the point of flow separation at which other solution methods fail to yield results. Their results for uniform wall temperature revealed that without using the actual local free stream velocity distributions, it is not possible to assess accurately the real characteristics of the local surface heat transfer rate.

The present work is an extention of the earlier analysis [1] by the present authors and deals with the case in which a uniform surface heat flux is prescribed at the surface of the cylinder. The study encompasses the entire regime of mixed convection, ranging from pure forced convection to pure free convection. The problem is formulated in a manner similar to that given in reference [1], as is the solution method. Numerical results for fluids having a Prandtl number of 0.7 are presented and compared with those for the case of uniform wall temperature [1].

Analysis

Envision a long horizontal cylinder which is aligned normal to a uniform, undisturbed oncoming free stream with velocity u_∞ and temperature T_∞. The radius of the cylinder is R. The gravitational acceleration g is acting downward, while the forced flow is assumed to be moving upward in the opposite direction. The x-coordinate is measured along the circumference of the cylinder from the lower stagnation point and the y-coordinate is measured normal to the surface. For the case of downward forced flow, however, the x-coordinate is measured from the upper stagnation point. Let the surface of the cylinder be maintained at a constant heat flux q_w. The analysis parallels are given in reference [1]. To conserve space, its details are omitted here.

The conservation equations and the boundary conditions describing the present problem are identical to those given by equations (1)–(4) of reference [1], except that the uniform wall temperature condition therein is now replaced by the uniform surface heat flux condition $\partial T/\partial y = -q_w/k$ at $y = 0$. In general, the local free stream velocity distributions across the cylinder have the expression [4]

$$U/u_\infty = A(x/R) + B(x/R)^3 + C(x/R)^5 + \ldots \quad (1)$$

where A, B, C, etc., are constants. For the ideal case of an inviscid flow, the $U(x)$ expression has the form

$$U/u_\infty = 2\sin(x/R) \quad (2)$$

with $A = 2$, $B = -1/3$, $C = 1/60$, etc., from the sine series expansion.

The first step in the analysis is to transform the conservation equations and their boundary conditions from the (x, y) coordinates to dimensionless coordinates by a proper choice of transformation variables for the forced-flow dominated case and the buoyancy-force

dominated case. The combination of these two cases then encompasses the entire regime of mixed convection.

Forced-Flow Dominated Case. In this case, the buoyancy force is of the secondary importance and the transformation can be patterned after that for pure forced convection. To this end, use is made of the Görtler-Meksyn variables [5]

$$\xi = \int_0^x \frac{U}{u_\infty} \frac{dx}{R}, \qquad \eta = y\frac{U}{(2\nu R u_\infty \xi)^{1/2}} \quad (3)$$

along with a reduced stream function $f(\xi, \eta)$ and a dimensionless temperature $\theta(\xi, \eta)$ defined, respectively, by

$$f(\xi, \eta) = \frac{\psi(x,y)}{(2\nu R u_\infty \xi)^{1/2}}, \qquad \theta(\xi, \eta) = \frac{[T(x,y) - T_\infty]\mathrm{Re}^{1/2}}{q_w R/k} \quad (4)$$

in which Re is the Reynolds number and $\psi(x, y)$ is the stream function that satisfies the mass conservation equation with

$$u = \partial\psi/\partial y, \qquad v = -\partial\psi/\partial x \quad (5)$$

By introducing equations (3)–(5) into the conservation equations, one can arrive at the following system of equations

$$f''' + ff'' + 2\frac{\xi dU}{U d\xi}(1 - f'^2) \pm 2\Omega\frac{\xi\sin(x/R)}{(U/u_\infty)^3}\theta$$
$$= 2\xi\left(f'\frac{\partial f'}{\partial\xi} - f''\frac{\partial f}{\partial\xi}\right) \quad (6)$$

$$\frac{1}{\mathrm{Pr}}\theta'' + f\theta' = 2\xi\left(f'\frac{\partial\theta}{\partial\xi} - \theta'\frac{\partial f}{\partial\xi}\right) \quad (7)$$

$$f'(\xi, 0) = 0, \qquad f(\xi, 0) + 2\xi\partial f(\xi, 0)/\partial\xi = 0,$$
$$\theta'(\xi, 0) = -\sqrt{2\xi}/(U/u_\infty), \qquad f'(\xi, \infty) = 1, \qquad \theta(\xi, \infty) = 0 \quad (8)$$

In the foregoing equations, the primes stand for partial derivatives of η and the buoyancy parameter Ω has the expression

$$\Omega = |\mathrm{Gr}|/\mathrm{Re}^{5/2} \quad (9)$$

wherein the Grashof number Gr and the Reynolds number Re are defined, respectively, as

$$\mathrm{Gr} = g\beta q_w R^4/k\nu^2, \qquad \mathrm{Re} = u_\infty R/\nu \quad (10)$$

It is noted here that the plus and minus signs in front of the buoyancy parameter Ω in equation (6) refer, respectively, to assisting and opposing flows.

The ξ-dependent coefficients appearing in the second and third terms on the left-hand side of equation (6) can be evaluated when the local free stream velocity distribution $U(x)$ is prescribed. At the stagnation point, equations (6)–(8) can be simplified to

$$f''' + ff'' + (1 - f'^2) \pm \Omega\theta/A^2 = 0 \quad (11)$$

$$\frac{1}{\mathrm{Pr}}\theta'' + f\theta' = 0 \quad (12)$$

$$f'(0) = f(0) = 0, \qquad \theta'(0) = -1/\sqrt{A}, \qquad f'(\infty) = 1, \qquad \theta(\infty) = 0 \quad (13)$$

where $A = 2$ for $U(x)$ from potential flow solution and $A < 2$ from measurements [4].

The physical quantities of interest here include the local friction factor C_f and the local Nusselt number Nu. They are defined, respectively, by

$$C_f = \tau_w/(\rho u_\infty^2/2), \qquad \mathrm{Nu} = hR/k \quad (14)$$

From the definitions of wall shear stress $\tau_w = \mu(\partial u/\partial y)_{y=0}$, local heat transfer coefficient $h = q_w/(T_w - T_\infty)$, and Fourier's law $q_w = -k(\partial T/\partial y)_{y=0}$, it can be shown that

$$C_f\mathrm{Re}^{1/2} = \sqrt{2}(U/u_\infty)^2 f''(\xi, 0)/\xi^{1/2}, \qquad \mathrm{NuRe}^{-1/2} = 1/\theta(\xi, 0) \quad (15)$$

Buoyancy-Force Dominated Case. When the buoyancy force dominates the flow field, it is logical to transform the governing

equations after the pattern of pure free convection. The transformation variables (X, Y), the reduced stream function $F(X, Y)$, and the dimensionless temperature $\phi(X, Y)$ for this case are now defined as

$$X = x/R, \qquad Y = (y/R)|\mathrm{Gr}|^{1/5} \qquad (16)$$

$$F(X, Y) = \frac{\psi(x, y)}{\nu X |\mathrm{Gr}|^{1/5}}, \qquad \phi(X, Y) = \frac{[T(x, y) - T_\infty]|\mathrm{Gr}|^{1/5}}{q_w R/k}$$
$$(17)$$

With equations (16) and (17), the transformation leads to

$$F''' + FF'' - F'^2 + \frac{1}{X} \frac{U}{u_\infty} \frac{d}{dX} \left(\frac{U}{u_\infty}\right) \Lambda + \frac{\sin X}{X} \phi$$
$$= X \left(F' \frac{\partial F'}{\partial X} - F'' \frac{\partial F}{\partial X}\right) \quad (18)$$

$$\frac{1}{\mathrm{Pr}} \phi'' + F\phi' = X \left(F' \frac{\partial \phi}{\partial X} - \phi' \frac{\partial F}{\partial X}\right) \qquad (19)$$

$$F'(X, 0) = 0, \qquad F(X, 0) + X\partial F(X, 0)/\partial X = 0, \qquad \phi'(X, 0) = -1$$

$$F'(X, \infty) = (1/X)(U/u_\infty)\Lambda^{1/2}, \qquad \phi(X, \infty) = 0 \qquad (20)$$

where the primes now stand for partial derivatives with respect to Y and the forced-flow effects are described by the parameter

$$\Lambda = \mathrm{Re}^2/|\mathrm{Gr}|^{4/5} = \Omega^{-4/5} \qquad (21)$$

The coefficients in front of Λ in equation (18) and in the boundary condition $F'(X, \infty)$ can be readily evaluated once the local free stream velocity $U(x)$ is specified. At the stagnation point, equations (18)–(20) reduce to

$$F''' + FF'' - F'^2 + A^2\Lambda + \phi = 0 \qquad (22)$$

$$\frac{1}{\mathrm{Pr}} \phi'' + F\phi' = 0 \qquad (23)$$

$$F'(0) = F(0) = 0, \qquad \phi'(0) = -1, \qquad F'(\infty) = A\Lambda^{1/2}, \qquad \phi(\infty) = 0$$
$$(24)$$

The local friction factor C_f and the local Nusselt number Nu for this case have the expressions

$$C_f\mathrm{Re}^{1/2} = 2XF''(X, 0)/\Lambda^{3/4}, \qquad \mathrm{NuRe}^{-1/2} = 1/[\phi(X, 0)\Lambda^{1/4}]$$
$$(25)$$

In the numerical computations, which covered $0 \le \Omega \le \infty$ (i.e., from pure forced convection to pure free convection), equations (6)–(8) were used for $0 \le \Omega \le 10$ and equations (18)–(20) for $1 \le \Omega \le \infty$ (i.e., $1 \ge \Lambda \ge 0$). They were solved by an efficient and accurate finite difference method described by Keller and Cebeci [2 and 3]. It was verified that the two sets of equations yielded the same results for the same values of Ω.

Results and Discussion

Numerical results were obtained for gases having a Prandtl number of 0.7 for buoyancy force parameter $\mathrm{Gr}/\mathrm{Re}^{5/2}$ ranging from 0 (i.e., pure forced convection) to ∞ (i.e., pure free convection with $\mathrm{Re}^2/\mathrm{Gr}^{4/5} = 0$) for assisting flow and from 0 to -2.0 for opposing flow. Two typical $U(x)$ expressions for free stream velocity distributions were used in the calculations. They are the inviscid flow velocity solution given by equation (2) and the velocity distributions from the measurements of Sogin and Subramanian [4] at a Reynolds number of $\mathrm{Re} = 61,000$, as given by equation (1) with $A = 1.820$, $B = -0.40$, and $C = 0$. This latter profile is valid for an angle of about 90 deg from the stagnation point. Thus, the results to be presented are terminated at $\Phi = 90$ deg.

The angular distributions of the local wall shear stress results $C_f\mathrm{Re}^{1/2}$ and the local Nusselt number results $\mathrm{NuRe}^{-1/2}$ are shown, respectively, in Figs. 1 and 2. As can be seen from the figures, the local wall shear and the local Nusselt number increase with increasing buoyancy force for assisting flow ($\mathrm{Gr}/\mathrm{Re}^{5/2} > 0$). This is because in
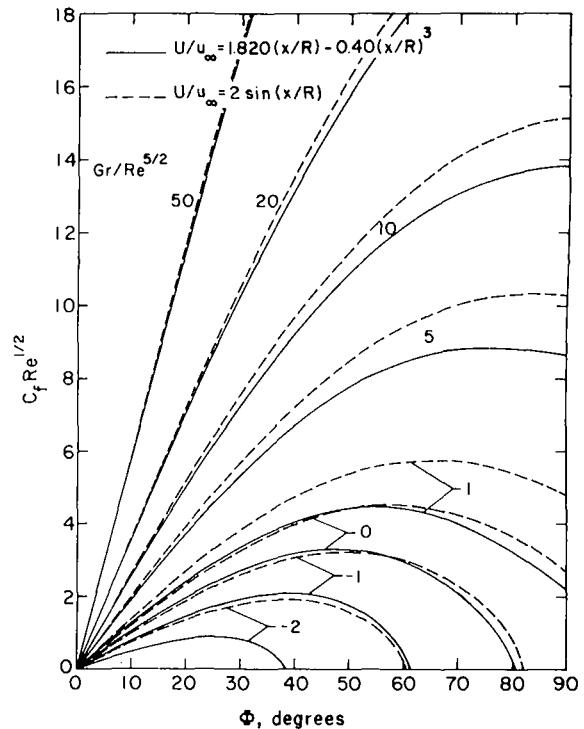

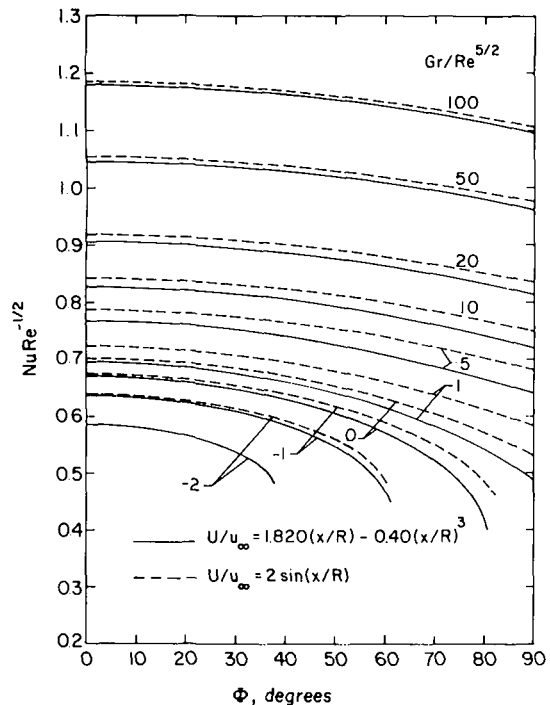Fig. 1   Angular distributions of the local wall shear stress, Pr = 0.7

Fig. 2   Angular distributions of the local Nusselt number, Pr = 0.7

the assisting flow case the buoyancy force induces a favorable pressure gradient which retards the flow separation and increases the velocity and temperature gradients at the wall. An opposite trend is in evidence for the opposing flow ($\mathrm{Gr}/\mathrm{Re}^{5/2} < 0$). An inspection of Figs. 1 and 2 also reveals that the variation of the local free stream velocity has a strong effect on the flow and heat transfer characteristics. For a given buoyancy force, the inviscid flow velocity distribution provides

local friction factor and Nusselt number that are much larger than those provided from measured forced convection flow. This effect is rather pronounced at large angles for small and moderate buoyancy forces, particularly for the opposing flow. However, for assisting flow with strong buoyancy forces ($Gr/Re^{5/2} \geq 20$), the dependence of the local friction factor and the local Nusselt number on the variation of the local free stream velocity distributions is seen to diminish as $Gr/Re^{5/2}$ increases.

It needs to be pointed out that the measured free stream velocity distribution used in the computations, equation (1), is for pure forced convection. For mixed convection flow with buoyancy force assisting, the actual local free stream velocity $U(x)$ is expected to lie between the measured forced convection flow [4] and the inviscid flow. Thus, the actual local wall shear and surface heat transfer results for the assisting flow case will probably lie somewhere between the values calculated by applying the two $U(x)$ expressions, with the results from the measured forced convection flow as the lower bounds and those from the inviscid flow as the upper bounds. For the opposing flow, the buoyancy force advances flow separation, and the results based on $U(x)$ from the measured forced convection flow may, therefore, be considered as the upper bounds. Thus, it can be concluded that the use of inviscid flow velocity distribution fails to provide reliable results in the region away from the stagnation point, particularly for the opposing flow.

The angular distributions of the local Nusselt number for large buoyancy parameters ($5 \leq Gr/Re^{5/2} \leq \infty$) are shown in Fig. 3 in terms of $NuGr^{-1/5}$. The curve for $Gr/Re^{5/2} = \infty$ (i.e., $Re^2/Gr^{4/5} = 0$) corresponds to the case of pure free convection and agrees very well with the results of Koh [6]. As the buoyancy parameter increases to ∞, the effect of the variation of the local free stream velocity distributions on the local Nusselt number diminishes completely.

It is of practical interest to compare the present local Nusselt number results for the Uniform Surface Heat Flux (UHF) with those for the Uniform Wall Temperature (UWT) reported in [1]. The dimensionless temperature and the Grashof number for the uniform wall temperature case are defined, respectively, by

$$\theta(\xi, \eta)_{UWT} = \phi(X, Y)_{UWT} = (T - T_\infty)/(T_w - T_\infty) \qquad (26)$$

$$Gr^* = g\beta(T_w - T_\infty)R^3/\nu^2 \qquad (27)$$

The corresponding expressions for the buoyancy parameter Ω^* and the local Nusselt number Nu_{UWT} for the forced-flow dominated case

are given by [1]

$$\Omega^* = |Gr^*|/Re^2 \qquad (28)$$

$$Nu_{UWT}Re^{-1/2} = -[(U/u_\infty)/\sqrt{2\xi}]\theta'(\xi, 0)_{UWT} \qquad (29)$$

and the forced-flow parameter Λ^* and the local Nusselt number for the buoyancy-dominated case by

$$\Lambda^* = Re^2/|Gr^*| \qquad (30)$$

$$Nu_{UWT}Re^{-1/2} = -\phi'(X, 0)_{UWT}\Lambda^{*-1/4} \qquad (31)$$

To facilitate a comparison of the results between the uniform surface heat flux and the uniform wall temperature, an equivalent buoyancy parameter Ω_e (or an equivalent forced-flow parameter Λ_e) between the two cases is defined by introducing the buoyancy parameter for the uniform wall temperature in terms of the local surface heat flux $q_w(x) = -k(\partial T/\partial y)_{y=0}$ such that

$$\Omega_e = [g\beta|q_w(x)|R^4/k\nu^2]/Re^{5/2} = |Gr_e|/Re^{5/2} \qquad (32)$$

For the forced-flow dominated case, one can obtain

$$\Omega_e = \Omega^* Nu_{UWT}Re^{-1/2} \qquad (33)$$

Similarly, for the buoyancy-force dominated case, one can find

$$\Lambda_e = \Lambda^{*4/5}[Nu_{UWT}Re^{-1/2}]^{-4/5} \qquad (34)$$

The Nusselt number ratio between the uniform surface heat flux and the uniform wall temperature, Nu_{UHF}/Nu_{UWT}, can be determined when $\Omega_e = \Omega_{UHF}$ (or $\Lambda_e = \Lambda_{UHF}$). This ratio is plotted against $Gr_e/Re^{5/2}$ in Fig. 4 for the angular positions of $\Phi = 0, 30, 60,$ and 90 deg. It can be seen from the figure that for a given buoyancy force the ratio Nu_{UHF}/Nu_{UWT} increases from unity as the angle Φ increases from 0 deg. In addition, for a given angular position, this ratio is seen to decrease as the buoyancy force increases. Thus, under equivalent buoyancy force effect, heating by uniform surface heat flux provides higher local Nusselt numbers than heating by uniform wall temperature.

Acknowledgments

References

1. Mucoglu, A., and Chen, T. S., "Analysis of Combined Forced and Free Convection Across a Horizontal Cylinder," (*Canadian Journal of Chemical Engineering*, in press.)
2. Keller, H. B., and Cebeci, T., "Accurate Numerical Methods for Boundary-Layer Flows. II: Two-Dimensional Turbulent Flows," *AIAA Journal*, Vol. 10, 1972, pp. 1193–1199.
3. Cebeci, T., "Laminar Free Convective Heat Transfer From the Outer Surface of a Vertical Slender Circular Cylinder," *Proceedings of the 5th In-*
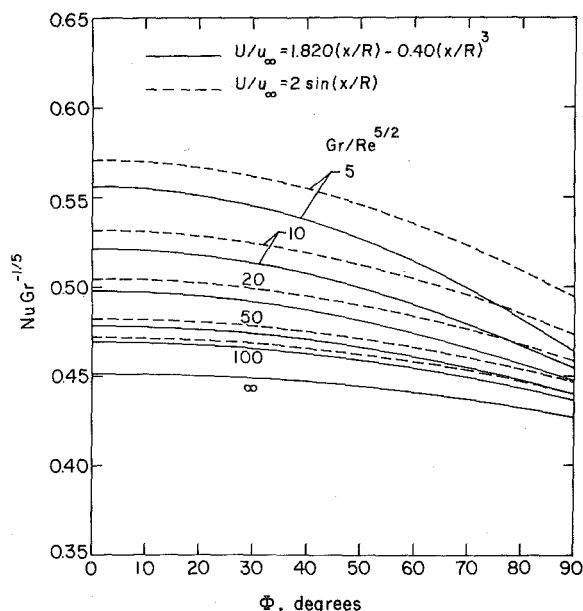

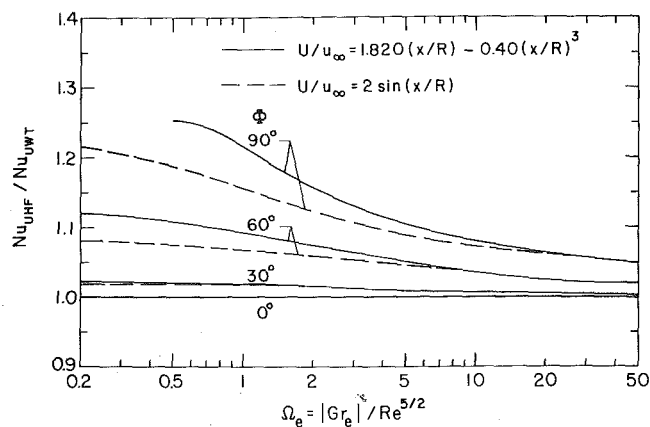**Fig. 3** Angular distributions of the local Nusselt number in terms of $NuGr^{-1/5}$, $Pr = 0.7$

Fig. 4 A comparison of local Nusselt numbers between uniform surface heat flux and uniform wall temperature

ternational Heat Transfer Conference, Vol. 3, Paper No. NC1.4, 1974, pp. 15–19.

4. Sogin, H. H., and Subramanian, V. S., "Local Mass Transfer From Circular Cylinders in Cross Flow," JOURNAL OF HEAT TRANSFER, TRANS. ASME, Series C, Vol. 83, 1961, pp. 483–493.

5. Sparrow, E. M., Quack, H., and Boerner, C. J., "Local Nonsimilarity Boundary-Layer Solutions," *AIAA Journal*, Vol. 8, 1970, pp. 1936–1942.

6. Koh, J. C. Y., "Laminar Free Convection From a Horizontal Cylinder With Prescribed Surface Heat Flux," *International Journal of Heat and Mass Transfer*, Vol. 7, 1964, pp. 811–813.

Laminarization in Low Reynolds Number Turbulent Duct Flows

H. Tanaka[1]
Jun-ichi Shimizu[2]

Introduction

In recent years much attention has been paid to the problem of reverse transition of turbulent to laminar flow caused by a strong acceleration. A number of experimental investigations [1–3][3] have been carried out on external boundary layer flows at relatively high Reynolds numbers. It has been found that the critical value of the acceleration parameter, $K = (\nu/U^2)(dU/dx)$ (U is the free stream velocity, ν the kinematic viscosity and x the distance in the streamwise direction), for the occurrence of reverse transition in external flows is 3×10^{-6}, independent of the Reynolds number [1]. A turbulent gas flow in a tube strongly heated will also revert to a laminar flow at a Reynolds number considerably higher than the lowest Reynolds number at which fully turbulent, isothermal flow can be maintained. Several investigators [4, 5] have suggested that the onset of laminarization in a heated pipe can be also predicted well by the acceleration parameter K, in which the mean flow velocity is adopted instead of the free stream velocity. The experimental results of reverse transition in internal flows, however, seem less complete because of the severe variations of physical properties imposed by large wall to bulk temperature ratios. The purpose of this investigation is to examine the laminarization phenomena in internal flows, under essentially constant property conditions, at relatively low Reynolds numbers, as have been encountered in the experiments on laminarization of heated pipe flows [4, 5].

Experiment

Heat transfer measurements have been performed for air flows in a horizontal, rectangular channel which is 1500 mm in length and 150 mm in width. Throughout the experiments, the height of the channel over the first 900 mm length has been kept constant as $h_0 = 30$ mm and the flow attains the fully developed state before being subjected to acceleration. In the succeeding accelerating section, the height of the duct, h, has been varied linearly by using a hinged roof plate. From the condition of continuity, this realizes the accelerated flow with a prescribed constant value of K according to the relation:

$$K = 2\beta/\text{Re} \qquad (1)$$

where β signifies the inclination of the roof plate, dh/dx, and the Reynolds number is defined by introducing a hydrodynamic equivalent diameter, d_e, as:
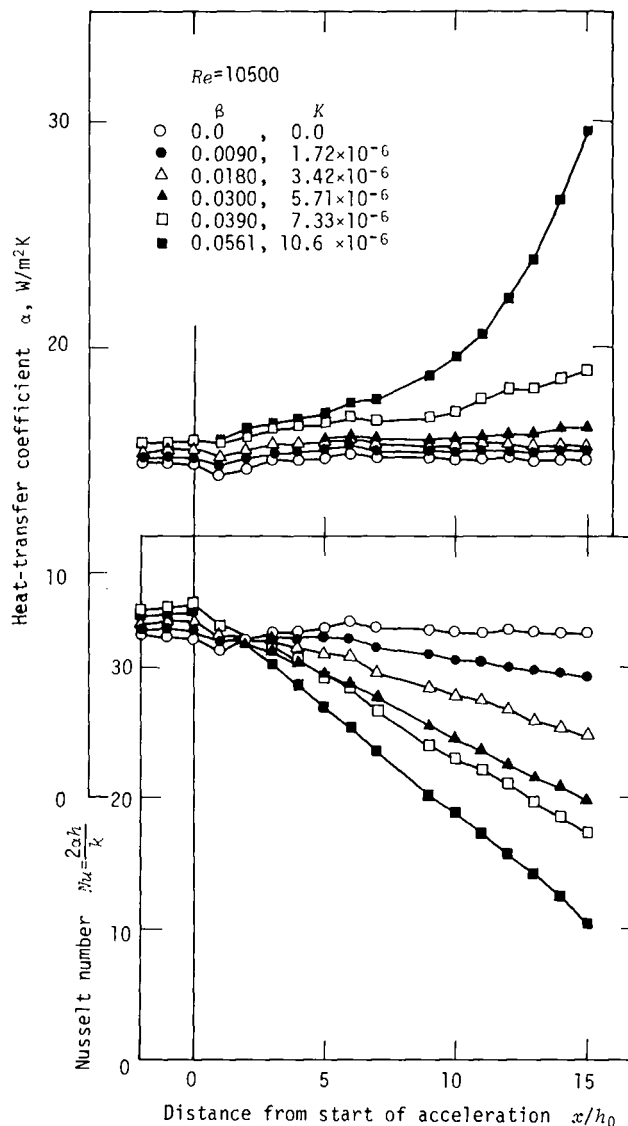
Fig. 1 Variations of the local heat-transfer coefficient and of the local Nusselt number with the distance from the start of acceleration

$$\text{Re} = d_e U/\nu = 2hU/\nu \qquad (2)$$

with the assumption of two-dimensional flow. The so defined Reynolds number becomes constant along the entire channel length, even if local values of h and U are introduced. It is noted that even a small gradient of $\beta = 0.015$ suffices to yield $K = 3 \times 10^{-6}$ when $\text{Re} = 1 \times 10^4$, as is easily understood from equation (1). As a heat transfer surface foil, a stainless steel plate, 0.1 mm thick and 130 mm wide, is fastened on the bottom plate over the entire channel length, and is slightly heated electrically by an A.C. power supply.

Results

The local heat transfer-coefficient α is determined from the measured wall temperature t_w and the bulk fluid temperature t_b as $\alpha = q/(t_w - t_b)$. The heat flux q is calculated from the electric input with the compensation for radiation. The variations of α and the local Nusselt number, $\text{Nu} = d_e\alpha/k = 2h\alpha/k$ (k is the thermal conductivity of air), along the distance from the beginning of acceleration are shown in Fig. 1 for various K's under $\text{Re} = 10,500$. Since the flow approaching the accelerating section has been designed to be both hydrodynamically and thermally developed, Nu's at $x/h_0 = 0$ are almost in agreement with the Dittus-Boelter formula: $\text{Nu} = 0.023 \, \text{Re}^{0.8} \text{Pr}^{0.4}$. Since

ternational Heat Transfer Conference, Vol. 3, Paper No. NC1.4, 1974, pp. 15–19.

4. Sogin, H. H., and Subramanian, V. S., "Local Mass Transfer From Circular Cylinders in Cross Flow," JOURNAL OF HEAT TRANSFER, TRANS. ASME, Series C, Vol. 83, 1961, pp. 483–493.

5. Sparrow, E. M., Quack, H., and Boerner, C. J., "Local Nonsimilarity Boundary-Layer Solutions," AIAA Journal, Vol. 8, 1970, pp. 1936–1942.

6. Koh, J. C. Y., "Laminar Free Convection From a Horizontal Cylinder With Prescribed Surface Heat Flux," International Journal of Heat and Mass Transfer, Vol. 7, 1964, pp. 811–813.

Laminarization in Low Reynolds Number Turbulent Duct Flows

H. Tanaka[1]
Jun-ichi Shimizu[2]

Introduction

In recent years much attention has been paid to the problem of reverse transition of turbulent to laminar flow caused by a strong acceleration. A number of experimental investigations [1–3][3] have been carried out on external boundary layer flows at relatively high Reynolds numbers. It has been found that the critical value of the acceleration parameter, $K = (\nu/U^2)(dU/dx)$ (U is the free stream velocity, ν the kinematic viscosity and x the distance in the streamwise direction), for the occurrence of reverse transition in external flows is 3×10^{-6}, independent of the Reynolds number [1]. A turbulent gas flow in a tube strongly heated will also revert to a laminar flow at a Reynolds number considerably higher than the lowest Reynolds number at which fully turbulent, isothermal flow can be maintained. Several investigators [4, 5] have suggested that the onset of laminarization in a heated pipe can be also predicted well by the acceleration parameter K, in which the mean flow velocity is adopted instead of the free stream velocity. The experimental results of reverse transition in internal flows, however, seem less complete because of the severe variations of physical properties imposed by large wall to bulk temperature ratios. The purpose of this investigation is to examine the laminarization phenomena in internal flows, under essentially constant property conditions, at relatively low Reynolds numbers, as have been encountered in the experiments on laminarization of heated pipe flows [4, 5].

Experiment

Heat transfer measurements have been performed for air flows in a horizontal, rectangular channel which is 1500 mm in length and 150 mm in width. Throughout the experiments, the height of the channel over the first 900 mm length has been kept constant as $h_0 = 30$ mm and the flow attains the fully developed state before being subjected to acceleration. In the succeeding accelerating section, the height of the duct, h, has been varied linearly by using a hinged roof plate. From the condition of continuity, this realizes the accelerated flow with a prescribed constant value of K according to the relation:

$$K = 2\beta/\text{Re} \qquad (1)$$

where β signifies the inclination of the roof plate, dh/dx, and the Reynolds number is defined by introducing a hydrodynamic equivalent diameter, d_e, as:
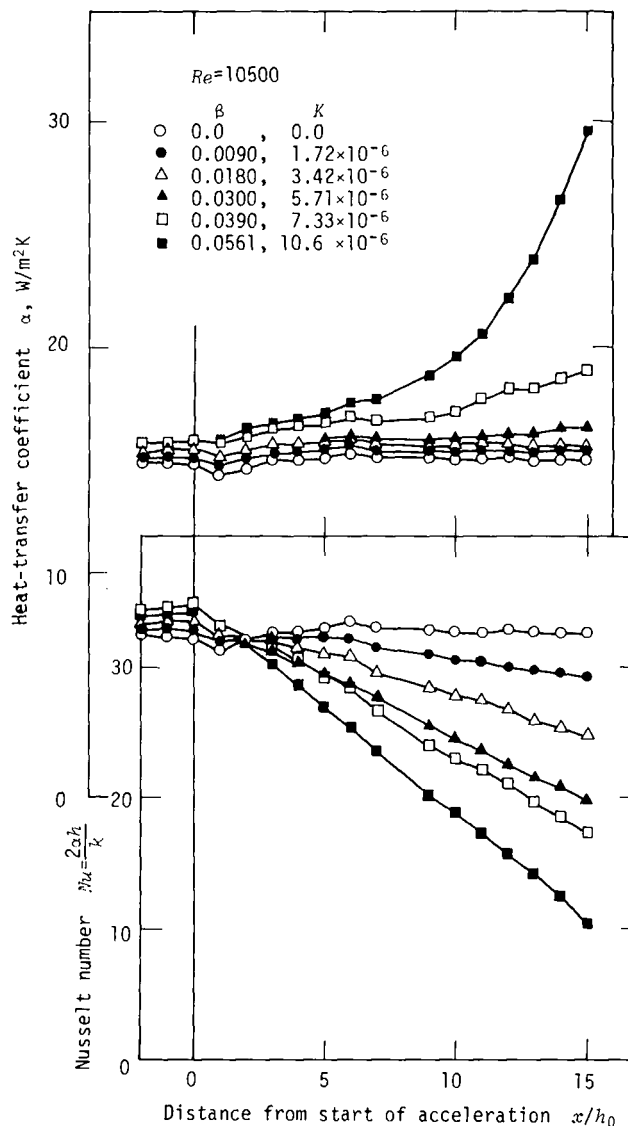

Fig. 1 Variations of the local heat-transfer coefficient and of the local Nusselt number with the distance from the start of acceleration

$$\text{Re} = d_e U/\nu = 2hU/\nu \qquad (2)$$

with the assumption of two-dimensional flow. The so defined Reynolds number becomes constant along the entire channel length, even if local values of h and U are introduced. It is noted that even a small gradient of $\beta = 0.015$ suffices to yield $K = 3 \times 10^{-6}$ when Re = 1×10^4, as is easily understood from equation (1). As a heat transfer surface foil, a stainless steel plate, 0.1 mm thick and 130 mm wide, is fastened on the bottom plate over the entire channel length, and is slightly heated electrically by an A.C. power supply.

Results

The local heat transfer-coefficient α is determined from the measured wall temperature t_w and the bulk fluid temperature t_b as $\alpha = q/(t_w - t_b)$. The heat flux q is calculated from the electric input with the compensation for radiation. The variations of α and the local Nusselt number, Nu = $d_e \alpha/k = 2h\alpha/k$ (k is the thermal conductivity of air), along the distance from the beginning of acceleration are shown in Fig. 1 for various K's under Re = 10,500. Since the flow approaching the accelerating section has been designed to be both hydrodynamically and thermally developed, Nu's at $x/h_0 = 0$ are almost in agreement with the Dittus-Boelter formula: Nu = 0.023 $\text{Re}^{0.8}\text{Pr}^{0.4}$. Since
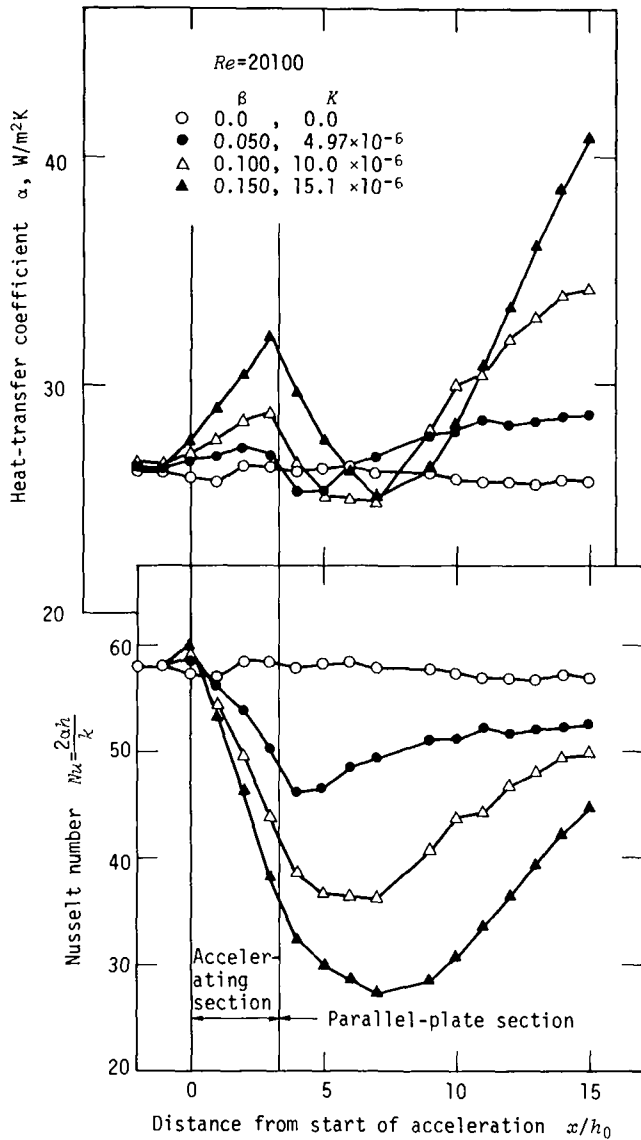
Copyright © 1977 by ASME

Fig. 2 Experimental results for an accelerating section 100 mm long succeeded by a parallel-plate section 500 mm long
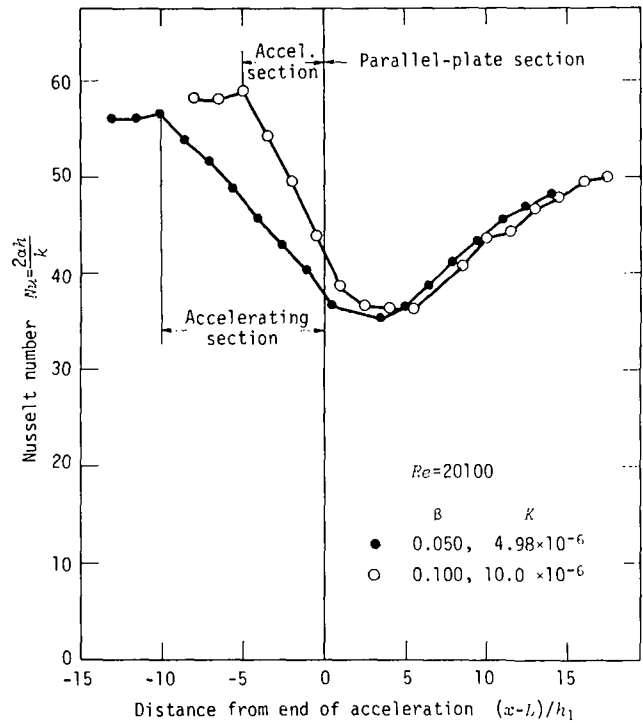

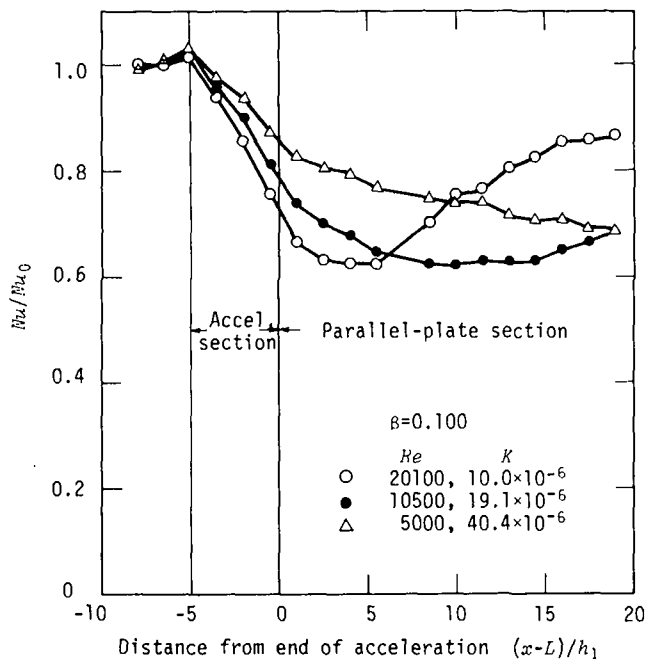Fig. 3 Experimental results for two accelerating ducts with different lengths but with the same terminal height

Fig. 4 Experimental results for various Reynolds numbers with the same accelerating duct

Re defined by equation (2) remains constant even in the accelerating section, Nu is expected to retain its initial value Nu_0, provided the flow achieves the fully turbulent structure from station to station, conforming to the local mean flow velocity. Then α will increase downstream owing to the increase in the mean flow velocity (i.e. with constant Nu, α increases as $2h$ decreases). From Fig. 1, however, the streamwise variation of the measured α appears nearly constant (for lower values of K) by the effect due to acceleration. Therefore, Nu decreases virtually in proportion to the duct height h and shows substantial deteriorations as K is increased (in proportion to β). The laminarization effect is certainly appreciable even for $K = 1.72 \times 10^{-6}$ ($\beta = 0.009$). When K becomes very large, α shows a tendency to increase markedly downstream (see $K = 10.6 \times 10^{-6}$ in Fig. 1).

In the second set of experiments, the flow, which is fully developed in the initial 900 mm entrance section, is accelerated during the finite length of linear contraction, and then is passed through a parallel-plate section. Fig. 2 shows the experimental results obtained for comparatively large β's (besides $\beta = 0$) under Re = 20100, by using an accelerating section 100 mm long which is succeeded by a parallel-plate section 500 mm long. In this figure, again (also in Figs. 3 and 4), Nu, in the approach to the accelerating section, satisfies the

Dittus-Boelter formula. Fig. 2 along with Figs. 3 and 4 demonstrates how the laminarized Nusselt number behaves in the parallel-plate section and ultimately recovers the initial level. It is noticeable in the upper part of Fig. 2 that α does not increase monotonously but turns to decrease at the initial region of the parallel-plate section, and then takes its minimum somewhat downsam. This behavior is quite similar to the experimental results by Mills [6], where heat transfer mea-

surement has been made in the entrance region of a circular pipe with various entrance configurations. According to [6], in the case of a bellmouthed intake the hydrodynamic and thermal boundary layers start simultaneously along the wall surface, at first in laminar state, then change through a transition region to turbulent flow. It is plausible that a physical mechanism similar to these qualitative changes of flow characteristics underlies the previously mentioned behavior of the heat-transfer coefficient in Fig. 2. The following observations will give further explanation of this mechanism.

The extent of laminarization at a particular station may be represented by the proportion of Nu at that station to Nu$_0$ of the fully developed flow. In the experiment shown in Fig. 3, two kinds of accelerating ducts have been employed, the lengths L which are different by a factor of two, but the heights of which at the terminal end, h_1, are the same. It appears from Fig. 3 that the flow which has been laminarized, to the same extent through any accelerating section, traces almost the same process of retransition to turbulence. In addition, from Fig. 2, it can be said that the retransition point shifts downstream as the laminarization effect becomes stronger. (This shifting will be more pronounced if we normalize the distance from the end of acceleration, $(x-L)$, by the terminal height h_1, as in Fig. 3). Finally, the retransition point goes upstream with increasing Re, as

is demonstrated in Fig. 4. From a practical point of view, it must be mentioned that when Re becomes considerably small, the laminarization effect retains its influence farther downstream.

References

1 Moretti, P. M., and Kays, W. M., "Heat Transfer to a Turbulent Boundary Layer with Varying Free-Stream Velocity and Varying Surface Temperature," *International Journal of Heat and Mass Transfer*, Vol. 8, 1965, pp. 1187–1202.

2 Back, L. H., and Seban, R. A., "Flow and Heat Transfer in a Turbulent Boundary Layer with Large Acceleration Parameter," *Proceedings of the 1967 Heat Transfer and Fluid Mechanics Institute*, edited by P. A. Libby et al., pp. 410–426.

3 Patel, V. C., and Head, M. R., "Reversion of Turbulent to Laminar Flow," *Journal of Fluid Mechanics*, Vol. 34, Part 2, 1968, pp. 371–392.

4 Coon, W. C., and Perkins, H. C., "Transition from the Turbulent to the Laminar Regime for Internal Convective Flow with Large Property Variations," JOURNAL OF HEAT TRANSFER, TRANS. ASME, Series C, Vol. 92, No. 3, 1970, pp. 506–512.

5 Bankston, C. A., "The Transition from Turbulent to Laminar Gas Flow in a Heated Pipe," JOURNAL OF HEAT TRANSFER, TRANS. ASME, Series C, Vol. 92, No. 4, 1970, pp. 569–579.

6 Mills, A. F., "Experimental Investigation of Turbulent Heat Transfer in the Entrance Region of a Circular Conduit," *Journal of Mechanical Engineering Science*, Vol. 4, No. 1, 1962, pp. 63–77.

Heat Transfer in Micropolar Laminar Radial Channel Flow

M. S. Khader[1] and R. I. Vachon[2]

Nomenclature

C_p = specific heat
Pr = Prandtl number based on the apparent viscosity, $C_p \mu_0/K$
P = pressure
P_0 = reference pressure at r_0
Re = channel Reynolds number based on the apparent viscosity, $\rho U_0 t/\mu_0$
Q = flow rate
r = radial coordinate
r_i = inlet radius of the channel
r_0 = outlet radius of the channel
T = temperature of the fluid
T_w = wall temperature
T_0 = initial fluid temperature
t = half the clearance between disks
u = radial velocity
W = angular velocity of particle in the θ-direction
x_i = nondimensional inlet radius, r_i/t
z = axial coordinate
$\overline{Nu}$ = average Nusselt number
μ = shear viscosity coefficient
μ_0 = apparent viscosity
μ_1 = rotational viscosity coefficient
γ = microrotational gradient viscosity
β = nondimensional parameter, $U_0^2\mu/C_p(T_w - T_0)\mu_0$
θ = dimensionless temperature, $(T - T_w)/(T_0 - T_w)$
ρ = density

[1] Assistant Professor, Mechanical Engineering Department, Cairo University, Giza, Egypt. Assoc. Mem. ASME.

[2] Professor, Mechanical Engineering Department, Auburn University, Auburn, Ala. Mem. ASME.

Introduction

Fluids with substructures occur in many engineering applications and in nature. Fluids with polymeric additives, fluid suspensions, liquid crystals, and blood are good examples of fluids with substructures. Anzelius [1][3] was one of the first to observe the unexpected behavior of fluids containing oblong molecule substructures in shear flow. Jeffery [2] discussed the modification produced in the motion of a classical or Stokesian fluid of infinite extent by the presence of single ellipsoidal particles. Moreover, Henniker [3] noted that some real fluids showed an increase in viscosity when they flow in very thin channels. He described an experiment where the viscosity of water exhibited a tenfold increase for flow between a 2500 Å width glass plate channel.

Recently, several new developments in mechanics of fluid with substructures have been based on a continuum approach and are referred to using the terms microcontinua or Cosserat continuum. Grad [4] was the first to introduce the linear constitutive equation for a polar fluid (fluid with substructures) based on a statistical approach. Aero, et al. [5], Cowin [6], and Condiff and Dahler [7] later developed the same constitutive equations from different points of view, either based on statistical mechanics or the Cosserat continuum. Eringen [8] introduced the general theory of nonlinear microcontinua where the governing and constitutive equations were formulated. Various classes of these structured fluids were introduced by Eringen [9, 10]. As a subclass of these fluids, Eringen introduced micropolar fluids [10] in which the particles were assumed to be rigid and were allowed to undergo only rigid rotations. Such materials exhibit only microrotational effects and can support body and surface couples.

Also Ericksen [11 and 12] has developed a continuum theory which takes into account the presence of substructures in the fluid. Allen, et al. [13], among others, have extended Ericksen's theoretical model to account for particle interactions as well as the explicit inertial characteristics of the substructure. Kline, et al. [14] have investigated experimentally the Ericksen continuum model and found the model to be in agreement with measurements to determine the forces on suspended particles in Poiseuille flow. Turk, et al. [15] presented a comparison of blood flow obtained by using micropolar fluid theory with the experimental data of actual blood flow.

In the field of heat transfer, Eringen [16], Kazakia and Ariman [17],

[3] Numbers in brackets designate References at end of technical note.

surement has been made in the entrance region of a circular pipe with various entrance configurations. According to [6], in the case of a bellmouthed intake the hydrodynamic and thermal boundary layers start simultaneously along the wall surface, at first in laminar state, then change through a transition region to turbulent flow. It is plausible that a physical mechanism similar to these qualitative changes of flow characteristics underlies the previously mentioned behavior of the heat-transfer coefficient in Fig. 2. The following observations will give further explanation of this mechanism.

The extent of laminarization at a particular station may be represented by the proportion of Nu at that station to Nu_0 of the fully developed flow. In the experiment shown in Fig. 3, two kinds of accelerating ducts have been employed, the lengths L which are different by a factor of two, but the heights of which at the terminal end, h_1, are the same. It appears from Fig. 3 that the flow which has been laminarized, to the same extent through any accelerating section, traces almost the same process of retransition to turbulence. In addition, from Fig. 2, it can be said that the retransition point shifts downstream as the laminarization effect becomes stronger. (This shifting will be more pronounced if we normalize the distance from the end of acceleration, $(x-L)$, by the terminal height h_1, as in Fig. 3). Finally, the retransition point goes upstream with increasing Re, as

is demonstrated in Fig. 4. From a practical point of view, it must be mentioned that when Re becomes considerably small, the laminarization effect retains its influence farther downstream.

References

1 Moretti, P. M., and Kays, W. M., "Heat Transfer to a Turbulent Boundary Layer with Varying Free-Stream Velocity and Varying Surface Temperature," *International Journal of Heat and Mass Transfer*, Vol. 8, 1965, pp. 1187–1202.

2 Back, L. H., and Seban, R. A., "Flow and Heat Transfer in a Turbulent Boundary Layer with Large Acceleration Parameter," *Proceedings of the 1967 Heat Transfer and Fluid Mechanics Institute*, edited by P. A. Libby et al., pp. 410–426.

3 Patel, V. C., and Head, M. R., "Reversion of Turbulent to Laminar Flow," *Journal of Fluid Mechanics*, Vol. 34, Part 2, 1968, pp. 371–392.

4 Coon, W. C., and Perkins, H. C., "Transition from the Turbulent to the Laminar Regime for Internal Convective Flow with Large Property Variations," JOURNAL OF HEAT TRANSFER, TRANS. ASME, Series C, Vol. 92, No. 3, 1970, pp. 506–512.

5 Bankston, C. A., "The Transition from Turbulent to Laminar Gas Flow in a Heated Pipe," JOURNAL OF HEAT TRANSFER, TRANS. ASME, Series C, Vol. 92, No. 4, 1970, pp. 569–579.

6 Mills, A. F., "Experimental Investigation of Turbulent Heat Transfer in the Entrance Region of a Circular Conduit," *Journal of Mechanical Engineering Science*, Vol. 4, No. 1, 1962, pp. 63–77.

Heat Transfer in Micropolar Laminar Radial Channel Flow

M. S. Khader[1] and R. I. Vachon[2]

Nomenclature

C_p = specific heat

Pr = Prandtl number based on the apparent viscosity, $C_p \mu_0/K$

P = pressure

P_0 = reference pressure at r_0

Re = channel Reynolds number based on the apparent viscosity, $\rho U_0 t/\mu_0$

Q = flow rate

r = radial coordinate

r_i = inlet radius of the channel

r_0 = outlet radius of the channel

T = temperature of the fluid

T_w = wall temperature

T_0 = initial fluid temperature

t = half the clearance between disks

u = radial velocity

W = angular velocity of particle in the θ-direction

x_i = nondimensional inlet radius, r_i/t

z = axial coordinate

$\overline{Nu}$ = average Nusselt number

μ = shear viscosity coefficient

μ_0 = apparent viscosity

μ_1 = rotational viscosity coefficient

γ = microrotational gradient viscosity

β = nondimensional parameter, $U_0^2\mu/C_p(T_w - T_0)\mu_0$

θ = dimensionless temperature, $(T - T_w)/(T_0 - T_w)$

ρ = density

Introduction

Fluids with substructures occur in many engineering applications and in nature. Fluids with polymeric additives, fluid suspensions, liquid crystals, and blood are good examples of fluids with substructures. Anzelius [1][3] was one of the first to observe the unexpected behavior of fluids containing oblong molecule substructures in shear flow. Jeffery [2] discussed the modification produced in the motion of a classical or Stokesian fluid of infinite extent by the presence of single ellipsoidal particles. Moreover, Henniker [3] noted that some real fluids showed an increase in viscosity when they flow in very thin channels. He described an experiment where the viscosity of water exhibited a tenfold increase for flow between a 2500 Å width glass plate channel.

Recently, several new developments in mechanics of fluid with substructures have been based on a continuum approach and are referred to using the terms microcontinua or Cosserat continuum. Grad [4] was the first to introduce the linear constitutive equation for a polar fluid (fluid with substructures) based on a statistical approach. Aero, et al. [5], Cowin [6], and Condiff and Dahler [7] later developed the same constitutive equations from different points of view, either based on statistical mechanics or the Cosserat continuum. Eringen [8] introduced the general theory of nonlinear microcontinua where the governing and constitutive equations were formulated. Various classes of these structured fluids were introduced by Eringen [9, 10]. As a subclass of these fluids, Eringen introduced micropolar fluids [10] in which the particles were assumed to be rigid and were allowed to undergo only rigid rotations. Such materials exhibit only microrotational effects and can support body and surface couples.

Also Ericksen [11 and 12] has developed a continuum theory which takes into account the presence of substructures in the fluid. Allen, et al. [13], among others, have extended Ericksen's theoretical model to account for particle interactions as well as the explicit inertial characteristics of the substructure. Kline, et al. [14] have investigated experimentally the Ericksen continuum model and found the model to be in agreement with measurements to determine the forces on suspended particles in Poiseuille flow. Turk, et al. [15] presented a comparison of blood flow obtained by using micropolar fluid theory with the experimental data of actual blood flow.

In the field of heat transfer, Eringen [16], Kazakia and Ariman [17],

[1] Assistant Professor, Mechanical Engineering Department, Cairo University, Giza, Egypt. Assoc. Mem. ASME.

[2] Professor, Mechanical Engineering Department, Auburn University, Auburn, Ala. Mem. ASME.

[3] Numbers in brackets designate References at end of technical note.

and Kline and Allen [18] introduced the energy equation for heat-conducting micropolar fluids. Constitutive equations appropriate to describe the thermal and mechanical response of micropolar fluids were postulated and subsequently linearized, and the energy equation was derived. An updated review of the theory of microcontinua fluids and the application of the theory is given by Ariman, et al. [19] and Cowin [20].

The evidence continues to grow that these recent theories for the behavior of fluids with microstructures will help in clarifying some of the unusual behavior of real fluids.

In this work, the theory for fluids with microstructures (micropolar) is used to analyze the flow and heat transfer in radial channel flow as a first approximation to the cases of thrust bearings, radial diffusers and compact heat exchangers, when the fluid is structures and/or when the characteristic geometric dimension of flow is small.

Flow Field. For the present problem, the analysis assumes steady, slow, imcompressible, symmetrical flow between two circular disks with $t/r_0 \ll 1$, as shown in Fig. 1. Moreover, for the region of flow far from the inlet, i.e., $r/t \gg 1$, the velocity in the axial direction is so small compared with the main radial velocity, u, that it may be neglected as a first approximation. Under these assumptions, the flow governing equations with vanishing inertia, body and couples terms are:

$$\frac{\partial}{\partial r}(ru) = 0 \tag{1}$$

$$\left.\begin{array}{l} \dfrac{\partial P}{\partial r} = (\mu + \mu_1)\left[\nabla^2 u - \dfrac{u}{r^2}\right] + 2\mu_1 \dfrac{\partial W}{\partial z} \\[2mm] \dfrac{\partial P}{\partial z} = 2\mu_1\left(\dfrac{\partial W}{\partial r} + \dfrac{W}{r}\right) \end{array}\right\} \tag{2}$$

$$-2\mu_1\left(\frac{\partial u}{\partial z} + 2W\right) + \gamma\left(\nabla^2 W - \frac{W}{r^2}\right) = 0 \tag{3}$$

with

$$\nabla^2 = \frac{\partial^2}{\partial r^2} + \frac{1}{r}\frac{\partial}{\partial r} + \frac{\partial^2}{\partial z^2}$$

(For complete derivation of the fundamental equations, the reader is referred to [8, 21]).

Where the other components of the angular velocity are found to be vanished by virtue of the foregoing assumptions and inspection of the equations of motion in the three directions, the boundary conditions are taken as:

$$u = 0 \text{ at } z = \pm t, \quad W = 0 \text{ at } z = \pm t$$

The last boundary condition represents the condition of a wall that prevents the spin of the microstructures, which is one extreme case. The opposite extreme occurs when the wall offers no resistance to spin. Therefore, the condition of zero spin is one of the possible boundary conditions which depends on the nature of the fluid and the confining wall.
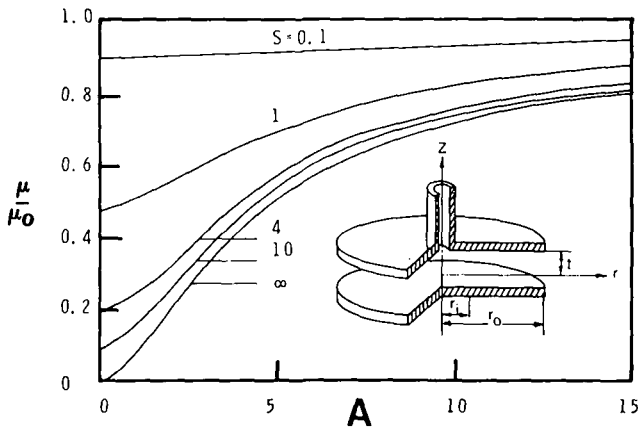
By introducing the following nondimensional variables

$$x = r/t, \quad y = z/t, \quad \bar{u} = u/U_0, \quad \text{and } \overline{W} = Wt/U_0$$

where $U_0 = Q/t^2$, equation (1) can be integrated to give

$$\bar{u} = F(Y)/x \tag{4}$$

As the velocity in the z-direction is small in comparison to the main velocity, u, in the r-direction, the flow is then parallel and $\partial P/\partial z$ is small, and the second equation of (2) then gives

$$\overline{W} = G(y)/x \tag{5}$$

Substituting equations (4) and (5) into equations (1) and (2), the nondimensional equations of motion become

$$(1 + s)F'' + 2sG' = x(dP/dx)(t/\mu U_0) \tag{6}$$

and

$$\frac{\gamma}{\mu t^2}G'' - 2s(F' + 2G) = 0 \tag{7}$$

where $s = \mu_1/\mu$ while the boundary conditions transform to

$$F(1) = F(-1) = 0 \text{ and } G(1) = G(-1) = 0 \tag{8}$$

The source discharge at the center of the channel is given by

$$Q = \int_{-t}^{t} 2\pi r u \, dz = \int_{-1}^{+1} 2\pi t^2 F U_0 dy; \quad \text{or } \int_{-1}^{+1} F dy = \tfrac{1}{2}\pi \tag{9}$$

Solution. Equations (6) and (7) are coupled total differential equations which give the solutions of both $\overline{U}$ and $\overline{W}$ in terms of dP/dx, and, upon using equation (9) for the discharge to eliminate the pressure gradient, the following solutions are obtained:

$$F = \frac{\left[1 - y^2 + \dfrac{2s}{1+s}\dfrac{1}{m}\dfrac{\cosh m}{\sinh m}\left(\dfrac{\cosh my}{\cosh m} - 1\right)\right]}{4\pi\left[\dfrac{1}{3} + \dfrac{s}{1+s}\dfrac{1}{m^2} - \dfrac{s}{1+s}\dfrac{1}{m}\dfrac{\cosh m}{\sinh m}\right]} \tag{10}$$

and

$$G = \frac{\left[y - \dfrac{\sinh my}{\sinh m}\right]}{4\pi\left[\dfrac{1}{3} + \dfrac{s}{1+s}\dfrac{1}{m^2} - \dfrac{s}{1+s}\dfrac{1}{m}\dfrac{\cosh m}{\sinh m}\right]} \tag{11}$$

While the pressure distribution is given by

$$\frac{(P - P_0)t^3}{Q\mu} = \frac{-1}{4\pi\left[\dfrac{1}{3} + \dfrac{s}{s+1}\dfrac{1}{m^2} - \dfrac{s}{s+1}\dfrac{1}{m}\dfrac{\cosh m}{\sinh m}\right]}\ln\left(\frac{r}{r_0}\right) \tag{12}$$

where

$$m = \left[\frac{s}{1+s}A^2\right]^{1/2} \text{ and } A^2 = \frac{4\mu t^2}{\gamma}$$

The parameter m^2 can be viewed physically as the ratio of two Reynolds numbers, the apparent and vortex Reynolds numbers. The parameter s is the coupling number and measures the magnitude of the ratio of viscous forces of relative rotation to the Newtonian viscous forces. In addition, A is a nondimensional length ratio of flow characteristic length, t, to a fluid characteristic length $(\gamma/4\mu)^{1/2}$. From the previous analysis, one can predict the apparent viscosity μ_0 if the micropolar fluid behaved as a homogeneous Newtonian fluid. The volumetric flow rate Q is given in terms of $P - P_0$ for a Newtonian fluid as

$$Q = \frac{-\dfrac{1}{3}(P - P_0)t^3 4\pi}{\mu_0 \ln(r/r_0)} \tag{13}$$

Fig. 1 Effective viscosity as a function of A

Equating (13) and the resulting equation for Q from (12), one obtains

$$\mu_0 = \frac{\frac{1}{3}\mu}{\left[\frac{1}{3} + \frac{s}{s+1}\frac{1}{m^2} - \frac{s}{s+1}\frac{1}{m}\frac{\cosh m}{\sinh m}\right]} \quad (14)$$

for the apparent viscosity of the flow μ_0.

Heat Transfer. The solution of the momentum equation gives the starting point for solving the energy equation. The configuration of the thermal field for the present problem is shown in Fig. 1. The two disks are maintained at the constant temperature T_W from r_i to r_0. The fluid enters at r_i with constant temperature T_0 and leaves at r_0. The fluid is assumed to be thermally conducting with constant properties. By considering $t/r_0 \ll 1$, it is possible to perform an order of magnitude estimate on the terms of the energy equation in a manner comparable to that used in developing the boundary layer equations. This estimate showed that the conduction in the r-direction is negligible in comparison with the axial conduction. Since the flow is symmetrical and parallel, i.e., the axial velocity is zero, then the energy equation takes the form

$$\rho C_p u \frac{\partial T}{\partial r} = K \frac{\partial^2 T}{\partial z^2} + (\mu_1 + \mu)\left(\frac{du}{dz}\right)^2$$
$$+ \mu_1\left(2W\frac{\partial u}{\partial z} + 2W^2\right) + \gamma\left(\frac{\partial W}{\partial z}\right)^2 \quad (15)$$

Also, the thermal entrance effect can be neglected for extremely small clearance between the disks ($t/r_0 \ll 1$).

For a constant wall temperature the boundary and initial conditions are stated as

$$T = T_w \text{ at } z = \pm t, \quad T = T_0 \text{ at } r = r_i \text{ and } z \quad (16)$$

The energy equation becomes

$$\frac{F}{x}\frac{\partial \theta}{\partial x} = \frac{1}{RePr}\frac{\partial^2 \theta}{\partial y^2} + \frac{\beta}{Re}\frac{1}{x^2}[(1+s)F'^2 + 2s(GF' + G^2) + sAG'^2]$$
$$\quad (17)$$

after introducing the dimensionless temperature, the velocity and microrotation functions, F and G, from the previous field flow analysis. Inspection of equation (17) shows that the temperature distribution is of the form $\theta = \theta\,(x, y, PrRe, \beta, Re, s, A)$. This functional dependency of the temperature distribution is different from that of the case of a zero microrotation (Newtonian) fluid solved by Kreith [21], in that it includes the three parameters, β, s and A. However, by taking the limit and $s \to 0$, one can obtain the solution for the case of zero microrotation, and as $\beta \to 0$ and $s \to 0$, one gets the case solved by Kreith [21] (i.e., no dissipation).

In order to facilitate the comparison of the results of the present study with the case of a zero microrotation fluid of reference [17], equation (17) is written in terms of the Graetz number Gz, by introducing the transformation

$$\eta = \frac{x^2 - x_i^2}{2RePr} = \frac{x^2 - x_i^2}{2Pe} = \frac{1}{Gz} \quad (18)$$

Equation (17) becomes

$$F\frac{\partial \theta}{\partial \eta} = \frac{\partial^2 \theta}{\partial y^2} + \frac{\beta}{(2Re + x_i^2/Pr)}[(1+s)F'^2$$
$$+ 2s(GF'^2 + G'^2) + sAG'^2] \quad (19)$$

with the boundary and initial conditions

$$\theta(0, y) = 1, \quad \theta(\eta, 1) = 0, \quad \theta(\eta, -1) = 0 \quad (20)$$

Solution

Because of the nonhomogeneity in the coordinate variables, the energy equation (20) developed in the last section does not lend itself to the general methods of analytical solution. A numerical solution

utilizing a finite difference technique is developed and used for the solution. When the finite difference scheme is employed, the derivatives in the partial differential equation are replaced by difference quotients, and this results in a set of difference equations. The solution can then be obtained by solving these algebraic equations, provided that the parameters Re, Pr, β, s, A, and x_i are known values; however, the solution can be made more general by reducing the number of these parameters.

Kreith [22] established an experimental relationship between the entrance length parameter x_i, at which the flow is laminar fully developed, and the Reynolds number of the channel as $x_i = 4\pi B$ $Re^{1/2}$ with B as an experimental constant ranging from 0.24–0.32 with an average value of 0.28.

By introducing the above relation for the entrance length into the energy equation (19), one obtains

$$F\frac{\partial \theta}{\partial \eta} = \frac{\partial^2 \theta}{\partial y^2} + \frac{E}{(2\eta + C/Pr)}[(1+s)F'^2$$
$$+ 2s(GF'^2 + G'^2) + sAG'^2] \quad (21)$$

where $E = \beta/Re$ and $C = 4\pi B^2 \simeq 1$. Equation (21) together with equation (20) represent the final dimensionless form of the thermal field governing equation which is solved numerically. After the temperature distribution θ is evaluated, the average Nusselt number can be determined, thereby enabling the temperature of the fluid leaving the channel to be calculated. For micropolar fluids, the heat flux at the wall is coupled with the gradient of microrotation in the radial direction. However, for the present analysis this gradient is zero ($\overline{W} = G(Y)/x$, and $\partial \overline{W}/\partial x)_{wall} = -G(0)/x^2$). The average Nusselt number is defined as

$$\overline{Nu} = \frac{2t h_m}{K} = \frac{1}{\eta_0}\int^\eta -\frac{\partial \theta}{\partial y}\bigg|_{y=1} d\eta \quad (22)$$

This Nusselt number is based on the difference between the initial temperature T_0 and the wall temperature T_w.

Discussion

From the previous analyses of the flow and the thermal fields of a micropolar fluid, one finds that in addition to the Newtonian flow parameters, two more parameters are shown, namely s & A. The first parameter designates the coupling of equations (6) and (7). For the limiting case of $s \to 0$, these equations become uncoupled and reduce to the usual Newtonian flow equations with a solution giving a parabolic velocity distribution and temperature distribution, as given in [21]. The second parameter A, is viewed as a measure of the relative size of the microstructure relative to the channel characteristic length, t. This parameter is similar in a sense to the Knudsen number used to characterize flow regimes. As A becomes small, the microstructure size relative to the channel becomes small. In the limit as $A \to 0$, the expression for velocity, pressure and temperature become similar to the case of Newtonian fluid with effective viscosity equal to $(\mu + \mu_1)$. On the other hand, as A becomes large, the effect of microstructures becomes more pronounced. As $A \to \infty$, the fluid flow and thermal field will correspond to those for a Newtonian fluid with effective viscosity equal to μ. Fig. 1 represents the effective viscosity as a function of A for different values of s. Since an order of magnitude of one for A represents the case of microstructure size comparable to the channel width, it was decided to show the results for a fixed value of $A = 1$. Furthermore, it was found that the value of A does not influence the results of both the flow and heat transfer, as its limit of influence is to change the apparent viscosity from μ to $\mu + \mu_1$ only for changes $0 \leq A \leq \infty$.

Fig. 2 shows a plot for the pressure distribution inside the channel. The effect of the presence of microstructures in the fluid is indicated by the parameter s. As the value of s increases, the magnitude of pressure also increases for the same flow rate. In this plot, the case $s = 0$ represents the classical case of Newtonian fluid with zero-microrotation (no microstructures). This increase in the pressure drop inside the channel is a consequence of the increase in the wall shear stress.
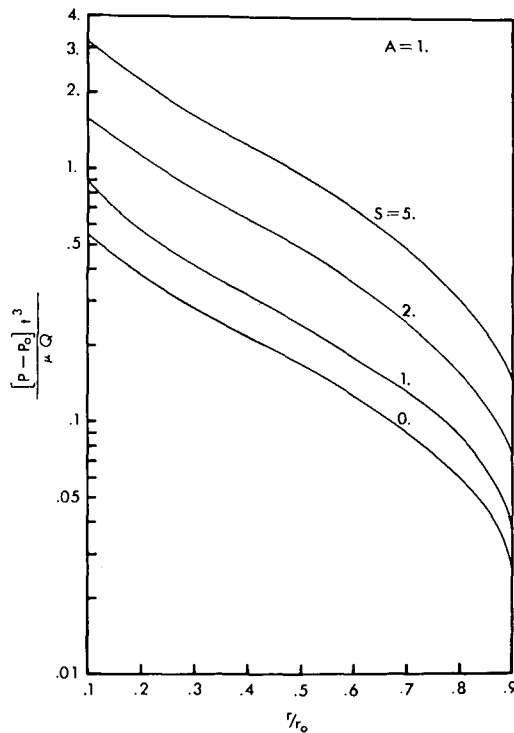
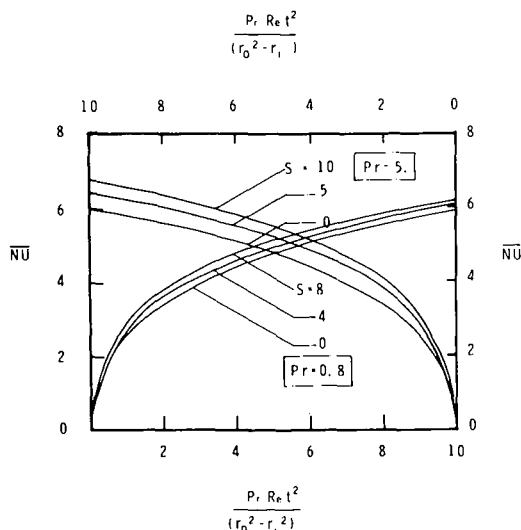**Fig. 2   Pressure distribution**

Fig. 3   Variation of average Nusselt number with Graetz number

Equation (21) is solved numerically, using an implicit finite difference scheme to obtain the temperature distribution and then the Nusselt number. The effect of the microstructure on the heat transfer characteristics is demonstrated by Fig. 3, where the average Nusselt number $\overline{Nu}$ is plotted for two different values of Prandtl number of 0.8 and 5. and different values of s. It is noticed that for fluids with microstructures, the average Nusselt number increases with the increase of s. However, the increase in the average Nusselt number with s is more pronounced in the case of Prandtl number greater than unity. Since the effect of the microstructures in the fluid is manifested by an increase in the apparent viscosity and an increase in the dissipation due to the work done on the rotation of the microstructures, the thermal field will be strongly influenced by Prandtl and Reynolds numbers.

References

1 Anzelius, A., *The Annual of the University of Uppsala*, 1931.
2 Jeffery, G. B., *Proceedings of the Royal Society*, Series A, Vol. 102, 1922, p. 171.
3 Henniker, J. C., "The Depth of the Surface Zone of a Liquid," *Rev. Mod. Phys.*, Vol. 21, 1949, p. 322.
4 Grad, M., "Statistical Mechanics, Thermodynamics, and Fluid Dynamics of Systems," *Commun. Pure App. Math.*, Vol. 5, 1952, p. 455.
5 Aero, E. L., Bulygin, A. N., and Kuvshinskii, E. V., "Asymmetric Hydromechanics," *App. Math. Mech.*, Vol. 29, 1965, p. 333.
6 Cowin, S. C., "Mechanics of Cosserat Continua," Ph.D. dissertation, The Pennsylvania State University, 1962.
7 Condiff, D. W., and Dahler, J. S., "Fluid Mechanical Aspects of Antisymmetric Stress," *Phys. Fluids*, Vol. 7, 1964, p. 842.
8 Eringen, A. C., "Simple Microfluids," *Int. J. Eng. Sci.*, Vol. 2, 1964, p. 205.
9 Eringen, A. C., "Theory of Micropolar Fluids," *J. Math. Mech.*, Vol. 16, p. 1.
10 Eringen, A. C., "Micropolar Fluids With Stretch," *Int. J. Eng. Sci.*, Vol. 7, 1969, p. 115.
11 Ericksen, J. L., "Transversely Isotropic Fluide," *Kolloid Z.*, Vol. 173, 1960, p. 117.
12 Ericksen, J. L., "Anisotropic Fluids," *Arch. Ration. Mech. Anal.*, Vol. 4, 1960, p. 231.
13 Allen, S. J., DeSilva, C. N., and Kline, K. A., "Theory of Simple Deformable Directed Fluids," *Phys. Fluids*, Vol. 10, 1967, p. 2551.
14 Kline, K. A., Allen, S. J., and DeSilva, C. N., "A Continuum Approach to Blood Flow," *Biorheology*, Vol. 5, 1968, p. 111.
15 Turk, M. A., Sylvester, N. D., and Ariman, T., *Developments in Theoretical and Applied Mechanics*, University of South Florida, Vol. 6, 1972, p. 3.
16 Eringen, A. C., "Theory of Thermomicrofluids," *J. Math. Analysis and Applic.*, Vol. 38, 1972, p. 480.
17 Kazakia, and Ariman, T., "Heat Conducting Micropolar Fluids," *Rheol. Acta*, Vol. 10, 1971, p. 319.
18 Kline, K. A., and Allen, S. J., "Heat Conduction in Fluids with Substructure," *Z. Angew Math. Mech.*, Vol. 48, 1968, p. 435.
19 Ariman, T., Turk, M. A., and Sylvester, N. D., "Microcontinuum Fluid Mechanics—A Review," *Int. J. Eng. Sci.*, Vol. 11, 1973, p. 905.
20 Cowin, S. C., "The Theory of Polar Fluids," *Adv. Appl. Mech.*, Vol. 14, 1974, p. 279.
21 Kreith, F., "Transfert de Chaleur et de Masse Dans un Ecoulement Radial Entre deux Disques Paralleles Fixes on Tournant a'la Meme Vitesse," *Int. J. Heat & Mass Transfer*, Vol. 9, 1966, p. 265.
22 Kreith, F., "Reverse Transition in Radial Source Flow Between Two Parallel Disks," *The Physics of Fluids*, Vol. 8, 1965, p. 1189.

Freezing of an Advancing Tube Flow

M. Epstein[1] and G. M. Hauser[1]

Nomenclature

a = crust profile exponent; equation (9)
B = solidification parameter; equation (3)
c = heat capacity
D = tube diameter; Fig. 1
f_0 = dimensionless friction parameter; equation (6)
k = thermal conductivity
L = latent heat of fusion
P_e = pressure at channel entrance; Fig. 1
P_0 = initial pressure in empty channel; Fig. 1
Pr = α/ν, liquid Prandtl number
R = distance from tube centerline to liquid-solid interface; Fig. 1
R_0 = $D/2$, tube radius
R^* = R/R_0, dimensionless location of liquid-solid interface
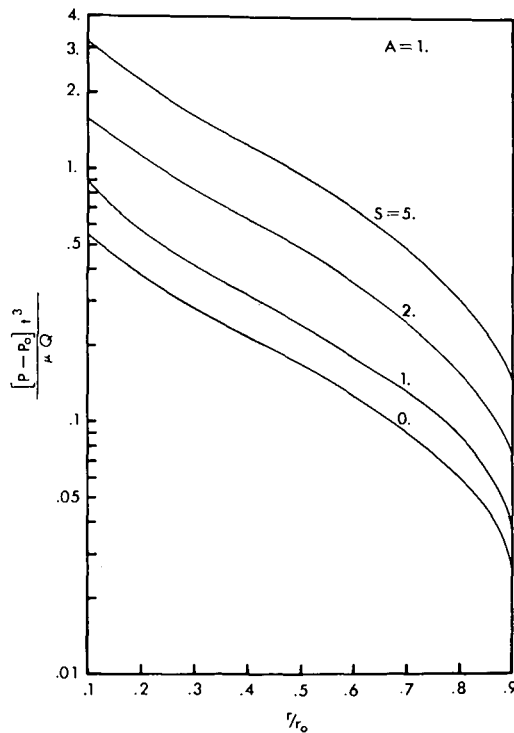Re = $(2\Delta P/\rho)^{1/2} D/\nu$, Reynolds number based on pressure drop

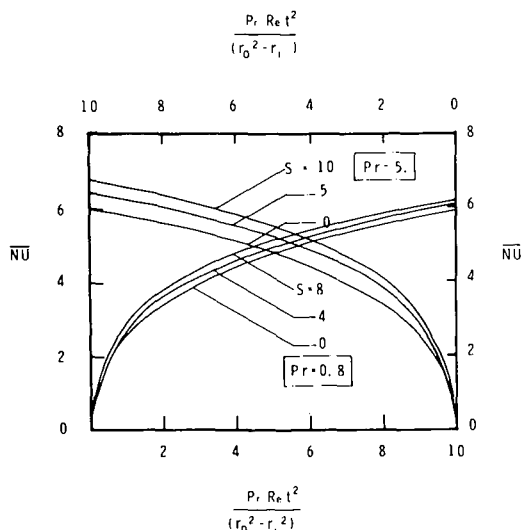**Fig. 2   Pressure distribution**

Fig. 3   Variation of average Nusselt number with Graetz number

Equation (21) is solved numerically, using an implicit finite difference scheme to obtain the temperature distribution and then the Nusselt number. The effect of the microstructure on the heat transfer characteristics is demonstrated by Fig. 3, where the average Nusselt number $\overline{Nu}$ is plotted for two different values of Prandtl number of 0.8 and 5. and different values of s. It is noticed that for fluids with microstructures, the average Nusselt number increases with the increase of s. However, the increase in the average Nusselt number with s is more pronounced in the case of Prandtl number greater than unity. Since the effect of the microstructures in the fluid is manifested by an increase in the apparent viscosity and an increase in the dissipation due to the work done on the rotation of the microstructures, the thermal field will be strongly influenced by Prandtl and Reynolds numbers.

References

1 Anzelius, A., *The Annual of the University of Uppsala*, 1931.
2 Jeffery, G. B., *Proceedings of the Royal Society*, Series A, Vol. 102, 1922, p. 171.
3 Henniker, J. C., "The Depth of the Surface Zone of a Liquid," *Rev. Mod. Phys.*, Vol. 21, 1949, p. 322.
4 Grad, M., "Statistical Mechanics, Thermodynamics, and Fluid Dynamics of Systems," *Commun. Pure App. Math.*, Vol. 5, 1952, p. 455.
5 Aero, E. L., Bulygin, A. N., and Kuvshinskii, E. V., "Asymmetric Hydromechanics," *App. Math. Mech.*, Vol. 29, 1965, p. 333.
6 Cowin, S. C., "Mechanics of Cosserat Continua," Ph.D. dissertation, The Pennsylvania State University, 1962.
7 Condiff, D. W., and Dahler, J. S., "Fluid Mechanical Aspects of Antisymmetric Stress," *Phys. Fluids*, Vol. 7, 1964, p. 842.
8 Eringen, A. C., "Simple Microfluids," *Int. J. Eng. Sci.*, Vol. 2, 1964, p. 205.
9 Eringen, A. C., "Theory of Micropolar Fluids," *J. Math. Mech.*, Vol. 16, p. 1.
10 Eringen, A. C., "Micropolar Fluids With Stretch," *Int. J. Eng. Sci.*, Vol. 7, 1969, p. 115.
11 Ericksen, J. L., "Transversely Isotropic Fluide," *Kolloid Z.*, Vol. 173, 1960, p. 117.
12 Ericksen, J. L., "Anisotropic Fluids," *Arch. Ration. Mech. Anal.*, Vol. 4, 1960, p. 231.
13 Allen, S. J., DeSilva, C. N., and Kline, K. A., "Theory of Simple Deformable Directed Fluids," *Phys. Fluids*, Vol. 10, 1967, p. 2551.
14 Kline, K. A., Allen, S. J., and DeSilva, C. N., "A Continuum Approach to Blood Flow," *Biorheology*, Vol. 5, 1968, p. 111.
15 Turk, M. A., Sylvester, N. D., and Ariman, T., *Developments in Theoretical and Applied Mechanics*, University of South Florida, Vol. 6, 1972, p. 3.
16 Eringen, A. C., "Theory of Thermomicrofluids," *J. Math. Analysis and Applic.*, Vol. 38, 1972, p. 480.
17 Kazakia, and Ariman, T., "Heat Conducting Micropolar Fluids," *Rheol. Acta*, Vol. 10, 1971, p. 319.
18 Kline, K. A., and Allen, S. J., "Heat Conduction in Fluids with Substructure," *Z. Angew Math. Mech.*, Vol. 48, 1968, p. 435.
19 Ariman, T., Turk, M. A., and Sylvester, N. D., "Microcontinuum Fluid Mechanics—A Review," *Int. J. Eng. Sci.*, Vol. 11, 1973, p. 905.
20 Cowin, S. C., "The Theory of Polar Fluids," *Adv. Appl. Mech.*, Vol. 14, 1974, p. 279.
21 Kreith, F., "Transfert de Chaleur et de Masse Dans un Ecoulement Radial Entre deux Disques Paralleles Fixes on Tournant a'la Meme Vitesse," *Int. J. Heat & Mass Transfer*, Vol. 9, 1966, p. 265.
22 Kreith, F., "Reverse Transition in Radial Source Flow Between Two Parallel Disks," *The Physics of Fluids*, Vol. 8, 1965, p. 1189.

Freezing of an Advancing Tube Flow

M. Epstein[1] and G. M. Hauser[1]

Nomenclature

a = crust profile exponent; equation (9)
B = solidification parameter; equation (3)
c = heat capacity
D = tube diameter; Fig. 1
f_0 = dimensionless friction parameter; equation (6)
k = thermal conductivity
L = latent heat of fusion
P_e = pressure at channel entrance; Fig. 1
P_0 = initial pressure in empty channel; Fig. 1
Pr = α/ν, liquid Prandtl number
R = distance from tube centerline to liquid-solid interface; Fig. 1
R_0 = $D/2$, tube radius
R^* = R/R_0, dimensionless location of liquid-solid interface
Re = $(2\Delta P/\rho)^{1/2} D/\nu$, Reynolds number based on pressure drop

ΔP.

s = dimensionless location of advancing liquid front; equation (5)

t = time

t' = time of arrival of flow front at location z

T_f = freezing point of liquid

T_w = temperature of tube wall

X = location of advancing liquid front; Fig. 1

$\dot{X}$ = velocity of advancing liquid front

z = axial coordinate measured from tube inlet

α = thermal diffusivity

γ = ratio of crust sensible heat to latent heat; equation (3)

δ = distance from tube centerline to liquid-solid interface at tube inlet; Fig. 1

Δ = δ/R_0 dimensionless location of liquid-solid interface at tube inlet

$\Delta P = P_e - P_0$, pressure drop over the instantaneous flow penetration length

ν = kinematic viscosity

ξ = dummy integration variable

ρ = density

τ = dimensionless time, equation (5)

Subscripts

p = at completion of freezing

s = solid phase

w = tube wall

0,1,2,3 . . . successive iterative approximations for s.

Introduction

Solidification of a liquid at its fusion temperature as it penetrates into an initially empty tube cooled on the outside was treated theoretically and experimentally in [1].[2] The analysis was based on an approximate method which involves postulating a reasonable functional form for the instantaneous shape of the frozen layer along the tube wall. In the present note we verify this approximate "crust profile" method theoretically, using a numerical approach in which the governing integro-differential equation of liquid motion is rigorously solved on a digital computer.

Physical Model

With the exception that we here confine our attention to the frequently encountered limiting case of negligible liquid flow inertia, our model is identical with that of [1], viz. we consider a turbulent liquid flow at its freezing temperature T_f penetrating into a cold tube (see Fig. 1). The tube wall is maintained at constant temperature T_w. As before [1], the assumption of negligible axial heat conduction within the frozen layer implies that the layer is thin compared with its extension in the direction of flow and that the crust thickness is maximum at the tube entrance (at $z = 0$). The problem is formulated by

---

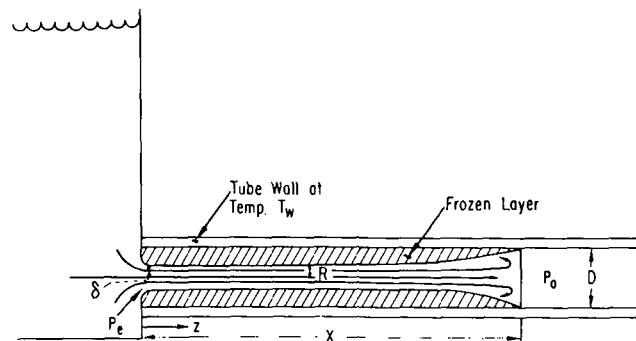[2] Numbers in brackets designate References at end of paper.

Fig. 1   Solidification in flow into a tube

asking what the flow penetration length $X(t)$ is at the moment solidification is complete in the inlet region of the tube.

Analysis

Assuming that the turbulent friction factor is given by the Blasius formula, the momentum balance between pressure and frictional forces over the instantaneous liquid penetration length X takes the form [1]

$$\dot{X}^2 = 12.64 \,(\Delta PR_0/\rho)(2R_0\dot{X}/\nu)^{1/4} \int_0^X \left(\frac{R_0}{R}\right)^{19/4} dz \qquad (1)$$

The crust shape $R(z, t)$ must now be determined from the one-dimensional conduction equation applied to the frozen layer. Unfortunately, no exact solution for freezing a saturated liquid inside a cylinder is available. Stefan [2] utilized an approximate collocation method which takes full account of the movement of the phase conversion front and transient heat conduction within the frozen layer. This technique yields the inverted solution for the instantaneous tube radius $R(z, t)$ at axial location z:[3]

$$\frac{4\alpha_s B}{R_0^2}(t - t') = 2\left(\frac{R}{R_0}\right)^2 \ln\left(\frac{R}{R_0}\right) - \left(\frac{R}{R_0}\right)^2 + 1 \qquad (2)$$

where

$$B = [1 + 2\gamma]^{1/2} - 1; \qquad \gamma = c_s(T_f - T_w)/L \qquad (3)$$

In equation (2), t' ($0 < t' < t$) is the time of arrival of the flow front at location z $[0 < z < X(t)]$. Clearly, the time of arrival is given by the implicit relation

$$X(t') = z \qquad (4)$$

We now introduce the dimensionless variables s and τ:

$$s = \left(\frac{8B^2\alpha_s{}^2 f_0\rho}{\Delta PR_0^5}\right)^{1/3} X \qquad \tau = \frac{4B^2\alpha_s}{R_0^2} t \qquad (5)$$

where the constant f_0 is given by

$$f_0 = 0.0628\left(\frac{64\nu^3\rho}{\alpha_s B\Delta PR_0^2}\right)^{1/11} \qquad (6)$$

Replacing dz in the integrand of equation (1) by $[dX(t')/dt']dt'$ (see equation (4)), integrating the result by parts and using definitions (5), we find that $s(\tau)$ satisfies the integral equation

$$s(\tau) = \int_0^\tau \left[s(\xi) - \frac{19}{16} \int_0^\xi \frac{s(\tau')d\tau'}{[R^*(\xi - \tau')]^{27/4} \cdot \ln[R^*(\xi - \tau')]} \right]^{4/7} d\xi \qquad (7)$$

where the normalized local cavity radius function $R^*(\xi - \tau')$ is given by equation (2) in the dimensionless form

$$2(R^*)^2 \ln(R^*) - (R^*)^2 + 1 = \xi - \tau' \qquad (8)$$

Equation (7) is now solved for s by a numerical iteration procedure. A zeroth order approximation $s_0(\tau)$ for $s(\tau)$ is assumed (see below). When this approximation is substituted for s in the integral of (7), we denote the resulting relation obtained by numerical integration by $s_1(\tau)$. Substituting $s_1(\tau)$ in the right-hand side of (7), we find the approximation $s_2(\tau)$. This procedure is repeated. Each successive iteration is used to generate a more exact approximation. A converged solution is obtained after six iterations.

---

[3] A comparison with available numerical solutions for the inward solidification of cylindrical bodies [3] indicates that equation (2) constitutes an accurate result for most situations of practical interest. In the limit $\gamma \to 0$, equation (2) converges to the exact quasi-steady result; it underpredicts solidification times by less than 20 percent for $\gamma < 2.0$. Unlikely physical situations characterized by $\gamma > 5.0$ lead to somewhat larger errors (>30 percent).
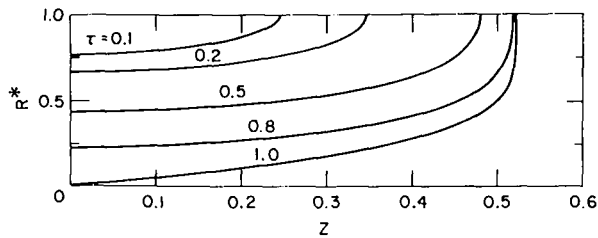
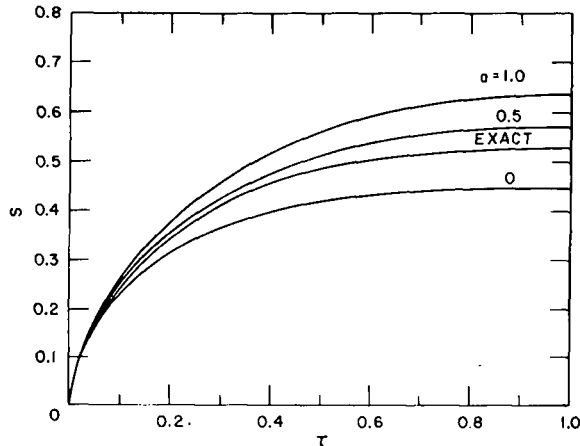Fig. 2 The effects of time on the actual crust shape for flow into a tube

Fig. 3 Comparison of the numerically exact penetration-time history with results obtained from the crust profile approximation for flow into a tube

Equation (1) can also be solved by the following approximate procedure. As discussed in reference [1], we suspect intuitively that the true crust shape must be convex (as viewed from the liquid) and look something like the crust shape sketched in Fig. 1. Therefore, the actual crust shape must be bounded by a linear crust profile and a uniform crust profile. Let us now choose a specific function $R(z, t)$ that gives a reasonable description of the crust shape. $R = \delta$ at $z = 0$ and, of course, $R = 0$ at $z = X$. This suggests that

$$\frac{R}{R_0} \approx 1 - \left(1 - \frac{\delta}{R_0}\right)\left(1 - \frac{z}{X}\right)^a \qquad (9)$$

might be an appropriate choice. The exponent appearing in the above equation takes on values in the range $0 \leq a \leq 1$. When $a = 0$ the solid phase is deposited uniformly; i.e., $R(z, t) = \delta(t)$. We have a square-root solidification profile and linear profile for $a = \frac{1}{2}$ and $a = 1$, respectively. Thus, the profiles given by (9) span the entire range of physically possible profiles. Substituting (9) into (1) leads to separable penetration velocity laws. For example, for $a = \frac{1}{2}$ we have (when cast in dimensionless notation)

$$s^{4/7}\frac{ds}{d\tau} = \left[\frac{8/15(\Delta^{-15/4} - 1) - 8/11(\Delta^{-11/4} - 1)}{(1 - \Delta)^2}\right]^{-4/7} \qquad (10)$$

The normalized cavity radius at the entrance, $\Delta = \delta/R_0$, is related to τ by (2) with $t' = 0$ and $R = \delta$; i.e., $2\Delta^2 \ln(\Delta) - \Delta^2 + 1 = \tau$.

Results and Discussion

Equation (10) (which must be integrated numerically by, say, Simpson's rule) can be used as the zeroth order approximation $s_0(\tau)$ to derive $s_1(\tau)$ from (7). The converged solution to (7), showing the evolution of both the crust shape and flow penetration distance, is displayed in Figs. 2 and 3. The penetration behavior predicted by the crust profile approximation for $a = 0, \frac{1}{2}, 1$ is also shown in Fig. 3.

The linear profile ($a = 1.0$) yields the upper bound for s, since this profile provides the maximum cross-sectional area for flow. On the other hand, the uniform profile ($a = 0$) gives the lower bound for s.

We note that the upper and lower bounds are sufficiently close together so that the choice of the square root profile ($a = \frac{1}{2}$) that lies approximately midway between the bounding linear and uniform profiles must yield results wihin approximately 25 percent of an exact calculation. We see that the actual error incurred is considerably less than this, with equation (10) for $a = \frac{1}{2}$ representing the exact penetration history to better than 8 percent. This result justifies the crust profile approximation introduced in reference [1] for treating problems of this type.

The numerical iteration solution yields $s_p = 0.54$. In terms of the physical variables

$$\frac{X_P}{D} = 0.141 \, Re^{8/11}\left[\frac{Pr(\alpha/\alpha_s)}{B}\right]^{7/11} \qquad (11)$$

The crust profile approximation with $a = \frac{1}{2}$ gives a solution of the same form as (11) except that the numerical coefficient is 0.152.

Acknowledgments

References

1 Epstein, M., Yim, A., and Cheung, F. B., "Freezing-controlled Penetration of a Saturated Liquid into a Cold Tube," JOURNAL OF HEAT TRANSFER, TRANS. ASME, Series C Vol. 99, No. 2 1977, pp 233-238.
2 Stephan, K., "Influence of Heat Transfer on Melting and Solidification in Forced Flow," Int. J. Heat Mass Transfer, Vol. 12, 1969, pp. 199-214.
3 Stephan, K., and Holzknecht, B., "Heat Conduction in Solidification of Geometrically Simple Bodies," Waerme Stoffübertragung, Vol. 7, pp. 200-207.

Transient Heat Conduction in Cryogenic Current Cables Following a Loss-of-Coolant Accident

A. Bejan[1]

The current supply cables of large superconducting magnet systems are cooled with an axial stream of cold helium vapor. If the flow of coolant is suddenly interrupted the current cables may overheat and burn up causing extensive damage to the entire system. The transient temperature distribution in the cable after the loss-of-coolant accident is derived analytically. The paper presents the maximum cable temperature versus time for a cryogenic current cable which stretches from room temperature (300 K) to a liquid helium-cooled superconducting system (4.2 K).

Introduction

Large superconducting magnets are energized through current cables which span the large temperature difference between ambient and liquid helium. In order to diminish the heat leak conducted into the cold space, the cryogenic cable is cooled axially with a stream of helium gas which runs against the conduction heat flow present in the cable (see Fig. 1).

[1] Miller Research Fellow, Department of Mechanical Engineering, University of California, Berkeley, Berkeley, Cal.
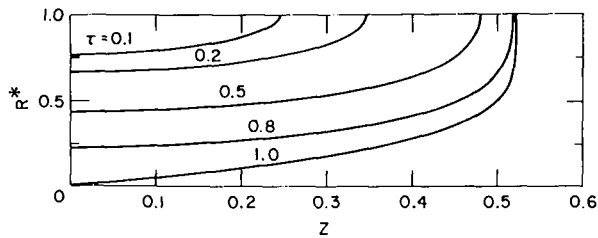
Fig. 2 The effects of time on the actual crust shape for flow into a tube

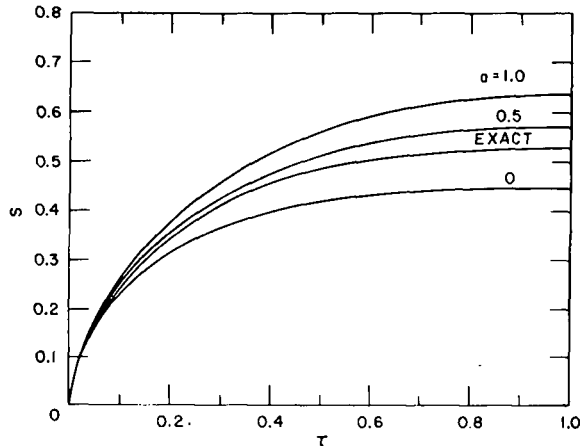**Fig. 3 Comparison of the numerically exact penetration-time history with results obtained from the crust profile approximation for flow into a tube**

Equation (1) can also be solved by the following approximate procedure. As discussed in reference [1], we suspect intuitively that the true crust shape must be convex (as viewed from the liquid) and look something like the crust shape sketched in Fig. 1. Therefore, the actual crust shape must be bounded by a linear crust profile and a uniform crust profile. Let us now choose a specific function $R(z, t)$ that gives a reasonable description of the crust shape. $R = \delta$ at $z = 0$ and, of course, $R = 0$ at $z = X$. This suggests that

$$\frac{R}{R_0} \approx 1 - \left(1 - \frac{\delta}{R_0}\right)\left(1 - \frac{z}{X}\right)^a \tag{9}$$

might be an appropriate choice. The exponent appearing in the above equation takes on values in the range $0 \leq a \leq 1$. When $a = 0$ the solid phase is deposited uniformly; i.e., $R(z, t) = \delta(t)$. We have a square-root solidification profile and linear profile for $a = \frac{1}{2}$ and $a = 1$, respectively. Thus, the profiles given by (9) span the entire range of physically possible profiles. Substituting (9) into (1) leads to separable penetration velocity laws. For example, for $a = \frac{1}{2}$ we have (when cast in dimensionless notation)

$$s^{4/7}\frac{ds}{d\tau} = \left[\frac{8/15(\Delta^{-15/4} - 1) - 8/11(\Delta^{-11/4} - 1)}{(1 - \Delta)^2}\right]^{-4/7} \tag{10}$$

The normalized cavity radius at the entrance, $\Delta = \delta/R_0$, is related to τ by (2) with $t' = 0$ and $R = \delta$; i.e., $2\Delta^2 \ln(\Delta) - \Delta^2 + 1 = \tau$.

Results and Discussion

Equation (10) (which must be integrated numerically by, say, Simpson's rule) can be used as the zeroth order approximation $s_0(\tau)$ to derive $s_1(\tau)$ from (7). The converged solution to (7), showing the evolution of both the crust shape and flow penetration distance, is displayed in Figs. 2 and 3. The penetration behavior predicted by the crust profile approximation for $a = 0, \frac{1}{2}, 1$ is also shown in Fig. 3.

The linear profile ($a = 1.0$) yields the upper bound for s, since this profile provides the maximum cross-sectional area for flow. On the other hand, the uniform profile ($a = 0$) gives the lower bound for s.

We note that the upper and lower bounds are sufficiently close together so that the choice of the square root profile ($a = \frac{1}{2}$) that lies approximately midway between the bounding linear and uniform profiles must yield results wihin approximately 25 percent of an exact calculation. We see that the actual error incurred is considerably less than this, with equation (10) for $a = \frac{1}{2}$ representing the exact penetration history to better than 8 percent. This result justifies the crust profile approximation introduced in reference [1] for treating problems of this type.

The numerical iteration solution yields $s_p = 0.54$. In terms of the physical variables

$$\frac{X_P}{D} = 0.141 \, \mathrm{Re}^{8/11}\left[\frac{\mathrm{Pr}(\alpha/\alpha_s)}{B}\right]^{7/11} \tag{11}$$

The crust profile approximation with $a = \frac{1}{2}$ gives a solution of the same form as (11) except that the numerical coefficient is 0.152.

Acknowledgments

References

1   Epstein, M., Yim, A., and Cheung, F. B., "Freezing-controlled Penetration of a Saturated Liquid into a Cold Tube," JOURNAL OF HEAT TRANSFER, TRANS. ASME, Series C Vol. 99, No. 2 1977, pp 233- 238.

2   Stephan, K., "Influence of Heat Transfer on Melting and Solidification in Forced Flow," Int. J. Heat Mass Transfer, Vol. 12, 1969, pp. 199 214.

3   Stephan, K., and Holzknecht, B., "Heat Conduction in Solidification of Geometrically Simple Bodies," Waerme Stoffübertragung, Vol. 7, pp. 200–207.

Transient Heat Conduction in Cryogenic Current Cables Following a Loss-of-Coolant Accident

A. Bejan[1]

The current supply cables of large superconducting magnet systems are cooled with an axial stream of cold helium vapor. If the flow of coolant is suddenly interrupted the current cables may overheat and burn up causing extensive damage to the entire system. The transient temperature distribution in the cable after the loss-of-coolant accident is derived analytically. The paper presents the maximum cable temperature versus time for a cryogenic current cable which stretches from room temperature (300 K) to a liquid helium-cooled superconducting system (4.2 K).

Introduction

Large superconducting magnets are energized through current cables which span the large temperature difference between ambient and liquid helium. In order to diminish the heat leak conducted into the cold space, the cryogenic cable is cooled axially with a stream of helium gas which runs against the conduction heat flow present in the cable (see Fig. 1).

---

[1] Miller Research Fellow, Department of Mechanical Engineering, University of California, Berkeley, Berkeley, Cal.
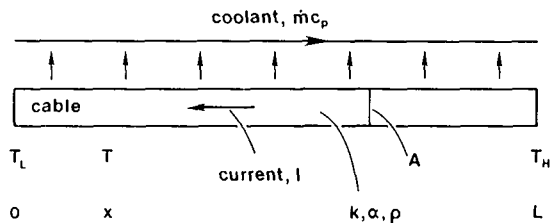
Fig. 1 Schematic of cryogenic current cable with continuous cooling effect provided by a stream of cold helium vapor

As superconducting magnets are more frequently used in large scale power systems, the reliability of the magnet and its current supply cables occupies a central position. This article considers the transient behavior of the cryogenic cable following a total loss-of-coolant accident. Without the customary axial flow of helium, the current in the cable is usually large enough to overheat the cable and, if the current is not interrupted in time, the cable may burn up locally. The loss of coolant can simultaneously lead to other damaging effects such as the burn-up of the superconducting winding. The question of what damage occurs first depends on the particular design, i.e., on the manner in which the liquid helium inventory is distributed through the cryogenic system. Experience with superconducting systems indicates that it is not uncommon for the cable burn-up to take place before or in the absence of superconductor failure [1].[2]

The objective of this technical note is to report the time dependence of the cable peak temperature, i.e., the time lapse between the loss-of-coolant accident and overheating.

Model for conductor properties

A set of simplifying assumptions is necessary in order to derive an analytical solution for the cable temperature following a loss-of-coolant accident. It is assumed that the conductor thermal conductivity k and diffusivity α are constant. In addition, the electrical resistivity ρ is assumed proportional to the absolute temperature T,

$$\rho = bT \tag{1}$$

Since in most applications the cable material is copper, these simplifying assumptions are valid approximations if the cable temperature exceeds 100 K. Due to the fact that overheating and burn-up are phenomena developing at temperatures of the order of 300 K and higher, this model costitutes an appropriate description of the conductor properties.

Problem Statement and Solution

The temperature history in the cryogenic cable is found by solving the following unsteady one-dimensional heat conduction problem. The heat conduction equation can be written as

$$\frac{\partial^2 T}{\partial (x/L)^2} - \frac{\partial T}{\partial (t\alpha/L^2)} + F^2 T = 0 \tag{2}$$

where T is the absolute temperature along the cable and F is a dimensionless parameter proportional to the electric current I carried by the arrangement shown in Fig. 1,

$$F = I \frac{L}{A} \left(\frac{b}{k}\right)^{1/2} \tag{3}$$

Equation (2) must be solved subject to the two end conditions

$$T(0, t) = T_L \tag{4}$$

$$T(L, t) = T_H \tag{5}$$

and the initial condition

$$T(x, 0) = f(x) \tag{6}$$

In general, the initial temperature distribution $f(x)$ depends on the steady-state operating conditions (current level, helium flow rate) present just before the loss-of-coolant accident. For the sake of brevity, a single initial temperature distribution is used,

$$f(x) = T_L \exp\left(\frac{x}{L} \ln \frac{T_H}{T_L}\right) \tag{7}$$

Expression (7) approximates fairly well the steady-state temperature distribution in cryogenic cables operating at high ratios of current to helium flow rate [2]. Moreover, it has been shown [3] that the temperature distribution of equation (7) corresponds to those cases in which the cable operates optimally from a thermodynamic standpoint. In such cases, the total power consumption, i.e., the electric power dissipated in the resistive cable plus the refrigerator power needed for cooling the cable, reaches a minimum.

The problem stated by equations (2)–(7) was solved using the Laplace transformation method [4]. Since the actual work follows a standard procedure, only the final result is presented. The temperature distribution in the cable following the sudden loss of coolant is

$$T(x, t)/T_L = \exp\left[Dt + (x/L) \ln\left(T_H/T_L\right)\right]$$
$$+ (T_H/T_L)\Phi(x, t) + \Phi(L - x, t) \tag{8}$$

where

$$\Phi(x, t) = \frac{\sin(F\,x/L)}{\sin(F)} - \exp(Dt)\frac{\sinh[(x/L)\ln(T_H/T_L)]}{\sinh[\ln(T_H/T_L)]}$$
$$+ 2\pi[F^2 + \{\ln(T_H/T_L)\}^2]$$
$$\cdot \sum_{n=1}^{\infty} \frac{n(-1)^n \sin(n\pi x/L)\exp\{-[(n\pi)^2 - F^2]\alpha t/L^2\}}{[(n\pi)^2 - F^2][(n\pi)^2 + \{\ln(T_H/T_L)\}^2]} \tag{9}$$

and

$$D = \alpha[F^2 + \{\ln(T_H/T_L)\}^2]/L^2 \tag{10}$$

Discussion

The analytical solution for the cable temperature distribution, equations (8)–(10) is plotted in Fig. 2 for a cryogenic cable stretching from 300 K (room temperature) to 4.2 K (normal boiling point of helium). This particular choice of T_H and T_L is representative of current cables to liquid helium-cooled superconducting magnets. The current level F spans a range of values encountered in practice.

In plotting the curves of Fig. 2 the time was increased up to the point where the maximum cable temperature starts to rise quickly above the warm end temperature, T_H. The figure shows that, as the current level F increases, the time lapse between loss of coolant and overheating decreases. At the same time, the hot spot develops at places increasingly closer to the warm end.

As a summary to the cases illustrated in Fig. 2, the last figure, Fig. 3, shows only the peak cable temperature as a function of time. For low current levels $F < \pi$, the cable temperature approaches the distribution corresponding to the steady-state solution to equation (2),

$$\frac{T}{T_L} = \left(\frac{T_H}{T_L} - 1\right)\frac{\sin(xF/L)}{\sin(F)} + \cos(xF/L) \tag{11}$$

If $\pi/2 < F < \pi$, the peak temperature levels off to the value

$$\left(\frac{T}{T_L}\right)_{max} = \left[1 + \left(\frac{T_H/T_L - 1}{\sin(F)}\right)^2\right]^{1/2} \tag{12}$$

If $F < \pi/2$, the cable temperature never rises above the warm end temperature T_H. For high current levels $F > \pi$, no steady temperature distribution exists.

The characteristic overheating time of a given set of cryogenic current cables can be estimated based on Fig. 3 by first calculating the electric current parameter F. As a numerical example, consider

---

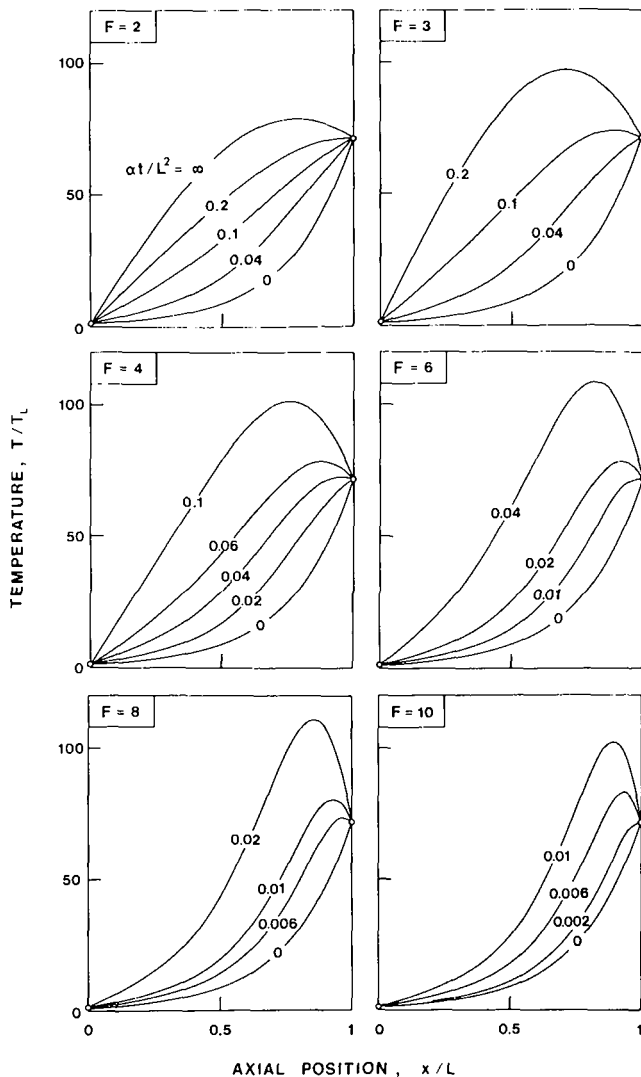[2] Numbers in brackets designate References at end of technical note.

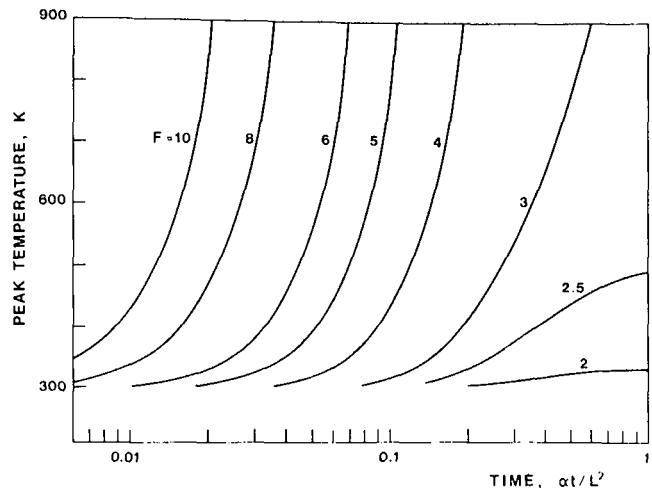Fig. 2 **Temperature distribution in a cryogenic current cable following a loss-of-coolant accident**

Fig. 3 **Cable maximum temperature as a function of time and electric current level parameter F**

above 200 K $\alpha \simeq 1.2$ cm^2/s, the calculated overheating time is 33 s.

The overheating time derived from Fig. 3 based on the constant thermal diffusivity present above 200 K is somewhat optimistic, i.e., slightly higher than the real time. This effect is caused by the thermal diffusivity of copper which increases rapidly as the temperature falls under 60 K. In terms of the cable temperature history plotted in Fig. 2, the small specific heat of copper at very low temperatures will cause the formation of a minor hot spot near the cold end. This minor spot will grow fast in its early stages but will slow down as its temperature approaches 60 K. From this point on, the warm end hot spot of Fig. 2 will dominate the overheating process, since the Joule heating is the most intense near the warm end. Overall, the cable temperature distribution will lie above the curves of Fig. 2 and the peak temperature traces will fall slightly to the left of the curves of Fig. 3.

the 200A current cables constructed by Claudet and Senet [5]. Each cable is 0.6 m long and has a cross-sectional area of 3.93 mm^2. Since for copper above 100 K $b \simeq (5.5)10^{-11}$ Ωm/K and $k \simeq 4$W/(cmK), using equation (3) we find $F_{max} = 11.3$. This value is slightly larger than the maximum F curve plotted on Fig. 3. However, towards large F's the peak temperature curves of Fig. 3 are similar so that the $F = 11.3$ curve can be located through extrapolation: The peak temperature reaches 600 when $\alpha/L^2 = 0.011$. Since $L = 0.6$ m and for copper

References

1 Hsieh, S. Y., et al., "A Survey of Failure Experience in Existing Superconducting Magnet Systems and Its Relevance to Fusion Power Reactors," *IEEE Transactions on Magnetics*, Vol. MAG-13, No. 1, 1977, p. 90.

2 Rauh, M., "Die Optimalen Dimensionen Elektrischer Zuleitungen für Tieftemperaturanlagen," Ph.D. dissertation No. 4656, Federal Institute of Technology, Zurich, Switzerland, Sept. 1970, p. 90.

3 Bejan A., "Improved Thermal Design of Cryogenic Cooling System for a Superconducting Synchronous Generator," PhD thesis, Massachusetts Institute of Technology, Cambridge, Mass., Feb. 1975, p. 108.

4 Carslaw, H. S., and Jaeger, J. C., *Conduction of Heat in Solids*, Second ed., Oxford University Press, London 1959, pp. 404.

5 Claudet, G. and Senet, L., "Current Leads for 4.2K Cryostats," *Cryogenics*, Vol. 13, 1973, pp. 44–46.

discussion

Approximate Solution for Convective Fins With Variable Thermal Conductivity[1]

A. Aziz.[2] The author compares in Fig. 3 the fin efficiency results based on the Galerkin method with those obtained using perturbation approach of the present discusser [1].[3] In [1] an error had crept in the derivation of equations for heat flux and fin efficiency. These were identified and corrected by Krane [2]. It seems that in the work under discussion the author used the incorrect fin efficiency equation of [1] for comparison appearing in Fig. 3. No wonder that he finds the perturbation results to be in significant error compared with the numerical results and his own approximate results based on Galerkin-type approach. If one uses the correct perturbation solution for fin efficiency [2] and compares the results as shown in Fig. 1, both the perturbation and the author's results are seen to be in good agreement

with the numerical results throughout the range of ϵ from −0.6 to +0.6. Furthermore, it must be emphasized that the perturbation solution is much simpler compared to the author's solution and that it has the additional merit of facilitating the evaluation of optimum fin dimensions. With the author's Galerkin type solution it is not possible to carry out the optimisation procedure.

Additional References

1 Aziz, A., and Enamul Huq, S. M., "Perturbation Solution for Convecting Fin With Variable Thermal Conductivity," JOURNAL OF HEAT TRANSFER, TRANS. ASME, Series C, Vol. 97, May 1975, pp. 300–301.

2 Krane, R. J., Discussion on a previously published paper by A. Aziz and S. M. Enamul Huq, JOURNAL OF HEAT TRANSFER, TRANS. ASME, Series C, Vol. 98, Nov. 1976, pp. 685–686.

Author's Closure

As stated in the paper under discussion, the comparison reported in Fig. 3 is referred to the fin efficiency equation given in [1]. Since this relationship has proved incorrect the comparison turns out to be misleading. In fact, the correct solution developed by Krane [2] shows a good agreement with the numerical results. In this connection it may be worthwhile to remark that there seems to be a slight discrepancy between the numerical results shown plotted in Fig. 3 and those reported by the discusser in Fig. 1. For instance, with $N = 2$ and $\epsilon = -0.6$ from the discusser's results one can estimate $\eta = 0.393$ while the
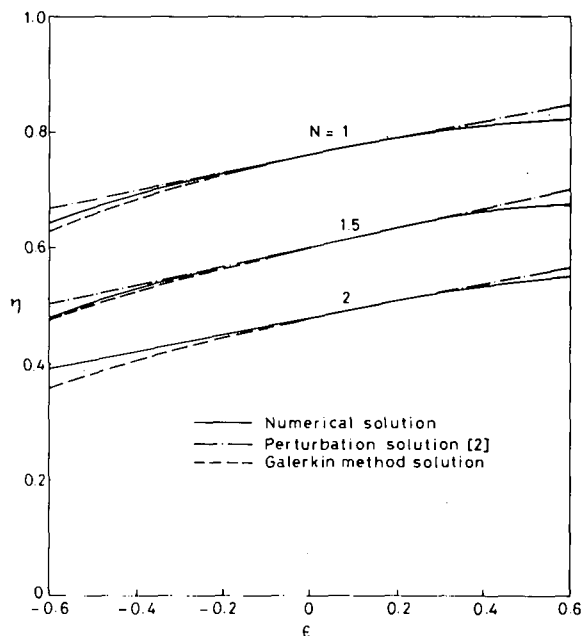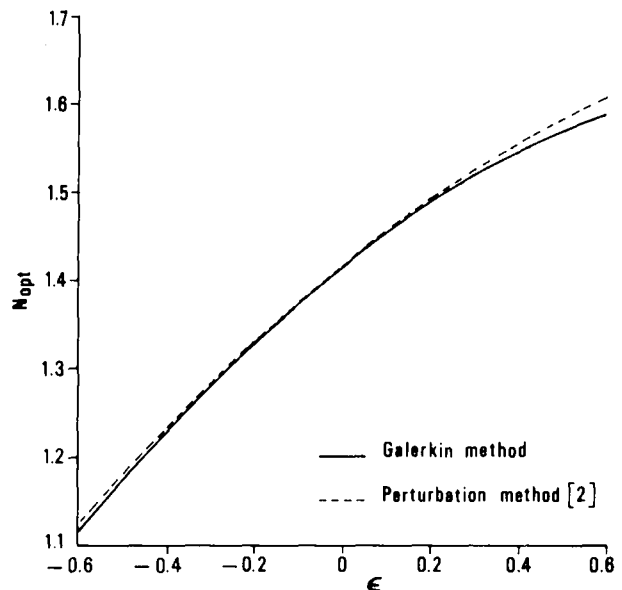

Fig. 1: Aziz

Fig. 1: Muzzio

author finds $\eta = 0.378$.

In any case, the Galerkin method solution seems to give a better accuracy, even though at the cost of a greater computation effort. Furthermore, it may be readily seen that, contrary to the discusser's claim, there is no difficulty in carrying out the optimization procedure.

The optimum values of N are obtained by solving the equation:

$$(\sinh 2N - 6N)\left(1 - C\frac{\tan h^2 N}{1 + \tanh^2 N}\right)$$

$$+ 6N\frac{dC}{dN}\frac{\tanh^3 N \cosh^2 N}{1 + \tanh^2 N} + 12NC\frac{\tanh^2 N}{(1 + \tanh^2 N)^2} = 0$$

where:

$$\frac{dC}{dN} = \frac{\alpha'C^2 + \beta'C + \gamma'}{2\alpha c + \beta}$$

The primes denote differentiation with respect to N. While the details of the calculation are not reported here, the results are shown plotted in Fig. 1 along with the perturbation solution [2].
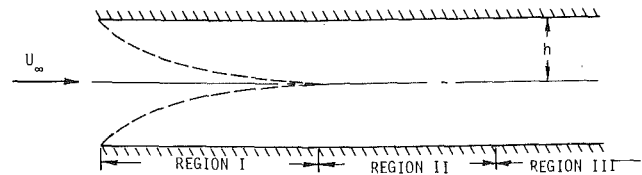

Fig. 1 Schematic representation of duct flow

The Numerical Prediction of the Turbulent Flow and Heat Transfer in the Entrance Region of a Parallel Plate Duct[1]

T. Cebeci,[2] R. S. Hirsh,[3] and K. C. Chang.[4] The two previous calculations of entry flow in a duct [1, 2][5] have both used rather complex turbulence models, i.e., a mixing-length model with twelve constants, and a k-ϵ model which requires six constants. The present communication describes a much simpler approach to this problem based on the essential physics of the duct flow. As such it is applicable only to this particular flow, but a similar concept has been utilized for the calculation of shock wave/boundary-layer interactions [3].

The entry flow in a duct is shown schematically in Fig. 1. There are three identifiable regions in the flow field. In region I the flow behaves as an external boundary layer interacting with an inviscid flow; this is called the "displacement-interaction" region. By region III, the character of the flow is wholly described by internal concepts; this is the "fully developed" region. Region II is a transition zone from external to internal flow.

In region I, we use the well-tested Cebeci-Smith eddy-viscosity model [4] for the boundary-layer-like development. This is given by

$$\epsilon^{\mathrm{I}} = \begin{cases} (0.4y)^2[1 - \exp(-y/A)]^2 \left|\dfrac{\partial u}{\partial y}\right| \gamma_{tr} & (1a) \\[2em] 0.0168 \displaystyle\int_0^\infty (u_e - u)dy \cdot \gamma_{tr} & (1b) \end{cases}$$

In a pipe, the flow in region III can be described by the classical mixing length model of Nikuradse [5]

$$\epsilon^{\mathrm{III}} = \ell^2 \left|\frac{\partial u}{\partial y}\right| [1 - \exp(-y/A)]^2 \qquad (2a)$$

$$\ell = r_0\left[0.14 - 0.08\left(1 - \frac{r}{r_0}\right)^2 - 0.06\left(1 - \frac{r}{r_0}\right)^4\right] \qquad (2b)$$

where for axisymmetric flow for constant r_0

$$r = r_0 - y$$
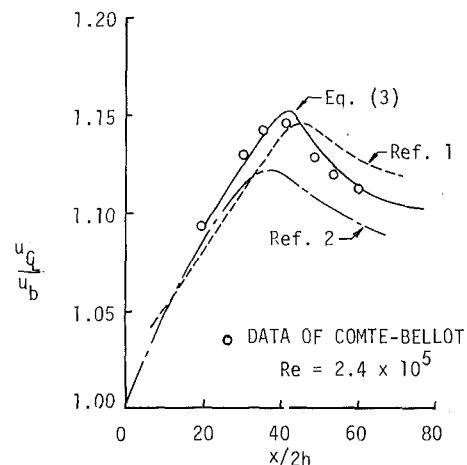
so that

$$1 - \frac{r}{r_0} = \frac{y}{r_0}$$

Fig. 2 Comparison of predictions for center-line velocity

To use this for two-dimensional duct flows we simply set $r_0 = h$ to get

$$1 - \frac{r}{r_0} = \frac{y}{h} \qquad (2c)$$

Either one of these can be used separately to calculate the developing duct flow using the numerical procedure described below, however, the overall agreement is poor. The solution was to model the entire flow situation based on our knowledge of the physics. A composite eddy viscosity is prescribed which changes smoothly from an external model (ϵ^{I}) to an internal model (ϵ^{III}) as follows

$$\epsilon = \epsilon^{\mathrm{I}} + (\epsilon^{\mathrm{III}} - \epsilon^{\mathrm{I}})\left[1 - \exp-\left(\frac{x - x_0}{20h}\right)\right] \qquad (3)$$

where x_0 is the length down the pipe where the two "external" boundary layers merge, and the denominator giving the relaxation scale was prescribed by divine intervention.

Using this model, the "nonlinear eigenvalue" procedure of Cebeci and Keller for laminar flows [6] was used to calculate the developing duct flow. For further details and heat transfer results see reference [7]. Fig. 2 shows the experimental results of Compte-Bellot for center-line velocity decay, along with the predictions of references [1, 2], and equation (3). The composite model provides strikingly improved results. The same comparison of predicted results for the displace-

author finds $\eta = 0.378$.

In any case, the Galerkin method solution seems to give a better accuracy, even though at the cost of a greater computation effort. Furthermore, it may be readily seen that, contrary to the discusser's claim, there is no difficulty in carrying out the optimization procedure.

The optimum values of N are obtained by solving the equation:

$$(\sinh 2N - 6N)\left(1 - C\frac{\tan h^2 N}{1 + \tanh^2 N}\right)$$

$$+ 6N\frac{dC}{dN}\frac{\tanh^3 N \cosh^2 N}{1 + \tanh^2 N} + 12NC\frac{\tanh^2 N}{(1 + \tanh^2 N)^2} = 0$$

where:

$$\frac{dC}{dN} = \frac{\alpha'C^2 + \beta'C + \gamma'}{2\alpha c + \beta}$$

The primes denote differentiation with respect to N. While the details of the calculation are not reported here, the results are shown plotted in Fig. 1 along with the perturbation solution [2].
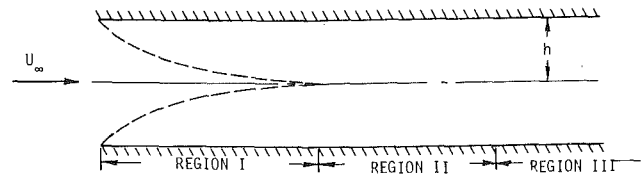

Fig. 1   Schematic representation of duct flow

The Numerical Prediction of the Turbulent Flow and Heat Transfer in the Entrance Region of a Parallel Plate Duct[1]

T. Cebeci,[2] R. S. Hirsh,[3] and K. C. Chang.[4] The two previous calculations of entry flow in a duct [1, 2][5] have both used rather complex turbulence models, i.e., a mixing-length model with twelve constants, and a k-ϵ model which requires six constants. The present communication describes a much simpler approach to this problem based on the essential physics of the duct flow. As such it is applicable only to this particular flow, but a similar concept has been utilized for the calculation of shock wave/boundary-layer interactions [3].

The entry flow in a duct is shown schematically in Fig. 1. There are three identifiable regions in the flow field. In region I the flow behaves as an external boundary layer interacting with an inviscid flow; this is called the "displacement-interaction" region. By region III, the character of the flow is wholly described by internal concepts; this is the "fully developed" region. Region II is a transition zone from external to internal flow.

In region I, we use the well-tested Cebeci-Smith eddy-viscosity model [4] for the boundary-layer-like development. This is given by

$$\epsilon^{\mathrm{I}} = \begin{cases} (0.4y)^2[1 - \exp(-y/A)]^2 \left|\dfrac{\partial u}{\partial y}\right| \gamma_{tr} & (1a) \\[2mm] 0.0168 \displaystyle\int_0^\infty (u_e - u)dy \cdot \gamma_{tr} & (1b) \end{cases}$$

In a pipe, the flow in region III can be described by the classical mixing length model of Nikuradse [5]

$$\epsilon^{\mathrm{III}} = \ell^2 \left|\frac{\partial u}{\partial y}\right| [1 - \exp(-y/A)]^2 \tag{2a}$$

$$\ell = r_0\left[0.14 - 0.08\left(1 - \frac{r}{r_0}\right)^2 - 0.06\left(1 - \frac{r}{r_0}\right)^4\right] \tag{2b}$$

where for axisymmetric flow for constant r_0

$$r = r_0 - y$$

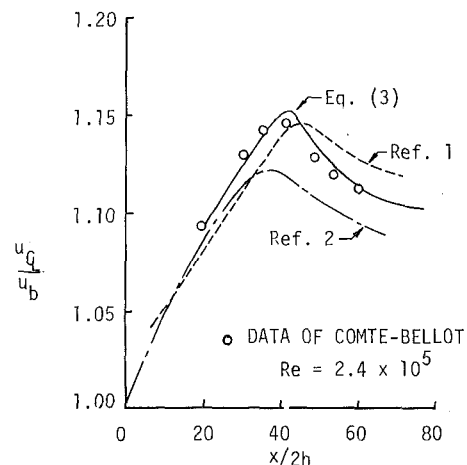so that

$$1 - \frac{r}{r_0} = \frac{y}{r_0}$$

Fig. 2   Comparison of predictions for center-line velocity

To use this for two-dimensional duct flows we simply set $r_0 = h$ to get

$$1 - \frac{r}{r_0} = \frac{y}{h} \tag{2c}$$

Either one of these can be used separately to calculate the developing duct flow using the numerical procedure described below, however, the overall agreement is poor. The solution was to model the entire flow situation based on our knowledge of the physics. A composite eddy viscosity is prescribed which changes smoothly from an external model (ϵ^{I}) to an internal model (ϵ^{III}) as follows

$$\epsilon = \epsilon^{\mathrm{I}} + (\epsilon^{\mathrm{III}} - \epsilon^{\mathrm{I}})\left[1 - \exp - \left(\frac{x - x_0}{20h}\right)\right] \tag{3}$$

where x_0 is the length down the pipe where the two "external" boundary layers merge, and the denominator giving the relaxation scale was prescribed by divine intervention.

Using this model, the "nonlinear eigenvalue" procedure of Cebeci and Keller for laminar flows [6] was used to calculate the developing duct flow. For further details and heat transfer results see reference [7]. Fig. 2 shows the experimental results of Compte-Bellot for center-line velocity decay, along with the predictions of references [1, 2], and equation (3). The composite model provides strikingly improved results. The same comparison of predicted results for the displace-

---

[2] Chief Aerodynamics Engineer, Research, Douglas Aircraft Co., Long Beach, Calif.
[3] Senior Engineer/Scientist, Douglas Aircraft Co., Long Beach, Calif.
[4] Research Associate, California State University at Long Beach, Long Beach, Calif.
[5] Numbers in brackets designate Additional References at end of discussion.
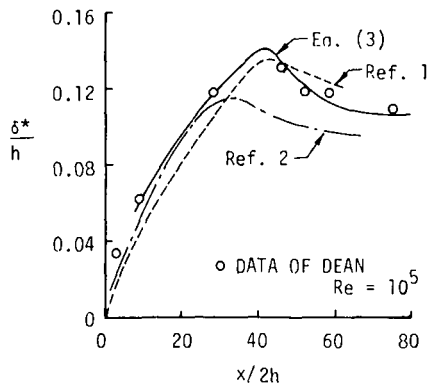
Fig. 3 Comparison of predictions for displacement thickness

ment thickness measured by Dean is shown in Fig. 3. Again, equation (3) gives the best comparison. The typical computation time, for a case using 41 points across the duct, and 35 axial stations down the duct, was less than 2 s on an IBM 370/175. Consequently, we conclude that simple models can be used to predict some complex flows by using a great deal of empiricism.

References

1 Emery, A. F., and Gessner, F. B., "The Numerical Prediction of the Turbulent Flow and Heat Transfer in the Entrance Region of a Parallel Plate Duct," JOURNAL OF HEAT TRANSFER, TRANS. ASME, Series C, Vol. 98, 1976, pp. 594–600.

2 Mujumdar, A. S., and Li, Y. K., Discussion of reference [1], JOURNAL OF HEAT TRANSFER, TRANS. ASME, Series C, Vol. 99, 1977, pp. 347–349.

3 Baldwin, B. S., and Rose, W. C., "Calculation of Shock Separated Turbulent Boundary Layers," *Aero. Analyses Requiring Adv. Comp.*, NASA SP-347, 1975, pp. 401–418.

4 Cebeci, and Bradshaw, P., *Momentum Transfer in Boundary Layers,* Hemisphere-McGraw Hill, Washington, 1977.

5 Schlichting, H., *Boundary-Layer Theory,* McGraw Hill, New York, 1960.

6 Cebeci, T., and Keller, H. B., "Flows in Ducts by Boundary-Layer Theory," Fifth Australasian Conference on Hydraulics and Fluid Mechanics, Christchurch, New Zealand, 1974.

7 Cebeci, T., and Chang, K. C., "A General Method for Calculating Momentum and Heat Transfer in Laminar and Turbulent Duct Flows," to be published in *Numerical Heat Transfer,* 1977.

Authors' Closure

The discussers have proposed a viable alternative to the length-scale model we proposed in our paper [1]. The discussers' claim that their model is "much simpler" because it is based on physical prin-

ciples is open to question. In reality, the eddy viscosity model which is proposed requires the specification of nine constants (four in equation (1) with two constants implicit in the expression for γ_{tr}, three in equation (2), and two in equation (3)). The total number of constants may, in fact, be even greater than nine if x_0 in equation (3) is not identically constant, but is allowed to vary for matching purposes with experimental data.

Although it may be argued that the constants in the discussers' model are well specified on the basis of previous experience with the expressions for ϵ^I and ϵ^{III}, the fact still remains that all of the coefficients are empirically determined quantities. Furthermore, the transition zone model given by equation (3) is not based on "our knowledge of the physics" but, instead, is simply an empirical expression which models experimentally observed behavior. Admittedly, the length-scale model we have proposed involves the specification of twelve constants, but these constants are also used in our three-dimensional length-scale model for developing flow in rectangular ducts of arbitrary aspect ratio [8]. We thus feel that our model offers more flexibility than the one proposed by the discussers, which admittedly is restricted to developing, two-dimensional duct flow.

On the basis of the comparisons shown in Figs. 2 and 3 the discussers conclude that their model gives "strikingly improved results" and "the best comparison." These statements are based, however, on unfair comparisons made in these figures. As we have carefully noted in our paper [1], our predicted distributions for $U_{CL}(x)$ and $\delta^*(x)$ are based on assumed uniform flow at the duct inlet. The corresponding experimental distributions measured by Dean [9] and Comte-Bellot [10] are not based on this condition, however, because the flow was partially developed at the inlet of their experimental configurations. With reference to Dean's results, for example, we stated that it was necessary to match initial conditions at $x/2h = 2.2$ in order to make direct comparisons with his data. If this is done then the distribution for δ^* based on our model (shown in Fig. 3 and labelled "reference [1]") will shift 3.8 duct widths upstream. The level of agreement between our results and Dean's data is then comparable to that observed between the discussers' results and the same data. Similar comments apply for the predicted and experimental profiles shown in Fig. 2. It should also be noted that the discussers' predictions are apparently based on matched initial conditions well downstream of the duct inlet, i.e., at $x/2h = 20$ (Fig. 2) and at $x/2h = 8.3$ (Fig. 3). This simple expedient will always enhance the likelihood of good agreement between predictions and data downstream of the matching location. A preferred procedure is to base comparisons on matched conditions at the first station for which data are available (e.g., at $x/2h = 2.2$ for Dean's data), and this is the approach we took in making our comparisons.

Additional References

8 Gessner, F. B., and Emery, A. F., "A Length-Scale Model for Developing Turbulent Flow in a Rectangular Duct," *Journal of Fluids Engineering,* TRANS. ASME, Series I, Vol. 99, June 1977, pp. 347–356.

9 Dean, R. B., "An Investigation of Shear Layer Interaction in Ducts and Diffusers," PhD thesis, University of London, Feb. 1974.

10 Comte-Bellot, G., "Turbulent Flow Between Two Parallel Walls," PhD thesis, University of Grenoble, France, 1963 (also available as ARC 31 609).